A Symphony on the Past: Deciphering Galaxy Formation Histories from a Composition of Stellar Tracers

Lucas Manuel Valenzuela



Munich 2026

Eine Symphonie der Vergangenheit: Entschlüsselung galaktischer Entstehungsgeschichten durch eine Komposition stellarer Tracer

Lucas Manuel Valenzuela



München 2026

A Symphony on the Past: Deciphering Galaxy Formation Histories from a Composition of Stellar Tracers

Lucas Manuel Valenzuela

Dissertation
an der Fakultät für Physik
der Ludwig-Maximilians-Universität
München

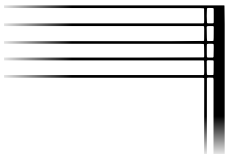
vorgelegt von
Lucas Manuel Valenzuela
aus Böblingen

München, den 2. Juni 2026

Erstgutachter: Apl. Prof. Klaus Dolag
Zweitgutachter: Prof. Rolf-Peter Kudritzki
Tag der mündlichen Prüfung: 17. Juli 2026



Zusammenfassung



In dieser Dissertation untersuche ich mithilfe kosmologischer Simulationen und Modelle, wie sich Entstehungsgeschichten heutiger Galaxien anhand dreier stellarer Tracer entschlüsseln lassen. Zunächst untersuche ich, wie die *stellare Komponente* in äußeren Haloregionen mit vergangenen Akkretionsereignissen zusammenhängt, da diese Überreste von Galaxienverschmelzungen in Form von Gezeitenstrukturen hinterlassen. Anhand einer umfassenden Erhebung von Gezeitenstrukturen zeige ich, dass radiale große Galaxienverschmelzungen zu langsam rotierenden Galaxien mit Gezeitenschalen führen, während Galaxien mit kinematisch entkoppelten Kernen und Gezeitenströmen auf eine von kleinen Verschmelzungen dominierte Akkretionsgeschichte hindeuten. Darüber hinaus zeige ich, dass die projizierten Eigenschaften von Gezeitenstrukturen nicht direkt den tatsächlichen Eigenschaften ihrer Vorläufergalaxien entsprechen und die in Simulationen vorhergesagten Bias daher berücksichtigt werden müssen.

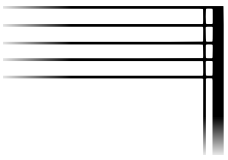
Aufgrund ihrer Nutzung als stellare Tracer in den äußeren Galaxienbereichen entwickle ich ein neuartiges Modell für *planetarische Nebel* in kosmologischen Simulationen (PICS) zur Interpretation von Beobachtungen. Mit PICS zeige ich, dass die Metallizität zentral für die Entstehung heller planetarischer Nebel in alten Sternpopulationen ist. Außerdem kann ich erstmals durch die Anwendung von PICS auf Simulationen einen Großteil des universellen hellen Endes der Leuchtkraftfunktion planetarischer Nebel über verschiedene Morphologien und mehrere Größenordnungen der Galaxienmasse erklären. Durch Vergleiche mit beobachteten planetarischen Nebeln in Galaxien frühen Typs zeige ich, dass helle planetarische Nebel mit dem Massenanteil von Sternen mittleren Alters (2–10 Milliarden Jahre) zusammenhängen und so Einblicke in die Sternentstehungsgeschichte ermöglichen.

Schließlich betrachte ich alte und dichte Sternhaufen, *Kugelsternhaufen*, als weitere Tracerpopulation zur Entschlüsselung der Galaxienentstehung. Mithilfe eines zuvor von mir entwickelten Modells zeige ich, dass die Altersverteilung von Kugelsternhaufen auf vergangene gasreiche Galaxienverschmelzungen hindeutet. Dies teste ich erfolgreich an der Milchstraße und rekonstruiere die Gaia-Sausage/Enceladus-Verschmelzung vor 10 Milliarden Jahren. Außerdem sage ich eine bimodale Altersverteilung für Gaia-Sausage/Enceladus voraus, die inzwischen durch neuere Beobachtungen bestätigt wurde. Anschließend führe ich die erste modellübergreifende Vergleichsstudie von Kugelsternhaufenmodellen durch und stelle unterschiedliche Vorhersagen ihrer Entstehungszeiten fest. Nur einige Modelle sagen voraus, dass die kürzlich beobachteten jungen Sternhaufen bei hohen Rotverschiebungen bis zu $z = 10$ potenzielle Vorläufer heutiger Kugelsternhaufen sein könnten. Dies verdeutlicht die Notwendigkeit verbesserter Kugelsternhaufenmodelle, um die Entstehung von Sternhaufen und ihre Rolle in der frühen Galaxienentstehung weiter einzugrenzen.

Zusammenfassend enthalten stellare Tracer eine Fülle an Informationen über die Entstehungsgeschichte von Galaxien. Die Kombination ihrer individuellen Hinweise ermöglicht es uns, ein umfassendes Bild der Vergangenheit von Galaxien zu gewinnen.



Abstract

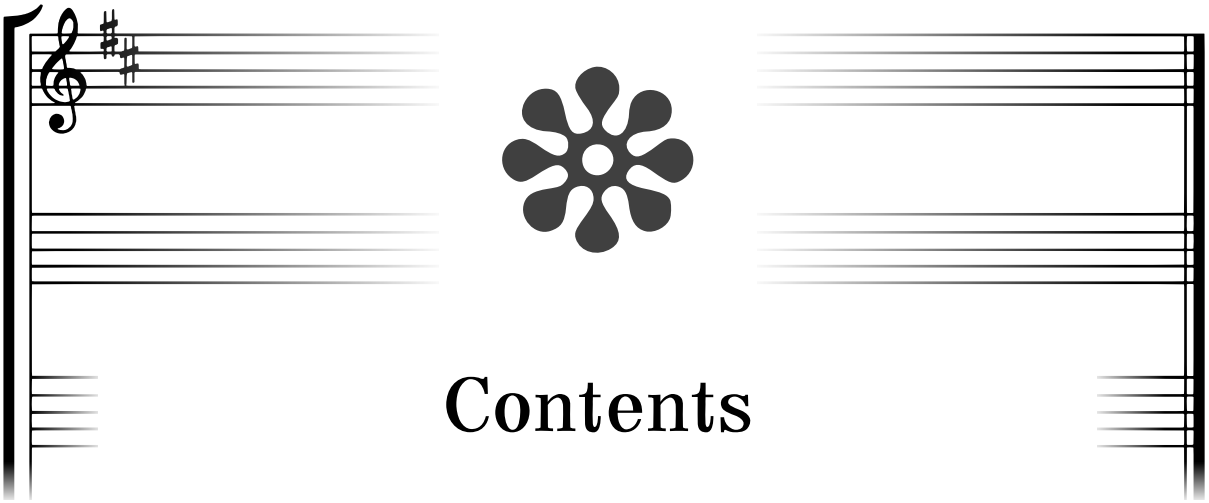


In this thesis, I explore how galaxy formation histories can be deciphered through three different stellar tracers in present-day galaxies using cosmological simulations and models. First, I investigate how the *stellar component* in the outer halo regions is related to past accretion events, which leave behind merger remnants such as tidal features. From a comprehensive tidal feature census, I find that radial major mergers lead to a correlation between slow rotation and the presence of tidal shells, whereas galaxies with kinematically distinct cores and tidal streams indicate accretion histories dominated by mini and minor mergers. Furthermore, I demonstrate that the projected properties of tidal features are not directly equivalent to the actual progenitor galaxies' properties, making it crucial to account for the biases predicted by the simulations.

As widely used stellar tracers of galaxy outskirts, I develop an entirely novel model for *planetary nebulae* in cosmological simulations (PICS) to provide a theoretical basis for interpreting the observations. Through PICS, I find that metallicity is a key ingredient for successfully producing bright planetary nebulae even in old stellar populations. Moreover, by applying PICS to simulated galaxies with cosmologically self-consistent star formation histories, I provide the first theoretical explanation for the universal bright-end cutoff of the planetary nebula luminosity function across different morphologies and several orders of magnitude in galaxy mass. Through comparisons with observed planetary nebulae in early-type galaxies, I present that bright planetary nebulae are related to the mass fraction of intermediate-age stars (2–10 Gyr old) in a galaxy and therefore provide insight into the underlying star formation history.

Finally, I consider *globular clusters*, old and dense stellar clusters and another commonly used tracer population, and their use in deciphering galaxy formation. Through a model that I previously developed, I find that the age distribution of globular clusters in a galaxy traces past gas-rich mergers, which I successfully test on the Milky Way, recovering the Gaia-Sausage/Enceladus merger 10 Gyr ago. From these data, I additionally predict a bimodal age distribution for Gaia-Sausage/Enceladus, which has in the meantime been confirmed by more recent observations. I then perform the first direct comparison of globular cluster models, focusing on their predicted formation times and finding substantial differences. With recent observations of young stellar clusters at high redshifts up to $z = 10$, only some of the models predict these to be potential progenitors of present-day globular clusters. This furthermore shows that improved globular cluster models will be necessary to better constrain cluster formation and their role in early galaxy formation.

To conclude, stellar tracers contain a wealth of information on the galaxy formation history imprinted in their present-day properties. Combining their individual clues provides us with the means to gain a comprehensive picture of the past of galaxies.



Contents

1 Introduction **1**

1.1 Structure and galaxy formation 2
1.2 The outskirts of galaxies 4
1.3 Stellar tracers of galaxy formation 6

2 Cosmological Simulations **9**

2.1 Magneticum Pathfinder simulations 10
2.2 Galaxy scaling relations through cosmic time 12
2.2.1 Galaxy sample and properties 13
2.2.2 Star-forming main sequence 14
2.2.3 Stellar mass-age relation 16
2.2.4 Stellar mass-metallicity relation 17
2.2.5 Stellar mass-size relation 18
2.2.6 Specific angular momentum relation 20
2.2.7 Resolved stellar kinematics 21

I The Stellar Component **25**

3 Introduction to the Stellar Component **27**

3.1 Stellar accretion onto galaxies 28
3.2 Satellite systems 29
3.2.1 Satellite planes 29
3.2.2 Predictions from simulations 30

3.3 Tidal features . . . 31
3.3.1 Tidal feature types . . . 32
3.3.2 Formation and evolution in simulations . . . 33
3.4 Scope of this Movement . . . 34

4 Connecting Tidal Features to Kinematics 35
4.1 Simulations and observations . . . 36
4.1.1 The Magneticum Pathfinder simulations . . . 36
4.1.2 The MATLAS sample . . . 37
4.2 Methods and definitions . . . 37
4.2.1 Tidal features: Shells, streams, and tidal arms . . . 37
4.2.2 Satellite planes . . . 39
4.2.3 Fast and slow rotators, and kinematic classes . . . 39
4.2.4 Morphological classes . . . 40
4.3 Results . . . 40
4.3.1 Feature statistics and mass, morphology, and size . . . 40
4.3.2 Correlations of tidal features and satellite planes with kinematic classes 43
4.3.3 Correlations of tidal features and satellite planes with the inner rotational support . . . 44
4.4 Conclusion . . . 48

5 Properties and Progenitors of Tidal Shells and Streams 51
5.1 Tidal feature sample . . . 53
5.2 Properties of shells and streams . . . 53
5.2.1 Spatial properties and masses . . . 53
5.2.2 Kinematics and stellar population properties . . . 57
5.3 Progenitors of shells and streams . . . 59
5.3.1 Properties of tidal feature progenitors . . . 60
5.3.2 Evolution of tidal feature spatial distributions . . . 64
5.4 Young in-situ stream-like features . . . 64
5.5 Summary and conclusion . . . 67

6 Further Studies on Tidal Features 69
6.1 Shells and inner kinematics in SAMI . . . 70
6.2 Tidal feature occurrence for simulated satellites . . . 72
6.3 Conclusion . . . 75

II Planetary Nebulae 77

7 Introduction to Planetary Nebulae 79
7.1 A phase of stellar evolution . . . 80
7.2 Planetary nebula luminosity function . . . 82

7.2.1 Bright-end cutoff of the PNLF . . . 82
7.2.2 The PNLF puzzle . . . 84
7.2.3 Faint part of the PNLF . . . 84
7.3 Planetary nebulae as stellar tracers . . . 85
7.3.1 Spatial and kinematic tracers . . . 85
7.3.2 Stellar population tracers . . . 86
7.4 Modeling planetary nebula populations . . . 86
7.5 Scope of this Movement . . . 87

8 PICS: Planetary Nebulae In Cosmological Simulations 89
8.1 Model . . . 90
8.1.1 Single stellar population properties . . . 91
8.1.2 Stellar lifetime function . . . 91
8.1.3 Initial-to-final mass relation . . . 94
8.1.4 Post-AGB stellar evolution tracks . . . 96
8.1.5 Planetary nebula model . . . 96
8.1.6 Circumnebular extinction . . . 100
8.1.7 Number of planetary nebulae . . . 102
8.2 The effect of metallicity and helium abundances . . . 102
8.2.1 Metallicity . . . 102
8.2.2 Helium abundance . . . 104
8.3 Single stellar population PNLFs . . . 106
8.3.1 PNLFs with nebular metallicity correction . . . 106
8.3.2 PNLFs with circumnebular extinction . . . 109
8.3.3 PNLFs with different IFMRs . . . 111
8.3.4 Normalized PNLFs . . . 114
8.4 Summary and conclusion . . . 118

9 The PNLF from Realistic Stellar Populations 123
9.1 PICS model . . . 124
9.2 Application to a cosmological simulation . . . 125
9.2.1 The importance of metallicity . . . 125
9.2.2 Normalization and shape of the PNLF . . . 127
9.3 Summary and conclusion . . . 128

10 Circumnebular Extinction Around Planetary Nebulae 131
10.1 Method . . . 132
10.1.1 PICS model . . . 132
10.1.2 Circumnebular extinction variations . . . 133
10.2 Results . . . 135
10.2.1 Extinction of Hβ . . . 135
10.2.2 Extinction effects on the PNLF . . . 137

10.2.3 Extinctions of de-reddened PNe . . . 137
10.3 Discussion . . . 140

11 Solving the Mystery of the PNLF Cutoff 143
11.1 Methods . . . 144
11.1.1 PN properties from the PICS model . . . 144
11.1.2 PNLF fitting . . . 144
11.1.3 Cosmological simulation . . . 145
11.2 PNe reaching the bright end . . . 145
11.3 The universal bright end of the PNLF . . . 149
11.4 Discussion and conclusion . . . 151

12 The PNLF in Cosmological Simulations 153
12.1 Methods . . . 155
12.1.1 PICS model for planetary nebulae . . . 155
12.1.2 Planetary nebula luminosity function fitting . . . 155
12.1.3 Cosmological simulations . . . 157
12.1.4 Galaxy sample and classifications . . . 158
12.2 PNLFs of the galaxy classes . . . 160
12.2.1 PNLF variations among simulations . . . 161
12.2.2 PNLF variations in the inner and outer regions . . . 166
12.2.3 PNLF bright-end cutoff magnitude . . . 168
12.3 Conclusion . . . 171

13 Stream Photometry Combined with PN Kinematics 173
13.1 Simulation and model . . . 174
13.1.1 Magneticum Pathfinder simulation . . . 174
13.1.2 Tidal feature census . . . 175
13.1.3 The PICS model . . . 175
13.2 Tracing tidal stream dynamics . . . 176
13.2.1 Dynamical decomposition of the stellar component . . . 177
13.2.2 Planetary nebulae as kinematic tracers for tidal features . . . 177
13.3 Summary and conclusion . . . 178

14 Planetary Nebulae as Stellar Population Tracers 181
14.1 Observed ETGs and their simulated analogs . . . 183
14.1.1 Observational data . . . 183
14.1.2 Simulated analog galaxies . . . 185
14.2 Comparison to simulated analog galaxies . . . 186
14.2.1 Stellar populations and the PNLF bright-end cutoff . . . 187
14.2.2 Stellar populations and the luminosity-specific PN number . . . 190
14.3 Observations of M 105 . . . 192

14.4 Comparison to PNe modeled in single stellar populations 194
14.4.1 Stellar populations and the PNLF bright-end cutoff 194
14.4.2 Stellar populations and the luminosity-specific PN number 194
14.5 Summary and conclusion 197

III Globular Clusters 201

15 Introduction to Globular Clusters 203
15.1 A type of star cluster 204
15.2 Globular cluster systems 206
15.2.1 Color bimodality 206
15.2.2 Extragalactic globular clusters 207
15.2.3 Galactic globular clusters 208
15.3 Globular clusters as stellar tracers 208
15.3.1 Spatial and kinematic tracers 209
15.3.2 Tracers of past star formation 210
15.4 Modeling globular cluster populations 210
15.5 Scope of this Movement 212

16 Globular Clusters as Dark Matter Tracers 213
16.1 Globular cluster model 214
16.2 Smooth accretion 216
16.3 Conclusion 216

17 Tracing Wet Mergers Through GC Ages 219
17.1 Data & method 221
17.1.1 Globular cluster model 221
17.1.2 Globular cluster observational data 223
17.2 Age dating wet mergers with GCs in the Milky Way 226
17.2.1 GC age distribution observations in the Milky Way 226
17.2.2 Model predictions 227
17.3 Discussion: GCs in the Milky Way 230
17.3.1 Milky Way diagnostics 230
17.3.2 Model diagnostics 233
17.4 Discussion: Extension to nearby galaxies 234
17.5 Conclusion 239

18 High-Redshift Stellar Clusters in GC Models 241
18.1 Data 242
18.1.1 Observations 243
18.1.2 Stellar particle tracer model 244
18.1.3 E-MOSAICS model 244

18.1.4 EMP-Pathfinder model . . . 245
18.1.5 Rapid mass growth model . . . 246
18.1.6 Two-phase model . . . 246
18.1.7 Dual formation pathway model . . . 247
18.1.8 Other models . . . 248
18.2 GC age distributions for MW-like galaxies . . . 248
18.2.1 Modelled GC age distributions . . . 249
18.2.2 Differences between the models . . . 251
18.2.3 Empirical and subgrid GC models . . . 252
18.3 GC age distributions for other MW-mass galaxies . . . 254
18.4 Predictions for high-redshift clusters . . . 257
18.5 Conclusion . . . 260

19 Globular Clusters as Dynamical Tracers 263
19.1 Dynamically modeling the halo of Centaurus A . . . 264
19.2 Comparison with simulations . . . 266
19.3 Conclusion . . . 267

20 Summary & Conclusion 269
20.1 Results from the stellar component . . . 269
20.2 Results from planetary nebulae . . . 270
20.3 Results from globular clusters . . . 272
20.4 A symphony on the past . . . 273

A Rescaling the Cumulative Distribution 275

B Tidal Feature Compilation 277
B.1 Overview of the extracted tidal shells and streams . . . 277
B.2 Potential trigger for an in-situ stream-like feature . . . 277

C Tidal features in projected phase space 281

D PICS Model Details 283
D.1 Post-AGB track interpolation . . . 283
D.2 Nebular model recipes . . . 284
D.2.1 Intensity ratio recipe . . . 284
D.2.2 Absorption factor recipe . . . 284
D.3 Nebular metallicity . . . 286
D.4 Circumnebular extinction . . . 286
D.5 Luminosity-specific bright PN numbers . . . 286
D.6 Extended PNLFs . . . 288

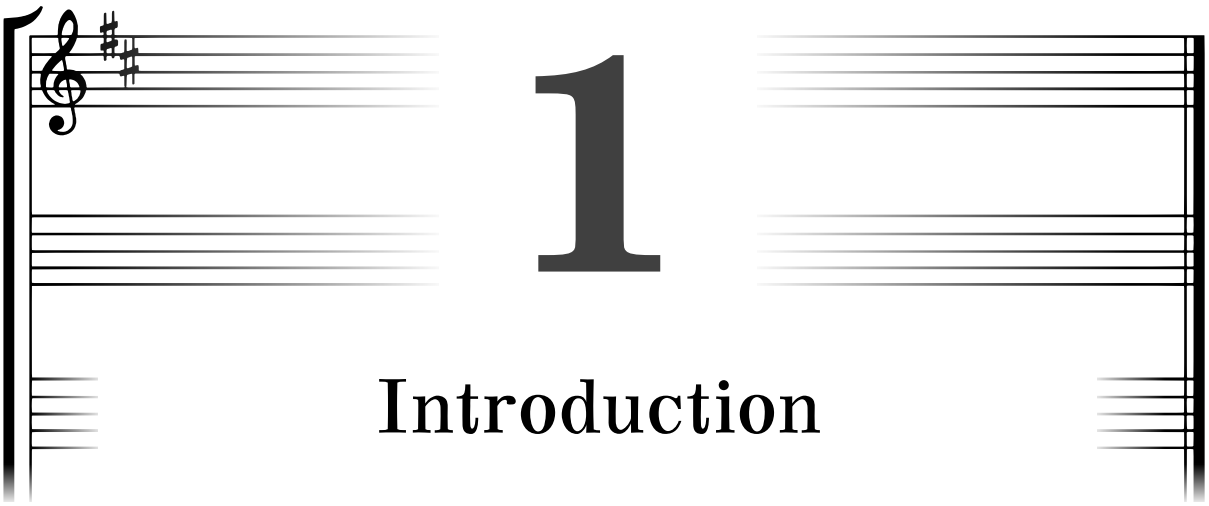
E PNe at the Bright End of the PNLF **291**
E.1 Maximal metal-poor PN [O III] magnitude evolution 291
E.2 PNLF bright end in Box4 at $z = 0$ 292
E.3 Stellar populations and bright-end cutoff in TNG50 293

F PNLFs of Simulated Galaxy Classes **297**
F.1 Maximum likelihood estimation of the PNLF 297
F.2 Corrected ages in Magneticum Box4 (uhr) for $z = 0$ 298
F.3 Central galaxies in Magneticum Box4 (uhr) 298
F.4 PNLF bright-end cutoff magnitudes in TNG50 298

G The Milky Way GC Age Distribution **303**
G.1 Milky Way globular cluster age distributions 303
G.1.1 Age distributions of all globular clusters 303
G.1.2 Alternative progenitor associations 305
G.1.3 Age distributions of a single study 305
G.1.4 Age histograms 306
G.2 Other Milky Way-mass modeled globular cluster age distributions 306

H GC Model Age Comparisons **311**
H.1 Globular cluster formation time distributions of other models 311
H.2 Ages including young GCs 312

References **315**



1 Introduction

Astronomy in the last century has taken an enormous leap forward thanks to the increasingly powerful telescopes available. In this time, observations of the night sky have let us move from the idea that the Universe only consists of our own Galaxy, the Milky Way, to the concept of an ever-expanding Universe containing over a trillion galaxies[1]. These advances have been accompanied by improving computational capabilities, enabling simulations of the non-linear processes that govern structure formation and evolution (e.g., White & Rees 1978; Vogelsberger et al. 2020). Such simulations cover the full range of astrophysical processes, from the formation of structure on the largest scales and the diverse population of galaxies found therein, all the way down to the formation of stars from intergalactic gaseous clouds, as it also happened for our very own Sun. The predictions from these simulations have been essential for interpreting the observational results and the underlying physical processes, which generally occur on timescales of billions of years and are thus far too long to probe observationally. On the observational side, galaxy surveys have studied a plethora of galaxies, which have demonstrated an astounding diversity of properties. Their morphologies as spiral, elliptical, or irregular galaxies have been classified through a sequence (Hubble 1926, 1936; Sandage 1961), their colors have been established to show a clear bimodality (Strateva et al. 2001; Bell et al. 2004), some galaxies are actively in the process of forming stars from their gas, whereas others are not (e.g., Kauffmann et al. 2004; Pearson et al. 2018; Popesso et al. 2023), their masses and luminosities range across many orders of magnitude from ultra-faint dwarfs up to massive elliptical galaxies (White & Frenk 1991), and their kinematics have been found to show a surprising variety of behaviors (e.g., Emsellem et al. 2007; Krajnović et al. 2011).

[1]The number of galaxies in the Universe up to redshift $z = 8$ is estimated as 2×10^{12} (Conselice et al. 2016).

This diversity in properties must be related to the individual galaxy formation histories that give rise to the characteristics seen in present-day galaxies. While we cannot turn back time for the observed galaxies, the components that carry these characteristics nevertheless retain traces of former times, as though singing a song of their past. As these components reveal distinct aspects of galaxy formation, together they form a larger narrative. In essence, their composition becomes a symphony. It is for this reason that this thesis carries the title *A Symphony on the Past*. With the aim of deciphering galaxy formation histories through simulations and models, this thesis considers three different stellar tracers and investigates what they reveal about the past. It is therefore structured in three Movements[2], one devoted to each stellar tracer: the stellar component (in the form of stellar structures in the galaxy outskirts; Movement I), planetary nebulae (a stage of late stellar evolution; Movement II), and globular clusters (dense and old star clusters; Movement III).

Each stellar tracer is introduced in an opening chapter of the respective Movement. The subsequent chapters then present the relevant studies that I have authored or co-authored during the work on my thesis, each introducing their individual context and science case at the beginning. Most of these studies have already been published in or submitted to astrophysical journals, comprising the works by Valenzuela (2023), Valenzuela & Remus (2024), Valenzuela et al. (2024b, 2025a,b,c,d, 2026), Stoiber, Valenzuela et al. (2025, 2026), Soemitro, Valenzuela et al. (2025), Rutherford et al. (2024), Veršič et al. (2024a), and Khalid et al. (2025). Additionally, the current status is presented of three further studies that are still in preparation, namely Valenzuela et al. (in prep. a,b) and Hartke, Ennis, Valenzuela et al. (in prep.). For the studies that I have published as first author, I have generally only adapted the introduction to integrate well within the respective Movement. For the studies that I have co-authored, I state my contributions at the beginning of the chapter and place the results within the context of this thesis. The main results of this thesis are finally summarized and concluded in Chapter 20.

Since several parts of this thesis make use of a cosmological simulation from the Magneticum Pathfinder simulation suite, I introduce this suite in Chapter 2. Having contributed significantly to the *Encyclopedia Magneticum* by Dolag, Remus, Valenzuela et al. (2025), I furthermore give an overview of the simulated galaxy scaling relations relevant to this thesis and how they compare to observations. Finally, the purpose of this first introduction chapter is to set the scene for the three Movements, giving a brief overview of the overarching processes that drive galaxy formation and motivating how stellar tracers may be useful to decipher galaxy formation histories.

1.1 Structure and galaxy formation

A central discovery for our understanding of structure formation has been the measurement of the cosmic microwave background (CMB; Penzias & Wilson 1965; Smoot et al. 1992;

[2]While the four-movement symphony became standard in the Classical period, earlier symphonies were often written in three movements, as seen in early works by Haydn and Mozart.

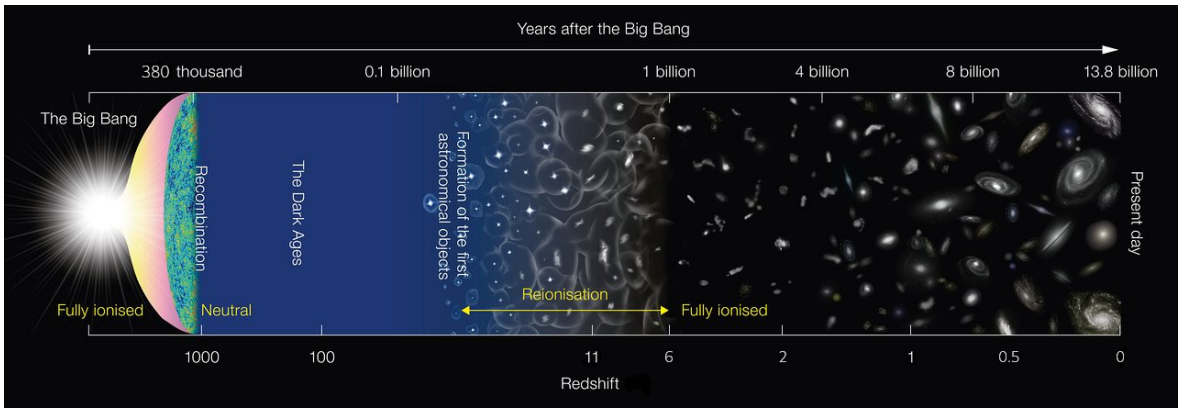


Figure 1.1: Overview of the central processes across cosmic time. The fully ionized Universe after the Big Bang becomes neutral after recombination, 380 000 yr later (at $z \approx 1100$). The time before the first astronomical objects are formed is referred to as the *Dark Ages*. Through the formation of stars, galaxies, and quasars, the UV radiation led to the reionization of the Universe, which took place until about 1 Gyr after the Big Bang ($z \approx 6$). Over the course of the following ~13 Gyr, galaxy formation continued with increasing cosmic star formation rate with a peak at $z \approx 2$ (age of the Universe of 3.3 Gyr), after which it has declined up to the present day ($z = 0$). *Image credit: NAOJ*[3]. *Modified to state the more accurate recombination time and adapted the redshift axis.*

Planck Collaboration 2020) radiation, which has a blackbody temperature of 2.725 K across the whole sky and exhibits fluctuations on the order of only 10^{-5}. It originates from the epoch of recombination of electrons and protons, which allowed photons to decouple from the baryons and to become observable to us already a mere 380 000 yr after the Big Bang (~13.8 Gyr ago). Figure 1.1 visualizes the evolution of the Universe over cosmic time, where the epoch of recombination can be seen as one of the first events in the timeline. The CMB fluctuations have provided us with a view of the early density perturbations that grow and collapse into the large-scale structure of the Universe, forming the cosmic web and dark matter (DM) halos, within which galaxies can form. In the following, this process is briefly outlined. Note that it is not intended to be exhaustive, for a more detailed overview of structure and galaxy formation, see for example Padmanabhan (1993) and Mo et al. (2010).

In the ΛCDM model of cosmology, where DM is assumed to be cold (the C in CDM) and interacts only gravitationally, the density perturbations initially grow linearly as the Universe expands (Zel'dovich 1970). When an overdensity reaches a critical density threshold, it collapses into a gravitationally bound structure, a DM halo (Gunn & Gott 1972). These halos grow hierarchically through mergers and form increasingly massive structures in a self-similar manner (Press & Schechter 1974; Blumenthal et al. 1984), thereby building up the cosmic web of nodes, filaments, and sheets. During this build-up, the DM halos gain angular momentum through tidal torques from the surrounding matter distribution (Peebles 1969; Doroshkevich 1970; Vitvitska et al. 2002). Simultaneously, the DM halos provide a gravitational potential into which baryonic matter can condense (White & Rees 1978), initially in the form of pristine gas, mostly composed of hydrogen and helium. As the gas cools, it falls to the center of the halo while redistributing its angular momentum and can form a disk (Mestel 1963; Fall & Efstathiou 1980). In the cool and dense gas, the first stars were born,

[3]https://www.eso.org/public/images/eso1620a/

referred to as *Population III* stars. Their formation details and properties are still a matter of current investigation, where current models suggest they form at redshifts of $z \approx 15$–30 (e.g., Klessen & Glover 2023, and see the formation of the first astronomical objects in Figure 1.1). Their feedback through stellar winds and supernovae chemically enriches the surrounding gas, giving rise to *Population II* stars, which are observable today as old and metal-poor stars.

Over cosmic time, these islands of stars, which we call *galaxies*, grow and evolve through accretion and star formation. The James Webb Space Telescope (JWST) has recently provided a much more detailed view of galaxies in the early Universe up to redshifts of $z = 14$ (∼300 Myr after the Big Bang; Carniani et al. 2024), revealing the rapid formation of compact and intensely star-forming galaxies (e.g., Matthee 2025). The high-redshift galaxies at $z \gtrsim 5$ have been found to exhibit star formation histories dominated by starbursts (e.g., Asada et al. 2024; Dressler et al. 2024). At the same time, JWST has revealed numerous unexpectedly massive and evolved galaxies that are already quiescent (i.e., have ceased forming stars, implying rapid early stellar mass assembly and efficient quenching) at redshifts of $z \sim 3$–7 (e.g., de Graaff et al. 2025; Kakimoto et al. 2024; Weibel et al. 2025; Kawinwanichakij et al. 2026). This occurs alongside the global rise of the cosmic star formation rate (SFR) density, which peaks at $z \approx 2$ (∼10.5 Gyr ago; Madau & Dickinson 2014). Since then it has decreased again, leading to an increased number of quiescent galaxies (Brammer et al. 2011).

Disk galaxies are commonly understood to form through the cooling of gas into rotationally supported structures and were historically classified as late-type galaxies (LTGs). Observations have shown that they are generally blue and star-forming. In contrast, elliptical early-type galaxies (ETGs) have been found to arise from galaxy mergers (e.g., Toomre 1977; White & Rees 1978; Gerhard 1981; Burkert & Naab 2003) and tend to be red and quiescent. It was also observed that galaxies are larger in size at later times for a fixed mass or luminosity, which is particularly the case for elliptical galaxies (e.g., Daddi et al. 2005; van der Wel et al. 2014). In this setting, the picture of a two-phase galaxy formation scenario has been established (Oser et al. 2010), where galaxies formed their *in-situ* stars rapidly through gas accretion and gas-rich mergers before $z \sim 2$ (e.g., Dekel et al. 2009), followed by a phase of growth through gas-poor minor mergers, bringing in accreted *ex-situ* stars. While these general descriptions of galaxy formation help explain trends found in the overall galaxy populations (see Chapter 2 for a selection of galaxy scaling relations across cosmic time), the details for individual galaxies will vary, giving rise to the large diversity of galaxies seen today (right end of the timeline in Figure 1.1).

1.2 The outskirts of galaxies

While the central regions of galaxies are bright and therefore easier to observe, they occupy only a small fraction of their host DM halos. They are also characterized by short dynamical timescales due to the higher central densities and smaller characteristic radii, leading to efficient phase-mixing that erases signatures of past events. On the other hand, the outskirts of galaxies encompass a much larger volume and evolve on much longer timescales. As a result,



Figure 1.2: Example galaxy (NGC 3923) and its outskirts imaged by the Dark Energy Camera. Symmetrical tidal shells are seen in the inner outskirts, whereas asymmetric structures in the halo can be seen in the further outskirts and indicate a more complex accretion history. This system has a large number of shells (up to 42, Bílek et al. 2016). *Image credit: DESI Legacy Imaging Surveys/LBNL/DOE & KPNO/CTIO/NOIRLab/NSF/AURA. Image processing: T.A. Rector (University of Alaska Anchorage/NSF NOIRLab), M. Zamani (NSF NOIRLab), R. Colombari (NSF NOIRLab) & D. de Martin (NSF NOIRLab). This is a cutout of the original image*[4].

structures in these outer regions are retained over longer periods of time, thereby providing a deeper window into the past. The outskirts are not only where lower-mass satellite galaxies reside, which are expected to merge with the central galaxy, but also where accreted structures deposit much of their material after having been disrupted by tidal forces (e.g., Bullock & Johnston 2005; Amorisco 2015). During the process of accretion, such structures can be observed either as still intact satellite galaxies or tidal features (e.g., Johnston et al. 2008; Karademir et al. 2019). Over time, a diffuse stellar halo is built up that for more massive galaxies is dominated by accreted stars (e.g., Cooper et al. 2013; Remus & Forbes 2022). From their spatial properties and dynamics, both the underlying DM potential and the imprint of past accretion events can be probed. Figure 1.2 shows deep imaging of an example galaxy with a prominent shell system in its outskirts, where the more distant outskirts furthermore reveal asymmetric structures, indicative of a more complex assembly history.

One major challenge of studying the outskirts of galaxies has been their low surface brightness (LSB). This requires deep imaging through long exposure times, which limited early studies to small samples of galaxies and shallower surface brightness limits (e.g., Malin & Carter 1983; Mihos et al. 2005). As observational facilities have become more powerful, larger galaxy samples and deeper imaging have become possible (e.g., Tal et al. 2009; Bílek et al. 2020; Martínez-Delgado et al. 2023a). With the recent and upcoming launches of the

[4]https://noirlab.edu/public/images/noirlab2325a/

Euclid mission and the Nancy Grace Roman Space Telescope, as well as the recent first light of the Vera C. Rubin Observatory, the near future promises LSB measurements in unprecedented abundance and depth. To fully exploit this wealth of incoming data, theoretical predictions and diagnostic methods for interpreting LSB structures and their formation are essential, which I address in Movement I.

1.3 Stellar tracers of galaxy formation

As the diffuse stellar component in the outskirts of galaxies has been challenging to observe, tracer populations are commonly used: individual bright objects that trace the outer spatial distribution and kinematics. To this end, the two tracer populations typically used in the outer regions are planetary nebulae (PNe; e.g., Hui et al. 1993) and globular clusters (GCs; e.g., Peng et al. 2004a). With their exceptionally bright [O III] emission line, PNe have long been detected through narrow-band imaging in extragalactic systems. As a late phase of stellar evolution, they trace the underlying diffuse stellar halo. An example of PNe tracing the stellar outskirts of a simulated galaxy through their spatial and kinematic properties is seen in Figure 1.3, where the overplotted PNe in the left panel (blackberry points) indicate the shape of the diffuse stellar halo. In the right panel, the PN kinematics in the outskirts reveal how the stellar halo is in fact counter-rotating to the inner galaxy, indicating a more complex assembly history. This example further underlines the potential of cosmological simulations and models to provide a theoretical basis for interpreting observations of galaxy outskirts through simulated analogs and the possibility of tracing back formation histories through time.

The details of the PN luminosity function have moreover been found to vary between galaxies with different formation histories, suggesting that they can be used to trace the underlying stellar populations. With recent advances in measuring PNe as well as the underlying stellar populations with integral field units (IFU) like MUSE (e.g., Kreckel et al. 2017; Roth et al. 2021), this has become a growing field of research. However, the theoretical understanding for the observed properties of PNe is still limited (e.g., Ciardullo 2022). To this end, I investigate this tracer population through models and simulations in Movement II.

As massive and dense star clusters, GCs are intrinsically bright and can thus be observed in the far outer regions of extragalactic systems. In general, GCs have been found to be old ($\gtrsim$10 Gyr) and have therefore co-evolved with their host galaxies over most of cosmic time. While their formation details are still a matter of research (e.g., Kruijssen 2026), the observed color bimodality of red and blue GCs is commonly interpreted as reflecting different formation pathways, representing the in-situ and accreted subpopulations, respectively (e.g., Forbes et al. 2018a). Given the differences observed between GC and PN populations in the outskirts of galaxies (e.g., Coccato et al. 2013), studying GC populations is complementary to that of PNe in what they can reveal about a galaxy's formation. Furthermore, measuring the stellar populations of GCs can reveal details about their origins. With recent JWST observations of young stellar clusters at high redshifts up to $z \sim 10$ (e.g., Adamo et al. 2024), the question has been raised whether these could be the progenitors of today's GCs. To address these

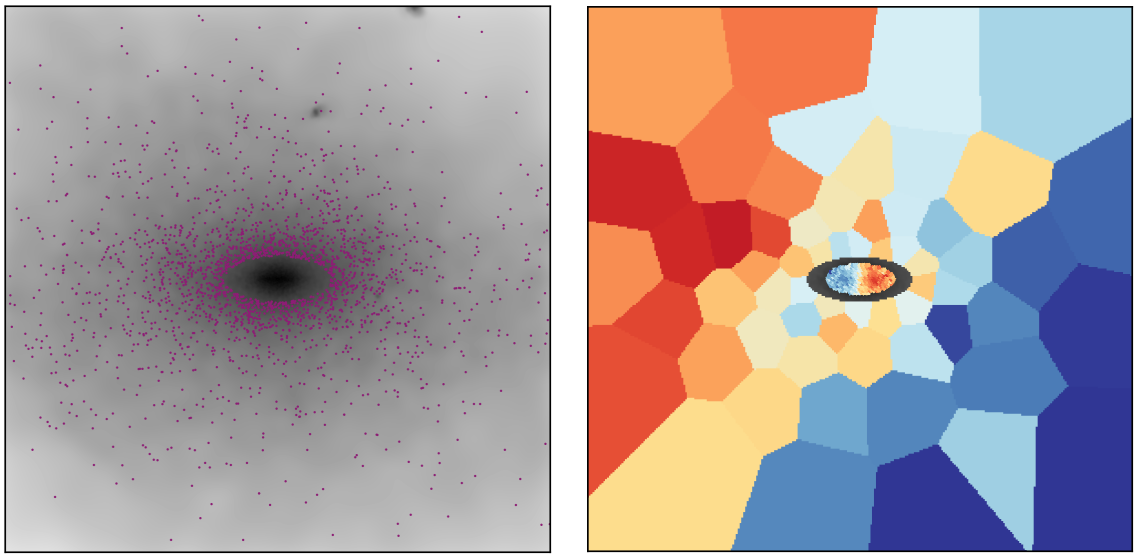


Figure 1.3: *Left*: Mock r-band image of a galaxy from the Magneticum Box4 (uhr) simulation (see Chapter 2) out to the outskirts. Its PN population (modeled with PICS, see Chapter 8) is overplotted in the outer regions (blackberry points). These are useful spatial tracers for the shape of the stellar halo. *Right*: Line-of-sight velocity map of the inner galaxy based on its stellar component (inner elliptical map) and of the outer regions based on the PN population seen on the left (outer map). The maps were created using the Voronoi tessellation method by Cappellari & Copin (2003). Dark red and dark blue represent line-of-sight velocities of $\pm 150\,\mathrm{km\,s^{-1}}$. The PNe are effective tracers of the outer kinematics of the stellar halo, which for this example galaxy is counter-rotating to the inner galaxy.

questions, I finally investigate this second tracer population through models and simulations in Movement III.

2

Cosmological Simulations

This chapter summarizes parts of the work accepted for publication in A&A
by Dolag, Remus, Valenzuela et al. (2025),
for which I created the data pipeline & catalogs and led the analysis efforts:
Encyclopedia Magneticum: Scaling Relations from Cosmic Dawn to Present Day

While observations are our primary means of accessing our Universe, we can only observe structures such as galaxies from a certain projection and at a specific moment in time. To unveil the physical processes and evolution that led up to the observed structures, other approaches have to be taken. Simulations have proven to be an effective tool to study how the complex interactions of matter and different physical processes affect the resulting structures. Early simulations of galaxies showed bars forming in isolated disk galaxies (Hohl 1971) and revealed how elliptical galaxies form from mergers (Toomre 1977), while first cosmological simulations displayed the evolution of large-scale structure across cosmic time (Davis et al. 1985). As computational capabilities have exponentially expanded, today's state-of-the-art cosmological simulations are able to resolve galaxies in large-scale volumes, simulate the gas hydrodynamics and star formation, and beyond that model a plethora of physical processes relevant to the evolution of galaxies and large-scale structure (also see the reviews by Vogelsberger et al. 2020; Valentini & Dolag 2025). Such simulations have been crucial in comparing to and interpreting the results of observational surveys of galaxies at different redshifts (e.g., SDSS, York et al. 2000; COSMOS, Scoville et al. 2007; MaNGA, Bundy et al. 2015). Some of the most prominent hydrodynamical cosmological simulations targeting galaxy formation

include Magneticum Pathfinder (Biffi et al. 2013; Hirschmann et al. 2014; Dolag et al. 2025), HorizonAGN (Dubois et al. 2014), Illustris (Vogelsberger et al. 2014), EAGLE (Schaye et al. 2015), IllustrisTNG (Nelson et al. 2018), and COLIBRE (Schaye et al. 2026).

Several parts of this thesis rely on the use of cosmological simulations to analyze simulated galaxies with realistic assembly and star formation histories in the cosmological context. The simulation that is mainly used here is Magneticum Box4 (uhr) from the Magneticum Pathfinder simulation suite (Teklu et al. 2015; Dolag et al. 2025). For this reason, this chapter provides an overview of Magneticum Pathfinder (Section 2.1) and characterizes the galaxies found therein through a variety of scaling relations (Section 2.2). The scaling relations presented here are chosen because of their relevance to the analyses in the subsequent chapters. Note that since the individual studies compiled in this thesis address different science cases, the respective chapters specify how the galaxy sample was selected for the objective at hand.

2.1 Magneticum Pathfinder simulations

The Magneticum Pathfinder simulation suite[1] (Dolag et al. 2025) is a set of hydrodynamical cosmological simulations ranging from large-scale volumes for galaxy cluster and cosmology studies to smaller high-resolution volumes targeting galaxy formation. The large-scale structures found in the simulations Box0, Box1a, Box2b, Box2, Box3, and Box4 at present-day redshift $z = 0$ are shown in the top panels of Figure 2.1, additionally highlighting exemplary zoomed regions of a galaxy cluster (bottom left and center) and two galaxies (bottom right). All simulations were run with a modified version of GADGET-2 (Springel 2005) with improvements on the smoothed particle hydrodynamics (SPH) treatment (Dolag et al. 2004, 2005; Donnert et al. 2013), active galactic nuclei (AGN) feedback (Fabjan et al. 2010; Hirschmann et al. 2014), stellar formation (Tornatore et al. 2004; Tornatore et al. 2007), and metal enrichment through stellar feedback (Wiersma et al. 2009), among others. The adopted ΛCDM cosmology is based on the seven-year results of WMAP (Komatsu et al. 2011), with $h = 0.704$, $\Omega_\Lambda = 0.728$, $\Omega_m = 0.272$, $\Omega_b = 0.0456$, $\sigma_8 = 0.809$, and $n_s = 0.963$. Because of the large differences in simulation volumes, the resolutions differ across runs, where the flagship runs of Box0 and Box1a are at medium resolution (mr), Box2b and Box2 at high resolution (hr), and Box3 and Box4 at ultra-high resolution (uhr; though Box3 was only run until $z = 1.9$ at this resolution). The particle masses and gravitational softening at the different resolutions are listed in Table 2.1. The box side lengths and initial particle numbers of the simulations are listed in Table 2.2.

Galaxies are identified using the subhalo finder SUBFIND (Springel et al. 2001; Dolag et al. 2009). It identifies halos through a friends-of-friends algorithm and detects substructures based on the density field, which are called subhalos and correspond to the individual galaxies. We refer to the most massive subhalo in a given halo as the *main* or *central* galaxy, and to the others as satellite galaxies. In the following analysis of galaxy scaling relations, we focus on a

[1] www.magneticum.org

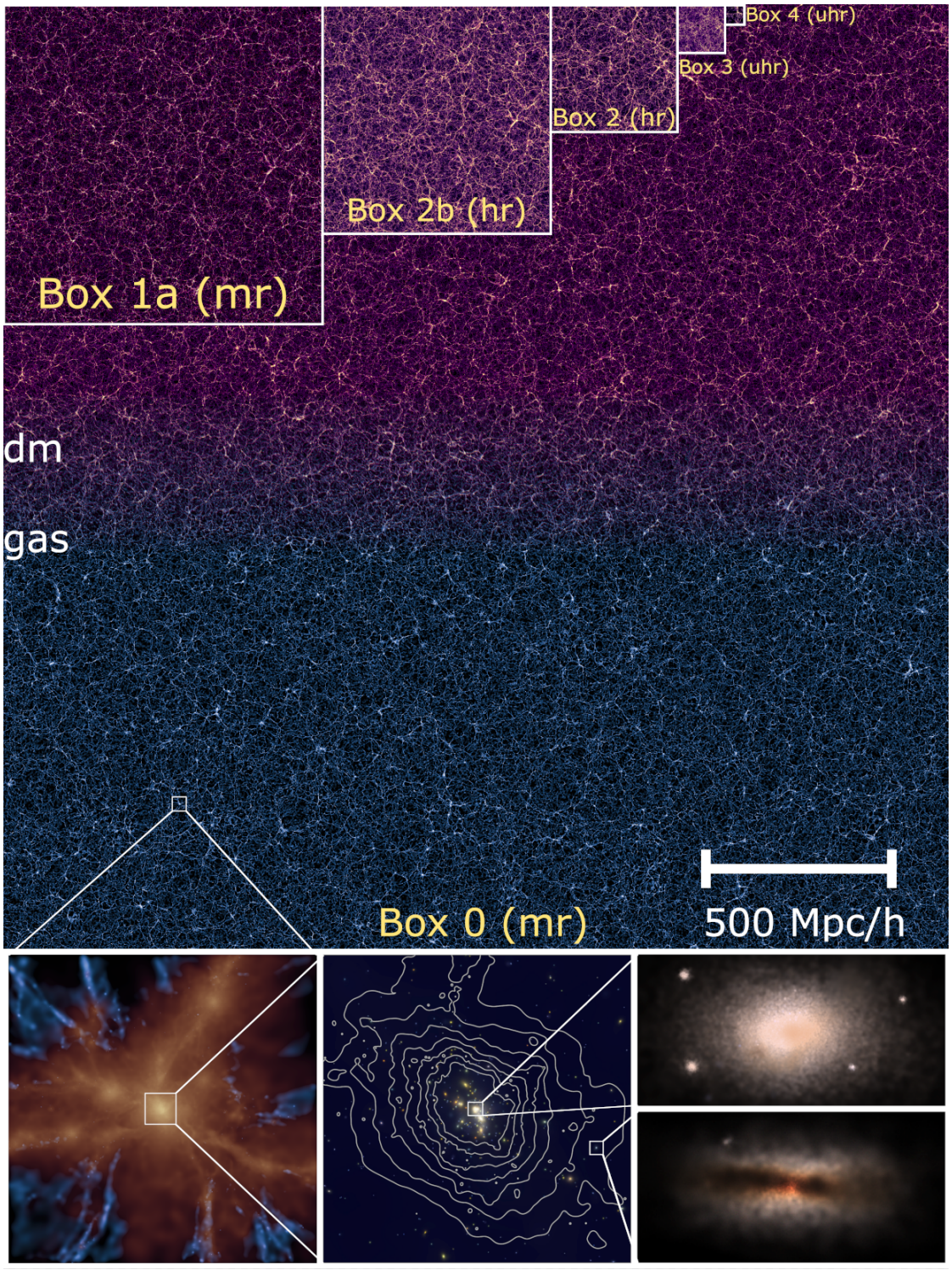


Figure 2.1: Visualization of the Magneticum Pathfinder simulations and exemplary zoomed regions of a galaxy cluster and two galaxies at $z = 0$. *Top*: Gas (blue) and DM (purple) surface density maps of the large-scale structure contained in the simulations. The simulation sizes are to scale (scale indicated at the bottom right of Box0). The name of the simulation and its resolution are stated in each subpanel (mr: medium resolution; hr: high resolution; uhr: ultra-high resolution). *Bottom left*: Gas surface density map of a massive galaxy cluster from Box2 (hr), displaying the hot (red-yellow) and cold (blue) gas. *Bottom center*: Stellar visualization with overlayed gas surface density contours for a zoomed region of the same galaxy cluster from Box2 (hr), with the stellar visualization created with Splotch (Dolag et al. 2008). *Bottom right*: Mock images of an elliptical galaxy (top) and an edge-on disk galaxy (bottom) from Box4 (uhr), created with `Skirt` (Baes et al. 2011; Camps & Baes 2020). *This is figure 1 from Dolag et al. (2025).*

Table 2.1: Gravitational softening ϵ and particle masses m corresponding to the simulation resolutions. The gas particle mass $m_{\rm gas}$ given here is only their initial mass as they can form up to four stellar particles over time, thereby losing mass, or gain mass through stellar feedback. The stellar particle mass m_* is stated here as a quarter of the gas particle mass, though in practice their masses also vary. The resolutions are colored in the same colors as used in the figures of Section 2.2. *This is part of table 2 from Dolag et al. (2025).*

	$\epsilon_{\rm gas/DM}$ $[h^{-1}{\rm kpc}]$	ϵ_* $[h^{-1}{\rm kpc}]$	$m_{\rm DM}$ $[h^{-1}M_\odot]$	$m_{\rm gas}$ $[h^{-1}M_\odot]$	m_* $[h^{-1}M_\odot]$
mr	10	5	1.3×10^{10}	2.6×10^{9}	6.5×10^{8}
hr	3.75	2	6.9×10^{8}	1.4×10^{8}	3.5×10^{7}
uhr	1.4	0.7	3.6×10^{7}	7.3×10^{6}	1.8×10^{6}

Table 2.2: Simulation side lengths and initial number of DM and gas particles $N_{\rm DM/gas}$ (i.e., the total initial number of particles is twice the value given here). The simulation names are colored in the same colors as used in the figures of Section 2.2. *The data is taken from table 1 of Dolag et al. (2025).*

Simulation	side length [Mpc]	$N_{\rm DM/gas}$
Box0 (mr)	3820	4536^3
Box1a (mr)	1300	1512^3
Box2b (hr)	910	2880^3
Box2 (hr)	500	1564^3
Box3 (uhr)	180	1536^3
Box4 (uhr)	68	576^3

subselection of the simulations, namely Box0 (mr), Box2b (hr), Box2 (hr), Box3 (uhr; only until $z = 1.9$), and Box4 (uhr).

2.2 Galaxy scaling relations through cosmic time

Galaxy scaling relations describe correlations between fundamental galaxy properties, such as mass, luminosity, size, kinematics, or star formation rate. These relations reveal the interdependence of different properties and reflect underlying physical processes governing galaxy formation and evolution (e.g., D'Onofrio et al. 2021). They additionally serve as crucial constraints for cosmological simulations of galaxy formation and provide insight into the key mechanisms that shape the observed galaxy population. We derived multiple properties of galaxies in the Magneticum simulations in a consistent manner to compare the galaxy populations between Magneticum and observations through scaling relations across four different redshifts. In the following, only some selected scaling relations are presented that are relevant to the research presented in this thesis. Note that here the description and discussion are furthermore kept brief. For a comprehensive comparison of 28 scaling relations including the ones presented here between Magneticum and observations, refer to Dolag et al. (2025).

2.2.1 Galaxy sample and properties

From each of the simulations, we selected all subhalos (i.e., both central and satellite galaxies) above a stellar mass threshold that depends on the resolution level and simulation volume. The computation of the stellar mass used for these cuts is described in the following. The stellar mass threshold for Box0 (mr) is $5 \times 10^{11}\,\mathrm{M}_\odot$, for Box2 (hr) it is $1 \times 10^{10}\,\mathrm{M}_\odot$, for Box2b (hr) it is $4 \times 10^{10}\,\mathrm{M}_\odot$ (to complement Box2 at the higher-mass end), and for Box3 (uhr) and Box4 (uhr) it is $1 \times 10^{9}\,\mathrm{M}_\odot$.

For each galaxy, we first shifted the particle positions and velocities to be adequately centered on the stellar component. We followed the method described by Valenzuela et al. (2024a), where the spatial center is obtained by a shrinking sphere method (Power et al. 2003). The velocity center is determined as the mass-weighted mean stellar velocity, where outlier particles in the velocity distribution are ignored to prevent fast flyby structures from biasing the result.

From the centered galaxy, the stellar mass M_* is determined as the total stellar mass contained within $0.1\,R_{\mathrm{vir}}$, where R_{vir} is the virial radius of the galaxy's host halo as determined by SubFind. The half-mass radius $R_{1/2}$ is then the 3D radius within which half of the stellar mass is contained.

To measure global properties of the galaxies without overemphasizing their halos and potential structures therein, we determine the following four quantities for the respective particles within $3\,R_{1/2}$. The stellar specific angular momentum j_* is computed as (Teklu et al. 2015)

$$j_* = \left| \frac{\sum_i m_i \boldsymbol{r}_i \times \boldsymbol{v}_i}{\sum_i m_i} \right| \tag{2.1}$$

with the sums running over the stellar particles i with positions $\boldsymbol{r}_i$, velocities $\boldsymbol{v}_i$, and masses m_i. This is a measure for the angular momentum per stellar mass in a galaxy. The stellar age t^* is computed as the mass-weighted stellar age, and the stellar metallicity Z^* as the mass-weighted metal mass fraction of the stellar particles (i.e., the mass fraction of all elements more massive than helium). Finally, the star formation rate SFR is determined as the summed star formation rates of all gas particles within $3\,R_{1/2}$.

Furthermore, we decided to measure two projected 2D properties from the edge-on view. We determined these as light-weighted properties in the rest-frame r-band using the stellar population synthesis code with the CB07 models by Bruzual & Charlot (2003), assuming a Chabrier (2003) IMF. This ensures a more direct comparison to observations through the light-weighting while simultaneously reducing the scatter from projection effects through the consistent edge-on view. The edge-on projection is obtained following the method by Valenzuela et al. (2024a), where the galaxy is rotated into the frame of reference defined by its shape tensor at $3\,R_{1/2}$. Here, instead of using the mass-weighted approach, we also use the r-band light weighting.

In the edge-on projection, we first determine the 2D effective radius R_e containing half of the r-band flux within $0.1\,R_{\mathrm{vir}}$ (mimicking the procedure for the 3D half-mass radius). Then,

the ellipticity $\epsilon_e = 1 - b/a$ is obtained from the light-weighted elliptical shape at 1 R_e with its semi-major axes a and b, following Valenzuela et al. (2024a). It is a measure for how circular or elliptical a galaxy is. Within this ellipse, the light-weighted 2D angular momentum proxy λ_{R_e} (Emsellem et al. 2007, 2011) is computed following Jesseit et al. (2009) and Schulze et al. (2018): after binning the stellar particles through the centroidal Voronoi tesselation method (Cappellari & Copin 2003), we compute

$$\lambda_{R_e} = \frac{\sum_k F_k R_k |\overline{V}_k|}{\sum_k F_k R_k \sqrt{\overline{V}_k^2 + \sigma_k^2}}, \tag{2.2}$$

where the sums run over the Voronoi cells k, with their fluxes in the r-band F_k, their 2D radial distances R_k, their line-of-sight velocities $|\overline{V}_k|$, and their line-of-sight velocity dispersions σ_k. The difference to Schulze et al. (2018) is that here we actually use the light weighting instead of mass weighting. The λ_{R_e} parameter quantifies how dispersion or rotation dominated a galaxy is. Due to the higher resolution that is necessary for an accurate determination of the ellipticity and λ_{R_e}, we increased the lower stellar mass limits for which these were determined. Specifically, the limit for Box2 (hr) is $4 \times 10^{11}\,\mathrm{M}_\odot$, and for Box3 (uhr) and Box4 (uhr) it is $2 \times 10^{10}\,\mathrm{M}_\odot$. We did not compute these quantities for the larger simulation volumes Box0 and Box2b.

We determined all of these properties at four simulation snapshots at redshifts $z = 4$ (lookback time $t_{\mathrm{lb}} \approx 12.2\,\mathrm{Gyr}$), $z = 2$ ($t_{\mathrm{lb}} \approx 10.4\,\mathrm{Gyr}$), $z = 1$ ($t_{\mathrm{lb}} \approx 7.8\,\mathrm{Gyr}$), and $z = 0$ (today). With the galaxy properties consistently computed across the simulations and snapshots, we present a selection of scaling relations from the simulations in the following, comparing them to galaxy observations and empirical relations available at the different redshifts.

2.2.2 Star-forming main sequence

The star-forming main sequence (SFMS) describes the relation between SFR and stellar mass, where observations have shown that the star-forming galaxies follow a power-law relation with SFR increasing with stellar mass. The SFMS has been empirically found to drop toward lower SFRs as time passes, that is, with decreasing redshift. We show the Magneticum SFMS of the different simulation resolutions (colored points and colored lines for the star-forming medians) at four redshifts ($z = 4$, 2, 1, 0) in comparison to observations (black and gray markers and lines) in Figure 2.2. Since Box3 (uhr) was run with a more advanced black hole model than Box4 (uhr), it is referred to as uhr-S in the legend (the S stands for Steinborn et al. 2015, who introduced the new model). We find that the different simulations and resolutions converge at all redshifts, even between the different uhr black hole models. Overall, we also find good agreement with the observed data at all four redshifts, in particular at $z = 4$ and 2, and at later times at higher stellar masses of $\log M_*/\mathrm{M}_\odot \gtrsim 10$–11. At lower masses, the Magneticum simulations tend to have lower SFRs than observed on average, though it should also be noted that there are large observed scatters and systematic deviations between the different observational studies for the SFMS.

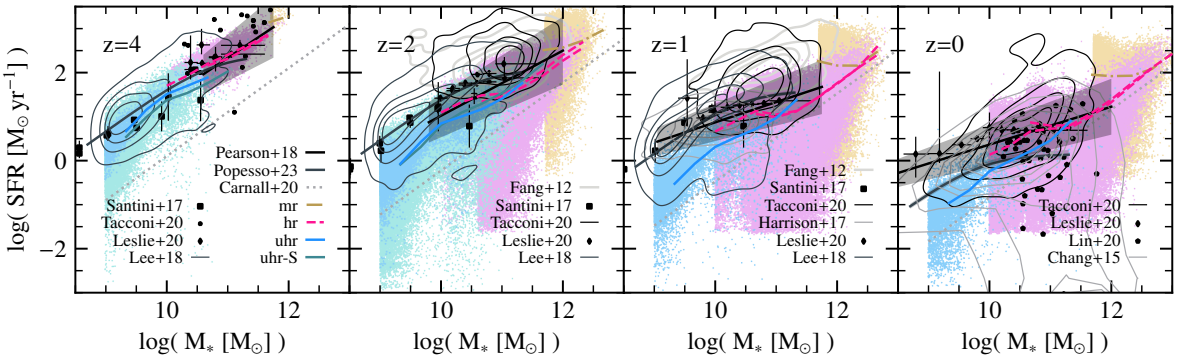


Figure 2.2: Star-forming main sequence (SFMS) of the Magneticum simulations at the four redshifts z = 4, 2, 1, and 0 (from left to right, indicated in the top left of each panel), with the star formation rate SFR shown as a function of stellar mass M_*. The simulated galaxies are shown as colored points: Box0 (mr) in gold, Box2 and Box2b (hr) in pink, Box3 (uhr) listed as uhr-S in green, and Box4 (uhr) in blue. The median relations of the star-forming galaxies (those above the dotted gray line following Carnall et al. 2020) are overplotted as a darker line in the corresponding color. Observational results are indicated by black and gray markers and lines. Two fits to the SFMS are shown by Pearson et al. (2018, with the scatter shown as a shaded region) and Popesso et al. (2023) at all four redshifts. Across the different redshifts, five larger samples of galaxies are shown through contour lines (Fang et al. 2012; Chang et al. 2015; Harrison et al. 2017; Lee et al. 2018; Tacconi et al. 2020). Smaller samples of galaxies at a given redshift are shown through individual markers (Santini et al. 2017; Leslie et al. 2020; Lin et al. 2020; Tacconi et al. 2020). The observations consist of data obtained from a variety of different methods and surveys, including data from UV, IR, and radio measurements, and in part through spectral energy distribution (SED) fitting. *This is figure 24 from Dolag et al. (2025).*

While it would appear as though galaxies evolve along the SFMS over time, Fortuné et al. (2025) show from Magneticum Box4 that in fact most of today's star-forming galaxies have had several periods of quiescence and rejuvenation. This explains some of the scatter seen for the simulated galaxies toward lower SFRs in Figure 2.2. The general decrease of SFR for the SFMS has been studied by Teklu et al. (2023), who showed that at later times the gas is distributed out to larger radii and thus has a lower star forming efficiency due to lower surface densities. Another picture has been drawn by Kelson (2014), who argue that hierarchical structure growth can also lead to the SFMS by the central limit theorem. In summary, the evolution of galaxies and galaxy populations with respect to their star formation over time is still a matter of active study. Further analysis of the interaction between gas accretion, star formation, and stellar feedback processes will be necessary to improve our understanding of galaxy quenching and rejuvenation.

The star-forming properties of galaxies become relevant in multiple parts of this thesis. The high star formation rates seen at early times are especially important for the formation of globular clusters (Movement III), and enhanced star formation rates as a result of gas-rich mergers can also lead to their formation (Chapter 17). We furthermore classify galaxies according to their star formation rate into star-bursting, star-forming, and quiescent galaxies in Chapter 12.

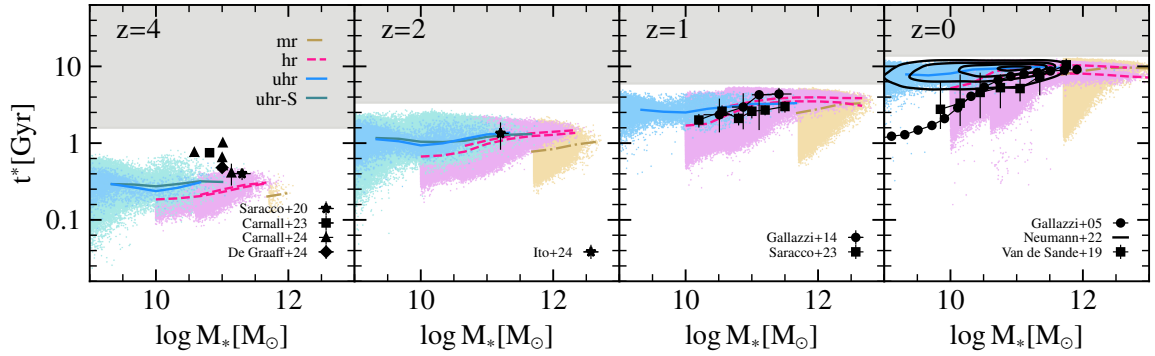


Figure 2.3: Stellar mass-age relation for the Magneticum simulations at four redshifts $z = 4$, 2, 1, and 0 (from left to right), with the stellar age t^* shown as a function of stellar mass M_*. The colored data points represent the galaxies from the different simulations as in Figure 2.2, and here the colored lines indicate the median relations for each simulation. The gray shaded region indicates ages that are beyond the age of the Universe at the respective redshift. Observations of individual massive passive galaxies are shown at $z = 4$ and 2 (Saracco et al. 2020; Carnall et al. 2023, 2024; de Graaff et al. 2025; Ito et al. 2025), with the error bars indicating measurement uncertainties. At $z = 1$ and 0, binned observational results are shown with their uncertainties (Gallazzi et al. 2005, 2014; van de Sande et al. 2019; Saracco et al. 2023), and contours of the results from MaNGA are shown from Neumann et al. (2022). *This is figure 27 from Dolag et al. (2025).*

2.2.3 Stellar mass-age relation

As a result of star formation, stars are born that form today's stellar component in galaxies. By measuring their ages, they reveal the time at which the bulk of a galaxy's stellar content was formed. In Figure 2.3 we show the stellar mass-age relation for the Magneticum galaxies at the same four redshifts as before ($z = 4$, 2, 1, and 0), again colored by the simulations and resolutions (with the colored points indicating the individual galaxies and the colored lines the median relations). The gray shaded region marks the age range beyond the age of the Universe at the respective redshift. The age relations are almost identical for simulations at the same resolution level (comparing blue and green at uhr level, and the two pink lines at hr level). Between simulations of different resolutions, the convergence is adequate, though with a trend toward younger ages in the lower-resolution runs. This is likely due to the efficient star formation at early times at higher resolutions (e.g., Tornatore et al. 2007; Kimmig et al. 2025).

Overall, we find a slight increase of age with mass across the different redshifts, which is also found in observations at $z = 1$ and $z = 0$ and indicates how more massive structures had earlier formation epochs and formed their stars on short timescales. At the highest redshift of $z = 4$, the age observations of massive passive galaxies show that they were formed at earlier times than the simulated galaxies. However, given that these are likely some of the most extreme galaxies, it is not surprising that they reside on the early assembly side of the simulated average predictions (see also the results on simulated early massive quenched galaxies by Kimmig et al. 2025; Remus & Kimmig 2025). At $z = 2$, however, the one observation by Ito et al. (2025) falls exactly on the simulated values, and also at $z = 1$, the observed relations are well in agreement with the simulations. At $z = 0$, the simulations predict old ages on the order of 10 Gyr (though note that the age axis scale is logarithmic) for most of the mass

range, which is consistent with the MaNGA results by Neumann et al. (2022), though previous results by Gallazzi et al. (2005) from SDSS and by van de Sande et al. (2019) from SAMI suggested that lower-mass galaxies would be considerably younger, differing from Neumann et al. (2022) by as much as an order of magnitude below $M_* \sim 10^{10}\,\mathrm{M}_\odot$.

These results also show the difficulty of measuring stellar ages from observations for other galaxies, where effects like the degeneracy between ages and metallicity in the resulting colors of stellar populations increase the uncertainties significantly, especially at older ages beyond several Gyr (e.g., Worthey 1994; Boecker et al. 2020). Stellar ages are a recurring theme in this thesis, where they play an important role for planetary nebulae (Movement II) and in particular the mass-age relation becomes relevant when studying planetary nebula populations in galaxies of different masses (see Chapters 11, 12, and 14). Finally, Chapters 17 and 18 focus on the ages of globular clusters and their comparison between observations and simulations.

2.2.4 Stellar mass-metallicity relation

Besides their age, a key property of stellar populations is their metallicity. Later generations of stars are generally formed from the gas that was chemically enriched by the stellar feedback of earlier generations (specifically through stellar winds and supernovae) and thus tend to have higher metallicities. In Figure 2.4, we show the stellar mass-metallicity relation for the Magneticum galaxies at the same four redshifts of $z = 4$, 2, 1, and 0, with the same coloring scheme (colored points as individual galaxies and colored lines as medians). The metallicity is normalized by the solar metallicity of $Z_\odot = 0.0142$ (Asplund et al. 2009). Similar to the stellar mass-age relation (Figure 2.3), simulations at the same resolution level are overall well converged, whereas there are systematic differences between the different resolutions: simulations at higher resolution tend to have more metal-rich galaxies, which may again be related to the more efficient early star formation found at higher resolution (Tornatore et al. 2007; Kimmig et al. 2025). Overplotted in black are stellar metallicity observations, whereas the gray markers and lines indicate observations of the gas-phase metallicity.

At all redshifts, more massive galaxies are generally found to be more metal-rich from the simulations and observations. This is also the case for the observed gas, which had already been found well before stellar metallicities could be constrained for larger samples of galaxies (e.g., Lequeux et al. 1979; Tremonti et al. 2004). Together with the older ages of massive galaxies, this suggests that efficient star formation at early times leads to rapid self-enrichment in such systems. While we find good agreement between the simulations and newer local observations at $z = 0$ (Kudritzki et al. 2021; Sextl et al. 2023; Kudritzki et al. 2024), most other stellar metallicity measurements tend to find systematically lower values at all redshifts. An exception are some $z = 4$ observations by Saracco et al. (2020) and Carnall et al. (2024), which feature galaxies largely consistent with the simulation predictions. While here we will not focus on the gas-phase metallicity, the observations show them to be systematically higher than the stellar metallicity measurements. In principle, this results from gas being

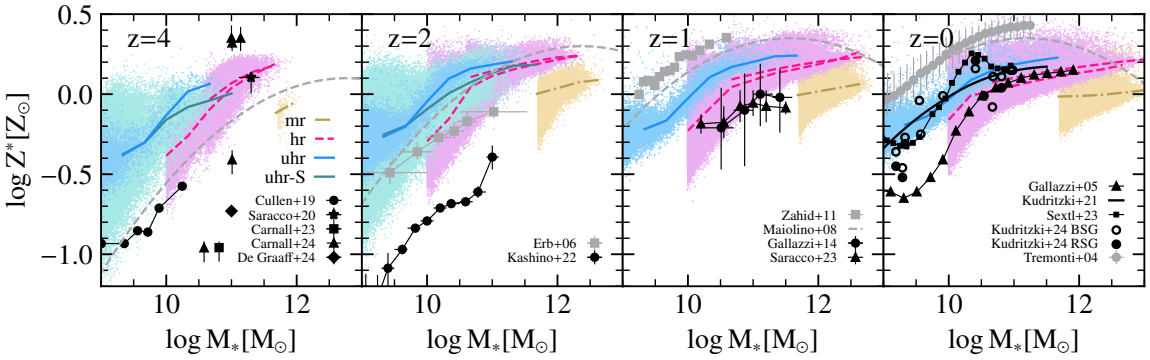


Figure 2.4: Stellar mass-metallicity relation for the Magneticum simulations at four redshifts z = 4, 2, 1, and 0 (from left to right), with the stellar metallicity Z^* shown as a function of stellar mass M_*. The colored data points and lines indicate the simulated galaxies and median values as in Figure 2.3. Black points and lines indicate stellar metallicity measurements, whereas gray points and lines indicate gas-phase metallicity measurements. Stellar metallicity observations of individual galaxies (Saracco et al. 2020; Carnall et al. 2023, 2024; Kudritzki et al. 2024; de Graaff et al. 2025) and averaged relations for larger samples of galaxies (Gallazzi et al. 2005, 2014; Cullen et al. 2019; Kudritzki et al. 2021; Kashino et al. 2022; Saracco et al. 2023; Sextl et al. 2023) in black (BSG indicates blue supergiant and RSG red supergiant measurements from the study on local galaxies by Kudritzki et al. 2024). The gas-phase metallicity relation fits to the data by Maiolino et al. (2008) are shown as the gray dashed line at all redshifts, and further observed gas-phase metallicity relations are included as well (Tremonti et al. 2004; Erb et al. 2006; Zahid et al. 2011). *This is figure 28 from Dolag et al. (2025).*

continuously enriched by stellar feedback over time, whereas stars keep the metallicity of the gas they were formed from and are not further enriched.

While the details of early enrichment in galaxies still remain unclear due to the large scatter of observations at z = 4, we conclude that the higher-resolution simulations (uhr and hr) generally well reproduce the present-day stellar mass-metallicity relation of galaxies. Further improvements on the observational side to reduce systematics in the local Universe and especially at higher redshifts will be necessary to provide the necessary constraints to better understand how the general galaxy population is chemically enriched over time. To this end, measuring alpha abundances at high redshifts may be helpful in bringing new insights to the early enrichment because the production channels of different elements change over time (Kobayashi et al. 2020; Kimmig et al. 2025).

Stellar metallicities will be discussed in multiple parts of this thesis. The stellar mass-metallicity relation has been relevant in the estimation of stellar masses for tidal feature progenitors, which is investigated in Chapter 5. Stellar metallicities are furthermore a key ingredient for planetary nebulae (Movement II). Their relevance for planetary nebulae is highlighted especially in Chapters 8 and 9 with a focus on stellar physics and in Chapters 12 and 14 considering the galaxy regime.

2.2.5 Stellar mass-size relation

One of the most fundamental properties of a galaxy besides its mass is its size. Different spatial distributions of the stars within galaxies are generally related to other properties varying as well and have been known to differ between elliptical and disk galaxies (e.g., van der Wel

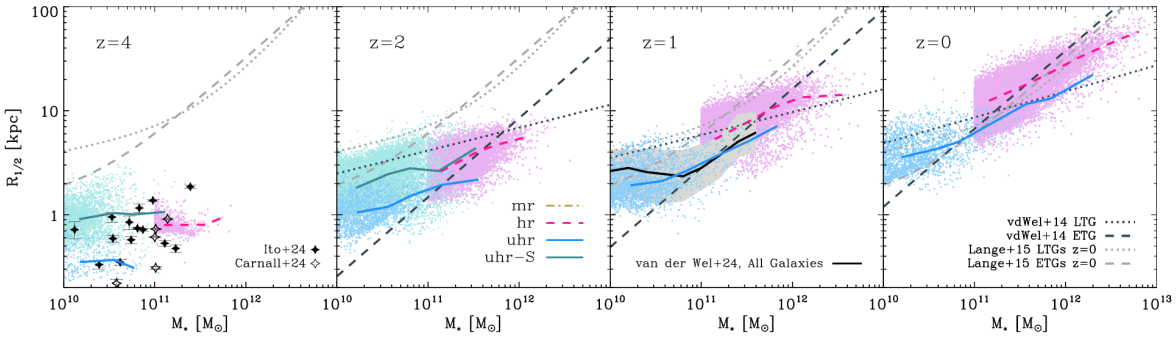


Figure 2.5: Stellar mass-size relation for the Magneticum simulations at four redshifts $z = 4$, 2, 1, and 0 (from left to right), with the stellar half-mass radius $R_{1/2}$ shown as a function of stellar mass M_*. The colored data points and lines indicate the simulated galaxies and median values as in Figure 2.3. The gray lines in all four panels indicate the relations found for early-type galaxies (ETGs, dotted) and late-type galaxies (LTGs, dashed) from GAMA at $z = 0$ by Lange et al. (2015). The black dashed and dotted lines indicate the relations for ETGs and LTGs, respectively, observed at the corresponding redshifts by van der Wel et al. (2014). Individual measurements of quiescent galaxies at $z = 4$ are shown with black markers (Carnall et al. 2024; Ito et al. 2024), and the mass-size relation of all galaxies (not split by morphology) at $z = 1$ observed with JWST by van der Wel et al. (2024) is shown as a black line, including its scatter (gray shaded region). *This is figure 30 from Dolag et al. (2025).*

et al. 2014). In Figure 2.5, we show the stellar mass-size relation for the Magneticum galaxies at the same four redshifts of $z = 4$, 2, 1, and 0, with the same coloring scheme as for the previous relations (colored points as individual galaxies and colored lines as medians). The Box0 (mr) galaxies are left out here because of their large gravitational softening that smear out the galaxy centers. The different simulations and resolutions show worse convergence compared to some of the previous scaling relations, where now even the two uhr simulations (Box3 and Box4) show a systematic offset from each other. The updated black hole model in Box3 (uhr, labeled uhr-S in the legend) produces systematically larger galaxies than Box4 (uhr) by a factor of ∼2. Between Box4 (uhr) and the lower resolution simulations Box2 and Box2b, the lower resolution galaxies are also systematically larger by a similar factor, which can be explained by the larger softening lengths.

The mass-size relation is found to evolve with time, where at a given mass galaxies increase in size towards lower redshifts. The same is true when considering observations at different redshifts, where the fits to early-type galaxies (ETGs) and late-type galaxies (LTGs) by van der Wel et al. (2014) show the same general behavior. For the high-resolution Box4 (uhr), we find very good agreement with observations at $z = 1$ and $z = 0$, in particular at $z = 1$ given the mixed-morphology sample by van der Wel et al. (2024). Note that at $z = 0$ the different morphologies in Magneticum have already been shown in several works that they follow the observed ETG and LTG relations (e.g., Schulze et al. 2018; Remus & Forbes 2022). Finally, at the high redshifts of $z = 4$, there is a large scatter in individual observed quiescent galaxies, and also the simulations show a larger deviation from each other than at later redshifts. As also shown by Remus & Kimmig (2025), Box3 (uhr, green) features galaxy sizes and a scatter that agree very well with the observations, which is a result of more extended disks. For elliptical galaxies, van der Wel et al. (2014) find a stronger increase in

size for elliptical galaxies (compared to the disks), which indicates their early rapid formation through starbursts (e.g., Forrest et al. 2020; Nanayakkara et al. 2024; Kimmig et al. 2025) and later increase in size through mergers (e.g., Naab et al. 2009; Schulze et al. 2020).

In this thesis, the sizes of galaxies have been especially relevant in the analysis of galaxies with tidal features around them (Chapter 4). The mass-size relation was also used to characterize the progenitors of the tidal features themselves (Chapter 5).

2.2.6 Specific angular momentum relation

On the dynamical side, an important relation has been observed to exist between the stellar mass and the stellar specific angular momentum of galaxies, which arises from theoretical considerations of the relation between halo mass and angular momentum (Fall 1983; Romanowsky & Fall 2012). One important finding has been that elliptical and disk galaxies follow two offset power laws in the stellar mass-specific angular momentum plane that have the same power law slope, with disk galaxies having the higher specific angular momenta. In Figure 2.6, we show the stellar mass-specific angular momentum relation for the Magneticum galaxies at the same four redshifts of $z = 4$, 2, 1, and 0, with the same coloring scheme as for the previous relations (colored points as individual galaxies and colored lines as medians). The convergence between the different simulations and resolution levels is overall very good, and the median lines are consistent with power laws as expected, roughly maintaining the same power law slope across all redshifts. This is consistent with the slope of $2/3$ of the scaling relations proposed by Fall & Romanowsky (2013, black and gray lines) for ETGs and LTGs. Over time, the specific angular momenta increase as the redshift decreases, where the evolution agrees well with the theoretical scaling of $j_* \propto (1+z)^{-1/2}$ proposed by Obreschkow et al. (2015), which we applied to the $z = 0$ relations of Fall & Romanowsky (2013) for the earlier redshifts $z = 4$,2, and 1 (black and gray lines).

Besides the work by Fall & Romanowsky (2013), most of the other observations are in fact of disk galaxies, which explains why they mostly scatter around the black LTG lines at all redshifts. The specific angular momenta spanned by the simulated galaxies, which include all types of morphologies, are therefore overall consistent with the observations, though not quite reaching the highest observed values. Note that the observed values are obtained from extrapolating the measured 2D rotation curves out to large radii, however, which makes a direct comparison to the simulated values difficult.

As shown by Teklu et al. (2015) for Box4 (uhr), the position of a galaxy in the stellar mass-specific angular momentum plane can be directly related to its morphology, building on the findings of Romanowsky & Fall (2012) and Fall & Romanowsky (2013). For this, they introduced the b-value, defined as the y-intercept of a 2/3 slope in the log-log space of the plane:

$$b = \log \frac{j_*}{\mathrm{kpc\,km\,s^{-1}}} - \frac{2}{3} \log \frac{M_*}{\mathrm{M_\odot}}. \tag{2.3}$$

As the simulations are well-converged and are consistent with observations of the specific angular momentum, the b-value has been an excellent measure for morphology in simulated

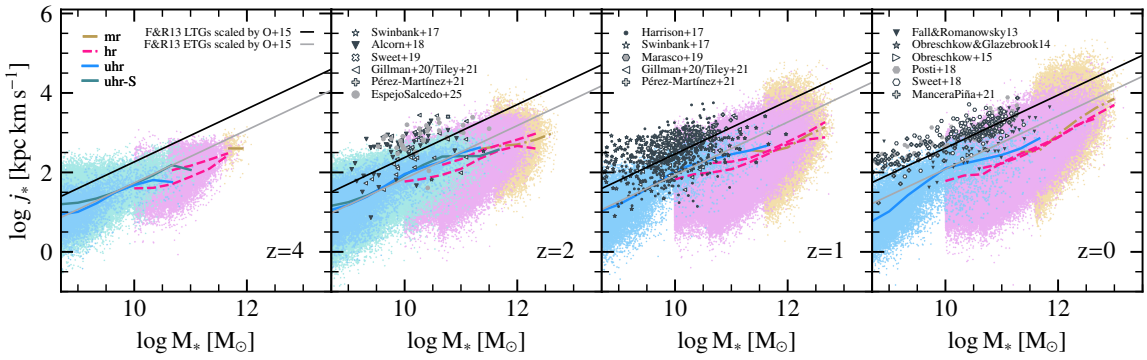


Figure 2.6: Stellar mass-specific angular momentum relation for the Magneticum simulations at four redshifts z = 4, 2, 1, and 0 (from left to right), with the stellar angular momentum j_* shown as a function of stellar mass M_*. The colored data points and lines indicate the simulated galaxies and median values as in Figure 2.3. The black and gray lines in all four panels indicate the relations found for LTGs (black) and ETGs (gray) at z = 0 by Fall & Romanowsky (2013), but scaled to higher redshifts following the model of Obreschkow et al. (2015). Individual galaxy observations are shown at all four redshifts by black and gray markers (Fall & Romanowsky 2013; Obreschkow & Glazebrook 2014; Obreschkow et al. 2015; Harrison et al. 2017; Swinbank et al. 2017; Alcorn et al. 2018; Posti et al. 2018; Sweet et al. 2018, 2019; Gillman et al. 2020; Mancera Piña et al. 2021; Tiley et al. 2021; Pérez-Martínez et al. 2021; Espejo Salcedo et al. 2025). *This is figure 29 from Dolag et al. (2025).*

galaxies. The commonly used thresholds at z = 0 have been $b = -4.73$ and -4.35 between early-type, intermediate, and late-type galaxies, respectively (e.g., Teklu et al. 2017; Emami et al. 2021; Valenzuela et al. 2024a).

Many parts of this thesis rely on a classification of galaxy morphologies, where the b-value is used as the morphological measure. The b-value is used for connecting the morphologies to the presence of tidal features (Chapter 4) and for measuring the morphology of the tidal feature progenitors (Chapter 5). Furthermore, the galaxies are split by morphology to investigate the differences between their planetary nebula populations (Chapters 11 and 12) and to aid selecting appropriate analogs for observed elliptical galaxies (Chapter 14).

2.2.7 Resolved stellar kinematics

Finally, we discuss the 2D projected inner kinematic properties of galaxies. The inner kinematics and shapes of galaxies are a powerful measure to probe galaxy formation models as cosmological simulations have long struggled to reproduce the observed kinematic properties (e.g., van de Sande et al. 2019; Pulsoni et al. 2020; van de Sande et al. 2021). In Figure 2.7, we show the λ_{R_e}-ϵ_e plane for the Magneticum galaxies at the same four redshifts of z = 4, 2, 1, and 0, with the same coloring scheme as for the previous relations (colored points as individual galaxies, but here without overplotted medians). As the simulations contain galaxy samples with significantly different mass ranges, their different locations in the plane in fact reflect the types of galaxies: the more highly resolved but smaller simulations Box3 (uhr) and Box4 (uhr) consist of many disk galaxies with high values of λ_{R_e} and ϵ in the fast rotator region (above the solid curves, see Emsellem et al. 2011), whereas the lower resolved but larger Box2 (hr) simulation mostly contains massive elliptical galaxies with low rotational

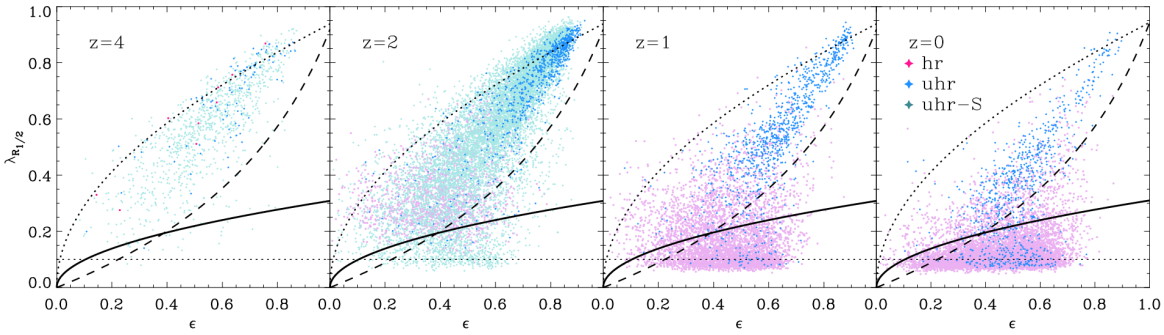


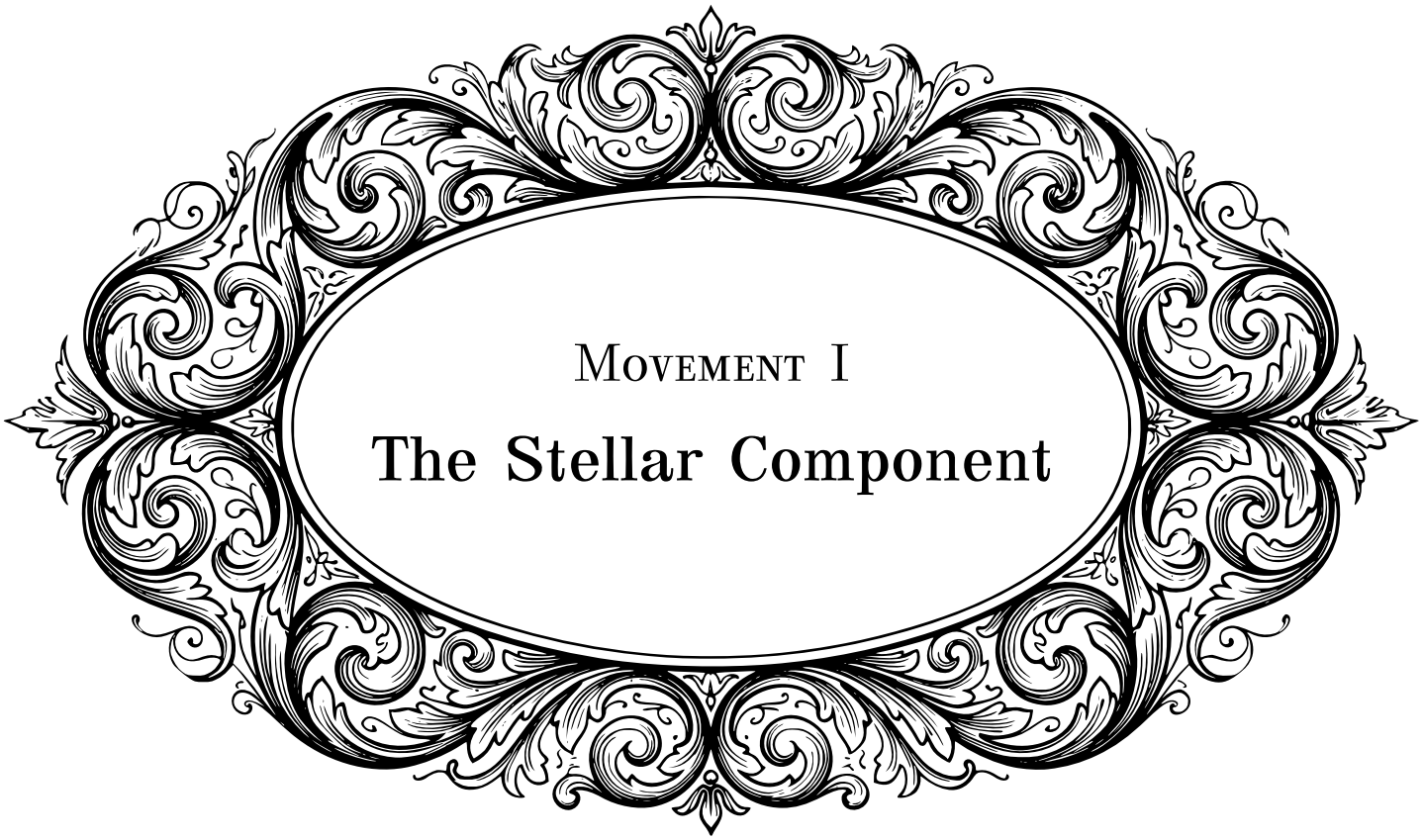
Figure 2.7: Projected rotational support-ellipticity plane for the Magneticum simulations at four redshifts $z = 4$, 2, 1, and 0 (from left to right), with the projected angular momentum proxy λ_{R_e} shown as a function of ellipticity ϵ_e. Both λ_{R_e} and ϵ_e were computed from the edge-on perspective of the galaxies with a rest-frame r-band light weighting. The solid curves mark the limit between fast and slow rotators based on Emsellem et al. (2011, $\lambda_{R_e} = 0.31\sqrt{\epsilon_e}$, with fast rotators above and slow rotators below). The dashed and dotted curves trace the theoretical predictions for galaxies with anisotropies of $\delta = 0.8\epsilon_e$ and $\delta = 0$, respectively, for an edge-on ellipsoidal galaxy (Binney 2005; Emsellem et al. 2011; Schulze et al. 2018). The horizontal dotted lines indicate an estimated lower limit of $\lambda_{R_e} = 0.1$ for simulated galaxies due to limited resolution (e.g., Bois et al. 2010; Naab et al. 2014; Schulze et al. 2018). *This is figure 32 from Dolag et al. (2025).*

support (many in the slow rotator region below the solid curves). While we do not show observational data in Figure 2.7, several studies have shown the Magneticum galaxies to be consistent with observations from numerous integral field unit (IFU) surveys at $z = 0$ (e.g., Schulze et al. 2018; van de Sande et al. 2019; Valenzuela et al. 2024a). There are still some differences, however, where at a given ellipticity, Magneticum galaxies tend to have lower values of λ_{R_e}. This also leads to an overpopulation of elongated slow rotators (e.g., Schulze et al. 2018), though this behavior is still less extreme than found in other simulations (e.g., Pulsoni et al. 2020). At higher redshifts, observations are still limited, with some individual recent studies at intermediate redshifts of $z < 0.75$ (e.g., Derkenne et al. 2024; Mozumdar et al. 2025a,b).

The simulated galaxies in Figure 2.7 show how early galaxies mostly populate the very high region of λ_{R_e} and ϵ, indicating their disk-like nature. Over time, galaxies become less rotationally supported and populate the dispersion-dominated slow rotator regime below the solid curves. This is seen especially nicely for the galaxies of Box4 (uhr), but it is also the case for Box2 (hr). Regarding the higher-redshift kinematics, predictions have been made by Schulze et al. (2018) for the galaxy populations up to $z = 2$. More recently, using Box3 (uhr) Kimmig et al. (2025) predicted high-redshift massive quenched galaxies to remain fast rotators even after quenching, which agrees well with observations of fast-rotating quenched galaxies at $z \sim 2$ by Newman et al. (2018). However, to improve our understanding of the overall kinematic evolution of the total galaxy population and the build-up of the slow rotator regime, further improved observations of the stellar kinematics will be necessary at high redshifts.

In this thesis, the inner kinematics of galaxies play a central role in being connected to the presence of tidal features or of a satellite plane around the host (Chapter 4). Moreover, the

classification of galaxies into fast and slow rotators based on the inner kinematics is also used to study the differences between their planetary nebula populations in Chapter 12.



Movement I

The Stellar Component

3

Introduction to the Stellar Component

This chapter contains parts from the introduction of Valenzuela & Remus (2024), whose results are presented in the subsequent chapter.

The stellar component of disk galaxies has classically been divided into three parts: the disk, bulge, and halo. Whereas the flat rotating disk and the central bulge[1] make up the main visible part of a galaxy and are used for its morphological classification (e.g., Hubble 1926, 1936; Freeman 1970; Kormendy & Kennicutt 2004), the stellar halo covers a significantly more extended volume beyond the other inner components. These outer stellar regions of both disk and elliptical galaxies encode clues about their formation histories because the relaxation times are longer and because they are where much of the accreted matter is deposited (e.g., Bullock & Johnston 2005). In the ΛCDM model of structure formation, galaxies grow hierarchically through the accretion of lower-mass structures, which are typically deposited in these outskirts. Studying this accretion through satellite galaxies and the low-surface-brightness (LSB) structures within the halo therefore promises to reveal clues about the merger history. For this reason, the first Movement of this thesis focuses on investigating the stellar component in the outskirts of galaxies as a stellar tracer for galaxy formation history.

[1] Note that what is referred to as a bulge can be diverse in nature, including a classical bulge, a nuclear disk, or a bar (e.g., Athanassoula 2005; Gadotti 2026).

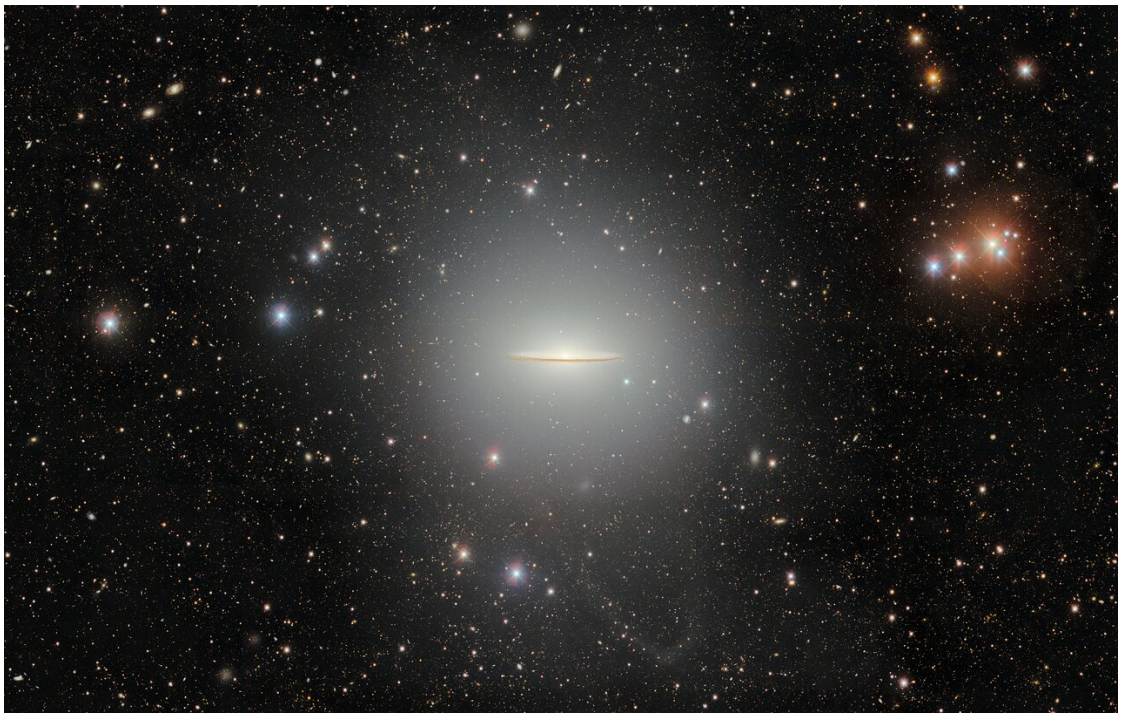


Figure 3.1: Example of a stellar halo imaged with the Dark Energy Camera (DECam), found around the Sombrero galaxy (M 104), at a distance of ∼9 Mpc. At the lower side of the halo, a tidal stream in the form of a loop can be seen. Two satellite galaxies can also be spotted as diffuse extended "smudges" (see figure 1 of Crosby et al. 2024): one right beneath the Sombrero galaxy, roughly half-way in between the outer stream edge and the galaxy center, and one to the lower right of the halo, at about the same height as the other satellite, to the left of a bright star (a tiny bit higher). *Image credit: CTIO/NOIRLab/DOE/NSF/AURA. Image processing: T.A. Rector (University of Alaska Anchorage/NSF NOIRLab), D. de Martin & M. Zamani (NSF NOIRLab)*[2].

Figure 3.1 shows an example of a galaxy and its stellar halo (the Sombrero galaxy, at a distance of about 9 Mpc; Fahrion et al. 2026). Deep imaging is required to detect the faint halo regions, including the tidal stream seen at the bottom right of the halo.

3.1 Stellar accretion onto galaxies

While lower-mass galaxies form many of their stars themselves (in-situ stars), more massive galaxies contain larger fractions of stars accreted from other systems where they were formed (ex-situ stars), which can reach over 80% (e.g., Cooper et al. 2013; Rodriguez-Gomez et al. 2016; Davison et al. 2020; Remus & Forbes 2022). This is a result of the ΛCDM model, where structure grows hierarchically from the bottom up: stars are first formed in smaller systems and are successively accreted onto more massive structures (e.g., White & Rees 1978; Gu et al. 2016). As satellite galaxies orbit in the gravitational potential of their host galaxies, they experience tidal forces that strip away their mass over time. Through this process, stars are gradually removed, and in the case of smaller mass ratios they are deposited in the halo, thereby increasing the size of the host (e.g., Naab et al. 2009; Hilz et al. 2012). In the case of gas-poor (dry) mergers, simulation studies have shown that minor mergers leave the inner

[2]https://noirlab.edu/public/images/noirlab2612a/

regions unchanged, whereas gas-rich (wet) mergers lead to newly formed stars in the inner galaxy (e.g., Hilz et al. 2013; Lagos et al. 2018). Moreover, more massive mergers deposit their stellar content at smaller radii (e.g., Karademir et al. 2019). As a result, the outer halo regions are oftentimes dominated by accreted stars (e.g., Cooper et al. 2013), but depending on the accretion history, even the central regions can become accretion dominated (e.g., Remus & Forbes 2022). Furthermore, the inner and outer kinematics may be affected differently depending on the accretion history, leading to a possible decoupling of the galaxy and its halo (e.g., Schulze et al. 2020; Pulsoni et al. 2021).

These accretion processes lead to several different types of structures that can be observed in the outer halos of galaxies. Satellite galaxies orbit around their host galaxies and represent those galaxies that have not yet merged with the host or been tidally disrupted. Tidal features are the disrupting remnants of former satellite galaxies that can still be observed as coherent LSB structures in the halo. Finally, after sufficient time has passed, an accreted galaxy becomes fully mixed with the outer regions, now belonging to the stellar halo and thereby increasing its mass. Like tidal features, the diffuse stellar halo can also be observed through deep imaging, as the example shows in Figure 3.1.

3.2 Satellite systems

Satellite systems represent the current galaxy population orbiting the host within its gravitational potential. Their distribution and kinematics are therefore influenced by the dark matter (DM) halo, which has been leveraged to estimate the total halo mass of the Milky Way (e.g., Li et al. 2017; Fritz et al. 2020) and of other structures (e.g., Shi et al. 2024). The abundance of the Milky Way satellite system had in fact led to an apparent tension with ΛCDM predictions, where many more satellites were expected to be observed based on DM-only cosmological simulations of Milky Way-mass halos (the *missing satellites problem*; e.g., Klypin et al. 1999; Moore et al. 1999). This tension has been resolved through the inclusion of baryonic matter in simulations, an improved understanding of the stellar mass-halo mass relation, and further observations, where now high-resolution simulations agree well with the observed satellites (e.g., Wetzel et al. 2016; Sales et al. 2022).

3.2.1 Satellite planes

Lynden-Bell (1976) already found that the Magellanic Clouds and a number of globular clusters form a thin plane around the Milky Way. More satellites have been identified to lie within this plane since then (e.g., Kroupa et al. 2005). Other well-known systems with satellite planes are the Andromeda galaxy (e.g., Ibata et al. 2013) and Centaurus A (e.g., Müller et al. 2018). More recently, Heesters et al. (2021) found that about 25% of MATLAS galaxies feature a flattened satellite plane in their outskirts, and the satellite system of NGC 4490 has

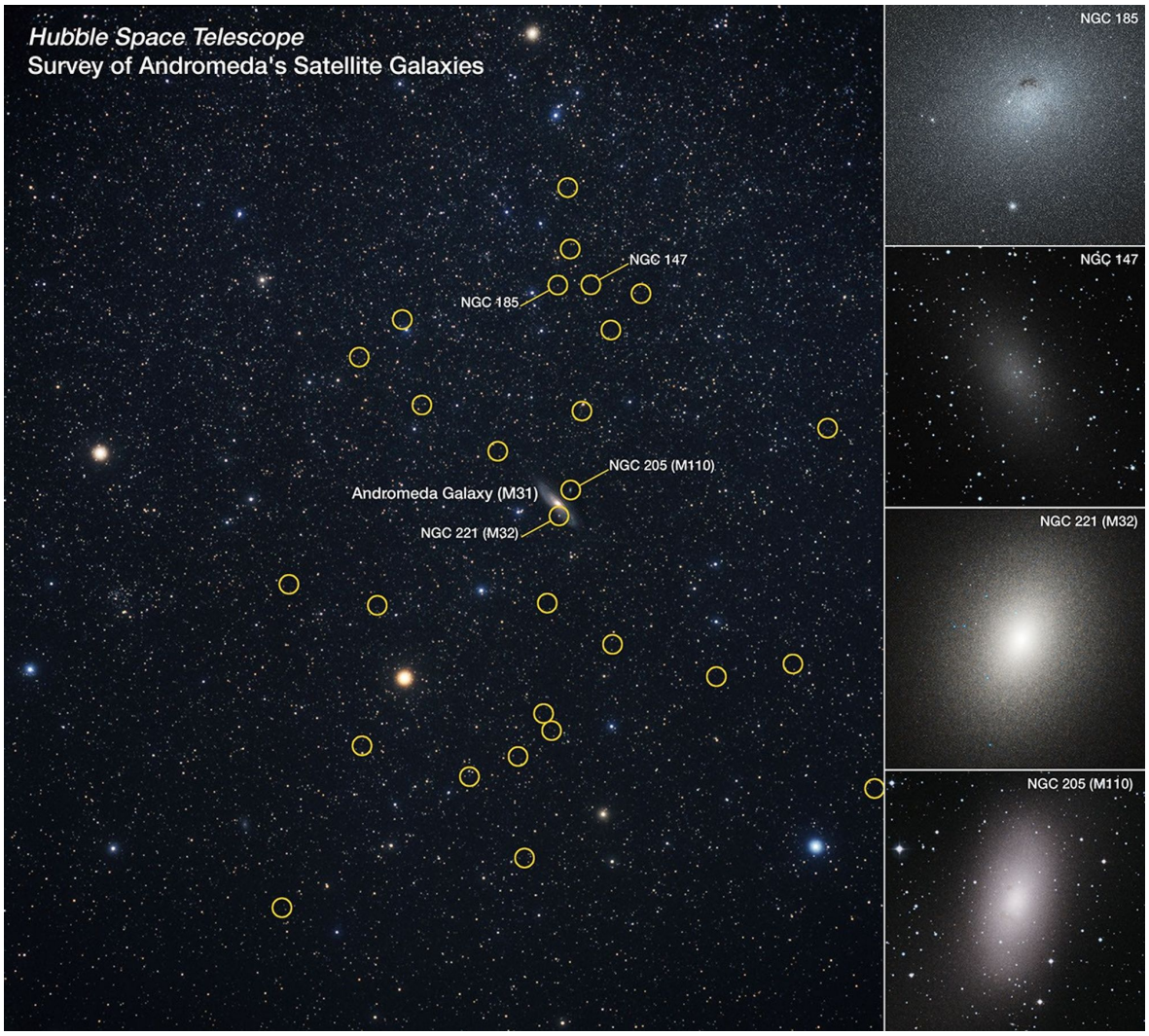


Figure 3.2: Example of a satellite plane with highlighted satellites found around the Andromeda Galaxy (M 31, at a distance of ~760 kpc Li et al. 2021). The known satellite galaxies of M 31 are indicated by the yellow circles and also appear to be orbiting in the same direction within a plane. The wide-field image is created from ground-based photography, and the satellite galaxy image panels on the right are from the Hubble Space Telescope survey of Andromeda's satellite galaxies (Savino et al. 2022). *Image credit: NASA, ESA, DSS2, Alessandro Savino (UC Berkeley), Joseph DePasquale (STScI), Akira Fujii*[3].

also been determined to have a plane of satellites around it (Karachentsev & Kroupa 2024). Figure 3.2 shows the satellite plane around M 31.

3.2.2 Predictions from simulations

The observed satellite planes have led to many studies trying to understand their origin. Simulations have predicted satellites to be arranged more isotropically, with very few systems having such satellite planes (e.g., Pawlowski et al. 2014; Pawlowski 2021). Other studies have found better agreement with observations (e.g., Wang et al. 2013; Pham et al. 2023), and specifically for the Milky Way, the presence of the LMC (e.g., Vasiliev 2024) and the local environment have been found to play an important role (e.g., Xu et al. 2023). Simulations

[3]https://science.nasa.gov/asset/hubble/survey-of-andromedas-satellite-galaxies/

furthermore suggest that the arrangement of satellites is connected to the surrounding cosmic web (e.g., Welker et al. 2018), or, like tidal features, may also be the result of galaxy interactions and mergers (e.g., Pawlowski et al. 2011; Smith et al. 2016; Bílek et al. 2018). Some studies have concluded that thin planes of satellite galaxies are short-lived (Fernando et al. 2017) and that this is the case for the Milky Way (Sawala et al. 2023). However, the origin of these satellite planes is still strongly debated (e.g., Kumar et al. 2025; Crosby et al. 2026). Finally, there have been several methods introduced to measure the flattening and dynamics of satellite systems to characterize them in simulations and observations (e.g., Shao et al. 2019; Förster et al. 2022; Seo et al. 2024). While overall motivated by the satellite plane tension, it should be highlighted that the method by Förster et al. (2022, the satellite plane data used in Chapter 4 originates from this method) was developed to quantify the flattening of satellite systems aligned in angular momentum with each other. In conclusion, while the origins of satellite planes are still a matter of investigation, their occurrence promises to reveal insights into the formation histories of galaxies, which among others may be through a larger accreted group of satellites or through a particular accretion orbit induced by the larger-scale environment.

3.3 Tidal features

As satellite galaxies are exposed to tidal forces, they form tidal features in the halo region over time, and also interacting galaxies can lose material in the form of tidal features. Since the galaxy outskirts as well as such features have a low surface brightness, deep imaging is necessary to detect these faint structures that store information about the merger history (e.g., Johnston et al. 2008). Early work by Malin & Carter (1983) already cataloged shell systems around elliptical galaxies. Deeper LSB observations (reaching a V-band depth of 28.5 mag arcsec^{-2}) later were able to reveal the complex diffuse intracluster light (ICL) in the Virgo Cluster (Mihos et al. 2005). Fainter tidal features were found around individual galaxies in subsequent studies (e.g., Martínez-Delgado et al. 2008), and brighter features were probed around large samples of galaxies through multiple works (e.g., Tal et al. 2009; Miskolczi et al. 2011; Atkinson et al. 2013; Morales et al. 2018), mostly reaching 28 mag arcsec^{-2}. Deeper imaging has become available for the outskirts of nearby galaxies through the MATLAS survey (Duc et al. 2015; Bílek et al. 2020; Sola et al. 2022) or the Stellar Stream Legacy Survey (Martínez-Delgado et al. 2023a), reaching surface brightnesses as faint as 29 mag arcsec^{-2}. The features are often identified through visual inspection, but fully automated approaches have been developed as well (e.g., Kado-Fong et al. 2018; Sola et al. 2022). However, these automated methods sometimes encounter problems caused by their sensitivity to LSB features.

Tidal features have been found to be especially common around prolate rotating galaxies (rotation around the major axis instead of the minor axis), indicating recent signs of interaction and merging (Ebrová et al. 2021). Other studies have investigated the correlation of tidal features with their local environment, finding that the local density has no effect, whereas galaxies near galaxy cluster centers exhibit significantly fewer tidal features around them (Adams et al. 2012). However, for the most massive elliptical galaxies, Yoon et al. (2024a)

have found that those in lower-density environments tend to have tidal features more often. After the publication of Valenzuela & Remus (2024, see Chapter 4), further work connecting tidal features with the inner galaxy kinematics has been performed (e.g., Rutherford et al. 2024; Yoon et al. 2024b).

With the recent launch of Euclid and first light of Rubin, a wealth of LSB data up to 30 mag arcsec^{-2} is incoming across large portions of the sky, which promise to reveal diffuse stellar structures in unprecedented quantity (e.g., Khalid et al. 2024; Urbano et al. 2025). Having a firm understanding of the types of tidal features and their meaning is crucial to interpret these observations.

3.3.1 Tidal feature types

Most often, three types of tidal features are distinguished: tidal shells, streams, and tails (e.g., Bílek et al. 2020). Tidal shells are found as concentric arcs centered on the host galaxy with a sharp outer edge (see the left panel of Figure 3.3 for an example of a shell galaxy at a distance of 80 Mpc[4]). They are known to form from nearly radial mergers with the host (e.g., Quinn 1984; Bílek et al. 2015; Pop et al. 2018; Karademir et al. 2019). Note that a shell is actually not a coherently moving structure, but is a stellar overdensity at the orbital apocenter of many stars oscillating within the host galaxy's potential. With each passage of the infalling satellite within the potential, a new shell forms on alternating sides of the central galaxy, thereafter propagating outwards as a density wave (e.g., Quinn 1984; Ebrová et al. 2010). Studies have furthermore shown that shell systems preferentially occur around red, massive elliptical galaxies (e.g., Kado-Fong et al. 2018) Tidal streams are the diffuse remnants of tidally disrupted lower-mass galaxies on more circular orbits around the host galaxies (see Figure 3.1 for an example of a galaxy with a tidal stream around it). Note that stellar streams have also been identified around the Milky Way from Gaia phase space data of individual stars, where many streams would not be identified purely from photometry (e.g., Borsato et al. 2020). Streams have been targeted to constrain the DM halo shape and mass of the Milky Way (e.g., Johnston et al. 1999; Koposov et al. 2010; Law & Majewski 2010) and of other galaxies (e.g., Pearson et al. 2022; Walder et al. 2025). Further morphological properties of streams like feathers and bifurcation have also been studied in previous work (e.g., Amorisco 2015). Tidal tails are structures that extend away from the host galaxy caused by interaction with another galaxy (see the right panel of Figure 3.3 for an example of a galaxy with two tails at a distance of 140 Mpc[5]). Unlike shells and streams, tidal tails are made up of the stars originating from the host galaxy itself, tidally stripped away from the inner regions in the form of a tail. Note that some studies have also classified umbrella structures as their own class, which generally look like a shell at the end of a stream oriented toward the host galaxy (e.g., Martínez-Delgado et al. 2023b, 2025).

[4]https://esahubble.org/images/heic1516a/
[5]https://esahubble.org/images/potw2252a/



Figure 3.3: *Left*: Example of a galaxy with tidal shells (ESO 381-12, at a distance of ~80 Mpc). *Image credit: NASA, ESA, P. Goudfrooij (STScI). Right*: Example of a galaxy with tidal tails (ESO 415-19, at a distance of ~140 Mpc). *Image credit: ESA/Hubble & NASA, J. Dalcanton, Dark Energy Survey/DOE/FNAL/DECam/CTIO/NOIRLab/NSF/AURA.*

3.3.2 Formation and evolution in simulations

Isolated merger simulations have been an important avenue for simulating the formation and evolution of different types of tidal features. Early simulations were already able to show how shells are formed on rather radial mergers (Quinn 1984), streams are tidally disrupted with a leading and a trailing arm along their orbits around a galaxy (Oh et al. 1995), and tails are the relics of close encounters of galaxies (Toomre & Toomre 1972). These features have recently been examined more closely in high-resolution simulations (e.g., Amorisco 2015; Hendel & Johnston 2015; Karademir et al. 2019; Bílek et al. 2022) with the aim of better understanding their connection with the merger histories of galaxies. For instance, Karademir et al. (2019) was able to disentangle where the stars are deposited depending on the merger mass and impact parameter, and they confirmed that radial and non-radial orbits preferentially lead to shells and streams, respectively. Bílek et al. (2022) analyzed the extreme shell system of NGC 474 through isolated merger simulations, constraining the orbital configuration necessary to form the observed system.

Methods of identifying tidal features across large samples as in observational surveys have also been applied to cosmological simulations. The possibility of tracing back individual galaxies and their tidal features through time enables one to directly connect the LSB structures to the formation histories of galaxies: as predicted by isolated merger simulations, in the cosmological context shells also typically form through mergers on radial orbits (e.g., Pop et al. 2018). Investigating the survival timescales in addition to the origin of different tidal features, Mancillas et al. (2019) found that shells and streams survive longest (~4 and 3 Gyr, respectively) and tails are the shortest-lived features (~2 Gyr). Studies of the appearance of certain tidal features have also been performed in hydrodynamical cosmological simulations, such as for shells by Pop et al. (2018), who found that more massive galaxies are more likely

to have shells around them and that shells are typically created through infalling satellites with low orbital angular momenta. Blumenthal et al. (2020) studied the occurrence of tidal features in simulations in the context of interacting galaxies and reported that tidal features and disturbed morphologies are more likely to be observed around interacting pairs of galaxies. Vera-Casanova et al. (2022) found that the brightest stellar streams formed from early accretion events.

3.4 Scope of this Movement

As stellar structures orbiting their host galaxies, tidal features and satellite systems are important tracers for their hosts' accretion histories. While satellite systems present the galaxies currently being accreted onto the host, tidal features are the remnants of past accretion events, often involving gas-poor satellites. Cosmological simulations are an attractive way to study these structures in a statistical manner to provide predictions for the incoming wealth of observations in the far outskirts of galaxies. They further allow one to connect such present-day structures to their original properties before infall, and to investigate to what extent they are correlated with the inner host's properties, which are also the result of galaxy formation.

In this Movement, I present several studies investigating tidal features in the context of cosmological simulations and their comparison to observations. In Chapter 4, I first introduce a full census of all three types of tidal features as well as satellite planes and correlate them with the inner host galaxies' kinematics. In Chapter 5, I then discuss the results of two follow-up studies I significantly contributed to, which focused on the stellar populations of the simulated tidal features and connecting the features back to their progenitor galaxies. Finally, I present a brief summary of two subsequent works I contributed to in Chapter 6, where we analyzed the connection between tidal features and kinematics in observations, and where we investigated the presence of tidal features in different environments from several cosmological simulations.

4

Connecting Tidal Features to Kinematics

This chapter was published as Valenzuela & Remus (2024), A&A 686, A182[1]:
A stream come true: Connecting tidal tails, shells, streams, and planes with galaxy kinematics and formation history

The long relaxation timescales in the outskirts of galaxies allow the structures therein to survive for longer than in the inner regions, providing insights into the recent accretion history of galaxies. Faint structures such as tidal features and special satellite configurations such as satellite planes can be connected to past accretion events and even the larger-scale environment. A direct imprint of the formation history of a galaxy is also found in its kinematics. While late-type galaxies (LTGs) usually exhibit regular rotation patterns, early-type galaxies (ETGs) show a wide variety of rotational properties. A kinematic classification of ETGs was introduced by Emsellem et al. (2007, 2011) for the SAURON and ATLAS^{3D} surveys, where ETGs are split into fast and slow rotators, depending on how rotationally supported they are. These rotation patterns are closely related to the formation of the galaxy, and slow rotators usually indicate a more violent accretion history (e.g., Schulze et al. 2018, 2020; Lagos et al. 2022). Moreover, special kinematic features such as kinematically distinct cores (KDCs) have been shown to indicate specific formation pathways. For example, large, old KDCs are formed through minor and mini mergers, in which only the inner rotating old disk is preserved (Schulze et al. 2020),

[1]Minor adjustments have been made, and the introduction has been adapted for this thesis.

while small, young KDCs consist of stars that formed during major mergers with gas fractions of 15–40% (Hoffman et al. 2010) within the last 3–4 Gyr (Schulze et al. 2017). Prolate rotation patterns have been discussed to originate from excessive merging, often through radial orbits, but no clear singular formation pathway has been established for these galaxies so far (Ebrová & Łokas 2017; Hegde et al. 2022).

Between the outer faint structures and the inner kinematics, which each give a different view on the past of a galaxy, the question then arises how these may be correlated and what further insights the combination of the two reveals. While tidal features typically indicate ongoing or past encounters and mergers with other galaxies, many galaxies still reside in the outskirts of the host galaxy, forming its satellite population. These are expected to eventually merge with the central galaxy in the future, potentially forming tidal features in the process. Therefore, these satellites are reservoirs for future tidal features. In this paper, we are also interested in the question whether the appearance of tidal features is influenced by the infall of satellite galaxies being isotropic or anisotropic, that is, whether they are more common around galaxies whose satellites are aligned in planes.

As both the internal kinematics and the faint structures found in the outskirts of galaxies are remnants of their formation history, we investigate the correlation between these two tracers in simulations and observations in this work. We consider features related to interactions and mergers with other galaxies and their remnants, that is, tidal features, and also satellite planes. We first introduce the simulations and observations in Section 4.1, followed by the details of our methods and the definition of the relevant properties in Section 4.2. Finally, the results are presented and discussed in Section 4.3, and we conclude in Section 4.4.

4.1 Simulations and observations

4.1.1 The Magneticum Pathfinder simulations

The galaxies classified in this work were extracted from the Magneticum Pathfinder[2] simulation suite (Dolag et al., in prep.), which consists of hydrodynamical cosmological simulations performed with Gadget-3, an extended version of Gadget-2 (Springel 2005; for details of the implementations, see Teklu et al. 2015). In particular, we used Box4 (uhr) (side length: 68 Mpc, with a stellar particle mass $\langle m_* \rangle = 1.3 \times 10^6\,\mathrm{M}_\odot\,h^{-1}$ and a softening length $\epsilon_* = 1\,\mathrm{kpc}$). Galaxies were identified using a modified version of SubFind adapted for baryonic matter (Springel et al. 2001; Dolag et al. 2009).

The galaxies from Magneticum Box4 (uhr) have been shown to agree well with observations, including their angular momenta (Teklu et al. 2015), kinematics (Schulze et al. 2018; van de Sande et al. 2019; Schulze et al. 2020), dynamics (Remus et al. 2017; Teklu et al. 2017; Harris et al. 2020), and their in situ component fractions (Remus & Forbes 2022).

In this work, we included all main galaxies with virial masses $M_{\mathrm{vir}} \geq 7.1 \times 10^{11}\,\mathrm{M}_\odot$ and stellar masses $M_* \geq 2.4 \times 10^{10}\,\mathrm{M}_\odot$ to ensure a sufficient resolution for identifying stellar tidal

[2] www.magneticum.org

features. Additionally, we limited the sample to galaxies with stellar half-mass radii larger than 2 kpc, that is, twice the stellar softening length (following Schulze et al. 2018). The resulting sample consists of 520 galaxies. Their ellipticities and λ_{R_e}-values (a 2D projected proxy for the angular momentum within the effective radius, R_e; see Section 4.2.3 for more details) at one half-mass radius were taken from Schulze et al. (2018) and the satellite plane properties were adopted from Förster et al. (2022). For more details of these properties, we refer to the original papers.

4.1.2 The MATLAS sample

The observational comparison sample was taken from the MATLAS survey (introduction by Duc et al. 2015; the full sample was presented by Bílek et al. 2020; the dwarf galaxy sample was presented by Habas et al. 2020), which includes 177 massive ETGs with deep optical images. The MATLAS sample is part of the ATLAS^{3D} sample (Cappellari et al. 2011), which comprises 260 nearby galaxies (<42 Mpc) as a complete volume-limited sample. The MATLAS sample contains all ATLAS^{3D} galaxies that do not belong to the Virgo cluster and are not located near bright stars.

Specifically, we used the results obtained by Bílek et al. (2020) for the tidal features around the 177 MATLAS galaxies, where tidal shells, streams, and tails were visually identified, and we used the identifications of satellite planes from Heesters et al. (2021). The ellipticities and λ_{R_e} values at one effective radius were taken from Emsellem et al. (2011).

4.2 Methods and definitions

For the comparison between the simulated and observed galaxies, we introduce in the following the different features and properties we used. These include the tidal features we classified, the method with which the satellite planes were identified, and the distinction between fast and slow rotators.

4.2.1 Tidal features: Shells, streams, and tidal arms

The three types of tidal features we considered are shells, streams, and tails. Examples of each feature are shown in Figure 4.1. They indicate past or ongoing gravitational interactions with other galaxies. Shells appear as circular arcs centered around a galaxy (top panel of Figure 4.1). They have sharp outer borders and are thought to form through the radial infall and disruption of (massive) satellites (e.g., Quinn 1984; Pop et al. 2018; Karademir et al. 2019; Bílek et al. 2022). Streams are thin slivers of stars around the host galaxy (middle panel of Figure 4.1) that are formed through the tidal disruption of an infalling galaxy on a circular orbit (e.g., Karademir et al. 2019; Tutukov et al. 2021). Tails are stellar arms that are stripped from the host galaxy (bottom panel of Figure 4.1). They are the result of tidal interaction with another galaxy, where the interaction is either ongoing or occurred recently, up to 2 Gyr ago (Mancillas et al. 2019).

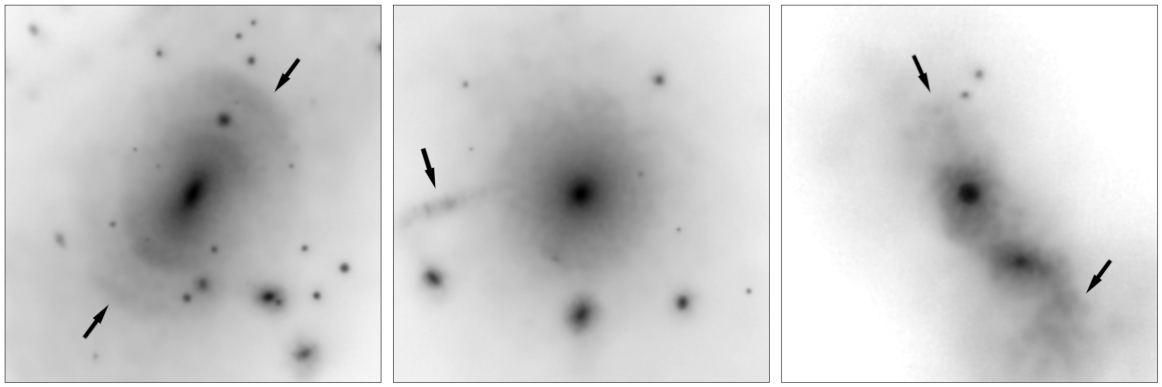


Figure 4.1: Mock images of simulated galaxies from Magneticum Box4 (uhr) with prominent tidal features: Shells (right; the outer two shells are marked), a stream (center), and tails (left). The mock images were created with the software from Martin et al. 2022 for the r band.

We classified the galaxies in Magneticum with respect to the existence of these tidal features by visual inspection of the 3D stellar component to find any sufficiently prominent features independent of their orientation and possible projection effects. Similar to the classification of Bílek et al. (2020) for the MATLAS sample, many people visually classified the galaxies, and no detection algorithm was used. A key difference between the classification methods is that the simulated galaxies were viewed in 3D, whereas the observations of the MATLAS galaxies only provide data for one projection. We opted for this approach to use the full potential of the simulation and find the actually existing tidal features around the simulated galaxies to obtain results independent of projection because Pop et al. (2018) found, for example, that the shells of only 40% of the galaxies with shells are visible in all three considered projections, whereas most shells are only visible in two projections. By performing the classification in 3D, we aimed to find all tidal features, which enabled us to investigate the underlying connection of the features with the formation history and especially galaxy kinematics. The comparison to observations is intended to determine whether the same trends are found in observations. The comparison is not intended as a verification of the simulation. A verification like this has already been shown in previous studies, especially for the kinematics (Teklu et al. 2015; Schulze et al. 2018, 2020).

Seven scientists (two of which are experienced scientists in galaxies and their dynamics, while the other five were instructed through observed examples about the look of the different tidal features) participated in the classification, for which they were presented with a 3D rendering of a given galaxy that was rotated to be viewed from all sides. The local environment around the individual galaxies was visible as well. The classification was performed independently by the participants. Each person stated whether they identified any tidal shells, streams, and tails, or no features. Analysis of the classifications did not result in a significant difference between the classifications of the experienced and less experienced scientists. One difference to point out is that the more experienced scientists found that more galaxies had streams. However, this difference was negligibly small.

In the following, we consider a galaxy to have a given tidal feature if at least half of the participants were in favor of this. For the MATLAS classification by Bílek et al. (2020), this

is considered to be the case if the classification score is at least 1 (the maximum score for them is 2, where 1 means that the respective feature is likely to be present).

We did not emulate a surface brightness limit cut for the simulations in this study. We refrained from this approach for the following reason: First, we would have had to introduce a model to obtain luminosities from the simulated masses, which has its own set of uncertainties, especially as we wished to make the comparison based on the true 3D findings from the simulations, as discussed above. Furthermore, the intrinsic mass resolution of the simulation results in a surface brightness limit that by chance is similar to that of the MATLAS survey when a constant mass-to-light ratio is assumed (see also Remus & Forbes 2022 for more details of surface brightness comparisons for the simulation). While this should be kept in mind, we therefore do not consider the comparability to be an issue given the fortunate similarity between the simulation resolution and the surface brightness limits of the MATLAS survey.

4.2.2 Satellite planes

We considered a galaxy to have a satellite plane when at least 80% of its satellite galaxies build a plane with a thickness $\leq 0.2\, R_{\rm vir}$ and when the in-plane angular momentum makes up at least 90% of their total angular momentum. These properties were computed through the momentum in the thinnest plane (MTP) method (Förster et al. 2022).

4.2.3 Fast and slow rotators, and kinematic classes

To distinguish fast from slowly rotating ETGs, we followed the approach taken by Emsellem et al. (2011). They determined an empirical cut in the λ_{R_e}-ϵ_e plane, where ϵ_e is the ellipticity at the effective radius. The λ_R value was introduced by Emsellem et al. (2007) as part of the SAURON project, defined as

$$\lambda_R = \frac{\langle R|V|\rangle}{\left\langle R\sqrt{V^2+\sigma^2}\right\rangle}, \tag{4.1}$$

with the projected radius R, the line-of-sight velocity V, the line-of-sight velocity dispersion σ, and the flux-weighted averages $\langle\cdot\rangle$. The adaptation for simulations, where no fluxes but only the masses M are available, requires $\langle\cdot\rangle$ to be the mass-weighted averages over the quantities (e.g., Jesseit et al. 2009; Naab et al. 2014; Schulze et al. 2018), assuming a constant mass-to-light ratio (see Schulze et al. 2018 for more details). As defined by Emsellem et al. (2011), galaxies that fulfill $\lambda_{R_e} > 0.31\sqrt{\epsilon_e}$ are classified as fast rotators, and all other galaxies are classified as slow rotators.

We obtained these parameters for the simulated galaxies from the simulation for the edge-on projections of the galaxies because this maximizes the λ_{R_e} values, and thus, the full kinematic properties are best identified. The distribution of λ_R-ϵ using random projected values are, however, comparable to observations, as shown by Schulze et al. (2018) and van de Sande et al. (2019), who not only compared the simulation to observations from SAMI and ATLAS^{3D}, but also to other cosmological simulations.

Galaxies were further classified based on their kinematic patterns within the half-mass radius. The classes used for this study are regular rotators, nonrotators, KDCs, and prolate rotators, based on the classifications from Schulze et al. (2018). These classes are similar to those presented by Krajnović et al. (2011) for ATLAS^{3D} galaxies, with the addition of the prolate rotators as an individual class, while the KDCs encompass all galaxies with separate cores independently of the outer rotation pattern.

4.2.4 Morphological classes

The galaxies from Magneticum were subdivided into morphological types using the classification from Teklu et al. (2017) based on the b value (Teklu et al. 2015), which is a good proxy for distinguishing LTGs from lenticular galaxies and ETGs (Romanowsky & Fall 2012; Teklu et al. 2015). The parameter is based on the location of the galaxies in the stellar mass-stellar angular momentum plane and has been shown to successfully determine the morphological galaxy types in simulations (e.g., Teklu et al. 2017; Schulze et al. 2018; Emami et al. 2021). We distinguished between clear disk galaxies (LTGs), clear elliptical galaxies (ETGs), and intermediate galaxies. The latter mostly contain S0-like galaxies and are thus often associated with ETGs. In this work, we treated them separately because the formation pathways of S0 galaxies can differ from those of typical elliptical galaxies and are still debated.

4.3 Results

4.3.1 Feature statistics and mass, morphology, and size

When the galaxies with a given tidal feature are highlighted in the mass-size relation, all three types of tidal features occur at all sizes and masses, with a clear preference for larger and more massive systems (first three panels of Figure 4.2), that is, the fraction of galaxies with tidal features increases with stellar mass (Figure 4.3). The figure also shows that the given mass bins have a larger fraction of galaxies with shells in MATLAS than in Magneticum, even though the MATLAS sample does not include the most massive galaxies with $M_* > 5.5 \times 10^{11}\,\mathrm{M}_\odot$, and thus, the highest-mass bin cannot be compared to MATLAS. The lowest-mass bin also includes relatively more streams and tails in MATLAS galaxies. Similarly, relatively more MATLAS galaxies have any one type or multiple types of tidal feature around them than in Magneticum. To cover the high-mass end, we included the tidal feature measurements around brightest cluster galaxies (BCGs) by Tal et al. (2009) and Kluge et al. (2020). The observations of Tal et al. (2009) for shells around BCGs are consistent with the simulated fraction in the highest-mass bin, while the observations from Kluge et al. (2020) are lower bounds for the fractions of shell and stream galaxies because of the large distance to their observed BCGs (see Kluge et al. 2020). Simulations and observations both indicate that tidal features are generally more common around more massive galaxies, and multiple features are the most common around BCGs.

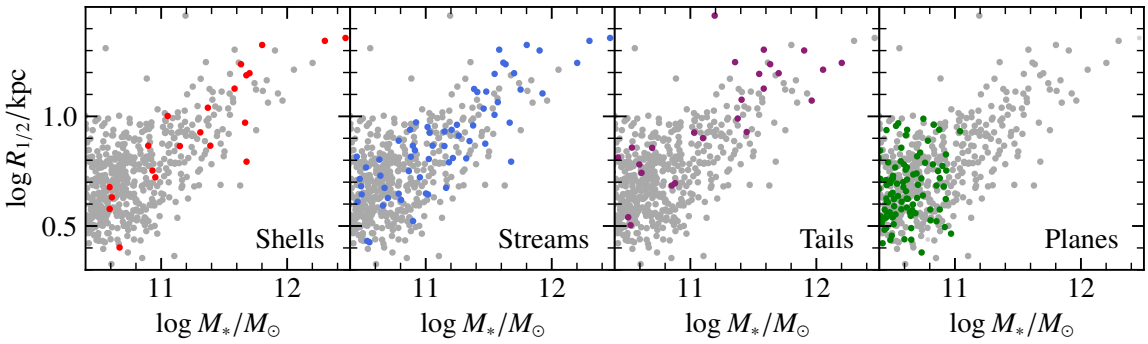


Figure 4.2: Mass-size relation of the Magneticum galaxy sample. Galaxies are classified as having tidal features or satellite planes in color.

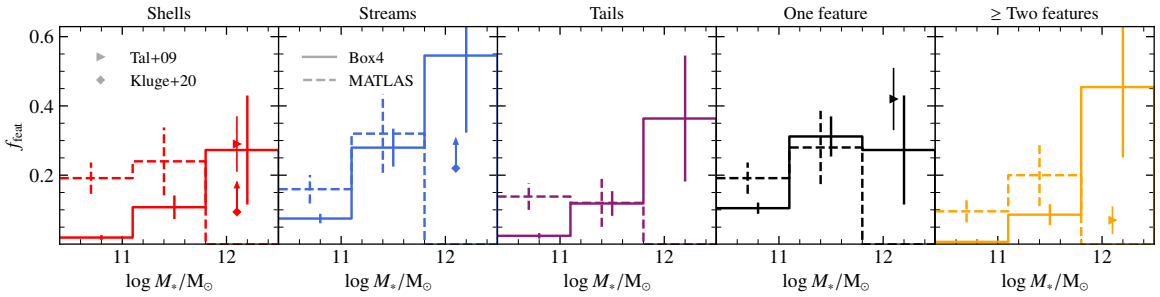


Figure 4.3: Fraction of galaxies with a given tidal feature (first three panels), any of the three tidal feature types (fourth panel), or a combination of multiple different types of features (fifth panel), $f_{\rm feat}$, in three stellar mass bins for Magneticum, MATLAS (Bílek et al. 2020), and for brightest cluster galaxies (BCGs) from Tal et al. (2009) and Kluge et al. (2020). The masses for MATLAS galaxies are taken from the dynamical masses obtained by Cappellari et al. (2013), which roughly correspond to the stellar masses. The vertical lines indicate the 1σ uncertainties.

When only galaxies with stellar masses $M_* \geq 10^{11}\,\mathrm{M}_\odot$ are considered, about 10% to 30% have a given tidal feature (see Table 4.1). Streams are by far the most common of these tidal features, while shells and tails are found with similar frequencies. The occurrence of shells in (11 ± 3)% of the Magneticum galaxies agrees within the uncertainty limits with 12% from Atkinson et al. (2013), who used a different stellar mass range and somewhat different categories (see the discussion by Bílek et al. 2020), and (17 ± 7)% from Bílek et al. (2020) for MATLAS (for the same stellar mass cut of $10^{11}\,\mathrm{M}_\odot$), but the uncertainty range does not reach the lower limit of (18 ± 3)% from Pop et al. (2018) for the Illustris simulation. The fraction of galaxies with streams in Magneticum ((29 ± 5)%) is consistent with the (25 ± 9)% found for MATLAS. Finally, the fraction of galaxies with tails in Magneticum ((12 ± 4)%) is larger than that in MATLAS ((6 ± 4)%), although the values are consistent within the uncertainty limits. Overall, the abundance of stellar tidal features found in the Magneticum Box4 simulation for the galaxies with higher stellar masses is consistent with previous findings.

The numbers of galaxies in each morphological class containing tidal features are listed in Table 4.2. While shells preferentially occur around ETGs, streams are found to be equally likely in all three types, and tails are more likely in intermediate galaxies and LTGs, although the uncertainty ranges overlap in the latter case. Because a number of galaxies feature multiple tidal structures in their outskirts, we also determined the fraction of galaxies that contains at

Table 4.1: Number and fraction of galaxies with a type of tidal feature.

Feature	Number	Fraction
Shells	14	$(11 \pm 3)\%$
Streams	38	$(29 \pm 5)\%$
Tails	16	$(12 \pm 4)\%$

Notes. Only the galaxies with stellar masses $M_* \geq 10^{11}\,M_\odot$ were considered for the numbers and fractions. The total number of galaxies analyzed in this mass range is 131.

Table 4.2: Numbers and fractions of ETGs, intermediates (Intm.), or LTGs with shells, streams, tails, or satellite planes.

Type	All	Shells	Streams	Tails	Planes
ETGs	295	17	37	9	49
		$(6 \pm 2)\%$	$(13 \pm 3)\%$	$(3 \pm 2)\%$	$(17 \pm 3)\%$
Intm.	172	4	20	12	37
		$(2 \pm 2)\%$	$(12 \pm 3)\%$	$(7 \pm 3)\%$	$(22 \pm 4)\%$
LTGs	53	0	5	5	14
		$(0 \pm 2)\%$	$(9 \pm 5)\%$	$(9 \pm 5)\%$	$(26 \pm 8)\%$

Notes. The full classified sample of 520 galaxies is considered for the numbers and fractions. The morphological classes of the galaxies were taken from Teklu et al. (2017).

least one type of tidal feature (shells, streams, or tidal arms): $(18 \pm 3)\%$ of ETGs, $(17 \pm 4)\%$ of intermediate type galaxies, and $(17 \pm 6)\%$ of LTGs. Overall, the fractions of LTGs ($(2 \pm 2)\%$) are similar, with multiple types of tidal feature as for intermediate-type galaxies ($(3 \pm 2)\%$) and ETGs ($(3 \pm 2)\%$).

For the satellite planes, we find that only galaxies with stellar masses $\lesssim 10^{11}\,M_\odot$ are surrounded by thin planes of satellites. This is consistent with the results from Förster et al. (2022), who found that the more massive systems lack thin planes. We find indications that planes are slightly more common around LTGs ($(26 \pm 8)\%$) than ETGs ($(17 \pm 3)\%$), with the intermediate galaxies in between ($(22 \pm 4)\%$). This does not reflect the findings for tidal features and clearly shows that the appearance of satellite planes is not directly connected to the appearance of tidal features. This shows that tidal features do not depend on the large-scale inflow field, but rather on the orbits and mass ratios of the infalling satellites.

The fraction of galaxies with a plane of satellites of the galaxies with certain tidal features shows a consistent behavior between the simulation and observations (Figure 4.4). The largest difference is found for galaxies with shells, where there is an indication that more observed shell galaxies are surrounded by satellite planes. There is also an indication that the fraction of galaxies without features (last vertical bar) surrounded by a satellite plane is larger than for galaxies with tidal features (first four bars). This means that there may be a slight preference for satellite planes to occur around galaxies without tidal features. The same slight trend is also found when we compare the fraction of galaxies with any type of tidal feature for galaxies with satellite planes versus galaxies without satellite planes: $(13 \pm 4)\%$ of the simulated galaxies ($(25 \pm 9)\%$ for observed galaxies) with a satellite plane have at least one type of tidal

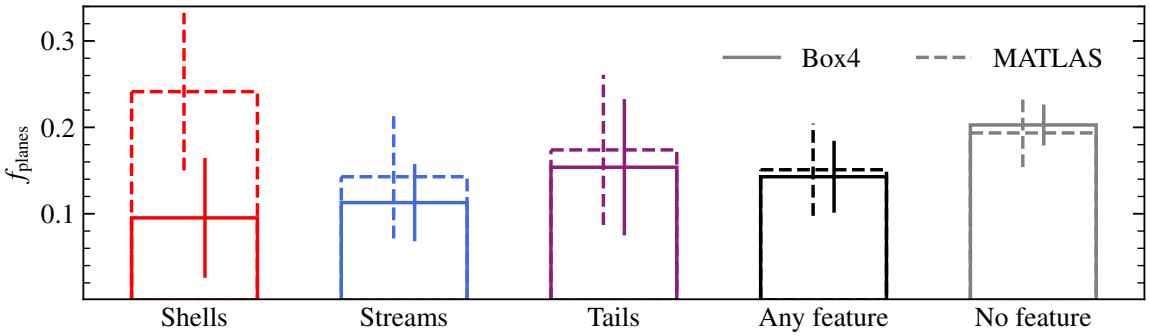


Figure 4.4: Fraction of galaxies with a satellite plane for different types of galaxies in Box4 (uhr) (Förster et al. 2022) and MATLAS (Bílek et al. 2020; Heesters et al. 2021): galaxies with shells, streams, tails, at least one of these features, and with none of these features. The vertical lines indicate the 1σ uncertainties.

feature, while $(19 \pm 3)\%$ ($(31 \pm 5)\%$) of the galaxies without a satellite plane have at least one type of tidal feature.

4.3.2 Correlations of tidal features and satellite planes with kinematic classes

Using the kinematic classification for the simulated galaxies from Schulze et al. (2018) as described in Section 4.2.3, we determined the numbers and fractions of galaxies with the different kinematic classes that have the respective tidal features or a satellite plane (Table 4.3). In the table, we combined the distinct core (DC) and KDC classes into a single class of KDCs (as also done by Valenzuela et al. 2024a; Remus et al., in prep.). The trend emerges that regular rotators are less likely to have tidal features, with the exception of tidal tails, which are found at a similar fraction around nonrotators and regular rotators. In contrast, nonrotators and especially prolate rotators have higher overall fractions of shells and streams than regular rotators, although the uncertainty limits overlap in part due to low number statistics.

We again determined the fraction of galaxies that contains at least one type of tidal feature (shells, streams, or tidal arms): $(12 \pm 3)\%$ of regular rotators, $(19 \pm 5)\%$ of nonrotators, $(27 \pm 11)\%$ of KDCs, and $(44 \pm 17)\%$ of prolate rotators. The much higher fraction of prolate rotators with at least one type of tidal feature compared to any single given feature shows that they are more likely to contain multiple tidal features in their outskirts, whereas the overlap of different types of features around a galaxy is less pronounced for the other kinematic classes.

These results agree with those from Ebrová et al. (2021), who found that a large fraction of observed prolate rotators are surrounded by multiple shells, and all of them show signs of interactions. Their determined fraction of 10 out of 19 systems ($(53 \pm 17)\%$) is significantly higher than the 3 out of 16 Magneticum galaxies ($(19 \pm 11)\%$). However, when we consider only the simulated prolate galaxies with stellar masses of $\geq 10^{11}\,\mathrm{M}_\odot$, which all but one of the galaxies considered by Ebrová et al. (2021) satisfy (but only 9 of our 16 galaxies), we find that 3 out of 9 galaxies have shells ($(33 \pm 20)\%$), which is consistent within the uncertainty limits

Table 4.3: Numbers and fractions of galaxies, with the given kinematic class having shells, streams, tails, or satellite planes.

Type	All	Shells	Streams	Tails	Planes
RR	286	2	26	8	63
		$(1 \pm 1)\%$	$(9 \pm 2)\%$	$(3 \pm 1)\%$	$(22 \pm 3)\%$
NR	108	10	16	2	19
		$(9 \pm 3)\%$	$(15 \pm 4)\%$	$(2 \pm 2)\%$	$(18 \pm 5)\%$
KDC	26	1	6	2	1
		$(4 \pm 4)\%$	$(23 \pm 10)\%$	$(8 \pm 6)\%$	$(4 \pm 4)\%$
PR	16	3	3	2	2
		$(19 \pm 11)\%$	$(19 \pm 11)\%$	$(13 \pm 9)\%$	$(13 \pm 9)\%$

Notes. Only the subset of our full sample that was kinematically classified by Schulze et al. (2018) was considered for the numbers and fractions. This subsample comprises 436 galaxies. The kinematic classes include regular rotators (RR), nonrotators (NR), KDCs, and prolate rotators (PR).

with the observed fraction of 9 out of 18 from that study ($(50 \pm 17)\%$). This reflects the mass trend for shells to be more common around more massive galaxies.

Of all kinematic classes, KDCs show the strongest probability of exhibiting a certain tidal feature, driven by the stream feature. The fact that almost every fourth KDC has streams in its outskirts is consistent with many KDCs having decreasing λ_R profiles at radii larger than the half-mass radius, which is usually caused by merger histories dominated by small mergers (Schulze et al. 2020). Kinematically distinct cores with these radial λ_R profiles are remnants of old disks that have assembled their outskirts by multiple minor mergers on mostly circular orbits (Schulze et al. 2020). When we traced the six simulated KDC galaxies with streams back until redshift $z = 1$, all of these galaxies had only grown in mass through mini and minor mergers. Therefore, this connection between the appearance of a stream and a KDC feature is a good indicator that the particular KDC was likely formed through the multiple merger scenario and not through the gas-rich recent major merger scenario, which is the other known formation pathway for KDCs (Hoffman et al. 2010; Schulze et al. 2017).

Finally, satellite planes again show the opposite behavior of tidal features. They are most common around regular rotators and least common around KDCs and prolate rotators. This shows that the alignment of satellite galaxies in a plane is not connected to the appearance of these features or might possibly even be anticorrelated (as shown in Figure 4.4).

4.3.3 Correlations of tidal features and satellite planes with the inner rotational support

We investigated the correlation between two known tracers of the accretion history of a galaxy, the appearance of tidal features, and the internal galaxy kinematics. To measure the latter, we used the position of galaxies in the λ_{R_e}-ϵ_e plane for both the observed and simulated galaxies (top and bottom of Figure 4.5, respectively). The values of λ_{R_e} and ϵ_e of the observed galaxies were obtained from a random projection, while the simulated values are the highest possible

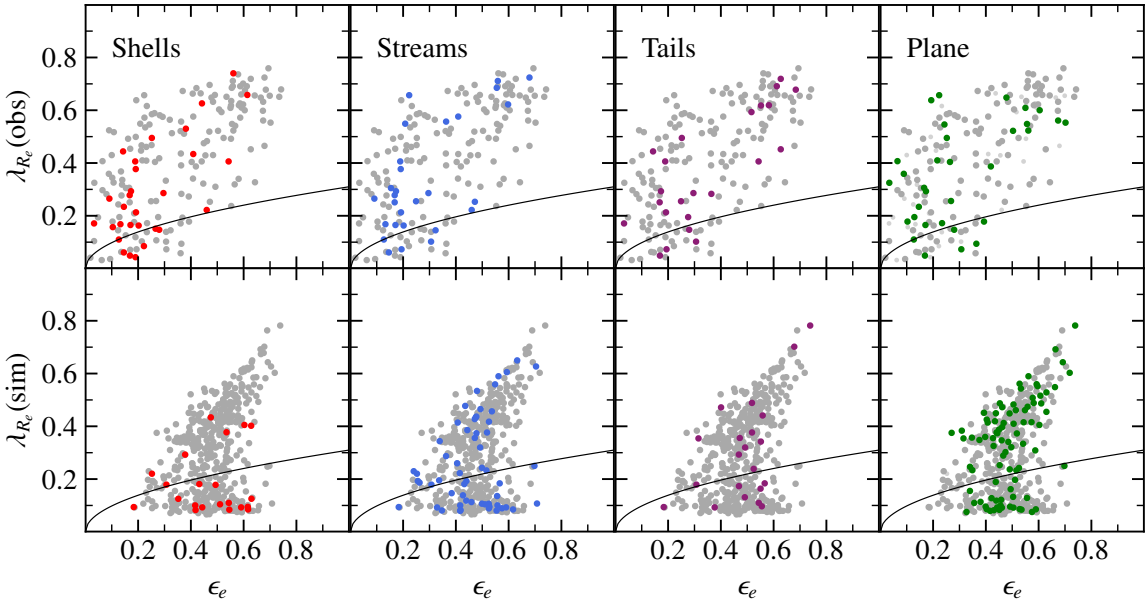


Figure 4.5: Galaxies classified as having tidal features or a satellite plane in the λ_{R_e}-ϵ_e plane in the MATLAS survey (*top row*) and in Magneticum Box4 (*bottom row*). Only the ETGs and intermediate-type galaxies are shown for the simulated sample. The colored data points represent galaxies with the respective feature. The large gray dots were classified as lacking the respective feature, and small gray dots were not classified (only the case for the observed satellite planes). The values of λ_{R_e} and ϵ_e were determined at one effective radius for the observations and at one half-mass radius for the simulations. For the simulations, they were determined in the edge-on projection. The solid black lines indicate the border between fast and slow rotators (Emsellem et al. 2011), with fast rotators lying above the border. The measurements of shells, streams, and tails of MATLAS galaxies are taken from Bílek et al. (2020) and the measurements of the planes are taken from Heesters et al. (2021).

values because they are obtained from the edge-on projections (for the projection effects found in this λ_{R_e}-ϵ_e space, see also the results from Cappellari et al. 2007). To do this, we limited the simulated sample of galaxies to ETGs and intermediate-type galaxies because the MATLAS sample does not contain LTGs. At first glance, there are no clear differences between the distributions of galaxies with tidal features and the total sample for the observations and simulations. The trend of shells lying around slow rotators is immediately visible only for the simulated galaxies. Similarly, the galaxies with satellite planes are uniformly distributed and do not show any preference for slow or fast rotation, or for particularly round or elongated shapes (right panel of Figure 4.5).

The differences between the edge-on and random projection of galaxies in the λ_{R_e}-ϵ_e plane were discussed in detail by Schulze et al. (2018), especially with respect to the ellipticity, ϵ_e, clearly showing the problems when comparing ellipticities between simulations and observations. In contrast, λ_{R_e} is more directly comparable because its values change only slightly for most projections, except when seen nearly face on. Thus, we determined the cumulative histograms of λ_{R_e} for the total simulated and observed galaxy samples, and for the galaxies with the respective tidal features or satellite planes (Figure 4.6). Because the λ_{R_e} distributions of the full samples are not identical (leftmost panel), a direct comparison between

the λ_{R_e} distributions of galaxies with a certain tidal feature requires a correction to the values in the cumulative histograms. The method for this correction is described in Chapter A.

By adapting the simulated cumulative histograms to the observed parent distribution, the colored lines in Figure 4.6 are directly comparable with each other. For the following comparisons, we used the two-sample Kolmogorov–Smirnov test with the null hypothesis that the underlying distributions of two random samples are the same. Very similar distributions of λ_{R_e} are found for galaxies with a given tidal feature in the simulations and observations (p-values[3] of 0.07, 0.32, 0.91, and 0.23 for shells, streams, tails, and planes, respectively).

For individual tidal features, we find a very clear trend that shells are mostly found around slow rotators, both in the simulation and in observations (p-values of 0.014 and 0.008 for Box4 and MATLAS, respectively, when comparing the tidal feature λ_{R_e} distributions to the simulated or observed total sample distributions). Streams have a slight preference to appear around slow and intermediate rotators, but this is only statistically significant here for the observations (p-values of 0.23 and 0.02 for Box4 and MATLAS, respectively). Tidal tails are found around both slow and fast rotators with similar probabilities (p-values of 0.84 and 0.39 for Box4 and MATLAS, respectively). The overall trends agree with the findings of Bílek et al. (2023), who determined a negative correlation between tidal features and rotational support. A direct comparison is not possible, however, because the definitions of rotational support differ.

The same is also true for the satellite planes: Planes are found equally around galaxies with any amount of rotational support in both Magneticum and MATLAS (p-values of 0.09 and 0.59 for Box4 and MATLAS, respectively). While Heesters et al. (2021) stated that 40% of their slow rotators featured satellite planes and only 16% of the fast rotators do this, they also remarked that these results are not that statistically significant given the small number of slow rotators in the sample. Even though the satellite planes are detected through entirely different methods, with the observed planes being determined from 2D data (Heesters et al. 2021) and the simulated planes from 3D data, it can be expected that the general correlation of the existence of such planes with the internal kinematics of galaxies would be found to be similar between observations and simulations. This is precisely what we have found between Box4 and MATLAS galaxies.

The result that shells are more common around slow rotators suggests that the processes leading to low rotational support and the appearance of shells are related. Shells have been found to originate from radial merger events, which are more pronounced the more similar the two merging galaxies are in mass (e.g., Amorisco 2015; Pop et al. 2018; Karademir et al. 2019). Slow rotators are found to often have formed through merger events, in which a large amount of mass has been accreted over a short period of time, most commonly through (major) merger events with mass ratios higher than 1:10 (e.g., Schulze et al. 2018; Lagos et al. 2022). Therefore, the existence of a shell strongly indicates that the observed slow rotator formed through a recent radial merger event with a mass ratio higher than 1:10. When we trace the

[3]For the Kolmogorov–Smirnov test, the p-value is the probability that two samples were drawn from the same underlying distribution, the null hypothesis. This means that the underlying distributions can be concluded to be different for p-values below 0.05 (by convention).

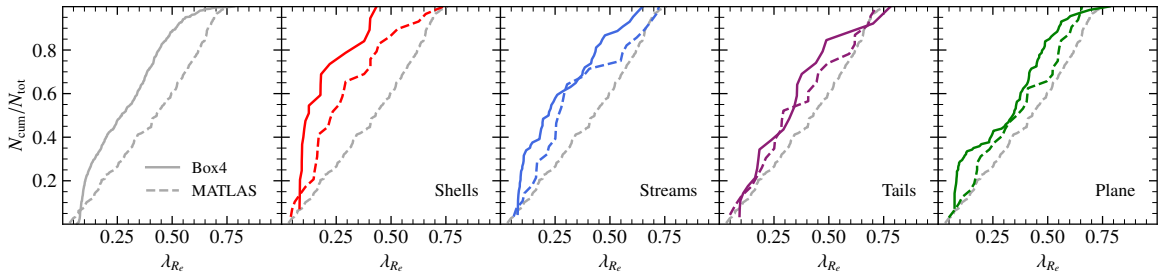


Figure 4.6: Cumulative histograms of λ_{R_e} for the galaxies in the MATLAS survey (dashed lines) and in Magneticum Box4 (uhr) (solid lines). Only the ETGs and intermediate-type galaxies were considered for the simulated sample. The first plot shows the difference in the distributions between observations and simulations. The cumulative histograms of the simulated galaxies in the other four panels were adapted to match the parent distribution of MATLAS to be directly comparable to the distributions of the MATLAS survey. The colored lines lying above the dashed gray line (the overall distribution of the MATLAS survey) indicate an increased presence of the respective tidal feature or satellite plane for galaxies with lower rotational support compared to those with higher rotational support. The measurements of shells, streams, and tails of MATLAS galaxies are taken from Bílek et al. (2020), and the measurements of the planes are taken from Heesters et al. (2021).

formation history of the slow rotators with shells back in the simulation, only 2 out of the 21 simulated galaxies with shells lack mergers above a mass ratio of 1:10 occurring within the past 4 Gyr (the lifetime of shells as estimated by Mancillas et al. 2019). In seven cases ((33 ± 13)%), the major merger that created the shells also led to a sudden strong decrease in λ_{R_e}, such that a previous fast rotator was converted into a slow rotator. These slow rotators seem to have particularly late formation times, while the other slow rotators with shells have had a low value of λ_{R_e} for more than 4 Gyr, six of which became slow rotators already by $z = 2$. This shows that most galaxies in the simulation with shells became slow rotators at early times, in agreement with Bílek et al. (2023), whereas roughly one-third of them just became slow rotators at the same time as the shells were formed. Thus, in all cases where the progenitor galaxy was a fast-rotating galaxy 4 Gyr ago, the major merger that formed the shells also destroyed the inner rotation pattern of the galaxy.

As an example, Figure 4.7 shows the evolution of the most massive galaxy from our sample of galaxies with shells. The orbit of the infalling galaxy that triggered the formation of the shells is shown in red in the first row. The shells found around this galaxy were formed through a satellite with a stellar mass ratio of 1:2.5 falling in radially at $z = 0.20$ (almost 2.5 Gyr ago), then falling back in again on the other side at $z = 0.13$ (1.7 Gyr ago). The back-and-forth movement led to the double shell structure found on two sides of the galaxy at $z = 0.07$ (0.9 Gyr ago). This clearly supports the idea that shells form through mergers on radial orbits. In the second row of Figure 4.7, the velocity maps are shown. The system is transformed from a fast-rotating galaxy with $\lambda_{R_e} = 0.36$ to a slowly rotating galaxy with $\lambda_{R_e} = 0.09$ during the merger. Because these values are computed for the edge-on projection of the galaxy instead of the shown projection, the transformation into a slow rotator is physical. Finally, the last row shows the velocity dispersion, which overall increases through the merger and also contributes to decreasing the value of λ_{R_e}. Remarkably, the shells seen around the galaxy in the first row can also be clearly identified in the velocity dispersion maps, best seen

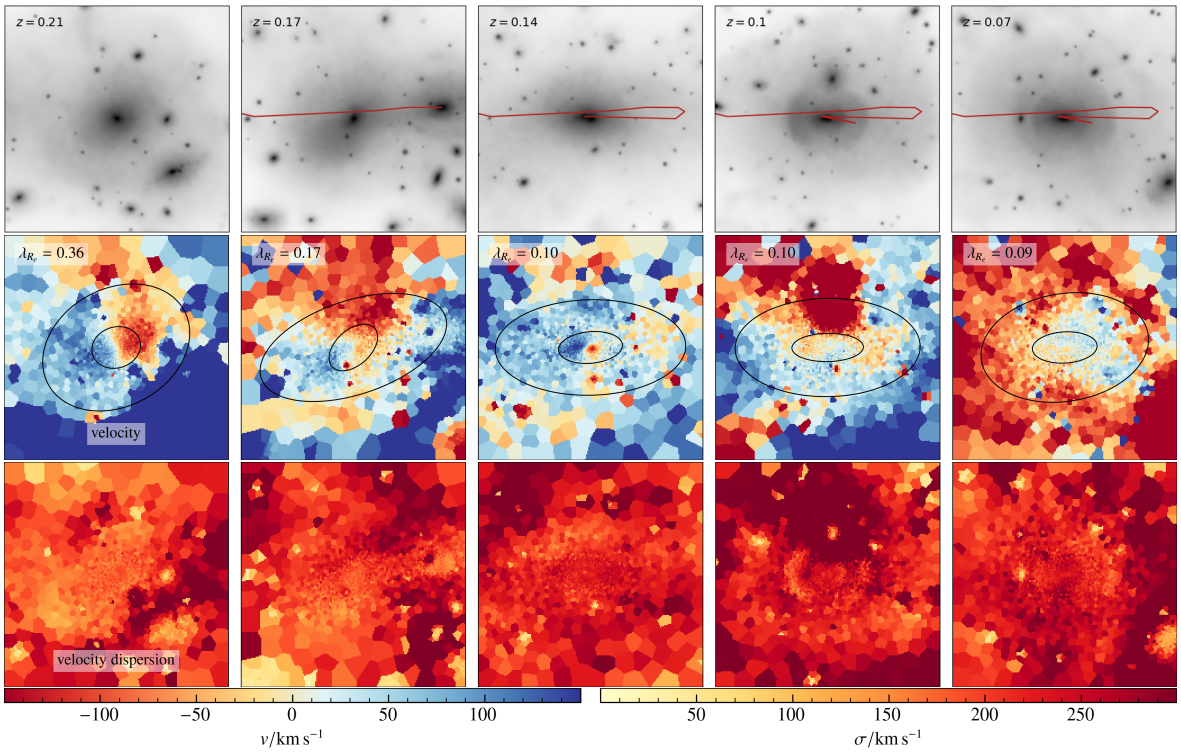


Figure 4.7: Evolution of the first example galaxy from Figure 4.1. The shells develop after a massive radial merger event, which also causes the value of λ_{R_e} to sharply drop and converts the galaxy into a slow rotator (where λ_{R_e} is measured from the edge-on projection). *Top*: Mock images of the stellar component from a projection in which the shells are especially clearly visible. The red lines trace the orbit of the infalling galaxy until the respective point in time. *Middle*: Velocity maps. The circles indicate the ellipses at one and three half-mass radii. *Bottom*: Velocity dispersion maps.

in the map at $z = 0.1$ as regions of comparably low velocity dispersion. This indicates that the kinematic studies of the outskirts of galaxies may be used to identify shells, for example, through tracer populations such as planetary nebulae (e.g., Roth et al. 2021).

4.4 Conclusion

We classified galaxies from the Magneticum Box4 (uhr) simulation with stellar masses above $2.4 \times 10^{10}\,\mathrm{M}_\odot$ according to the existence of tidal features in their outskirts and used data of satellite planes from Förster et al. (2022) to connect their appearance to the internal kinematics of the host galaxies. We compared the results to those from Bílek et al. (2020) and Heesters et al. (2021) for the MATLAS survey and observations of BCGs by Tal et al. (2009) and Kluge et al. (2020). The internal kinematic properties were taken from Schulze et al. (2018) and cover both overall rotational properties quantified by the λ_R parameter (Emsellem et al. 2011) and internal kinematic patterns such as regular rotation, nonrotation, prolate rotation, and KDCs.

The fractions of Magneticum galaxies with shells, streams, and tails are comparable to those reported in observations and other simulations. Streams are found to be the most common of these features, with 29% of galaxies above a stellar mass of $10^{11}\,\mathrm{M}_\odot$ exhibiting streams. We also see a clear trend with mass, with all types of features being more common

around galaxies with higher stellar masses, in agreement with results from observations. Galaxies with more than one type of feature are also much more frequent at high stellar masses, indicating a much more turbulent accretion history for more massive galaxies. This agrees well with previous studies (e.g., Remus & Forbes 2022).

Additionally, we find indications that tidal features are more common around early-type galaxies than late-type galaxies for shells and streams. No shells were found for late-type galaxies, while tails are most frequently found for disk-like galaxies and are rather rare around spheroidal galaxies. This agrees well with the current scenario in which shells are formed during massive radial merger events that would also destroy the disk of a galaxy, while streams can occur around all types of galaxies as they are remnants of disrupted galaxies that fell in on circular orbits (e.g., Amorisco 2015; Karademir et al. 2019). Tidal tails, on the other hand, are best visible if a merger occurs to a disk galaxy because these galaxies are more radially extended at a given mass and their stars are therefore less strongly bound than those of spheroidal galaxies.

When inspecting the connection between global kinematic properties and the appearance of tidal features, we found a remarkable agreement with observations for the distribution of the kinematic parameter λ_{R_e} for galaxies that have a given type of tidal feature. For both simulations and observations, slow rotators are most likely to have shells, while streams preferentially occur around galaxies with low to medium rotational support. Tracing these galaxies with shells back in time, we find that 30% of the galaxies lose their global angular momentum through the merger event that also caused the shells. The remaining 60% of shell galaxies had already been slowly rotating prior to the merger event that created the shells. About half of these galaxies had lost their global angular momentum even prior to redshifts of $z = 2$. Thus, we conclude that for all such cases where the galaxy was still rotationally supported, the massive merger event that caused the shells also led to a loss of the suppression of the rotational support. Moreover, we find that the orbits of these shell-forming satellite galaxies are radial, which agrees with previous simulation results from isolated merger experiments (e.g., Amorisco 2015; Karademir et al. 2019) and from the Illustris simulations by Pop et al. (2018).

Interestingly, we also find that shells appear in the velocity dispersion maps around their host galaxies as regions with a low-velocity dispersion, while they do not appear in the velocity maps. While the faint outskirts of galaxies are unlikely to be probed by IFU surveys in the near future, kinematic tracers such as globular clusters and planetary nebulae can be used to map these regions and might therefore help detect shell features from their velocity dispersion distribution (e.g., Roth et al. 2021). However, more detailed studies need to expand on these aspects in the future.

While we do not find a clear correlation between the overall rotational support of a galaxy and the appearance of streams beyond a slight tendency for streams to be the least common for galaxies with high rotational support, we find a connection between the appearance of streams and an internal kinematic feature: KDCs. For these galaxies, two different formation pathways are known: On the one hand, KDCs are made during gas-rich major mergers, with a

lifetime of about 4 Gyr (Hoffman et al. 2010; Schulze et al. 2017). On the other hand, these KDCs can be remnants of an old disk that grew into a spheroidal through multiple minor and mini mergers on circular orbits that mostly populate the outskirts of these galaxies (Schulze et al. 2020). About 30% of our KDC galaxies show stream features, the largest amount of any given tidal feature connected to a kinematic class. These clearly indicate that the formation pathway of these KDCs most likely corresponds to the multi-merger scenario.

The galaxies with the largest overall amount of features are prolate rotators for all types of tidal features. This agrees with observational results by Ebrová et al. (2021) and with the fact that there are multiple possible pathways reported for prolate rotators (i.e., Ebrová & Łokas 2017; Hegde et al. 2022), which also leads to a wide variety in possible tidal features. Overall, the large number of tidal features (sometimes even multiple different features) found around prolate rotators agrees with the idea that they are oftentimes formed through multiple merger events (effectively making them overmerged galaxies, as discussed by Remus & Forbes 2022), and thus, they are also rather frequent in high-mass galaxies.

Finally, we do not find any connection between the inner rotational support of the host galaxies and the existence of satellite planes. We find no strong indications of a connection between the appearance of tidal features and planes in addition to the possibility that tidal features may preferably occur around galaxies without satellite planes. Overall, satellite planes behave oppositely to the tidal features. They are most frequent around disk galaxies and regular rotators. This could either imply that the large-scale structure of accretion has no impact on the internal kinematics of a galaxy and the appearance of tidal features, or that these planes are the prestage of the merger events that leave the tidal features and change the kinematic properties of the host galaxy. Testing this in more detail will be an important step forward in the future.

5

Properties and Progenitors of Tidal Shells and Streams

This chapter summarizes the results submitted to A&A by Stoiber, Valenzuela et al. (2025) and to the IAU Symposium 403 proceedings by Stoiber, Valenzuela et al. (2026), for which I significantly contributed to the project development, analysis, and interpretation:

Living the stream: Properties and progenitors of tidal shells and streams around galaxies from Magneticum
&
Stream on: Evolution of stellar shells and streams – A case study

As the remnants of tidally disrupted galaxies, tidal shells and streams not only offer insights into the properties of the merger itself (e.g., Karademir et al. 2019; Mancillas et al. 2019), but also of the progenitor galaxies. This is achievable through color measurements (e.g., Kado-Fong et al. 2018; Khalid et al. 2026) or integral field unit (IFU) observations, from which the underlying stellar populations can be constrained (e.g., Fensch et al. 2020). While deep IFU observations of these low-surface-brightness (LSB) features are not yet feasible for large galaxy samples due to the extensive telescope time needed, individual galaxies and their tidal features have been investigated in considerable detail. Most prominently, the shell galaxy NGC 474 (e.g., Malin & Carter 1983; Turnbull et al. 1999) has been studied in great detail with respect to the merger (e.g., Bílek et al. 2022) as well as through IFU measurements of one of the shells (Fensch et al. 2020), revealing its kinematics and intermediate-metallicity stellar population.

Since galaxies follow different scaling relations with respect to their properties (see Section 2.2), including their stellar populations, measuring quantities like the metallicity can reveal indications about the progenitor's mass before its disruption. This is motivated by the stellar mass-metallicity relation (see Section 2.2.4; e.g., Gallazzi et al. 2005; Kirby et al. 2013), where observations have shown that the stellar metallicity in massive galaxies is higher than in low-mass galaxies. The stellar mass-metallicity relation has been used to estimate progenitor masses for both tidal streams (e.g., Laine et al. 2016) and shells (e.g., Fensch et al. 2020). However, these types of inferences may be biased by background stellar populations of the halo through the projection, which for massive tidal features are likely to be older and more metal-poor. Additionally, if galaxies that become tidal features around more massive galaxies tend to be outliers in the typical scaling relations, this would also result in biased conclusions about the progenitor systems.

To test the validity of these inferences and their potential biases, cosmological simulations provide an ideal way to self-consistently connect the visible tidal features to their progenitors. This allows one to investigate to what extent the tidal feature properties can provide insights into the progenitor galaxy. Several studies have previously analyzed the stellar populations of tidal features in cosmological simulations. For shell galaxies, Pop et al. (2017) identified shell galaxies in the Illustris simulation and found that the metallicity of the shells is higher than their surroundings and that the metallicity heavily depends on the progenitor. This was followed up by a study on the orbital properties of shell-forming mergers, where Pop et al. (2018) found that they have overall low angular momenta, which is consistent with other findings of rather radial orbits leading to shells (e.g., Quinn 1984; Amorisco 2015; Karademir et al. 2019). For tidal streams, Vera-Casanova et al. (2022) connected the brightest stellar streams to their progenitors in the Auriga cosmological zoom-in simulations for Milky Way-mass galaxies, finding a wide range of infall times with more massive progenitors being accreted at later times.

Similarly, cosmological simulations have been used to study the typical merger mass ratios that led to the formation of tidal shells and streams. Mancillas et al. (2019) used zoom-in simulations to estimate typical merger mass ratios of 1:4 for tidal shells and 1:10 for streams. For shell galaxies, Pop et al. (2018) even determined from Illustris that more than half of the shell systems are formed through mass ratios greater than 1:3. The reason for shells typically originating from more massive mergers is that dynamical friction removes angular momentum more rapidly for larger masses, thereby radializing the infall orbit (e.g., Vasiliev et al. 2022). This means that a larger range of initial infall parameters are possible for a more massive merger compared to less massive galaxies, which require a nearly pure radial trajectory (e.g., Pop et al. 2018).

This chapter presents the relevant findings of Stoiber et al. (2025, 2026) to this thesis. In the work of Stoiber et al. (2025) we first set out to identify and systematically characterize the tidal features around the simulated galaxies of Magneticum Box4 (uhr), in both their projected kinematics and stellar population properties, thereby building on the results from Valenzuela & Remus (2024, see Chapter 4). Then, by identifying the corresponding progenitor galaxies

before the mergers, we determined the merger mass ratios and placed the progenitor galaxies within the overall galaxy population with respect to the relevant metallicity and mass-size scaling relations. In the work by Stoiber et al. (2026), we additionally tracked the spatial evolution of tidally stripped stars to understand where they are deposited over time. Finally, we investigated the origins of a curious appearance of a young stream-like feature, for which no progenitor galaxy could be identified.

5.1 Tidal feature sample

Building on the work of Valenzuela & Remus (2024), we first selected the cataloged shell and stream galaxies from the Magneticum Box4 (uhr) simulation (Dolag et al. 2025) with stellar masses of $M_* \geq 10^{10}\,\mathrm{M}_\odot$ (note that this is a lower mass threshold than used by Valenzuela & Remus (2024)). We first rotated the galaxies to be face-on, where the 3D major axis is aligned with the x-axis. The reason for this is that we found that for the face-on projection, more shells and streams can be visually identified compared to the edge-on or side-on views. The difference between projections is most pronounced for shells, where the elongation axis of the merger remnant still largely follows the merger infall direction that led to the formation of the shells (e.g., Mancillas et al. 2019). Shells are rarely seen when viewed from the side-on view (line of sight along the major axis) due to their morphology appearing as a spherical cap, generally propagating along the major axis. Using stellar mock observations in the r-band (Martin et al. 2022) for the face-on projection, we manually marked the outlines of the tidal features, which we refer to as the projected shell or stream regions in the following.

The projected identification of these features resulted in a total of 24 shell galaxies and 56 stream galaxies for the simulated galaxies with $M_* \geq 10^{10}\,\mathrm{M}_\odot$. Compared to the original tidal feature census of 24 shell galaxies and 66 stream galaxies, for which 3D tooling was used, we could not identify the streams in the projected visualizations of ten of the originally classified stream galaxies. As 17 of the galaxies feature both shells and streams, there are a total of 63 galaxies with identified projected tidal feature regions, which we show in Figure 5.1. Several galaxies feature multiple projected stream regions, some of which are likely part of the same stream (e.g., UID 14247 or UID 20604). Most shell galaxies have several identified shells on both sides, and almost all of them are located along the major axis as expected (x-axis in each of the plots with the galaxies being rotated face-on).

5.2 Properties of shells and streams

5.2.1 Spatial properties and masses

To gain a better understanding of the general morphological properties of the identified tidal features, we quantify the spatial properties of the shells and streams. We determined the mean radial distance from the host's center for each tidal feature, where we find that shells tend to reside closer to the galaxy than streams (orange and blue distributions in the top left panel

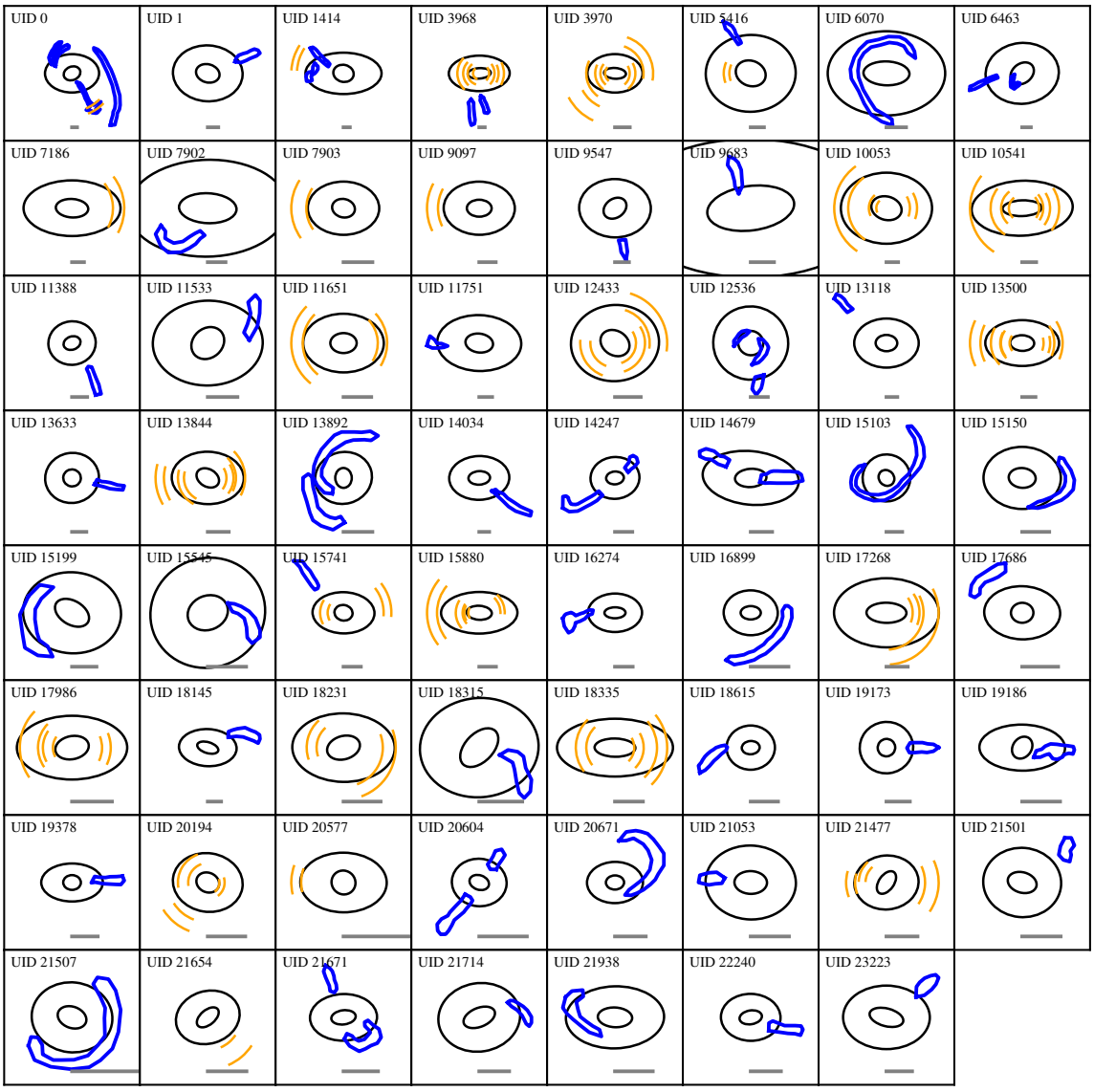


Figure 5.1: Projected tidal feature regions of the face-on Magneticum galaxies, with shells shown in orange (two arcs marking the inner and outer radii) and streams in blue. The black ellipses indicate the galaxies' shapes at 1 and 3 $R_{1/2}$. The gray horizontal lines mark the physical scale of 15 kpc in each panel. *This is figure 2 from Stoiber et al. (2025).*

of Figure 5.2). The median distances are at around 21 and 27 kpc for shells and streams, respectively (vertical lines), and the distribution tails reach values of up to 75 to 100 kpc, which correspond to the more massive galaxies in the sample, lying in the group to low-mass cluster regimes. Note that the median half-mass radius of the simulated galaxy sample is $\langle R_{1/2} \rangle \approx 7.3$ kpc and the mock observations used for the feature identification were made out to 7 $R_{1/2}$, such that the declining distribution tail toward higher distances is expected.

The shell distance distribution agrees very well with the observational results by Sola et al. (2025b, magenta dashed line) using CFHT (Canada-France-Hawaii Telescope) images from the MATLAS, UNIONS/CFIS, VESTIGE, and NGVS surveys, with a total of nearly 60 shell galaxies. In fact, our measured shell distance distribution is also quite similar to that of the shell system of NGC 474 (Bílek et al. 2022, light gray dashed line). In contrast, the extensive shell system of NGC 3923 (Bílek et al. 2015, 2016, dark gray dashed line) lies

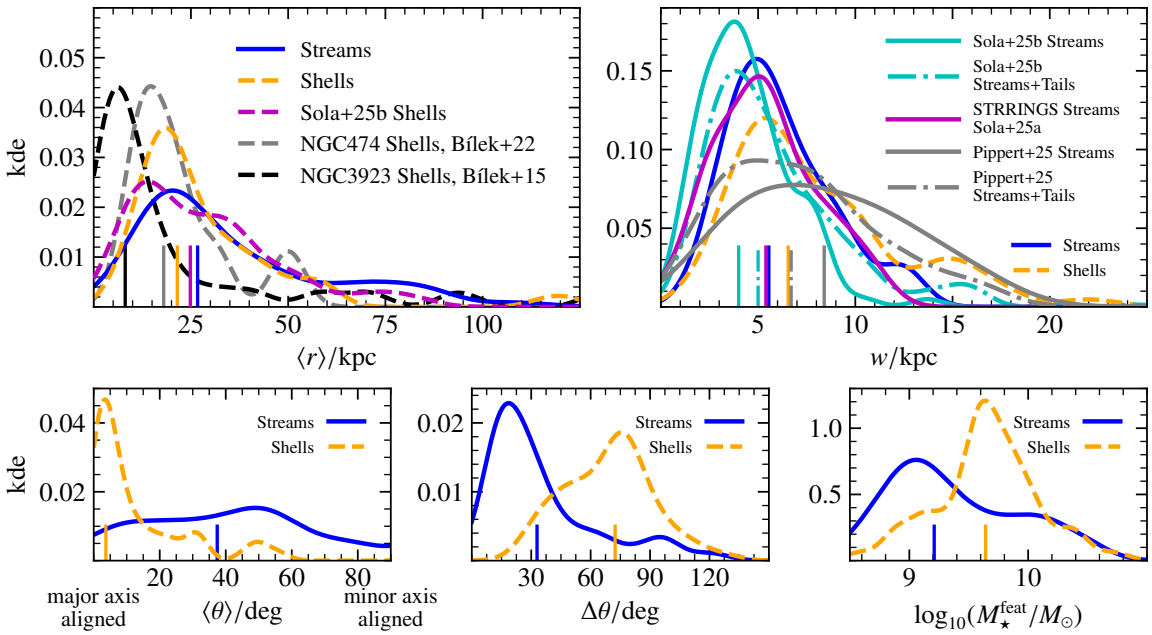


Figure 5.2: *Top row*: Distributions of the radial distance $\langle r \rangle$ from the host's center (left) and of the tidal feature widths w (right) for the shells (orange) and streams (blue) in Magneticum Box4. Observed shell radial distances are shown for the sample of Sola et al. (2025b), for NGC 474 (Bílek et al. 2022), and for NGC 3923 (Bílek et al. 2015, 2016). Observed stream widths are shown for the streams (solid lines) and combined streams+tails (dash-dotted lines) samples from Sola et al. (2025b) and Pippert et al. (2025), as well as from the STRRINGS streams sample by Sola et al. (2025a). *Bottom row*: Distributions of the mean angular position $\langle \theta \rangle$ (left, angle between the galaxy's major axis and the center of the feature region), the angular extent $\Delta\theta$ (middle, total angular region covered by the feature region, as measured from the galaxy center), and of the total stellar mass contained within the projected tidal feature region $M_\star^{\mathrm{feat}}$, for the shells (orange) and streams (blue) in Magneticum Box4. The vertical lines indicate the medians of the respective distributions. *This is figure 3 from Stoiber et al. (2025).*

closer to the galaxy center, though it should be noted that they subtracted a Sérsic light profile from the galaxy before identifying their shells, allowing them to reveal shells in the brighter inner galaxy regions. For streams, prominent streams have been observed to be consistent with our stream distance distribution, for example for M 83 the stream lies between 28 and 48 kpc (Barnes et al. 2014), and for NGC 5907 the mean radial distance is 46 kpc (Laine et al. 2016). Both of those streams thereby reside in the upper range of our distance distribution from the simulation.

As we had manually marked the projected feature regions (as shown in Figure 5.1), we could use these contours to determine the feature widths (top right panel of Figure 5.2). For the streams, we find a distribution and median (~5.5 kpc) very similar to the observations of 35 galaxies with streams by Sola et al. (2025a, magenta line) from the DESI Legacy Survey, where they also annotated their features manually on the low-surface-brightness images. The simulated stream widths also lie in between the tidal feature samples by Sola et al. (2025b) with 100 streams and 199 tails and by Pippert et al. (2025) with 9 streams and 4 tails, for which we show both the pure streams width as well as the combined streams+tails width distributions. Only Pippert et al. (2025) use a different approach for determining the feature widths, which is by determining the full width at half maximum for Gaussian fits to the streams, which may

bias their results to larger widths. However, given their small sample size, this may also be a result of the limited statistics. For the shell widths it is more difficult to define their width given that a shell is characterized by its sharp border where the stellar overdensity drops off towards the outer regions, whereas there is no such inner cutoff to a shell. Nevertheless, we also show the annotated shell widths for completeness (orange line), which have overall more narrow widths than streams.

Since all the tidal features were annotated in the face-on projection of the host, we determined the mean angular position of each feature $\langle\theta\rangle$, that is, the angle between the major axis of the galaxy and the projected feature center. We show the distribution of $\langle\theta\rangle$ for shells and streams in the lower left panel of Figure 5.2. As already seen in the feature overview panel (Figure 5.1), the shells are largely aligned with the photometric major axis with a median alignment below 5°. Since a radial merger is needed to form shells (e.g., Karademir et al. 2019), this merger leads to the elongation of a galaxy along the infall axis, leading to a major axis in the same direction. Also the prominent shell system of NGC 3923 has been found to be oriented along the major axis (Prieur 1988). In contrast, streams are almost uniformly distributed around the host galaxies, where they are only a little less likely to be centered around the minor axis. However, a more extensive sample of streams would be needed to confirm this indication. Regardless, the overall almost uniform distribution of stream angular position shows that their more circular infall orbits (e.g., Karademir et al. 2019) do not affect the host galaxy's shape.

The angular extent $\Delta\theta$ is the total angular region covered by the tidal feature as measured from the host's center. The lower middle panel of Figure 5.2 shows its distribution for shells and streams, where shells are found to have angular extents between around 30° to 100°, with a median of 72°. Individual stream regions have the potential to almost wrap around the entire galaxy (e.g., UID 6070 and UID 15103 as seen in Figure 5.1), but many streams are oriented radially toward the host's center (e.g., UID 1 and UID 15741), thereby significantly decreasing the typical angular extent of streams (median of 33°).

Finally, we computed the total stellar mass contained within each projected tidal feature region, $M_\star^{\mathrm{feat}}$. The lower right panel of Figure 5.2 shows its distribution for shells and streams, where clearly shell regions contain overall more mass (median of $4.4 \times 10^9\,\mathrm{M}_\odot$) than stream regions (median of $1.6 \times 10^9\,\mathrm{M}_\odot$). While on average shells reside slightly closer to the host galaxy than streams (top left panel of Figure 5.2), such that the host's halo contributes more to the projected mass, this is not sufficient to explain the significant projected mass difference between shell and stream regions. As a result, this suggests that shell progenitors are more massive than stream progenitors. Compared to stream observations, our typical values are higher than estimates for the stream of M 83 with $10^8\,\mathrm{M}_\odot$ from near-infrared observations (Barnes et al. 2014) or of NGC 5907 with $2.1 \times 10^8\,\mathrm{M}_\odot$ from the r-band (Laine et al. 2016). Even for the sample of 35 stream galaxies (Sola et al. 2025a), lower median stream stellar masses are found from the g- and r-bands compared to our values ($6.2 \times 10^8\,\mathrm{M}_\odot$). However, as Sola et al. (2025a) subtracted a galaxy model from the flux data before determining the stream mass, a systematic offset is expected to our values, reducing the differences between

simulated and observed projected stream masses. In general, it should be pointed out that a direct comparison between individual tidal feature properties is difficult: different stages of their evolution, where mass is stripped away over time, and varying projected distances of the progenitor's core from the host's center can heavily influence such measurements.

5.2.2 Kinematics and stellar population properties

As found by Valenzuela & Remus (2024) in their case study of a shell galaxy in Magneticum Box4, the velocity dispersion within the shells is lower than within their surroundings. For the Illustris simulation, Pop et al. (2017) found that the metallicity within shells is higher than within their surroundings. These previous findings indicate that the projected tidal features have distinct properties compared to the rest of the halo. In the following, we investigate for our entire tidal feature sample how the shells and streams compare to their surroundings with respect to the velocity dispersion, metallicity, and stellar age. For this, we used the same face-on projection of the galaxies as before and determined the mean projected velocity dispersion, mean metallicity, and mean stellar age within each projected tidal feature region, all computed in a light-weighted manner from the r-band mock observations. For the streams, this is computed across the entire stream region, whereas for the shells, we take the maximum radial velocity dispersion and metallicity and the minimum radial age within the shell region from radial bin slices to ensure that the actual shell structure is identified. The properties of the stream surroundings were determined within an annulus around the host galaxy with inner and outer radii equivalent to the radial extent of the stream. For the shell surroundings, we selected the immediate inner and outer regions surrounding the shell within the same circular sector, where we individually computed the projected properties and then took the mean between the two regions. This enables a comparison with the direct surroundings of both streams and shells.

Figure 5.3 shows how the feature properties (feat) compare to their surroundings (surr) directly (top panels) and relatively (lower panels) for the mean light-weighted line-of-sight velocity dispersion $\langle \mathrm{los}\sigma \rangle_{\mathrm{lw}}$ (left), stellar age $\langle t_\star \rangle_{\mathrm{lw}}$ (middle), and stellar metallicity $\langle [Z/\mathrm{H}] \rangle_{\mathrm{lw}}$ (right). The velocity dispersion within shells (orange) and streams (blue) is lower than that of the surroundings for most features, where only a few streams and a single shell show the opposite behavior. Even including the associated scatters, roughly two thirds of tidal features have statistically significant lower velocity dispersions than the surrounding halo. Since streams and shells are composed of stars with bulk motions that originate from a common progenitor, these stars dominate the light in those regions, significantly lowering the velocity dispersion. The relative relation (bottom panel) is largely independent of feature velocity dispersion, except that at the very lowest values the feature velocity dispersion can be much lower, up to a factor of 0.5–0.6. These low feature velocity dispersions are also only found for lower-mass host galaxies (less opaque data points), likely because of a combination of less material being contained in their halos as well as lower-mass galaxies having lower velocity dispersions in general.

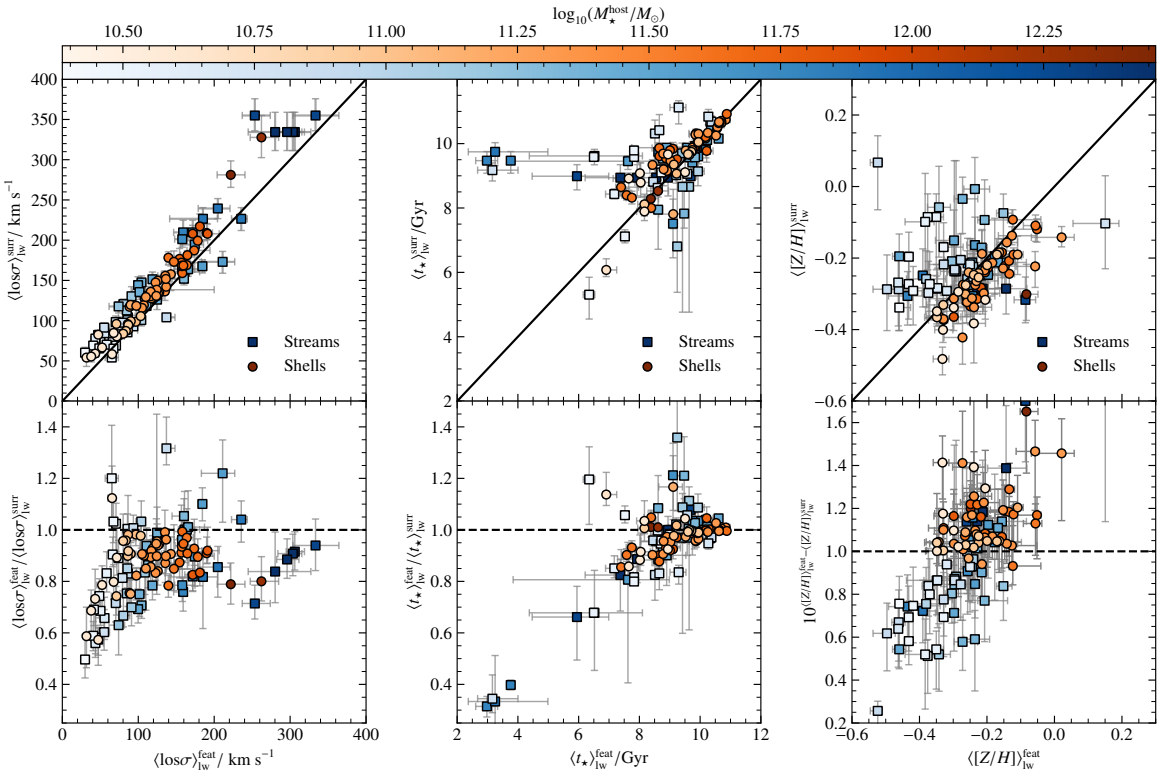


Figure 5.3: *Top row*: Quantity of the surroundings as a function of the tidal feature quantity for the mean light-weighted line-of-sight velocity dispersion $\langle \log\sigma \rangle_{\rm lw}$ (left), stellar age $\langle t_\star \rangle_{\rm lw}$ (middle), and stellar metallicity $\langle [Z/{\rm H}] \rangle_{\rm lw}$ (right). The 1:1 relation is indicated by the solid black lines. *Bottom row*: Relative ratio of the feature quantity divided by the quantity of the surroundings as a function of the feature quantity for the same three properties. The 1:1 relation is indicated by the dashed black lines. The data points are colored by feature type, with shells in orange and streams in blue, and have an opacity depending on the host galaxy's stellar mass (see the respective color bars). The error bars indicate the 1σ scatter within each region. *This is figure 4 from Stoiber et al. (2025).*

The tidal feature mean stellar ages are generally similar to their surroundings (middle panels of Figure 5.3), except for a set of eight young streams with ages below 7 Gyr, most of which are significantly younger than their surroundings. The general stream stellar ages are similar to those of some observed stellar streams, like of the Sagittarius stream around the Milky Way (7 Gyr; de Boer et al. 2015), the Giant Stellar Stream around M 31 (8.8 Gyr; Brown et al. 2006), or the stream around NGC 5907 (11.9 Gyr; Laine et al. 2016). For shells, Fensch et al. (2020) measured an age of around 3.6 Gyr for the most prominent outer shell of NGC 474 through full spectral fitting, which is much younger than any of the stellar ages we found for the simulated shell regions, which only reach as young as 7 Gyr. It is also younger than the core of NGC 474 (7.7 Gyr; McDermid et al. 2015), such that it may be an outlier among shells with a potential starburst during the collision. This may also be related to NGC 474 having had recent star formation and being a "blue outlier" among early-type galaxies (Jeong et al. 2012; Zaritsky et al. 2014) from its bluer color and high near-UV emission.

Finally, the metallicity of the Magneticum shells is almost always higher than that of their surroundings (right panels of Figure 5.3), consistent with the Illustris results from Pop et al. (2017). Due to the large scatter within the shells, this is only true for about a third of them when considering the 1σ scatter. Their values range between $\langle [Z/{\rm H}] \rangle_{\rm lw}^{\rm feat} = -0.35$ and

0.0. The prominent shell of NGC 474 was measured to have a metallicity of $[Z/\mathrm{H} = -0.83]$ (Fensch et al. 2020), which is significantly less metal-rich than our shells. In contrast, the Illustris shell metallicities were determined to lie well above our values, at $\log Z/Z_\odot = -0.02$ to 0.18. The differences in metallicity could arise from several different factors. On the observational side, uncertainties can arise from the full spectral fitting, among others through the age-metallicity degeneracy, and through the low-surface-brightness nature of the shell (e.g., Worthey 1994; Boecker et al. 2020). Different galaxy formation models as employed by Magneticum and Illustris as well as the specific yields employed for supernova and stellar wind feedback can lead to systematic offsets between each other. Here, the key conclusion is that shells tend to have higher metallicities than their outskirts, which is a result drawn from both of the simulations, independent of their underlying models. The reason for this is that shells tend to be formed by relatively massive infalling galaxies (see also the next section), which generally have larger metallicities according to the stellar mass-metallicity relation (e.g., Gallazzi et al. 2005) and thereby have a larger metallicity than the host's halo.

For streams, there is a tendency for them to have lower metallicities compared to their surroundings, though there are also a number of streams that have higher metallicities. Compared to the shells, the metallicities are lower, mostly ranging from $\langle [Z/\mathrm{H}] \rangle_{\mathrm{lw}}^{\mathrm{feat}} = -0.5$ to -0.15. On the observational side, the core of the Giant Stellar Stream around M 31 has been measured to have a metallicity of $[\mathrm{Fe/H}] \sim -0.7$ to -0.5 (Ferguson & Mackey 2016), which is at the lower end of our range. In contrast, the stream around NGC 5907 has a metallicity of $\log Z/Z_\odot = -0.3$ (Laine et al. 2016), which is significantly more metal-rich and agrees well with the simulated streams.

5.3 Progenitors of shells and streams

One of the central utilities of cosmological simulations is connecting present-day structures with their progenitors. In the following, we trace back the tidal features to their pre-merger progenitor galaxies and investigate the merger as well as the galaxy properties.

First, we matched the stellar particles found in each of the projected tidal feature regions with those found in nearby satellite galaxies in the preceding snapshots, such that we were able to identify which galaxies at earlier times correspond to the respective tidal feature in the last snapshot. This was possible for most tidal features, with the exception of several of the young stream-like objects, which we investigate in Section 5.4. By selecting only the particles that were part of the identified progenitor galaxy in the last snapshot, we could disentangle the pure and complete tidal features from the host galaxies. Figure 5.4 shows two examples of this for a shell (top) and a stream (bottom) galaxy, where the entire host galaxies and their outskirts are shown on the left, while the extracted tidal features are shown on the right. Clearly, much of the tidal features is covered by the host and its halo, such that only the brightest parts can be seen in the left maps. One can also see that the shell system is a lot more spatially extended compared to the full stream. The reason for this is that the radial orbit of the shell progenitor has a much closer encounter with the host and its gravitational potential, leading to

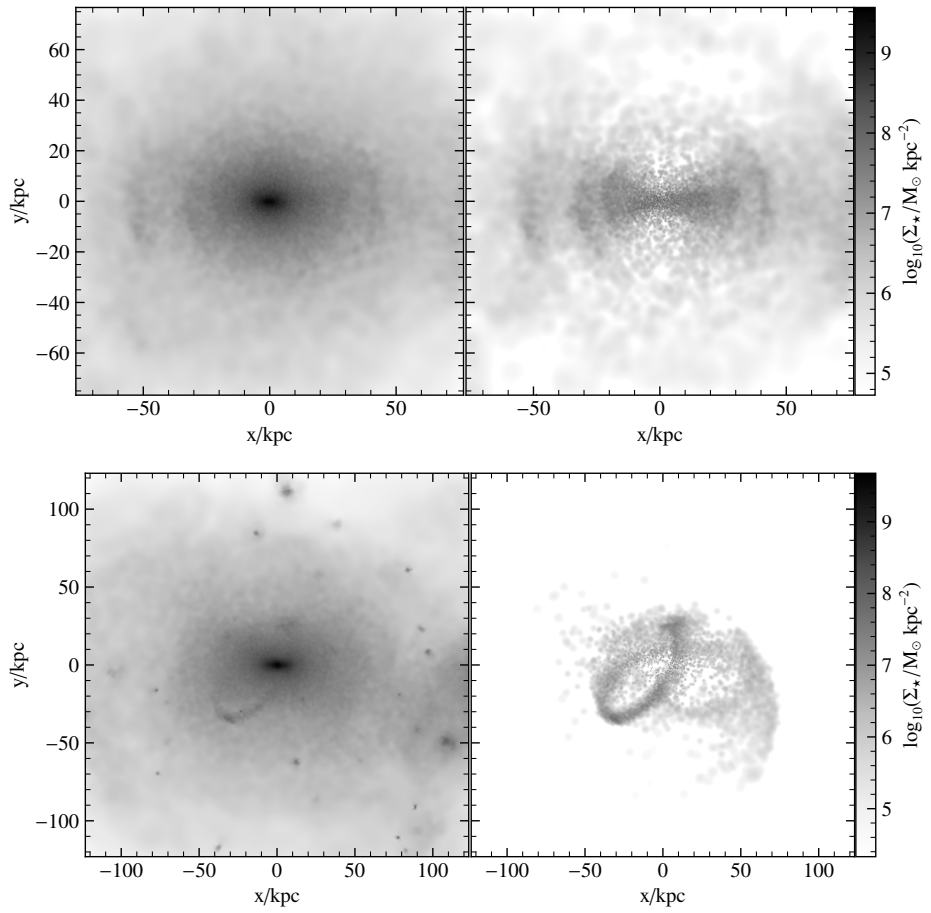


Figure 5.4: *Top row*: Stellar surface density map of a galaxy (UID 13500) with a prominent shell system (left) and of the isolated remnant of the identified shell progenitor galaxy (right). Both maps are of the same region in the same snapshot. *Bottom row*: Stellar surface density map of a galaxy (UID 7902) with a prominent stream (left) and of the entire isolated stream, which is the remnant of the isolated stream progenitor galaxy (right). The projections and orientations are the same as in Figure 5.1. *This is figure 5 from Stoiber et al. (2025).*

the stars being funneled into a wide circular sector (e.g., Quinn 1984; Hernquist & Quinn 1988). In contrast, a stream is tidally stripped along its orbit through tidal shocking at the orbit's pericenter and through evaporation of stars across the tidal boundary, which results in a leading and a trailing arm that make up the total stream. In Appendix B.1, we show the remaining isolated tidal feature structures.

5.3.1 Properties of tidal feature progenitors

With the identified progenitors, we determined their properties at merger time to characterize the tidal feature progenitor galaxies. A central merger property is the stellar merger mass ratio $M_\star^{\mathrm{prog}}/M_\star^{\mathrm{host}}$, for which we show its distribution in the left panel of Figure 5.5 for shell and stream mergers. As expected, mergers that lead to the formation of shells are on average relatively more massive than stream mergers, with most stellar mass ratios being major and minor and lying between 1:5 and 1:1, compared to the largely mini and minor stream mergers of <1:5. These results are consistent with those by Pop et al. (2018) and Mancillas et al.

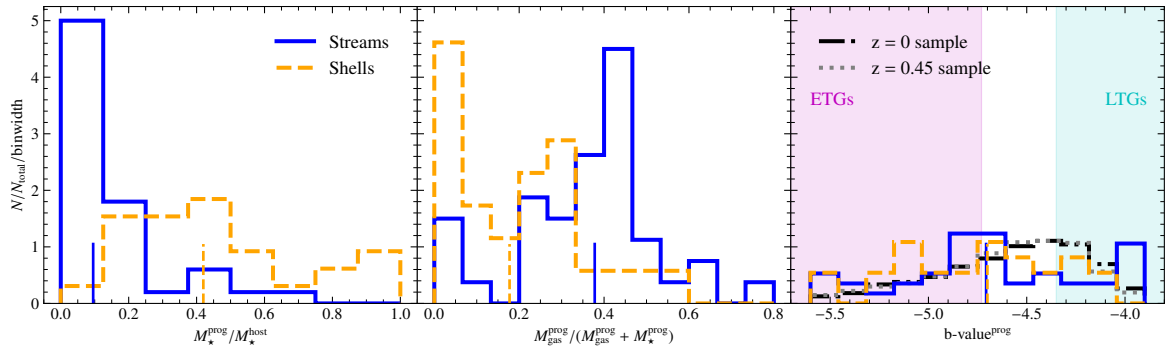


Figure 5.5: Distributions of the stellar merger mass ratio $M_\star^{\mathrm{prog}}/M_\star^{\mathrm{host}}$ (left), of the progenitor gas mass fraction $M_{\mathrm{gas}}^{\mathrm{prog}}/(M_{\mathrm{gas}}^{\mathrm{prog}}+M_\star^{\mathrm{prog}})$ (center), and of the morphology quantified by the b-value (right), of shell (orange) and stream (blue) progenitors. For the b-value, the overall distribution of all galaxies at $z = 0$ (dashed black line) and $z = 0.45$ (dotted gray line) are shown as well for comparison. The early-type galaxy (ETG) and late-type galaxy (LTG) classifications are indicated by the shaded areas. The thin vertical lines indicate the medians of the respective distributions. *This is figure 10 from Stoiber et al. (2025).*

(2019). Nevertheless, we also find cases of smaller mergers leading to shells, which is then linked to an especially radial merger orbit of the progenitor.

The gas mass fraction distribution of the progenitors is shown in the center panel of Figure 5.5, where stream progenitors generally have higher values than shell progenitors. In part, this may be caused by the intrinsically higher masses of shell progenitors (see figure 8 of Stoiber et al. 2025), which tend to have lower gas mass fractions (e.g., Catinella et al. 2018; Díaz-García & Knapen 2020). Note that here we do not distinguish between hot and cold gas, however.

The morphological distribution of shell and stream progenitors is very similar, as quantified by the b-value (right panel of Figure 5.5). However, compared to the overall morphological distribution of all galaxies in the original sample at $z = 0$ (black) and $z = 0.45$ (gray, corresponding to the typical redshift at which the progenitors reached their peak stellar mass), there are fewer late-type galaxies (LTGs) among the feature progenitors. While it is not conclusive what the primary reason for this difference is, it is possible that the typically higher fractions of cold gas in late-type galaxies change the merger dynamics sufficiently compared to the collisionless nature of a gas-poor merger.

To further investigate whether the tidal feature progenitors also deviate from the overall galaxy sample in other aspects, we consider two scaling relations, within which we place the progenitors. The first is the stellar mass-metallicity relation, which we show in the top panel of Figure 5.6. The data points are colored by the redshift at which they reached their peak stellar mass before the merger, z_{PSM}, for shells (circles) and streams (triangles). In general, the stellar masses of the progenitors tend to be more massive compared to the overall sample (gray points at $z = 0.45$ and black contours at $z = 0$), which is a result of these forming the prominent tidal features that could be identified clearly in the mock observations. Compared to the overall galaxy sample, the feature progenitors do not have a particular bias toward larger or smaller metallicities, but lie right on the general relation, in agreement with a stream

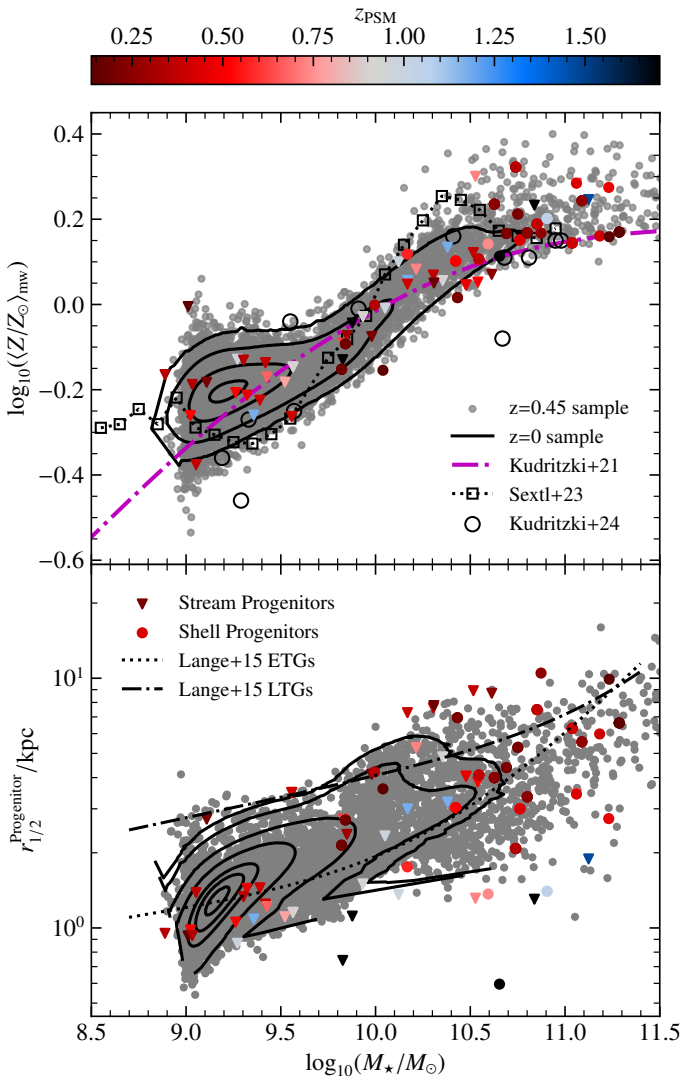


Figure 5.6: *Top*: Stellar mass-metallicity relation. The mass-weighted mean stellar metallicity $\log\langle Z/Z_\odot\rangle_{\rm mw}$ is shown as a function of stellar mass for the simulated galaxies in Magneticum Box4 (uhr) for the total sample at $z = 0.45$ (gray) as well as at $z = 0$ (black contours), and for the shell (colored circles) and stream (colored triangles) progenitors. Observed data points and relations are shown for Kudritzki et al. (2021) from a galaxy evolution lookback model, for Sextl et al. (2023) from stacked galaxy spectra, and for Kudritzki et al. (2024) as measured from individual blue supergiants. *Bottom*: Mass-size relation. The stellar half-mass radius $r_{1/2}$ is shown as a function of stellar mass. The data points and contours are plotted analogously to the top panel, and the observed relation for early-type galaxies (ETGs; dotted line) and late-type galaxies (LTGs; dash-dotted line) are shown from Lange et al. (2015). The properties are computed at the redshift of peak stellar mass of the respective feature progenitors, $z_{\rm PSM}$, according to which the data points are colored. *This is figure 11 from Stoiber et al. (2025).*

study in the FIRE simulations (Panithanpaisal et al. 2021). Metallicity observations obtained with different methods (Kudritzki et al. 2021; Sextl et al. 2023; Kudritzki et al. 2024) are also consistent with the galaxy sample, where there appears to only be a tendency for higher simulated metallicities at the high-mass end of $M_\star \gtrsim 10^{11}\,\mathrm{M}_\odot$. In particular, this means that the differences found for the metallicities of the projected tidal feature regions compared to observations (see Section 5.2) are not a result of systematically overly high simulated

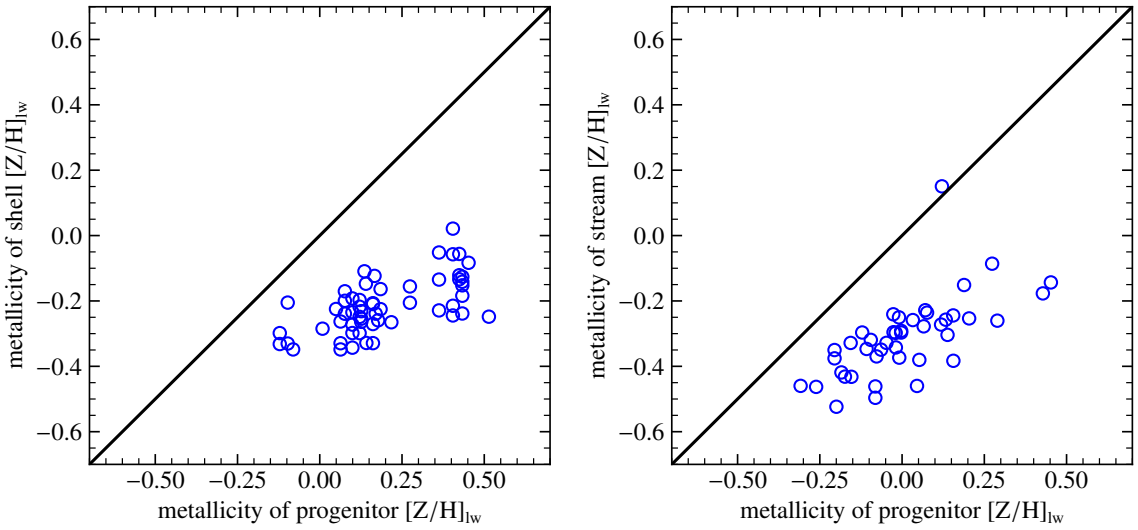


Figure 5.7: Light-weighted mean stellar metallicity $[Z/H]_{lw}$ of the projected tidal feature regions (y-axis) compared to the actual value of the corresponding progenitor galaxies (x-axis). *Left*: Relation for the shells and their progenitors. *Right*: Relation for the streams and their progenitors. *This figure was produced by Johannes Stoiber within the scope of the work by Stoiber et al. (2025).*

metallicities. Given the higher stellar masses of shell progenitors and their higher metallicities, this is also the underlying reason for the higher projected shell metallicities found in Figure 5.3.

The second scaling relation we consider is the mass-size relation, shown in the bottom panel of Figure 5.6. Again, the feature progenitors do not have a particular bias compared to the overall galaxy sample, which also follows the observed mass-size relation (Lange et al. 2015). Only a small number of galaxies with very early peak stellar mass times before $z = 1.5$ (dark blue) are found to be especially small, though this is consistent with the temporal evolution of the mass-size relation (see figure 30 of Dolag et al. 2025).

Having established the actual positions of the shell and stream progenitor galaxies in the stellar mass-metallicity relation, we next compared these to the originally observed values for the projected tidal feature regions in Section 5.2. Figure 5.7 shows for shells (right) and streams (left) how the stellar metallicity compares between the projected feature region and the actual mean metallicity of the progenitor galaxy. Nearly all projected shell and stream regions have significantly lower metallicities than the corresponding progenitor galaxies by around 0.2–0.6 dex, most likely heavily influenced by the metal-poor halo of the host galaxy. Only one stream has a similar metallicity similar to that of the progenitor, which is due to its remnant metal-rich core making up most of the selected stream region in an early state of its tidal disruption. Overall, our results show that directly inferring a progenitor's stellar mass from a projected metallicity measurement of the tidal feature through the mass-metallicity relation is severely biased toward lower masses because the projected metallicities are systematically lower than the actual progenitor's metallicity.

5.3.2 Evolution of tidal feature spatial distributions

Since the tidal feature progenitors typically also have internal gradients such as for metallicity and age, it is important to understand the spatial evolution of the stars that are tidally stripped from the infalling galaxy. To this end, we studied a shell and a stream galaxy as a case study for each type of tidal feature. For each stellar particle in the progenitor galaxy, we determined its initial radial distance from the progenitor's center in units of the half-mass radius $r_{1/2}$ at the same time, which we used to then track where the stars of each initial radius are deposited.

Figure 5.8 shows the evolution of a shell system over the course of almost 3 Gyr, centered on the gravitational potential of the host galaxy, which is not shown. The stellar component is colored by the initial radius, and we follow the infalling galaxy with a blue line for as long as it was still identified as a satellite by the subhalo finder. The blue line traces a radial orbit, just as expected for a shell progenitor (e.g., Karademir et al. 2019). Each shell that is formed is labeled with an incrementing unique number, where it becomes clear that the first shells are made up of stars that initially were in the outskirts of the progenitor galaxy (yellow shells). Later shells contain stars from regions that originally sat closer to the progenitor's core (orange to purple shells). This shows how the progenitor galaxy is tidally disrupted from the outside to the inside. The radial ordering means that intrinsic gradients found in the progenitor, such as a metallicity gradient, should also leave their imprint in the shell system. All of the shells propagate outward as density waves and simultaneously become fainter as they dissipate. Here it is important to note that a shell is not a structure composed of the same stars over time, but consisting of stars slowing down on their orbits as they reach the apocenter, after which they fall back toward the host galaxy (e.g., Amorisco 2015). The changing stars can be seen by following the color of the shell labeled 6, which starts with stars that initially mainly resided within $1\,r_{1/2}$ (purple) and later contains stars that initially were further outside (orange).

The evolution of the example stream progenitor is found in Figure 5.9. A clear difference from the shell progenitor is that it falls in on a much more circular orbit, as expected (e.g., Karademir et al. 2019). During the first orbit in the first two panels, a first tidal arm develops from the outer regions of the progenitor (dark yellow). Over time, the stream covers an increasingly large stretch of its orbit, with clear leading and trailing arms seen in several of the later panels around the progenitor's core marked by the red cross. Starting at a lookback time of $t_{\rm lb} = 0.85\,\mathrm{Gyr}$, even the core region within $1\,r_{1/2}$ begins to get tidally stripped, until it is almost fully disrupted by the last snapshot. The original stream annotation was based on the stream region right around the core (red cross) in the last snapshot, indicating that at the time of observation a stream can potentially only be identified by the stars originating from the progenitor's inner regions.

5.4 Young in-situ stream-like features

Not all the identified streams could be traced back to a progenitor galaxy. Several young streams with ages of $\langle t_\star \rangle < 7\,\mathrm{Gyr}$ do not originate from an infalling galaxy, but in fact are

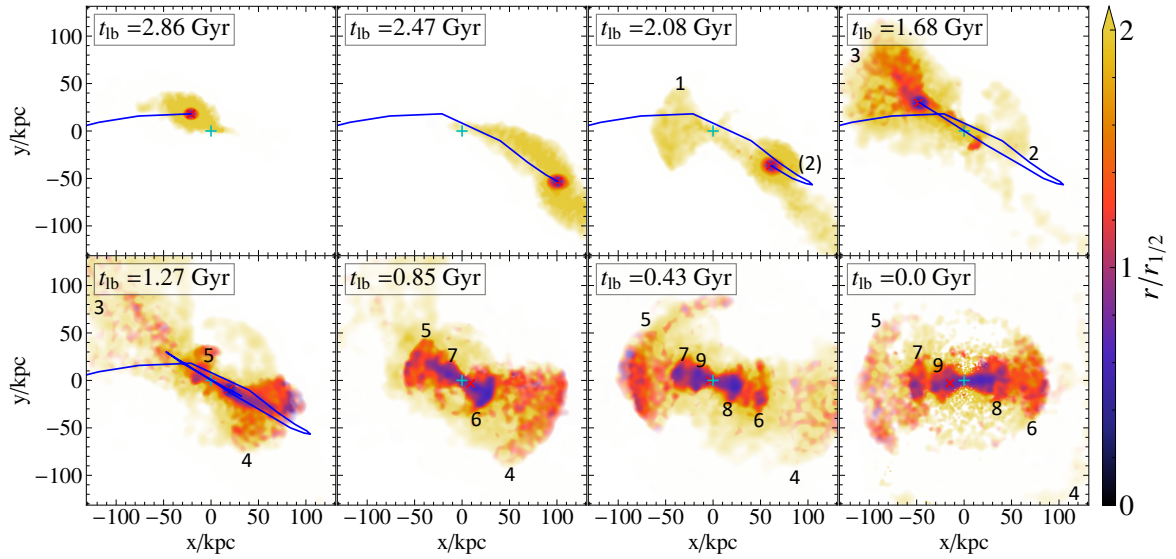


Figure 5.8: Evolution of an infalling shell progenitor galaxy. The stellar component is colored by the initial radial distance of the stars within the progenitor, and the opacity is determined by the underlying stellar surface density. The lookback time t_{lb} as measured from the last snapshot is shown in the top left of each panel. The green plus at the center indicates the center of the host galaxy, which itself is not shown. The red cross follows the stellar particle that was initially the closest to the center of the progenitor. The blue line traces the progenitor for as long as it is still identified as its own galaxy by the subhalo finder. The numbers label each unique shell in order of appearance. *This is figure 3 from Stoiber et al. (2026).*

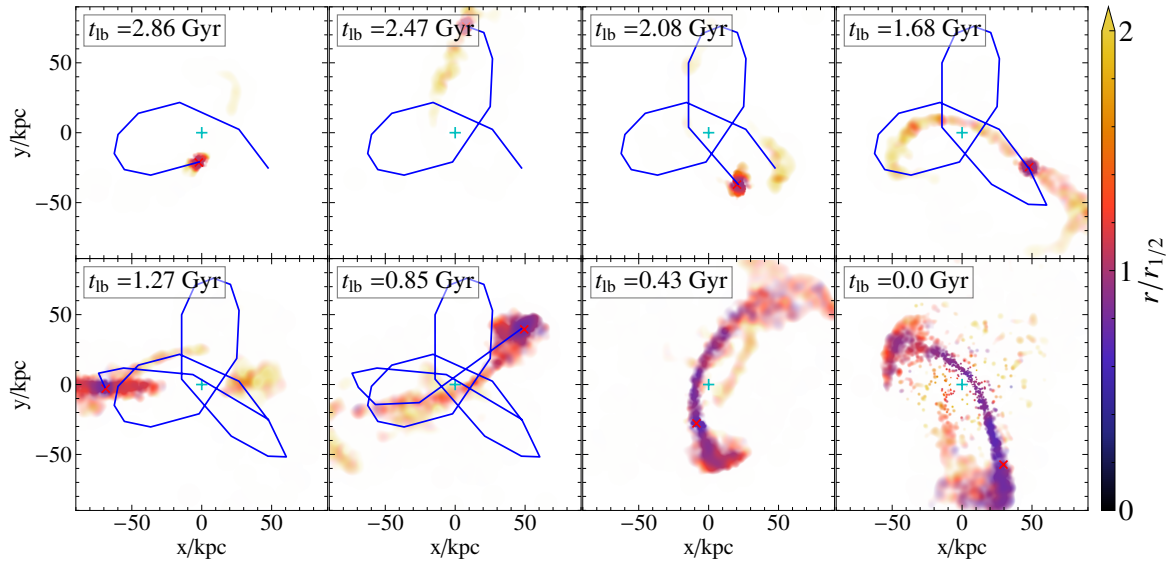


Figure 5.9: Same as Figure 5.8, but for the evolution of an infalling stream progenitor galaxy. *This is figure 2 from Stoiber et al. (2026).*

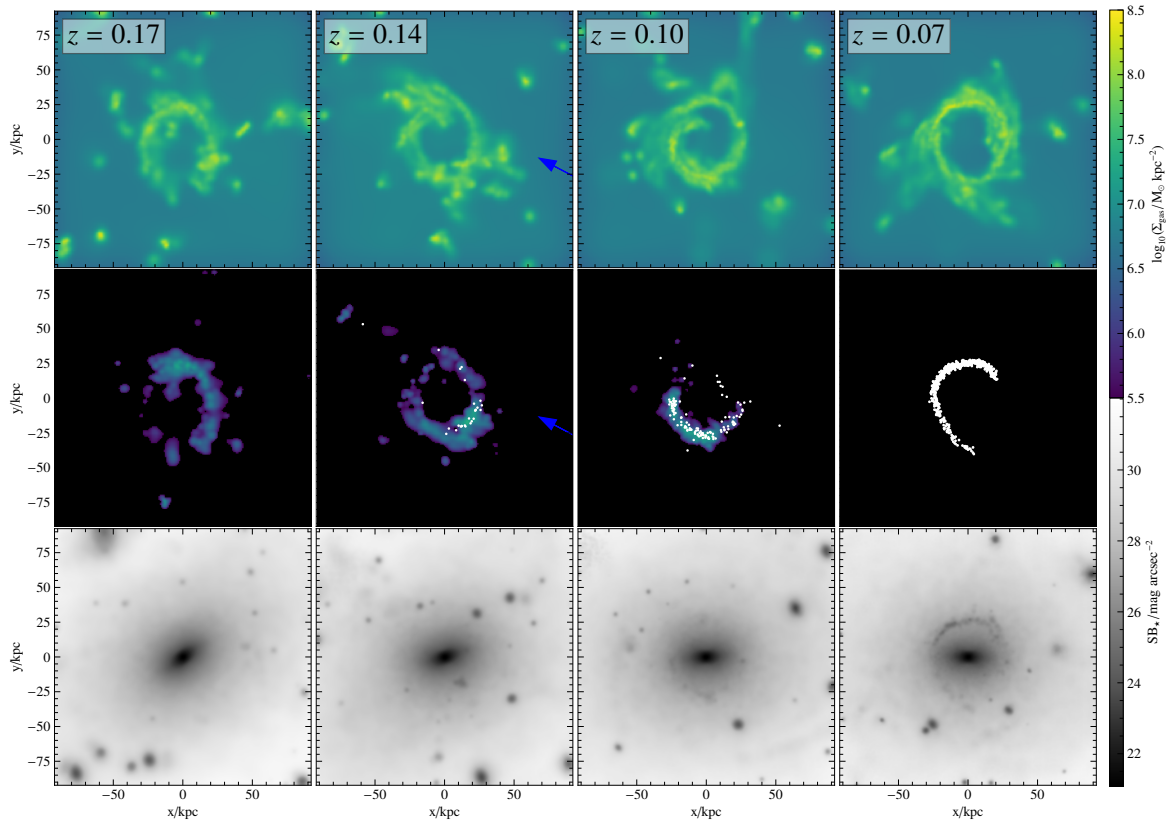


Figure 5.10: In-situ formation of a young stream-like feature (UID 6070) from a gas ring across four snapshots (from left to right), covering a time range of ∼1.3 Gyr. The redshift of a snapshot is stated in the top left of the top panels. *Top*: Gas surface mass density of the host galaxy. *Middle*: Gas surface mass density (color map) of the gas from which the stars of the young stream-like feature form (white dots). Only the stars younger than 1.2 Gyr from the originally selected projected stream region are shown. *Bottom*: Stellar mock observation of the host galaxy in the r-band. The last panel in this row is the map in which the stream-like feature was originally annotated, and the orientation is the same as in Figure 5.1. The blue arrows in the second column indicate the position and direction of the velocity of a satellite galaxy that potentially triggered the star formation in the gas ring (see Appendix B.2). *This is figure 12 from Stoiber et al. (2025).*

formed in-situ. We traced back the stars contained in one of these stream-like features to the gas they were formed from. We show the evolution of the gas and stars in Figure 5.10 from $z = 0.17$ until the last snapshot at $z = 0.07$, visualizing the gas surface density of the entire system (top), the stars of the stream-like feature as well as the gas that formed them (middle), and the r-band stellar mock observations (bottom). To avoid older foreground and background stars from the host galaxy's halo, we set an upper stellar age limit of $t_{\text{age}} \leq 1.2\,\text{Gyr}$ (corresponding to a formation after $z = 0.17$, the redshift of the first panel) for the stars in the second row. It becomes apparent that the young stream-like feature was formed within a gas ring around the host's center, with most stars appearing in the last two panels. Interestingly, it appears that the stars were mostly formed on one side of the gas ring, seen by the semi-circle ring of stars (white dots) in the third panel of the second row. These young stars are luminous and hence appear as a stream-like feature in the photometry (last panel in the third row). The gas ring remains in place over the entire sequence of snapshots (top row).

While the investigation of the origin of the gas ring is beyond the scope of this work, we found that similar formation pathways lead to the other young stream-like features without identified progenitor galaxies, making them in-situ stream-like features. For the case study highlighted here in Figure 5.10, a potential trigger for the star formation in the gas ring is the brief interaction with another galaxy as it passes by with the pericenter at $z = 0.14$ (blue arrows in the second column). As it passes the host galaxy in the same direction as the star formation appears to occur, we propose that the gas in the ring is compressed through the encounter and thereby forms stars on that side of the ring. We show the galaxy flyby in the larger environment of the host galaxy in Appendix B.2.

5.5 Summary and conclusion

Building on the study by Valenzuela & Remus (2024), we systematically investigated the tidal shells and streams around the galaxies of Magneticum Box4 (uhr). We first focused on the projected properties of the features, including their spatial properties, kinematics, and stellar populations. Overall, the results we found for the simulated galaxies are in agreement with observed shells and streams. This is the case for individual observed tidal features (e.g., Bílek et al. 2016, 2022) as well as for the distributions of positions and widths from larger samples (e.g., Sola et al. 2022; Pippert et al. 2025; Sola et al. 2025b). Shells are found to reside along the major axis of their host galaxy, just as expected from a radial merger forming the shells and simultaneously elongating the galaxy in the infall direction.

We confirmed the prediction of Valenzuela & Remus (2024) based on their case study that shells have lower line-of-sight velocity dispersions than their surroundings. The ages of tidal features are overall similar to their surroundings, with the exception of some especially young stellar streams. The metallicity of shells is generally higher than that of their surroundings, while streams have similar or slightly lower metallicities. Overall, the stellar ages and metallicities of the tidal features are comparable to the results from observations (e.g., Brown et al. 2006; Ferguson & Mackey 2016; Laine et al. 2016). Still, there is a significant difference compared to the results from full spectral fitting for NGC 474 by Fensch et al. (2020), who measure a very young and more metal-poor stellar population within the shell, though this may be an especially peculiar case. However, it is also possible that potential star formation within some shells cannot be captured in the simulation without increasing the resolution or further improving the star formation model.

We then identified the progenitor galaxies of the tidal features by tracing them backward in time to investigate the progenitor properties. The shell progenitors in Magneticum Box4 (uhr) differ from stream progenitors through higher merger mass ratios, higher stellar masses, and lower gas mass fractions. In particular, the higher merger mass ratio leads to a preference for radial infall because of dynamical friction, which is necessary for the formation of shells (e.g., Quinn 1984; Karademir et al. 2019). This is also consistent with previous work on shells in the Illustris simulation by Pop et al. (2018). Nevertheless, we find that even minor mergers

are capable of forming shells when the orbit is sufficiently radial, while most minor and mini mergers fall in on more circular orbits, leading to streams (e.g., Mancillas et al. 2019).

Shell and stream progenitors are not outliers in the stellar mass-metallicity and mass-size scaling relations. This also means that the age and metallicity differences to Fensch et al. (2020) are unlikely a result of systematic differences in galaxy properties. Instead, observational biases, improvements in the simulated star formation recipes and resolution, and larger simulated galaxy samples are likely necessary to explain these discrepancies. We also find that the projected metallicities measured within the projected tidal features are lower than the intrinsic values of the progenitors, which is a result of the more metal-poor overlaying host galaxies' halos. This has to be taken into account in any observational attempts to infer the progenitor galaxy's mass through the mass-metallicity relation based on metallicity measurements of a given tidal feature. Otherwise, progenitor masses are underestimated, which can be seen by differing mass estimates by Fensch et al. (2020) using several methods for the shells of NGC 474.

Tracing the evolution of infalling galaxies over time for a shell and a stream example, we find that the outer stars are first tidally stripped from the progenitor as expected. The first shells that are formed are therefore composed of outer stars, whereas later shells are made up of inner progenitor stars. As a result, a metallicity gradient in the progenitor should also be imprinted in the shell system. Stream progenitors initially develop tidal arms containing their outer stars, but as time passes the galaxy is tidally disrupted into a stream composed of its innermost stars. The former core region can then be observed as the brightest part of a stream (unless covered by the host galaxy in projection).

Finally, we investigated the nature of several young stream-like features without identified progenitors. These in fact form in-situ in their host galaxies and are therefore not actually stellar streams in the classical sense. For an exemplary case, we find that it is formed within a gas ring. The star formation was potentially triggered by a passing galaxy during its pericenter passage shortly before the stars begin forming. Future studies will be necessary to develop a deeper understanding of such occurrences.

With this study we have delivered the most extensive analysis to date of tidal shells and streams in a cosmological simulation, analyzing their projected properties and linking them to their progenitors. We find that the shells and streams in the Magneticum Box4 (uhr) simulation agree very well with observations across a large range of properties from spatial extent to stellar populations. The characterization of shell and stream merger mass ratios and progenitor properties furthermore expand on previous studies of shells or streams. Further work will be crucial to deliver more predictions for the currently and soon incoming wide-field low-surface-brightness observations from the Euclid, Rubin, and Roman facilities.

6

Further Studies on Tidal Features

This chapter summarizes the results published by Rutherford et al. (2024, incl. Valenzuela), MNRAS 529, 810, and by Khalid et al. (2025, incl. Valenzuela), MNRAS 543, 3391, for which I provided simulation data and contributed to the interpretations:

The SAMI Galaxy Survey:
using tidal streams and shells to trace the dynamical evolution of massive galaxies
&
Tidal features around simulated groups and cluster galaxies: enhancement and suppression of merger events through environment in LSST-like mock observations

Building on the work on tidal features in Magneticum Box4 (uhr) and the analysis on the relation between outer structures and the inner kinematics (Valenzuela & Remus 2024, see Chapter 4), I have contributed to two subsequent studies that further investigate tidal features and their occurrence in different galaxy populations. As tidal features are a temporary phenomenon, their presence indicates that a merger has occurred in the last few Gyr (Mancillas et al. 2019). Expanding on the results found for Box4 and the MATLAS survey with respect to the inner kinematics and the presence of tidal features, we used galaxies from the SAMI survey (Croom et al. 2012; Bryant et al. 2015) to identify tidal features and connect them to several different galaxy properties (Rutherford et al. 2024, incl. Valenzuela). Furthermore, it remains unclear to what extent tidal features are found around satellite galaxies as they fall into a more massive host galaxy, which would provide insights into the merger occurrence for the infalling

galaxies themselves. Using a tidal feature census for the galaxies in several cosmological simulations (including Box4; Khalid et al. 2024), we thus investigated how common tidal features are around satellite galaxies in different regions of phase space for galaxy to galaxy cluster environments (Khalid et al. 2025, incl. Valenzuela). In the following, the central results in the context of this thesis are presented for each of the two studies. Section 6.1 summarizes the results by Rutherford et al. (2024), Section 6.2 summarizes the results by Khalid et al. (2025), and Section 6.3 presents a conclusion to the two works.

6.1 Shells and inner kinematics in SAMI

Slow rotator galaxies with low values of the spin parameter λ_R (Emsellem et al. 2007, 2011, also see Section 4.2.3) have typically also been characterized by being massive and having old stellar ages, which appear to be the result of diverse formation paths (e.g., Lagos et al. 2022). While simulations have shown that in general slow rotators develop through galaxy mergers (e.g., Di Matteo et al. 2009; Bois et al. 2011; Choi & Yi 2017; Lagos et al. 2018; Schulze et al. 2020), some studies have found no relation between merger signatures and slow rotators (e.g., Oh et al. 2016), indicating that the relevant mergers occurred long ago to not be traceable anymore. Having established the correlation between tidal shells as a merger signature and a slowly rotating host galaxy for the Magneticum Box4 (uhr) simulation and the MATLAS survey (Valenzuela & Remus 2024), we used galaxies from the SAMI survey (Croom et al. 2012; Bryant et al. 2015) to consolidate the connection between slow rotators and recent mergers.

To this end, we selected galaxies from SAMI DR3 (Croom et al. 2021) that are early-type galaxies according to the classification by Cortese et al. (2016) and that live in non-cluster environments. These galaxies are covered by the Hyper Suprime-Cam Subaru Strategic Program (HSC-SSP; Aihara et al. 2019), which has a surface brightness limit of 27.8 mag arcsec^{-2} in the r-band. We set a stellar mass criterion of $M_* \geq 10^{10}\,\mathrm{M}_\odot$, resulting in a sample of 411 galaxies. Of these, 325 have λ_{R_e} measurements available from van de Sande et al. (2017), 405 have ellipticity measurements from D'Eugenio et al. (2021), and 386 have light-weighted age measurements from Vaughan et al. (2022).

Tidal features were identified by eye from r-band, rgb, and model-subtracted (using mult-Gaussian expansion fits, MGE, following D'Eugenio et al. 2021) images of the individual galaxies and their outskirts. Here we only distinguished between tidal streams and shells. Of the total galaxy sample, there are 71 galaxies with shells and 76 with streams (18 of which have both types of features). These fractions of galaxies with tidal features are overall comparable to the fractions found for MATLAS (Bílek et al. 2020) and Magneticum Box4 (Valenzuela & Remus 2024). The fraction of galaxies with tidal features is highest for young and massive galaxies, where around 35% of the galaxies with above-median stellar mass and below-median age have tidal features, whereas this value is 10–12% for older or lower-mass galaxies. For the total galaxy sample, neither λ_{R_e} nor the ellipticity ϵ is correlated with the presence of tidal features.

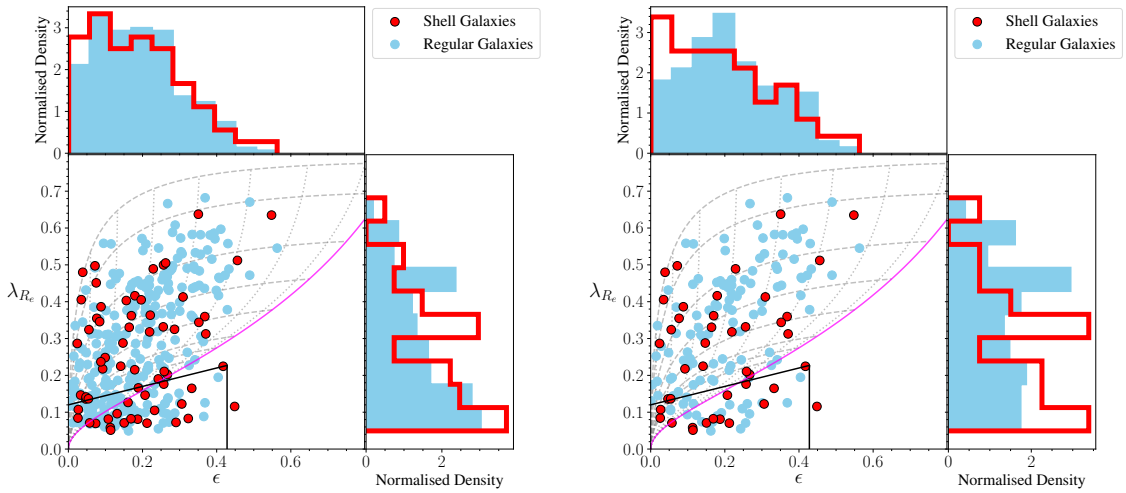


Figure 6.1: Location of SAMI galaxies in the λ_{R_e}-ϵ plane for the total galaxy sample (left) and galaxies with mean stellar ages below the median (right). Shell galaxies are marked in red, while galaxies without any tidal features (regular galaxies) are marked in blue. The histograms above and to the left of the main panels indicate the normalized probability density functions of ϵ and λ_{R_e}, respectively. The region contained by the solid black line marks the slow rotators according to the definition by van de Sande et al. (2021), $\lambda_{R_e} < 0.12 + 0.25\epsilon$ and $\epsilon < 0.428$, whereas galaxies outside the region are considered fast rotators. The solid magenta line traces the theoretical prediction for edge-on oblate galaxies with an anisotropy of $\beta = 0.7\epsilon$. The dotted gray lines indicate the same relation, but for different inclinations from 10° to 80°. The dashed gray lines also indicate the same relation, but for different fixed intrinsic ellipticities $\epsilon_{\rm intr} = 0.9$ to 0.35 as the viewing angle changes from face-on ($\epsilon = 0$) to edge-on (ϵ reaching the solid magenta line). *These are figures 6 and 7 from Rutherford et al. (2024).*

Since Valenzuela & Remus (2024) found that tidal shells are most strongly correlated with lower values of λ_{R_e}, we next placed a particular focus on the SAMI shell galaxies. In the left panel of Figure 6.1, we show the λ_{R_e}-ϵ plane for the SAMI galaxies with shell galaxies highlighted in red. Considering the overall distributions of λ_{R_e} and ϵ for galaxies with shells (red histogram) and galaxies without any tidal features (regular galaxies, blue histograms), there is no statistically significant difference between them. For both samples, the galaxies tend to have lower values of ellipticity and rotational support, which is expected based on the selection of massive early-type galaxies. However, the lack of any difference between the two samples stands in contrast to the results of Valenzuela & Remus (2024) for the simulation Box4 and the MATLAS survey.

Only when considering solely the younger galaxies (with mean light-weighted stellar ages younger than the median), for which the fraction of galaxies with tidal features is generally higher, the distributions of λ_{R_e} and ϵ differ between the shell galaxies and galaxies without tidal features (right panel of Figure 6.1). For this subsample, the young shell galaxies continue to have similar distributions of the two parameters (comparing the red histograms between the left and right panels), whereas the young galaxies without tidal features tend to have larger ellipticities and higher values of λ_{R_e} (comparing the blue histograms between the left and right panels). Here we finally do recover the same behavior found by Valenzuela & Remus (2024) for Box4 and MATLAS, just that for SAMI it is limited to the younger half of galaxies.

This trend is driven by the fraction of slow rotators among galaxies without tidal features falling for younger galaxies, while the fraction of slow rotators among shell galaxies stays almost constant.

If we assume that the mean light-weighted stellar age can be used as an indicator for the time of the last major merger, this would imply that old slowly rotating galaxies had their major merger and spin-down occur long ago, where any shell features would have dissipated by today (based on an estimated lifetime of ∼4 Gyr, Mancillas et al. 2019). As a result, the correlation between slow rotators and the presence of shells disappears for these old galaxies. In contrast, for young slowly rotating galaxies a recent major merger would be more likely to have a still observable remnant in the form of shells. For this latter case, a correlation between slow rotators and shells emerges. These results are consistent with the idea that a spin-down induced by a merger is only traceable through tidal shells for a limited period of time.

Finally, we also find that limiting the sample to strongly visible shells (which were also part of the visual classification scheme), the difference of λ_{R_e} between shell and tidal feature-less galaxies becomes even greater at younger ages. This indicates that weaker shell systems formed through less impactful mergers that do not affect the inner rotation of the galaxies as much, or through misclassified shells that are in reality a different type of feature, such as rings or weak spiral arms.

6.2 Tidal feature occurrence for simulated satellites

In denser environments, there are two effects that can affect the likelihood of merger events. On the one hand, more galaxies are contained in a smaller volume, such that generally more mergers can occur. On the other hand, in the densest regions, for instance near the center of a galaxy cluster, the relative velocities between satellite galaxies become so large that mergers occur less frequently. Cosmological simulations and semi-analytic models have predicted that galaxy interactions are most common in group environments and drop towards lower (field galaxy regime) and higher (galaxy cluster regime) halo masses (e.g., Gnedin 2003; Mihos 2004; Jian et al. 2012; Omori et al. 2023). Observations have in contrast discovered that galaxies in the cluster environment show a larger rate of post-merger features, which has been connected to regions of lower velocity dispersion such as the outer cluster regions or within infalling galaxy groups (e.g., Sheen et al. 2012; Oh et al. 2018; Kim et al. 2024). Putting this in the context of infalling galaxies into the potential of a more massive host, some studies have related the phase-space properties of satellite galaxies with their infall times into the cluster or group (e.g., Rhee et al. 2017; Pasquali et al. 2019).

Kim et al. (2024) performed a first analysis on several observed galaxy clusters, comparing the occurrence of merger and post-merger signatures with the location in projected phase space (projected distance from the cluster center vs. line-of-sight velocity). They find that merging galaxies are located predominantly in groups in the cluster outskirts, whereas post-merger signatures are found throughout phase space. To further probe the occurrence of post-merger signatures in different environments and thereby provide predictions for mergers of infalling

galaxies, we employ several cosmological simulations to analyze the occurrence of tidal features as post-merger indicators of satellite galaxies. To this end, we use the tidal feature census of Khalid et al. (2024) for the simulations Magneticum Box4 (uhr; Teklu et al. 2015; Dolag et al. 2025), EAGLE (Schaye et al. 2015), and TNG100 (Marinacci et al. 2018; Naiman et al. 2018; Nelson et al. 2018; Pillepich et al. 2018; Springel et al. 2018). The tidal features were visually identified through mock images designed to imitate the expected 10-year Vera C. Rubin Observatory Legacy Survey of Space and Time (LSST; Ivezić et al. 2019) data with its point spread function (PSF) and surface brightness limit of roughly 30 mag arcsec^{-2} in the g, r, and i bands.

For the classification, four types were distinguished: *tidal streams and tails* (as one group, in contrast to Bílek et al. 2020 or Valenzuela & Remus 2024), *tidal shells*, *plumes or asymmetric halos* as diffuse structures in the outer regions, and *double nuclei* as actively merging galaxies with two clearly distinguishable nuclei and tidal features being present. Khalid et al. (2024) find that the tidal feature occurrences are similar between the simulations and show the same behavior as a function of stellar and halo mass, despite differences in employed galaxy formation models and mass resolution. Satellite galaxies with stellar masses of $\log M_*/\mathrm{M}_\odot \geq 9.5$ are selected. For the environments we consider three halo mass bins based on the host galaxy's virial mass $M_{200,\mathrm{crit}}$ (total mass within a sphere with average density equaling 200 times the critical density of the Universe), with field galaxies ($\log M_{200} = 12$–13), galaxy groups ($\log M_{200} = 13$–14), and galaxy clusters ($\log M_{200} = 14$–14.7).

To investigate the occurrence of tidal features in different regions of phase space, we employ the regions in projected velocity-radius phase space by Pasquali et al. (2019). These regions generally trace the infall times associated with galaxies located in the respective regions, where they parametrized zones with values of $p = 1$–7 (see Pasquali et al. 2019 for details). We define the regions of $p = 1$–2 as *ancient infallers*, which have average infall times of (5 ± 2) Gyr, $p = 3$–4 as *intermediate infallers* with infall times of (4 ± 2) Gyr, and $p = 5$–7 as *recent infallers*, with infall times of (2 ± 1) Gyr. Note that these infall time estimates are based on data from the group and cluster regimes, but likely do not apply to lower-mass host galaxies. The zones are also limited to radii smaller than $R_{200,\mathrm{crit}}$ (the radius within which $M_{200,\mathrm{crit}}$ is determined).

While we consider the tidal feature occurrences in projected phase space in Appendix C, we here focus on the intrinsic 3D phase space, which furthermore shows clearer trends. Note that the originally defined regions by Pasquali et al. (2019) were defined for projected phase space, though for this analysis they suffice as general indicators for the infall times of satellite galaxies when directly applied to 3D phase space. Figure 6.2 shows the locations of galaxies with and without tidal features (blue crosses and red circles, respectively) in 3D phase space for the three halo mass bins (field galaxies, groups, and clusters, from left to right). The ancient, intermediate, and recent infaller regions are indicated by the solid gray lines, and the fourth outer region beyond $R_{200,\mathrm{crit}}$ is separated by the dashed gray line.

Considering the fractions of tidal features, there are large differences between the three environments. Most satellites of field galaxies in the ancient infaller region and thereby

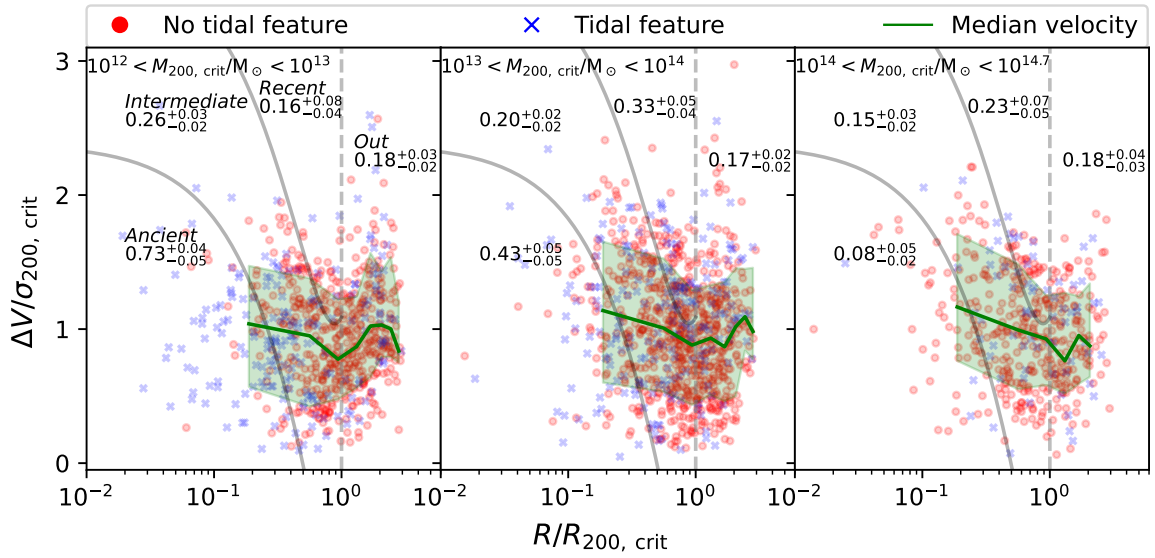


Figure 6.2: Phase-space diagram of satellite galaxies in host halos of three different mass bins, for field galaxies (log M_{200} = 12–13, left), galaxy groups (log M_{200} = 13–14, center), and galaxy clusters (log M_{200} = 14–14.7, right). The phase space is made up of the 3D radial distance to the host center R, normalized to $R_{200,\mathrm{crit}}$, and the 3D velocity relative to the host ΔV, normalized to the halo velocity dispersion $\sigma_{200,\mathrm{crit}}$. The markers indicate the combined sample of satellite galaxies from Magneticum Box4, EAGLE, and TNG100, differentiating between galaxies with (blue crosses) and without (red circles) tidal features. The solid green line indicates the median velocity as a function of radius and the shaded region its 1σ scatter. The solid gray lines mark the borders of the ancient, intermediate, and recent infaller regions (as specified in the left panel, based on the definitions of Pasquali et al. 2019), and the vertical dashed gray line marks the halo border of $R_{200,\mathrm{crit}}$, separating the outer fourth region (Out). The fractions of galaxies having tidal features and their corresponding upper and lower errors are indicated in each region. *This is figure D1 from Khalid et al. (2025).*

residing close to the host galaxy show tidal features (almost 75%, left panel), whereas ancient infaller satellites in galaxy clusters are unlikely to have tidal features (less than 10%, right panel). For group satellites, almost half have tidal features in this region (43%, center panel). This shows how the higher velocity dispersions in the dense environments lead to fewer galaxies showing signs of interaction, which would have to have occurred after their infall to still be visible, based on an assumed infall time of 5 Gyr ago, which is longer than the typical lifetime of tidal features (Mancillas et al. 2019).

In contrast, for field galaxies, the closer a satellite is to the host, the more likely it is to undergo interactions, where more distant intermediate and recent infallers have lower tidal feature fractions of 26% and 16%, respectively. This trend is less strong for groups, where the largest feature fraction is still found for ancient infallers, but the lowest fraction is in fact found for intermediate infallers. We suggest that this shows the two mechanisms working against each other, where denser environments increase the interaction rate, but higher velocity dispersions decrease it. Finally, the intermediate and recent infallers in galaxy clusters show the same trend as galaxy groups, with the central difference being that ancient infallers in clusters are much less likely to show signs of interaction, caused by the high-velocity encounters. In all environments, the outer regions show a constant ∼18% fraction of galaxies

having tidal features, indicating that these outer regions are still unaffected by the environment in their vicinity. In projected phase space, these intrinsic 3D trends are found to become less significant, but generally still show the same behavior (see Appendix C). The differences are mostly confined to the central ancient infaller region, whereas the other three regions are largely consistent between the feature fractions in the intrinsic regions and the projected regions, such that for those regions the intrinsic 3D results can generally be applied to observations.

6.3 Conclusion

In two further studies, we build on the results from Valenzuela & Remus (2024) with respect to tidal features found around galaxies in the Magneticum Box4 (uhr) simulation and the MATLAS survey. We extended the analysis of the relation between the presence of tidal shells and the inner galaxy kinematics to a larger galaxy sample from the SAMI survey, where we do not recover the originally expected correlation of tidal shells preferentially occurring around slow rotators (Rutherford et al. 2024, incl. Valenzuela). However, when reducing the sample to the younger half of the galaxies, we again find the same correlation. This indicates a subtlety not revealed through Box4 or MATLAS, where early major mergers that transformed galaxies into slow rotators are not traceable anymore after several Gyr because any remnant tidal features dissipate over time and cannot be identified anymore at the present day. In contrast, younger slowly rotating galaxies, of which a significant fraction presumably suffered a major merger more recently, will still display tidal shells around them.

We additionally expanded on the tidal feature statistics, differentiating not only between environments, but furthermore between the infall regions in phase space (Khalid et al. 2025, incl. Valenzuela). To this end, we used satellite galaxies from three cosmological simulations, specifically Magneticum Box4 (uhr), EAGLE, and TNG100, and considered the locations of tidal features in phase space based on the feature classifications by Khalid et al. (2024) and the phase space infall regions by Pasquali et al. (2019). We find that the inner regions of galaxy clusters (ancient infallers) suppress tidal features, whereas field galaxies and group environments show increased signs of interactions in those regions. The intermediate and recent infaller regions as well as the outer surrounding regions show tidal feature fractions more comparable to each other. For cluster environments, we suggest that mergers occur within infalling groups in the recent infaller region and dissipate by the time the satellites become ancient infallers.

These studies show the necessity of extensive analyses using both observations and simulations to statistically probe the occurrences of tidal features and their relations with other galaxy properties. Since tidal features are post-merger signatures, such endeavors lead to deeper insights and improve our understanding of mergers and their importance in galaxy formation.



Movement II

Planetary Nebulae

7

Introduction to Planetary Nebulae

This chapter contains parts from the introductions of Valenzuela et al. (2025b,c,d, 2026), whose results are presented in the subsequent chapters.

Planetary nebulae (PNe) have been established as important tracers in galaxies for decades because of their bright [O III] λ5007 emission line. They form as a late stellar evolutionary phase for intermediate-mass stars, during which a nebula forms around the central star. This nebula is ionized and becomes the source of multiple emission lines including [O III] λ5007, typically the brightest among them. A PN can re-emit up to 15% of the central star's total luminosity through the [O III] line (Dopita et al. 1992), which is the reason that it can be observed even in extragalactic systems, for instance through narrow-band filters. This has made PN detections possible out to 100 Mpc (Gerhard et al. 2005). Since PNe come from stars, they have become popular tracers for the underlying stellar component. For this reason, the second Movement of this thesis focuses on investigating PNe as stellar tracers and what their properties can reveal about galaxy formation histories.

Figure 7.1 shows an example of a Galactic PN (the Necklace Nebula[1], at a distance of about 4.6 kpc), which is spatially resolved. In contrast, more distant PNe outside the Local Group appear as point sources.

[1] https://esahubble.org/images/potw2117a/

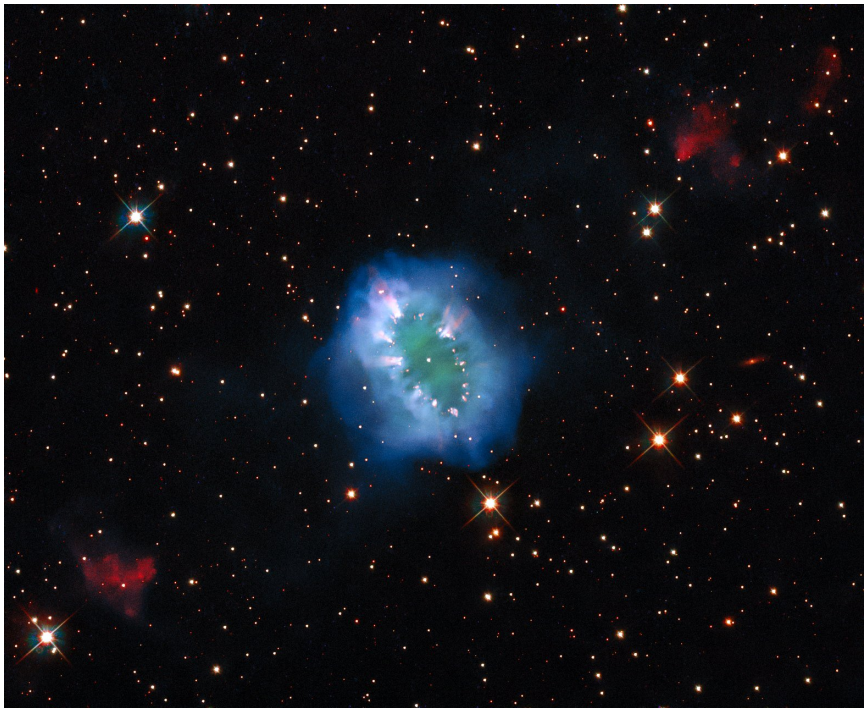


Figure 7.1: Example of a Galactic PN imaged with the Hubble Space Telescope, known as the Necklace Nebula, at a distance of ~4.6 kpc. At its center resides a binary star system, seen as the central bright dot in the image. *Image credit: ESA/Hubble & NASA, K. Noll.*

7.1 A phase of stellar evolution

Planetary nebulae can form for intermediate-mass stars with an initial mass of around 0.8–8 $M_\odot$ and are a phase of their stellar evolution. For most of its lifetime, a star on the main sequence burns hydrogen through nuclear fusion, converting it into helium (see Figure 7.2 for an example of the evolution of a solar-mass star in the Hertzsprung-Russell diagram). Once the hydrogen in the core has been converted to helium, the star leaves the main sequence on the red giant branch (RGB; beginning of the red line), where hydrogen is burned in a shell around the core and the star expands in size. When helium is able to ignite in the core (as a *helium flash* for lower-mass stars of $\lesssim 2\,M_\odot$, or more smoothly at higher masses, see Miller Bertolami 2016), the star leaves the RGB and converts helium to carbon and oxygen. Once helium runs out, the star begins to expand again, now entering the asymptotic giant branch (AGB; end of the red line), where helium and hydrogen are burned in two shells around the core. During this phase, thermal pulses, where the helium shell ignites, lead to a rapid expansion of the star. In the cooling outer layers, dust can condense and is then also pushed out through stellar winds. As a result of these processes, the star experiences significant mass loss, which finally leaves behind a shrinking and heating star in the post-AGB phase (brown line). As the effective temperature increases, the high-energy photons of the central star can photo-ionize the atomic gas in the gaseous envelope, resulting in nebular emission lines during this PN phase (pink line). A PN thereby arises in the late stellar evolution phase of the post-AGB and lasts for only up to 25 000–30 000 yr until the gas disperses or the ionizing radiation dies down (e.g., Pottasch 1984; Méndez et al. 1993). When nuclear fusion ceases in the central star, it begins to

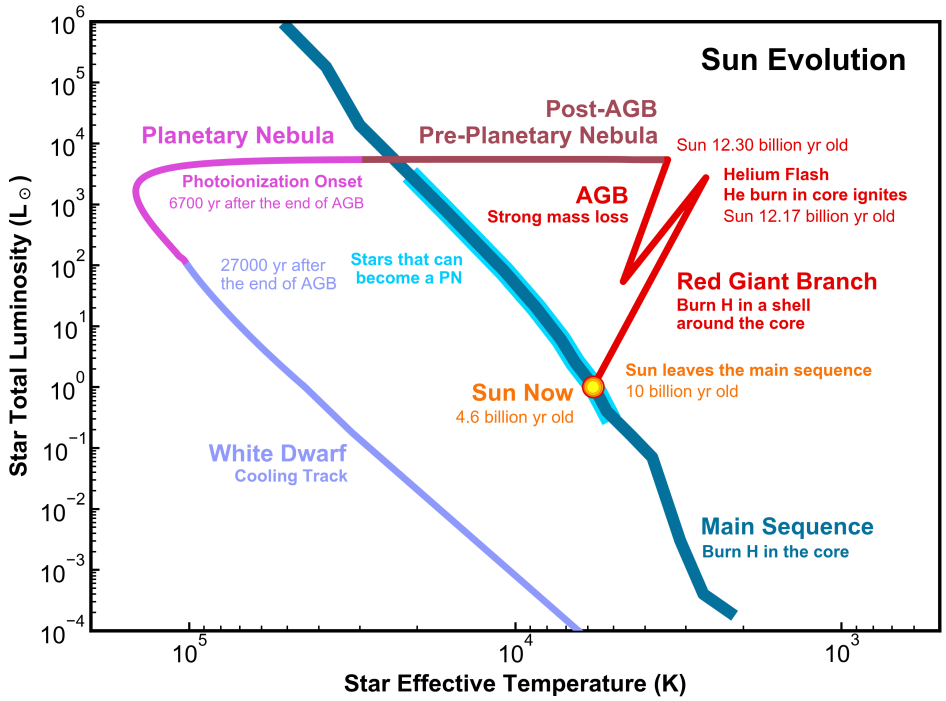


Figure 7.2: Evolution of the Sun in the Hertzsprung-Russell diagram with respect to its effective temperature and total luminosity. The Sun's current location on the main sequence is marked with the orange point. The main sequence is indicated by the thick blue line, where the subsection of stars that can become PNe is highlighted in cyan. The other colored lines show the subsequent stellar evolutionary phases of the Sun after it leaves the main sequence: the red giant branch (RGB), helium flash, and asymptotic giant branch (AGB) phases (red), the initial post-AGB phase (brown), the PN phase (pink), and finally the white dwarf phase (purple). *This is figure 2 from De Marco et al. (2025).*

cool and decrease its luminosity, thereby evolving into a white dwarf (purple line). For a more detailed description of the stellar evolution for such intermediate-mass stars, see Iben (1995). In the following, we highlight some of the key factors for PNe regarding their stellar evolution.

Mass loss. The mass loss during the AGB phase is significant, where a star can lose 50% to 80% of its initial mass. The resulting final mass of the central star is an important quantity that affects the star's luminosity, which stays roughly constant during the post-AGB phase and together with the rising temperature is responsible for the amount of ionizing radiation. The relation between the initial and final mass is also referred to as the initial-to-final mass relation (IFMR). It has been hard to constrain the IFMR observationally, where the reasons include uncertainties in stellar mass measurements and the difficulty to connect the main sequence stars to the white dwarfs at the same age and metallicity (e.g., in star clusters, Cummings et al. 2018). Even theoretically it is difficult to predict because of the challenges of modeling the thermal pulses during the AGB phase (e.g., Miller Bertolami 2016). Despite the challenges, there are several measured and modeled IFMRs in the literature, which mostly show a monotonically increasing IFMR (e.g., Miller Bertolami 2016; Cummings et al. 2018; Cunningham et al. 2024; Hollands et al. 2024).

Stellar lifetime. Since the stellar lifetimes on the main sequence and in the post-main sequence phases (until the end of the AGB) are shorter for more massive stars (e.g., Miller Berto-

lami 2016), this means that central stars of PNe in younger stellar populations are more massive (based on the increasing IFMR). In turn, a more massive central star has a larger luminosity (Miller Bertolami 2016) that ionizes the nebular envelope. The stellar lifetime before the PN phase amounts to a few 100 Myr up to ∼12 Gyr for initial masses of 4 $M_\odot$ and 1 $M_\odot$, respectively (Miller Bertolami 2016).

Nebular emission. Because of the very low densities of the nebular gas, it is possible for metastable excited energy levels to occur in different elements, which would normally be collisionally de-excited in denser environments. For this reason, electron transitions for certain ions are possible in PNe that otherwise rarely occur. This is most notably the case for the doubly-ionized oxygen forbidden line at 5007 Å, commonly referred to as [O III] λ5007 (e.g., Iben 1995). When conditions are optimal, up to 15% of the central star's total luminosity can be re-emitted in [O III] (Dopita et al. 1992), making PNe attractive extragalactic tracers.

7.2 Planetary nebula luminosity function

Due to their bright [O III] λ5007 line, a PN luminosity function (PNLF) can be determined for a galaxy's PN population. The PNLF is the histogram of the [O III] magnitudes, $m(5007)$, which are obtained from the [O III] fluxes (Jacoby 1989):

$$m(5007) = -2.5 \log F(5007) - 13.74, \tag{7.1}$$

where $F(5007)$ is the flux of the [O III] λ5007 line in erg s^{-1} cm^{-2}. As the apparent magnitudes are dependent on distance, the PNLF is oftentimes shown in terms of absolute magnitudes $M(5007) = m(5007) - 5 \log D/(10\,\mathrm{pc})$, for a distance D. The shape of the PNLF has generally been described by a function introduced by Ciardullo et al. (1989):

$$N(M(5007)) = c_1 e^{c_2 M(5007)} \left(1 - e^{3(M^*(5007) - M(5007))}\right), \tag{7.2}$$

where the parameter $M^*(5007)$ represents the absolute [O III] magnitude of the brightest PNe (also referred to as the bright-end cutoff of the PNLF), c_1 is the normalization, and $c_2 = 0.307$. An example of an observed PNLF and the overplotted fitted analytic PNLF of Equation 7.2 is shown in Figure 7.3. Some authors have also generalized this function by allowing the value of c_2 to vary as a second parameter (e.g., Longobardi et al. 2013; Hartke et al. 2017).

7.2.1 Bright-end cutoff of the PNLF

As it was found that the bright end of the PNLF is constant at around $M^*(5007) \approx -4.5$ mag in the local Universe, independent of galaxy type and stellar population, Ciardullo et al. (1989) introduced the PNLF as a standard candle by calibrating it through PN measurements in M 31 and its satellites. Since then, the PNLF has been determined for a large number of galaxies in the local Universe and more distant galaxies, and has since also been assessed as being

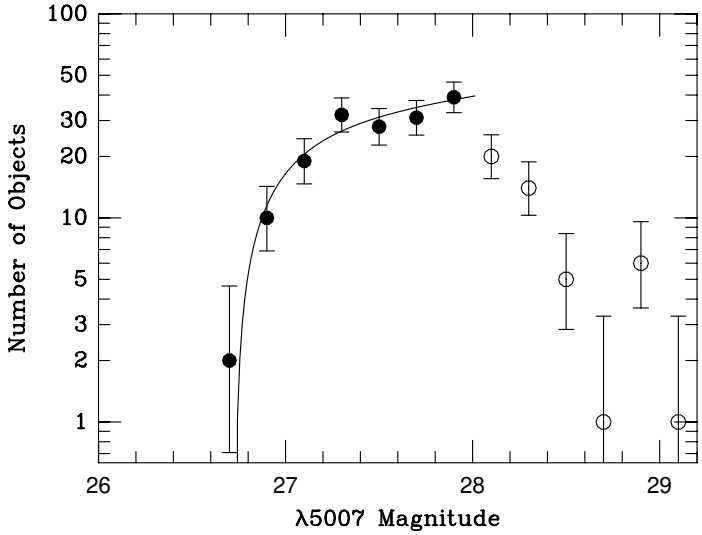


Figure 7.3: Observed PNLF of NGC 1399 (black circles) with the overplotted best fit PNLF (Equation 7.2; black line), shown in apparent magnitudes. The filled circles denote the magnitude bins where the PNe are statistically complete, the open circles where they are statistically incomplete. The error bars show the 1σ confidence intervals. *This is figure 22 from Jacoby et al. (2024).*

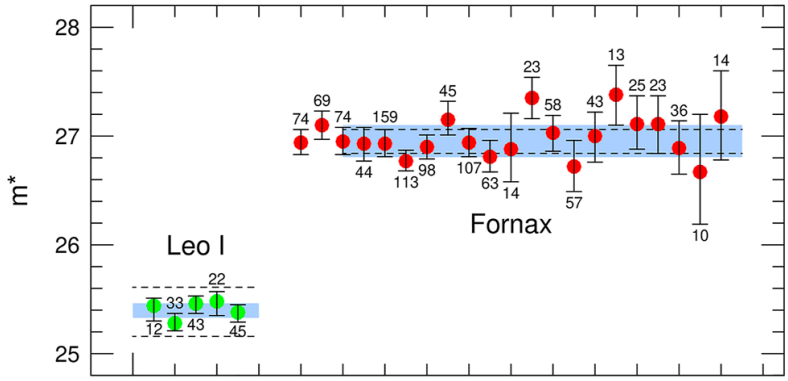


Figure 7.4: Apparent PNLF bright-end cutoff magnitudes m^* of galaxies in the Leo I group (green points) and Fornax cluster (red points). The blue shaded regions show the respective 1σ scatter of the cutoff magnitudes within Leo I and Fornax. The dashed lines indicate the equivalent distance offset of ± 1 Mpc from the mean. The error bars show the uncertainties of the cutoff magnitudes. The number of PNe used in each PNLF fit is indicated above or below the error bars. *This is figure 3 from Ciardullo (2022).*

a reliable distance indicator (Jacoby et al. 1990a; Rekola et al. 2005; Ciardullo 2012). The PNLF has been successfully used to measure distances for galaxies up to 10–15 Mpc, where it has complemented other distance measurement approaches (Ciardullo et al. 2002). However, it has been limited to within 20 Mpc because of the limitations of narrow-band filter imaging (Roth et al. 2021). Figure 7.4 shows the variations of the apparent bright end cutoff magnitude in the Leo I group and the Fornax cluster, where the galaxies can be expected to have almost the same distances. The small scatter of the cutoff magnitudes underlines how little variation there is even between different galaxy morphologies.

Advances on the observational side regarding integral field unit (IFU) measurements with the instrument MUSE have made it possible to obtain the full spectra for each individual pixel, thereby making the detection of PNe and the removal of contaminants possible without

follow-up measurements in pencil beam observations. This enables the study of PNe at larger distances, and complements previously existing methods like the PN Spectrograph (PN.S; Douglas et al. 2002; see also the extended PN.S early type galaxy survey, ePN.S; Pulsoni et al. 2018). In turn, the PN.S has the advantage of a significantly larger field of view (100 arcmin^2 vs. 1 arcmin^2 for MUSE) and higher spectral resolution, which has enabled detailed dynamical studies of galaxies using PNe (e.g., Aniyan et al. 2018, 2021, for face-on disks). Using MUSE, several works have analyzed extragalactic PN populations, getting better data for previously studied objects or investigating new systems (e.g., Kreckel et al. 2017; Spriggs et al. 2020; Roth et al. 2021; Scheuermann et al. 2022; Soemitro et al. 2023; Jacoby et al. 2024). Furthermore, the high spatial resolution and the IFU nature of MUSE are expected to make it possible to measure distances of up to 40 Mpc through the PNLF bright end, more than twice as far compared to previous limits (Roth et al. 2021).

While the universal PNLF bright-end cutoff appears to be independent of stellar age and metallicity, this has been found to be restricted to metallicities of $12 + [\mathrm{O/H}] \gtrsim 8.5$ (e.g., Ciardullo 2012). At lower metallicities, theory and observations have determined that there is a slight dependence of the PNLF bright end on metallicity, where the bright end becomes fainter for very metal-poor systems (e.g., Ciardullo & Jacoby 1992; Dopita et al. 1992; Ciardullo et al. 2002; Ciardullo 2010).

7.2.2 The PNLF puzzle

Despite the wide usage, the underlying physics of the universality of the PNLF has remained a mystery in particular due to the question how old elliptical galaxies should be able to host any PNe as bright as the ones observed at the magnitude cutoff (Ciardullo 2012). The theoretical reason for this is that old stars at the main-sequence turnoff should be too low in mass to produce such high emission in [O III] during the post-AGB phase. On the other hand, young stellar populations would be expected to have brighter intrinsic [O III] emission. To this end, there are observational indications that the stronger circumstellar dust extinction around more massive stars decreases the observed flux to the bright-end cutoff over a large range of central star masses, preventing overly luminous PNe (Jacoby & Ciardullo 2025). Over the years, many attempts have been made to resolve the tension between theory and observations, which is summarized in the section on PN models (Section 7.4).

7.2.3 Faint part of the PNLF

Not only has the bright end of the PNLF drawn attention, but so has the shape of the faint part of the PNLF: the general shape was introduced in its analytical form (Equation 7.2) by Ciardullo et al. (1989) as an exponential cutoff function with a parameter describing the slope on the faint side based on theoretical derivations of Henize & Westerlund (1963) and Jacoby (1980). This slope has been predicted to encode clues about the star formation history (e.g., Ciardullo 2010; Longobardi et al. 2013; Hartke et al. 2017) and has been investigated in particular for the different substructures in the outskirts of M 31 (Bhattacharya et al. 2021).

For this, Bhattacharya et al. (2021) also used the approach of fitting a superposition of two modes of the PNLF following Rodríguez-González et al. (2015). A further interesting feature that has been observed in the faint part of the PNLF is a dip for galaxies with recent star formation, that is a lower abundance of PNe at an intermediate magnitude (e.g., Jacoby & De Marco 2002; Reid & Parker 2010; Soemitro et al. 2023). Even some models have been able to find such a dip in the PNLF for younger stellar populations (e.g., Méndez et al. 2008; Valenzuela et al. 2019).

7.3 Planetary nebulae as stellar tracers

Arising during the late evolutionary stages of regular stars, PNe to first order trace the underlying stellar component. For this reason, they have long been used as stellar tracers in the outskirts of galaxies to infer the spatial and kinematic properties in the halo. However, since PNe correspond to a very particular phase of stellar evolution, to second order the PN population should also contain clues about the underlying stellar population properties.

7.3.1 Spatial and kinematic tracers

Spatial and kinematic studies of PNe have been performed for decades due to the ease of their observation via the [O III] line and because of being able to determine their radial velocities with good accuracy (Arnaboldi et al. 1998). Surveys such as SLUGGS (Brodie et al. 2014) and ePN.S (Pulsoni et al. 2018) have shown that PNe are generally good tracers for the stellar light in the outskirts of galaxies. One of the first large analyses of PN kinematics was done by Hui et al. (1995) for the massive elliptical galaxy Centaurus A, who also attempted to determine the mass distribution of its DM halo with the PNe. This study was extended a number of years later by Peng et al. (2004b) with an even larger sample of PNe in the outer halo.

The kinematics of PNe have also been measured in different environments. For galaxy clusters, they have for instance been studied in the cores and the member galaxies (Virgo Cluster: e.g., Arnaboldi et al. 1996; Teodorescu et al. 2011; Fornax Cluster: e.g., Arnaboldi et al. 1998; Spiniello et al. 2018), in their outer halo (e.g., Longobardi et al. 2018), and in the intracluster regions (e.g., Arnaboldi et al. 2002, 2004). Through this research, it has, for example, been possible to study the diffuse stellar component and to separate the stellar halos of various member galaxies from the intracluster light. Individual galaxies have also been targeted, such as elliptical (e.g., Coccato et al. 2009) and lenticular galaxies (e.g., Cortesi et al. 2011, 2013a,b), and the ePN.S survey for PNe in early-type galaxies (ETGs) aims at determining and analyzing the kinematic profiles of more than 30 ETGs by using PNe as tracers (Pulsoni et al. 2018). Through such studies, the PN data in the outskirts has helped further constrain the formation and merger histories of galaxies since the relaxation timescales in the outer regions are longer, thereby providing a deeper view into the past.

To date, there have not been many studies combining deep photometric observations of tidal features with kinematic PN measurements to gain further insights into the past. In one notable study, PNe were observed in a shell around NGC 474 (see Section 5.2 for a discussion on some of its properties) through MUSE observations (Fensch et al. 2020). They were able to kinematically associate the PNe with the shell and used the PN abundance to estimate the mass of the shell progenitor.

7.3.2 Stellar population tracers

Through the [O III] magnitude measurements of PNe, the information contained in a PN population is not only limited to their spatial and kinematic properties. As discussed above, the PNLF bright end loses its universality toward low metallicities and becomes fainter (Section 7.2.1; Ciardullo 2010), and the faint part of the PNLF has been shown to correlate with the stellar population (Section 7.2.3), for instance through its slope (e.g., Longobardi et al. 2013) or through a dip in the PNLF of young galaxies (e.g., Jacoby & De Marco 2002). Further studies indicate that the number of PNe per underlying bolometric luminosity (referred to as the luminosity-specific PN number α) also vary with the stellar population (e.g., Hartke et al. 2017).

A main difficulty in connecting PNe with their underlying stellar populations has been that narrow-band imaging and slitless spectroscopy, which were otherwise used in PN surveys, struggle to detect PNe in the central bright regions of galaxies (e.g., Hartke et al. 2026). However, this is where stellar population properties are most easily measured. With the advent of IFU instruments such as MUSE, co-spatial studies connecting PNe and stellar populations in the same region and from the same data have finally become possible even in the inner regions of galaxies (e.g., Scheuermann et al. 2022; Congiu et al. 2025; Hartke 2025). These observational advances require an improved theoretical understanding of the PNe and their properties to physically interpret the data.

7.4 Modeling planetary nebula populations

Overall, there have been several approaches to modeling PNe and their [O III] emission. One of the main difficulties is the modeling of stellar evolutionary tracks through the post-main sequence and post-AGB phases, of which only a few exist. Some of the early tracks were those by Schönberner (1983), Vassiliadis & Wood (1994), and Blöcker (1995). Based on those tracks, Méndez & Soffner (1997) improved on earlier models (Méndez et al. 1993) for the [O III] emission of PNe to constrain the properties of the underlying PN populations of observed galaxies. Through their model, they found that the nebulae cannot be entirely optically thick with respect to the central star's UV radiation to reproduce the PN abundances in galaxies. Further PN models were developed based on photoionisation models (e.g., Dopita & Meatheringham 1991a; Dopita et al. 1992; Marigo et al. 2004) and on hydrodynamical PN models to further improve the properties of the [O III] intensity (Schönberner et al. 2007;

Méndez et al. 2008; Schönberner et al. 2010). However, these studies predicted that older stellar populations would produce PNLFs with their bright end being significantly dimmer, which is not observed (e.g., Marigo et al. 2004; Ciardullo 2012, stating that the PNLF bright end should already be dimmer by more than 4 magnitudes for ages of 10 Gyr).

In the last decade, one important advancement has been a new set of post-AGB tracks for intermediate-mass stars (Miller Bertolami 2016). These tracks feature a much faster post-AGB evolution with timescales shorter by a factor of three to ten and with brighter post-AGB stars. These led to several PN models being developed in recent years with a particular focus on improving the understanding of the universal bright end of the PNLF. Overall, the brighter post-AGB evolution has slightly diminished the large discrepancy between the observed bright PNe in old stellar populations and the models (e.g., Gesicki et al. 2018; Valenzuela et al. 2019). In these types of models, the prescriptions were applied to mock PNe generated according to some empirical mass function for central stars of PNe.

Finally, further models have been developed with alternative attempts of explaining the bright end of the PNLF, including accreting white dwarfs (WDs; e.g., Soker 2006; Souropanis et al. 2023), blue straggler stars (e.g., Ciardullo et al. 2005), and WD mergers (e.g., Yao & Quataert 2023). Such models focused more on the general possibility of reaching the bright end of the PNLF rather than modeling an entire PN population, however.

7.5 Scope of this Movement

While PNe have the potential to be a powerful avenue to investigating galaxy formation histories through their spatial and kinematic properties as well as through the details of their PNLF, the challenges between theory and observation have limited the scope of interpreting their observations. The existing PN models have generally been based on mock stellar populations, oftentimes using the results from studies of Milky Way stars. However, such stellar populations may not be representative of the diverse star formation histories seen in real galaxies. As shown in Chapter 2, cosmological simulations provide the variety of galaxies and stellar populations that is also found in observations.

In this Movement, I introduce the first PN model (PICS; PNe In Cosmological Simulations) that can be applied to the galaxies of any hydrodynamical cosmological simulation, which I developed as a part of this thesis, and present multiple applications of it to investigate science cases from stellar and PN physics up to the galaxy regime. I describe PICS itself in Chapter 8, which includes several parameter tests relating to stellar and nebular processes, followed by a first application to simulated galaxies in Chapter 9. In Chapter 10, I present a second set of parameter tests based on the extinction caused by dust expelled during the AGB phase. In Chapters 11 and 12, I apply PICS to a large sample of galaxies to perform a statistical analysis of the PNLF bright end and its overall shape depending on several typical galaxy classifications. This in fact resolves much of the tension between theory and observations, significantly improving our understanding of PNe and their populations in galaxies. In Chapter 13, I use PICS to motivate how PNe can be used as kinematic tracers

in tidal features, through which one can benefit from combining two different stellar tracers. Finally, I present the results of two other PN studies that I significantly contributed to, focusing on the comparison between the observations and models of PN populations in Chapter 14.

8

PICS: Planetary Nebulae In Cosmological Simulations

This chapter was published as Valenzuela et al. (2025c), A&A 699, A371[1]:
The PICS Project. I. The impact of metallicity and helium abundance on the bright end of the planetary nebula luminosity function

With the multitude of observations and modeling approaches, the continual lack of fundamental understanding concerning the PNLF suggests that some of the previously employed assumptions are insufficient to address the problem as a whole. Indeed, there are two central assumptions that have been commonly made in PN models over the years that do not represent realistic stellar populations as they are found in actual galaxies: First, models have mostly only taken into account stellar evolution at metallicities around solar metallicity values, which has been done with respect to their main sequence (MS) and post-MS lifetimes, the initial-to-final mass relation (IFMR), and the post-AGB evolution (e.g., Gesicki et al. 2018; Valenzuela et al. 2019; Souropanis et al. 2023). Furthermore, even stellar evolution models employ many recipes based on measurements of the Sun and assume abundances based on the Milky Way (e.g., Miller Bertolami 2016). For example, the helium abundance has mostly been assumed to scale linearly with metallicity, though this has been put into question recently (e.g., Clontz et al. 2025). Second, the studies that have attempted to model the entire PN population have set up artificial mock stellar populations with the goal of mimicking selected real galaxies

[1]Minor adjustments have been made, and the introduction has been adapted for this thesis.

(e.g., Méndez & Soffner 1997; Valenzuela et al. 2019), but again relying on observations in the Milky Way, specifically the WD mass distribution. These models therefore fall short of accurately representing the large diversity of galaxies and star formation histories, which can strongly vary depending on intrinsic factors and the cosmological environment.

To overcome these limitations of current PN models, we introduce PICS (PNe In Cosmological Simulations), a modular framework for modeling PNe within any given stellar population, taking into account properties such as mass, age, metallicity, and the initial mass function (IMF). In the era of hydrodynamical cosmological simulations, a new approach is further possible: realistic stellar populations with self-consistent properties in the cosmological context can be directly obtained for a large variety of galaxies from such simulations. With PICS, we present the very first method for bringing PNe into cosmological simulations and simultaneously improve on previous PN models by fully considering the metallicity and specific abundances beyond solar values. Finally, the modular nature of the framework allows for controlled testing of different parameters and individual models, which we will also demonstrate in this paper.

In Section 8.1, we present the PICS model structure and the implementation of the fiducial model, including the metallicity dependence on the individual modules. By combining some of the modules, we then show how the metallicity and helium abundances affect the stellar evolution relevant for PNe in Section 8.2. In Section 8.3, we present grids of PNLFs resulting from different pairs of ages and metallicities and from varying the IFMR – these are the building blocks for any real PNLF. Finally, we summarize the results and conclude in Section 8.4.

8.1 Model

In the following, we describe the building blocks of the PICS model. Its target is to take a given single stellar population (SSP) parameterized by a set of properties and determine the contained PN population. The obtained PN properties in particular include the magnitude of the emitted [O III] line, as it is the primary intrinsic observable quantity of an extragalactic PN. This procedure will make it possible to apply PICS to both observed galaxy star formation histories discretized by SSPs and to the stellar particles extracted from cosmological simulations (Soemitro et al. in prep.; Valenzuela et al. in prep.). The end result is then a full population of PNe for an entire system like a galaxy or galaxy cluster.

The model is designed to be modular, meaning that the individual parts described in the following can be replaced with different underlying models, and the selection of models will also be continuously expanded in future versions. In this work, we present the fiducial model and some alternative relations for the IFMR and how they affect the PNLF. The source code and more information on using the model are made available online.[2] A summary of the general model functionality is presented in the proceedings by Valenzuela et al. (2025d). The

[2] `https://lucasvalenzuela.de/PICS/`

correction for nebular metallicity and the inclusion of circumnebular extinction are presented here for the first time.

8.1.1 Single stellar population properties

An SSP represents the population of stars having formed from a gas cloud where all the member stars share the same underlying age and chemical composition. The distribution of stellar masses within the SSP is given by an IMF. In its simplest form, the input SSP properties need to include its total mass, an IMF, and its age. The age is needed to determine the initial mass range of stars now residing within the PN phase after having left the AGB track. The IMF is used to determine the fraction of stars that are within that initial mass range, and the total mass sets the absolute number of those stars. In addition to these properties, further quantities significantly influence the processes relevant for stellar evolution and PNe: in particular, we show in this work that the stellar metallicity is a vital parameter that affects the duration of stellar evolution on the MS and post-MS. In the future, individual abundances like helium or α-element abundances will also be added as quantities that are taken into account.

In this work, each SSP is parameterized with the following quantities:

- IMF, for this work we only consider that by Chabrier (2003)
- total mass M_{tot} of the SSP
- age t, that is the time since the formation of the SSP stars
- metallicity Z, in this work quantified as the initial metal mass fraction: $Z = M_{\mathrm{met,init}}/M_{\mathrm{tot,init}}$. As a point of reference, the solar metallicity lies between $Z = 0.01$ and 0.02 (e.g., Asplund et al. 2009; Caffau et al. 2011; von Steiger & Zurbuchen 2016; Asplund et al. 2021).

8.1.2 Stellar lifetime function

In the context of PN modeling, we define the stellar lifetime as the time from the birth of a star until it leaves the AGB phase and enters the post-AGB phase, during which a star can become a PN. It therefore roughly corresponds to the combined MS and post-MS lifetimes from other works (e.g., Renzini 1981; Renzini & Buzzoni 1986; Padovani & Matteucci 1993). The purpose of this module in PICS is to return the initial stellar mass of the stars that now are passing through the PN phase after the age t. Due to the short-lived nature of the PN phase (assumed as 30 000 yr here), the time spent after the departure from the AGB phase is negligible for the initial mass of the star. Then, disregarding binary interactions, we can assume that all PNe in a single stellar population are descendants of stars with the same initial mass.

For this work we took the lifetimes of the stellar evolution simulations from Miller Bertolami (2016), given in their tab. 2. For each of their considered metallicities ($Z = 0.0001, 0.001, 0.01,$ and 0.02) and initial masses (ranging from $M_{\mathrm{init}} = 0.8$–$4.0\,\mathrm{M}_{\odot}$, depending on the metallicity), we added up all the stated lifetimes: MS, red giant branch (RGB), core He-burning, early AGB, and thermally pulsing AGB (TP-AGB) phases as an M-type and carbon star. Taking

Table 8.1: Lifetime function double power law fit parameters.

Z	a_{low}	k_{low}	a_{high}	k_{high}
0.0001	11.80	−3.58	7.98	−2.55
0.001	9.72	−3.52	6.54	−2.45
0.01	6.41	−3.45	4.64	−2.45
0.02	5.95	−3.40	4.75	−2.65

Notes. The fit parameters are for the low ($\leq$1.5 $\mathrm{M}_\odot$) and high initial masses ($\geq$1.5 $\mathrm{M}_\odot$) at the given metallicities Z from Miller Bertolami (2016), parameterized as $t/\mathrm{Gyr} = a \times (M_{\mathrm{init}}/\mathrm{M}_\odot)^k$.

these lifetimes and the initial masses from Miller Bertolami (2016), we fit a double power law for each of the four metallicities (Z = 0.0001, 0.001, 0.01, and 0.02) by fitting a power law to the lower masses up to and including 1.5 $\mathrm{M}_\odot$ and a power law to the higher masses starting at 1.5 $\mathrm{M}_\odot$ (i.e., with one value in common). Table 8.1 shows the fitting parameters for the free parameters of

$$t/\mathrm{Gyr} = a \times (M_{\mathrm{init}}/\mathrm{M}_\odot)^k \tag{8.1}$$

for the low and high masses at the four metallicities, which lead to very good descriptions of the original data points, even in logarithmic space.

These fits only correspond to the four discrete metallicities from Miller Bertolami (2016). To obtain a continuous representation of the lifetime function across metallicities, we found the following relations to describe the change of the four double power law parameters with metallicity[3]:

$$a_{\mathrm{low}} = 78.27 \times Z^{0.649} + 5.67, \tag{8.2}$$

$$a_{\mathrm{high}} = 107.5 \times Z^{0.880} + 4.58, \tag{8.3}$$

$$k_{\mathrm{low}} = -0.943 \times Z^{0.400} - 3.38, \tag{8.4}$$

$$k_{\mathrm{high}} = -3.29 - 0.654 \times (\log Z) - 0.124 \times (\log Z)^2. \tag{8.5}$$

The lifetime is then determined as the maximum between t_{low} and t_{high} computed from the respective power law parameters obtained from the stated relations. The lifetime function is shown for the original and some selected further metallicities in Figure 8.1, showing the continuous nature of the here derived expression. In Section 8.2, we present how the extrapolation of this relation to higher metallicities compares to detailed evolutionary models computed at such higher metallicities.

The obtained lifetime functions at the four original metallicities (Equations 8.2 to 8.5) as well as at intermediate and one lower metallicity (Z = 0.00001) are shown in Figure 8.1 as lines, colored by metallicity. The circular points indicate the values obtained from tab. 2 of Miller Bertolami (2016) and lie directly on the respective thick solid functional lines. The thin lines, which are at interpolated and lower metallicities, lie between the thick lines, just as they should. The power law slope k_{high} becomes steeper with decreasing metallicity, such that the extrapolation to Z = 0.00001 leads to a very small change in slope towards larger

[3]See the implementation in the source code on GitHub for the exact values with more significant digits.

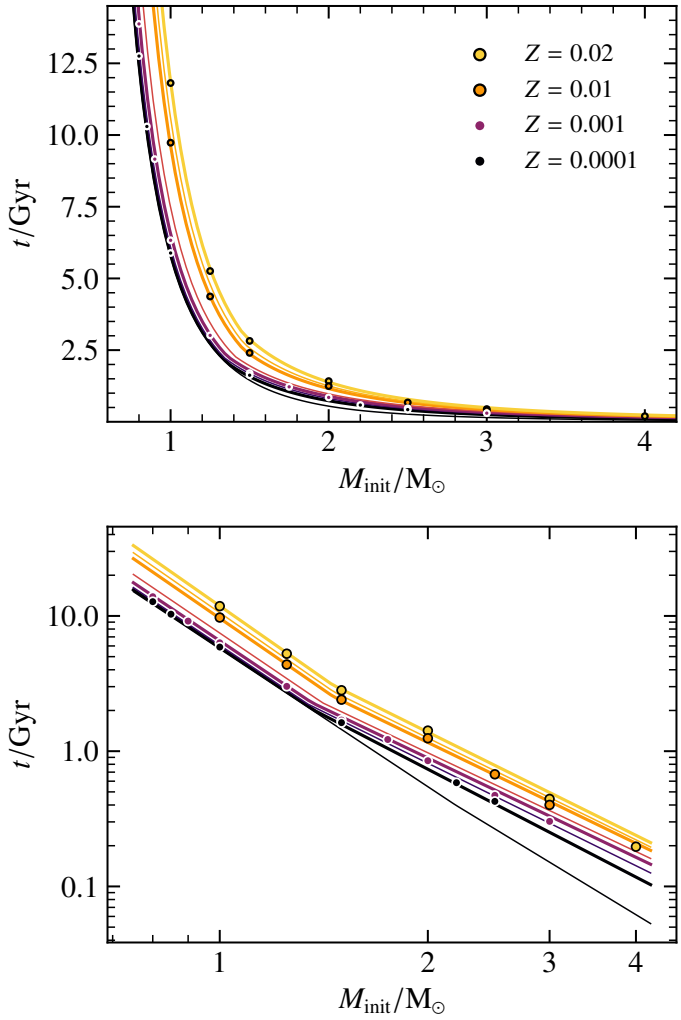


Figure 8.1: Lifetime function of stars until they reach the post-AGB phase as a function of their initial mass. *Top*: Linear axes. *Bottom*: Logarithmic axes, which makes it easier to distinguish the individual lines and data points. The points are from the models by Miller Bertolami (2016), and the lines are the fit relations to those data points. The thick lines are at the same metallicities as the ones from the original models ($Z = 0.0001$, 0.001, 0.01, and 0.02) and the thin lines are at $Z = 0.00001$, 0.0003, 0.003, and 0.014, where the latter three values are the logarithmic midpoints of the original metallicities.

masses. We therefore conclude that our determined analytical lifetime function is suitable for metallicities of at least $Z = 0.00001$–0.02.

While other PN studies have generally implicitly or explicitly assumed a fixed metallicity for their underlying mock stellar populations, oftentimes $Z = 0.01$ or $Z = 0.02$ (e.g., Gesicki et al. 2018; Souropanis et al. 2023; Valenzuela et al. 2019), Figure 8.1 shows that the metallicity plays a very significant role for stars of any age. For a fixed stellar age, varying the metallicity from low values of $Z = 0.0001$ to $Z = 0.02$ results in a change of more than $M_{\mathrm{init}} = 0.2\,\mathrm{M}_{\odot}$. In contrast, large absolute changes of stellar age for $t \gtrsim 5\,\mathrm{Gyr}$ only slightly affect the initial mass, which becomes relevant towards lower masses as the mass approaches the minimum viable mass for PNe to form, however. For old elliptical galaxies the metallicities tend to be high (e.g., Li et al. 2018), which means that especially for those types of galaxies it is important to take into account the actual underlying stellar metallicity. The implications of a higher

metallicity are the following: at a fixed stellar age, more metal-rich stars now passing through the PN phase are more massive than metal-poor stars that are PNe because more metal-rich stars evolve more slowly at a fixed stellar mass. This leads to more massive central stars with higher temperatures and luminosities, thus giving rise to brighter PNe, which is a possible way of populating the bright side of the PNLF with PNe from older stellar populations.

8.1.3 Initial-to-final mass relation

Having obtained the initial mass of stars that are now PNe, the IFMR is next used to determine the final mass based on the initial mass and metallicity of the star, that is how massive the central star of the PN is. This relation has been mainly investigated through WD stars in star clusters in the solar neighborhood (e.g., Cummings et al. 2018), though it has also been estimated from composite stellar populations (e.g., El-Badry et al. 2018).

For the fiducial model, we create a metallicity-dependent IFMR based on the values obtained from the models of Miller Bertolami (2016), which includes the four metallicities $Z = 0.0001$, 0.001, 0.01, and 0.02, just as for the lifetime function (Section 8.1.2). To sample more data points between the simulated pairs of initial and final mass values at each metallicity, a forward-looking quadratic interpolation (Bhagavan et al. 2024) is used. Then, a 2D linear interpolation is applied between the four logarithmic metallicities to the more finely sampled values, which is the resulting metallicity-dependent IFMR. This IFMR can be applied in two extrapolation modes: for metallicities outside of the range of $Z = 0.0001$–0.02, the values at the respective bounding metallicity can be used as a constant beyond that value, or the linear fit can be extrapolated beyond the original metallicity range. In Figure 8.2, we show the resulting IFMR with extrapolated values at the same metallicities as shown for the lifetime function in Figure 8.1, plus the higher metallicity of $Z = 0.05$. The colored dots show the original data points from table 2 of Miller Bertolami (2016), between which the interpolation took place.

The dependence on metallicity of the IFMR shows that more metal-rich stars at a fixed initial mass end up having lower final masses than metal-poor stars. As more massive stars are hotter and more luminous in the post-AGB phase and thus lead to brighter PNe, this counteracts the effect that metallicity has on the lifetime function, which leads to stars with higher initial masses entering the PN phase.

It is worth noting that the metallicity dependence of the IFMR of the models of Miller Bertolami (2016) is a consequence of the adopted winds. The metallicity dependence of cold winds is still poorly understood, in particular in the first RGB phase. The resulting theoretical IFMRs should therefore be taken as educated guesses. Most reliable IFMRs come from semi-empirical studies of star clusters in the solar neighborhood, which are only available for near-solar metallicities, however.

As the IFMR in general and also its metallicity dependence are still poorly understood, it is important to better understand the dependence of the resulting PNe in a given SSP on the used IFMR. For this, we additionally consider four IFMRs derived from observed WDs in the Milky Way: Cummings et al. (2018) determined their IFMR from 80 WDs located in 13 star clusters,

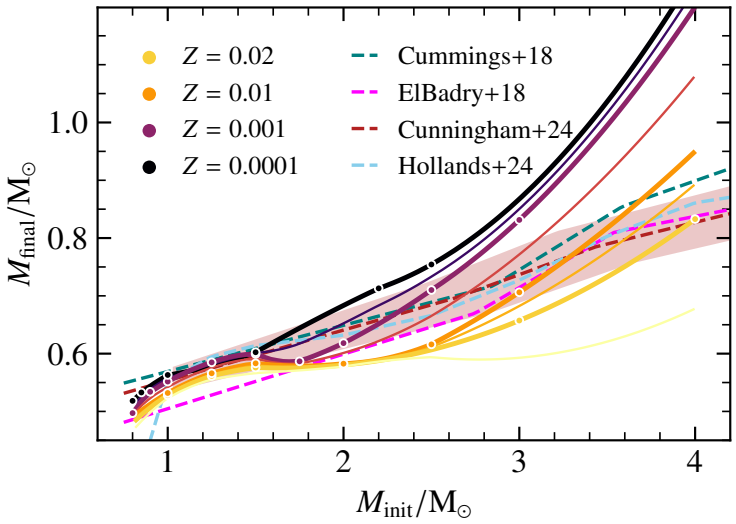


Figure 8.2: Initial-to-final mass relation of stars. The points are from the models by Miller Bertolami (2016), and the lines in the corresponding colors are the fit relations to those data points. The thick lines are at the same metallicities as the ones from the original models (Z = 0.0001, 0.001, 0.01, and 0.02) and the thin lines are at Z = 0.00001, 0.0003, 0.003, 0.014, 0.05, where the middle three values are the logarithmic midpoints of the original metallicities. Additionally, four observationally based IFMRs from nearby WD measurements at solar metallicity are shown from Cummings et al. (2018), El-Badry et al. (2018), Cunningham et al. (2024), and Hollands et al. (2024), as well as the 1σ uncertainty band of Cunningham et al. (2024).

El-Badry et al. (2018) estimated the IFMR from Gaia measurements of over 1000 WDs within 100 pc fo the Sun, Cunningham et al. (2024) studied 40 WDs with spectroscopic measurements from Gaia data within 40 pc of the Sun, and Hollands et al. (2024) studied 90 WD binaries from Gaia data with distances of up to 250 pc. All four of these IFMRs correspond to near-solar metallicities. We also show IFMRs from the four studies in Figure 8.2, where we use the adopted MIST-based IFMR of Cummings et al. (2018) and linearly extrapolate the IFMRs down to lower initial masses, as Cunningham et al. (2024) and Hollands et al. (2024) only fit their IFMRs down to 1 $\mathrm{M}_\odot$, and Cummings et al. (2018) to 0.83 $\mathrm{M}_\odot$. The uncertainties of these IFMRs are on the order of $\sigma_{M_{\rm final}} \approx 0.025\,\mathrm{M}_\odot$, for which we also show the uncertainty region of Cunningham et al. (2024). Further, the systematic uncertainties are on the order of 0.1 $\mathrm{M}_\odot$, as seen by using different underlying stellar evolution model is employed (Cummings et al. 2018). Only the low-mass IFMR from El-Badry et al. (2018) produces significantly lower final masses than the other relations. According to Cunningham et al. (2024), the reason for this is that El-Badry et al. (2018) use a different method for obtaining the minimum WD mass that can be created through single stellar evolution. While these relations are all monotonic, we note that it is still debated whether this is the case or if there is a dip around $M_{\rm init} \approx 1.5$–$2\,\mathrm{M}_\odot$ (e.g., Marigo et al. 2020) due to the large uncertainties.

Overall, there is a general agreement on what the IFMR looks like within the measurement uncertainties and their large systematics, where the theoretical metallicity-dependent IFMR from Miller Bertolami (2016) predicts overall lower final masses at solar metallicity than the observationally based IFMRs, especially at final masses of $M_{\rm init} \approx 1.5$–$3\,\mathrm{M}_\odot$ around the potential dip. Still, the small differences in final mass can lead to significant changes in the

resulting PN properties, especially moving towards final masses below $0.6\,M_\odot$. In Section 8.3, we investigate how the different IFMRs impact the resulting PN population with respect to their PNLF.

8.1.4 Post-AGB stellar evolution tracks

With the final mass of the star in question, the evolving properties of the central star can be obtained from post-AGB stellar evolution tracks. In particular, the luminosity L and effective temperature $T_{\rm eff}$ can be directly obtained with the tracks in the Hertzsprung-Russell diagram, given the final mass and an identifying time. For PICS, we assume the lifetime of a PN can be up to 30 000 yr (Valenzuela et al. 2019). For a given central star, the time since leaving the post-AGB phase is therefore randomly drawn from a uniform distribution between 0 and 30 000 yr, as the timescale is negligible compared to the timescale of the MS and post-MS.

In this work, we use the post-AGB tracks of the H-burning stars from Miller Bertolami (2016) and interpolate them to obtain the central star luminosity and effective temperature as a function of metallicity, final mass, and the post-AGB age (see Appendix D.1 for details on the interpolation). Following the approach of Valenzuela et al. (2019), we take the post-AGB age to be the time since the temperature reached a value of $T_{\rm eff} = 25\,000\,{\rm K}$ ($\log T_{\rm eff}/{\rm K} \approx 4.40$). The interpolated post-AGB tracks at two final masses of $M_{\rm final} = 0.55$ and $0.58\,M_\odot$ (of which only the former mass was explicitly computed by Miller Bertolami 2016) for a range of different metallicities can be seen in Figure 8.3. Clearly, the interpolations successfully produce intermedial values, in particular between the originally simulated metallicities. For metallicities outside of the range between $Z = 0.0001$ and 0.02, we simply use the respective tracks at $Z = 0.0001$ or $Z = 0.02$.

Additionally, it can here be seen that more metal-poor stars at a fixed final mass have a higher luminosity and can reach higher temperatures than metal-rich stars, as was also shown by Miller Bertolami (2016). Like the metallicity-dependent IFMR from Miller Bertolami (2016) presented in Section 8.1.3, this counteracts the effect the lifetime function has that one would expect more metal-rich stars to host brighter PNe, as well as the lower number of oxygen atoms in the nebula, which is also expected to limit the brightness of the [O III] line.. The dependence of the maximum luminosity and effective temperature of a star on its metallicity and age is therefore not trivial.

8.1.5 Planetary nebula model

The central star properties can finally be used to infer the PN emissions. Particularly, the [O III] intensity is of great importance for studies of extragalactic PNe. Additionally, properties such as the Hβ intensity may be of further relevance and has been studied for extragalactic PN populations as well (e.g., Reid & Parker 2010).

In this work we use the PN model from Valenzuela et al. (2019). To our knowledge it is the only current PN model that not only addresses the brightest PNe at the bright end of the PNLF, but can also be used to produce dim PNe that are consistent with observations, while

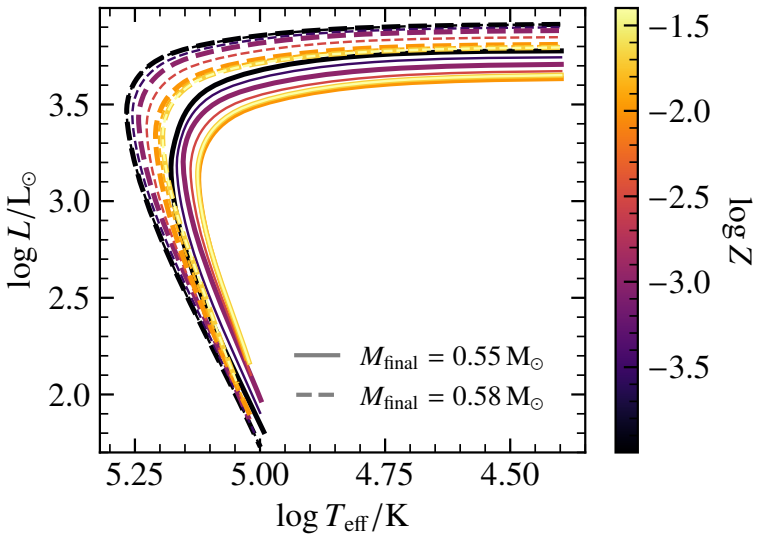


Figure 8.3: Post-AGB tracks in the Hertzsprung-Russell diagram of stars at two final masses $M_{\rm final} = 0.55\,{\rm M}_\odot$ and $0.58\,{\rm M}_\odot$ for a range of metallicities. The tracks are interpolated between the data tables from Miller Bertolami (2016). The metallicity colorbar corresponds to the same coloring as found in Figures 8.1 and 8.2. The thick lines are at the same metallicities as the ones from the original models ($Z = 0.0001$, 0.001, 0.01, and 0.02) and the thin lines are at $Z = 0.00001$, 0.0003, 0.003, 0.014, 0.05, where the middle three values are the logarithmic midpoints of the original metallicities.

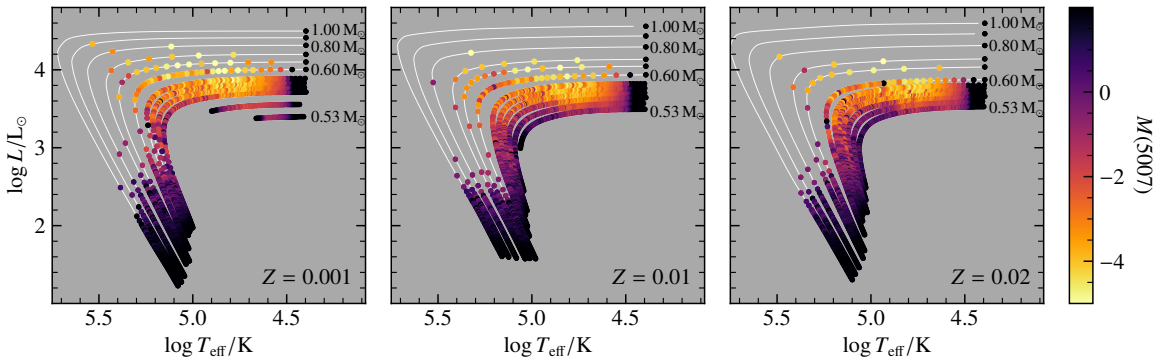


Figure 8.4: Post-AGB tracks in the Hertzsprung-Russell diagram of stars at metallicities $Z = 0.001$, 0.01, and 0.02 (left, middle, and right, respectively), colored by the λ5007 magnitude. The tracks are shown for stars at different final masses $M_{\rm final} = 0.53$, 0.54, 0.55, 0.56, 0.57, 0.58, 0.60, 0.65, 0.70, 0.80, 0.90, and $1.00\,{\rm M}_\odot$. For each final mass, stars at 600 evenly spaced post-AGB ages between 0 and 30 000 yr are plotted. The white lines indicate the tracks for the selected central star masses.

being applicable to large numbers of central stars without exceedingly high computational cost. The model computes the maximum total intensity of Hβ emission assuming optical thickness, $I({\rm H}\beta)$, based on the luminosity of the central star luminosity and its blackbody radiation given by the effective temperature. Next, the ratios between $I({\rm H}\beta)$ and the intensity of the [O III] emission line $I(5007)$ that have been observed for PNe in the Milky Way and the LMC are used to empirically obtain $I(5007)$ for a given PN. This ratio is drawn from a Gaussian distribution and is modified by some physically motivated prescriptions based on stellar mass and temperature. We give an overview of this prescription in Section D.2.1.

Finally, an absorbing factor μ is applied to the intensities to account for ionizing stellar photons that are not absorbed by the nebula. The absorbing factor is equivalent to the fraction

of ionizing photons that are actually absorbed and is simply multiplied with the previously obtained intensity to get the observed value of $I(5007)$. The absorbing factor for a given star is drawn randomly because of possible asymmetries in the nebula that can lead to a leakage of ionizing photons (for more details see Méndez & Soffner 1997; Valenzuela et al. 2019). Additionally, its maximally allowed value is decreased over the lifetime of the PN, which accounts for the nebula dissipating over time. The prescription for the absorbing factor is described in Section D.2.2. One aspect that is not included in the model of Valenzuela et al. (2019) is the internal dust extinction, which becomes more important for younger stars (e.g., Jacoby & Ciardullo 2025), which means in general for higher stellar masses. We add this effect as a further step in the PICS framework in Section 8.1.6.

In Figure 8.4 we show the post-AGB tracks in the Hertzsprung-Russell diagram of stars with certain final central star masses at metallicities of $Z = 0.001$, 0.01, and 0.02. The data points show individual PNe at evenly spaced ages between 0 and 30 000 yr starting from the given track reaching $T_{\mathrm{eff}} = 25\,000\,\mathrm{K}$. The PNe are colored according to their [O III] λ5007 absolute magnitude, $M(5007) = -2.5 \log I(5007) - 13.74$ with $I(5007)$ being the intensity seen 10 pc away, as defined by Jacoby (1989). According to the model, the brightest PNe for a given central star mass are located on the rising temperature track, after which the intensity of the [O III] line decreases again due to the dissipation of the nebula over time and the eventual drop of the star's luminosity. Here it also becomes apparent how quickly more massive stars ($M_{\mathrm{final}} \gtrsim 0.6\,\mathrm{M}_\odot$) evolve along the tracks compared to less massive stars, for example at $Z = 0.001$: two data points are separated by 50 yr, which means that after only a little more than 100 yr, a central star of mass $0.8\,\mathrm{M}_\odot$ reaches its peak temperature. As a result, even though more massive stars have the potential of developing brighter PNe, the likelihood of observing such a PN in its bright stage is much lower for more massive stars due to their fast evolution.

The PN model by Valenzuela et al. (2019) was originally developed for use with the post-AGB tracks from Miller Bertolami (2016) at a metallicity of $Z = 0.01$ and the [O III] to Hβ intensity ratio was empirically based on Milky Way and LMC PNe, which span a range of metallicities. As there is no obvious step in the model's recipes where it would be trivial to add a direct dependence on metallicity, in this work we apply the PN model to central stars of all metallicities without modification. While the model therefore statistically works well enough for composite populations of PNe that roughly have the same metallicity distribution as the Milky Way and LMC PNe, the intrinsic dependence on metallicity is lost, where lower abundances of oxygen should generally lead to less [O III] emission. For this reason, only applying the PN model by Valenzuela et al. (2019) to especially metal-poor PNe will result in overluminous PNe.

Multiple studies have investigated the dependence of the maximum [O III] flux on the metallicity. This relation is not straightforward as [O III] is also one of the primary coolants of the nebula (e.g., Jacoby 1989). Using nebular models, Jacoby (1989) found that small changes in the metallicity at solar-like abundances resulted in variations of the [O III] flux by the square root. Later models by Dopita et al. (1992) and Schönberner et al. (2010) showed

a quadratic form in logarithmic space around solar abundances for the peak luminosity of a given PN (see fig. 27 from Schönberner et al. 2010). In this work we consider all three possible relations as direct corrections to the obtained [O III] fluxes, extrapolating them beyond solar abundances to both low and high metallicities. As the nebular model by Valenzuela et al. (2019) was not based on a particular metallicity to which a simple nebular metallicity correction can be applied, we needed to estimate a base metallicity Z_{base} of the model from which it is possible to use the abundance differences to determine the correction required for the [O III] flux. Because Milky Way and LMC PNe were used for creating the empirical model by Valenzuela et al. (2019), the value has to be equal to or lower than the maximum metallicities of both galaxies. The overall more metal-poor LMC has an upper metallicity of around $Z = 0.008$ (Harris & Zaritsky 2009), which is consistent with the upper oxygen abundance found for its PNe of $12 + \log(\mathrm{O/H}) = 8.5$–$8.6$ (Dopita & Meatheringham 1991b; Richer 1993). At the same time the base metallicity value may not be too low as the observed nebulae have to have a sufficient amount of oxygen available to become PNe in the first place. We therefore estimate this base metallicity as $Z_{\mathrm{base}} = 0.007$, a value near the upper metallicity value of the LMC and also roughly half of the solar metallicity. We decided on this value because it is within the reasonable metallicity range of both the Milky Way and the LMC. However, it is important to note that this is not a physically derived value due to the nature of the empirical model being based on a distribution of metallicities.

For the square root relation of Jacoby (1989), we obtain a nebular metallicity correction factor of

$$p_{5007,\mathrm{J89}}(Z) = \left(\frac{Z}{Z_{\mathrm{base}}}\right)^{0.5}. \tag{8.6}$$

For Dopita et al. (1992), we assumed a linear conversion between the metallicity and oxygen abundance [O/H], so with our choice of the base metallicity we obtain a correction factor of

$$p_{5007,\mathrm{D92}} = 10^{\log F_{5007,\mathrm{D92}}(\log Z/Z_\odot) - \log F_{5007,\mathrm{D92}}(\log Z_{\mathrm{base}}/Z_\odot)}, \tag{8.7}$$

$$\log F_{5007,\mathrm{D92}}([Z]) = -0.8791 + 0.1459[Z] - 0.3013[Z]^2, \tag{8.8}$$

where the latter equation is taken from their eq. 4.1 with $[Z] = \log Z/Z_\odot$ and we take $Z_\odot = 0.0134$ from Asplund et al. (2009), which is also the solar metallicity that Schönberner et al. (2010) assumed in their models. Finally, for Schönberner et al. (2010) we fit two quadratic functions to their data points for their two final masses and used the mean of each of the fit parameters to obtain the following correction factor:

$$p_{5007,\mathrm{S10}} = 10^{\log F_{5007,\mathrm{S10}}(\log Z/Z_\odot) - \log F_{5007,\mathrm{S10}}(\log Z_{\mathrm{base}}/Z_\odot)}, \tag{8.9}$$

$$\log F_{5007,\mathrm{S10}}([Z]) = -0.24([Z] - 0.78)^2. \tag{8.10}$$

We show the direct comparison of the three correction factors as a function of metallicity in Section D.3. As the correction factor only depends on metallicity, the values of $M(5007)$ in

Figure 8.4 are simply offset by a fixed value per panel when applying one of the three nebular metallicity corrections.

While the nebular metallicity relations from the three works were originally constructed to describe how the fluxes of the brightest PNe vary with metallicity, we have decided to use these relations for correcting the [O III] fluxes of all PNe irrespective of their properties. We also note the caveat of applying the nebular metallicity correction to the resulting fluxes from the model by Valenzuela et al. (2019): as the model was tuned to PNe with a range of metallicities, having to pick a single base metallicity from which the correction is determined leads to an excessive brightness of PNe on the slightly metal-rich side and an excessively strong dimming on the slightly metal-poor side. As the disadvantages of not applying such a correction outweigh this caveat, however, we pick as the fiducial model the nebular metallicity correction by Dopita et al. (1992), which does not boost the [O III] flux as much as the other two relations (see Figure D.1).

Finally, we comment on the fact that for our current fiducial nebular model, we only take into account the general metallicity mass fraction Z and not any specific abundances. On the one hand, this has the big advantage of keeping the model simple, especially in light of the large parameter space already spanned through the stellar evolution models, which has also been the focus for this paper. With the aim of applying PICS to cosmological simulations, most chemical evolution models are not yet able to find good agreement with observed abundances, whereas the total metallicity mass fractions are in general consistent with observations. On the other hand, the simple linear scaling assumptions of different abundances like helium, oxygen, and iron with Z are certainly not entirely correct and may lead to systematics and biases in the modeled PN emission lines. For instance, accounting for alpha elements independently of iron-peak elements may be relevant when treating galaxies with different star formation histories like typical elliptical versus disk galaxies. Similarly, increased helium abundances could affect the number of ionizing photons available to ionize hydrogen (e.g., Osterbrock & Ferland 2006). As the focus of this paper is on the advances of stellar evolution modeling in the context of PNe, treating the nebular physics with a more detailed model will be the subject of future work, further improving the PICS model.

8.1.6 Circumnebular extinction

During the AGB phase stars create and eject dust through their stellar winds, which may lead to extinction of the PN emission. As more massive stars evolve more quickly along the post-AGB tracks and thus reach high temperatures to ionize the nebula shortly after the AGB phase, these PNe would suffer a larger extinction than PNe of low-mass stars when they reach their brightest [O III] magnitude. Ciardullo & Jacoby (1999) suggested that this effect could explain how the bright end of the PNLF is even universal for PNe in younger stellar populations, where the central stars of the PNe would be more massive. For the bulge of M 31, Davis et al. (2018) found that a significant fraction of the brightest PNe are strongly extincted. Most recently, Jacoby & Ciardullo (2025) presented the observed relation between central

star mass and circumnebular extinction measured for the brightest PNe in the LMC and M 31, which they fit through linear relations. Their work extends on Ciardullo & Jacoby (1999) and presents strong indications that this effect indeed could explain how younger galaxies have the same universal bright-end cutoff of the PNLF as the circumnebular extinction could bring the overly bright PNe down to the cutoff.

As PICS has the objective to produce PN properties for direct comparison with observations, accounting for circumnebular extinction is an important last step for obtaining the actually observed [O III] flux. While it is in part possible to determine the circumnebular extinction of PNe in the Local Group, this is impossible for most extragalactic systems. The relations for extinction as a function of final mass provided by Jacoby & Ciardullo (2025) are only valid for the PNe in the brightest magnitude. As the dust becomes more diffuse over the lifetime of a PN, the extinction is expected to decrease. Under the assumption that the evolution of dust extinction is the same for all PNe, we derived the extinction relation as a function of post-AGB age that recovers the relation by Jacoby & Ciardullo (2025) for the PNe at metallicity $Z = 0.01$ as they reach their peak brightness. We chose the metallicity of $Z = 0.01$ as a reasonable value between the expected metallicities of the brightest PNe in M 31 and the LMC. We note that using slightly lower or higher metallicities do not affect the resulting extinctions significantly.

We first determined the post-AGB age corresponding to the maximal brightness as a function of final mass at $Z = 0.01$ and fit the following broken linear relation to it (see Section D.4 for the details of the derivation):

$$M_{\mathrm{final,bright}} = \max \begin{Bmatrix} 1.014 - 0.1704 \log(t_{\mathrm{post-AGB}}/\mathrm{yr}) \\ 0.729 - 0.0479 \log(t_{\mathrm{post-AGB}}/\mathrm{yr}) \end{Bmatrix} \tag{8.11}$$

In this work we use the combined orthogonal regression fit to the bright LMC and M 31 PNe of Jacoby & Ciardullo (2025, Combined OR in their table 2), which takes the corresponding brightest final mass as argument (independent of what the actual final mass is):

$$c_{\mathrm{H}\beta} = 7.05 M_{\mathrm{final,bright}}/\mathrm{M}_\odot - 3.97, \tag{8.12}$$

where the extinction in Hβ, $c_{\mathrm{H}\beta}$, is used to obtain the [O III] extinction, A_{5007}, through the Cardelli et al. (1989) extinction law with $A_V = R_V E(B-V)$, $R_V = 3.1$, and $E(B-V) = c_{\mathrm{H}\beta}/1.47$ (Ciardullo & Jacoby 1999):

$$A_{5007} = \frac{c_{\mathrm{H}\beta}}{1.47} \left(R_V a(x) + b(x)\right), \tag{8.13}$$

where $a(x)$ and $b(x)$ are defined for the optical/near-infrared range in eqs. 3a and 3b from Cardelli et al. (1989) with $x = 1\,\mu\mathrm{m}/5007\,\text{Å}$. In this way, the extinction only depends on the post-AGB age of a PN. While in this work we only apply the one circumnebular extinction relation from Jacoby & Ciardullo (2025), we will investigate the effects of variations of the relation in a forthcoming paper (Valenzuela et al. in prep.).

8.1.7 Number of planetary nebulae

The previous sections dealt with the modeling of a single PN based on the IMF, age and metallicity of the SSP. How many PN this SSP produces is additionally dependent on the total mass. For this the IMF is integrated between the initial mass obtained from the SSP age (Section 8.1.2) and the initial mass obtained from the SSP age minus 30 000 yr because those are the stars that are still in the PN phase. The integrated value is then multiplied with the total mass to obtain the expected total number of PNe in that SSP. The actual integer number is then determined by rounding down or up randomly based on the decimal places, for example an expected value of 10.2 would lead to 10 PNe being selected with an 80% chance and 11 PNe with a 20% chance.

The number of PNe is obtained after the initial stellar mass has been found from the lifetime function. The final mass and the PN properties are then determined individually for each of those PNe since values such as the post-AGB age or the absorbing factor can be different for PNe even within the same SSP.

8.2 The effect of metallicity and helium abundances

8.2.1 Metallicity

In the previous section it can be seen that multiple aspects of the emergence of PNe depend on the metallicity: For a given initial mass, more metal-rich stars remain on the MS and post-MS for a longer period of time (Figure 8.1), and they lose more mass assuming the IFMR from Miller Bertolami (2016), leading to smaller final masses after the AGB phase (Figure 8.2). For the post-AGB tracks at a given final mass, more metal-rich stars have lower luminosities and reach lower maximum temperatures before entering the cooling track (Figure 8.3). Finally, while not depicted in this work, stars of a given final mass move along the Hertzsprung-Russell diagram at roughly the same speed, that is they heat up and cool down on a similar timescale (fig. 8 of Miller Bertolami 2016).

It is not directly clear from the individual relations themselves how the metallicity affects the central stars of the PNe when combining the lifetime function and the IFMR. To shed more light on this, we show how the final stellar mass depends on the age with varying metallicity in the left panel of Figure 8.5. For a large age range, most of the metallicities lead to similar final masses: at ages of 2–7 Gyr all but $Z = 0.001$ lie closely together, and at ages of 5–11 Gyr, all but $Z = 0.05$ lie closely together. Based on this model, this implies that there is a nearly universal final mass relation with age independent of metallicity for these ages, with variations of around 0.01–0.02 $M_\odot$ at a given age. For lower and higher ages, however, the final masses begin to deviate more from one another. For stellar populations less than 2 Gyr old, stars becoming PNe that are more metal-rich tend to have smaller final masses. For ages above 8–10 Gyr and with $Z > 0.001$, the trend emerges under the current model assumptions that more metal-rich stellar populations produce PNe with larger final masses due to their longer

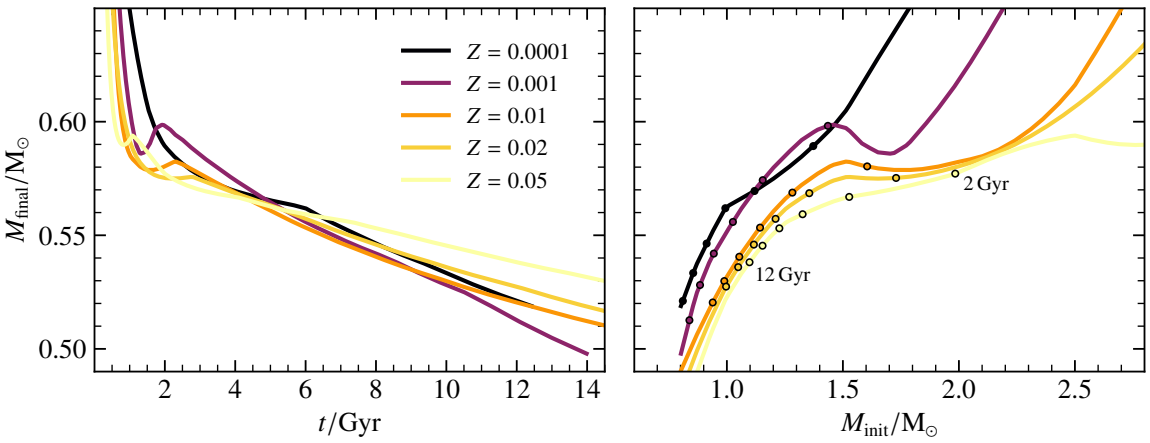


Figure 8.5: Final masses as a function of stellar lifetime (left) and of initial mass (right) for selected metallicities (Z = 0.0001, 0.001, 0.01, 0.02, and 0.05) based on the models of Miller Bertolami (2016). The final mass y-axis range is reduced to the primarily relevant values in the regime of older stellar populations of $t > 2$ Gyr. For the initial-to-final mass relation, the masses reaching the post-AGB phase after t = 2, 4, 6, 8, 10, and 12 Gyr are marked with circles.

lifetimes compared to their lower-mass counterparts. While these trends are not monotonic in the shown metallicity range, old stellar populations that are especially metal-rich above solar metallicity produce significantly more massive central stars of PNe than at lower metallicities, still reaching final masses of 0.55 $M_\odot$ after 9 Gyr.

Based on these relations, we can now highlight the importance of taking the metallicity into account for especially metal-rich systems: if one were to follow the approach of some previous studies of assuming a fixed roughly solar-like metallicity of $Z = 0.01$ (e.g., Gesicki et al. 2018; Valenzuela et al. 2019), then for ages above 5 Gyr the final masses at that fixed metallicity would be systematically lower than if taking the correct higher metallicity into account (see the left panel of Figure 8.5). The information can also be presented in the IFMR plot from Section 8.1.3 by marking specific times along the IFMRs at each metallicity. The right panel of Figure 8.5 shows the IFMR for a more limited range of initial and final masses than shown in Figure 8.2 where the points along the IFMRs are marked at equally spaced lifetimes between 2 and 12 Gyr. Especially at higher metallicities it can be seen that very old stellar populations with $t > 6$ Gyr have stars of higher initial and final masses reach the PN phase, resulting in old and metal-rich elliptical galaxies having more massive central stars of PNe than the old stellar population of a more metal-poor spiral galaxy, for example.

One caveat of the above conclusions based on the highest shown metallicity $Z = 0.05$ is that this metallicity lies outside the range originally modeled by Miller Bertolami (2016). Since those models only reached a metallicity of $Z = 0.02$, it cannot simply be assumed that the extrapolation of the lifetime function to higher metallicities is applicable using the fit analytic relation (Section 8.1.2). One difficulty in this matter is that stellar evolution and in particular the AGB phase are still poorly understood for super-solar metallicity stars. This is largely due to such metal-rich stars being mostly observed only in the Galactic bulge or in M 31 for massive stars (e.g., Pietrinferni et al. 2013; McDonald et al. 2022). Some studies have run models for super-solar metallicity stars, including the PARSEC (Bressan et al.

2012) and BaSTI (Pietrinferni et al. 2013) stellar evolution models, additionally Althaus et al. (2009) investigated potential high-metallicity progenitors of WDs, and Nanni et al. (2014) ran super-solar metallicity models to study the dust production in pulsing AGB stars. As stated by Pietrinferni et al. (2013), there are differences between their BaSTI and the PARSEC models in part because of different initial helium abundance assumed in the models.

8.2.2 Helium abundance

Not only the initial helium abundance is uncertain: its scaling with the overall metallicity has been primarily measured at lower metallicities in the Milky Way and in H II regions. Mostly, studies have quantified a slope $\Delta Y/\Delta Z$ as the cosmic production rate of helium, which has been estimated to be between 1 and 3 (e.g., Jimenez et al. 2003; Izotov & Thuan 2004; Casagrande et al. 2007). However, not all authors assume a linear slope, especially at the lowest metallicities (e.g. Keszthelyi et al. 2024). While Miller Bertolami (2016) assumed a slope of 2 for the initial abundances of the stellar evolution models, it is unclear how exactly the helium-to-metallicity relation continues beyond the upper metallicity of $Z = 0.02$. Casagrande et al. (2007) even suggest that the slope becomes smaller towards higher metallicities, though the large uncertainties of the helium abundances and the metallicities make it difficult to draw definite conclusions on the true relation.

For these reasons, we ran two additional models following the procedure by Miller Bertolami (2016) with a super-solar metallicity of $Z = 0.05$. The first assumes the same linear relation between the helium abundance Y and metallicity Z of $Y = 0.245 + 2Z$ (i.e., $Y = 0.345$, *linear He*), whereas the second assumes that a saturation of helium is reached at the linearly determined value at $Z = 0.02$ (i.e., $Y = 0.285$, *cutoff He*). The lifetime functions of the MS and post-MS for stars with these initial abundances as a function of the initial stellar mass are shown in Figure 8.6 as the blue (linear He) and red (cutoff He) data points. Additionally, the values from the analytic relation obtained in Section 8.1.2 are shown as lines for the original four metallicities as well as for the extrapolated metallicity $Z = 0.05$. We find that the blue linear helium data points at $Z = 0.05$ lie very close to the relation at the lower metallicity $Z = 0.02$ (light-orange line), whereas the red cutoff helium data points at $Z = 0.05$ also correspond to the extrapolated analytical function at $Z = 0.05$ (yellow line).

The newly run models show that the lifetime not only depends on metallicity, but is also heavily influenced by the helium abundance at $Z = 0.05$. Another finding is that the overall trend of the lifetimes increasing with metallicity is not valid when extrapolating the linear relation between Y and Z beyond $Z = 0.02$. This can be qualitatively explained by the following: in general, an increase of Z leads to higher bound-free opacities in the star, which lowers the radiative energy transport and overall luminosity. More metal-rich stars thus spend more time on the MS and post-MS. This is the case at lower metallicities, where the hydrogen abundance only minimally increases with higher Z. However, at higher metallicities, a relative increase of Z results in a significantly larger change of the helium abundance following the linear relation of $Y = 0.245 + 2Z$. As the hydrogen abundance is given by $X = 1 - Y - Z$, the

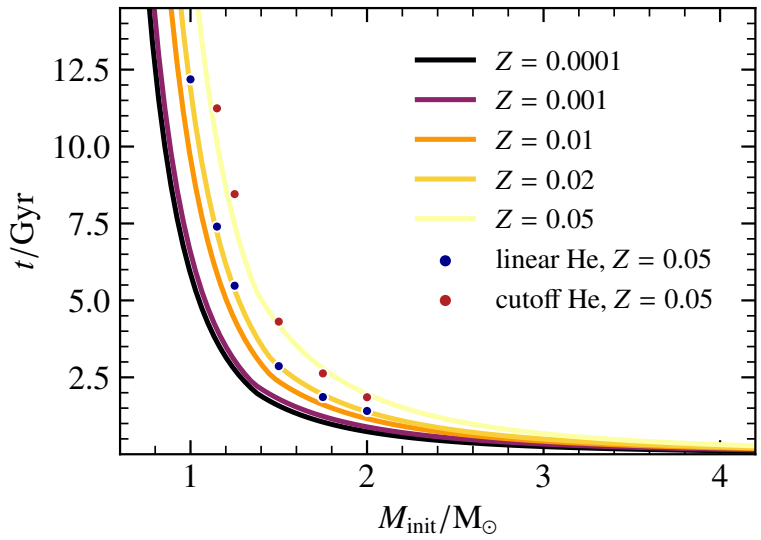


Figure 8.6: Lifetime function of stars until they reach the post-AGB phase as a function of their initial mass. The lines are the fit relations to the models of Miller Bertolami (2016) with original metallicities of $Z = 0.0001$, 0.001, 0.01, and 0.02, as in Figure 8.1. Here the extrapolation of these fits to $Z = 0.05$ is also shown. The points are the results of newly run models following the procedure of Miller Bertolami (2016) for $Z = 0.05$, and the lines are the fit relations to those data points. The linear helium abundance is at $Y = 0.345$ and the cutoff helium abundance at $Y = 0.285$. The thick lines are at the same metallicities as the ones from the original models ($Z = 0.0001$, 0.001, 0.01, and 0.02) and the thin lines are at $Z = 0.00001$, 0.0003, 0.003, and 0.014, where the latter three values are the logarithmic midpoints of the original metallicities.

higher value of Y means that the total amount of available hydrogen is decreased, resulting in less fuel for the MS and thus shorter MS lifetimes. Moreover, a higher helium abundance implies a higher mean molecular weight of the stellar material. Due to the high sensitivity of luminosity on the molecular weight ($L \propto \mu^4$; Kippenhahn et al. 2013), this leads to a larger luminosity and faster fuel consumption. In summary, when extrapolating the linear relation between Y and Z, the stellar lifetime increases with metallicity until the rising helium abundance counteracts that effect, leading to similar lifetimes at $Z = 0.05$ and $Z = 0.02$. In contrast, letting the helium abundance saturate and stay constant for values of $Z \geq 0.02$ means that the lifetimes continue to increase with metallicity.

For the saturated (cutoff) helium abundance, it is interesting that the simulated MS and post-MS lifetimes are overall very similar to the analytically computed values at $Z = 0.05$ for stars with initial masses $M_{\rm init} \gtrsim 1.5\,M_\odot$, but slightly higher at lower masses. This indicates that the extrapolation based on the lower metallicities (i.e., the analytic function that was fit to the original data points) corresponds to a slightly higher helium abundance than the saturated helium simulation. A thorough analysis of how the helium abundances affect the stellar lifetimes and the resulting PN populations is beyond the scope of this paper, however. It will be the subject of a future study.

Due to the poor observational constraints with respect to the Y-Z relation, we conclude that the analytically derived lifetime function from Section 8.1.2 at super-solar metallicities is still consistent with the stellar evolution simulations within the uncertainties of the observed helium

abundances. Moreover, there is recent observational evidence for the helium abundance to saturate beyond a certain metallicity as measured for Omega Centauri (Clontz et al. 2025). First evidence supporting the usage of this function even at high metallicities is presented by Valenzuela et al. (2025d), where the fiducial model of PICS was applied to several galaxies from a cosmological simulation, spanning a wide range of star formation histories, ages, and metallicities. The thereby obtained PN populations and their PNLF are consistent with observations and give a robust view of PNe, as will be fully shown in detail in the next paper of this series (Valenzuela et al. in prep.). In a future study we will further investigate how different assumptions regarding the helium abundances affect the PN populations of galaxies with different star formation histories in detail. Comparing the observed PN populations with modeled PNe based on simulated galaxies may even provide an independent way of probing the production rate of helium at high metallicities. In the following sections we apply the analytic function from Section 8.1.2 for all metallicities.

8.3 Single stellar population PNLFs

In Section 8.2 we have highlighted the importance of the metallicity and helium abundance when considering some of the individual blocks required to model the PNe within a stellar population. We now showcase how the SSP age and metallicity affect the resulting PNe by exploring the parameter space for the fiducial PICS model. For this, we paired ten SSP ages between $t_{\rm age} = 0.25$ and 13 Gyr with six metallicities between $Z = 0.0001$ and 0.08 to run PICS on and obtain corresponding PNLFs. To overcome the stochastic nature of the PN model itself with respect to the post-AGB age and the absorbing factor that determines the opacity of the nebula, we ran PICS on 10^6 stars for each pair of age and metallicity, with equally spaced post-AGB ages between 0 and 30 000 yr.

8.3.1 PNLFs with nebular metallicity correction

As a first step, Figure 8.7 shows the PNLFs without accounting for circumnebular extinction for a grid of SSPs with different ages (constant age per row) and metallicities (constant metallicity per column), that is the $M(5007)$ histograms for the 10^6 PNe. The colors represent the approaches to correcting for the nebular metallicity of Jacoby (1989), Dopita et al. (1992), and Schönberner et al. (2010) that were presented in Section 8.1.5, while the black PNLFs were created from PNe without applying such a correction and functions as a reference for what the corrections are doing. Statistically, the PNLFs in a given column are always shifted by the same amount relative to each other due to the way the metallicity corrections are implemented as a function solely of metallicity. For each panel, the final mass of the central stars is stated in the bottom right corner.

The effect of accounting for nebular metallicity is immediately obvious when comparing the left to the right columns: at low metallicities, the [O III] brightness drops considerably (colored lines), removing any PNe at $Z = 0.0001$ from bright magnitudes of $M(5007) < -4$

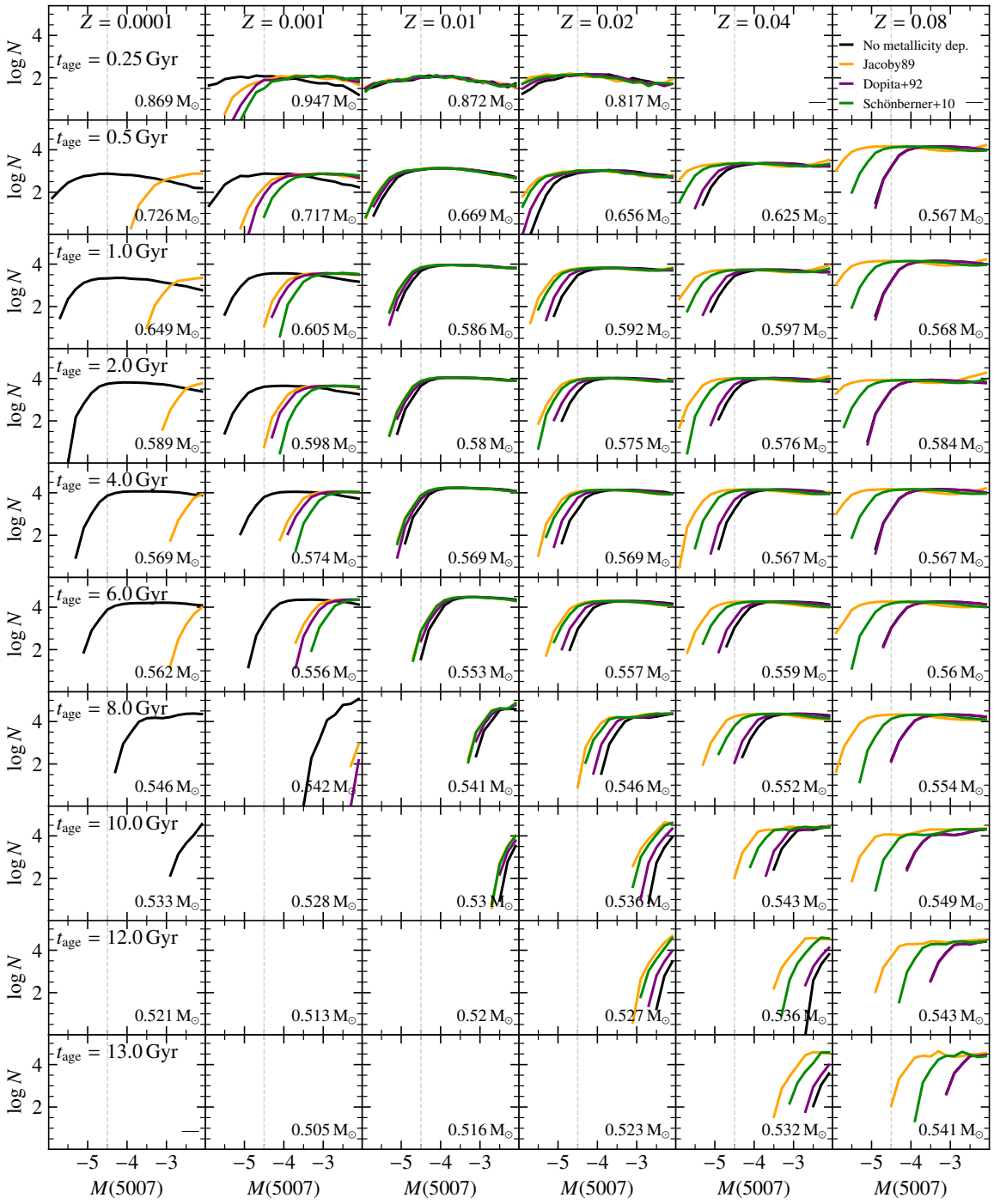


Figure 8.7: Single stellar population PNLFs depending on the age and metallicity for the fiducial model without circumnebular extinction, varying the nebular metallicity correction applied. Rows correspond to the different ages and columns to the metallicities. The final masses are computed from the IFMR of Miller Bertolami (2016) and are stated in the lower right corner of each panel. In the cases where the initial mass values lie outside the modeled range, only a dash is shown (this is only the case for two panels in the top right and one in the bottom left). The PNLFs are obtained from 10^6 stars of the respective final mass with equally spaced post-AGB ages between 0 and 30 000 yr. For the black PNLFs no nebular metallicity correction factor was applied, whereas the colored lines include the corrections by Jacoby (1989), Dopita et al. (1992), and Schönberner et al. (2010). The bright-end cutoff is marked by the vertical gray dashed line at $M(5007) = -4.5$.

compared to the metallicity-independent nebular model (black line), while at high metallicities the correction leads to overall brighter PNe. The corrections are close to zero at $Z = 0.01$, which is due to the chosen base metallicity of $Z_{\rm base} = 0.007$ at which the corrections are defined to not change the [O III] brightness. Among the three metallicity correction relations, the simple square root law by Jacoby (1989) always leads to the brightest PNe (yellow). At high metallicities, the relation by Dopita et al. (1992) enhances the PN brightness the least, as is expected from Section D.3, and again reaches a correction factor of 1 at around $Z = 0.08$, such that the purple and black lines are nearly the same in the last column of Figure 8.7.

The first finding is that not all combinations of age and metallicity contribute to the bright end of the PNLF at around $M(5007) = -4.5$ (e.g., Ciardullo 2012), marked by the vertical gray dashed lines. Especially old stellar populations with ages of $t_{\rm age} \gtrsim 8$–$10\,{\rm Gyr}$ generally produce fainter PNe. Note, however, that when nebular metallicity effects are not taken into account, the model predicts much brighter PNe at $Z = 0.0001$ and $Z > 0.04$. The final masses of the PNe in the stellar populations not reaching the bright end for the most part lie around $M_{\rm final} \sim 0.51$–$0.55\,{\rm M}_\odot$. This range lies well below the expected maximum final masses of older observed stellar population from previous studies needed to explain the brightest PNe (e.g., Méndez 2017; Valenzuela et al. 2019).

For intermediate-age stellar populations with $t_{\rm age} \sim 2$–$8\,{\rm Gyr}$, the bright end of the PNLF is well populated with PNe. Brighter nebulae are found for lower ages. When accounting for the nebular metallicity (colored lines), this is only true for intermediate to high metallicities of $Z \gtrsim 0.001$. Even at $Z = 0.001$, the older intermediate-age stellar populations ($t_{\rm age} \gtrsim 6$–$8\,{\rm Gyr}$) do not reach the bright end. Interestingly, there is a maximum of the non-metallicity-corrected PNLF between $M(5007) = -4.5$ and -4.0 for a number of the age-metallicity combinations in this intermediate-age regime, with a slow decline of the PNLF towards fainter PNe. This maximum is simply shifted to other magnitudes for the metallicity corrections. All of the SSP PNLFs here feature the recognizable typical shape of observed PNLFs, just with shifts towards brighter or fainter magnitudes. For the intermediate ages, the final masses lie between around 0.55 and $0.59\,{\rm M}_\odot$. This approximately lies in the expected maximum central star final mass range for intermediate-to-old stellar populations as found by Valenzuela et al. (2019) based on modeling PNe in mock stellar populations.

The younger stellar populations at $t_{\rm age} < 0.5\,{\rm Gyr}$ only feature the typical PNLF shape at the higher metallicities when not accounting for nebular metallicity (black lines). In contrast, lower-metallicities lead to much brighter PNe existing even well beyond $M(5007) = -5.0$. At high metallicities, the nebular metallicity corrections of Jacoby (1989) and Schönberner et al. (2010) also lead to such bright PNe. The absolute numbers are overall much lower than for older stellar populations, which is a result of the much faster evolution along the post-AGB tracks for these more massive central stars ($M_{\rm final} \gtrsim 0.6$). The stars reside on the heating track for only a short period of time (see the widely spaced data points in Figure 8.4 for the more massive central stars) before cooling down and dropping in luminosity, thus making bright nebulae around those massive stars rather rare.

8.3.2 PNLFs with circumnebular extinction

The fact that the PNLFs discussed in the previous section are able to reach magnitudes much brighter than the observed cut-off value is very likely due to the PN model of Valenzuela et al. (2019) not incorporating circumnebular dust extinction. The circumnebular dust extinction has been observed to rise with increasing PN brightness, thus pushing the brightest PNe back down to the bright end cutoff (e.g., Davis et al. 2018; Jacoby & Ciardullo 2025). In Figure 8.8 we show the full grid of PNLFs with respect to their unextincted and dust-extincted [O III] magnitudes. The unextincted PNLFs (dotted) are the same as those shown in Figure 8.7 for the non-metallicity dependent PNLFs (black) and those corrected for nebular metallicity (colored) through the relations of Dopita et al. (1992) and Schönberner et al. (2010). We do not show the PNLF by Jacoby (1989) to keep the figure from being too cluttered and since the simple square root relation is most likely the least accurate of the three. The solid PNLFs move to dimmer magnitudes by taking into account time-dependent dust extinction according to the Combined OR linear relation for circumnebular extinction, which is stronger in the early post-AGB phase. As a result, the extinction is seen the strongest for the fast evolving PNe of younger ages (top rows), where for $t_{\rm age} = 0.25\,$Gyr none of the PNe reach the brightest two magnitudes of the universal PNLF anymore ($M(5007) < -2.5$). At older ages of $t_{\rm age} \gtrsim 6\,$Gyr, there is practically no more extinction that can be observed: the solid and dotted PNLFs are almost perfectly overlayed.

For lower-to-intermediate ages of 1–4 Gyr, the extinction affecting the brightest PNe is on the order of 0.25–0.75 mag and also varies slightly with metallicity. This is expected as the lifetime function and the IFMR both affect the resulting final masses and thus how fast they evolve. Figure 8.8 nicely shows that circumstellar extinction is able to lower the SSP cutoff magnitude to the actually observed cutoff value of $M(5007) = -4.5$ for the age range of 1–4 Gyr. At younger ages with generally higher final masses, the adopted prescription leads to much higher extinction for the brightest PNe and is on the order of 1.5–2.5 mag for all but the highest metallicity. Only at $Z = 0.08$ the lower final masses at young-to-intermediate ages lead to significantly lower circumnebular extinction of the bright end. The extent to which this is true naturally depends on the nebular metallicity correction applied, as for example the relation by Schönberner et al. (2010) leads to significantly brighter PNe at the metal-rich end of $Z \gtrsim 0.02$. Even the circumnebular extinction recipe does not bring down the brightest PNe to the bright end for intermediate-aged metal-rich populations ($t_{\rm age} \sim 0.5$–$6\,$Gyr, $Z \gtrsim 0.02$) for Schönberner et al. (2010). We conclude that the fiducial model involving the nebular model by Valenzuela et al. (2019) with the correction by Dopita et al. (1992) is the most realistic with respect to our expectations from observations as it properly accounts for metallicity and simultaneously does not over-enhance the brightness of PNe at high metallicities.

As a result, we find that correcting for nebular metallicity through the relation of Dopita et al. (1992) and additionally accounting for circumnebular extinction (Jacoby & Ciardullo 2025) leads to a grid of PNLFs that are in general consistent with observations with respect to the bright end. They offer the basis for interpreting the observed PNLFs of composite stellar

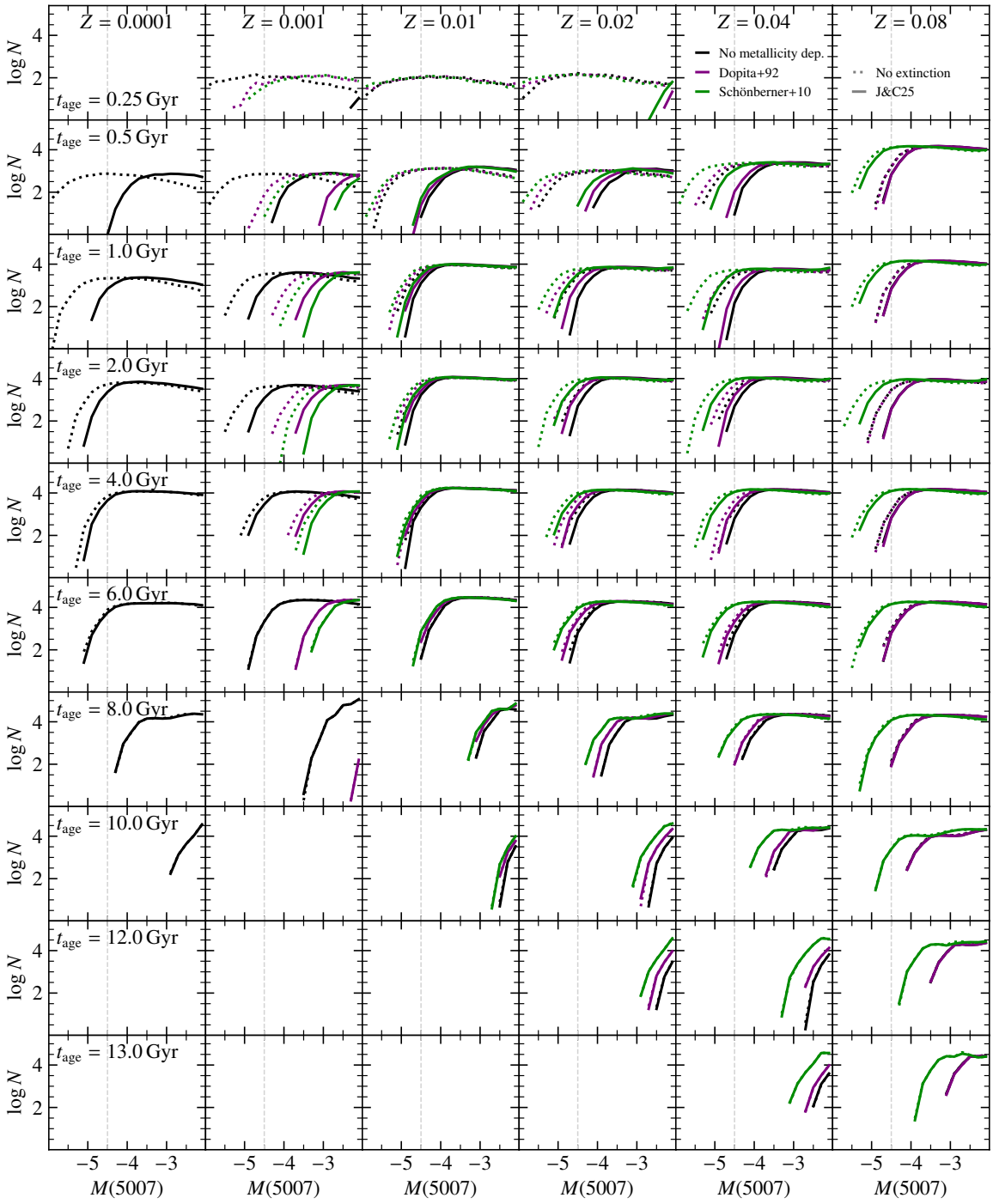


Figure 8.8: Single stellar population PNLFs depending on the age and metallicity for the fiducial model with different nebular metallicity corrections applied and showing the effect on the PNLFs from circumnebular dust extinction. The structure of the grid and the amount of PNe sampled for each PNLF are the same as in Figure 8.7. For the black PNLFs no nebular metallicity correction factor was applied, whereas the colored lines include the corrections by Dopita et al. (1992) and Schönberner et al. (2010). The dotted PNLFs are the same as those shown in Figure 8.7 and the solid PNLFs additionally take into account the circumnebular extinction from Jacoby & Ciardullo (2025) as described in Section 8.1.6.

populations. At the same time, the fact that the PNLFs vary significantly between different nebular metallicity corrections also indicates that improved modeling will be necessary to decrease the systematic uncertainties seen between methods. Developing a refined nebular model is beyond the scope of this work, however.

8.3.3 PNLFs with different IFMRs

In Section 8.1.3 we presented several IFMRs in addition to the one by Miller Bertolami (2016) used in the fiducial PICS model, namely those by Cummings et al. (2018), El-Badry et al. (2018), Cunningham et al. (2024), and Hollands et al. (2024). In Figure 8.9 we show the consequence of adopting an IFMR that does not depend on metallicity by using the latter four IFMRs instead of that of the fiducial PICS model by Miller Bertolami (2016). The black lines are the same as the blackberry lines in Figure 8.8 from the fiducial PICS model with the nebular metallicity correction by Dopita et al. (1992), while the colored lines correspond to the obtained PNLFs using the IFMRs of Cummings et al. (2018), El-Badry et al. (2018), Cunningham et al. (2024), and Hollands et al. (2024). The different IFMRs only show a similar PNLF for younger ages of around $t_{\mathrm{age}} \lesssim 6\,\mathrm{Gyr}$, and only the PICS fiducial IFMR shows a deviating behavior at higher metallicities in this age range with a larger number of PNe, but at the same time a fainter bright end of the PNLF. In the context of circumnebular extinction, as the final masses now vary even within a single panel based on which IFMR was used, the effect of extinction is different for each PNLF because of the final mass influencing how fast the central star evolves. This can especially be seen for the young metal-rich panels, where the dotted and solid black lines lie almost on top of each other for the fiducial model using the IFMR by Miller Bertolami (2016), while the other IFMRs lead to much higher final masses, thus resulting in significantly stronger extinction at the bright end (the colored solid lines lie much further to the right than their dotted counterparts).

The values of age and metallicity where similar PNLFs are found for all IFMRs roughly correspond to the initial mass range of $M_{\mathrm{init}} \gtrsim 1.3\,\mathrm{M}_{\odot}$ in which the alternative IFMRs do not lead to higher final masses than at even the lowest metallicities of the fiducial models (Figure 8.2). In contrast, for lower initial masses and thus for older stellar populations, Figure 8.2 shows that in particular the IFMR by Cummings et al. (2018) surpasses the final mass values of the fiducial model at all metallicities. At the lowest initial masses around $M_{\mathrm{init}} \approx 0.9\,\mathrm{M}_{\odot}$, both the models of Cummings et al. (2018) and Cunningham et al. (2024) show higher final masses than the fiducial models because their values result from linear fits in this mass range without a drop towards lower initial masses (in contrast to the fiducial model and that by Hollands et al. 2024). Since this leads to final masses of $M_{\mathrm{final}} \gtrsim 0.55\,\mathrm{M}_{\odot}$, even such old low-mass stars are able to produce bright PNe, as seen by the bright PNe in turquoise and red in Figure 8.9 for older systems of $t_{\mathrm{age}} \gtrsim 8\,\mathrm{Gyr}$. Overall, the PNe produced with the IFMR by Cummings et al. (2018) can be the brightest at older ages. The PNLFs obtained with their IFMR are surprisingly similar in bright end and shape across most ages and metallicities with only minor shifts of the bright end. Among the other four IFMRs, differences in the

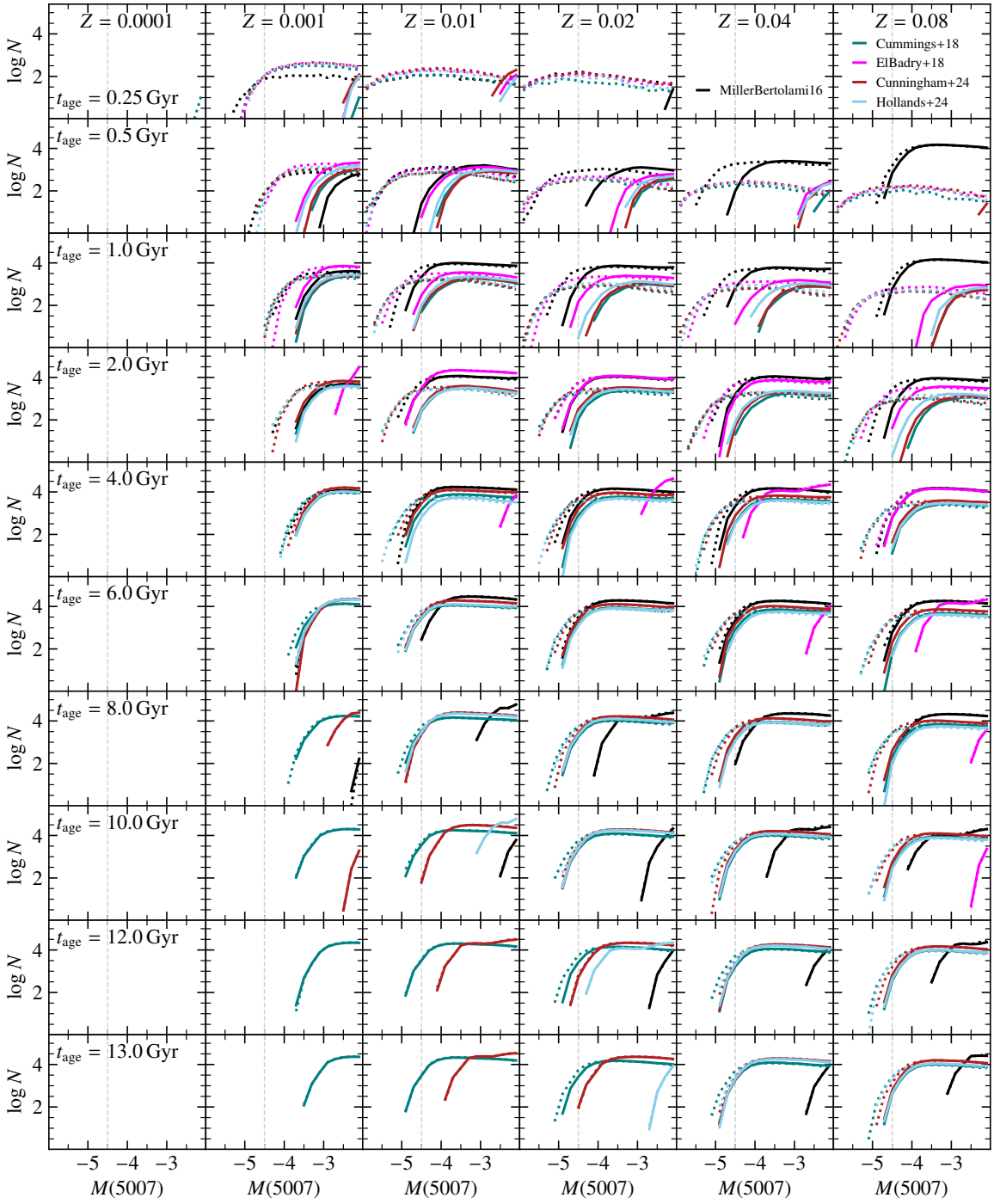


Figure 8.9: Single stellar population PNLFs depending on the age and metallicity for the fiducial model using the nebular metallicity correction by Dopita et al. (1992) and with variations of the IFMR (colored). The IFMRs are from Miller Bertolami (2016) in black, and Cummings et al. (2018), El-Badry et al. (2018), Cunningham et al. (2024), and Hollands et al. (2024) in turquoise, magenta, red, and light blue, respectively. The structure of the grid and the amount of PNe sampled for each PNLF are the same as in Figure 8.7. The dotted PNLFs are constructed from the intrinsic [O III] magnitudes and the solid PNLFs additionally take into account the circumnebular extinction from Jacoby & Ciardullo (2025) as described in Section 8.1.6.

bright end cutoff of up to half a magnitude can be found between the different IFMRs for $t_{\rm age} = 6\,$Gyr, one magnitude at 8 Gyr, and more than 2–3 magnitudes in stellar populations older than 10 Gyr. Finally, for the IFMR by El-Badry et al. (2018) the especially low final masses obtained from initial masses of $M_{\rm init} \lesssim 2\,{\rm M}_\odot$ lead to PNe dropping out of the brightest magnitudes of the PNLF for $t_{\rm age} \gtrsim 4\,$Gyr for metallicities approximately up to the solar value (a lack of magenta PNLFs in the center to bottom left panels). At higher metallicities this is the case for $t_{\rm age} \gtrsim 6\,$Gyr ($Z = 0.04$) and $t_{\rm age} \gtrsim 8\,$Gyr ($Z = 0.08$) as a result of the longer lifetimes of metal-rich stars leading to higher initial masses at a given age.

Despite the sharp drop in the IFMR of Hollands et al. (2024) towards lower masses in the range of $M_{\rm init} \lesssim 1\,{\rm M}_\odot$, which is even more extreme than the fiducial model shows, the light blue lines for Hollands et al. (2024) at high ages and metallicities show that bright PNe can still be produced (bottom right panels in Figure 8.9). This is a consequence of the alternative IFMRs not depending on metallicity, while the metallicity still influences the lifetime function, where higher metallicities lead to more massive stars reaching the post-AGB phase for a given SSP age. Because of the drastic drop of the final mass with lower initial masses, old low-metallicity SSPs do not produce bright PNe when using the IFMR by Hollands et al. (2024), leading to a lack of the light blue PNLFs in the bottom left panels in Figure 8.9.

For the younger ages at high metallicities (top right panels), it may seem curious that all alternative IFMRs lead to similar bright PNLFs before accounting for circumnebular extinction, whereas the fiducial IFMR by Miller Bertolami (2016) leads to a slightly dimmer bright end, but a significantly higher number of PNe. The reason for this can be understood by considering Figure 8.2. For young ages, the initial masses are above $2\,{\rm M}_\odot$. In this range, the high metallicity fiducial IFMRs show much lower final masses than the alternative IFMRs. The final masses are still high enough to produce relatively bright PNe, but not quite as bright as those obtained with higher final masses. However, the stars with lower final masses move more slowly across the Hertzsprung-Russell diagram before cooling down, thus allowing the nebula to survive for a longer period of time. The result is a larger number of PNe that can be observed.

The grid of PNLFs with different assumed IFMRs shows that the assumed IFMR strongly affects the PNLF that can be expected from a given stellar population, in particular for older systems. It is interesting that it is the regime of old stellar populations, where the abundance of PNe at the bright end has been a puzzle for a long time, that shows the highest sensitivity to the IFMR. This shows that understanding the IFMR dependence on metallicity (i.e., understanding the dependence of cold winds on metallicity) will play a significant role in the understanding of PNe and the PNLF in old stellar populations. We also note that here no potential intrinsic scatter of the IFMR is accounted for, which will also affect the resulting PN populations and the brightest PNe through the variations of the final mass (see also the discussion by Jacoby & Ciardullo 2025). Finally, even though the metallicity is not considered for the alternative IFMRs themselves, the metallicity dependence of the lifetime function and the post-AGB tracks leads to a shift of the bright end of the PNLFs, which can mostly be summarized as having a brighter PNLF cutoff at higher metallicities.

8.3.4 Normalized PNLFs

While the PNLF grids shown until this point were each constructed for a fixed number of 10^6 PNe and are useful for investigating the parameter space of the PICS model, their normalization still lacks the direct comparability to observations with respect to the underlying stellar populations. Since the PN central stars have different initial and final masses depending on the age and metallicity (the final masses are noted in the bottom left corner of each panel in Figure 8.7), varying numbers of PNe are expected to be found if the total SSP mass or luminosity is kept constant, based on the IMF. In Figure 8.10 we show the Dopita et al. (1992) nebular metallicity-corrected and circumnebular-extincted PNLFs for a fixed number of 10^6 PNe as shown in the other PNLF grids (black), for a fixed total stellar mass of $M_* = 10^{12}\,\mathrm{M}_\odot$ assuming a Chabrier (2003) IMF (red), and for a fixed total bolometric luminosity of $L_\mathrm{bol} = 10^{12}\,\mathrm{L}_\odot$ based on the GALAXEV CB07 SSP models by Bruzual & Charlot (2003) using a Chabrier (2003) IMF (orange).

For the luminosity-normalized PNLFs (orange), there are relatively more PNe compared to the fixed-number PNLFs (black) for older ages. The reason for this arises from the fact that younger stellar populations are intrinsically brighter than older ones, thus resulting in less total mass when keeping the total bolometric luminosity constant. In turn, this leads to a smaller number of PNe for young ages. The normalization to bolometric luminosity also gives us the possibility to determine the luminosity-specific PN numbers, typically denoted by α. As our model produces complete samples of PNe for a given SSP, it is possible to compute the actual value of α without having to assume an underlying PNLF shape based on which the number is estimated by extrapolation. Instead, the α value is obtained directly from counting the number of PNe in a given SSP brighter than a given magnitude. As the model can produce extremely dim magnitudes for objects that are essentially not PNe anymore, we limited the α determination to PNe with $M(5007) \leq +3.5$, which corresponds to the 8 brightest magnitudes with an assumed bright-end cutoff of $M(5007) = -4.5$. We chose this magnitude range to align with the estimation of Buzzoni et al. (2006) on PNe spanning roughly 8 orders of magnitude. The values of α for the same grid of SSPs found in Figure 8.10 are shown in Table 8.2, using the extincted PICS fiducial model and the same bolometric luminosity prescription by Bruzual & Charlot (2003) as described above. Note that this approach differs from that of Buzzoni et al. (2006) through our full modeling of PNe: we can simply count the PNe and do not have to make assumptions on the specific evolutionary flux, but rather can infer it from the model results themselves (see below).

These values for the most part lie between $5\times10^{-7}\,\mathrm{L}_\odot{}^{-1}$ for solar metallicities of $Z = 0.01$–0.02 and ages of $t_\mathrm{age} \gtrsim 2\,\mathrm{Gyr}$, which drop towards lower metallicities and ages, and rise towards higher metallicities and ages. These results are generally on the same order of magnitude as what Buzzoni et al. (2006) found, except that they find α to correlate much more strongly with age and much less with metallicity. The trend with metallicity that we find is largely due to the metallicity-dependent stellar evolution models employed from Miller Bertolami (2016) with respect to the stellar lifetimes and the IFMR, which was not taken into account by Buzzoni

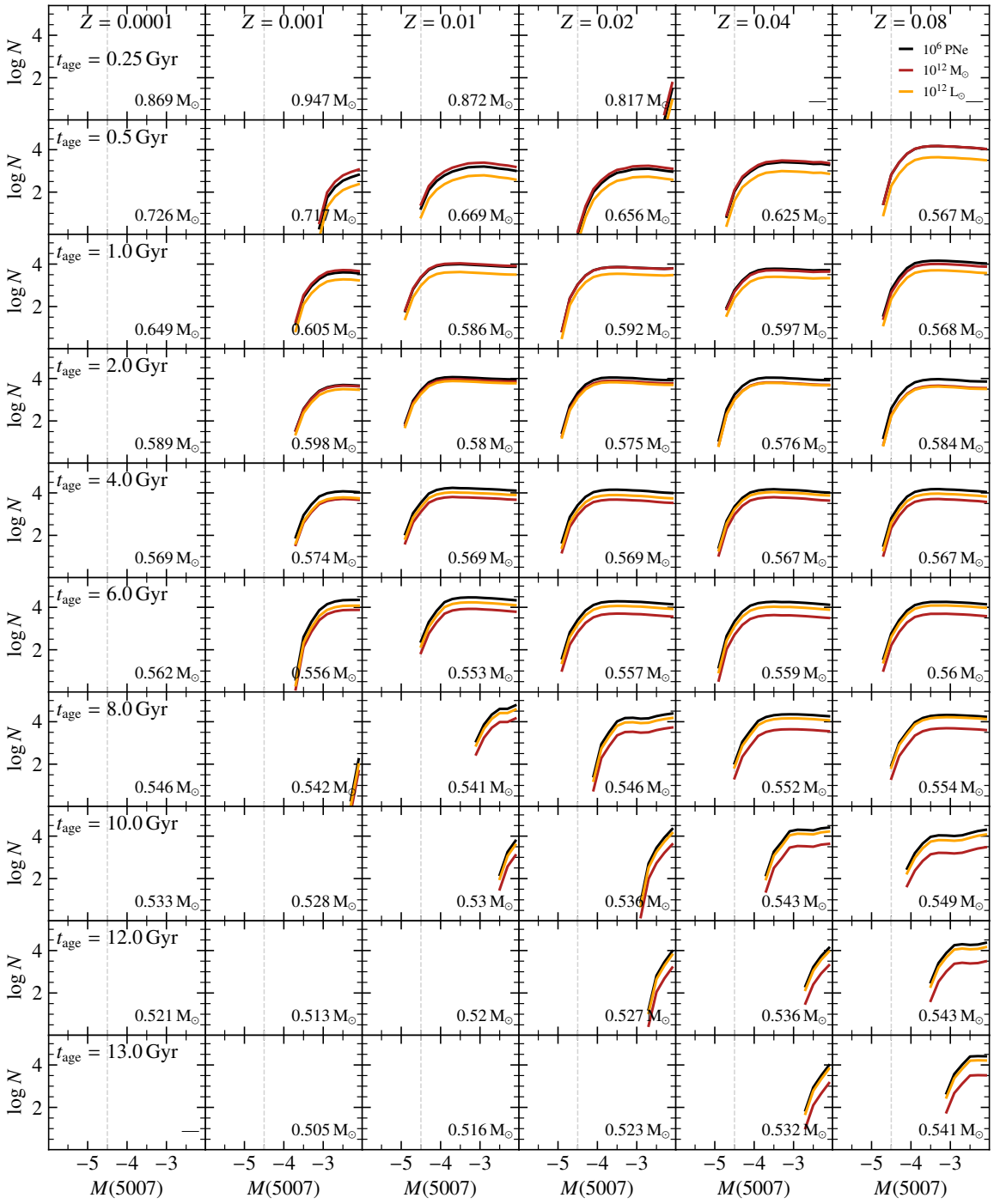


Figure 8.10: Single stellar population PNLFs depending on the age and metallicity for the fiducial model with the nebular metallicity correction by Dopita et al. (1992) and circumnebular extinction by Jacoby & Ciardullo (2025), normalized to different quantities. The structure of the grid and the amount of PNe sampled for each PNLF are the same as in Figure 8.7. The black lines are the PNLFs obtained from 1×10^6 stars of the respective final mass with equally spaced post-AGB ages between 0 and 30 000 yr. The red PNLFs are normalized to a total mass of $10^{12}\,\mathrm{M}_\odot$ assuming a Chabrier IMF (Chabrier 2003). The orange PNLFs are normalized to a total bolometric luminosity of $10^{12}\,\mathrm{L}_\odot$ based on the GALAXEV CB07 SSP models by Bruzual & Charlot (2003) using a Chabrier IMF.

Table 8.2: Luminosity-specific PN numbers α of the SSP PNLFs.

$t_{\rm age}$	Z					
(Gyr)	0.0001	0.001	0.01	0.02	0.04	0.08
0.25	–	0.429	2.036	2.075	–	–
0.5	0.033	1.419	2.845	3.348	3.125	2.669
1.0	0.138	2.467	3.555	4.224	3.602	3.157
2.0	0.432	3.580	5.511	5.390	5.093	3.925
4.0	0.825	3.341	5.413	5.101	6.642	5.460
6.0	1.370	3.655	5.245	5.486	5.326	6.084
8.0	2.151	4.986	5.763	5.640	5.844	7.025
10.0	1.825	3.880	5.758	5.892	5.937	5.344
12.0	–	–	–	6.391	6.148	5.642
13.0	–	–	–	–	6.277	5.787

α in units of $10^{-7}\,{L_\odot}^{-1}$

Notes. The luminosity-specific PN numbers α are given in units of $10^{-7}\,{L_\odot}^{-1}$, and are given for the brightest 8 magnitudes below the typical bright-end cutoff of $M(5007) = -4.5$ for each SSP PNLF. Each row corresponds to the given age $t_{\rm age}$ and each column to the given metallicity Z. The values were computed from the constant luminosity PNLFs shown in Figure 8.10 using the extincted PICS fiducial model with metallicity correction by Dopita et al. (1992), circumnebular extinction by Jacoby & Ciardullo (2025), and the same bolometric luminosity prescription by Bruzual & Charlot (2003).

Table 8.3: PN visibility lifetimes $\tau_{\rm PN}$.

$t_{\rm age}$	Z					
(Gyr)	0.0001	0.001	0.01	0.02	0.04	0.08
0.25	–	5.20	21.54	20.60	–	–
0.5	0.27	11.86	22.09	23.87	24.73	26.86
1.0	0.86	15.82	24.90	26.39	25.95	26.84
2.0	2.54	16.83	25.29	27.09	27.02	26.26
4.0	5.32	19.34	26.34	27.27	27.22	26.86
6.0	7.78	20.42	26.90	27.29	27.24	26.88
8.0	11.69	26.54	27.23	27.37	27.15	26.85
10.0	9.53	19.43	26.68	27.64	27.43	26.82
12.0	–	–	–	28.32	27.59	27.14
13.0	–	–	–	–	27.55	27.28

$\tau_{\rm PN}$ in units of 10^3 yr

Notes. The PN visibility lifetimes $\tau_{\rm PN}$ are given in units of 10^3 yr and are determined from the PNe resulting from the SSPs for the brightest 8 magnitudes below the typical bright-end cutoff of $M(5007) = -4.5$. Each row corresponds to the given age $t_{\rm age}$ and each column to the given metallicity Z.

et al. (2006). Our smaller trend with age, however, could arise from the assumption of the nebular model from Valenzuela et al. (2019) that PNe have a maximum lifetime of 30 000 yr. While this assumption is likely sufficient for most observed PNe, the dimmest PNe may very well also occur after this time frame. This could increase the total number of PNe for older stellar populations since their central stars have lower masses and thus evolve more slowly along the stellar tracks, leading to a slower loss of temperature and luminosity.

As Buzzoni et al. (2006) discuss, the α parameter can be linked to the PN visibility lifetime $\tau_{\rm PN}$. For the PICS model, it is possible to directly extract this lifetime for each age and metallicity as the time that a PN has a magnitude of $M(5007) \leq +3.5$. From the 10^6 modeled PNe uniformly sampled across 30 000 yr for each SSP, we took the fraction of PNe in that magnitude range as the factor to be multiplied with 30 000 yr to obtain the respective PN visibility lifetime, which we show in Table 8.3 for the same SSP grid. Around solar metallicity of $Z = 0.01$–0.02, the visibility lifetimes roughly range between 25 000 and 28 000 yr for SSP ages $t_{\rm age} \geq 1$ Gyr. Lower metallicities and ages lead to shorter PN visibility lifetimes, similar to the trends seen with α as expected. Note that the values do not reach the full 30 000 yr because of the stochastic nature of the model by Valenzuela et al. (2019) through the absorption parameter, which accounts for possible optical transparency of the nebula. This can drop the [O III] flux below the 8 magnitudes for the faintest PNe. Further, these values of the PN visibility lifetime are affected by the model's choice of 30 000 yr, a matter that will be addressed through improved nebular models in the future. From α and $\tau_{\rm PN}$ the specific evolutionary flux can be determined as their fraction $\mathcal{B} = \alpha/\tau_{\rm PN}$ (Buzzoni et al. 2006). For instance, at $Z = 0.01$ and $t_{\rm age} = 6.0$ Gyr, the specific evolutionary flux is $\mathcal{B} = 1.95 \times 10^{-11}\,{\rm L_\odot}^{-1}\,{\rm yr}^{-1}$, which exactly lies in the upper range shown in fig. 1 from Buzzoni et al. (2006).

In the literature the use of $\alpha_{2.5}$ has commonly been used due to the fact that observationally one is generally restricted to only the brightest magnitudes of the PNLF (e.g., Jacoby et al. 1990a; Longobardi et al. 2013; Hartke et al. 2017). Hereby only the 2.5 brightest magnitudes are taken into account for the luminosity-specific PN number. We show the predicted values of $\alpha_{2.5}$ and their corresponding visibility lifetimes $\tau_{\rm PN,2.5}$ in Section D.5.

For some nearby galaxies it has been possible to measure a statistically complete PNLF down to six magnitudes below the bright cutoff (e.g., Reid & Parker 2010; Bhattacharya et al. 2019), which has revealed significant variations of the PNLF shape at its faint end. We show the same grid of normalized PNLFs as in Figure 8.10 up to a magnitude of $M(5007) = +2$ in Appendix D.6, which is around 6.5 magnitudes below the bright end of the PNLF. These will be relevant in upcoming studies to compare the models with such nearby deep observations and provide a means for interpreting the variations of the PNLF shape. We highlight two insights from the extended magnitude PNLF grid: first, we find the dip or "camel" shape previously found in some galaxies with recent star formation like the Magellanic Clouds or NGC 300 (Jacoby & De Marco 2002; Reid & Parker 2010; Peña et al. 2012; Soemitro et al. 2023) and simulations of mock stellar populations with more massive central stars (Méndez et al. 2008; Valenzuela et al. 2019). Here we find that this dip already arises from the PNLF

of a sole SSP and is not necessarily the result of multiple stellar populations overlapping with each other, as has for example been proposed by Rodríguez-González et al. (2015). As proposed by Ciardullo (2010), the physical reason for the dip is that more massive post-AGB stars can host brighter PNe on their heating track than lower-mass stars, but their extremely fast evolution leads to them cooling down very quickly, resulting in a rapid decline of the [O III] emission before reaching a moderate brightness, where their evolution slows down and PNe accumulate, which is where the PNLF rises again. Second, the differences in shape and slope found at the faint end of the PNLF in observations indicate that these individual SSP PNLFs will help better understand and interpret the different behaviors found at the faint end of the PNLF, for example for PN populations in M 31 and its outskirts (Bhattacharya et al. 2021).

As a final comment, since any given stellar population is made up of many SSPs, any observed or simulated PNLF is in fact a superposition of these SSP PNLFs. In an upcoming study, we will use this fact to present a test using resolved star formation histories of observed galaxies to compare the PICS-predicted PNLF based on the observationally inferred stellar populations to the actually observed PNLF. With those tests we will demonstrate how successfully PICS is capable of modeling accurate PN populations self-consistently.

8.4 Summary and conclusion

This first paper in a series introduces PICS (PNe In Cosmological Simulations), a modular framework that models the PN population contained within an SSP. The SSP is described by its total mass, age, IMF, and optionally by its metallicity and/or further abundances. For our fiducial model, we consider the SSP metallicity mass ratio and use the metallicity-dependent lifetime function, IFMR, and post-AGB tracks from Miller Bertolami (2016) to model the central stars of the PNe. The nebula and its [O III] emission are modeled using the method from Valenzuela et al. (2019) and we account for the nebular metallicity according to the results by Dopita et al. (1992). Finally, time-dependent circumnebular dust extinction is applied to the [O III] emission derived from the observed relation by Jacoby & Ciardullo (2025). PICS thus produces the main observable quantity of extragalactic PNe and can be employed to compare theoretical models and hydrodynamical cosmological simulations with observations, which in turn can be used to interpret the properties of the PNe and underlying stellar populations.

We show how the initial metallicity of the star affects the stellar evolution relevant to PNe: higher metallicities lead to more massive stars reaching the post-AGB phase later than their lower-metallicity counterparts, while the final masses after the AGB phase are lower at constant initial mass. Higher metallicities also lead to lower luminosities and temperatures of the central stars for a fixed final mass. Considering both the lifetime function and the IFMR, the effect of the metallicity is strongest at ages below 3–4 Gyr, where lower metallicities lead to more massive PN central stars, and at higher ages above 6 Gyr, where higher metallicities lead to more massive central stars (Figure 8.5). The effect on final mass becomes strongest

at very young and at very old ages. The final mass is important for the maximal brightness of $M(5007)$ that can be reached throughout the post-AGB phase and reaching higher final masses will increase the probability of finding such a PN at the bright end of the PNLF. Furthermore, these relations provide the first indications that the metallicity is relevant for older stellar populations, in particular as these are oftentimes more metal-rich in massive elliptical galaxies than in disk galaxies like our own Milky Way.

One important finding of this work is that for high-metallicity stars, the metallicity is not the only property affecting the lifetime of stars. While higher metallicities generally do increase the opacity of the star, leading to longer lifetimes, the accompanying increase of the helium abundance counteracts this trend due to higher main sequence luminosities and less available fuel. As the relation of helium abundance with metallicity is still poorly constrained from observations, in particular at high metallicities, we explored the parameter space ranging from a linearly increasing helium abundance with metallicity to a constant helium abundance of $Y = 0.285$ above a metallicity of $Z = 0.02$. Such a constant helium abundance above a certain metallicity would be in line with recent observations of the metallicity of the stellar population of the globular cluster Omega Centauri (Clontz et al. 2025).

Assuming the linear relation, the lifetime function does not lead to longer timescales at higher metallicities above $Z = 0.02$ anymore, whereas assuming a saturation of the helium abundance results in longer lifetimes at $Z > 0.02$. The helium abundance relation is therefore especially relevant for metal-rich stellar populations, as it governs how the lifetime function behaves for the individual stars. A higher helium abundance causes shorter lifetimes, leading to less massive stars becoming PNe after a given time at fixed metallicity. This in turn means that the brightest possible magnitudes $M(5007)$ are dimmer. If the helium abundance is capped, however, the stellar lifetimes increase, leading to more massive central stars at older ages for super-solar metallicity stellar populations. Based on the metallicities originally used by Miller Bertolami (2016) of $Z = 0.0001$–0.02, we derived an analytic expression for the lifetime function, whose extrapolation lies between the simulated values for linear and constant helium abundance relations, but closer to the latter. Thus, for the fiducial model, we pick the constant helium abundance relation due to it lying closer to the analytic function. Since longer lifetimes of metal-rich stars increase the occurrence of bright-end PNe in old stellar populations, our findings indicate that a saturation of the helium abundance at high metallicities could be part of the solution for the universal bright-end cutoff of the PNLF. The implications would be that high-metallicity stars have longer lifetimes than expected from models assuming non-saturated helium abundances. In future studies we will extend our stellar grids to include the effect of the helium abundance consistently with the prediction from cosmological models.

To obtain a complete overview of how the SSP metallicity and age affect the resulting PN population, we produced a grid of PNLFs, each corresponding to a fixed pair of metallicity and age. The PNLF shapes are generally consistent with each other and have a varying bright end cutoff: older SSPs generally contain less luminous PNe. However, at older ages above 6 Gyr, higher metallicities again lead to brighter PNe forming. In addition, at almost all

ages the lowest metallicities of $Z = 0.0001$ and $Z = 0.001$ lead to a significant dimming of the PNe through any of the three nebular metallicity corrections we have implemented in this work (Jacoby 1989; Dopita et al. 1992; Schönberner et al. 2010), especially compared to not accounting for the nebular metallicity. In particular, the brighter old and metal-rich PNe could in part explain how old elliptical galaxies still retain a similar bright end of the PNLF compared to disk galaxies as they tend to be especially metal-rich. The grids of SSP PNLFs presented in this work set the theoretical foundation for interpreting the relations of the observed PNLF bright end with properties of the underlying stellar populations with respect to their age and metallicity.

We also present a grid of extended PNLFs down to six magnitudes below the bright end cutoff, which are needed for comparison and interpretation of PN studies of Local Universe galaxies, where it has been possible to obtain statistically complete samples even of very faint PNe, for example in the LMC or M 31 (Reid & Parker 2010; Bhattacharya et al. 2021). The extended PNLFs reveal that the "dip" or "camel shape" of the PNLF with a minimum at around $M(5007) \approx -2$–0, which has previously been seen in observations (e.g., Jacoby & De Marco 2002; Reid & Parker 2010; Peña et al. 2012; Soemitro et al. 2023) and models (e.g., Méndez et al. 2008; Valenzuela et al. 2019), is in fact an intrinsic property of PNe with more massive central stars and arises even in SSPs. It is thereby not only a result of two or more modes of PNLFs from multiple stellar populations, as has been suggested by Rodríguez-González et al. (2015). Of course, any real PNLF is a superposition of SSP PNLFs, which can lead to an even larger variety of observed faint PNLF shapes. This carries the potential of being another independent diagnostic tool for investigating the underlying star formation history and metallicity properties of galaxies and their formation histories, which we will also be presenting with a self-consistent test on observations in an upcoming study.

Through the PNLF grids we investigate the effects of applying different nebular metallicity corrections, which are critical to avoid overly luminous extremely metal-poor PNe. The square root law by Jacoby (1989) is the relation first found for solar-like metallicities and enhances the brightness of metal-rich PNe very strongly when extrapolated, and leads to the smallest dimming of metal-poor PNe. In contrast, the relations by Dopita et al. (1992) and Schönberner et al. (2010) enhance it less significantly at the metal-rich end, and the relation by Dopita et al. (1992) the least. Applying circumnebular extinction further decreases the brightness of the brightest PNe of very young stellar populations, such that the bright end of the PNLF can only be found at solar-like and higher metallicities for stellar ages of $\gtrsim 1$ Gyr.

Finally, we studied how different IFMRs affect the resulting PN populations by considering metallicity-independent IFMRs determined from the solar neighborhood in the Milky Way in addition to the relation used for the fiducial model from Miller Bertolami (2016). Most of the various IFMRs (except that by El-Badry et al. 2018) do not change the SSP PNLFs much for younger stellar populations of $\lesssim 6$ Gyr. However, at larger ages the metallicity-independent IFMRs mostly lead to brighter PNe being produced, in part even reaching the bright-end cutoff for the IFMR by Cummings et al. (2018). The reason for this is that some of these IFMRs do not see the final stellar masses drop as steeply towards low initial masses as the relations by

Miller Bertolami (2016). Only the IFMR by El-Badry et al. (2018) predicts much lower final masses in the low-mass regime, that is for old stellar ages. As a result, no PNe are produced in the brightest 4 magnitudes for ages of $\gtrsim$6 Gyr for this IFMR. Furthermore, the lack of metallicity dependence means that at high metallicities the PN central stars are more massive than when employing the metallicity-dependent IFMR, in turn leading to on average brighter PNe. The implications for the existence of bright PNe in old stellar populations are very important: The IFMR, in particular at initial masses of $M_{\rm init} \lesssim 1.2\,{\rm M}_{\odot}$, plays a significant role in how massive the central stars are and therefore how bright the PNe can get. Getting better constraints and developing a more robust theoretical understanding of the mass loss in the AGB phase is therefore essential for explaining the observed bright end of the PNLF in old stellar populations.

With PICS, we have laid the groundwork for populating cosmological simulations with PNe, thereby producing PN populations based on self-consistent star formation histories within a cosmological context. On the theoretical side, this allows us to make predictions for the PNLF behavior based on statistically significant samples of galaxies with diverse morphologies and star formation histories, which will aid our understanding of the universal bright end of the PNLF. Furthermore, the modular structure of PICS makes parameter studies possible, where controlled changes to one specific block in the pipeline can be used to understand its effect on the resulting PN population, just as done for the IFMR in this work. For the observational side, it will be possible to compare the modeled PN populations to observations by identifying appropriate simulated galaxy analogues, and to offer an interpretation for the observed PNe and their properties.

To conclude, we have shown in this study that it is essential to account for both the metallicity and helium abundances in PNe models, as well as improving the observations and models of the IFMR. These factors all particularly affect the brightest PNe, leading us one step further in our understanding of the universal bright end of the PNLF, which we will explore in more detail in future studies.

9

The PNLF from Realistic Stellar Populations

This chapter was published as Valenzuela et al. (2025d), IAU Symposium 384, 69[1]:
PICS: Planetary Nebulae in Cosmological Simulations –
Revelations of the Planetary Nebula Luminosity Function from Realistic Stellar Populations

A key finding of the PICS (PNe In Cosmological Simulations; Valenzuela et al. 2025c; see Chapter 8) framework is that taking metallicity into account for PNe is crucial to obtain PNe at the bright end of the PNLF. This not only applies to the effects metallicity has on the initial-to-final mass relation (IFMR; e.g., Marigo et al. 2004) and nebular physics (e.g., Jacoby 1989; Dopita et al. 1992), but also to the stellar lifetimes, where more metal-rich stars have longer lifetimes before reaching the post-asymptotic giant branch (post-AGB) phase (Romero et al. 2015). However, for certain use cases, metallicity-independent stellar lifetimes are employed, for instance in many cosmological simulations.

With the advent of hydrodynamical cosmological simulations in the past decade, it has become possible to obtain more realistic stellar populations with a large variety of cosmological star formation histories that are self-consistent with the actual assembly history of the simulated galaxy itself. In this work, we present the first application of the PICS framework to simulated galaxies from a cosmological simulation, with two objectives: to underline the importance of using metallicity-dependent stellar lifetimes for the PNLF shape to remain universal across

[1]Minor adjustments have been made, and the introduction has been adapted for this thesis.

different galaxies with realistic stellar populations, and to verify the normalization of a modeled PNLF with a volume-complete sample of PNe in the Milky Way. In Section 9.1, we describe the setup of the PICS framework used for this work. In Section 9.2, we present first results from applying PICS to a cosmological simulation, focusing on the relevance of metallicity and the reproduction of the Milky Way PNLF. Finally, we summarize and conclude our findings in Section 9.3.

9.1 PICS model

To introduce PNe in cosmological simulations, the PICS method provides a modular framework for determining the population of PNe for a given single stellar population (SSP). As each stellar particle in a cosmological simulation represents an SSP, this allows one to apply PICS to all the stellar particles in such a simulation in post-processing. As a result, PNe are obtained with all the inherited properties from their parent stellar particles, such as spatial and kinematic information or their ages, and with the properties of the PNe themselves, such as the [O III] λ5007 (from hereon simply referred to as [O III]) magnitude or the central star mass.

The framework consists of a sequence of models that determine the PNe population for an SSP, which is defined by its age, total mass, initial mass function (IMF), and its element abundances. In its basic form, the sequence is the following (note that here we used an early version of PICS without nebular metallicity correction or circumnebular extinction, both described in the introduction paper; Valenzuela et al. 2025c); see Sections 8.1.5 and 8.1.6:

1. Lifetime function for the SSP, through which the initial mass of the stars reaching the post-AGB phase can be determined from the SSP age.
2. IFMR, from which the central star mass is obtained.
3. Post-AGB stellar evolution tracks, which provide the central star properties for a given post-AGB age, that is the time passed since leaving the AGB. In particular, the stellar properties consist of the effective temperature and luminosity of the star.
4. Planetary nebula model, which determines the nebular properties, most importantly the [O III] magnitude.

For (1), the lifetime function, we consider two different prescriptions: The first is composed of the main sequence lifetime from Padovani & Matteucci (1993), which is the one used in the Magneticum Pathfinder simulations (the implemented stellar evolution models are described by Tornatore et al. 2007), and the post-main sequence lifetime from Renzini & Buzzoni (1986). The second is the group of lifetime functions as obtained from Miller Bertolami (2016), which vary with metallicity. The left panel of Figure 9.1 shows the lifetime functions, where it can be seen that the lifetime function from Padovani & Matteucci (1993) and Renzini & Buzzoni (1986) is most similar to the lifetime function at a metallicity of $Z = 0.01$ from Miller Bertolami (2016). It also becomes apparent that more metal-rich stars reach the PN phase after significantly longer times than metal-poor stars of the same initial mass. This is due to the impact of metallicity on bound-free opacities, which leads to larger luminosities at lower metallicities.

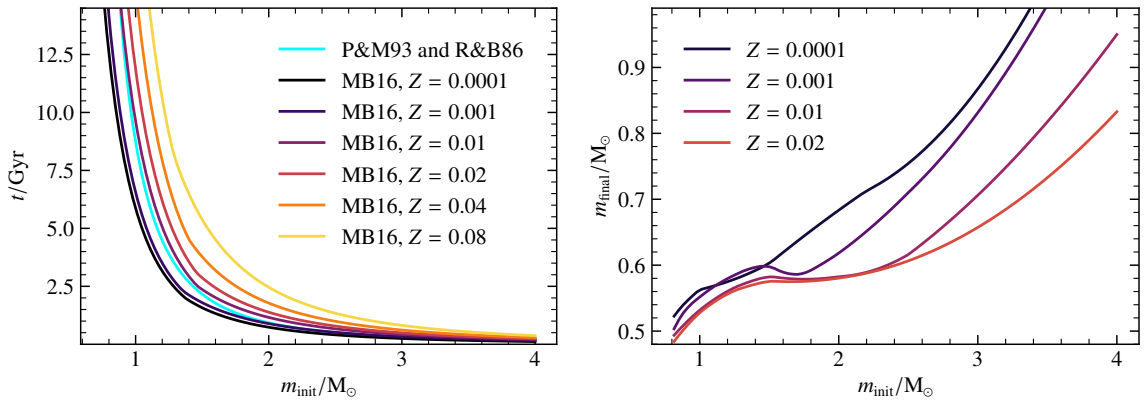


Figure 9.1: *Left*: Lifetime functions from the main sequence plus post-main sequence lifetime functions by Padovani & Matteucci (1993) and Renzini & Buzzoni (1986), respectively, and from the total lifetimes as computed by Miller Bertolami (2016) for different metallicities, Z, given the initial mass of a star. The lifetime functions for $Z = 0.04$ and 0.08 are extrapolated from the four computed ones. *Right*: Initial-to-final mass relations for the four computed metallicities from Miller Bertolami (2016).

For (2) and (3), the IFMR and post-AGB stellar evolution tracks, respectively, we use the metallicity-dependent results from Miller Bertolami (2016). The IFMRs for the four metallicities used by Miller Bertolami (2016) are shown in the right panel of Figure 9.1. All of the models are interpolated between the metallicities. The lifetime functions are extrapolated beyond the originally computed metallicities, as running new stellar evolutionary simulations for the higher metallicities is beyond the scope of this work. In future studies, we will have such simulated results available to replace the extrapolations. Finally, for (4), the PN model, we use the empirical model presented by Valenzuela et al. (2019), which is also based on the assumption that PNe can be optically thin, thus losing some of their [O III] intensity. The model will be presented in detail in a full paper (Valenzuela et al. 2025c).

9.2 Application to a cosmological simulation

As a first test in applying the model to a cosmological simulation, we use the Magneticum Pathfinder[2] Box4 (uhr) simulation, which has a side length of 68 Mpc and an average stellar particle mass of $1.8 \times 10^6\,\mathrm{M}_\odot$. We assume a Chabrier IMF (Chabrier 2003) as also used within the simulation. For more details on the simulation and an overview of comparisons with observations, see Teklu et al. (2015) and Valenzuela & Remus (2024), respectively.

9.2.1 The importance of metallicity

In recent studies of the PNLF through modeling, it has been customary to only consider PNe of a single fixed solar-like metallicity of $Z = 0.01$ or $Z = 0.02$ (e.g., Gesicki et al. 2018; Valenzuela et al. 2019; Souropanis et al. 2023; Yao & Quataert 2023). To evaluate

[2] www.magneticum.org

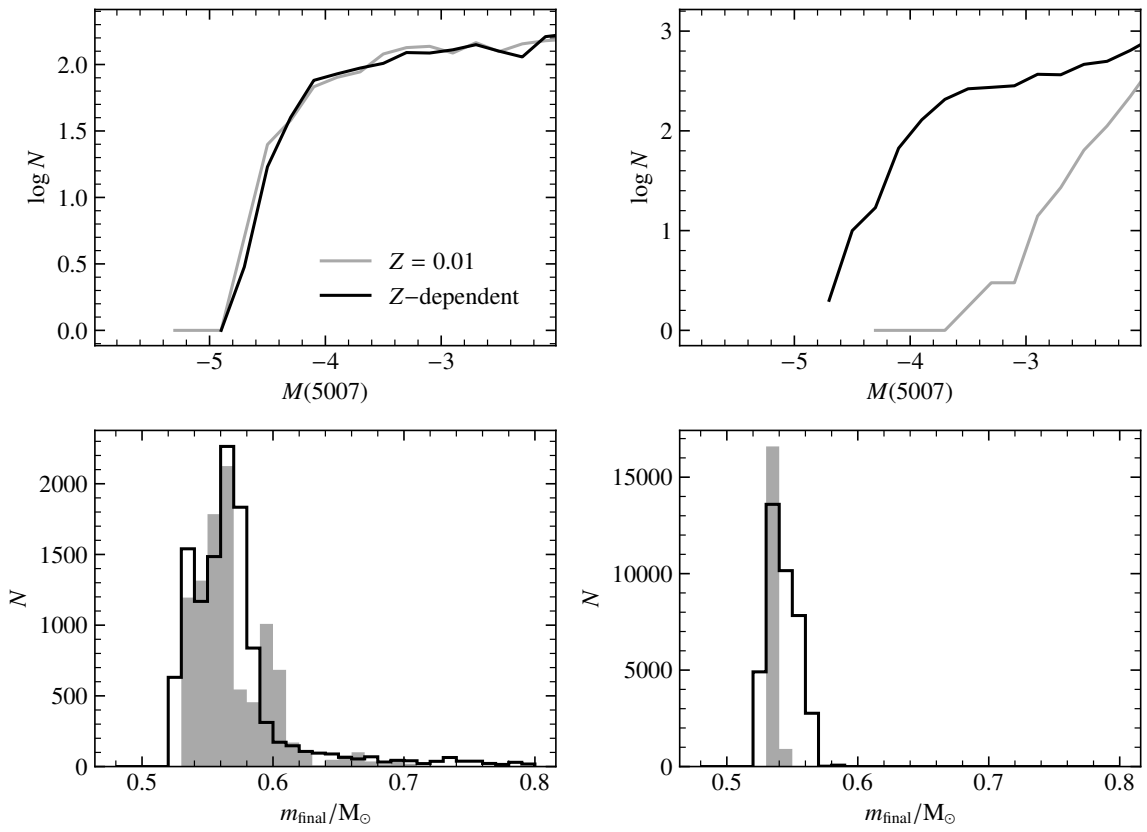


Figure 9.2: *Top*: Obtained PNLFs for two simulated galaxies (left and right panel each show the results for one galaxy) by running PICS with the models for $Z = 0.01$ (gray) and with the full metallicity-dependent models (black). *Bottom*: Final mass distributions of the PN central stars for the same two galaxies and running the same two varieties of PICS model sequences (in gray and black as for the top row).

the importance of taking the actual metallicities of PNe into account, we apply PICS with two different model sequences to the cosmological simulation. For the first, we only use the relations given for a metallicity of $Z = 0.01$ from Miller Bertolami (2016) and the lifetime function from Padovani & Matteucci (1993) and Renzini & Buzzoni (1986). For the second, we apply the full metallicity-dependent models to the stellar particles.

We applied the two model sequences of PICS to two different galaxies in the simulation, thus obtaining two PNe populations with [O III] magnitudes for each galaxy, leading to two PNLFs per galaxy. This led to very different results between the two galaxies. The first galaxy, which has a stellar mass of $M_* = 1.8 \times 10^{10}\,{\rm M}_\odot$, an average stellar age of $\langle t_{\rm age}\rangle = 6.5\,{\rm Gyr}$, and an average metallicity of $\langle Z\rangle = 0.013$, features the well-known PNLF bright end cutoff for both model sequences (top left panel of Figure 9.2). In contrast, the second galaxy, which is much more massive, older, and more metal-rich ($M_* = 1.2 \times 10^{11}\,{\rm M}_\odot$, $\langle t_{\rm age}\rangle = 9.3\,{\rm Gyr}$, $\langle Z\rangle = 0.022$), only features a normal PNLF for the metallicity-dependent model sequence, but completely lacks the brightest PNe when disregarding the metallicity on the stellar lifetimes (top right panel of Figure 9.2).

The reason for the large differences between the two PNLFs of the second galaxy can be found in the distribution of the final masses of the PN central stars (bottom row of Figure 9.2).

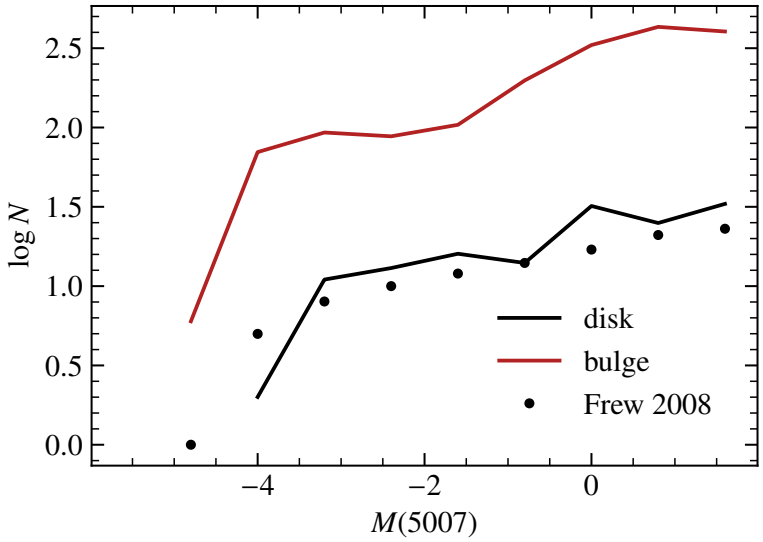


Figure 9.3: Planetary nebula luminosity functions of PNe in the Milky Way within 2 kpc of the Sun from Frew (2008) (black dots), for the modeled PNe within a sphere of 2 kpc radius with its center in the disk, 8 kpc away from the center of a selected simulated galaxy (black line), and for the modeled PNe within 2 kpc of the center of the simulated galaxy (red line). The simulated galaxy is a disk galaxy with a mass similar to that of the Milky Way. The PNe were modeled using the metallicity-dependent lifetime functions. Note that the $M(5007)$-axis reaches much deeper magnitudes than the ones in Figure 9.2.

While the $Z = 0.01$ model predicts final stellar masses of mostly $M_{\mathrm{final}} < 0.54\,\mathrm{M}_{\odot}$, the metallicity-dependent model finds final masses of up to $M_{\mathrm{final,max}} = 0.57\,\mathrm{M}_{\odot}$, which is only slightly lower than the required maximum final mass as obtained by Valenzuela et al. (2019) for old stellar populations. This is a consequence of the lifetimes being longer for any given stellar mass at higher metallicities (left panel of Figure 9.1), leading to the metal-rich, more massive stars reaching the PN phase at later times than metal-poor stars of the same mass. As the second galaxy is old and relatively metal-rich, the effect is strongly visible, whereas the first galaxy has metallicities close to the assumed $Z = 0.01$ of the metallicity-independent model, thus only leading to minor changes in the PNLF and final mass distribution. As a result, the metallicities clearly cannot be neglected in the general case when modeling the PNLF.

9.2.2 Normalization and shape of the PNLF

While we have shown that the general shape of the PNLF is qualitatively in agreement with observations, the question remains whether the absolute number of PNe found at a given [O III] magnitude is comparable with observations, that is the normalization of the PNLF. To not only compare this for the brightest PNe, but obtain a result reaching faint PNe as well, we decided to use the PNLF measured for PNe within 2 kpc of the Sun by Frew (2008). That PNLF is estimated to be statistically complete up to six orders of magnitude below the bright end cutoff and can be seen in Figure 9.3.

From the simulation, we selected a disk galaxy from Magneticum Box4 (uhr) with a Milky Way-like stellar mass ($M_* = 3 \times 10^{10}\,M_\odot$) to determine an analogous PNLF in the outer regions of the disk. For this, we only considered the stellar particles within a radius of 2 kpc from a point in the disk 8 kpc away from the galaxy center. The average stellar age in that region is $\langle t_{\rm age} \rangle = 5.6$ Gyr and the average metallicity $\langle Z \rangle = 0.027$, which is overall similar to the solar neighborhood. The resulting PNLF from PICS using the metallicity-dependent model sequence is very similar to that from Frew (2008), lying only around 0.2 dex higher than the observed PNLF at the dim end and dropping off slightly earlier at the bright end (Figure 9.3). As the simulated galaxy is of course not an exact Milky Way-analog, it is expected to also have differences with respect to its PNLF. However, the fact that the overall normalization and absolute number of PNe down to six orders of magnitude below the bright end are in agreement between the observations and simulations shows that the PNLF normalization obtained from the basic metallicity-dependent PICS model sequence is reasonable. In addition, it also shows that the assumption of PNe sometimes being optically thin is necessary to obtain the correct normalization since optically thick PNe lead to more particles being ionized and thus more [O III] emission. It should be noted that a perfect comparison is not only difficult because of the differences between the simulated galaxy and the Milky Way, but also because of the circumstellar extinction not being taken into account for the Milky Way PNe.

Finally, we also determined the PNLF of the inner stellar particles within 2 kpc of the galaxy center (red line in Figure 9.3). Due to the larger density of stars in the center, there are significantly more PNe in this region. Additionally, the shape of the PNLF is different than that of the disk, which is likely due to the bulge of the simulated galaxy being younger and more metal-rich than the disk (unlike the Milky Way bulge). This difference in stellar population affects the shape of the PNLF, as already observed in previous studies (e.g., Reid & Parker 2010; Valenzuela et al. 2019; Bhattacharya et al. 2021) and will be further investigated in a future study.

9.3 Summary and conclusion

In this work, we have presented first results from a novel method of integrating PNe in cosmological simulations through post-processing, called PICS (PNe In Cosmological Simulations). The method consists of a sequence of models that define the stellar lifetime function, the initial-to-final mass relation, the post-AGB stellar evolutionary tracks, and the nebular model. We employ the models of Miller Bertolami (2016) and Valenzuela et al. (2019) and use the lifetime function from Padovani & Matteucci (1993) and Renzini & Buzzoni (1986), which has been used independently of metallicity in the past, to compare the effect that metallicity-dependent models have: We show that a reasonable bright end of the PNLF of old metal-rich stellar populations can only be obtained when taking into account that metal-poor stars reach the PN phase more quickly than metal-rich stars of the same mass.

We also demonstrate that the metallicity-dependent model sequence of PICS is capable of producing the same shape and normalization (i.e., the same absolute number of PNe) of the

PNLF as is observed in the Milky Way disk around the Sun, down to at least six magnitudes below the bright end of the PNLF. As a result, PICS is shown to produce reasonably accurate populations of PNe and PNLFs for different underlying stellar populations. This work therefore lays the foundation for a more detailed analysis of the drivers behind the properties of the PNLF as well as for studies of the PNLF for galaxies across a diverse range of morphologies and formation histories, promising to significantly improve our understanding of the PNLF.

10

Circumnebular Extinction Around Planetary Nebulae

This chapter was published as Valenzuela et al. (2025b),
Front. Astron. Space Sci. 12, 1709047[1]:
The PICS project. II. Circumnebular extinction variations and their effect on the planetary nebula luminosity function

The tension regarding the observed universal bright end of the PNLF involves two sides, which theoretical models have had to address: limiting the [O III] brightness for PNe in young stellar populations, which would have more massive PN central stars compared to those in older populations, and increasing the [O III] brightness for PNe in old stellar populations (e.g., Ciardullo 2022). One proposal for bringing the brightness down for PNe in younger stellar populations has been the self-extinction through the dust formed in the winds during the asymptotic giant branch (AGB) phase preceding the PN phase (e.g., Ciardullo & Jacoby 1999; Ventura et al. 2014). Based on their findings and a model, Jacoby & Ciardullo (2025) showed how this circumnebular extinction seems to exactly compensate for the increasing potential brightness of PNe with more massive central stars over a large mass range, which could in part explain the constant PNLF bright-end cutoff. Considering the brightest PNe in the bulge of M 31, Davis et al. (2018) found very large circumnebular extinctions, implying intrinsic brightnesses well beyond the expectation for an older stellar population. Their results are

[1]Minor adjustments have been made, and the introduction has been adapted for this thesis.

also consistent with studies of other nearby galaxies (e.g., Méndez et al. 2005; Reid & Parker 2010). Furthermore, circumnebular extinction has been suggested as a way to understand the connection between UV measurements of post-AGB stars and PN central star candidates (Sarzi et al. 2011). The findings demonstrate that understanding the effects of circumnebular extinction on the bright end of the PNLF and on individual PNe is crucial to properly interpret the observations in both local and distant galaxies.

Recently, theoretical modeling of PNe has made large advances through the novel PICS (PNe In Cosmological Simulations) framework (Valenzuela et al. 2025c,d; see Chapter 8), a model that traces all the properties necessary to obtain a realistic PN population for any given single stellar population (SSP). Since it is built in a modular fashion, it allows one to study precisely how variations in the models and parameters impact the resulting PN and PNLF properties for any stellar population.

In this work, we use PICS to investigate how the chosen circumnebular extinction recipe affects the bright-end cutoff of the PNLF of different SSPs and compare the individual modeled extinctions of the bright PNe to observations. In Section 10.1, we give a brief overview of the PICS model and the extinction recipes tested. We then present the results in Section 10.2 and discuss them in Section 10.3.

10.1 Method

We use the fiducial model of the PICS framework presented by Valenzuela et al. (2025c), for which we test how the resulting PN properties change based on variations of the circumnebular extinction model. In the following, we give a brief overview of PICS and the circumnebular extinction recipe variations we tested.

10.1.1 PICS model

The PICS framework is composed of several modules that for a given SSP predict the PN population found therein. Such an SSP is parameterized by its total mass, age, metallicity, and initial mass function (IMF). In the PICS fiducial model, these properties are used to first determine the initial mass of the central stars of the current PNe through the lifetime function (Miller Bertolami 2016). The final stellar mass is obtained from the initial-to-final mass relation (IFMR) and the stellar properties from the post-AGB stellar tracks from Miller Bertolami (2016). All three of these steps are metallicity-dependent. Based on the stellar properties, the nebular model by Valenzuela et al. (2019) is applied together with a metallicity correction from Dopita et al. (1992). The nebular model also accounts for the possibility of the nebula being optically thin to the ionizing photons. The primary resulting quantity is the [O III] flux, $F(5007)$.

As shown by Jacoby & Ciardullo (2025), the [O III] flux can be significantly extincted by circumnebular dust that was expelled through the AGB winds. The extinction is expected to decrease over time during the post-AGB phase as the dust and nebula diffuse into the

interstellar medium (ISM) with age. The fiducial PICS model accounts for a post-AGB time-dependent circumnebular extinction consistent with the empirical findings from Jacoby & Ciardullo (2025), where we define the post-AGB time as the time after the central star reaches an effective temperature of $T_{\rm eff} = 25\,000\,\mathrm{K}$. The implemented extinction recipe is solely a function of post-AGB time of the central star, which in particular means we here assume it is independent of stellar mass.

To derive this equation, an intermediate step has to be taken because the relations from Jacoby & Ciardullo (2025, table 2) between stellar final mass and extinction, $c(\mathrm{H}\beta)$, are derived only from the brightest PNe. For this, we determined the post-AGB time at which a central star (with a metallicity of $Z = 0.01$) of given final mass reaches its brightest intrinsic [O III] magnitude. This will be needed to derive an "equivalent brightest PN final mass". The relation by Jacoby & Ciardullo (2025) returns an extinction based on the final mass of a brightest PN. From these two relations, we derived a direct dependence of extinction on post-AGB time: From the post-AGB time we obtain the "equivalent brightest PN final mass", from which we finally get the extinction. Because we make the simplifying assumption that the extinction depends only on post-AGB time and not on stellar mass, we use the resulting relation for all PNe. For the fiducial PICS model, we use their orthonormal regression fit to the combined Large Magellanic Cloud (LMC) and M 31 sample of PNe, the *Combined OR* (orthogonal regression) fit (from the table of Jacoby & Ciardullo 2025).

By running PICS for a given SSP, the result is a population of PNe, each with an [O III] magnitude. The resulting PNe differ from each other because the nebular model by Valenzuela et al. (2019) is stochastic in nature. Two reasons for this are the randomly drawn post-AGB lifetime and the randomness of the optical thickness of the nebula. In this work, we leave the fiducial PICS model fixed, with exception of the circumnebular extinction treatment. The variations thereof are described in the following.

10.1.2 Circumnebular extinction variations

While we used the Combined OR fit of Jacoby & Ciardullo (2025) for the fiducial PICS model, they also provided five additional fits to their PN data, varying both the subsample of PNe (Combined, LMC, M 31) and the fitting method (OR; ordinary least squares, OLS). They also include a fit that optimizes the final mass range over which the bright-end cutoff magnitude remains constant at $M^*(5007) \sim -4.5$ (named *Optimized*, see more details in Sect. 5 of Jacoby & Ciardullo 2025).

For the Combined OR fit, we assumed a metallicity of $Z = 0.01$ for the post-AGB evolution needed for the intermediate step (see the previous section). However, for the pure M 31 and LMC fits, it is more appropriate to assume metallicities that would more closely match those expected for their respective brightest PNe. Only for the Combined and Optimized fits did we assume $Z = 0.01$. For the LMC fits, we used $Z = 0.007$ based on the upper metallicity found for the LMC and its PNe (e.g., Dopita & Meatheringham 1991b). For M 31, we used a solar-like metallicity of $Z = 0.015$, based on metallicity measurements of luminous PNe in

M 31 (e.g., Balick et al. 2013). For each of the metallicities, we fit a broken linear fit (above and below $M_{\rm final} = 0.60\,{\rm M}_\odot$) to the relation of final mass versus post-AGB time at which an optically thick PN reaches its brightest [O III] luminosity, analogously to the $Z = 0.01$ fit by Valenzuela et al. (2025c, appendix D). The derived relations for the two metallicities are the following:

$$M^{Z=0.007}_{\rm final,bright}/{\rm M}_\odot = \max\begin{Bmatrix}1.023 - 0.1740\log(t_{\rm post-AGB}/{\rm yr})\\0.714 - 0.0432\log(t_{\rm post-AGB}/{\rm yr})\end{Bmatrix}, \tag{10.1}$$

$$M^{Z=0.015}_{\rm final,bright}/{\rm M}_\odot = \max\begin{Bmatrix}0.956 - 0.1477\log(t_{\rm post-AGB}/{\rm yr})\\0.743 - 0.0531\log(t_{\rm post-AGB}/{\rm yr})\end{Bmatrix}, \tag{10.2}$$

where the respective maximum of the two linear terms is taken. Based on the fit parameters presented in table 2 of Jacoby & Ciardullo (2025), the extinction $c({\rm H}\beta)$ is finally determined according to

$$c({\rm H}\beta) = {\rm S} \times M_{\rm final,bright} + I, \tag{10.3}$$

where S is the slope and I the intercept. One important note is that $M_{\rm final,bright}$ is not to be confused with the actual final mass of a PN. It is rather the "equivalent brightest PN final mass" as described in Section 10.1.1, based on the post-AGB time of a given PN (which can have any other final mass), and needed as input for the fits by Jacoby & Ciardullo (2025).

In addition to the relations taken directly from Jacoby & Ciardullo (2025), we also considered a shift of the OR extinction relations of $\Delta c({\rm H}\beta) = +0.08$. The motivation for this shift arises in Section 10.2.1 and is explained there in detail. Finally, the extinction in Hβ is converted to A_{5007} according to eq. 13 of Valenzuela et al. (2025c).

The result is an [O III] extinction, A_{5007}, as a function of post-AGB time, which we show in Figure 10.1. All recipes produce broken linear relations of A_{5007} with respect to the logarithmic post-AGB time and have the break at around 200 yr. The OR models have a significantly higher extinction than their OLS counterparts at young ages, but in turn have a slightly lower extinction at ages beyond ∼1500 yr. The modified OR models with the +0.08 shift have a slight offset to larger extinction by $\Delta A_{5007} = +0.18$. Between the different underlying observed PN samples, the LMC relations have the most extinction until about 1000 yr, with the LMC OLS relation being similar to the M 31 OR fit. The Combined relations respectively lie in between the LMC and M 31 relations, but align more closely with M 31 at later times. The Optimized relation leads to slightly stronger extinctions than the M 31 OR model.

These variations of the circumnebular extinction recipe were implemented within the PICS framework as described. They are used in the following to investigate their effect on the resulting PN population properties.

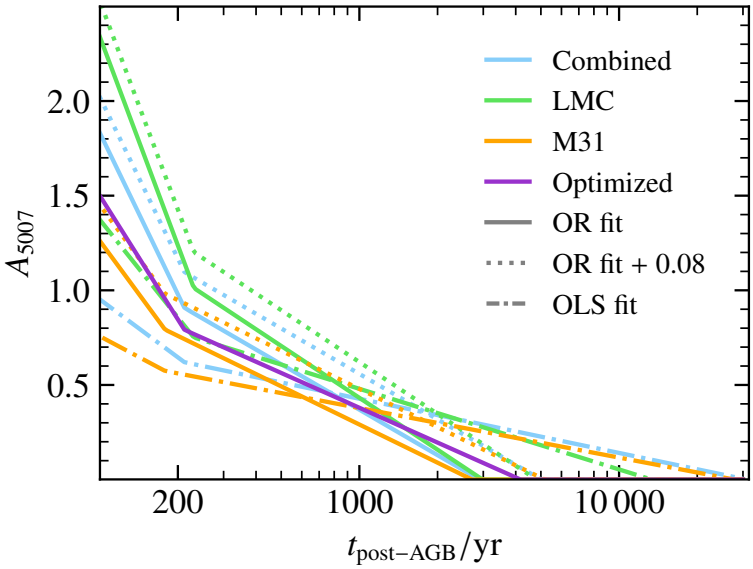


Figure 10.1: Circumnebular extinction of [O III], A_{5007}, as a function of post-AGB time of the central star for the different extinction recipes tested. The recipes are based on the relations by Jacoby & Ciardullo (2025) for the extinction $c(\mathrm{H}\beta)$ versus core mass for the brightest PNe in M 31 and the LMC. The colors indicate the Combined (blue), LMC (green), M 31 (orange), and Optimized (purple) fits, and the line styles denote the respective OR (solid), shifted OR (dotted), and OLS (dash-dotted) fits for all but Optimized. The dotted *OR fit + 0.08* lines are based on their OR relations shifted by $\Delta c(\mathrm{H}\beta) = +0.08$.

10.2 Results

While the recipe for extinction was derived from the maximal brightness of PNe with a given final stellar mass, the nebular model by Valenzuela et al. (2019) allows for escaping ionizing fractions and different [O III] to Hβ flux ratios. This leads to the possibility of dimmer PNe arising, leading to a range of possible [O III] magnitudes for a given final mass and post-AGB time.

10.2.1 Extinction of Hβ

As the recipe for circumnebular extinction was informed through the observations by Jacoby & Ciardullo (2025), this allows for a direct consistency check for the actually derived extinction values of the resulting PN population from the PICS model. To this end we ran PICS for an LMC-like PN population of $Z = 0.007$, for which we only kept those with extincted magnitudes $M(5007) \leq -3.5$ for comparison with the observational sample. We ran PICS with the extinction recipes based on the LMC OR, OLS, and the shifted OR relations. The $c(\mathrm{H}\beta)$ extinctions of the bright PNe are shown in the left panel of Figure 10.2, where the lines indicate the median extinctions found for the bright PNe at the individual final masses, and the shaded regions the 1σ-scatter. The observed extinctions of the LMC PNe are indicated with black points. The same is shown for an M 31-like PN population of $Z = 0.015$ in the right panel for the analogous three M 31 extinction fits to the observed M 31 PNe.

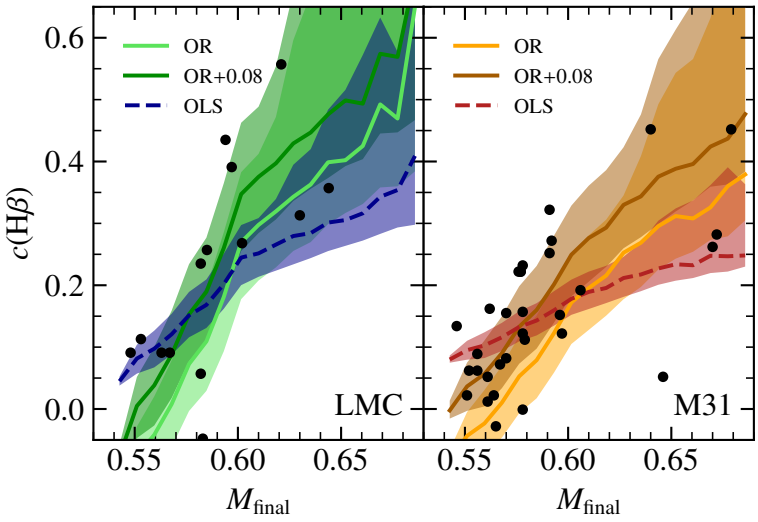


Figure 10.2: Circumnebular extinction of Hβ, $c(\mathrm{H}\beta)$, as a function of stellar final mass for the brightest observed and modeled PNe assuming different extinction recipes. LMC-like PNe ($Z = 0.007$) are shown on the left and M 31-like PNe ($Z = 0.015$) on the right. Bright PNe are selected according to $M(5007) \leq -3.5$, analogously to the observed PNe (black circles) as selected by Jacoby & Ciardullo (2025). The lines indicate the medians and the shaded regions the 1σ-scatter of the extinction values at the respective final masses. The extinction recipes correspond to the input fit relations from Jacoby & Ciardullo (2025), orthonormal regression (OR), shifted OR by $\Delta c(\mathrm{H}\beta) = +0.08$, and ordinary least squares (OLS).

For both PN populations, it can be seen that the OR model (light green and light orange) leads to overall lower extinctions of the PNe compared to the observations, though the slope stays the same. In contrast, the OLS model (dashed blue and red) results in too much extinction at lower masses ($\lesssim$0.56 $\mathrm{M}_\odot$) and underestimates the extinction at higher masses ($\gtrsim$0.59 $\mathrm{M}_\odot$) because of its overall more shallow slope.

We find that the OR models lead to systematically too low values of $c(\mathrm{H}\beta)$ by around 0.08. For this reason, we implemented a shifted OR relation with $\Delta c(\mathrm{H}\beta) = +0.08$. For the shifted models the PN extinction distributions are indeed brought into much better agreement with the observations (dark solid lines in Figure 10.2).

The motivation for such a shift is that the observations on which the relations are based are of the brightest PNe within one magnitude of the bright-end cutoff, and not only of the very brightest PNe. In contrast, our implemented recipe assumes the extinction from the fits of Jacoby & Ciardullo (2025) to correspond to the point in time where the PNe are at their brightest. After the time of reaching its brightest [O III] flux, a PN drops in brightness and the extinction declines. Such PNe could still reside in the brightest magnitude, but would have a lower extinction. For this reason it is expected that the average extinction of the brightest PNe ($M(5007) \leq -3.5$) will be underestimated through the application in the PICS model, suggesting that a correcting shift is necessary. We conclude that the shifted OR recipe leads to the most compatible extinctions with observations and that the shift is reasonable for adaptation within the PICS framework.

10.2.2 Extinction effects on the PNLF

Having verified the agreement of the modeled circumnebular extinction with the original observations, we next tested how much the variations of the extinction recipe actually affect the PNLF and its bright end. Running PICS for a sufficiently large number of PNe that arise from an SSP of certain age and metallicity produces the PNLF expected for such an SSP. Figure 10.3 shows a grid of such SSP PNLFs for five different metallicities from $Z = 0.001$ to 0.08 and ten SSP ages between 0.25 and 13 Gyr, using no circumnebular extinction (dotted black lines) and the different extinction recipes as described in Section 10.1 (solid lines for OR, dotted for shifted OR, and dash-dotted for OLS).

As expected, the extinction is the highest for the young SSPs with high-mass PN central stars, leading to dimmer bright-end cutoffs for the extincted PNe (colored lines) compared to the non-extincted PNe (dotted black lines) in the upper rows. Here it becomes clear that the OLS recipes lead to the smallest amount of dimming (dash-dotted lines) for young SSPs, followed by the OR (solid lines) and shifted OR recipes (dotted colored lines). Compared to the Combined OR recipe used in the fiducial PICS model, most extinction recipes lead to brighter PNLFs, except for the two LMC OR recipes. However, these differences become noticeably smaller for ages of 1 Gyr and older, reducing the differences between the circumnebular extinction recipes to $\lesssim$0.5 mag. These differences between the tested recipes remain rather constant for the metallicity range considered ($Z = 0.001$–0.08) and also moving towards older SSPs. For the oldest SSPs of $t_{\rm age} \gtrsim 8$ Gyr, the dimming becomes zero or near-zero for all but the OLS recipes. This is related to the more shallow slope of the OLS relations (see Figure 10.2), resulting in a generally stronger extinction even at the lower final masses below $0.55\,M_\odot$.

Having been optimized to recover a constant bright-end across a range of masses that is as large as possible, the Optimized PNLFs (purple lines in Figure 10.3) show a PNLF dimming that is right in the middle of the alternative models for younger SSPs. This leads to a slightly brighter cutoff than $M^*(5007) = -4.5$ for some SSPs, but it quickly approaches a negligible dimming for older SSPs when the lower-mass PNe become intrinsically dimmer. Thus, the Optimized recipe produces the most constant PNLF cutoff across SSPs of different ages and metallicities using the PICS model.

10.2.3 Extinctions of de-reddened PNe

Finally, we investigated the relation of intrinsic de-reddened [O III] magnitudes with their circumnebular extinctions. For this, we ran PICS for 100 000 PNe at an intermediate metallicity of $Z = 0.01$ with different circumnebular extinction recipes, 1000 PNe each for 100 uniformly spaced ages between 0.25 and 10 Gyr. The relation of their intrinsic [O III] magnitudes, $M_{\rm dered}(5007)$, with the [O III] extinction, A_{5007}, is shown in Figure 10.4. We also included observations of bright PNe from four nearby galaxies, as compiled by Davis et al. (2018). These are from M 31 (Davis et al. 2018), the LMC (Reid & Parker 2010), NGC 4697 (Méndez et al. 2005), and NGC 5128 (Walsh et al. 2012). The dashed line marks the location of the

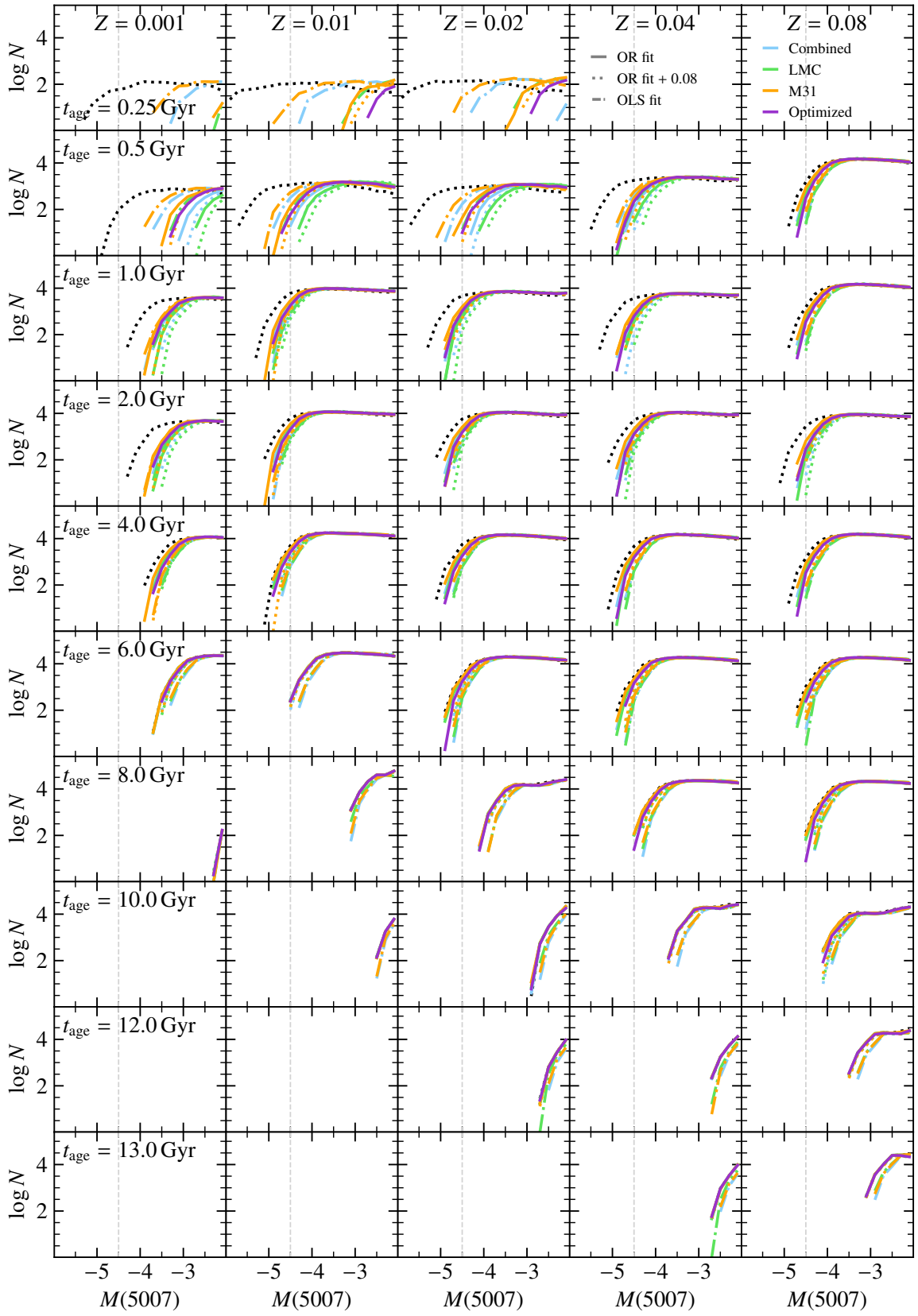


Figure 10.3: Grid of SSP PNLFs for different metallicities (columns; $Z = 0.001$, 0.01, 0.02, 0.04, 0.08) and ages (rows; $t_{age} = 0.25$ to 13 Gyr for the different circumnebular extinction recipes tested (colored lines), as well as without extinction (dashed black lines). The observed universal bright-end cutoff of $M(5007) = -4.5$ is indicated by the dashed gray lines.

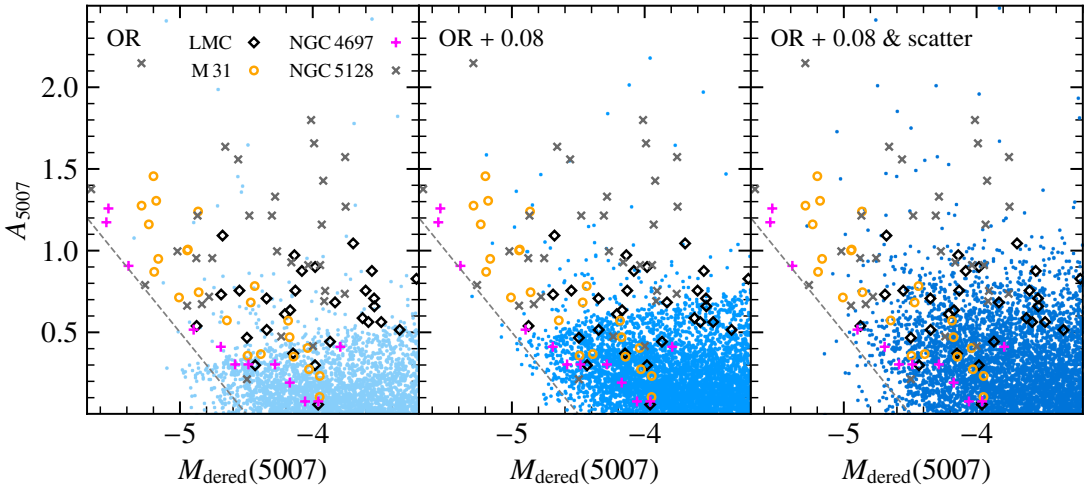


Figure 10.4: Circumnebular extinction of [O III], A_{5007}, versus the intrinsic de-reddened [O III] magnitude, $M_{\rm dered}(5007)$, of observed and modeled PNe for three different circumnebular extinction recipes. *Left*: Combined OR. *Middle*: Combined OR with a shift of $\Delta c(\mathrm{H}\beta) = +0.08$. *Right*: Combined OR with the same shift of +0.08 and an added normally distributed scatter in $c(\mathrm{H}\beta)$ of $\sigma = 0.1$. The values of the observed PNe are taken from Davis et al. (2018), who observed PNe in the bulge of M 31 and compiled the data from other works for three other galaxies: the LMC (Reid & Parker 2010), NGC 4697 (Méndez et al. 2005), and NGC 5128 (Walsh et al. 2012). The dashed gray lines indicate the bright-end cutoff of the PNLF of $M(5007) = -4.5$.

bright-end cutoff for PNe of different extinctions. In the left and middle panels, the Combined OR and shifted Combined OR recipes were applied, respectively. The elevation to higher extinctions can immediately be seen for the shifted OR recipe: first, the bulk of PNe reach higher values of A_{5007}, and second, there are fewer PNe that reside in the regime brighter than the bright-end cutoff (region below the dashed gray line). Overall, most PNe have lower extinction values of $A_{5007} \lesssim 0.5$ and 0.75 for OR and shifted OR, respectively. This stands in contrast to the observed PNe, where the extinctions of the PNe are more uniformly distributed. Only NGC 4697 contains a large fraction of PNe with $A_{5007} \lesssim 0.5$, but still has a significant amount of them at higher extinctions (3 out of 12), unlike the modeled PNe. Additionally, there is a larger fraction of intrinsically bright observed PNe with $M(5007) \lesssim -5.0$ compared to the modeled PNe.

Since the observed extinctions are much greater than the modeled ones in both cases (left and center panel of Figure 10.4), we decided to add a random normally distributed scatter to $c(\mathrm{H}\beta)$ after applying the respective linear relation from Jacoby & Ciardullo (2025). The motivation is that any asymmetric nebulae would be expected to also have varying amounts of dust along different lines of sight, thus changing the circumnebular extinction. We tested an additional Gaussian scatter with $\sigma = 0.1$ applied to the shifted Combined OR relation. This chosen value leads to a slightly larger scatter than is observed in the $c(\mathrm{H}\beta)$ relation showed in Figure 10.2, but which still has the same median behavior as the non-scattered versions. In the right panel of Figure 10.4 we show how the A_{5007} extinctions are able to reach higher values due to the increased scatter. However, even with this, the large relative amount of high-extinction PNe found in the observations is still not recovered. Finally, PNe brighter than

the bright-end cutoff (those found below the dashed diagonal line) are now on average also further away from the cutoff, with several ending up at magnitudes close to $M(5007) \sim -4.8$. Therefore, the larger scatter on the one hand increases the extinctions that can generally be reached, but on the other hand also leads to overly bright PNe, though there are also occasional observations of such PNe (e.g., Jacoby et al. 2024, fig. 59). We conclude that the simple additional scatter for the extinction is not sufficient in bringing the modeled and observed [O III] extinctions in agreement.

10.3 Discussion

For the [O III] circumnebular extinction, A_{5007}, the largest effect of the different tested extinction recipes is found at the beginning of the post-AGB phase (Figure 10.1). Because only the more massive central stars can come near the bright end within this short time frame due to their faster heating (e.g., Miller Bertolami 2016), the only SSP PNLFs that experience significant extinction differences between the recipes are those of the youngest SSPs with $t_{\rm age} \lesssim 0.5$ Gyr (Figure 10.3). This implies that in particular the early behavior of dust build-up in the nebula is of great importance for the resulting amount of circumnebular extinction. However, given that the implemented recipes were based on the empirical results of extinction related to final mass from Jacoby & Ciardullo (2025), we note that the regime of very large extinction is largely beyond the originally fitted range of $c(\mathrm{H}\beta) \lesssim 0.5$ ($A_{5007} \lesssim 1.2$). In turn, this range covers most of the PN lifetime after 200 yr, where the differences are much smaller as they are more constrained by the observations.

Overall, the modeled PNe have similar extinctions to the observed PNe for the different recipes, but neither the pure OR nor OLS recipes reproduce the same median extinction-final mass relation as the observations (Figure 10.2). This shows that the average extinction relation of the PNe in the brightest magnitude is not the direct desired input relation for the PICS model (Valenzuela et al. 2025c), though the slope of the OR recipe is similar to that of the observed median relation. We addressed this offset by shifting the OR relations up by the respective amount of $\Delta c(\mathrm{H}\beta) = 0.08$. However, in the future ideally the relation between extinction and final mass will be informed by a larger sample of PNe that directly lie at the bright end to limit the scatter around the fitted relation (see the discussion by Jacoby & Ciardullo 2025).

Despite the Combined OR recipes reaching the second highest extinctions (after the LMC OR recipes; see Figure 10.1) and generally reproducing the relation between extinction and final stellar mass, it is curious that the models using *Combined OR* do not reach as high extinctions for a full PN population as found in nearby galaxies (Figure 10.4). Even when including a scatter for the extinction that would produce higher values, the distribution still does not match the observations. There are multiple possible reasons for this discrepancy. For one, the modeled stellar population is artificially created with PNe at uniformly spaced ages and thus does not represent the true star formation history of any of the four observed galaxies. However, from the model side the only realistic possibility to obtain a similar amount of

high-extinction PNe would be to have a much larger fraction of younger stars, which is likely not the case for the observed galaxies.

Furthermore, potential model-intrinsic issues of the recipes used by PICS could lead to PN populations that do not entirely match the observed PNe. While the PNLF properties and many relations like the extinction-final mass relation do agree with observations, the properties of individual PNe could still be systematically offset because of unknown degeneracies. Another possible explanation is that PICS is missing relevant channels for forming PNe at the bright end, for example accreting white dwarfs (e.g., Soker 2006; Souropanis et al. 2023), blue stragglers (e.g., Ciardullo et al. 2005), and white dwarf mergers (e.g., Yao & Quataert 2023), which could result in different extinction properties. These additional possible pathways are supported by the evidence that a significant fraction of PNe are in binary systems (Jones & Boffin 2017; Jacoby et al. 2021; Csukai et al. 2025). Additionally, a random scatter of the final mass through the IFMR as proposed by Jacoby & Ciardullo (2025) could also increase the number of bright PNe with higher extinctions. Systematic biases in the extinction determination for the observations could lead to a preference of higher extinctions being predicted for the PNe. Then the slope parallel to the bright-end cutoff line seen in Figure 10.4 for M 31 and NGC 4697 could also be the result of selection bias coupled to systematically higher extinctions.

Finally, it is interesting to consider the effects that metallicity would have on the extinction, which are not accounted for in the tested recipes. At higher metallicity, there should be more metals to contribute to the formation of dust for equal stellar masses. As also pointed out by Jacoby & Ciardullo (2025), curiously their derived relations between extinction and final mass show no significant differences between M 31 and the LMC PNe, even though the PNe in the bulge of M 31 have roughly twice the metal mass fraction as those in the LMC. The LMC PNe even seem to reach higher extinctions at a given final mass (Figure 10.2), though this seems to stand in contrast to the overall lower measured [O III] extinctions (Davis et al. 2018), seen in Figure 10.4.

To conclude, while circumnebular extinction surely plays a central role in limiting the [O III] magnitude of PNe in intermediate-to-younger stellar populations to the universal bright-end cutoff, the details around its dependency on other physical properties are not straightforward. While recipe variations in the PICS model affect the youngest stellar populations the most due to being the least constrained observationally, the general discrepancies between the modeled extinctions and those determined from observations make it very difficult to disambiguate between the recipes. Further observations and advances on the understanding of circumnebular dust evolution will be necessary to improve the modeling.

11

Solving the Mystery of the PNLF Cutoff

This chapter presents the current status of work to be submitted
as Valenzuela et al. (in prep.):
Solving the mystery of the planetary nebula luminosity function cutoff

The tension caused by the observed universal bright end of the PNLF and the lack of a theoretical explanation for it has been a long-standing issue in PN studies (e.g., Ciardullo 2010, 2022). In the last decade, updated post-AGB stellar evolutionary tracks helped overcome some of the original conflict through overall more massive and thus brighter central stars (Miller Bertolami 2016; Gesicki et al. 2018; Valenzuela et al. 2019). However, to date, none of the proposed solutions have been shown to actually explain the universality of the PNLF for real galaxies.

To actually verify whether a model can explain the universal PNLF bright-end cutoff, it is necessary to employ realistic stellar populations found in the different galaxy morphologies and test the PN models on these. In this work, we apply the newly developed model *Planetary nebulae In Cosmological Simulations* (PICS; Valenzuela et al. 2025c; see Chapter 8) to the galaxies from the hydrodynamical cosmological simulation *Magneticum* (Dolag et al. 2025; see Chapter 2) to investigate whether the PN model together with a galaxy formation simulation can reproduce the observed PNLF properties. The stellar populations from Magneticum thus have self-consistent star formation histories related to the galaxy morphology in the cosmological

context. This allows us to produce the PNLFs for galaxies of all morphological types and test whether the combination of cosmological star formation histories from Magneticum and full stellar evolution modeling from PICS can finally explain the universality of the PNLF bright-end cutoff.

11.1 Methods

In the following, we introduce the relevant methods for this work. We first introduce the employed PN model and describe how we perform PNLF fits to the PN [O III] magnitudes, followed by an overview of the cosmological simulation and the selected galaxy sample therein.

11.1.1 PN properties from the PICS model

The PN properties in the simulated galaxies are obtained with the fiducial PICS model (Valenzuela et al. 2025c), which determines the PN populations for single stellar populations, each with a given initial mass function (IMF), total mass, age, and metallicity (here used as the mass ratio $Z = M_{\rm met}/M_{\rm tot}$). It first employs the results from a metallicity-dependent stellar evolution model (Miller Bertolami 2016) to compute the central star properties of the PNe: the lifetime function, which gives the time it takes a star on the main sequence to reach the post-AGB phase as a function of initial stellar mass, additionally the initial-to-final mass relation (IFMR), and the post-AGB evolution tracks of the central star. Next, an empirical nebular model with a recipe for nebular transparency is employed to obtain the [O III] flux (Valenzuela et al. 2019), where additionally a correction is applied to account for the metallicity (Dopita et al. 1992) relative to the zero point of $Z = 0.007$ (Valenzuela et al. 2025c). Finally, an empirical relation for the circumnebular extinction is applied based on the core mass of the central star (Jacoby & Ciardullo 2025).

We ran PICS on the individual stellar particles of each considered galaxy in the cosmological simulation. This provides us with the total PN population for the collection of stellar particles representing the discretized star formation history of the respective simulated galaxy. The result is a list of $M(5007)$ values per galaxy, from which the PNLFs can be computed.

11.1.2 PNLF fitting

Taking the values of $M(5007)$ obtained from PICS for each of the galaxies, we compute their PNLF and fit the generalized form of the PNLF to it (Longobardi et al. 2013). This is done by a least-squares method applied to the cumulative PNLF to avoid issues with binning. The three free parameters are the bright-end cutoff value $M^*(5007)$, an exponential slope, and a normalization for the PNLF. To obtain accurate values for $M^*(5007)$, we only fit the PNe with magnitudes brighter than $M(5007) \leq \max(-3.5, M_{\rm min} + 1)$, where $M_{\rm min}$ is the [O III] magnitude of the brightest PN found in the galaxy. This ensures a minimum magnitude range of 1 mag of the PNLF to be fitted.

Not all PNLF fits are successful in converging, such that we discard the non-converged fits. This only affects 2.5% of elliptical and 0.1% of lenticular galaxies, leaving us with 2958 elliptical, 2374 lenticular, and 1186 disk galaxies. Additionally, some of the PNLF fits that converged have significantly brighter cutoff values than the brightest PN magnitude in a galaxy. This happens most often for galaxies with low numbers of PNe at the bright end. For those cases, we fit the PNLF through a maximum likelihood method (described in Sect. 3.2 of Scheuermann et al. 2022) for the same PNe as the least-squares method and assuming a fixed slope of $c_2 = 0.307$, that is assuming a classical PNLF. This method performs better for low numbers of PNe, but for PNLFs with individual especially bright PNe it is too sensitive to the brightest PN. For that reason, we only use this method as a fallback for the poor-quality least-squares PNLF fits. For a more detailed description of the fitting methods, refer to Section 12.1.2 and Appendix F.1.

11.1.3 Cosmological simulation

The hydrodynamical cosmological simulation Magneticum Box4 (uhr) was run with the smoothed-particle hydrodynamics (SPH) code Gadget-3 (a modified version of Gadget-2; Springel 2005) has a box side length of 68 Mpc and an average stellar particle mass of $1.8 \times 10^6\,\mathrm{M}_\odot$. The galaxies were identified with SubFind (Springel et al. 2001; Dolag et al. 2009). For this study, we used all central and satellite galaxies from the last simulation snapshot at $z = 0.06$ with stellar masses of $M_* \geq 2 \times 10^9\,\mathrm{M}_\odot$, where these are determined as the total stellar mass contained within $0.1\,R_\mathrm{vir}$ (Dolag et al. 2025). For the morphological classification, we used the kinematic description thereof through the galaxy position in the stellar specific angular momentum-mass plane, quantified by the b-value (Teklu et al. 2015):

$$b = \log \frac{j_*}{\mathrm{kpc\,km\,s^{-1}}} - \frac{2}{3} \log \frac{M_*}{\mathrm{M}_\odot}, \tag{11.1}$$

where $j_* = J_*/M_*$ is the specific angular momentum, measured within $3\,R_{1/2}$ with $R_{1/2}$ being the 3D half-mass radius of the galaxy (Dolag et al. 2025). The morphologies are then defined as (Valenzuela et al. 2024a):

- disk galaxy: $b \geq -4.35$,
- lenticular galaxy: $-4.73 < b < -4.35$,
- elliptical galaxy: $b \leq -4.73$.

For this work, we only contrasted the disk and elliptical galaxies to demonstrate the two extremes of the morphological spectrum. The galaxy sample contains 2958 disk, 2374 lenticular, and 1186 elliptical galaxies.

11.2 PNe reaching the bright end

The PNe found at the bright end of the PNLF could originate from very different initial properties of their central stars. We evaluate which PNe are actually capable of reaching the

bright-end cutoff for a range of different initial central star properties. There are two important relations that impact what brightness individual PNe can reach over their own lifetime of around 30 000 yr. The first is the PN central star mass ($M_{\rm final}$) that is reached for different metallicities (defined here as metal mass fractions Z, where solar metallicity is $Z_\odot \approx 0.015$; Asplund et al. 2021) at fixed stellar population age, where higher central star masses can lead to higher intrinsic [O III] emission. The top panel of Figure 11.1 shows that at super-solar metallicities, the central star mass as modeled by the fiducial PICS model (Valenzuela et al. 2025c) decreases with increasing metallicity for young stellar populations younger than 1 Gyr, whereas for older stars, the star mass increases with metallicity. The stellar population ages range from 0.4 to 12.0 Gyr and are colored by different colors. Only at ∼1 Gyr is there an initial rise with metallicity up to a peak star mass at around $Z = 0.04$ before declining again. In particular, this means that old metal-rich PNe are expected to be brighter in [O III] emission than old solar-metallicity PNe. The second important relation is that circumnebular extinction is higher for massive stars at peak luminosity due to their fast heating after leaving the AGB. It has been observationally determined that there is a linear relation between central star mass and extinction in [O III], A_{5007} (Jacoby & Ciardullo 2025; Valenzuela et al. 2025b). Therefore, the extinction as a function of metallicity at fixed stellar population age qualitatively behaves similarly to the relation with the central star mass for the more massive younger central stars, where extinction declines with increasing metallicity (bottom panel of Figure 11.1).

In Figure 11.2, we track the temporal evolution of the maximal [O III] magnitudes $M(5007)$ for individual PNe of different metallicities and stellar ages, as modeled by the fiducial PICS model (Valenzuela et al. 2025c). Here, we investigate the maximal [O III] brightness to determine the potential that PNe in a given stellar population have to reach the bright-end cutoff of the PNLF, thereby assuming them to be optically thick. Optically thin PNe (e.g., caused by asymmetries) would evolve similarly, but with dimmer magnitudes. We ran PICS for a single PN of given stellar age and metallicity for post-AGB ages $t_{\rm PN} = 0$–$30\,000$ yr, which is the PN lifetime from the nebular model (Valenzuela et al. 2019). As the model is stochastic with respect to the optical thickness of the nebula, we ran the model 1000 times per post-AGB age to estimate the maximally possible brightness of such a PN. The figure thus shows the magnitude evolution for the brightest PNe in the given stellar populations. Most other PNe will actually be less luminous due to a lack of optical thickness, for example because of spatial asymmetries. Solar metallicity PNe are shown in the top panel, and the super-solar metallicities $Z = 0.04$ and 0.06 are shown in the middle and bottom panels, respectively. For sub-solar metallicities, the brightest magnitudes obtained for PNe are expected to become significantly dimmer towards lower metallicities (Jacoby 1989; Schönberner et al. 2010), thus not contributing as much to the bright end. We show the temporal evolution tracks for lower metallicities in Appendix E.1.

The general shape of the magnitude evolution shows a brightening of the PN over time, which corresponds to the stellar heating on the post-AGB track (Miller Bertolami 2016). This occurs over a shorter period of time for more massive central stars found in younger stellar populations (darker lines), and it takes longer for less massive stars (lighter lines).

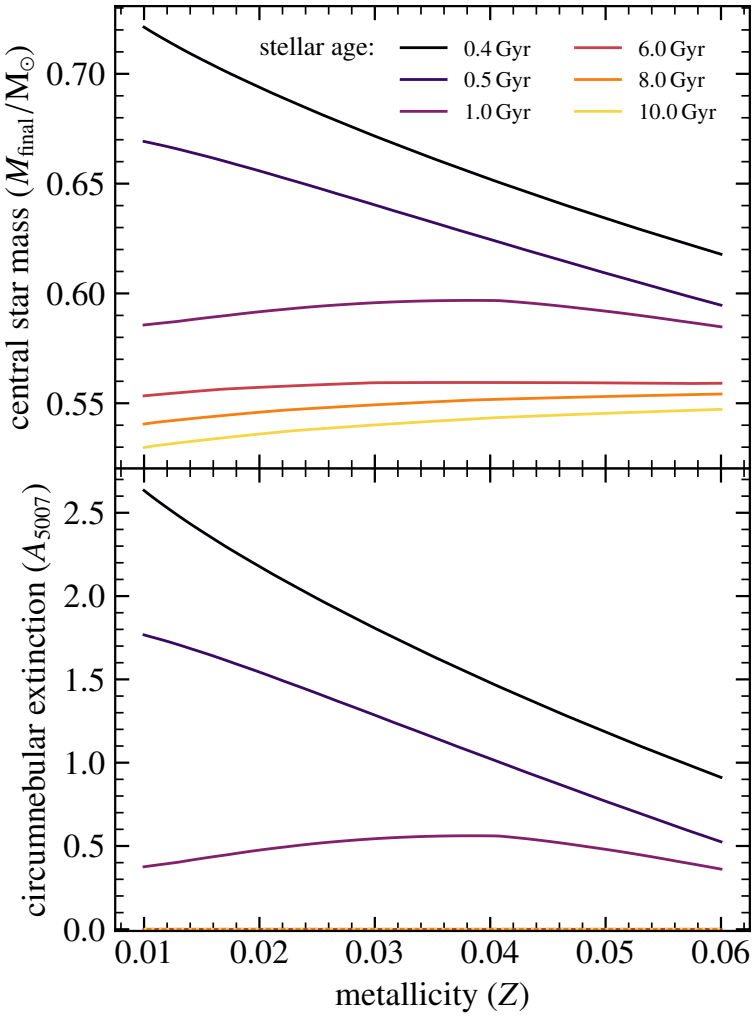


Figure 11.1: Final central star mass ($M_{\rm final}$; *top*) and circumnebular extinction at maximum brightness (A_{5007}; *bottom*) as a function of metallicity for PNe of different stellar ages from PICS (Valenzuela et al. 2025c). More massive stars can produce a brighter [O III] emission, while the extinction at maximum brightness is linearly related to mass and dims the emission (Jacoby & Ciardullo 2025). The circumnebular extinction reaches zero below a mass of around 0.56 $M_\odot$.

Here the high extinction at early PN times particularly dims the PNe from the younger stellar populations, which becomes less significant with increasing metallicity as expected from Figure 11.1. After reaching the peak luminosity, the nebula continues dissipating and the star cools down slowly after reaching its maximum temperature. Note that the double peak seen for many of the magnitude evolutions is a numerical artifact of the nebular model and does not imply an underlying physical process.

The PICS model predicts that, for the selected metallicities, PNe reach the bright-end cutoff for a short time over a large range of stellar population ages. At solar metallicity (top panel) this is the case for ages of 0.5–6 Gyr as can be seen by the two corresponding purple lines touching the bright-end cutoff (gray dashed line). At $Z \gtrsim 0.04$ (middle panel) the age range for which PNe reach the bright-end cutoff increases to 0.4–8 Gyr. Only older stellar populations beyond 8 Gyr (yellow) are not able to populate the bright end of the PNLF. The youngest and most massive PNe do not reach these bright values due to the even more

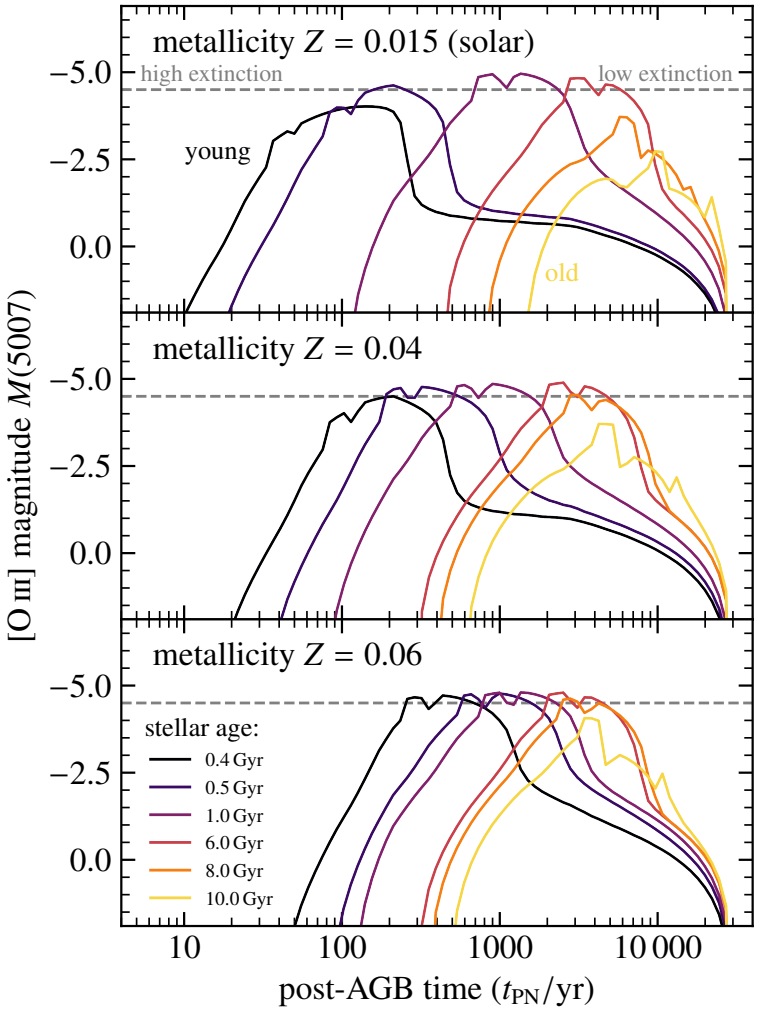


Figure 11.2: Temporal evolution of the magnitude $M(5007)$ for optically thick PNe of different stellar ages (indicated by the colors) at solar and super-solar metallicities ($Z = 0.015$, 0.04, 0.06 from top to bottom, corresponding to $\log Z/Z_\odot = 0.0$, 0.4, and 0.6, the first being solar, see Asplund et al. 2021) over the PN lifetime of 30 000 yr from PICS (Valenzuela et al. 2025c). The circumnebular dust extinction decreases over the PN lifetime, which significantly dims the peak brightness of the youngest PNe. The observed bright-end cutoff value of $M^*(5007) = -4.5$ is marked by the horizontal dashed lines.

significant circumstellar extinction around the corresponding massive central stars (Jacoby & Ciardullo 2025).

For our own Sun of mass 1 $M_\odot$, the corresponding maximal PN brightness evolution it could follow is the 10 Gyr line at solar metallicity $Z = 0.015$ (orange line in the top panel of Figure 11.2). The model predicts that in around 5.5 Gyr, when our Sun becomes a PN, it could contribute to the PNLF of the Milky Way with a magnitude of up to $M(5007) = -2.5$ at its maximum luminosity. This brightest phase would last around 1000 yr, as seen by the width of the peak of the orange curve at $t_{PN} \sim 10\,000$ yr in the top panel. However, the Sun is not sufficiently massive or metal-rich to reach the bright end of the PNLF.

In summary, older PNe can reach brighter magnitudes the higher their metallicity is due to the higher central star mass (top panel of Figure 11.1), but the oldest PNe always lack the stellar luminosity and temperature to reach the bright end. For the PNe that actually reach the

bright end, the time they remain there strongly depends on the intrinsic properties and ranges from around 100 yr (e.g., $t_{\rm age} = 0.5$ Gyr at $Z = 0.015$) to a couple 1000 yr (e.g., $t_{\rm age} = 6.0$ Gyr at $Z = 0.04$). Overall, it is very promising that the PNe across a large range of ages can reach the bright end. Next we can verify whether this is sufficient to produce PNLFs for realistic galaxies with a universal bright end consistent with observations.

The differences in bright-end cutoff magnitude and scatter at around $\log M_*/\mathrm{M}_\odot \approx 10$–$11$ for Box4 seen in Figure 11.4 can be explained by the different stellar populations found in the elliptical and disk galaxies. Figure 11.3 shows the mass-weighted mean stellar ages and metallicities as functions of the stellar mass, revealing significant differences in the stellar ages, in particular around the relevant mass range of $\log M_*/\mathrm{M}_\odot \approx 10$–$11$. In this range, elliptical galaxies tend to be older than disk galaxies by around $\Delta t_{\rm age} \approx 1$–$2.5$ Gyr. With the similar mass-metallicity relation for both types of galaxies (see Dolag et al. 2025 for more details about this relation in Magneticum and comparisons to observations), the generally older stellar populations of elliptical galaxies beyond ~9 Gyr lead to overall dimmer PNe, which also affects the bright-end cutoff. Observations and models also show that there is an expected decrease of bright PNe in older stellar populations (Soemitro et al. 2025). In contrast, the more massive elliptical galaxies have higher metallicities, which increases the potential PN brightness towards the bright-end cutoff magnitude at those super-solar metallicities (Figure 11.2).

11.3 The universal bright end of the PNLF

For the application of PICS to realistic galaxies, we use the Magneticum Box4 (uhr) simulation, which has been shown to agree well with observations across a large range of galaxy properties (Teklu et al. 2015; Dolag et al. 2025). To test the universality of the PNLF across morphologies, we select disk and elliptical galaxies from the simulation with stellar masses of $M_* \geq 2{\times}10^9\,\mathrm{M}_\odot$. We apply PICS to each of these galaxies to obtain a complete PN population per galaxy. From their [O III] magnitudes, the PNLF is computed and we fit an analytical form of the PNLF with an exponential cutoff to it (Ciardullo et al. 1989; Longobardi et al. 2013). For each galaxy, the bright-end cutoff then arises directly from the fit to its PNLF, such that we obtain a bright-end cutoff per galaxy.

In Figure 11.4 we show the PNLF bright-end cutoff $M^*(5007)$ as a function of stellar mass for the two morphological types, disk (blue) and elliptical (red) galaxies. The lines indicate the respective median of $M^*(5007)$ and the shaded regions the 1σ scatter of the values. The observed value of $M^*(5007) = -4.5$ is marked by the horizontal dashed line. We find an astonishing similarity between the median cutoffs of disk and elliptical galaxies with differences of only $\Delta M^*(5007) \sim 0.1$–$0.25$ across the entire considered mass range. Disk galaxies have a slightly brighter median cutoff value than elliptical galaxies for $\log M_*/\mathrm{M}_\odot \sim 9.8$–$11$, which is the same tendency that has always been theoretically expected, just without the large systematic difference. This therefore provides the first theoretical demonstration of the

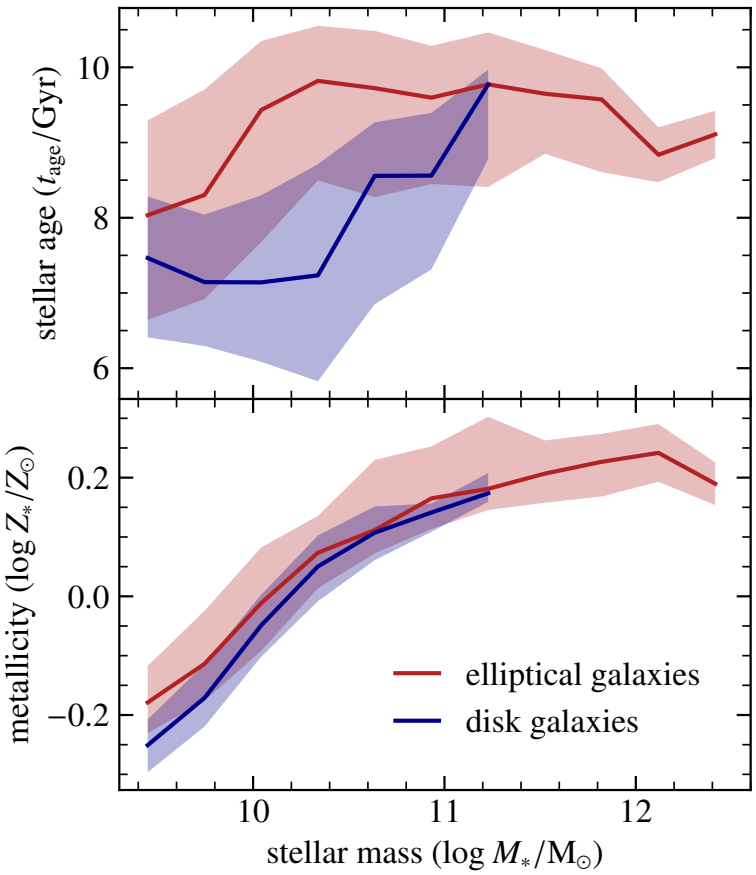


Figure 11.3: Mass-weighted mean stellar age t_{age} (top) and metallicity Z_* (bottom) as functions of stellar mass for the simulated galaxies of the Magneticum Pathfinder Box4 (uhr) simulation, split by morphological type into disk (blue) and elliptical (red) galaxies. The solid lines show the respective median age or metallicity value, with the shaded regions indicating the 1σ scatter.

observed universality of the PNLF between galaxies of different morphologies for a large statistical sample.

Additionally, there is a surprising constancy of the median cutoffs across the entire mass range, where disk galaxies show no significant dependence of $M^*(5007)$ on their stellar mass for the considered mass range. Elliptical galaxies also feature a very constant behavior of the cutoff value, but become brighter as the mass increases above $\log M_*/M_\odot \gtrsim 10.2$. In contrast, the cutoff of lower-mass elliptical galaxies becomes brighter with decreasing mass. These results finally support the observed universality of the PNLF bright-end cutoff across disk and elliptical galaxies for a large range of galaxy masses.

Since Magneticum Box4 (uhr) was only run until $z = 0.06$, we also fit the PNLFs to stellar populations with artificially increased ages to correct for the difference to $z = 0$ and present the results in Appendix E.2. There the dip toward fainter cutoff magnitudes increases for ETGs around $M_* \approx 10^{10}\,M_\odot$ due to their generally older ages increasing even further into the regime where PICS struggles to form PNe at the bright end (Valenzuela et al. 2025c). We also ran PICS on the galaxies in the simulation TNG50 (Nelson et al. 2019), which has a smaller volume than Magneticum Box4, and found the same universal PNLF cutoff (see Appendix E.3), except that the median cutoff of elliptical galaxies is only dimmer by up to

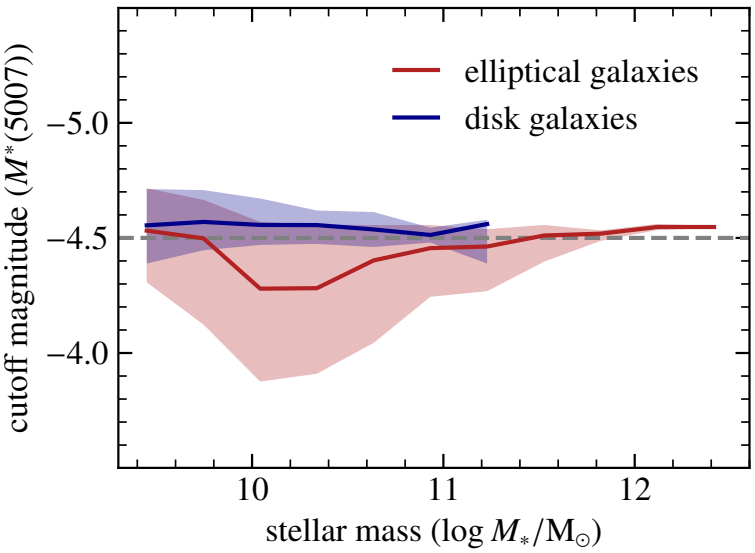


Figure 11.4: Bright-end cutoff magnitude $M^*(5007)$ as a function of stellar mass for the simulated galaxies of the Magneticum Pathfinder Box4 (uhr) simulation, split by morphological type into disk (blue) and elliptical (red) galaxies. The solid lines show the respective median $M^*(5007)$ value, with the shaded regions indicating the 1σ scatter. The observed bright-end cutoff value of $M^*(5007) = -4.5$ is marked by the horizontal dashed line. Galaxies of both morphologies feature PNLF cutoffs around the observed value over a large range of stellar masses.

~0.1 mag than that of disk galaxies, and there is no dip in the ETG cutoff relation. Both simulations therefore support the theoretical motivation of a universal bright end of the PNLF.

While here the cutoff median is found to be universal, the scatter differs for morphologies and stellar masses. Elliptical galaxies at all masses have a larger scatter than disk galaxies, and lower-mass galaxies have a larger scatter for a given morphology. These differences arise from the larger variety of star formation and enrichment histories of both lower-mass and elliptical galaxies. Observationally, the dimmer cutoff values have been found for more metal-poor galaxies like the Small Magellanic Cloud or NGC 5253 (Ciardullo 2010). The scatter to lower PNLF cutoffs for elliptical galaxies found in the simulation at around $M_* = 10^{10}\,\mathrm{M}_\odot$ is further also consistent with the lower values observed in the local Universe for metal-poor galaxies (Ciardullo 2010) or for the dim PNLF cutoff galaxies based on tip of the red-giant branch (TRGB) distance measurements (Scheuermann et al. 2022). It is also consistent with PNLF measurements of the low-metallicity outskirt regions of the Andromeda Galaxy (Bhattacharya et al. 2021), though these observed systems are of even lower mass than we can study in the simulation.

11.4 Discussion and conclusion

Clearly, the combination of a cosmological simulation with the full treatment of metallicity-dependent stellar evolution and of the nebula itself is necessary to solve the mystery of the universal bright end of the PNLF. In a previous study investigating the bright-end cutoff through the newly computed post-AGB stellar tracks from 2016 (Miller Bertolami 2016), the

authors investigated PNe at solar metallicity and considered artificial star formation histories with simple assumptions on the nebular opaqueness (Gesicki et al. 2018). The authors found a large range of ages for which PNe are able to reach the bright end of the PNLF (Gesicki et al. 2018), though they only showed the post-AGB $M(5007)$ evolution without application of circumnebular extinction. Our results here demonstrate that with consideration of super-solar metallicities, the bright end is reached by PNe with an even broader range of ages. In particular, these high metallicities aid the production of bright PNe in old elliptical galaxies despite their overall older ages, for which dimmer PNe would be expected. On the other hand, single stellar populations and simplified composite stellar populations fall short of being adequate representations of real galaxies, thus being insufficient to fully test PNLF properties.

Nevertheless, the difference in scatter of the bright-end cutoff for disk and elliptical galaxies shows that the star formation histories do in fact affect the PNLF bright end, just not in the systematic way that had originally been expected from theory. Additionally, the downward scatter of the bright-end cutoff increases towards lower stellar masses up to $M_* \sim 10^{10}\,\mathrm{M}_\odot$, especially for elliptical galaxies, in line with the observed mass-metallicity relation (Gallazzi et al. 2005; Kudritzki et al. 2024) and the observed dimmer cutoffs at lower metallicities (Ciardullo 2010). This also shows how the diversity found in lower-mass galaxies directly impacts the range of possible PN populations found therein, providing a direct prediction for comparison with local Universe observations of PNe. The lowest-mass galaxies are made up of far fewer particles in the simulation and contain supermassive black holes near the resolution limit, which can affect the star formation histories and ongoing star formation rates. This low-mass regime and the scatter of $M^*(5007)$ for these galaxies should therefore be taken with some caution. In contrast, for TNG50, the resolution is higher and there is no significant increase of $M^*(5007)$ or an obvious decrease in scatter, which can be linked to the different stellar population properties of the galaxies caused by differences in the galaxy formation model.

To conclude, this study shows how the overall behavior of PNe in their cosmological context leads to a universal bright-end cutoff across a large range of morphologies and stellar masses and simultaneously predicts differences in the cutoff scatter depending on the galaxy properties. In the future, these can be further tested through an increased number of targets for PN studies, both in the low-mass regime as well as at higher masses.

12

The PNLF in Cosmological Simulations

This chapter presents the current status of work to be submitted
as Valenzuela et al. (in prep.):
The PICS Project. III. The planetary nebula luminosity function in cosmological simulations

The PNLF has been observed for many galaxies over the years, ranging from elliptical galaxies (e.g., Jacoby et al. 1990a; Arnaboldi et al. 1994; Méndez et al. 2001; Teodorescu et al. 2011; Hartke et al. 2017) over lenticular (e.g., Ciardullo et al. 1991, 2002) to disk galaxies (e.g., Ciardullo et al. 1989; Jacoby et al. 1989; Feldmeier et al. 1997; Bhattacharya et al. 2019; Scheuermann et al. 2022). Across these measurements, the universality of its bright-end cutoff magnitude $M^*(5007)$ has remained at odds with theoretical models (e.g., Méndez & Soffner 1997; Marigo et al. 2004; Ciardullo 2010). Understanding the origins of the bright-end cutoff and general shape of the PNLF has been the target of multiple theoretical studies (e.g., Méndez et al. 1993; Gesicki et al. 2018; Valenzuela et al. 2019; Souropanis et al. 2023; Yao & Quataert 2023), though the limitation has been that they do not self-consistently model an entire PN population that can be directly compared to the observations.

In the past, PNe have mostly been measured in the outskirts of galaxies outside our Local Group because of the lower surface brightness compared to the inner galaxy regions (e.g., Hui et al. 1993; Arnaboldi et al. 1994, 1996; Méndez et al. 2001; Peng et al. 2004b; Douglas et al. 2007). As a result, many observed PNLFs do not actually represent the total PN populations

of the respective galaxies, but rather of their outskirts. On the other hand, PNe have long been observed in the bulge of M 31 (e.g., Ciardullo et al. 1989), across the Magellanic Clouds (e.g., Ford & Jacoby 1978; Jacoby 1980; Meatheringham et al. 1988; Jacoby et al. 1990b; Reid & Parker 2010), or in M 32 (e.g., Sarzi et al. 2011), and as of recently, MUSE observations have enabled the detection of PNe in the centers of other elliptical galaxies in recent years (e.g., Spriggs et al. 2020; Roth et al. 2021; Scheuermann et al. 2022; Jacoby et al. 2024; Congiu et al. 2025; Ennis et al. 2026). Galaxies can have intrinsic radial stellar population gradients, where age (e.g., Zibetti et al. 2020; Parikh et al. 2021; Liao & Cooper 2023) or metallicity (e.g., Kobayashi & Arimoto 1999; Tortora et al. 2010; Parikh et al. 2021) vary radially. For this reason, the inner and outer PNLFs can be expected to show differences, where several studies have investigated the properties of the PNLF at different radii (e.g., Hartke et al. 2020; Congiu et al. 2025; Soemitro et al. 2025).

On the theoretical side, PNe have mostly been studied based on mock stellar populations around solar metallicity (e.g., Méndez et al. 1993; Méndez & Soffner 1997; Schönberner et al. 2007; Valenzuela et al. 2019). To reliably model PNe for more complex star formation histories, the newly developed PICS (PNe In Cosmological Simulations) framework (Valenzuela et al. 2025c,d) has adopted the approach of modeling PNe self-consistently for single stellar populations (SSPs) with a given stellar age and metallicity, finding that taking into account the metallicity is crucial for old stellar populations. Cosmological simulations offer an ideal environment to obtain diverse star formation histories in galaxies that are self-consistent with their cosmological evolution and assembly histories. Because these types of simulations generally contain stellar particles that represent SSPs, PICS can be directly applied to these and predict a PN population for each stellar particle. While first case studies have been successfully completed with PICS on simulated galaxies (e.g., Valenzuela et al. 2025d; Soemitro et al. 2025; Hartke et al. in prep., see Chapter 14), it is important to perform a comprehensive study on a larger galaxy sample to understand the underlying PN populations in a more statistical manner, which corresponds to the main objective of the PICS project (hence the acronym PICS).

In this work we present the first systematic study of PN populations and their PNLFs modeled in simulated galaxies from different cosmological simulations. By splitting the galaxies into commonly used classes based on several global galaxy properties, we make predictions for the PNLFs measured in such systems and analyze the PNLF behavior between galaxy classes. We additionally compare the PNLFs found in the inner and outer regions of galaxies to identify trends that may be relevant when measuring PNe in a certain subregion of a galaxy. This work is structured as follows. In Section 12.1, we introduce the models and simulations as well as the PNLF fitting methods and the galaxy classifications employed. We then present and discuss the PNLFs of the different galaxy classes with respect to their shapes and bright-end cutoff magnitudes in Section 12.2. We finally summarize our findings and conclude in Section 12.3.

12.1 Methods

In the following, we describe the PN model and the method used to fit the analytical PNLF to the PN populations in each galaxy. We then introduce the cosmological simulations used for this study as well as the galaxy sample selection and the different galaxy classification schemes used throughout this work.

12.1.1 PICS model for planetary nebulae

We model PNe with the framework PICS (PNe In Cosmological Simulations; Valenzuela et al. 2025c,d), which models PN populations for SSPs given their properties. Specifically, the relevant SSP input quantities for PICS are the IMF, total mass, age, and metallicity as a metal mass fraction $Z = M_{\rm met}/M_{\rm tot}$. While PICS is a modular framework for the different stellar evolution phases and the nebular properties needed for the PN [O III] magnitude, in this work we use the fiducial model as presented by Valenzuela et al. (2025c). The stellar lifetime function, initial-to-final mass relation, and post-AGB stellar evolution tracks are all taken from the metallicity-dependent models of Miller Bertolami (2016). The empirical nebular model presented by Valenzuela et al. (2019) predicts the PN [O III] magnitude based on the central star properties and takes into account a random optical thickness for the possibility of optically thin nebulae (e.g., Méndez et al. 1992).The [O III] emission is then modified by a metallicity correction based on the results of Dopita et al. (1992). Finally, an empirical model for circumnebular extinction is applied, which builds on the observations of Jacoby & Ciardullo (2025) (also see Valenzuela et al. 2025b for a study on how variations in the circumnebular extinction influence the PN [O III] magnitudes). For the details of the individual models, please refer to Valenzuela et al. (2025c). The PICS model has successfully been compared with Milky Way PNe in the solar neighborhood (Valenzuela et al. 2025d), and it has been used to interpret and explain observations of elliptical galaxies (Soemitro et al. 2025).

The hydrodynamical cosmological simulations used in this work contain stellar particles that represent SSPs (see Section 12.1.3). Therefore, we apply PICS to each stellar particle to obtain a PN population for the respective SSP, assuming a Chabrier (2003) IMF. The PNe obtained for the stellar particles of a given simulated galaxy together form the galaxy's PN population.

12.1.2 Planetary nebula luminosity function fitting

From each PN population of a galaxy, we create the PNLF from the individual [O III] magnitudes, $M(5007)$. We fit an analytic PNLF function in two different manners to each measured PNLF, both of which come with their own advantages and drawbacks. The classical analytical PNLF by (Ciardullo et al. 1989) as a function of the absolute [O III] magnitude $M(5007)$ is

$$N(M(5007)) = c_1 e^{c_2 M(5007)} \left(1 - e^{3(M^*(5007) - M(5007)}\right), \tag{12.1}$$

where c_1 is the normalization constant, $c_2 = 0.307$ is the slope at dim magnitudes, and $M^*(5007)$ is the absolute bright-end cutoff magnitude with an observed value of around -4.5 (e.g., Ciardullo 2010; Jacoby et al. 2024). Leaving c_2 as a free parameter results in the generalized PNLF (e.g., Longobardi et al. 2013).

Cumulative PNLF fitting

For the first approach, following Bhattacharya et al. (2019), we fit the generalized PNLF (Equation 12.1) by a least-squares method applied to the cumulative PNLF (Rodríguez-González et al. 2015), given as

$$N(\leq M) = c_1 e^{c_2 M}\left(\frac{e^{c_2 M}}{c_2} + \frac{1}{3-c_2} e^{3M^* - (3-c_2)M} - \left(\frac{1}{c_2} + \frac{1}{3-c_2}\right) e^{c_2 M}\right), \tag{12.2}$$

where we shortened $M(5007)$ and $M^*(5007)$ to the abbreviated forms M and M^*. The fit to the cumulative distribution is preferred as it avoids the arbitrary choice of bins, which can bias the resulting PNLF fit. We perform the fit to the bright PNe with $M(5007) \leq \max(-3.5, M_{\mathrm{min}}(5007) + 1)$, that is, to the PNe brighter than -3.5 mag, or to the PNe within 1 mag of the brightest PN in the galaxy, whichever threshold includes the larger magnitude range. This approach ensures that the bright end of the PNLF is sufficiently accounted for, even for PN populations without any particularly bright PNe. Simultaneously, it limits the fit to the brightest PNe such that deviating PNLF shapes in the dimmer regime from the analytical functions do not impact the fit significantly as the primary purpose of the fits is to obtain the bright-end cutoff $M^*(5007)$. The downside of this method is that the fit does not always converge, and in some cases the PNLF cutoff is selected to be much too bright when there is a small sample of PNe. For these reasons, we needed a fallback method to use when the cumulative fitting fell short.

Maximum likelihood PNLF estimation

The second PNLF fitting approach we employ is by maximum likelihood estimation (MLE). This kind of method has oftentimes been used to fit the PNLF in the literature (e.g., Ciardullo et al. 1989; Scheuermann et al. 2022) and is robust even for small sample sizes of PNe. We apply the method as described by Scheuermann et al. (2022), where the PNLF normalization is given by the number of PNe up to the fitting magnitude threshold of $M(5007) \leq \max(-3.5, M_{\mathrm{min}}(5007) + 1)$. The logarithmic likelihood for a PNLF is determined by the sum of logarithmic probabilities of each PN existing at its magnitude, $\log \mathcal{L} = \sum_i \log p(M_i(5007))$. Here the individual probabilities are computed as the integral over the PNLF multiplied with a Gaussian, where we assume a small fixed magnitude uncertainty of $\sigma_m = 0.01$ mag for all PNe. To our knowledge, this integral has previously only been computed numerically, which is computationally expensive, especially when used in the context of a Markov Chain Monte Carlo (MCMC) method. We show in Appendix F.1 the analytical solution to the integral, which is computationally significantly faster.

We apply the MLE method to all galaxies fitting the classical PNLF with the sole free parameter of $M^*(5007)$ through MCMC with 50 000 iterations, from which we determine the bright-end cutoff through the median value, ignoring a burn-in phase of the first 2000 iterations. While this method is ideal for small numbers of PNe and for PNLFs that have a clear exponential cutoff at the bright end, it does not deal well with overluminous PNe. The MLE method leads to best-fit bright-end cutoffs that are dominated by the brightest PN, regardless of the remaining PNLF shape. For this reason, we only use the determined MLE bright-end cutoff in the cases where the cumulative PNLF fitting method fails to converge or where it leads to a bright-end cutoff beyond 0.3 mag brighter than the brightest PN.

12.1.3 Cosmological simulations

To test the effects of the PNLF on realistic galaxies with self-consistent star formation histories in a cosmological context, we apply PICS to the simulated galaxies from several cosmological simulation suites. These were run with different galaxy formation models, such that the resulting stellar populations and galaxy properties can differ, which would also affect the PN populations. In the following, we give a brief overview of the simulations used in this work.

Magneticum Pathfinder

The Magneticum Pathfinder simulation suite (Dolag et al. 2025) consists of a set of cosmological simulations covering a large range of resolutions and sizes. They were run with GADGET-3, a modified version of GADGET-2 (Springel 2005) with improved physics treatments (see Dolag et al. 2025 for details). The simulations were run with ΛCDM parameters corresponding to the seven-year results of WMAP (Komatsu et al. 2011): $h = 0.704$, $\Omega_\Lambda = 0.728$, $\Omega_m = 0.272$, $\Omega_b = 0.0456$, $\sigma_8 = 0.809$, and $n_s = 0.963$. Due to its high resolution, we here use the hydrodynamical simulation Magneticum Box4 (uhr) for the study of PN populations in the simulated galaxies, which has a volume of $(68\,\mathrm{Mpc})^3$, a mean stellar particle mass of $\langle m_* \rangle \approx 1.8 \times 10^6\,\mathrm{M}_\odot$, and a stellar softening length of $\epsilon_* \approx 1\,\mathrm{kpc}$. This particular simulation was run to $z \approx 0.066$, corresponding to a lookback time of $t_\mathrm{lb} \approx 0.88\,\mathrm{Gyr}$. The galaxies were identified with a baryonic-compatible version of SUBFIND (Springel et al. 2001; Dolag et al. 2009). Magneticum Box4 has been shown to agree well with galaxy properties across a wide range of properties, including angular momenta (e.g., Teklu et al. 2015), kinematics (e.g., Schulze et al. 2018; van de Sande et al. 2019; Schulze et al. 2020), dynamics (e.g., Remus et al. 2017; Harris et al. 2020; Remus & Forbes 2022), faint structures in the outskirts (e.g., Valenzuela & Remus 2024; Stoiber et al. 2025), star formation (e.g., Kudritzki et al. 2021; Fortuné et al. 2025), and stellar populations (e.g., Dolag et al. 2025).

IllustrisTNG

The IllustrisTNG simulation suite consists of a set of cosmological simulations targeting galaxies at several different resolutions and sizes. For this work, we use TNG50 (Nelson et al. 2019; Pillepich et al. 2019), which was run with AREPO (Springel 2010) with an updated galaxy

formation model. The simulation uses a ΛCDM cosmology consistent with Planck 2015 results (Planck Collaboration 2016): $h = 0.6774$, $\Omega_\Lambda = 0.6911$, $\Omega_m = 0.3089$, $\Omega_b = 0.0486$, $\sigma_8 = 0.8159$, and $n_s = 0.9667$. The simulation volume of TNG50 is $(52\,\mathrm{Mpc})^3$, the stellar particle mass is $m_* \approx 8.5 \times 10^4\,\mathrm{M}_\odot$, and the stellar softening length is $\epsilon_* \approx 0.3\,\mathrm{kpc}$. The galaxies were identified with SubFind (Springel et al. 2001; Dolag et al. 2009). These simulations have been used to compare galaxy population properties to observations, including stellar populations (e.g., Boecker et al. 2023), kinematics (e.g., Pillepich et al. 2019; Pulsoni et al. 2020), morphology (e.g., Rodriguez-Gomez et al. 2019), faint structures in the outskirts (e.g., Khalid et al. 2024), and star formation (e.g., Piotrowska et al. 2022; Popesso et al. 2023). In this work we use this simulation to demonstrate whether there is an expected systematic difference that could be related to different galaxy formation models.

12.1.4 Galaxy sample and classifications

For the simulated galaxies, we compute the stellar mass M_* within $0.1\,R_{\mathrm{vir}}$ around the stellar center of mass following the method of Valenzuela et al. (2024a). From each of the simulations, we include the galaxies (central galaxies as well as satellites) with stellar masses $M_* \geq 2 \times 10^9\,\mathrm{M}_\odot$ in our sample. Because we are primarily interested in the stellar population, we do not apply further selection criteria such as on the size. In the following, we introduce the five galaxy classification schemes we use in addition to the distinction between central and satellite galaxies to split the galaxy population. Table 12.1 shows an overview of the number of galaxies in each simulation and the different classes.

Morphology

For a morphological classification, we follow the definition of Teklu et al. (2017) for disk, elliptical, and intermediate simulated galaxies based on the b-value (Teklu et al. 2015). The b-value is defined by a galaxy's location in the stellar angular momentum-stellar mass plane, which is closely related to the morphology (Romanowsky & Fall 2012; Teklu et al. 2015). It has already been used in several simulation studies (e.g., Schulze et al. 2018; Emami et al. 2021). The class of intermediate galaxies mostly consists of lenticular galaxies. This classification scheme is particularly useful for simulations as the dynamic information contained in the angular momentum is less affected by resolution compared to the intrinsic shapes of galaxies.

Star formation

For the star formation, we distinguish between star-forming, star-bursting, and quiescent galaxies. We define the SFR thresholds following the observed star-forming main sequence (SFMS) by Popesso et al. (2023) because of the good agreement with the simulations (see also Fortuné et al. 2025). For this, we define all galaxies with a SFR more than 0.5 dex above the SFMS at the given stellar mass to be star-bursting, those more than 0.5 dex below the SFMS as quiescent, and the rest as star-forming. This follows common definitions such as that by Bluck et al. (2020), though we combine their green valley and quenched classes as quiescent.

Table 12.1: Galaxy counts for the different classes in the cosmological simulations.

		Magneticum Box4 (uhr)			TNG50		
	Class	Total	Centrals	Satellites	Total	Centrals	Satellites
General	total	6518	3991	2527	2204	1299	905
	centrals	3991	3991	0	1299	1299	0
	satellites	2527	0	2527	905	0	905
Morphology	disk	1186	827	359	1334	903	431
	intermediate	2374	1553	821	465	251	214
	elliptical	2958	1611	1347	405	145	260
Star formation	star-bursting	65	45	20	103	65	38
	star-forming	1634	1172	462	1375	1003	372
	quiescent	4819	2774	2045	726	231	495
Kinematics	fast rotator	874	546	328	2127	1268	859
	slow rotator	317	226	91	76	30	46
Age	young	1677	1178	499	1484	999	485
	middle-age	4185	2530	1655	616	278	338
	old	656	283	373	104	22	82
Metallicity	metal-poor	936	661	275	50	40	10
	solar	4582	2760	1822	1201	807	394
	metal-rich	1000	570	430	953	452	501

Notes. The total counts are the sum of the central and satellite galaxy counts for a given class. Note that for Magneticum Box4 (uhr), only the more massive galaxies have kinematic classifications.

Kinematic behavior

For the kinematic classification, we separate the galaxies into slow rotators and fast rotators. We follow the definition by Emsellem et al. (2011) first introduced for the ATLAS^{3D} survey according to a galaxy's location in the λ_R-ϵ plane, where λ_R parametrizes the extent to which a galaxy is rotationally or dispersion dominated from the line-of-sight kinematics (Emsellem et al. 2007), and ϵ is the 2D ellipticity. For the computation of these parameters, we follow Schulze et al. (2018) by first rotating the galaxies edge-on before determining these quantities to maximize the line-of-sight rotational properties and avoid random projection effects. Both parameters are computed for a radius of 1 R_e, and λ_R is determined from light-weighted kinematic maps to ensure compatibility with observations. These values are computed following Dolag et al. (2025), which are only determined for galaxies with stellar masses above 2×10^{10} $M_\odot$ for Magneticum Box4 (uhr) because of its more limited mass resolution compared to TNG50. We consider galaxies with $\lambda_R > 0.31\sqrt{\epsilon}$ to be fast rotators, the others are slow rotators (Emsellem et al. 2011).

Stellar age

For the stellar age classification, we distinguish between young, middle-age, and old galaxies. We measure the stellar age of a galaxy following Dolag et al. (2025) as the mean mass-weighted age $t_{\rm age}$ of all stellar particles within 3 $R_{1/2}$, where $R_{1/2}$ is the 3D half-mass radius. We define the old galaxies to have ages of >10 Gyr, which is a threshold that has been used in recent PN work (e.g., Soemitro et al. 2025) due to this being the age range in which current PN models like PICS are not able to populate the bright end of the PNLF (see fig. 10 of Valenzuela et al. 2025c). Since there is only a small number of galaxies with young ages of a few Gyr in the simulations, we defined the young galaxies to be those with ages of <7 Gyr, and the middle-age galaxies with ages of 7–10 Gyr.

Stellar metallicity

For the stellar metallicity classification, we classify galaxies as metal-poor, solar, and metal-rich galaxies. We measure the stellar metal mass fraction Z of a galaxy following Dolag et al. (2025) as the mean mass-weighted metal mass fraction of all stellar particles within 3 $R_{1/2}$. Assuming a solar metallicity of $Z_\odot = 0.015$ (Asplund et al. 2021), we compute the metallicity $[Z] = \log Z/Z_\odot$. We then define the metal-poor galaxies by $[Z] < -0.2$, solar metallicity galaxies by $-0.2 \leq [Z] \leq 0.1$, and metal-rich galaxies by $[Z] > 0.1$. These thresholds were chosen to keep the number of galaxies in each class from becoming too small in all considered cosmological simulations.

12.2 PNLFs of the galaxy classes

Based on the galaxy classifications, we investigated to what extent the PNLF and its bright-end cutoff magnitude $M^*(5007)$ vary depending on different galaxy properties. In this section, we

study the modeled PNLFs and their scatter for each class and then compare them between the inner and outer regions of the galaxies, where stellar population gradients oftentimes play an important role.

12.2.1 PNLF variations among simulations

We ran PICS on each simulated galaxy to obtain the PN populations and their magnitudes, from which we determined the PNLFs. To make the PNLFs comparable to each other, we normalized each PNLF to a total stellar mass of $10^{11}\,M_\odot$ based on the galaxy's actual stellar mass. In Figure 12.1 we show the median PNLFs for each class in the different classification schemes (one panel per classification scheme) with their 1σ scatters (shaded regions). Across all classes, the bright-end cutoff magnitudes of the median PNLFs appear to deviate at most by 0.2 mag from the observed cutoff magnitude of $M^*(5007) = -4.5$ mag, except for the old galaxies having a significantly fainter cutoff at around -3.9 mag. As a first result, this shows that the age of a galaxy is the most significant factor in determining where the bright end of the PNLF lies. This is further supported by the three age classes (young, middle-age, and old) having the smallest scatters of the PNLF compared to the classes of other classification schemes. Of course, this does not contradict our previous findings that metallicity plays an important role (Valenzuela et al. 2025c), however, the metallicity effect carries more weight when the stellar age is held constant. In general, most of the scatter in the PNLFs of the classification schemes besides age is a result of the galaxies having a variety of ages in each class.

Interestingly, all PNLFs converge to an almost identical point at $M(5007) \approx -1.7$ mag with a surprisingly small scatter before moving apart again at fainter magnitudes. This behavior has not been documented before for PICS, but may be related to the assumed maximum PN lifetime of 30 000 yr and the dimming of the [O III] emission. This magnitude still lies at brighter magnitudes compared to where the additional exponential term becomes relevant for the deep observed PNLFs for M 31 substructures, which is roughly 5 mag below the bright end (Bhattacharya et al. 2021). Also looking at the deep modeled SSP PNLFs of Valenzuela et al. (2025c, fig. F.1), it is not apparent where the PNLF convergence comes from. While investigating this further is beyond the scope of this work, one of the future plans for PICS is to examine the faint end of the PNLF in more detail and to improve on the currently employed nebular model of Valenzuela et al. (2019).

Just as the universality of the PNLF has been discovered to hold across different morphologies (e.g., McMillan et al. 1993; Feldmeier et al. 1997; Ciardullo et al. 2002), we here also find closely aligned PNLFs for disk, intermediate, and elliptical galaxies (top left panel). The expected age trend of disk galaxies tending to have younger stellar populations, followed by intermediate and elliptical galaxies that are increasingly old, is found through the slight shift of the PNLFs toward fainter magnitudes. Also, the larger scatter of elliptical galaxies indicates how they have a larger diversity in ages right around the limit of PICS to produce PNe at the bright end, as seen by the Box4 analog galaxies used by Soemitro et al. (2025).

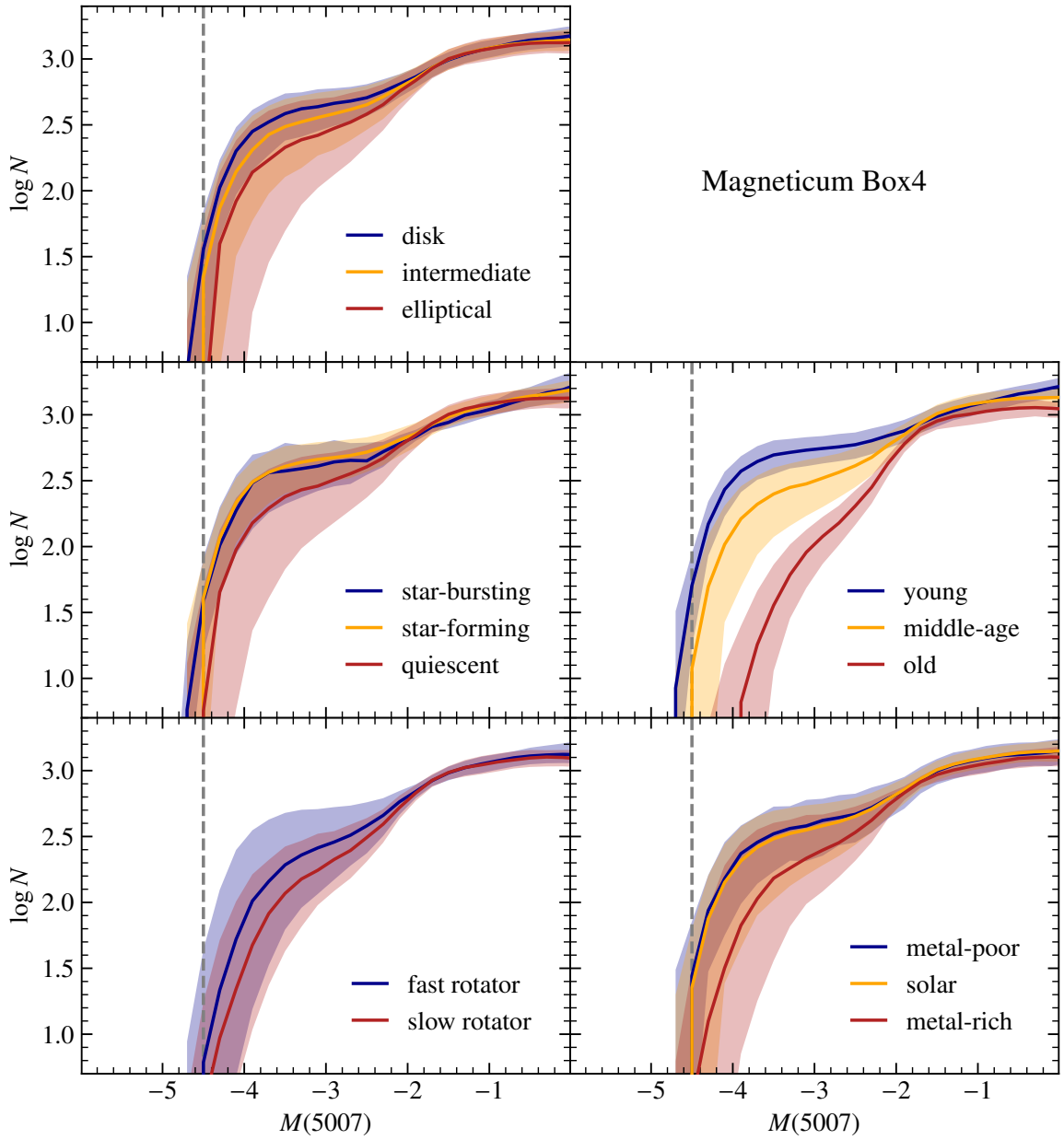


Figure 12.1: Median PNLFs of galaxy classes in Magneticum Box4 (uhr) from the different classification schemes, that is, morphology, star formation, kinematic behavior, age, and metallicity, from top to bottom and left to right, respectively. For each galaxy class, the normalized PNLFs to a total stellar mass of $10^{11}\,M_\odot$ are considered, where for each magnitude bin in steps of 0.2 mag the median (solid lines) and the 1σ scatter (shaded regions) are computed. The observed bright-end cutoff magnitude $M^*(5007) = -4.5$ mag is marked by the vertical dashed gray lines.

These differences lead to more significant changes in the slope of the PNLF, where elliptical galaxies have steeper PNLF slopes around $M(5007) = -3.5$ mag compared to intermediate and disk galaxies (the latter having the most shallow slopes). The slopes are a result of the much stronger variations in slope found for the age classifications, where older stellar populations have overall fewer bright PNe. These results support observational findings of differing PNLF slopes depending on the fraction of low-mass stellar cores or stellar age, where there is evidence that older stellar populations have steeper PNLFs (e.g., Longobardi et al. 2013, 2015).

Ciardullo et al. (2004) had also previously proposed that star-forming galaxies have more shallow PNLFs, where the PNLFs of M 33 and the SMC flatten at $M(5007) \gtrsim -3.5$ mag, in excellent agreement with our results for star-bursting and star-forming galaxies (middle left panel). For these two classes, we find no significant differences between their PNLFs, which is likely due to their definition according to the current SFR: this corresponds to stellar populations with ages well below the regime where PNe are expected to be seen, due to their rapid evolution in the post-AGB phase (Miller Bertolami 2016) and their high circumnebular extinction (e.g., Jacoby & Ciardullo 2025). Also note that the number of star-bursting galaxies is rather low (see Table 12.1). Quiescent galaxies, on the other hand, have PNLFs similar to those of elliptical galaxies, both with respect to the median as well as to the scatter. This is unsurprising since many elliptical galaxies are found to be quiescent (e.g., Renzini 2006). The difference between the PNLFs of quiescent and star-forming/star-bursting galaxies is similar to that between disk and elliptical galaxies.

For the kinematic classification between fast and slow rotators (bottom left panel), we find that the fast rotator PNLFs are closer to those of elliptical and quiescent galaxies, except that they also have a larger scatter toward brighter magnitudes. This is due to the limited galaxy sample of Magneticum Box4 for which we determined the kinematic properties ($M_* \geq 2 \times 10^{10}\,\mathrm{M}_\odot$), which leads to a lower fraction of disk galaxies with younger stellar populations. Additionally, many elliptical galaxies are in fact fast rotators (e.g., Emsellem et al. 2011). Since slow rotators are essentially only comprised of elliptical galaxies, this most likely leads to the further shift of the PNLF toward fainter magnitudes and a steeper slope. The large scatters seen for both classes, however, suggest that this kinematic classification is not as closely related to the stellar populations relevant for PNe as the other classes. However, the general independence of these quantities means that combining kinematic information with deep observations of PNe should deliver further insights into the past of a galaxy, such as has been exploited from some observations (e.g., Sambhus et al. 2006; Bhattacharya et al. 2021; Hartke et al. 2022, in prep., see Chapter 14).

Focusing on the PNLFs split by galaxy age classes (middle right panel), as stated earlier we find the clearest differences between PNLFs, all classes also having small scatters. The largest scatter is found for middle-age galaxies despite its comparatively small age range of 7–10 Gyr. This shows the importance of the ages approaching 10 Gyr for the PNLF in PICS, as also discussed by Valenzuela et al. (2025c). This general trend with age is weaker than predicted by previous models (e.g., Marigo et al. 2004), but arises from the same issue of old stellar populations containing PN central stars that are not massive and luminous enough to produce a sufficiently bright [O III] emission in their nebula (e.g., Ciardullo 2012; Valenzuela et al. 2019). These PNLFs also reveal the actual origin of differing slopes in the modeled PNLFs, where old stellar populations lack the brighter PNe, but still reach the same convergence point at $M(5007) \approx -1.7$ mag just like the younger galaxies, thus resulting in a steeper slope (also see Longobardi et al. 2013, 2015; Ciardullo et al. 2004).

There are observational indications that the dimming of the PNLF bright-end cutoff for old galaxy ages is not as strong as found by PICS. For example, Soemitro et al. (2025) determined

through full spectral fitting that most of their studied elliptical galaxies have mean ages of around 12–13 Gyr. All of these galaxies have bright-end cutoffs of $M^*(5007) \approx -4.5$ mag, which in fact become even brighter when assuming alternative distance measures to the galaxies. Based on our findings here, reaching the universal bright-end cutoff for such old galaxies should be the exception, not the norm. However, the total stellar mass, the precise star formation histories, and possible measurement systematics must also be taken into account to draw more final conclusions. For the PICS models, this means that further PN pathways such as blue stragglers should be explored in the future, which also have the potential to resolve this tension (e.g., Ciardullo et al. 2005).

The PNLFs of the metallicity class (bottom right panel) show the interesting trend of more metal-poor galaxies having brighter PNLF cutoffs, which at first seems counter-intuitive. However, this has to be considered in the context of the stellar ages, which are not held fixed here: as elliptical galaxies tend to be old and metal-rich, whereas disk galaxies are generally younger and more metal-poor, the resulting PNLFs of the metal-rich galaxies are mostly driven by their older ages. The fact that not all metal-rich galaxies purely consist of old stars can be seen by the large scatter of their PNLFs. Metal-poor and solar metallicity galaxies do not have any significant differences between them. Finally, we tested the effect of restricting the galaxy sample to only the central galaxies, finding that it leads to overall slightly brighter PNLF cutoffs for those that currently reside at fainter magnitudes than −4.5 mag.

As Magneticum Pathfinder implements a different galaxy formation model than IllustrisTNG, we can expect the galaxy properties and their stellar populations to differ between the two simulation suites. We thus also applied PICS to the IllustrisTNG simulations to investigate to what extent the predictions for the PNLFs vary depending on the galaxy formation model employed. In Figure 12.2 we show the median PNLFs (normalized to $M_* = 10^{11}\,\mathrm{M}_\odot$) with their scatters for each class of the different classification schemes in the same way as for Magneticum Box4 (uhr) in Figure 12.1. Note that here the kinematic classification is applied to the entire galaxy sample, unlike for Box4 (see Section 12.1.4). The first important finding is that in general, the PNLFs take on the same shapes as in Box4. We also recover the convergence point of the PNLFs at $M(5007) \approx -1.7$ mag, indicating that this is indeed more closely related to the PICS model itself and not to the particular star formation histories. We also again find the clearest distinction between PNLFs for the age classes, which again have small scatter. A significant difference to the Box4 PNLFs, however, is the tendency of all PNLFs except for those of the old galaxies to look rather similar to those of the young and middle-age galaxies. In particular, they also have elevated numbers of bright PNe at $M(5007) \gtrsim -3$ mag compared to the Box4 galaxies, leading to even more shallow slopes. This is related to the systematically younger galaxies in TNG50 compared to Box4 despite Box4 only having reached $z = 0.066$, such that most TNG50 galaxies fall in the young and intermediate-age classes (see Table 12.1). Another systematic difference is the significantly higher metallicity in TNG50, leading to an enhanced brightness of the PNe, which is especially relevant for the older stellar populations. For the stellar population differences, we refer the reader to Dolag et al. (2025, figs. 27 and 28) and Boecker et al. (2023, fig. 13) for Magneticum

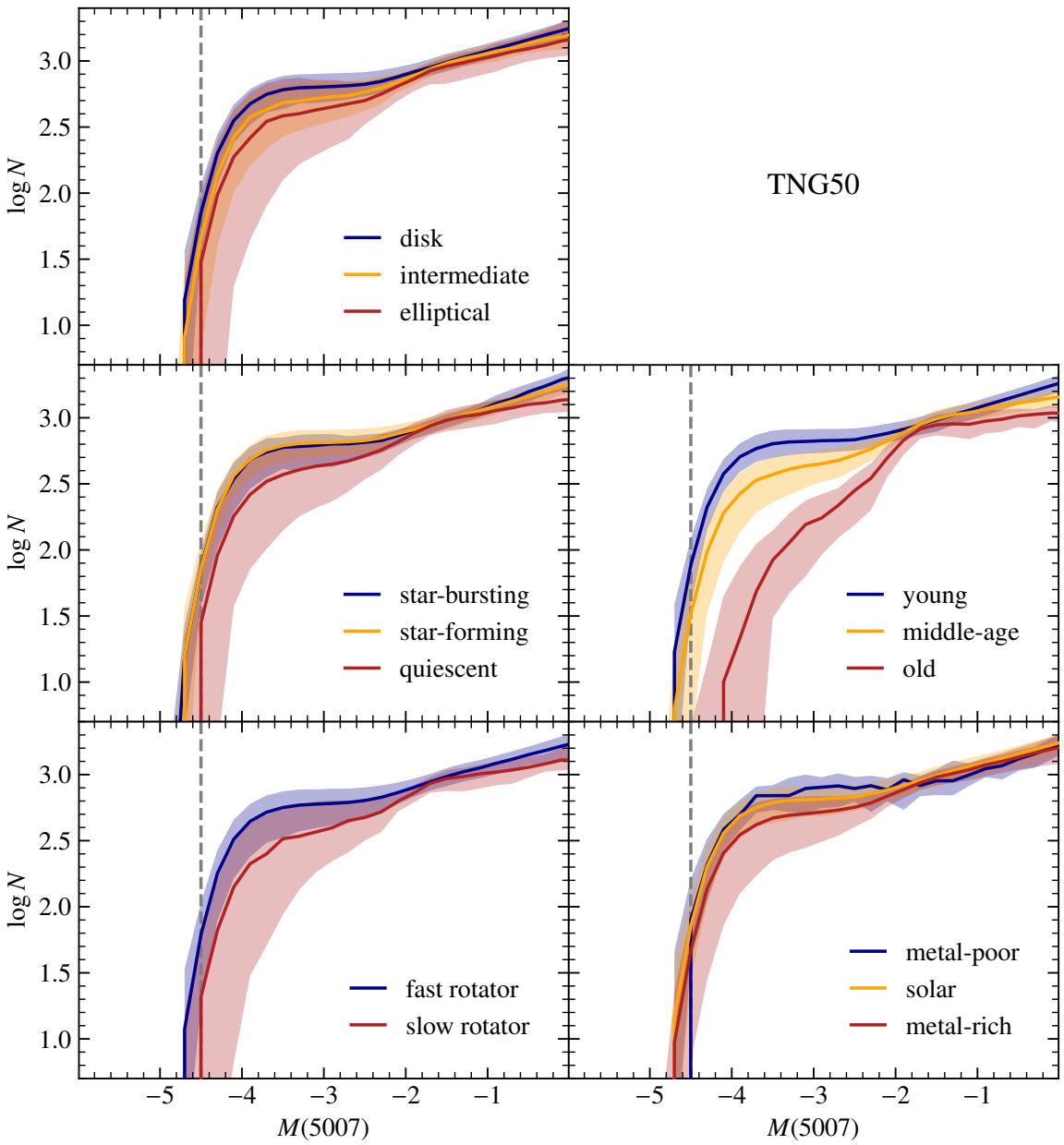


Figure 12.2: Median PNLFs of galaxy classes from the different classification schemes as in Figure 12.1, but for the galaxies in TNG50.

and IllustrisTNG, respectively. We also investigate their differences with respect to the modeled PNe in a companion paper (Valenzuela et al. in prep., see Chapter 11).

As a result, the disk, intermediate, and elliptical galaxies have PNLFs that resemble each other more than the Box4 morphological classes. The biggest difference between the three classes besides slight changes in brightness is the increased scatter for the elliptical galaxies. The increased scatter for the classes that contain the older elliptical galaxies, that is, the quiescent, slow-rotator, and metal-rich galaxies, is seen for the other classification schemes as well. Similar to Box4, the star-bursting and star-forming, and the metal-poor and solar metallicity galaxies have nearly indistinguishable PNLFs. Compared to Box4, here the PNLFs of the fast rotator galaxies are more similar to those of the disk galaxies because of the kinematic classes having been determined for all TNG50 galaxies instead of only the more

massive galaxies. Since galaxy age is the most relevant factor for the shape of the PNLF, the PNLFs for the age classes are quite similar to those of Box4. Besides the systematic differences to Box4, the general relative trends between classes with respect to the PNLF brightness and shape as well as its scatter for the galaxies within a class remain the same.

12.2.2 PNLF variations in the inner and outer regions

Since PNe have mostly been measured in the outskirts of galaxies due to the lower surface brightness (e.g., Hui et al. 1993; Arnaboldi et al. 1996; Douglas et al. 2007), with some exceptions in the Local Group (e.g., Ciardullo et al. 1989; Reid & Parker 2010; Sarzi et al. 2011), our findings shown above for the total PN populations are not directly comparable to those PNLF measurements. As newer instrumentation has allowed for PNe to be detected even in the centers of other elliptical galaxies (e.g., Spriggs et al. 2020; Roth et al. 2021), PNLFs are now also being measured for these inner regions beyond the Local Group. For these reasons, it is useful to present the predictions for inner and outer PN populations, not only for comparisons with observations, but also to investigate intrinsic trends within the galaxies. These could arise from age or metallicity gradients in the galaxies that affect the stellar populations in the inner and outer regions (e.g., Kobayashi & Arimoto 1999; Parikh et al. 2021; Liao & Cooper 2023).

Following the general concept of Stoiber et al. (2025), we split the PNe of each simulated galaxy in two subpopulations, those within 1 $R_{1/2}$ and those outside (considering the actual 3D radial distances). Given the definition of $R_{1/2}$, this means that the inner and outer PNLFs arise from the same underlying stellar mass, specifically, from half of the total galaxy's stellar mass. Figure 12.3 shows the median normalized PNLFs of the inner and outer regions of the Magneticum Box4 (uhr) galaxies for the same set of classes as in Figure 12.1, normalized to half of the previously used stellar mass, $M_* = 5 \times 10^{10}\,\mathrm{M}_\odot$. In general, we find that the inner and outer PNLFs do not differ significantly, both following the median behavior of the total PNLFs seen in Figure 12.1. Yet there are several interesting indications of radial trends, which we highlight in the following.

For the morphological classes, the disk and elliptical galaxies experience opposite radial trends. The outer PNLFs of disk galaxies appear to have a slightly larger number of brighter PNe than the inner regions, whereas the outer PNLFs of elliptical galaxies have fewer bright PNe than the inner regions, also having a larger logarithmic difference between the median PNLFs. The PNLF slope differs especially for the elliptical galaxies, where the outer regions have steeper slopes. This points to generally older stellar populations in the outskirts of the simulated elliptical galaxies, leading to the smaller number of bright PNe. The slope of the outer PNLF of elliptical galaxies is in excellent agreement with the observations of the halo PNe of NGC 4697 (black points; Méndez et al. 2001), though the observed bright end is still more consistent with the typical value of $M^*(5007) = -4.5$ mag compared to the fainter elliptical galaxy bright end. A more complete comparison would have to take into account further information of star formation histories and stellar mass, which is beyond the scope of

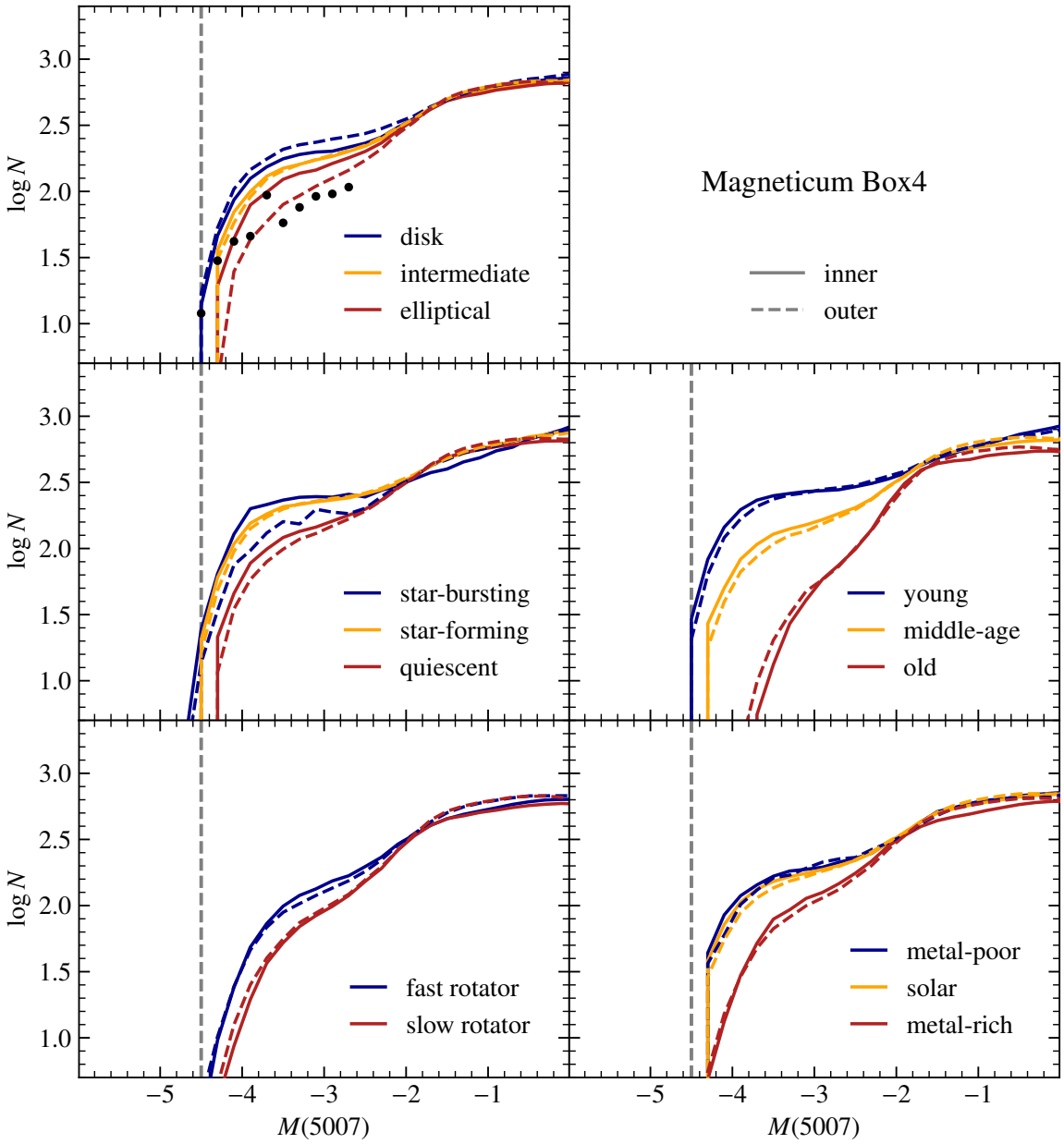


Figure 12.3: Median PNLFs of galaxy classes in Magneticum Box4 (uhr) from the different classification schemes as in Figure 12.1, but split for the inner ($r < R_{1/2}$; solid lines) and outer ($r \geq R_{1/2}$; dashed lines) PN populations. The normalization is chosen as half of that used for Figure 12.1 because of the split in two subpopulations, $M_* = 5 \times 10^{10}\,\mathrm{M}_\odot$. In the morphology panel (top left), we over-plot the suitably re-scaled statistically complete part of the PNLF of NGC 4697 (black dots; Méndez et al. 2001) to compare directly to the median outer elliptical regions. The observed bright-end cutoff magnitude $M^*(5007) = -4.5$ mag is marked by the vertical dashed gray lines.

this work. Lastly, the lower number of bright PNe in the outer regions stands in contrast to multiple observations of the luminosity-specific PN number α increasing toward the outskirts of galaxies (e.g., Longobardi et al. 2013; Hartke et al. 2017, 2020). In future work we will investigate to what extent this discrepancy is due to the PN model, observational biases, or specifics of the stellar population gradients. On the other hand, the simulated disk galaxies do exhibit the observed trend, which has also been found for disk galaxies (e.g., Bhattacharya

et al. 2019). This may be related to younger stellar populations tending to reside in the outer disk (e.g., Wang et al. 2011).

The star-bursting galaxies present another interesting case: like the elliptical galaxies, their outskirts have a smaller number of bright PNe ($\lesssim -2.5$ mag) than the inner regions. While the starburst itself cannot directly contribute to the PNLF because those young stellar populations would not yet produce sufficiently bright PNe if any at all, there appears to be a general behavior of star-bursting galaxies to contain more PNe in the outer regions. However, this behavior may be a result of low number statistics for these galaxies (see Table 12.1). There is also a very slight indication of slow rotators and old galaxies featuring the opposite trend, that is, having slightly more bright PNe than in the outer compared to the inner regions. As especially old galaxies are more likely to accrete younger structures in their outskirts, younger stars would be deposited in their halos, increasing the probability of obtaining brighter PNe in those regions. The inner and outer PNLFs of all other classes have generally similar behaviors to each other, where the outer regions have slightly fewer bright PNe, most likely due to a slightly positive age gradient. However, the differences are well within the scatter of PNLFs (see Figure 12.1) and should not be over-interpreted. Since Box4 (uhr) was only run to $z = 0.066$, we show the PNLFs based on stellar populations with accordingly increased ages in Appendix F.2.

We also show the inner and outer PNLFs for the TNG50 galaxies in Figure 12.4 for comparison with Box4. Curiously, in almost all cases the trend is contrary to the Box4 galaxies. Most classes show that they have more PNe in the outer compared to the inner regions, with the exception of old galaxies (again the opposite of Box4). This is especially seen for disk, star-bursting/star-forming, and fast rotator galaxies, as well as all metallicity classes, and may be related to negative age gradients found in disk galaxies (e.g., Wang et al. 2011). However, it is unclear why this trend is not found for any of the other classes that typically contain disk galaxies, such as star-bursting and star-forming galaxies. For the old galaxies, the outer regions are most likely less metal-rich, resulting in higher α-values for old stellar populations beyond 10 Gyr (see Valenzuela et al. 2025c). Comparing the outer PNLF of the elliptical galaxies to the PNLF data points for NGC 4697, we find that the observed PNLF slope is much steeper, unlike the outer PNLFs found in Box4.

12.2.3 PNLF bright-end cutoff magnitude

For each of the simulated galaxies, we fit the PNLFs as described in Section 12.1.2 to obtain the respective bright-end cutoff magnitudes $M^*(5007)$. In Figure 12.5 we show the median value of $M^*(5007)$ as a function of stellar mass for the different classes and classification schemes, arranged as in Figure 12.1. In general, we observe as before a remarkable constancy of the bright-end cutoff magnitudes, even across multiple orders of magnitude in mass. The scatter found for $M^*(5007)$ is larger than observed within the galaxies of individual observed galaxy groups or clusters, however (e.g., Spriggs et al. 2021; Ciardullo 2022). The overall

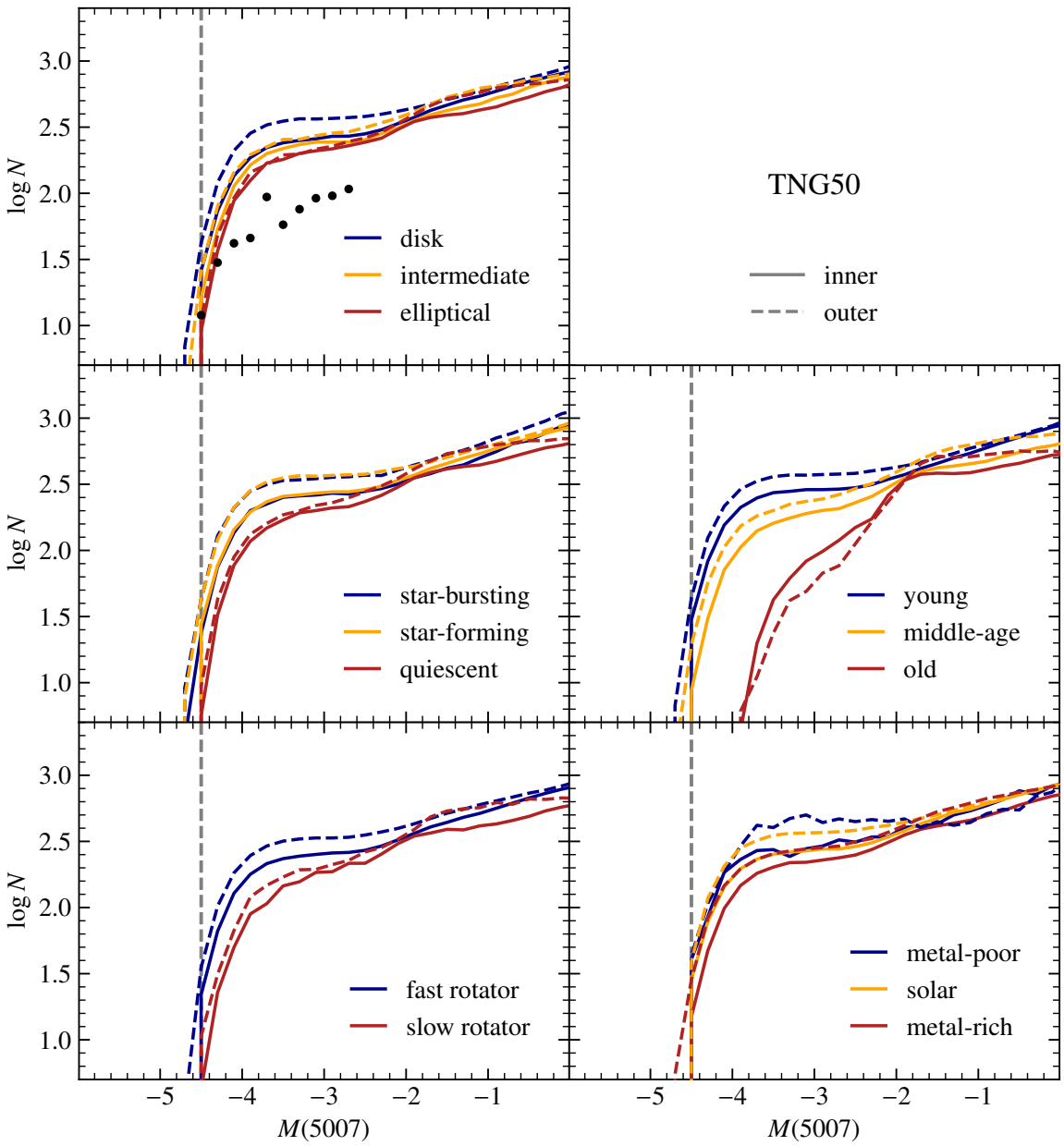


Figure 12.4: Median inner and outer PNLFs of galaxy classes from different classification schemes as in Figure 12.3, but for the galaxies in TNG50.

shifts in magnitude of the PNLFs between the classes are consistent with the findings above, but we discover that there are some significant trends with mass that are only revealed now.

As the main factor for the PNLFs, we find that the age classes reveal the largest differences between the cutoff magnitudes. While the young and middle-age galaxies have almost entirely constant bright-end cutoffs across the mass range, the old galaxies show a clear correlation with stellar mass. Old low-mass galaxies have significantly fainter values of $M^*(5007)$, with a median of -3.8 mag for the least massive bin of $\sim 2 \times 10^9\,\mathrm{M}_\odot$. This value becomes brighter toward higher masses until it reaches the observed value of -4.5 mag at $\sim 2 \times 10^{11}\,\mathrm{M}_\odot$, where it remains. There are three key factors that lead to this increase in cutoff brightness with mass. First, because of the stellar mass-metallicity relation (Gallazzi et al. 2005; Kudritzki et al. 2024; Dolag et al. 2025), massive galaxies are more metal-rich and therefore can produce

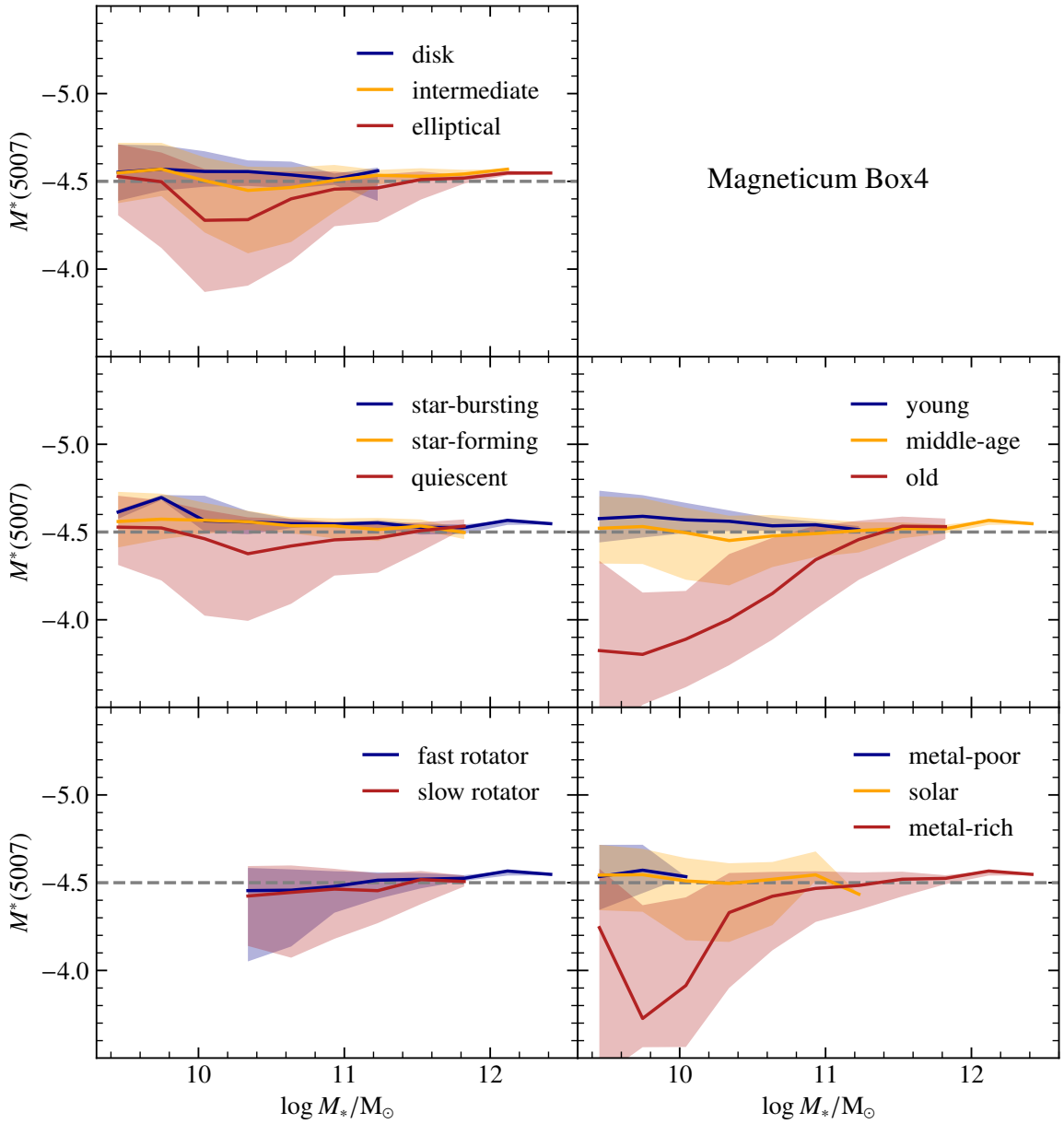


Figure 12.5: Median PNLF bright-end cutoff magnitudes $M^*(5007)$ as a function of stellar mass M_* for the galaxy classes in Magneticum Box4 (uhr) from the different classification schemes, that is, morphology, star formation, kinematic behavior, age, and metallicity, from top to bottom and left to right, respectively. For each mass bin, the median (solid lines) and the 1σ scatter (shaded regions) are computed. The observed bright-end cutoff magnitude $M^*(5007) = -4.5$ mag is marked by the vertical dashed gray lines.

brighter PNe (see Valenzuela et al. 2025c). Second, massive galaxies generally also have a larger fraction of intermediate-age stellar populations, which can populate the bright end of the PNLF (see Soemitro et al. 2025). Third, more stars mean the probability increases that the bright end of the PNLF is fully sampled and captured. The deviating bright-end cutoff from −4.5 mag found for old galaxies is the principal cause for galaxies in other classes to find fainter median cutoffs and larger downward scatters, specifically for elliptical and metal-rich galaxies, and to lesser extent also for quiescent galaxies. In contrast, galaxies of all other classes follow the universal bright-end cutoff remarkably well. We conduct a more detailed analysis of the differences for the morphological classes in the companion paper, Valenzuela et

al. (in prep., see Chapter 11). Finally, the lack of a trend for metal-poor galaxies having fainter cutoffs is because of our threshold choice of $[Z] < -0.2$, which is still roughly 0.2 dex higher than the metallicity below which the bright end of the PNLF is expected to become fainter (e.g., Dopita et al. 1992; Ciardullo et al. 2002; Scheuermann et al. 2022). In Appendix F.3, we show what effect it has to restrict the galaxy sample to the central galaxies, finding that it leads to overall more constant values of $M^*(5007)$. For TNG50, we show the same relation between $M^*(5007)$ and stellar mass in Appendix F.4, where due to the systematically younger ages the other classes find almost no deviation of $M^*(5007)$, except for the trend that we also found for old galaxies in Box4.

12.3 Conclusion

We have applied the PN model PICS (Valenzuela et al. 2025c) to the galaxies in several cosmological simulations to investigate their PNLFs with respect to common galaxy classification schemes. Specifically, we classify the simulated galaxies according to morphology, star formation, kinematics, stellar age, and stellar metallicity. This presents the first systematic study of the PNLF through the combination of a theoretical PN model and galaxies from cosmological simulations, which have self-consistent star formation histories in a cosmological context.

By comparing the median PNLFs and their shapes for each galaxy class, we find that the galaxies generally follow the expected PNLF shape found in observations and also have their cutoff around the observed value of $M^*(5007) \approx -4.5$ mag. The key driver for the bright-end cutoff magnitude as well as for the slope of the PNLF is a galaxy's mean age. Older galaxies have fainter cutoff magnitudes and thereby also feature steeper PNLF slopes. The strongest effect of this is seen at around 10 Gyr, where PICS does not produce PNe at the bright end anymore. The other classes largely follow this trend to different degrees, depending on the distribution of galaxy ages within the respective classes. As a result, elliptical, quiescent, slow rotator, and metal-rich galaxies all have PNLFs that tend toward fainter magnitudes due to them containing a larger fraction of old galaxies. Curiously, there is a point at $M(5007) \approx -1.7$ mag where the PNLFs appear to converge to similar PN numbers in that bin. We suggest that this may be related to the assumed PN lifetime of 30 000 yr in the nebular model.

Between the cosmological simulations, these trends are found for the simulations Magneticum Box4 (uhr) and TNG50, with the difference that TNG50 has systematically younger and more metal-rich galaxies, thus resulting in the PNLFs deviating less from each other besides for the age classification. Compared to observations, more galaxies are expected to be older and less metal-rich. The PNLFs of young and middle-age galaxies appear to be consistent with expectations from observations. The steeper slope of the PNLF for older stellar populations is also generally in agreement with observations. However, as we find the lower-mass old galaxies to have a significantly fainter cutoff magnitude, this stands in contrast with PNLF measurements of old elliptical galaxies, where $M^*(5007) \approx -4.5$ mag is also reached. Interestingly, more massive old galaxies ($M_* \gtrsim 2 \times 10^{11}\,\mathrm{M}_\odot$) are again

predicted to have the observed bright-end cutoff magnitude, primarily due to a larger amount of intermediate-age stars (e.g., Soemitro et al. 2025). While the age measurements may be subject to systematic biases, it seems likely that additional pathways for PNe to arise from old stellar populations have to be considered, such as through blue stragglers (e.g., Ciardullo et al. 2005) or a scatter in the stellar initial-to-final mass relation (e.g., Jacoby & Ciardullo 2025).

Finally, we considered how the PNLFs vary between the inner ($<1\ R_{1/2}$) and outer ($>1\ R_{1/2}$) regions of the simulated galaxies. Here the cosmological simulations predict different relative behavior, which is coupled to different galaxy formation models and the resulting stellar population gradients in the galaxies. While in Box4, young and middle-age galaxies have nearly identical PNLFs, but slightly fewer bright PNe in the outer regions, and old galaxies have slightly more bright PNe, the exact opposite is true for TNG50, with stronger differences between the inner and outer PNLFs. These predictions can be tested by comparing the PNLF slopes to observations. For instance, comparing the outer elliptical galaxy PNLF with the observations of NGC 4697, Box4 recovers the steep slope, whereas TNG50 does not. However, Box4 does not reproduce the PNe at the bright end, though an in-depth comparison will require taking more properties such as star formation history and galaxy mass into account. In both simulations, disk galaxies have more bright PNe in their outskirts, which is consistent with observations of higher luminosity-specific PN numbers in the outer regions (e.g. Bhattacharya et al. 2019), whereas for elliptical galaxies this is only the case in TNG50, but at the cost of overly young stellar populations and more shallow PNLF slopes.

In summary, this study has revealed a surprising constancy of the PNLF shape and cutoff magnitude obtained from theoretical models, which relieves much of the tension surrounding the PNLF between theory and observations from the past decades, underlining the theoretical basis for using the PNLF as an extragalactic distance indicator. Through the systematic analysis, however, we have also identified several points of tension between the models and observations that require further investigation on both sides. In particular, improved measurements of stellar populations that can be linked to their PNe are a promising avenue, where in particular IFU instruments like MUSE or MICADO at the upcoming ELT (e.g., Sturm et al. 2024; Hartke 2025) can pave the way forward for a better understanding of PNe and their capabilities as tracers.

13

Stream Photometry Combined with PN Kinematics

This chapter was submitted as Valenzuela et al. (2026)
to the IAU Symposium 403 proceedings:
Deep Imaging Meets Motion:
Complementing Stream Photometry Through Planetary Nebula Kinematics

Current and upcoming wide-field deep imaging facilities like Euclid, Rubin, and Roman will deliver vast amounts of low-surface-brightness data in the outskirts of galaxies (e.g., Trujillo et al. 2021; Euclid Collaboration 2022; Martin et al. 2022). These outer structures not only hold clues to the formation history of the host galaxy, but also to its underlying gravitational potential (e.g., Hendel & Johnston 2015; Pearson et al. 2022). As tidal streams are the extended remnants of tidally disrupted galaxies (see Movement I) orbiting a more massive host galaxy, these structures are useful in constraining the host galaxy's potential. Stellar streams have been used to this end by tracing their morphology and reconstructing their orbit, not only in the Milky Way from 6D phase space information (e.g., Koposov et al. 2023; Starkman et al. 2023), but also extragalactically (e.g., Walder et al. 2025).

On the extragalactic front, the projected view of faint integrated stellar light complicates the process of modeling the gravitational potential due to the limited information available. Pure photometric information provides the means to constrain the form of the potential, but an additional velocity measurement is necessary to obtain absolute values for the scale radius

and enclosed total mass (e.g., Pearson et al. 2022; Walder et al. 2025). Line-of-sight velocity measurements of faint structures are currently possible for individual tidal features (e.g., Fensch et al. 2020), but this will not be feasible for the wealth of upcoming deep photometric observations of galaxy outskirts. As a possible solution, kinematic tracer populations such as planetary nebulae (PNe) could be employed, as they have long been used to trace the low-surface-brightness Universe given their bright emission in [O III] λ5007 (e.g., Arnaboldi et al. 1994; Méndez et al. 2009).

Hydrodynamical cosmological simulations have proven to be useful tools to study and interpret the occurrence of low-surface-brightness structures (e.g., Pop et al. 2018; Mancillas et al. 2019; Valenzuela & Remus 2024; Khalid et al. 2025; Stoiber et al. 2025). Additionally, PN models have made significant advances in recent years, where new methods like PICS (PNe In Cosmological Simulations; Valenzuela et al. 2025c; see Chapter 8) have been developed to model PNe in cosmological simulations and provide direct counterparts to compare to PN observations.

In this work, we present a first case study applying the PN model PICS (Valenzuela et al. 2025c) to the simulation Magneticum Pathfinder (Dolag et al. 2025) to predict the effectiveness of PNe in tracing the dynamics of a stream. In Section 13.1, we introduce the simulation and tidal feature sample from which the stream is selected as well as the PICS framework. In Section 13.2, we analyze the galaxy halo and stream kinematics, for which we then demonstrate how well the PNe trace them. Finally, we summarize and conclude our findings in Section 13.3.

13.1 Simulation and model

To investigate the usefulness of kinematic tracer populations for tidal features, cosmological simulations with a sufficient resolution are needed as they contain galaxies with self-consistent star formation histories in a cosmological context. In this section, we first introduce the cosmological simulation used in this work and the census of tidal features found therein, followed by a description of the PN model that we applied to the stellar component.

13.1.1 Magneticum Pathfinder simulation

The Magneticum Pathfinder simulation suite (Dolag et al. 2025) includes simulations ranging from large cosmologically relevant volumes down to smaller high-resolution box sizes useful for galaxy studies. For the investigation of tidal features, we use Magneticum Box4 (uhr), which has a side length of 68 Mpc and was initialized with 2×576^3 DM and gas particles (stellar particle masses $m_* = 1.3 \times 10^6\,\mathrm{M}_\odot\,h^{-1}$ and softening length $\epsilon_* = 1\,\mathrm{kpc}$). It was run with an extended version of Gadget-2 (Springel 2005) with smoothed-particle hydrodynamics (SPH). For details about the implemented physics, refer to Dolag et al. (2025). The galaxies were identified with SubFind, adapted for baryonic simulations (Springel et al. 2001; Dolag et al. 2009).

The galaxies and associated scaling relations in Box4 have been shown to agree well with observations (Dolag et al. 2025), including their outer kinematics (e.g., Schulze et al. 2020), dynamics (e.g., Harris et al. 2020), and matter distribution and in situ component fractions (e.g., Remus & Forbes 2022). For the simulated galaxies, we have created a census of tidal features around the galaxies in previous work and showed that their occurrence as well as connection to the inner galaxy kinematics is consistent with observations from MATLAS (Valenzuela & Remus 2024), with subsequent work finding good agreement with the SAMI survey (Rutherford et al. 2024). In a follow-up study, we compared the sizes and positions of streams and shells between the simulation and several observations, again finding good agreement (Stoiber et al. 2025). As a result, the Magneticum Box4 (uhr) simulation is an ideal simulation for the purposes of studying tidal features and their dynamics in closer detail.

13.1.2 Tidal feature census

For the tidal feature census by Valenzuela & Remus (2024), streams, shells, and tails were visually identified around 520 galaxies with stellar masses of $M_* \geq 2.4 \times 10^{10}\,\mathrm{M}_\odot$ and half-mass radii of $R_{1/2} > 2\,\mathrm{kpc}$. The classification resulted in 62 galaxies with streams, 21 with shells, and 26 with tails, where the fraction of galaxies with a given type of feature increases with stellar mass, just as in observations (see fig. 3 of Valenzuela & Remus 2024). By tracing the stellar particles of each tidal feature back in time, we additionally identified the respective progenitor galaxies, enabling us to separate the present-day features from the galaxy and halo (Stoiber et al. 2025). This is particularly important in the context of this work for separating the feature dynamics from that of the halo. An example galaxy with a prominent stream is shown in the left panel of Figure 13.1, which we use in this work for the case study. The host galaxy has a mass of $M_* = 4 \times 10^{11}\,\mathrm{M}_\odot$ and a projected half-mass radius of $R_{1/2} = 13.5\,\mathrm{kpc}$, while the stream originates from a galaxy with $M_* = 2.4 \times 10^{10}\,\mathrm{M}_\odot$. The stream wraps around the galaxy, with a still identifiable core located at the top of the stream.

13.1.3 The PICS model

We obtain the PN populations from the PICS framework (Valenzuela et al. 2025d,c), which models the relevant physical processes for PNe given a stellar particle that represents a single stellar population. Stellar evolution including the post-asymptotic giant branch (post-AGB) phase and initial-to-final mass relation is followed through the metallicity-dependent models by Miller Bertolami (2016). The nebular [O III] emission is determined through an empirical nebular model (Valenzuela et al. 2019) with a metallicity correction motivated from theory (Dopita et al. 1992). Finally, circumnebular extinction is accounted for through an empirical relation from recent observations (Jacoby & Ciardullo 2025; Valenzuela et al. 2025b). The result is a population of PNe with their respective [O III] magnitudes. The model has already been successfully used to interpret observations of elliptical galaxies and their PN populations (Soemitro et al. 2025).

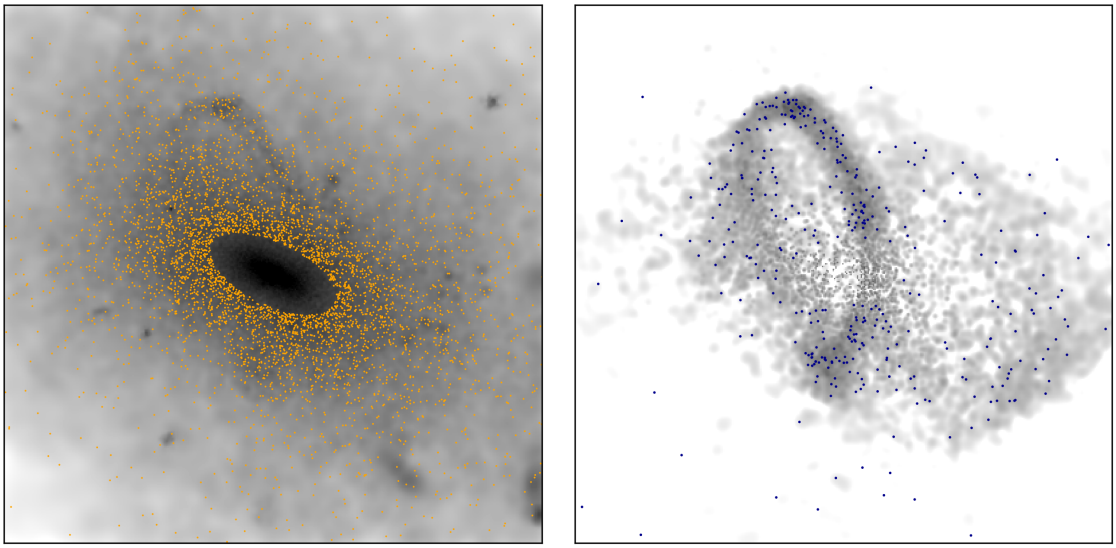


Figure 13.1: *Right*: Mock observation of a prominent stream to the upper left of its host galaxy from Magneticum Box4 in the r-band with overplotted PNe modeled with PICS (orange points) in the outer galaxy regions. The galaxy is viewed from a random projection. *Left:* Stream separated from the host galaxy, as identified by the stellar particles originating from the stream progenitor galaxy. The PNe associated with these stellar particles are overplotted in blue. The PNe shown in both panels are those brighter than the threshold absolute magnitude of $M(5007) \leq -2.0$ mag, which corresponds to the PNe in the brightest 2.5 mag below the bright-end cutoff. Both panels have a side-length of 140 kpc and cover the same area.

Applying the fiducial PICS model to the selected galaxy with the prominent stream reveals a PN population that largely follows the underlying stellar component in spatial distribution. Because the PNe are modeled for the individual stellar particles, we were also able to separate those belonging to the stream from those of the host galaxy. The orange and blue points in Figure 13.1 show the PNe in the brightest 2.5 mag of the PNLF, where for old elliptical galaxies a luminosity-specific PN number on the order of around $\alpha_{2.5} \sim 10^{-8}\,\mathrm{L}_{\odot}{}^{-1}$ is expected from observations (i.e., the number of PNe per underlying bolometric luminosity; e.g., Hartke et al. 2022).

13.2 Tracing tidal stream dynamics

Given the identified tidal features with their positions and spatial distributions, it is possible to model the potential of the host galaxy. In particular, there are significant efforts for this based on streams in the outskirts (e.g., Pearson et al. 2022; Walder et al. 2025). However, because of uncertainties in distance to the respective systems, the constraints are generally limited to a relative description of the density profile. To determine the absolute mass of the host halo, a single line-of-sight velocity measurement of a given stream is in fact sufficient. In the following, we present the stellar kinematics of the example galaxy as well as of its tidal stream and to what extent it is traced by the PNe.

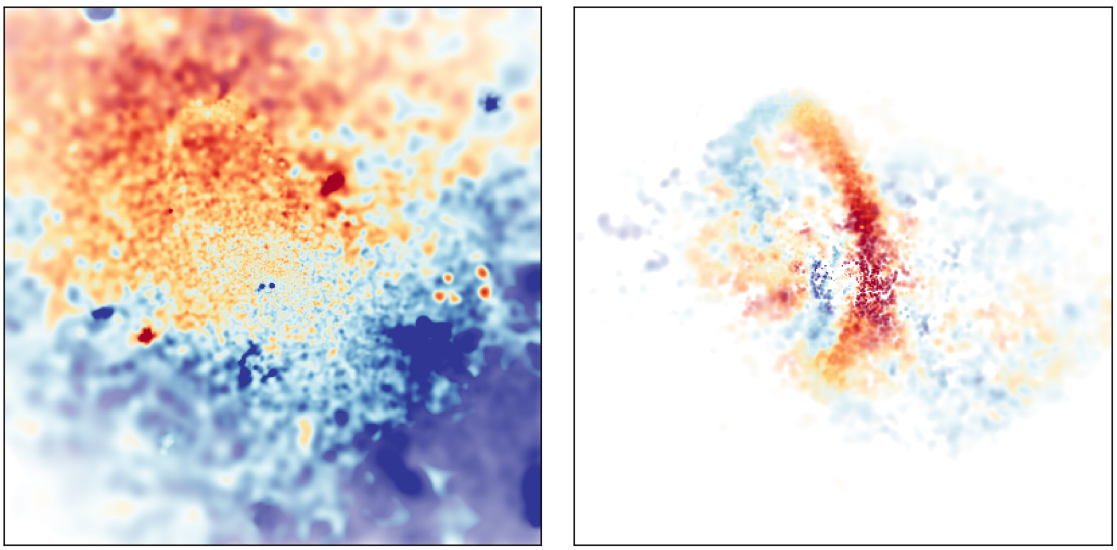


Figure 13.2: Line-of-sight stellar velocity maps of the same galaxy and stream as in Figure 13.1 with the same projection and area displayed. The color map ranges from -150 to $150\,\mathrm{km\,s^{-1}}$ for the dark red and dark blue extremes, respectively. The color opacity is furthermore set by the r-band flux shown in Figure 13.1, with fainter regions appearing more white in the velocity maps. *Right*: Velocity map of the entire galaxy including the stream. *Left*: Velocity map of the stream stellar particles. For the visualizations, each of the stellar particles is smoothed according to the local density, after which the displayed line-of-sight velocities in each pixel are determined by the light-weighted mean.

13.2.1 Dynamical decomposition of the stellar component

To this end, we show the line-of-sight stellar velocities as they would be observed for the entire galaxy in Figure 13.2 (left panel), as well as the line-of-sight velocities of the separated stream stellar particles (right panel). The halo shows a clear sign of ordered rotation around a rotational axis drawn from the top right to the bottom left. Interestingly, this is slightly misaligned with respect to the inner galaxy shape and its position angle (PA), which is generally related to the merger history (e.g., Foster et al. 2016; Schulze et al. 2020; Valenzuela et al. 2024a). The stream kinematics are hardly visible in the full galaxy velocity map, where only a slight drop in velocity can be seen at the top right of the galaxy (left panel), which corresponds to the location where the stream is best visible in the photometric map (left panel of Figure 13.1). The pure stream kinematics primarily show how the stream follows an orbit around the host, but also to what extent phase space mixing has already made the strongly stripped stellar component (seen to the very right in the maps) nearly indistinguishable from the rest of the halo component (comparing the right-most region between the left and right panels).

13.2.2 Planetary nebulae as kinematic tracers for tidal features

While only one kinematic measurement along the stream would suffice to anchor the halo mass in absolute terms, the question arises to what extent it is possible to obtain this from individual PNe without knowing whether they belong to the stream or halo. In Figure 13.3, we show the same PN population as in Figure 13.1, but colored by line-of-sight velocity

(top row). The PN kinematics overall show the same behavior as the stellar kinematics in Figure 13.2, that is, they clearly trace the halo's global rotation. Given that PNe trace the stellar component, this was to be expected. Additionally, now the individual line-of-sight velocities of the PNe simultaneously provide some insight into the underlying velocity dispersion, where in particular in the inner regions there are strongly varying PN line-of-sight velocities found close together.

The following rows show the zoomed-in region of the bright upper stream part with the overplotted PN population colored by velocity. They show the PNe with varying magnitude limits per row where the first of those rows shows the largest magnitude range of $M(5007) \leq -2.0$ mag (same as the top row of Figure 13.3), followed by -3.0 and -3.5 mag. The decreasing number of PNe with each row raises the stochasticity of whether it is possible to detect a sufficient number of PNe associated with the stream to obtain the necessary corresponding velocity measurement. While the stream kinematics are clearly traced by the brightest 2.5 mag PNe (right panel in the second row of Figure 13.3, $M(5007) \leq -2.0$ mag), there are few PNe in the brightest 1 mag (fourth row) with only five PNe lying along the main stream section seen on the right side of the right zoom-in panel. The additional halo PNe seen within the stream in the left zoom-in panel of the fourth row hinder a precise estimate of the stream dynamics.

For the intermediate deep PN sample of the brightest 1.5 mag (third row of Figure 13.3, $M(5007) \leq -3.0$ mag), the stream PNe are sufficient to trace the stream dynamics well through their line-of-sight velocities (right panel). In particular, the smooth velocity gradient along the brightest stream section is recovered, from light blue points at the top to dark red points at the bottom right. Further including the halo PNe (left panel), the PNe found within the projected brightest stream section still largely trace the stream dynamics, with only some contaminating outliers. The total stream mass displayed in the zoomed-in panels of the right column is $M_{*,\text{zoom-stream}} = 6.7 \times 10^9\,\mathrm{M}_\odot$, which corresponds to between a third and a fourth of the original progenitor galaxy's mass.

This means that for a massive stream such as in the case study here, detecting the brightest 1.5 mag PNe is sufficient to obtain a robust dynamic measurement of the stream along the brightest section of the stream. This method even promises to deliver a velocity gradient along the stream, which is expected to further improve the constraints that can be placed on the absolute halo mass of the host galaxy with methods such as those employed by Pearson et al. (2022) and Walder et al. (2025).

13.3 Summary and conclusion

In this work, we have applied the PICS framework for modeling PNe (Valenzuela et al. 2025c) to the cosmological simulation Magneticum Box4 (uhr; Dolag et al. 2025) to investigate to what extent PN kinematics can trace the dynamics of tidal streams. We present a case study for a prominent tidal stream around a massive elliptical galaxy, where the line-of-sight stellar kinematics along the stream show a clear velocity gradient. By applying different brightness

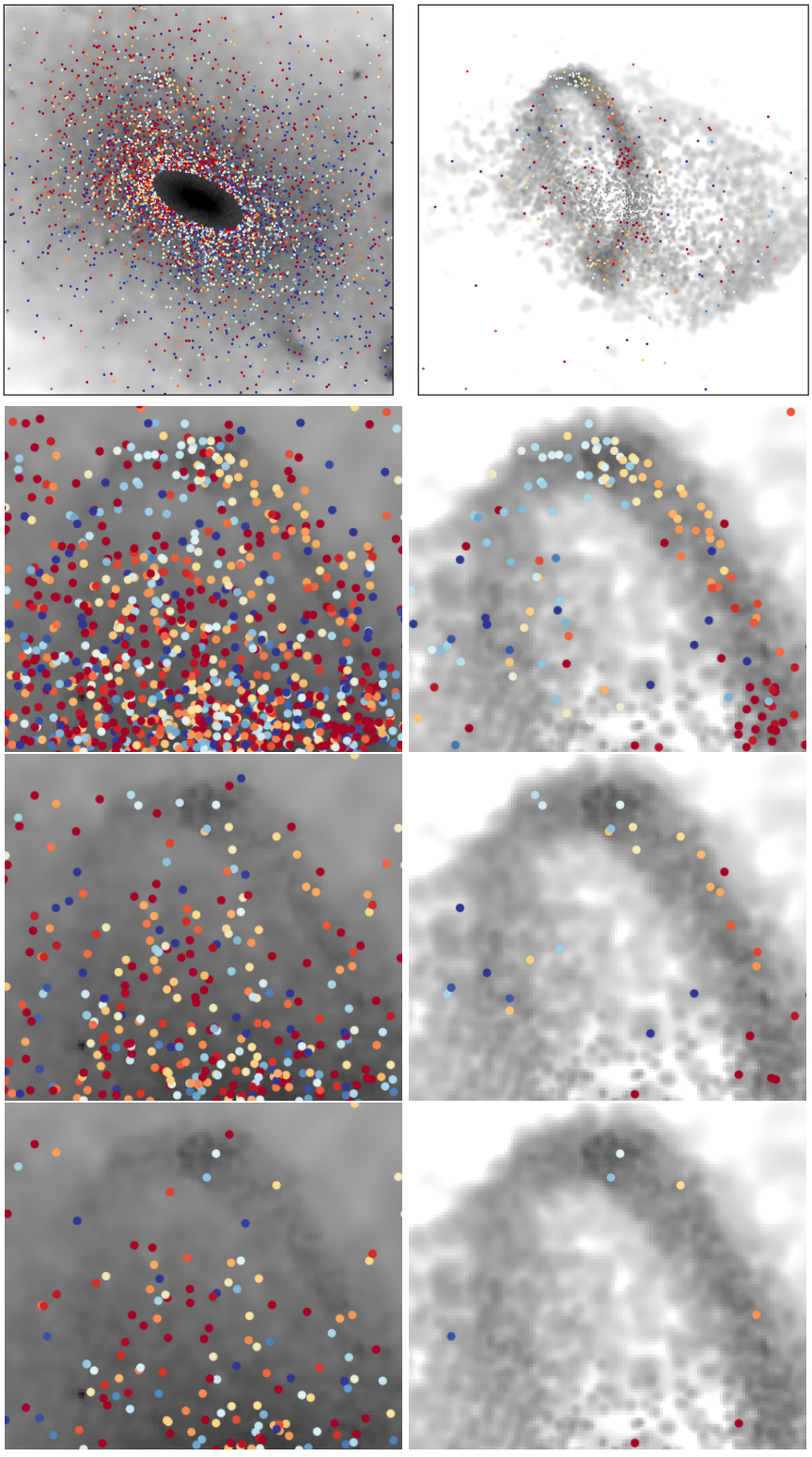


Figure 13.3: Mock observations of the same galaxy and stream as in Figures 13.1 and 13.2 with overplotted PNe colored by their line-of-sight velocities. The color map ranges from −150 to 150 km s^{-1} for the dark red and dark blue extremes, respectively. *Top row*: Same projection and area as shown in Figures 13.1 and 13.2, where only PNe are displayed that are brighter than a magnitude limit of $M(5007) \leq -2.0$ mag, just as in Figure 13.1. *Bottom rows*: Zoomed-in region of the bright upper stream part, where the overplotted PNe are subject to magnitude cuts of $M(5007) \leq -2.0$, −3.0, and −3.5 mag, from top to bottom. These correspond to the brightest 2.5, 1.5, and 1.0 mag of the PNLF, respectively. The zoomed-in region has a width of around 36.5 kpc.

cutoffs for the PNe with respect to their bright [O III] emission line, we analyze to what extent the stream can be disentangled from the underlying halo kinematics solely based on the PN line-of-sight velocities and positions. Over the brightest stream region with a mass of 6.7×10^9 $M_\odot$, the brightest 1.5 mag PNe are sufficient to recover the stream dynamics within the host galaxy's halo.

As a result, we show that PNe are effective tracers of the underlying stellar kinematics, even for tidal streams when they are massive enough. Moving towards lower-mass tidal features, deeper observations will be required to obtain a sufficient sample of PNe. We find that tracer populations are an attractive alternative to expensive low-surface-brightness kinematic measurements for obtaining the velocity data, which are needed to recover the halo profile and mass from stream detections (e.g., Pearson et al. 2022; Walder et al. 2025). In the era of wide-field deep photometric surveys, where tidal features are being discovered around increasingly large samples of galaxies (e.g., Martínez-Delgado et al. 2023a; Gordon et al. 2024), PN surveys targeting the tidal features are a viable approach to complement the photometry. In particular, wide-field narrow-band imaging can be used to identify PN candidates. Later spectroscopic follow-up measurements could then deliver the relevant kinematic information. We conclude that PN kinematics are a feasible way forward for delivering the much-needed complementary information to the low-surface-brightness imaging of galaxy outskirts from the observational side.

14

Planetary Nebulae as Stellar Population Tracers

This chapter summarizes the results published by Soemitro, Valenzuela et al. (2025), A&A 704, A303, and by Hartke, Ennis, Valenzuela et al. (in prep.), for which I contributed the simulation and model analysis:

Towards precision cosmology with improved PNLF distances using VLT-MUSE: III. Impact of stellar populations in early-type galaxies
&
The halo of M105 and its group environment as traced by planetary nebulae populations: III. Metallicity-dependent variations in the planetary nebula populations

One of the novelties of the PICS framework (Valenzuela et al. 2025c) is that it takes into account several stellar population properties to fully model the relevant processes from stellar evolution to the nebular emission itself. For this reason, it is possible to compare its predictions in a direct manner to PN observations within galaxies that have measured stellar population properties. The previous chapters have mainly dealt with the predictions from applying PICS to cosmological simulations, showing that it resolves several of the tensions previously found between theory and observations of PNe (see in particular Chapters 8, 11, and 12). However, it is also important to understand to what degree PICS can reproduce and explain the observed PN populations in individual galaxies.

Observationally, there have been significant advances made in the past two decades on the measurement of stellar populations from integrated spectra. In particular, new possibilities

have opened up through integral field unit (IFU) observations with the MUSE (Multi Unit Spectroscopic Explorer; Bacon et al. 2010) instrument at the Very Large Telescope (VLT). Its spectral resolution in the optical regime and high spatial resolution across a 1 arcmin^2 field of view make it possible to perform spatially resolved stellar population synthesis for extragalactic systems to an unprecedented degree. Furthermore, it covers the relevant emission lines to identify PNe and PN interlopers such as H II regions or supernova remnants, including the primary emission line [O III] λ5007, but also Hα, Hβ, and the doublet [S II] $\lambda\lambda$6717, 6731 (e.g., Reid & Parker 2010; Roth et al. 2021). The IFU nature of MUSE has additionally enabled the identification of PNe further in the inner regions of galaxies with higher stellar surface brightness (e.g., Spriggs et al. 2021; Scheuermann et al. 2022; Soemitro et al. 2023; Congiu et al. 2025). As a result, it is possible to directly link the PNe and their underlying stellar populations from the observational side (e.g., Galán-de Anta et al. 2021; Ennis et al. 2026), which is ideal to compare with the results from PICS.

Two of the challenges for theoretical models of PN populations have been related to properties of the PNLF. The first is how its bright-end cutoff of $M^*(5007)$ may vary with properties such as age and metallicity (e.g., Marigo et al. 2004; Ciardullo 2012). The second concerns the luminosity-specific PN number $\alpha = N_{\rm PN}/L_{\rm bol}$, the number of PNe brighter than a given magnitude per bolometric luminosity of the underlying stellar component (Jacoby 1980), where α has been observed to increase toward the outer regions of galaxies (e.g., Doherty et al. 2009; Longobardi et al. 2013; Hartke et al. 2020). This increase in luminosity-specific PN number likely arises from a gradient in stellar population properties, which is generally difficult to measure out to large radii due to the low surface brightness of galaxy outskirts, however. Despite the challenging observations, several empirical relations between α and the underlying stellar populations have been studied in the past (e.g., Ciardullo et al. 2005; Buzzoni et al. 2006), finding that α decreases with older stellar ages.

The MUSE instrument provides a promising avenue for approaching these questions through improved stellar population measurements with full spectral fitting compared to methods using line indices (e.g., Ciardullo et al. 2005). Specifically, this allows us to connect the PNLF measures of $M^*(5007)$ and α to the underlying stellar ages, metallicities, and their respective distributions. To help interpret the findings, state-of-the-art models like PICS can be applied to simulated analog galaxies that are selected to match the observed objects. By investigating the simulated and observed counterparts in the same way, the properties and relations can be compared and physically interpreted. In addition to the complex composite stellar populations found in galaxies from cosmological simulations, parameter tests of PICS with single stellar populations (SSPs) are furthermore useful to put observations in context with respect to the basic parameters of age and metallicity.

This chapter presents the relevant findings of Soemitro et al. (2025) and Hartke et al. (in prep.) on comparing individual observed PN populations with their stellar populations from observations and models. In the work by Soemitro et al. (2025), we build on the previous studies by Roth et al. (2021) and Jacoby et al. (2024), which used archival MUSE data of nearby galaxies ($\lesssim$30 Mpc) to identify their PNe and use the PNLFs as distance indicators to

obtain an independent value for H_0. We targeted the central regions of five early-type galaxies (ETGs) in their sample to analyze the PN properties and stellar populations, specifically the ages and metallicities. With the aim of comparing and interpreting the observed results through theory, we additionally ran PICS on simulated analog galaxies selected for each observed galaxy to study the modeled PN populations with respect to $M^*(5007)$ and α.

In the work by Hartke et al. (in prep.), we build on the previous studies by Hartke et al. (2020, 2022), which used photometric and PN Spectrograph (PN.S; Douglas et al. 2002) observations to analyze the PNe in the halo and intra-group light (IGL) around the ETG M 105. By complementing the data with MUSE observations of the center of M 105, we were able to compare the underlying stellar metallicities and PN properties between the core, the halo, and the envelope (tracing the IGL). We then applied the PICS model to a grid of SSP models with different ages and metallicities. We compared its predictions to the observations in the three galaxy regions with distinct metallicities with the aim to understand the invariance of $M^*(5007)$ as well as the large increase of α in the envelope.

14.1 Observed ETGs and their simulated analogs

In the following, we introduce the ETG sample and the simulated galaxy analogs used by Soemitro et al. (2025). For each of the galaxies, we split the PN populations into an inner and an outer component to then be able to compare their trends with the stellar populations. This has the advantage that systematics from different observational conditions are avoided and that the distance is the same, thereby allowing relative statements about quantities such as the bright-end cutoff of the PNLF.

14.1.1 Observational data

We selected five ETGs from the samples of Roth et al. (2021) and Jacoby et al. (2024), which all have more than 80 PNe identified. This ensures a good measurement of the PNLF cutoff, even when splitting the PNe into two subsamples, as it requires more than 30 PNe in the brightest magnitude of the PNLF (Roth et al. 2021; Jacoby et al. 2024). Each of these galaxies has archival MUSE data available for their cores, for which we show the flux maps of two of them in Figure 14.1. Based on the PNe identified in the archival MUSE data of each of these galaxies, we split them into an inner and outer equal-number subsample according to the elliptical galaxy isophotes (orange circles and purple squares split by the middle black ellipse). The innermost region is also avoided due to the high surface brightness limiting the PN detection completeness (inner black ellipse), and the outer limit is given by the most elliptically distant PN (outer black ellipse).

For each of the PN subsamples, we fit the classical form of the PNLF (Equation 7.2) with $c_2 = 0.307$ through a maximum likelihood fit following the method by Chase et al. (2023). This approach takes into account foreground Galactic extinction according to (Schlafly & Finkbeiner 2011). From the best fit, we obtained the bright-end cutoff $M^*(5007)$ and

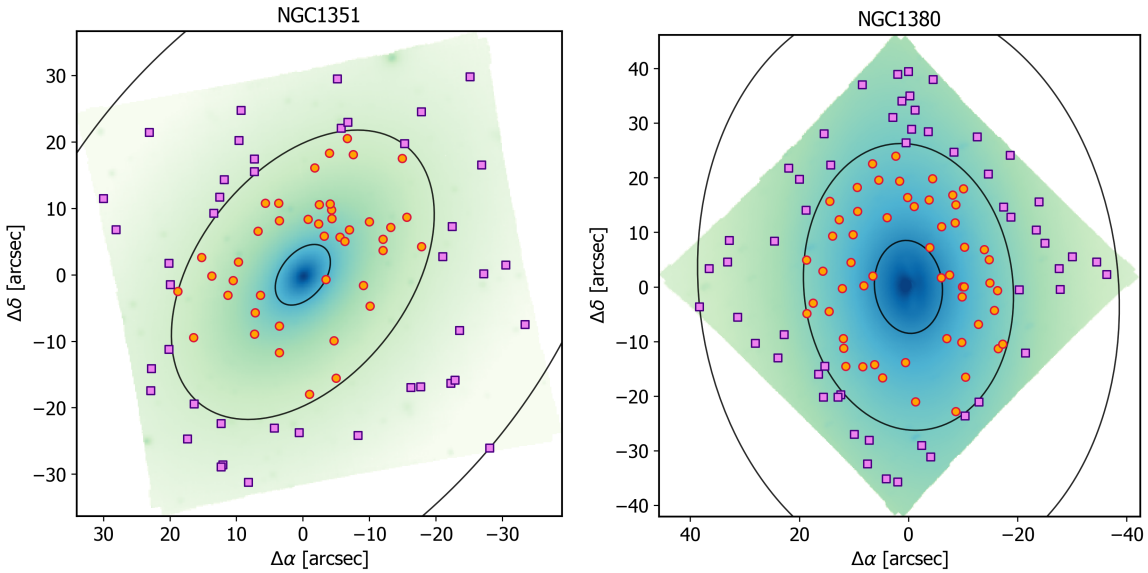


Figure 14.1: Subsamples of the PNe overlaid on the MUSE flux maps for two of the five studied ETGs (NGC 1351 and NGC 1380). The equal-number PN subsamples are positionally selected between elliptical isophotes (black lines) with the inner PNe shown as orange circles and the outer PNe as purple squares. *These are two of the panels in figure 1 from Soemitro et al. (2025).*

the luminosity-specific PN number within the brightest 0.5 mag, $\alpha_{0.5}$, assuming the V-band bolometric correction by Buzzoni et al. (2006).

We then performed stellar population synthesis for each of the subsample regions given by the elliptical isophotes to obtain the most likely distributions of stellar ages and metallicities. The spectral fitting was done with `pPXF` (Cappellari & Emsellem 2004; Cappellari 2023) using the sMILES SSP models (Knowles et al. 2021, 2023) with a grid of 53 ages, 10 metallicities, and 4 alpha abundances ($[\alpha/\mathrm{Fe}]$) assuming the universal Kroupa (2001) IMF (here we do not discuss the results on the alpha abundances, for more details on them and their results, see Soemitro et al. 2025). Based on the resulting SSP mass weights, we computed the mean light-weighted ages and metallicities [M/H] as well as their statistical errors. We additionally constructed the star formation histories according to the SSP ages and subdivided them into three age bins, separated by the age limits at 2 and 10 Gyr. These were chosen based on the findings by Valenzuela et al. (2019) that PN central masses of 0.53–0.58 $M_\odot$ are needed to explain the PNLF of the ETG NGC 4697, which correspond to stellar ages of around 2–10 Gyr (Miller Bertolami 2016; Valenzuela et al. 2025c). At the higher-mass end, several authors have stated that central stars at the PNLF cutoff require masses larger than 0.58 $M_\odot$ (e.g., Schönberner et al. 2007; Gesicki et al. 2018) or around 0.57–0.58 $M_\odot$ (e.g., Galera-Rosillo et al. 2022; Morisset et al. 2023, for PNe in M 31). These three age bins allow us to disentangle which stellar populations contribute the most to the production of bright PNe in a composite stellar population. For more details on the spectral fitting methodology, refer to Soemitro et al. (2025). We show an overview of the relevant galaxy properties in Table 14.1.

Table 14.1: Properties of the five ETGs studied. We list the number of PNe $N_{\rm PN}$, the PNLF distance D from Jacoby et al. (2024), the effective radius R_e in kpc and arcsec from Forbes et al. (2017) and Iodice et al. (2019a), the semi-major axes of the elliptical isophotes defining the two PN subsample regions $a_{1/2/3}$, and the $g-r$ color from Iodice et al. (2019b), just for NGC 1351 from Watkins et al. 2022 and converted via the method of Jester et al. 2005. *The data are composed of tables 1 and 2 from Soemitro et al. (2025) and additionally include the $g-r$ colors.*

Galaxy	$N_{\rm PN}$	D/Mpc	R_e/kpc	$R_e/''$	$a_1/''$	$a_2/''$	$a_3/''$	$g-r$
NGC 1052	86	17.9	1.9	21.9	9.9	28.4	59.9	–
NGC 1351	86	19.0	2.5	27.6	5.2	24.8	60.3	0.791
NGC 1380	112	16.6	5.9	72.7	8.5	52.9	222.5	0.59
NGC 1399	232	17.6	29.5	346.0	15.2	44.3	111.1	0.7
NGC 1404	107	18.8	18.4	201.5	5.6	25.2	57.7	0.71

14.1.2 Simulated analog galaxies

To interpret the observed properties of PN populations and their differences between galaxies and their radial behaviors, we use PICS applied in post-processing to the Magneticum Box4 (uhr) simulation (Dolag et al. 2025). Since the simulation run only reaches $z \approx 0.066$, which corresponds to a lookback time of 0.88 Gyr, the stellar ages can reach at most 12.9 Gyr. In this work, the stellar ages are not adapted for this as the general trends with stellar populations should be unaffected by this.

To select six simulated analog galaxies for each observed object, we took into account the morphological type (i.e., only elliptical and lenticular galaxies) and the literature values for the effective radius and the $g-r$ color (see Table 14.1). To reduce the selection of simulated galaxies to the most suitable analogs for a given observed galaxy, we first discarded galaxies classified as late-type by their morphology as measured by the b-value (Teklu et al. 2015) according to the same classification as used in Section 4.2.4. Next we only kept galaxies with effective radii within 30% of the observed effective radius and with $g-r$ colors within an absolute difference of ±0.4. Finally, we defined a metric to identify the best six candidates out of these remaining galaxies by

$$m = \left(\frac{R_{e,\rm sim} - R_{e,\rm obs}}{0.3 R_{e,\rm obs}}\right)^2 + \left(\frac{(g-r)_{\rm sim} - (g-r)_{\rm obs}}{0.4}\right)^2, \tag{14.1}$$

where we took the galaxies with the lowest values of m as analogs. We only skipped duplicate analogs across different observed galaxies. The $g-r$ color term was not applied for NGC 1052. The reason for limiting the number of selected analogs per observed galaxy is the limited simulation volume, through which there are only a small number of galaxies that can actually be used as suitable analogs when matching specific galaxy properties. We therefore decided on selecting six analogs per observed galaxy as the compromise between not being restricted to a single analog galaxy and still being sufficiently similar in galaxy properties to the observations.

For each of the galaxy analogs, we ran the fiducial PICS model on each stellar particle belonging to the respective galaxy, resulting in a PN population with their corresponding positions and $M(5007)$ magnitudes. To obtain two PN subsamples per galaxy in radial bins

like in the observations, we used the values of a_1, a_2, and a_3 given in Table 14.1 and converted them from arcsec to kpc, assuming the listed PNLF distances. We oriented each analog simulated galaxy in a random direction and then defined the two elliptical radial regions according to its 2D shape with the inner and outer semi-major axes converted to kpc from the values given in Table 14.1. The PNe located in the respective projected regions are used as the corresponding PN subsamples to compare to the observations. We fit the generalized PNLF as described in Section 12.1.2 to the PN populations through the cumulative method and obtain values for $M^*(5007)$ and $\alpha_{0.5}$, for which we divide the number of PNe in the brightest 0.5 mag by the total bolometric luminosity determined with the models by Bruzual & Charlot (2003). We also computed the mean mass-weighted stellar ages and metallicities [M/H] in each region, and we determined the mass fraction of stars in each of the three age bins split at 2 and 10 Gyr.

The analog galaxies have self-consistent cosmological star formation histories and thereby serve as the hosts of PN populations that arise from the composite stellar populations, which we can directly compare with the observed galaxies. Furthermore, the differences between the simulated galaxies allow us to gain a deeper understanding of the underlying physics and on the connection between the PNe and the stellar populations. It should be noted that the simulated galaxies were not formed in targeted constrained simulations to reproduce the observed systems, but were taken as the most suitable analogs from an independent cosmological simulation.

14.2 Comparison to simulated analog galaxies

As we did not select the analogs based on age or metallicity, we first compared these two properties between the observations and the simulation. For each observed galaxy, we computed the mean and standard deviation of the stellar properties for the inner and outer regions of the respective analog galaxies. We show the comparison between observed and simulated mass-weighted stellar ages and metallicities in Figure 14.2 for the inner and outer galaxy regions. The ages are systematically younger for four of the simulated galaxies by up to 5 Gyr, which is significantly more than the offset caused by the simulation having stopped at $z = 0.066$ (0.88 Gyr). Only NGC 1351 has consistent ages in both the observations and simulations. The differences could arise from systematics in the galaxy color selection or from an overly extended late-time cosmic star formation history in the simulations, though comparisons with high-redshift observations do not support that scenario for Magneticum Box4 (uhr; see figure 12 of Dolag et al. 2025 for the cosmic star formation rate density compared to observations). On the observational side, systematics caused by the employed spectral libraries lead to larger total uncertainties (see appendix A of Soemitro et al. 2025), and it is possible that there are further biases with possible effects from the age-metallicity degeneracy (e.g., Worthey 1994; Boecker et al. 2020). Between the inner and outer galaxy regions there is no clear age correlation, which is consistent with studies showing that ETGs

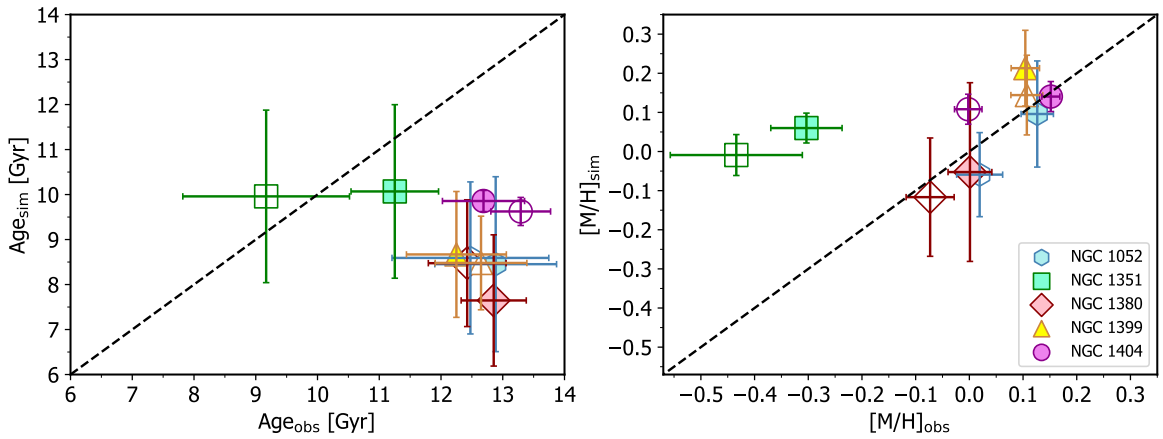


Figure 14.2: Comparison between the observed (obs) and simulated (sim) stellar populations in the inner (filled markers) and outer (open markers) galaxy regions of the five ETGs (see the legend), for the mean mass-weighted age (left) and metallicity [M/H] (right). The dashed line indicates the one-to-one relation. The error bars for the observed properties show the statistical uncertainties from the spectral fitting, while those for the simulated properties show the scatter among the six analog galaxies. *This is figure 7 from Soemitro et al. (2025).*

generally have rather flat age gradients (e.g., Parikh et al. 2021), though there are differing results on this matter (e.g., Zibetti et al. 2020; Liao & Cooper 2023).

In contrast, the metallicities lie nearly on the one-to-one line between the observed and simulated galaxies, with the exception of NGC 1351, which is curiously also the only galaxy that is consistent in age. Across both observations and the simulation, there is evidence for a negative metallicity gradient (i.e., higher metallicities in the inner regions), which is consistent with observations of larger samples of ETGs (e.g., Kobayashi & Arimoto 1999; Tortora et al. 2010; Parikh et al. 2021). However, the metallicity differences between inner and outer regions are comparable to the respective error bars.

In the following, these analog galaxies are used to compare the modeled PN populations to the observations. For this, it is important to keep the general similarities and systematic differences of the stellar populations in mind.

14.2.1 Stellar populations and the PNLF bright-end cutoff

We first consider the bright-end cutoff magnitude of the PNLF, $M^*(5007)$, in the observed galaxies. The left panels of Figure 14.3 show the relation between $M^*(5007)$ and the two stellar population properties, metallicity and age. There is no clear correlation of the bright-end cutoff with these parameters, which is not overly surprising for two reasons: first, the bright-end cutoff has been found to be universal across different galaxy types (e.g., Ciardullo et al. 1989, 2002; Spriggs et al. 2021), and second, the absolute magnitudes in the left panels are set according to the distance determined through the PNLF method, which already assumes a universal cutoff. However, the lower metallicity of NGC 1351 ([M/H] ≈ -0.4 to -0.3) actually comes close to the regime where dimmer bright-end magnitudes would be expected from theory and observations (e.g., Dopita et al. 1992; Ciardullo 2012), though there is significant scatter observed in this range. The relative differences between the $M^*(5007)$

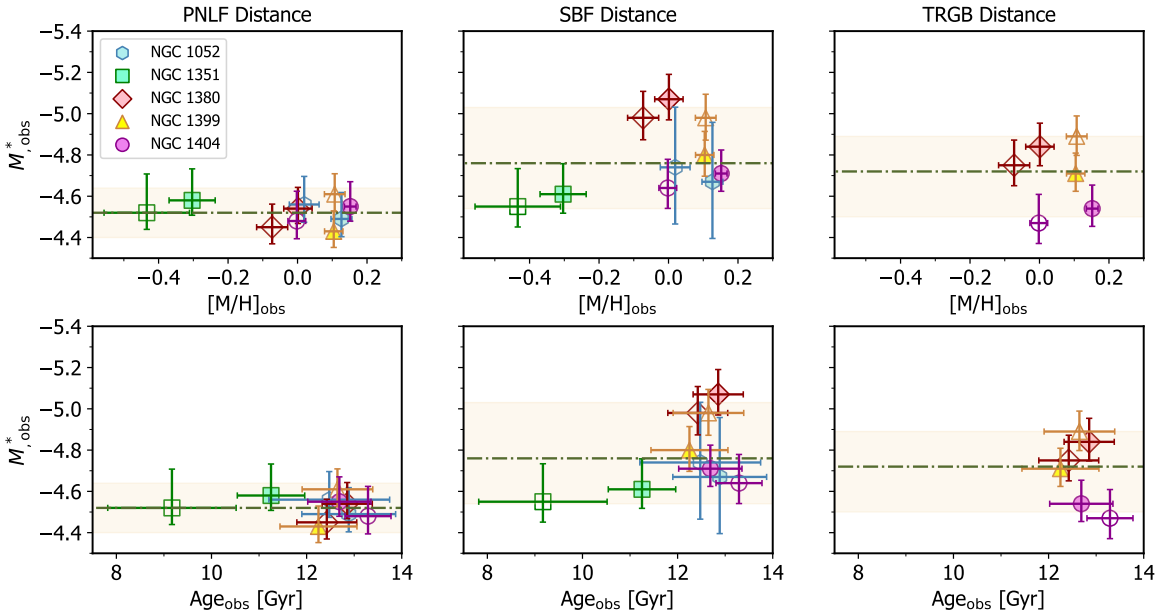


Figure 14.3: Observed bright-end cutoff magnitude $M^*(5007)$ of the PNLF compared to the underlying stellar metallicity (top) and age (bottom), where the absolute magnitudes are determined assuming three different distance measures: PNLF (left), SBF (middle), and TRGB (right). The five galaxies are shown with respect to their inner (solid markers) and outer (open markers) regions. The error bars indicate the statistical uncertainties. The PNLF distances are taken from Roth et al. (2021) and Jacoby et al. (2024), and they assumed a cutoff magnitude of $M^*(5007) = -4.53$ and -4.54 mag, respectively. The SBF distances are taken from Tonry et al. (2001) and Blakeslee et al. (2009), and the TRGB distances from Anand et al. (2024). Currently, there are no TRGB distance measurements for NGC 1052 and NGC 1351. The dash-dotted horizontal lines indicate the mean cutoff value, and the shaded areas indicate its standard deviation. *This is figure 9 from Soemitro et al. (2025).*

values of the inner and outer regions still give insight into its sensitivity to the changes in the stellar population properties. Since these differences are smaller than the error bars, we conclude that the relative differences of age and metallicity within the galaxies do not have a significant effect on the bright-end cutoff.

The left two columns of Figure 14.3 show the same relations for the absolute cutoff magnitudes, but assuming two other distance measures for the galaxies, the surface brightness fluctuations (SBF; middle; Tonry & Schneider 1988) and tip of the red giant branch (TRGB; right; Lee et al. 1993) methods. In both cases we find an increased scatter of $M^*(5007)$ and a systematic shift toward brighter magnitudes by 0.25 mag for SBF and 0.2 mag for TRGB, originating from larger inferred distances. The offset of PNLF distances to the SBF method is well known and may be caused by errors in the assumed internal extinction of the galaxies, which would affect PNLF and SBF distances in opposite directions (e.g., Ciardullo et al. 2002; Ciardullo 2012). For the TRGB distances, it is possible that metallicity corrections are necessary to correct the zero-point (e.g., Bellazzini et al. 2001; Rizzi et al. 2007), though solving these systematic offsets is beyond the scope of this work. For both alternative distance measures, we find no clear trends between $M^*(5007)$ and the metallicities or ages. Only the dimmer SBF cutoff magnitude for NGC 1351, which has a lower metallicity and age, indicates that metal-poor and younger stellar populations could lead to a dimmer bright-end cutoff,

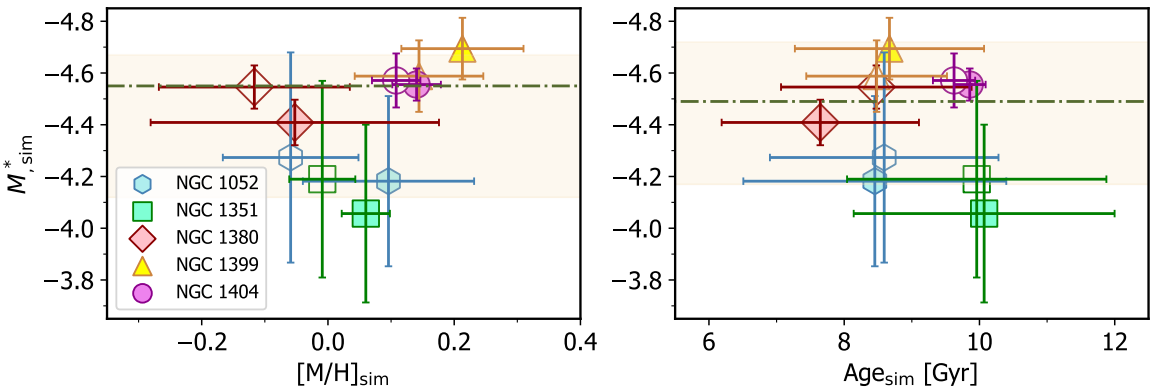


Figure 14.4: Bright-end cutoff magnitude $M^*(5007)$ of the PNLF for the simulated analog galaxies compared to the underlying stellar metallicity (left) and age (right). The galaxies are shown with respect to their inner (solid markers) and outer (open markers) regions. The error bars indicate the scatter among the six analog galaxies per observed counterpart. The dash-dotted horizontal lines indicate the mean cutoff value, and the shaded areas indicate its standard deviation. Note that the ranges of the x- and y-axes differ from Figure 14.3. *This is figure 10 from Soemitro et al. (2025).*

which for metallicity would be consistent with expectations (e.g., Dopita et al. 1992; Ciardullo 2012). A TRGB measurement for this galaxy would be interesting to verify this result for NGC 1351. In general, the zero-point differences between the methods appear to be unrelated to stellar population details.

For the simulated analog galaxies, there is no correlation of $M^*(5007)$ with the metallicity (left panel of Figure 14.4). In contrast to the observations, the analogs of two of the galaxies have significantly fainter bright-end cutoffs by around ∼0.3 mag (NGC 1052 and NGC 1351), though they also have the largest scatter. Both having on average solar metallicities, the metallicity is unlikely to be the reason for the fainter $M^*(5007)$. Turning to the relation with age (right panel), there is little correlation with $M^*(5007)$, except for the indication that younger galaxies are less likely to have faint bright-end cutoffs (which is consistent with the SSP models of Valenzuela et al. 2025c). Here, the overall older ages of the NGC 1351 analogs ($\gtrsim$10 Gyr) are likely a main reason for the dimmer PNe, together with the comparatively small size (Table 14.1), which implies a lower mass and thereby fewer PNe that could potentially populate the bright end. While the NGC 1052 analogs are on average younger by around 1.5 Gyr, the even smaller size (Table 14.1) is likely responsible for the relatively faint cutoffs. Overall, individual simulated galaxies with a combination of low metallicities ([M/H] $\lesssim -0.1$) as well as old ages ($\gtrsim$10 Gyr) can have cutoff values of up to $M^*(5007) \approx -4.0$ mag. At the other extreme, individual young and metal-rich galaxies can have cutoffs significantly brighter than −4.5 mag. As a result, the simulated analog galaxies display a wider range of cutoff values while still finding an average value of $M^*(5007) = -4.49$ mag, in excellent agreement with the empirically expected universal cutoff.

Finally, we considered the relative differences of $M^*(5007)$ and the stellar population properties between the inner and outer regions of the galaxies. However, we did not find any clear trends between these differences, which may also be related to the statistical errors of the PNLF fits to the limited numbers of PNe. While previous studies have shown that

$M^*(5007)$ varies with metallicity, this is restricted to metal-poor systems (e.g., Dopita et al. 1992; Ciardullo et al. 2002; Bhattacharya et al. 2021), whereas the galaxies studied here are sufficiently metal-rich ([M/H] > -0.4) for this to have an effect.

14.2.2 Stellar populations and the luminosity-specific PN number

Related to the bright-end cutoff magnitude itself are the PNe that actually populate the bright end of the PNLF. To better understand the relation of these brightest PNe with the underlying stellar population, we consider the luminosity-specific PN number $\alpha_{0.5} = N_{\mathrm{PN},0.5}/L_{\mathrm{bol}}$, where $N_{\mathrm{PN},0.5}$ is the number of PNe in the brightest 0.5 mag of the PNLF. In the simulation, this value is the actual count of PNe brighter than $M(5007) < -4.0$ mag, while for the observations, it is determined from the best-fit PNLF parametrization (Equation 7.2).

Drawing on the star formation histories determined for the observed and simulated galaxies through the three age bins (limits at 2 and 10 Gyr), we compared the stellar mass fractions in each of these bins to $\alpha_{0.5}$ (Figure 14.5). Note that in the literature, $\alpha_{2.5}$ is commonly used as a measure of the brightest to intermediate PNe, which has been put in relation with stellar populations (e.g., Buzzoni et al. 2006; Longobardi et al. 2013; Hartke et al. 2017). The top row shows the relations for the observations in each of the three age bins (left to right), where there is no correlation with the youngest stars (<2 Gyr), which show a very low mass fraction (<5%), as expected from rather quiescent ETGs. In contrast, both of the other age bins show a correlation with $\alpha_{0.5}$: for the intermediate age bin (2 Gyr $\leq t_{\mathrm{age}} \leq$ 10 Gyr), $\alpha_{0.5}$ increases with larger stellar mass fraction in that age range (dash-dotted green line in the middle panel), and the opposite is true for the oldest age bin ($t_{\mathrm{age}} >$ 10 Gyr; dash-dotted green line in the right panel). Both of these linear correlations have a p-value of 0.001, which means the relation is statistically significant. At first sight the trend seems to be primarily driven by NGC 1351, which has a much larger amount of intermediate-age stars ($\gtrsim$30%) compared to the other galaxies ($\lesssim$10%). However, even without taking into account NGC 1351 in the fit, we still find the same overall trends (dashed brown lines), though the p-value increases to 0.11, meaning that the result is not statistically significant anymore. Further measurements of galaxies with more intermediate-age stars will be needed to verify the trends found here.

For the simulated analog galaxies (bottom row of Figure 14.5), there is also no clear correlation between the young mass fraction and $\alpha_{0.5}$ (left panel), similar to the observations. Again, the young mass fraction is rather low ($\lesssim$10%). While the intermediate-age mass fractions are overall significantly higher (and therefore the old mass fraction lower) because of the systematic age differences (Section 14.2), we again find a positive correlation with $\alpha_{0.5}$ (and a negative correlation for the old mass fractions). Here the p-values for the correlations are 0.01 and 0.02 for intermediate and old ages, respectively, which are both statistically significant. While the slopes are shallower than the observed fits, the observed values at lower $\alpha_{0.5}$ ($\sim 1 \times 10^{-9}\,\mathrm{L_\odot}^{-1}$) lie very close to the extrapolated simulated fit, indicating good agreement with the observations despite the systematic age offset of the simulations. The observed and simulated correlations are consistent with the results by Valenzuela et al. (2019,

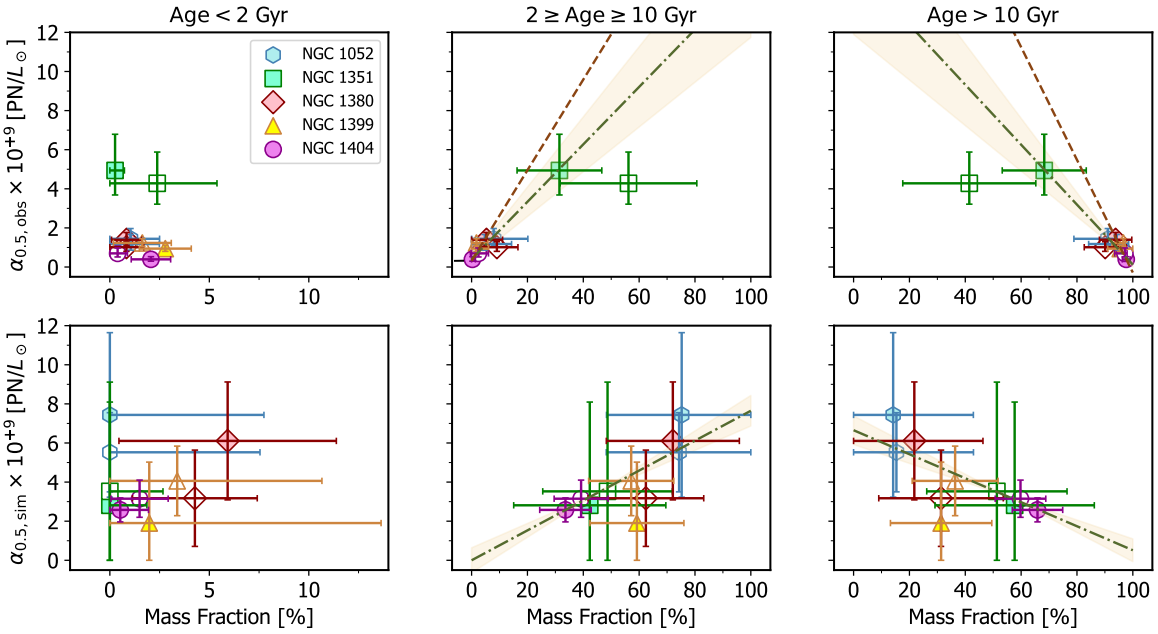


Figure 14.5: *Top*: Observed luminosity-specific PN number $\alpha_{0.5}$ in the brightest 0.5 mag of the PNLF compared to the underlying stellar age mass fractions in three bins of young (<2 Gyr), intermediate (2–10 Gyr), and old (>10 Gyr) stars. The five galaxies are shown with respect to their inner (solid markers) and outer (open markers) regions. The error bars indicate the statistical uncertainties. The dash-dotted green lines indicate the linear fits for the intermediate-age and old bins, and the shaded areas indicate the fit uncertainty range. The dashed brown lines are the linear fits excluding the data points of NGC 1351. *Bottom*: Same relations as in the top panels, but for the simulated analog galaxies. The error bars indicate the scatter among the six analog galaxies per observed counterpart. *This is figure 12 from Soemitro et al. (2025).*

2025c) that the bright-end of the PNLF is populated by PNe with ages between 2 and 10 Gyr. For older stellar populations to reach the bright end, further pathways such as blue straggler stars (e.g., Ciardullo et al. 2005) or a scatter of the initial-to-final mass relation (e.g., Jacoby & Ciardullo 2025) would be necessary.

Comparing the $\alpha_{0.5}$ values with the metallicity [M/H], we see for both simulations (left) and observations (right) in Figure 14.6 that $\alpha_{0.5}$ is higher in more metal-poor galaxies. The linear fit is shallower for the observations (comparing the dash-dotted green lines), but again the statistically significant correlation ($p = 0.001$) in the observations becomes statistically insignificant without taking NGC 1351 into account ($p = 0.48$). In the simulations, the scatter is relatively large among the galaxies and also among the respective analog galaxies for a given observation (seen by the error bars), leading to a larger uncertainty of the fit with a non-statistically significant correlation ($p = 0.33$). Nevertheless, the slight trend found here is consistent with some findings of high α parameters in the metal-poor outskirts of ETGs (e.g., Longobardi et al. 2013, 2015; Hartke et al. 2017, 2020). As for the trend with ages, additional galaxies with a stellar population similar to that of NGC 1351 are needed to confirm the present results, especially given that NGC 1351 is an outlier in multiple respects. In both the simulation and the observations, there is no clear trend between the inner and outer parts of the galaxies with respect to their values of $\alpha_{0.5}$. Differences in the conclusions of previous studies with respect to a trend with metallicity (e.g., Ciardullo et al. 2005; Galán-de Anta

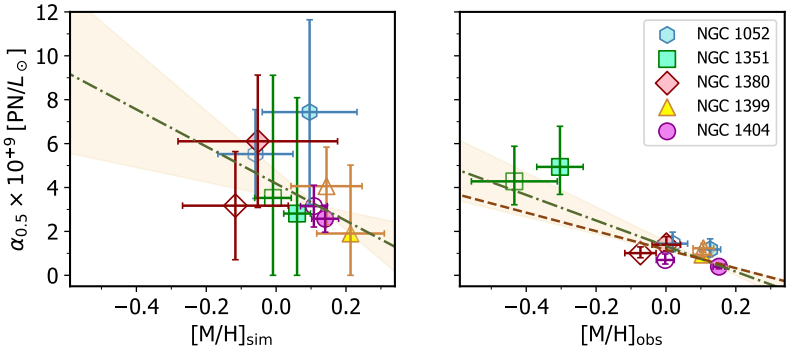


Figure 14.6: Luminosity-specific PN number $\alpha_{0.5}$ in the brightest 0.5 mag of the PNLF compared to the underlying stellar metallicity [M/H] from the simulated analog (left) and observed (right) galaxies. The five galaxies are shown with respect to their inner (solid markers) and outer (open markers) regions. The simulated error bars indicate the scatter among the six analog galaxies per observed counterpart, and the observed error bars the statistical uncertainties. The dash-dotted green lines indicate the linear fits, and the shaded areas indicate the fit uncertainty range. The dashed brown line for the observations is the linear fit excluding the data points of NGC 1351. *These are two of the panels in figure 13 from Soemitro et al. (2025).*

et al. 2021) may be related to variations in α-element abundances [α/Fe], which includes oxygen. Since PICS currently does not take into account α-element abundances, we refer to Soemitro et al. (2025) for a more detailed discussion of [α/Fe] for the five ETGs, where there is a positive correlation with $\alpha_{0.5}$.

14.3 Observations of M 105

In the following, we present the observational data of M 105 used by Hartke et al. (in prep.), which combines observations from multiple instruments and programs. The two preceding works by Hartke et al. (2020, 2022) analyzed PNe from the extremely-extended PN.S (e^{2}PN.S) ETG survey and from narrow-band photometry from Suprime-Cam at the Subaru telescope (Miyazaki et al. 2002), which are shown in the right panel of Figure 14.7. Of the 319 PNe with line-of-sight velocity measurements from e^{2}PN.S, Hartke et al. (2022) determined 225 of them to be associated with M 105 (colored points) and the rest with NGC 3384 (gray points), where both galaxies are part of the Leo I group. The M 105 PNe are colored by the probability to be associated with the envelope (tracing the IGL) of M 105, w_{envelope}. The 137 PNe identified with Suprime-Cam have more accurate [O III] magnitude measurements (with uncertainties of $m(5007)$ of around ±0.05 mag) compared to PN.S (±0.2 mag) and are indicated by the dark gray circles. We split the PN population into three components: core (inner effective radius R_{eff} = 2.7 kpc, as measured by Capaccioli et al. 1990), halo (1–7.5 R_{eff}), and envelope ($\gtrsim$7.5 R_{eff}). The PNe detected in the inner 1 arcsec^2 MUSE region are considered the core PNe. The PNe from Hartke et al. (2022) with $w_{\text{envelope}} \leq 0.5$ are classified as halo PNe, and the others are envelope PNe. For each of the PN subsamples, we fit the classical PNLF (Equation 7.2 with $c_2 = 0.307$) following Scheuermann et al. (2022) and assuming the SBF distance of 10.3 Mpc obtained by Tonry et al. (2001).

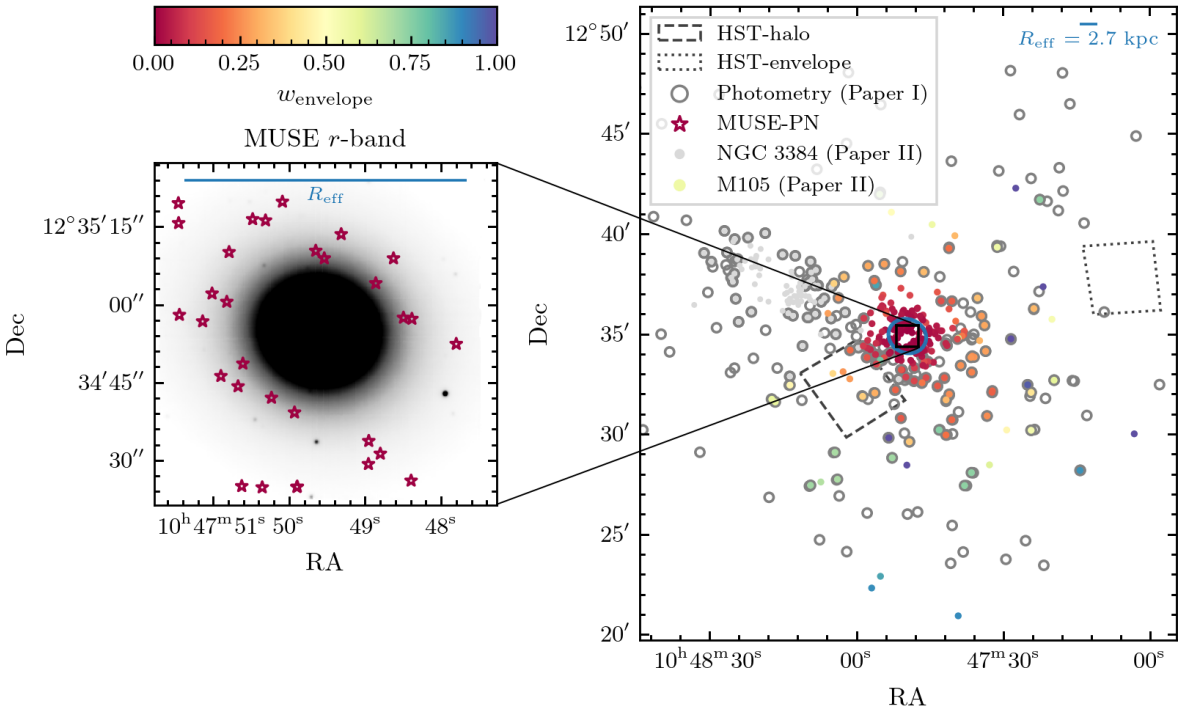


Figure 14.7: Positions of PNe around M 105. *Left*: Central region of M 105 as measured with MUSE in the reconstructed r-band with overplotted PNe (red stars). *Right*: Environment of M 105 and the detected PNe from PN.S data belonging to M 105 (colored points) and NGC 3384 (gray points) based on the decomposition of Hartke et al. (2022). Dark gray circles indicate PNe with accurate [O III] magnitude measurements from Suprime-Cam (Hartke et al. 2020). The color of PNe belonging to M 105 indicates the probability of being associated with the envelope, w_{envelope}. The solid black square shows the region observed by MUSE shown in the left panel, and the dashed and dotted black rectangles mark the halo and envelope regions observed by HST (Harris et al. 2007; Lee & Jang 2016), respectively. The length of the effective radius $R_{\mathrm{eff}} = 2.7$ kpc is indicated by the top blue bars in both panels, and by the blue ellipse in the right panel. *This is figure 1 from Hartke et al. (in prep.).*

In this work, we also used data from the MUSE wide-field mode commissioning, during which the center of M 105 was also observed. The PNe were identified in the MUSE data using an automated version of the DELF method (Roth et al. 2021; Ennis et al. 2026), building on the version used for the five ETGs discussed in Section 14.1.1, and by removing interlopers like supernova remnants, H II regions, or other background sources. The PNe detected in the MUSE data are shown in the left panel of Figure 14.7.

We also determined stellar population properties from the MUSE data using `GIST` (Bittner et al. 2019), measuring a mean light-weighted stellar metallicity of [M/H] = 0.04 and an age of 12.4 Gyr for this core region. To compare the core to the halo and envelope, we use the results from Harris et al. (2007) and Lee & Jang (2016) for the outer regions from red giant branch (RGB) stars observed with the Hubble Space Telescope (HST). For the halo, the stellar metallicity is [M/H] = 0.01 and the age 12 Gyr, and for the envelope, the metallicity is [M/H] = −1.10 and the age also 12 Gyr. The halo and envelope regions observed with HST are shown as dashed and dotted rectangles in Figure 14.7.

14.4 Comparison to PNe modeled in single stellar populations

In the following, we compare the stellar population properties found for the three components (core, halo, and envelope) with the PN populations associated with them. We additionally employ theoretical results from the fiducial PICS model (Valenzuela et al. 2025c) for SSPs, using the results from the SSP grid shown in Figure 8.10.

14.4.1 Stellar populations and the PNLF bright-end cutoff

The bright-end cutoff $M^*(5007)$ of the PN populations in all three components are similar to each other, with values of $-4.60^{+0.21}_{-0.33}$, $-4.48^{+0.10}_{-0.15}$, and $-4.42^{+0.15}_{-0.23}$ mag for the core, halo, and envelope, respectively. Note that the slightly fainter bright-end cutoff for the envelope could be related to the small number of PNe brighter than the completeness limit to which the PNLF was fit, consisting of only 10 PNe (compared to 24 and 31 for the core and halo, respectively). We show the relation of $M^*(5007)$ with metallicity in Figure 14.8, where we compare the data points for the three components to the theoretical predictions of Dopita et al. (1992, gray line) and Valenzuela et al. (2025c, cross markers and dotted lines). The core and halo data points for M 105 agree well with the predictions by Dopita et al. (1992). For PICS, only the intermediate-age PICS models ($\lesssim$6 Gyr) follow a similar relation, thereby leading to similar cutoff magnitudes as the core and halo observations. However, older stellar populations, as measured for M 105, lead to much fainter cutoffs at [M/H] ≈ -0.1, by 1.5–2 mag. The differences become more severe for the metal-poor envelope: while the observed bright-end cutoff is only slightly fainter than for the core and halo, the theoretical models all predict significantly dimmer cutoffs (by $\gtrsim$0.6 mag), even for intermediate-age and young stellar populations that follow the relation of Dopita et al. (1992). Based on this comparison, there is a clear lack of bright PNe in the PICS models for old stellar populations, and simultaneously the question is raised why the envelope PNe do not exhibit a fainter PNLF cutoff magnitude compared to the more metal-rich core and halo PNe.

14.4.2 Stellar populations and the luminosity-specific PN number

For each of the three components, we determined the luminosity-specific PN number $\alpha_{2.5}$ of the brightest 2.5 mag of the PNLF fits to the corresponding PNe. Figure 14.9 shows the observed values of $\alpha_{2.5}$ as a function of metallicity compared to the predictions by Buzzoni et al. (2006, top panel) and Valenzuela et al. (2025c, bottom panel). Buzzoni et al. (2006) assumed an initial-to-final mass relation with a mass loss parameter of $\eta = 0.3$ (Iben & Renzini 1983), for which we scaled the α_8 values to $\alpha_{2.5}$ according to the classical PNLF form by Ciardullo et al. (1989). The values by Valenzuela et al. (2025c) are taken from Table D.1, which are based on the actual counts of PNe brighter than −2 mag. The observations show a

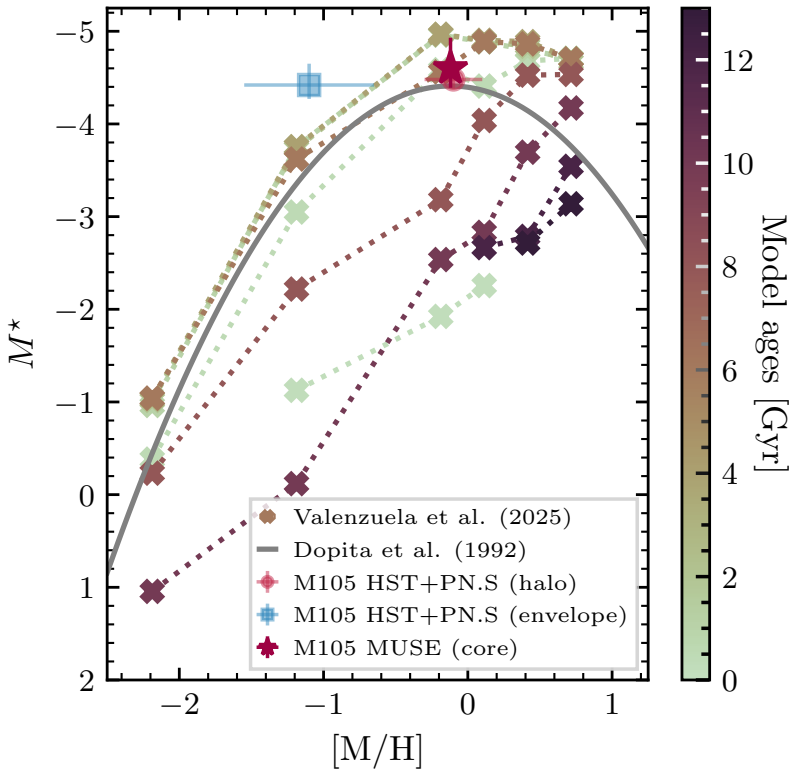


Figure 14.8: Bright-end cutoff magnitude $M^*(5007)$ of the PNLF as a function of metallicity compared between observations and models. The observations are for the core (red triangle), halo (red circle), and envelope (blue square) PNe, where the error bars indicate the measurement uncertainties. The theoretically predicted relation from Dopita et al. (1992) is shown as the gray line. For the PN populations obtained from PICS by Valenzuela et al. (2025c) for different SSPs, we take the respective brightest PN magnitude (i.e., the brightest magnitude that each PNLF reaches in Figure 8.10), indicated by the cross markers. The PICS models of the same SSP age are connected with dotted lines and colored according to the respective SSP age. No data points are plotted for some of the youngest and oldest models at lower metallicities where no PNe are predicted by PICS. *This is figure 9 from Hartke et al. (in prep.).*

significantly higher value of $\alpha_{2.5}$ in the metal-poor envelope compared to the halo and core at solar metallicity, with the core having the lowest $\alpha_{2.5}$ value.

The model predictions interestingly show contrasting results as a function of age and metallicity. Buzzoni et al. (2006) predict $\alpha_{2.5}$ being rather constant as a function of metallicity at old ages and showing a decrease toward higher metallicities around the solar value at younger ages. They also find an increase in $\alpha_{2.5}$ toward older stellar ages. As a result, their predictions are close to the observed $\alpha_{2.5}$ value for the envelope of M 105 at old ages, while the more metal-rich but equally old PN populations in the core and halo have significantly lower values compared to the corresponding predictions for 12 Gyr. In contrast, Valenzuela et al. (2025c) predict rather constant values of $\alpha_{2.5}$ at intermediate-ages of 2–8 Gyr, but an increase of $\alpha_{2.5}$ toward super-solar metallicity systems at older and younger ages. Their results for old stellar populations agree well with the observed values for M 105 in the core and halo, but at the low metallicity of the envelope, only the much younger stellar population of 6 Gyr

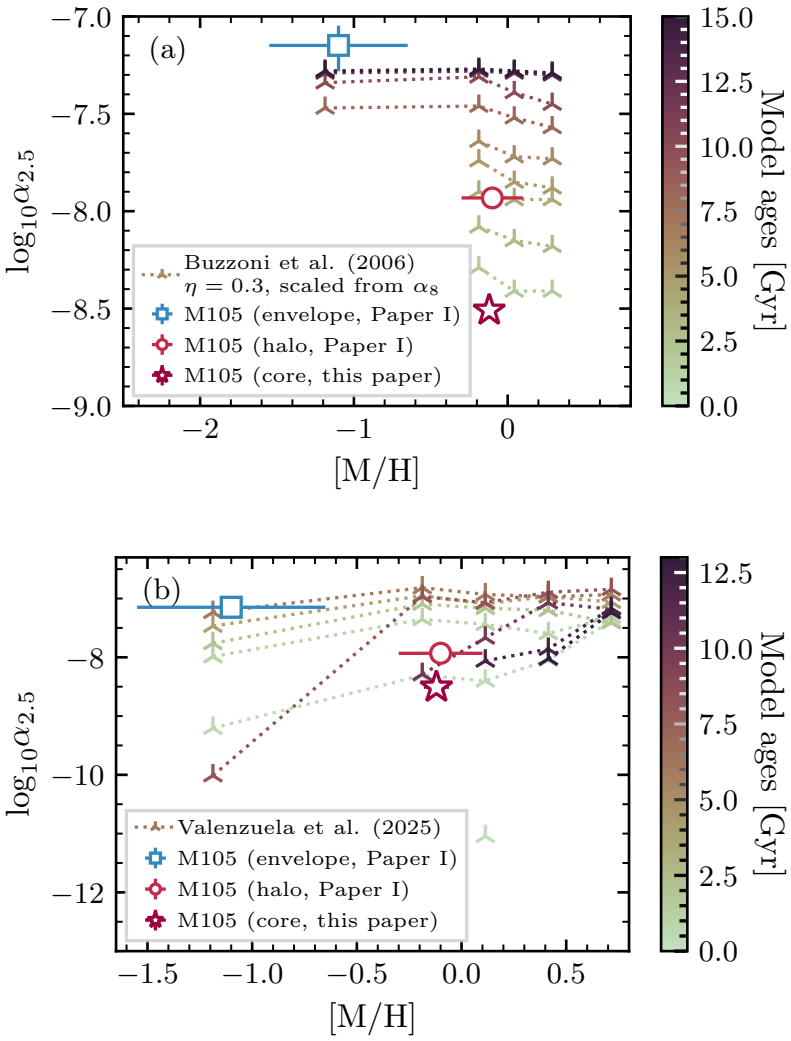


Figure 14.9: Luminosity-specific PN number $\alpha_{2.5}$ for the brightest 2.5 mag of the PNLF as a function of metallicity [M/H] compared between observations of M 105 and models by Buzzoni et al. (2006, top) and Valenzuela et al. (2025c, bottom). The observations are for the core (red triangle), halo (red circle), and envelope (blue square) PNe, where the error bars indicate the measurement uncertainties. The model lines connect data points corresponding to the same SSP age, which also determines the color. No data points are plotted for some of the youngest and oldest models at lower metallicities where no PNe are predicted. Note that the axis and color bar ranges are different between the top and bottom panels. *This is figure 10 from Hartke et al. (in prep.).*

would match the observed envelope value. Each of the models therefore can explain one part of the observations, but fails to be in agreement with the other.

One possibility to resolve some of the tension between the models with respect to $\alpha_{2.5}$ lies in its assumed scaling from α_8 (the luminosity-specific number of PNe in the brightest 8 mag) by Buzzoni et al. (2006), based on the classical PNLF form by Ciardullo et al. (1989). Assuming a bright-end cutoff magnitude of $M^*(5007) \approx -4.5$ mag and a faint-end slope of $c_2 = 0.307$, the scaling between the two quantities becomes $\log_{10}\alpha_8 \approx \log_{10}\alpha_{2.5} + 1$. However, the faint part of the PNLF can take on different slopes (e.g., Longobardi et al. 2013; Hartke et al. 2017), include an additional exponential term (Bhattacharya et al. 2021), or contain dips (e.g., Jacoby & De Marco 2002; Hernández-Martínez & Peña 2009; Longobardi et al. 2015, 2018; Soemitro et al. 2023). These features have been related to the underlying

stellar populations and have also been found in PN models (e.g., Méndez et al. 2008; Gesicki et al. 2018; Valenzuela et al. 2019, 2025c), indicating that the classical form of the PNLF cannot be assumed to hold over eight magnitudes below the bright end.

In the top two panels of Figure 14.10, we compare the model predictions of Buzzoni et al. (2006) and PICS (Valenzuela et al. 2025c, see the values in Table 8.2) for α_8 as a function of stellar age for different metallicities. While Buzzoni et al. (2006) predict a slow increase of α_8 with stellar age independent of the metallicity, PICS finds a steep increase at young ages of $\lesssim$2 Gyr, followed by an almost constant value with age, and there is an overall trend of larger α_8 with metallicity. Only for the lowest metallicity at around [M/H] ≈ -2, there is a more gradual increase across the ages, and α_8 is significantly lower than for higher metallicities. Overall, the values around solar metallicity (green) agree well between the two models for old ages at $\gtrsim$10 Gyr. We also show the results of the typically used scaling between α_8 and $\alpha_{2.5}$ through the models of Valenzuela et al. (2025c) in the bottom panel (also see the corresponding values of $\alpha_{2.5}$ in Table D.1). Clearly, the relations with stellar age differ from the actual values of α_8 predicted from PICS (middle panel). This is especially the case for low metallicities (where no bright PNe are found in the brightest 2.5 mag) and for ages larger than ∼8 Gyr for solar and super-solar metallicities (green and yellow), where α_8 is actually higher than suggested by $\alpha_{2.5}$.

The tension between models and observations with respect to $M^*(5007)$ and $\alpha_{2.5}$ could also be related to missing physics in the models or observational biases as discussed in Section 14.2.2. For the analysis performed for M 105, we also propose that the presence of intermediate-age stars could explain the more luminous PNe as well as the higher luminosity-specific PN number in the metal-poor envelope. While several observations agree that the stars are overall old in the outer halo (e.g., Vazdekis et al. 1997; Trager et al. 2000), Harris et al. (2007) noted how stars older than ∼5 Gyr differ little in color, such that the presence of an intermediate-age stellar population is not excluded. However, Harris et al. (2007) ruled out younger stellar populations based on the resolved stellar observations. Also for the core of M 105, it is actually composed of a composite stellar population instead of an SSP (as implicitly assumed in the figures shown here), where a subset of stars in the intermediate-age regime could bring the observational results closer to the predictions as suggested in Figure 14.5.

14.5 Summary and conclusion

From MUSE archival data, we have analyzed the stellar and PN populations in a total of six ETGs to compare them to the results from simulations and models. The IFU measurements with MUSE enable PNe to be detected and stellar population synthesis to be performed from the same data. For each of the five ETGs from the samples of Roth et al. (2021) and Jacoby et al. (2024), we split the identified PNe into an inner and an outer group to compare them based on the variations of the stellar populations parameters. We further selected six simulated analog galaxies per observed galaxy based on morphology, size, and color, for which we modeled the PN populations with the framework PICS to perform the analysis analogously.

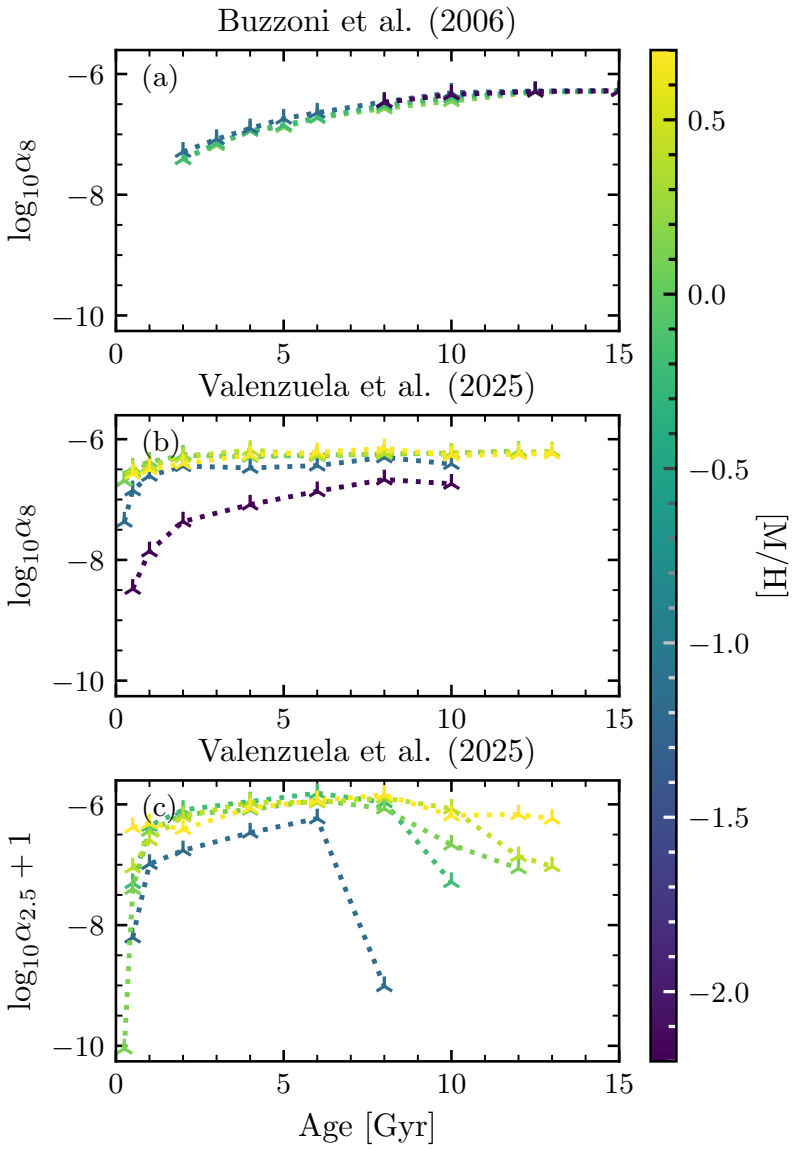


Figure 14.10: Luminosity-specific PN number α_8 for the brightest 8 mag of the PNLF as a function of stellar age compared between the models by Buzzoni et al. (2006, top) and Valenzuela et al. (2025c, middle), additionally including the typically used scaling of $\log_{10}\alpha_8 \approx \log_{10}\alpha_{2.5} + 1$ applied to the results from Valenzuela et al. (2025c, bottom). The data points and connecting dashed lines are colored by metallicity [M/H]. *This is figure 11 from Hartke et al. (in prep.).* No data points are plotted for some of the more metal-poor models at older ages where no PNe are predicted.

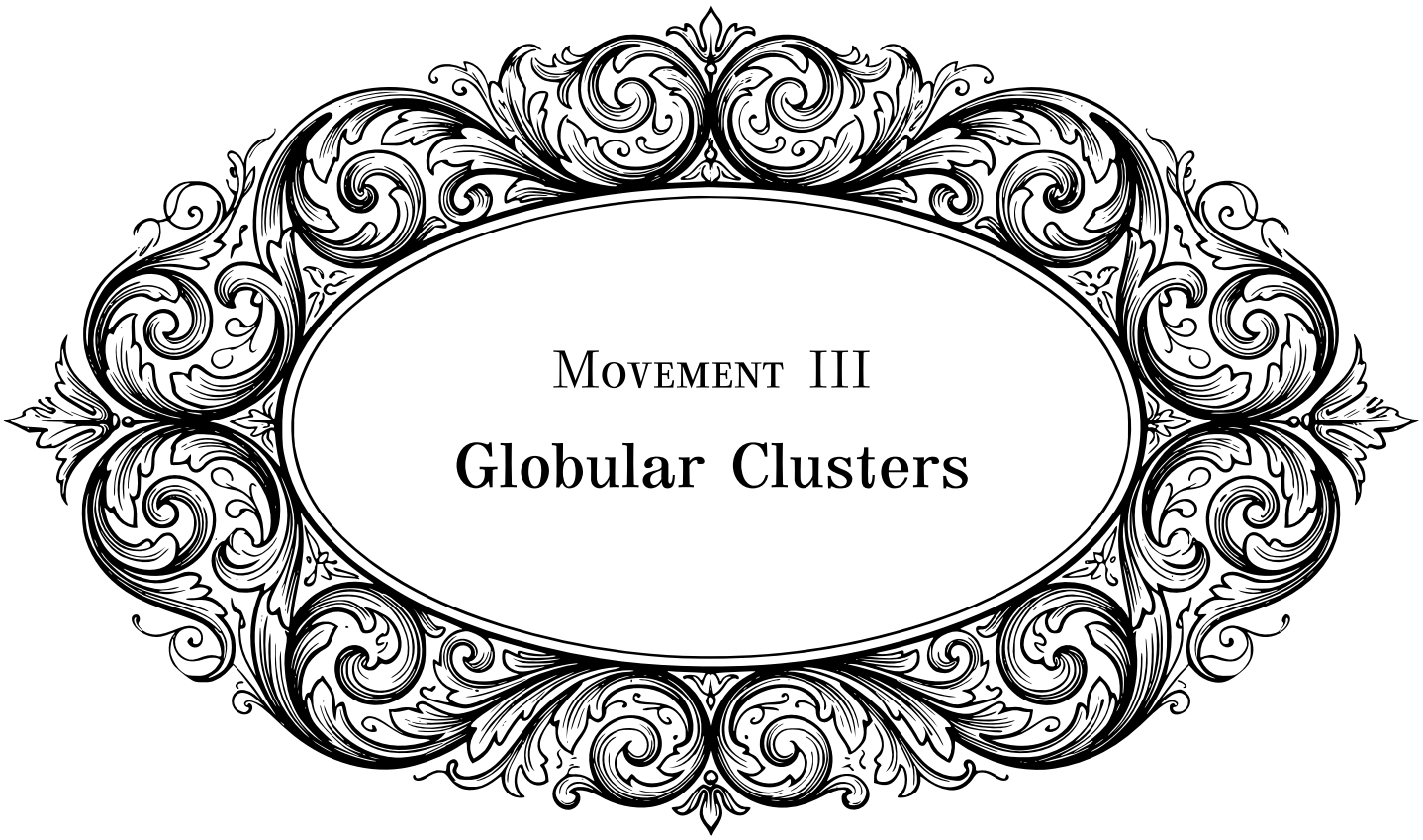
Furthermore, building on the results of Hartke et al. (2020, 2022), we combined PN and stellar population data of the outskirts of M 105 from PN.S and HST with MUSE commissioning data of the galaxy's core. This yielded measurements for three components: the core of M 105 within an effective radius, its halo, and the extended envelope as a tracer of the IGL in the Leo I group. We compared these results to the predictions by Dopita et al. (1992), Buzzoni et al. (2006) and Valenzuela et al. (2025c) for SSPs.

To relate the PNe to the underlying stellar populations, we considered several properties. For the PNe, we determined their PNLF bright-end cutoff magnitude $M^*(5007)$ and the luminosity-specific PN number α for the PNe brighter than a certain magnitude. For the stellar population, we considered the stellar age and metallicity, and for the five ETGs, we also considered the stellar mass fractions within three age bins (with limits at 2 and 10 Gyr).

Across all observations, we recover similar PNLF bright-end cutoffs for PN populations belonging to the same galaxy (where the distance does not vary) despite variations in stellar populations, and in general do not find a significant dependence on age or metallicity. The same holds true for the simulated galaxies, though there is a larger scatter to brighter and fainter cutoff magnitudes, similar to the observed scatter when assuming SBF or TRGB distance measures. While the simulated analogs are systematically younger than the measured observed ages, we still find a strong positive correlation of $\alpha_{0.5}$ with the stellar mass fraction of intermediate-age stars (2–10 Gyr) for both the observed and simulated galaxies. This is accompanied by a negative correlation with the stellar mass fraction of old stars (>10 Gyr). We conclude that most PNe near the bright-end cutoff of the PNLF originate from intermediate-age stellar populations. The relation of $\alpha_{0.5}$ with metallicity has a larger scatter, but we find indications of $\alpha_{0.5}$ being larger for metal-poor systems from both the observed and simulated galaxies.

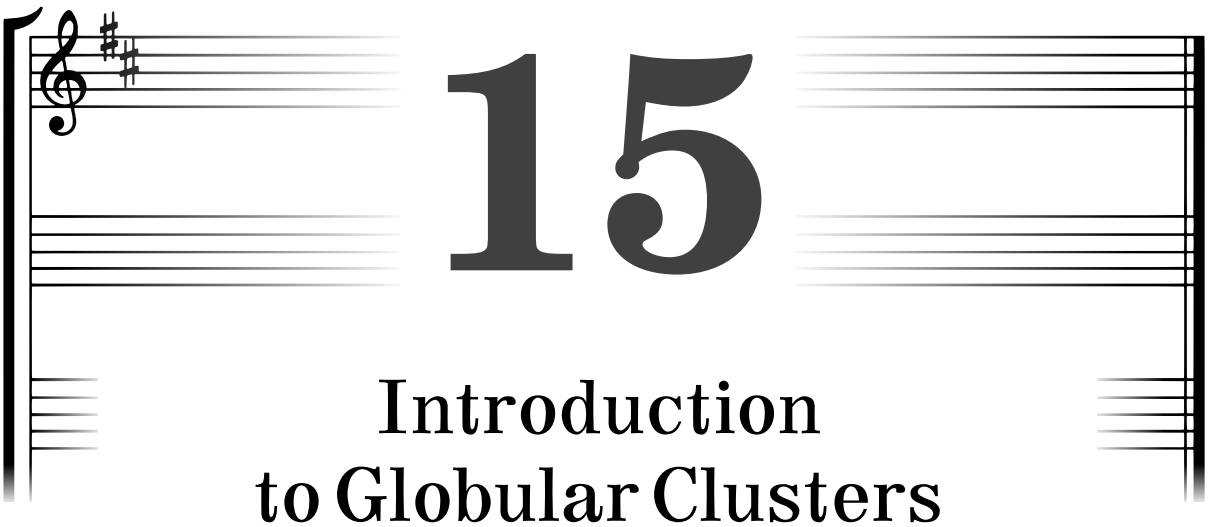
From the core, halo, and envelope regions of M 105, we find that the PNLF bright-end cutoff remains rather constant despite metallicity differences of an order of magnitude. In contrast, $\alpha_{2.5}$ is significantly higher in the metal-poor envelope than in the core and halo at solar metallicity. These results stand in conflict with models predicting $M^*(5007)$ to get significantly dimmer toward lower metallicities. Even the core and halo cutoff magnitudes are only consistent with PNe from younger stellar populations according to the PICS model. Moreover, while the $\alpha_{2.5}$ values of the core and halo are consistent with old stellar populations from PICS, and $\alpha_{2.5}$ of the envelope PNe is consistent with the predictions for old stellar populations of Buzzoni et al. (2006), the models do not agree with $\alpha_{2.5}$ of the respective other component(s). To resolve these tensions, we propose two possible factors. On the model side, further physics may need to be included. On the observational side, the results indicate that a small fraction of intermediate-age stars may be present in addition to the overall old stellar population. Such intermediate-age and metal-poor stars could have been accreted through mini mergers (e.g., Amorisco 2017; Nipoti 2025).

To conclude, these first comparisons between the predictions from PICS and observations of PNe and their underlying stellar populations mark a major step forward for PN studies. Future refinements to the models will allow us to explore further possibilities regarding the formation of bright PNe, especially in metal-poor or old stellar populations. Additionally, more observations connecting PNe to the stellar populations and improved stellar population synthesis methods will be necessary to draw a fuller picture of PN populations and their origins. To this end, the upcoming era of extremely large telescopes such as the ELT will begin enabling these kinds of measurements in much higher quality and at significantly larger distances.



Movement III

Globular Clusters



15

Introduction to Globular Clusters

This chapter contains parts from the introductions of Valenzuela (2023) and Valenzuela et al. (2024b, 2025a), whose results are presented in the subsequent chapters.

As bright and compact star clusters, globular clusters (GCs) have long been studied in the Milky Way (MW) and many other galaxies. They have generally been found to be old and metal-poor, with no compelling evidence for residing within their own dark matter halos. With masses between 10^4 and $10^6\,M_\odot$ and sizes of only a few pc (Baumgardt & Hilker 2018), GCs appear as bright point sources outside the Local Group, where they have been detected out to very large distances at $z \approx 0.44$ ($\sim$1.7 Gpc) with JWST (Harris et al. 2025), and even to $z \approx 1.4$ through gravitational lensing (Mowla et al. 2022). Their old ages and the fact that they are found in galaxies of all types and masses enable them to be used as tracers for galaxy formation, evolution, and multiple present-day galaxy properties. For this reason, the third Movement of this thesis focuses on investigating GCs as stellar tracers[1] and what their properties can reveal about galaxy formation histories.

[1] In this context, the term *stellar* tracer should not imply that the underlying stellar component is necessarily traced by GCs, but rather that GCs consist of stars and can be used as tracers for the host galaxy.

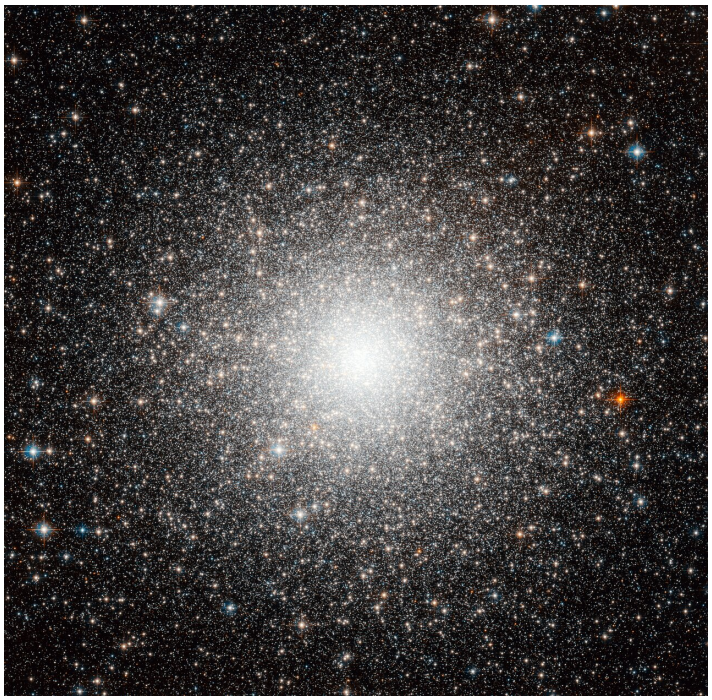


Figure 15.1: Example of a GC imaged with the Hubble Space Telescope, known as Messier 54, at a distance of ~25 kpc. It is associated with the Sagittarius Dwarf Elliptical Galaxy, a satellite of the Milky Way. *Image credit: ESA/Hubble & NASA.*

Figure 15.1 shows an example of a GC belonging to the MW's dwarf satellite Sagittarius (M 54[2], at a distance of about 25 kpc), which is spatially resolved. In contrast, more distant GCs outside the Local Group generally appear as point sources.

15.1 A type of star cluster

As massive and dense agglomerates of stars, GCs are a type of star cluster that is gravitationally bound, unlike open clusters. Compared to them, they are overall more massive (~10^4 to 10^6 $M_\odot$) and significantly more compact, with half-mass radii between 1 and 30 pc (as measured by Baumgardt & Hilker 2018 for the GCs in the MW). In terms of their size and luminosity, GCs lie directly next to ultracompact dwarfs (UCDs), which are more luminous and larger (see Figure 15.2), but appear to be a distinct class of objects (Brodie et al. 2011). In general, GCs have been measured to be old, with ages mostly beyond ~10 Gyr in the MW (e.g., Forbes & Bridges 2010; Massari et al. 2023) and are believed to have had their formation peak before that of cosmic star formation, potentially playing an important role in early galaxy formation and reionization (e.g., Renzini 2017; Gratton et al. 2019). Moreover, GCs have been found to be metal-poor, with metallicities of MW GCs being measured to be in the range of [Fe/H] ~ −2.2 to −0.6 (e.g., Forbes & Bridges 2010; Dotter et al. 2010, 2011; VandenBerg et al. 2013). With respect to their origins, testing theoretical predictions of GC formation is challenging due to their old ages. However, with the recent launch of JWST and

[2] `https://esahubble.org/images/potw1145a/`

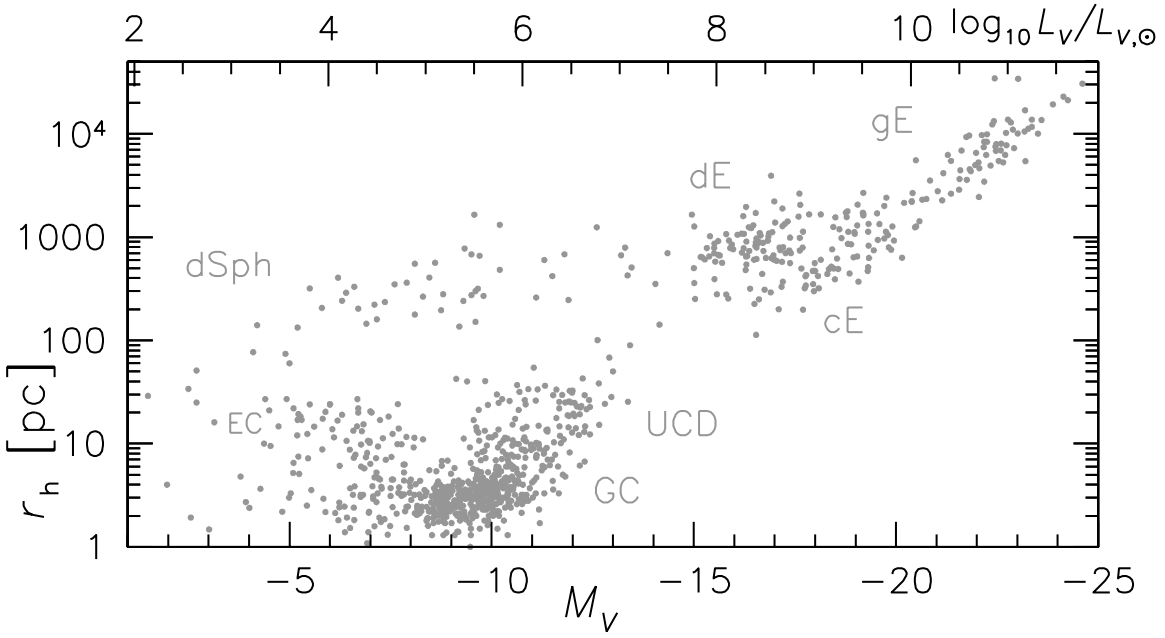


Figure 15.2: Magnitude-size relation of different types of stellar structures, where the half-light radius is shown as a function of absolute magnitude (or luminosity, see the top axis) in the V-band. The annotated galaxy types include GCs, ultracompact dwarfs (UCD), extended clusters (EC), dwarf spheroidals (dSph), dwarf ellipticals (dE), compact ellipticals (cE), and giant ellipticals (gE). *This is the top panel of figure 8 from Brodie et al. (2011).*

observations of young stellar clusters in strongly-lensed high-redshift galaxies, new insights into their formation are likely to emerge in the near future.

Further internal properties of GCs are also matters of ongoing research, which are briefly mentioned here, but are not central to the aims of the subsequent chapters. Analyses of stellar populations within GCs have shown that nearly all GCs host significant spreads of abundances, indicative of multiple stellar populations within them (e.g., Renzini 2008; Bastian & Lardo 2018). The most massive GC in the MW, Omega Centauri, even features a wide metallicity range among its stars, which has been interpreted as being the remnant of an accreted dwarf galaxy (e.g., Lee et al. 1999; Bedin et al. 2004; Bastian & Lardo 2018). Many exotic objects are found in GCs due to the high fraction of binary star systems, including blue stragglers, millisecond pulsars, and X-ray binaries (Gratton et al. 2019). Binaries are furthermore important for the dynamical evolution of GCs as they lead to dynamical heating (e.g., Heggie 1975; Hills 1975). Over time, mass segregation can occur where massive stars are concentrated toward the center (e.g., Spitzer 1969; Hillenbrand & Hartmann 1998; Guszejnov et al. 2022). Several internal and external processes such as dynamical evaporation, stellar evolution, and tidal shocks additionally lead to mass loss of a GC (McLaughlin & Fall 2008; Baumgardt et al. 2019; Webb et al. 2019, e.g.,), where tidal arms can also be seen extending from some GCs (e.g., Odenkirchen et al. 2003).

In the following, further details are outlined on two important topics concerning GCs. They relate to the formation of GCs and are relevant to the subsequent chapters.

Ages. While measurements of their ages have large uncertainties, observations of GCs in and beyond the MW suggest that they are generally old, with ages mostly older than 10 Gyr (e.g., Salaris et al. 1997; Cohen et al. 1998; Strader et al. 2005; VandenBerg et al. 2013; Usher et al. 2019). Some galaxies have been found to contain younger GC populations as well, with ages below 8 Gyr (e.g., Sharina et al. 2006) or even below 3 Gyr (e.g., Goudfrooij et al. 2001b; Sharina et al. 2006; Chomiuk et al. 2008; Martocchia et al. 2018; Sesto et al. 2018), though such systems still contain a significant old GC population (e.g., Goudfrooij et al. 2001a, for NGC 1316, consistent with models of 14 Gyr old GCs), and only lower-mass galaxies like the Magellanic Clouds may host mostly younger GCs, where the SMC only has GCs below 8–9 Gyr, with most lying around 2–5 Gyr (e.g., Parisi et al. 2014).

Formation scenarios. Despite GCs having been studied in detail in galaxies, their formation is still poorly understood. Many different theoretical approaches have been formulated for GC formation, with early ideas proposing them to have formed before galaxies in gravitationally bound clouds (Peebles & Dicke 1968), through infalling cold gas fragmentation (Fall & Rees 1985) or formation through a gas-rich merger (Ashman & Zepf 1992). Later ideas included GCs forming in their own dark matter (DM) halos (e.g., Bromm & Clarke 2002; Bekki 2006; Boley et al. 2009) and GCs being former nuclear star clusters (e.g., Mackey & van den Bergh 2005; Lee et al. 2009). Some of the recent proposals are based on colliding scenarios like dwarf galaxy mergers (Lahén et al. 2019) or collisions of DM subhalos (Madau et al. 2020). Other scenarios include relative streaming velocities between baryons and DM (e.g., Naoz & Narayan 2014; Lake et al. 2021, though it has been put into question whether this channel could reach sufficiently high masses, see Schauer et al. 2021), formation within accreting gas filaments (van Donkelaar et al. 2023), accreted nuclear star clusters within dwarfs (Gray et al. 2025), or disc fragmentation (Mayer et al. 2025). However, as of yet it is still under debate which of these channels are actually responsible for the formation of real GCs and how frequent they are.

15.2 Globular cluster systems

Considering the entire GC system of a galaxy has been a key to better understanding both GCs and their host galaxies. In the following, I highlight the observed color bimodality of GC systems and then give an overview of extragalactic and Galactic GC systems as well as what can be learned from them.

15.2.1 Color bimodality

Observations have shown that there is a color bimodality of GCs around more massive galaxies, where the GCs come in two groups of colors and metallicities: red, metal-rich GCs, and blue, metal-poor GCs (e.g., Brodie & Strader 2006; Usher et al. 2012). The fraction of red GCs has been found to increase with halo mass (Harris et al. 2015). The MW itself has long

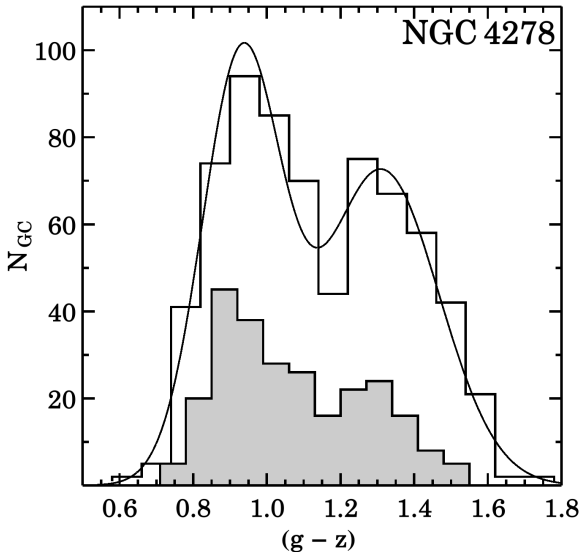


Figure 15.3: Color distribution of the GC system in NGC 4278 with a clear bimodality. The empty and filled histograms indicate the candidate and confirmed GCs, respectively. The solid curve shows the mixture model fit to the candidate histogram. *This is the middle right panel of figure 5 from Pota et al. (2013).*

been known to have a bimodal metallicity distribution (e.g., Zinn 1985). An example of a particularly strong GC color bimodality for a galaxy is shown in Figure 15.3. Both types are found in most massive galaxies, where the red GCs tend to populate the inner regions and trace the stellar light distribution (e.g., Peng et al. 2004a; Schuberth et al. 2010; Dolfi et al. 2021), whereas blue GCs lie further out and can have a different spatial distribution (e.g., Forbes et al. 1997; Schuberth et al. 2010; Faifer et al. 2011; Kluge et al. 2023). These differences have suggested that red and blue GCs are formed through different pathways (e.g., Forbes et al. 2018a): blue GCs may tend to form in small galaxies at early times, later being accreted onto more massive galaxies (e.g., Côté et al. 1998; Schuberth et al. 2010; Forbes & Remus 2018), whereas red GCs may later form after the gas has been enriched, for example in starbursts caused by major gas-rich mergers (e.g., Ashman & Zepf 1992; Goudfrooij et al. 2001b; Schuberth et al. 2010; Harris et al. 2017b). However, the origin of this bimodality and the GC formation itself are still matters of research, and several formation mechanisms are currently being discussed (e.g., Kruijssen 2015; Kang & Lee 2021).

15.2.2 Extragalactic globular clusters

It has been found that GC systems are more abundant in more massive galaxies, where the mass of the galaxies' dark matter halos is strongly correlated with the number of GCs (e.g., Blakeslee et al. 1997; Harris et al. 2017a). This relation has in fact been found to be nearly linear and reaches from the dwarf galaxy regime (where galaxies can have as little as one GC or none at all; Forbes et al. 2018b) up to galaxy clusters with tens of thousands of GCs (Harris et al. 2016; Burkert & Forbes 2020). Even exotic systems such as ultra-diffuse galaxies (UDGs) with high DM fractions and abundant GC systems compared to their stellar component appear to follow this relation (e.g., Burkert & Forbes 2020; Forbes & Gannon 2025). In contrast,

the stellar mass of galaxies is not as closely correlated to the GC counts due to the nonlinear behavior and scatter of the stellar mass-halo mass relation (e.g., Harris et al. 2017a). As a result, the tight relation with the DM halo mass has led to GC abundances being used as a tracer for halo masses of galaxies (e.g., Spitler & Forbes 2009).

Beyond GC counts, multiple studies have attempted to infer GC stellar population statistics from extragalactic GC systems (see an overview of age measurements in Section 15.1; e.g., Puzia et al. 2005; Strader et al. 2005; Mora et al. 2008; Usher et al. 2019). A challenge for these types of studies is that, in contrast to GCs in the MW and its neighborhood, extragalactic GCs are observed as point sources. Because of this, measuring their ages is subject to large uncertainties, as only the integrated GC properties can be measured. For this reason, stellar population models and evolutionary tracks have to be used for extragalactic systems to estimate the ages.

15.2.3 Galactic globular clusters

In contrast to most extragalactic GCs, in the MW the stars of GCs can be individually observed, such that reasonably good measurements of their ages and metallicities can be determined through the color-magnitude diagram (CMD), which has been done for various GC subsamples in the MW (e.g., Salaris & Weiss 1998; Dotter et al. 2008; Marín-Franch et al. 2009). Figure 15.4 shows an example for the age determination of a MW GC by fitting isochrones to the CMD data of the cluster stars. Many of the now close to 200 known GCs in the Milky Way have been studied with respect to their stellar populations, including many recently detected GC candidates located in the Galactic bulge (e.g., Garro et al. 2024).

In the last decade, Gaia measurements have furthermore added phase space information on over a billion stars in the MW. From the wealth of data, the phase space properties of GCs have also been determined (e.g., Gaia Collaboration 2018a; Vasiliev 2019; Vasiliev & Baumgardt 2021), which has helped uncover more details of the early MW's history (e.g., Deason & Belokurov 2024). From the field stars, new structures in the phase space have been identified that likely fell into the MW at early times, such as Gaia-Sausage/Enceladus (GSE; Belokurov et al. 2018; Helmi et al. 2018). The GC phase space information has also provided researchers with the means to distinguish in-situ and ex-situ formed GCs (e.g., Belokurov & Kravtsov 2024; Chen & Gnedin 2024a) or even attempt to associate GCs with their progenitor host galaxy (e.g., Massari et al. 2019; Myeong et al. 2018; Forbes 2020; Callingham et al. 2022). As a result, the GC system of our own MW can be used as a dynamical probe and tracer of the assembly history in a uniquely powerful way.

15.3 Globular clusters as stellar tracers

Owing to their old ages, GCs have co-evolved with their host galaxies over cosmic time, indicating their potential to serve as valuable tracers for galaxy formation. Their spatial distribution and kinematics have long been used to trace properties in the outskirts of galaxies.

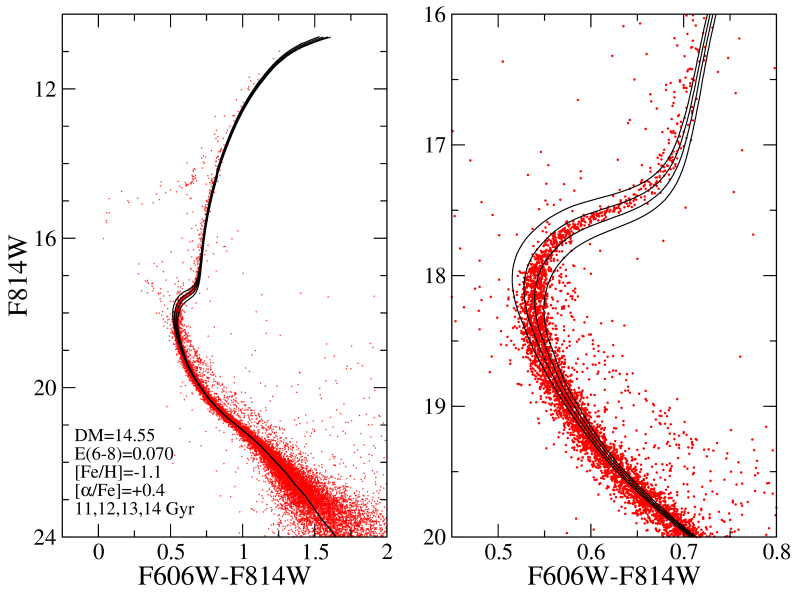


Figure 15.4: Color-magnitude diagram (CMD) of the stars (red points) in the MW GC NGC 6362 with four isochrone fits overplotted (black lines). *Left*: Full CMD showing the stellar main sequence (MS; straight sequence beginning at the lower right), the red giant branch (RGB; the upper curved sequence ending at the top right), and the subgiant branch (section right after the MS turnoff between the MS and RGB). *Right*: Zoom on the MS turnoff region, where the differences between the isochrone fits are more clearly seen. This is the relevant region for determining the age. The parameters of the four isochrones are shown in the bottom left of the left panel, stating the distance modulus (DM), color excess (E(6-8)), metallicity ([Fe/H]), alpha abundance ([α/Fe]), and the four ages used: 11, 12, 13, and 14 Gyr, with the oldest age corresponding to the isochrone with the shortest MS section. *This is figure 3 from Dotter et al. (2010).*

However, given the massive and compact nature of GCs, their formation must be linked to significant star formation and thus they should also serve as tracers for the past star formation.

15.3.1 Spatial and kinematic tracers

Because of their intrinsic brightness, GCs have also been used as tracer populations in the outskirts of other galaxies to study their mass distribution, kinematics, and formation history. One of the early large kinematic studies of GC systems was conducted by Peng et al. (2004a) for Centaurus A, a giant early-type galaxy (ETG), to constrain its evolution by studying the ages, metallicities, and kinematics of the GCs. They found that red GCs tend to match the kinematics of the planetary nebula population in their kinematic behavior, whereas blue GCs showed differences in their velocity dispersion and less kinematic correlation to the stars. Many GC studies have since then been performed on galaxy clusters and their member galaxies (e.g., Bridges et al. 2006; Lee et al. 2010; Strader et al. 2011; Li et al. 2015; Pota et al. 2015; Zhang et al. 2015; Fahrion et al. 2020) as well as on individual galaxies (e.g., Forbes et al. 2011; Foster et al. 2011; Norris et al. 2012; Dowell et al. 2014), including the Milky Way (e.g., Piatti 2019) and M 31 (e.g., Veljanoski et al. 2013, 2014). Moreover, systematic investigations of GC spatial and kinematic properties have also been made possible through surveys like SLUGGS (e.g., Pota et al. 2013; Brodie et al. 2014; Alabi et al. 2017; Dolfi et al. 2021). These

studies have collectively drawn a picture of GCs being good tracers for the enclosed mass and the spatial distribution of the DM halo (e.g., Zhu et al. 2014; Veršič et al. 2024b) and for past accretion events (e.g., Coccato et al. 2013), where red GCs generally trace the stellar light and blue GCs sometimes deviate from it (e.g., Dolfi et al. 2021). As described in Section 15.2.1, the color bimodality has been put into relation with the formation pathways of the GCs, where the blue GCs would tend to have formed ex-situ and were then later accreted onto the main galaxy, thus tracing the accreted halo, whereas red GCs would mostly have formed in-situ and thereby trace the in-situ material (e.g., Li & Gnedin 2014; Harris et al. 2015; Forbes & Remus 2018). Support for this idea has also been found through observations of the blue GCs following the DM halo measured through X-ray gas emission (e.g., Forte et al. 2005; Forbes et al. 2012; Kluge et al. 2023).

15.3.2 Tracers of past star formation

Because of their dense and massive nature and being composed of nearly equal-age stars, the conditions under which GCs formed require massive gas clouds and high gas pressure. Such expectations are motivated by observations in the local Universe for young massive cluster formation (e.g., Wei et al. 2012; Kruijssen 2026). Several studies have connected GC formation to giant molecular clouds (GMCs) with high pressure (e.g., Harris & Pudritz 1994; Elmegreen & Efremov 1997), where it has been found that their maximum mass is correlated with the local star formation rate (Kravtsov & Gnedin 2005). With high surface density clumps of molecular gas having been detected in the interstellar medium (ISM) of star-forming galaxies at redshifts of $z \sim 2$–3 (e.g., Genzel et al. 2010; Swinbank et al. 2011), where conditions are intensified within merging galaxies, these present environments suitable for the formation of the metal-rich GCs (Shapiro et al. 2010). Recent observations of strong clustered star formation at even earlier redshifts with HST and JWST have further made clear that the general conditions needed for GC formation are already met within the first billion years of the Universe, even if it is still unclear whether these objects survive to the present day (e.g., Vanzella et al. 2023; Adamo et al. 2024; Messa et al. 2024; Mayer et al. 2025). As old surviving clusters, GCs are the relics of early galaxy assembly and their populations can therefore be expected to serve as tracers for past intense star formation episodes.

15.4 Modeling globular cluster populations

To investigate the formation and evolution of GCs, numerous GC models have been developed to improve our understanding concerning GCs. These models are developed to explain GC properties seen at $z = 0$, and many provide a means to constrain the details of their formation as well as to predict what clues today's GC populations can reveal about galaxy formation. One of the most common approaches has been to study GCs through empirical and semi-analytic GC formation models applied to cosmological merger trees. For this, different formation prescriptions have been employed, including high-redshift GC formation (e.g., Boylan-Kolchin

2017), gas pressure and density conditions El-Badry et al. (2019); Carleton et al. (2021); De Lucia et al. (2024), accretion rate criteria (e.g., Li & Gnedin 2014; Choksi et al. 2018; Chen & Gnedin 2023, 2024b; Pal et al. 2026). One of the central findings has been that the linear relation between GC numbers and the DM halo mass (see Section 15.2.2) is a result of hierarchical merging and the central limit theorem and is almost unaffected by the GC formation details.

Some models also build on the GC color bimodality to form GCs through two pathways such as early formation in small galaxies and later formation in gas-rich mergers or strong accretion (e.g., Beasley et al. 2002a; Valenzuela et al. 2021). These types of models enable one to test the parameter space of a limited number of free parameters for a large number of galaxies and can improve our understanding of the statistical properties of GC formation that are necessary to reproduce GC properties and relations as they are observed today (see Section 15.2). In particular, the model by Valenzuela et al. (2021) was able to show that two formation pathways are necessary to overcome previous limitations of empirical and semi-analytic models, which did not manage to reproduce the observed GC systems in lower-mass galaxies and simultaneously a reasonable GC age distribution. Some models additionally tag particles with GCs in galaxy simulations to trace their spatial and kinematic properties (e.g., Chen & Gnedin 2022, 2023). Despite not all models tracing GC spatial properties, many even implement recipes for mass loss and cluster disruption (e.g., Choksi et al. 2018; Chen & Gnedin 2022).

Another group of GC models has explored GC formation and evolution through the use of sub-grid models applied to isolated or cosmological hydrodynamical simulations, where the GC formation sites are inferred through the local gas properties, but are not actually resolved (e.g., Bekki et al. 2005; Kruijssen et al. 2011). An especially well-known model is E-MOSAICS (Pfeffer et al. 2018), which was applied to galaxies from the EAGLE cosmological simulation (Schaye et al. 2015), where stellar particles keep track of their sub-grid clusters. Many subsequent studies have used E-MOSAICS to analyze the star and cluster formation histories, to connect the GCs to the early assembly of the host galaxies, or to study the underlying DM potential, among others (e.g., Kruijssen et al. 2019a; Reina-Campos et al. 2019; Trujillo-Gomez et al. 2021; Dolfi et al. 2022; Reina-Campos et al. 2023). Building on the E-MOSAICS model, Reina-Campos et al. (2022) more recently developed an updated model for stellar clusters, *EMP-Pathfinder*, which they applied to the same galaxies to test different cluster formation and evolution prescriptions.

In recent years, a number of very high-resolution simulations have been performed to resolve GC formation through different models and scenarios (e.g., Kim et al. 2018; Lahén et al. 2019; Schauer et al. 2021; McKenzie & Bekki 2021; Reina-Campos et al. 2025). While such high-resolution simulations have shed light on potential formation mechanisms of GCs, in contrast to the empirical and semi-analytical models they are not suitable for a statistical comparison with observations of large or numerous GC systems as they are restricted to small volumes or very early times because of their large computational cost. Finally, there are several models that focus on the evolution and kinematics of GC systems and seed the GCs

according to certain spatial distributions or by tagging stellar or DM particles at a specific time (e.g., Bekki et al. 2005; Veljanoski & Helmi 2016; Amorisco 2019; Carlberg & Keating 2022; Doppel et al. 2023; Pagnini et al. 2023). Such models are not suitable for studying GC formation, however.

15.5 Scope of this Movement

As the GC color bimodality has inspired models with two distinct formation pathways, the question arises what other implications these models have and what their predictive power is. One of the best testbeds for such a study is the MW itself because of the wealth of data available on its GCs and past accretion history. Furthermore, the availability of a large number of models for GC formation means that these can be compared with each other to learn about the consequences of different model approaches. The recent measurements of high-redshift young stellar clusters from JWST have additionally opened up the question whether these young clusters could be the progenitors of present-day GCs.

In this Movement, I build on the GC model with dual formation pathways that I developed previously to this thesis (Valenzuela et al. 2021), where in Chapter 16 I first summarize the model itself together with the properties of the two formed GC populations and quantify the connection between the GCs and the DM accretion history. In Chapter 17, I then test the model prediction that the GC age distribution should trace past gas-rich mergers on the MW as well as nearby galaxies, finding evidence for a GC formation episode during the encounter with Gaia-Sausage/Enceladus, the MW's last major merger. Furthermore, I present the first cross-model comparison of six state-of-the-art GC models and connect their predictions of GC formation times to the high-redshift observations of young stellar clusters in Chapter 18. Finally, I summarize the results of a further work I contributed to in Chapter 19, where we model the DM halo of Centaurus A from GC dynamics and gain insight into its recent assembly through a comparison with cosmological simulations.

16

Globular Clusters as Dark Matter Tracers

This chapter was published as Valenzuela (2023), Mem. Societa Astronomica Italiana 94, 47[1]:
Lights in the Dark: Globular clusters as dark matter tracers

Empirical models of globular clusters (GCs) have proven useful for studying GC populations and their formation in a statistical manner. As introduced in Section 15.4, many of these models are built on merger trees obtained from cosmological simulations or through generating mock merger trees. As observations have found that the number and total mass of GCs correlate linearly with the virial mass of the host system (e.g., Blakeslee et al. 1997; Harris et al. 2017a; Forbes et al. 2018b, see Section 15.2.2), empirical GC models have been used to investigate the origins of this correlation. Such studies have shown the linear relation between the GC abundances and the halo virial masses to result from hierarchical merging and the central limit theorem. The models have generally either assumed GCs to form at very early times (e.g., Beasley et al. 2002a; Boylan-Kolchin 2017; Burkert & Forbes 2020) or to form by high accretion rates with sufficient available gas (e.g., Beasley et al. 2002a; Choksi et al. 2018; El-Badry et al. 2019). However, the former models do not take younger GC populations into consideration, while the latter models only find GC populations in the more massive galaxies, which does not agree with the results from Forbes et al. (2018b).

[1]Minor adjustments have been made, and the introduction has been adapted for this thesis.

To address this issue, Valenzuela et al. (2021) introduced a model that combines both pathways of GC formation, finding that only the combination of the two can reproduce the observations: the relation between virial mass and GC numbers as well as the observed GC age distribution. Another key finding was that the GC number of a galaxy at a fixed virial mass is related to the amount of smoothly accreted matter onto the host dark matter halo.

This work expands on the findings of Valenzuela et al. (2021) by considering the individual contributions of the two GC formation pathways to the age distribution and by quantifying the relation between GC abundances and dark matter smooth accretion. This provides a direct measure of the extent to which GCs trace past smooth accretion, a quantity that is otherwise very difficult to measure. In Section 16.1, the GC model and its two formation pathways are summarized, followed by an analysis of the GC age distribution and its decomposition into the two GC subpopulations. In Section 16.2, the relation between GC numbers and dark matter smooth accretion is quantified, and finally Section 16.3 concludes this work.

16.1 Globular cluster model

The two GC formation pathways employed by the model from Valenzuela et al. (2021) follow the idea that GCs are either formed in small galaxies at early times or in gas-rich mergers of more massive galaxies. Both pathway models are kept as simple as possible to allow probing the whole parameter space, meaning that the number of free parameters is kept to a minimum. These models track the number of GCs in each galaxy and the individual GC formation times. They were run on the merger tree of a dark matter-only cosmological simulation with a side length of 30 Mpc within the empirical model EMERGE (Moster et al. 2018). The stellar and gas components are empirically inferred from the dark matter halos and their merger trees by EMERGE. For more details on this see Moster et al. (2018).

Small Halo Pathway In the first model, GCs are formed as soon as the virial mass of a galaxy surpasses a threshold seeding mass, the first free parameter. On average one GC is formed: either 0, 1, or 2 are formed at random. By adapting the threshold seeding mass, the observed relation between the virial mass and the number of GCs from Burkert & Forbes (2020) can be reproduced (left panel of Fig. 16.1). However, when comparing the cumulative age distribution of the GCs, the model lacks the younger GCs found in local galaxies by Usher et al. (2019) (left panel of Fig. 16.2). Clearly, the model forming GCs in small halos is not sufficient for explaining the observed GC populations.

Wet Merger Pathway The second model follows the one introduced by Choksi et al. (2018): when the mass accretion rate surpasses an accretion rate threshold (the first free parameter), GC formation is triggered. The total GC mass is determined from the cold gas mass through a conversion factor (the second free parameter), from which the number of GCs formed is derived by an exponential cluster initial mass function with a slope of -2. This model only forms GCs in galaxies with virial masses above roughly $10^{10.5}\,M_\odot$ and therefore lacks the

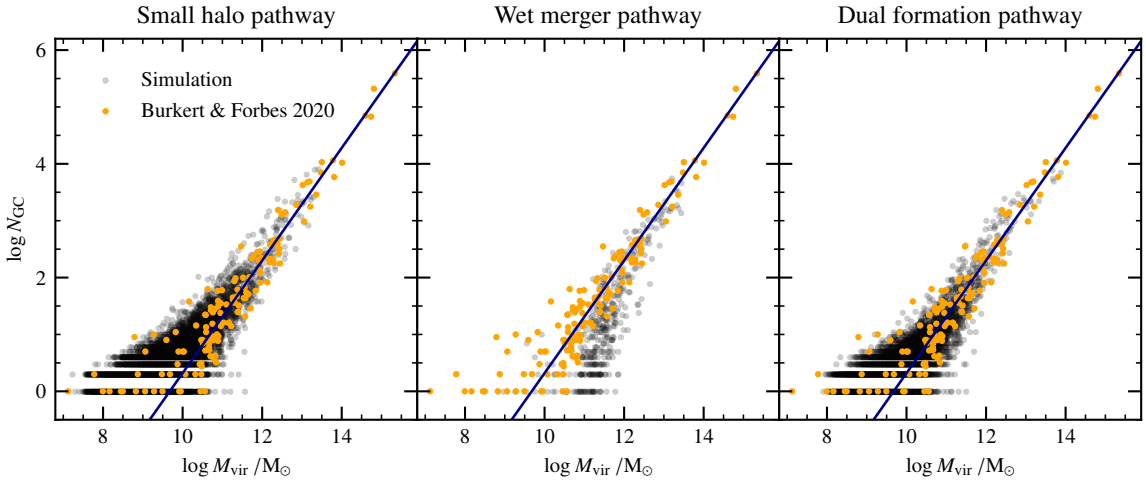


Figure 16.1: Relation between the virial mass and the number of GCs of galaxies in observations (Burkert & Forbes 2020) and from the GC models. From left to right the first model, the second model, and the combined models, respectively. The solid blue lines indicate the fit relation to the observed galaxies. The virial masses of the simulated galaxies are shown with a random measurement uncertainty of 0.3, 0.25, and 0.25 dex, respectively.

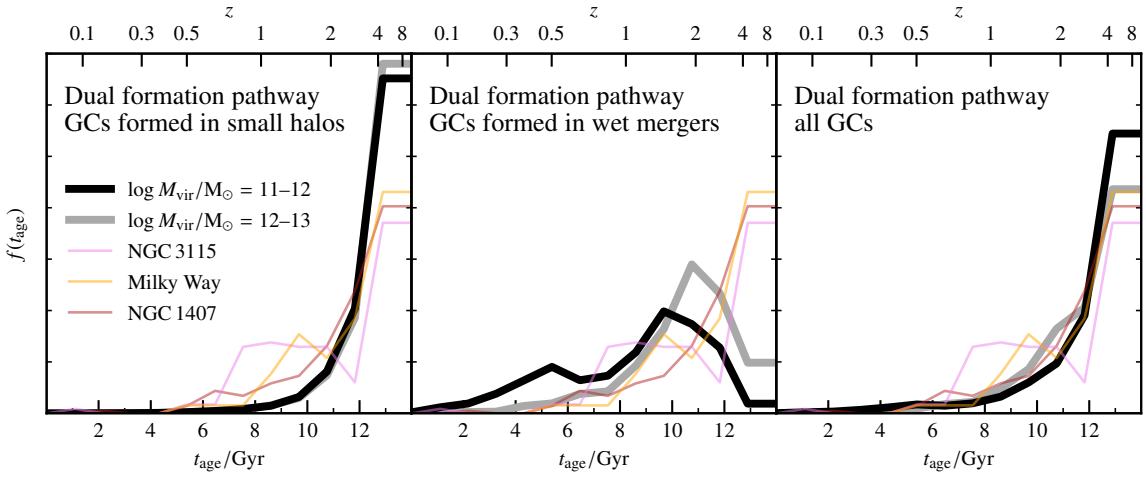


Figure 16.2: Age distributions of three local galaxies including the Milky Way (Usher et al. 2019) compared to the mean age distributions of the modeled GC populations in the two relevant virial mass bins (i.e., the age probability density function of the GCs found in an individual observed galaxy in color, and of all GCs around galaxies within the respective virial mass bins in gray). The GC age t_{age} indicates the lookback time of the GC formation, with the corresponding formation redshift z shown on the top x-axes. All panels show the GCs from the dual formation pathway model, where the first two panels show only the GCs formed through the small halo pathway and the wet merger pathway, respectively. The third panel shows the total GC population.

GCs in low-mass galaxies as seen in the middle panel of Fig. 16.1. This model is therefore also not sufficient to explain the GC observations.

Dual Formation Pathway Running both models at the same time makes it possible to reproduce the GC number-virial mass relation again (right panel of Fig. 16.1), and in contrast to the first model, now also results in a similar age distribution to that of the Milky Way and NGC 1407 for simulated galaxies of the corresponding virial mass bins (right panel of Fig. 16.2). This arises from the much younger GCs formed in wet mergers (middle panel of Fig. 16.2). In summary, the first pathway contributes the older GC population, whereas the second forms younger GCs. Varying the parameters either leads to an increasingly non-linear relation between the number of GCs and the virial mass, or to much too old GC populations, or to unreasonably low or high thresholds for GC formation in wet mergers (for more details, see Valenzuela et al. 2021).

16.2 Smooth accretion

Despite the limited number of free parameters, the model results in a non-negligible scatter of GCs for a given virial mass. The main driver of this scatter is the amount of smoothly accreted matter throughout a galaxy's formation history, where anything that was accreted with a virial mass below $10^{8.8}\,M_\odot$ (the GC seeding mass of the first model) is considered to have been smoothly accreted. The relation between the logarithmic over- or underabundance and the above- or below-average smooth accretion for galaxies with the same virial masses is anti-correlated with a slope of roughly -1 (Fig. 16.3). In conclusion, this means that galaxies with more GCs than average have had less smooth accretion than other galaxies of the same virial mass and vice versa.

16.3 Conclusion

By combining two common approaches to empirically modeling GCs in a dual formation scenario, GC numbers and ages can be found that agree with those observed in galaxies of all masses. The individual models either fail to obtain young GC populations or lack GCs in dwarf galaxies. The necessity of two formation pathways suggests that also the spatial and kinematic properties of GCs may trace different aspects of galaxies. First results on red GCs tracing the stellar light and blue GCs tracing the dark matter halo (Kluge et al., in prep.) are a good indication for distinct formation pathways of these GC populations, as proposed by the model. Furthermore, the over- or underabundance of GCs with respect to the average number found in galaxies of the same virial mass gives a measure for the smooth accretion onto a galaxy, a nearly untraceable property of galaxy formation history.

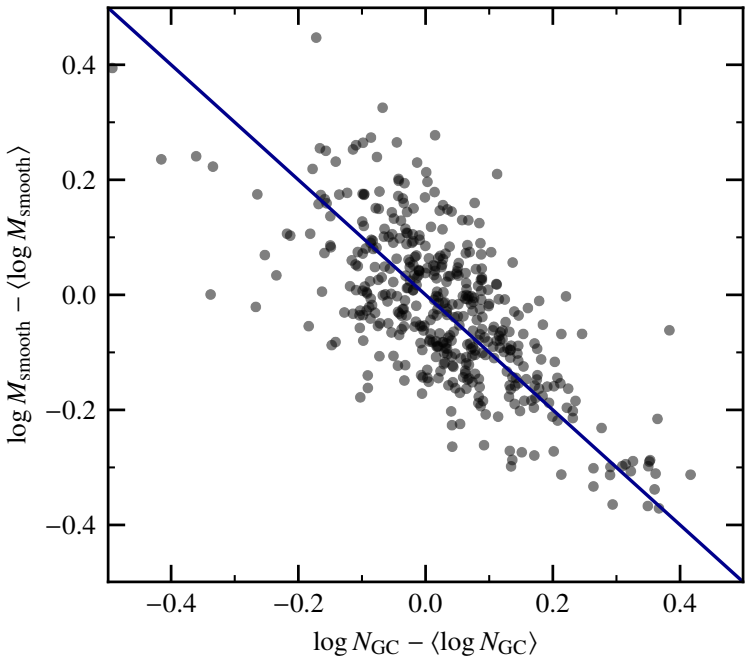


Figure 16.3: Relation between the overabundance of GCs and the deviation from the average smoothly accreted matter of the simulated galaxies with virial masses above $10^{11}\,\mathrm{M}_{\odot}$. The solid blue line indicates the negative 1:1 relation.

17

Tracing Wet Mergers Through GC Ages

This chapter was published as Valenzuela et al. (2024b), A&A 687, A104[1]:
Galaxy archaeology for wet mergers:
Globular cluster age distributions in the Milky Way and nearby galaxies

Over the course of galaxy formation and evolution, in situ formed structures mix with accreted matter, concealing their origin and thereby the formation history of the galaxy. Through precise measurements of star and gas properties, such as their distribution in space, their velocities, their chemical compositions, and the stellar ages, it is possible to disentangle many of the individual clues on the formation history. This is the aim of galaxy archaeology (e.g., Freeman & Bland-Hawthorn 2002; Binney 2013; Helmi 2020). In particular, stellar structures and overdensities, such as stellar streams and other tidal features, can reveal details on a galaxy's history, where especially stellar streams are generally the remains of a tidally disrupted satellite galaxy. This has been done extensively for the Milky Way (MW; e.g., Helmi et al. 1999; Belokurov et al. 2006, 2007; Bell et al. 2008; Shipp et al. 2018), aided particularly by the Gaia mission (Gaia Collaboration 2016, 2018b, 2023) in recent years with 6D phase-space data (e.g., Helmi et al. 2018; Helmi 2020; Prudil et al. 2022; Malhan et al. 2022; Ruiz-Lara et al. 2022). It is also possible to detect tidal features for other galaxies in a more limited way through photometric and integral field unit (IFU) observations. Such

[1]Minor adjustments have been made, and the introduction has been adapted for this thesis.

identified structures have also been connected to the merger history of their host galaxies in observations (e.g., Bílek et al. 2020, 2023; Chandra et al. 2023) and simulations (e.g., Bullock & Johnston 2005; Johnston et al. 2008; Amorisco 2015; Hendel & Johnston 2015; Pop et al. 2018; Karademir et al. 2019; Valenzuela & Remus 2024; see Movement I). However, all of these are tracers for stellar-dominated merger events and cannot trace the gas that has been accreted through such mergers.

For our own Galaxy, data are available in unprecedented detail, including measured proper motions. By detecting kinematic substructures of stars clustered in phase space, it has been possible to identify a number of past and ongoing mergers for the MW. The Sagittarius Dwarf Spheroidal Galaxy was the first merger discovered with the MW through positional and line-of-sight kinematic data by Ibata et al. (1994). Using Hipparcos data and line-of-sight distances and velocities, Helmi et al. (1999) discovered substructures in the inner halo now known as the Helmi streams. Through the Gaia mission and the 6D kinematic data that were obtained for stars in the MW, a large number of halo stars were found to have distinct kinematics in phase space, which were attributed to a major merger event that is expected to have taken place around 10 Gyr ago, Gaia-Sausage/Enceladus (GSE; Belokurov et al. 2018; Haywood et al. 2018; Helmi et al. 2018; Mackereth et al. 2019). It is the last major merger that the MW experienced, as well as the most massive one, forming a large part of the stellar halo. There are also other interpretations of the kinematic signatures, however, that the local halo cannot be dominated by GSE alone, but is composed of the remains of multiple mergers over a prolonged time (e.g., Donlon et al. 2020, 2022; Donlon & Newberg 2023). Finally, Myeong et al. (2019) find a second group of halo stars kinematically and chemically different from GSE stars with overall retrograde motions, which they attribute to a separate merger event, referred to as Sequoia. Further groups of stars in phase space have been found, which are likely the debris of disrupted galaxies that fell into the MW, though the connection to specific merger events is not yet clear (see Dodd et al. 2023 and Horta et al. 2023 for a current overview of structures found in phase space).

Through Gaia data, globular clusters (GCs) in the MW have also been used to further disentangle the Galactic formation history. Based on their 6D phase-space properties and their age-metallicity relations, some studies have linked the GCs with their likely progenitor host galaxies (Myeong et al. 2018; Massari et al. 2019; Forbes 2020; Horta et al. 2020; Callingham et al. 2022; Belokurov & Kravtsov 2024; Chen & Gnedin 2024a), such as to the MW itself as in situ GCs, or to some of the inferred accreted galaxies. These studies also reveal unassociated groups of GCs with low and high orbital energies, where it is proposed that a group of unassociated low-energy GCs are part of a further past merger event (Massari et al. 2019; Forbes 2020; Callingham et al. 2022). Similar structures in phase space with overlapping properties are identified through different methods (e.g., Kruijssen et al. 2019b; Forbes 2020; Horta et al. 2021, 2023). However, it has also been shown that GCs can migrate in phase space over time, potentially making it difficult to disentangle the origin of GCs based on their phase-space properties alone (Pagnini et al. 2023). An overview of the positions on

the sky and in phase space of the streams and GCs detected in the MW can be found in the figures of Riley & Strigari (2020), Malhan et al. (2022), and Mateu (2023).

While the ages of MW GCs can be measured with reasonable accuracy through the color-magnitude diagram (CMD; see Section 15.2.3), obtaining reliable age estimates for extragalactic GCs is much more difficult (Section 15.2.2). Ages have been estimated from photometric studies of the integrated light of extragalactic GCs (e.g., Chies-Santos et al. 2011; Georgiev et al. 2012; de Brito Silva et al. 2022), a technique which will also become increasingly important with the upcoming generation of observatories such as Euclid, the Nancy Grace Roman Space Telescope, and the Vera C. Rubin Observatory (e.g., Lançon et al. 2021; Dage et al. 2023; Usher et al. 2023). Even integrated spectroscopic measurements of extragalactic GCs are oftentimes biased towards younger ages compared to the CMD method. This bias arises from hot horizontal branch (HB) stars, whose presence is degenerate with younger stars (e.g., Worthey 1994; de Freitas Pacheco & Barbuy 1995; Beasley et al. 2002b; Cabrera-Ziri & Conroy 2022) and even causes issues when using state-of-the-art models (e.g., Perina et al. 2011; Gonçalves et al. 2020). This has been done for GCs in galaxies in the Local Group (e.g., Beasley et al. 2005; Schiavon et al. 2013; Wang et al. 2021) and for selected nearby galaxies (e.g., Usher et al. 2019).

In this work, we use a recent empirical GC formation model with two formation pathways (Valenzuela et al. 2021; Valenzuela 2023, see Chapter 16, the first pathway forms GCs in small halos, while the second forms GCs in gas-rich mergers) to study how its second pathway of forming GCs in gas-rich wet mergers (e.g., Ashman & Zepf 1992) can help shed light on the formation history of the MW and other nearby galaxies. The model has been shown to agree well with the observed numbers of GCs in galaxies from dwarf to galaxy cluster masses, where a linear relation has been found to exist between the number of GCs and the dark matter (DM) halo virial mass (e.g., Blakeslee et al. 1997; Harris et al. 2017a; Forbes et al. 2018b), as well as with GC age distributions of the MW and nearby galaxies. We introduce the GC model and observational data in Section 17.1. In Section 17.2, we present a bimodal feature found in the observed GC age distribution of the MW and how it could be related to the predictions of the GC model. We then test and discuss these predictions in detail for the MW in Section 17.3 and for other nearby galaxies in Section 17.4. Finally, we summarize and conclude the results in Section 17.5.

17.1 Data & method

In the following, the empirical GC model and the GC observational data used in this work are presented. The main property studied is the GC age distribution of galaxies.

17.1.1 Globular cluster model

In this work, we used the empirical GC formation model introduced by Valenzuela et al. (2021), which builds on previous models and investigations by Boylan-Kolchin (2017), Choksi

et al. (2018), and Burkert & Forbes (2020). The model employs two formation pathways for GCs: The first, the small halo pathway, forms GCs in small haloes as soon as a halo's virial mass surpasses a given threshold value, M_{seedGC}. With equal probability, 0, 1, or 2 GCs are formed. The second, the wet merger pathway, is the formation pathway introduced by Choksi et al. (2018) and triggers GC formation when the relative halo mass accretion rate surpasses a given threshold value, A_{min}. The formed number of GCs is then determined by converting the available cold gas mass M_{gas} to a total GC mass via a conversion factor, η_{GC} (Kravtsov & Gnedin 2005; Li & Gnedin 2014; Choksi et al. 2018; Valenzuela et al. 2021):

$$M_{\mathrm{GC}} = 1.8 \times 10^{-4} \eta_{\mathrm{GC}} M_{\mathrm{gas}}. \tag{17.1}$$

By assuming a cluster initial mass function of

$$\frac{dN}{dM} \propto M^{-2}, \tag{17.2}$$

the expected number of formed GCs is obtained as (combining eqs. 3, 6, and 7 of Valenzuela et al. 2021)

$$\langle N \rangle = \exp\left(W\left(\frac{1.8 \times 10^{-4} \eta_{\mathrm{GC}} M_{\mathrm{gas}}}{M_{\mathrm{min}}}\right)\right) - 1, \tag{17.3}$$

where W is the Lambert W function, $\eta_{\mathrm{GC}} = 0.5$ for the best-fitting model, and $M_{\mathrm{min}} = 10^5\,\mathrm{M}_\odot$ is the minimum mass that a GC needs at formation time to survive for a few Gyr (Li & Gnedin 2014; Choksi et al. 2018). For more details on the models, see Valenzuela et al. (2021). Note that recent work by Chen & Gnedin (2023) now uses a smaller value of $M_{\mathrm{min}} = 10^4\,\mathrm{M}_\odot$, although they note that GCs with low initial masses of for example $10^4\,\mathrm{M}_\odot$ have an estimated lifetime of around 1 Gyr at 3 kpc distance of the center of a MW-mass galaxy. The model only tracks the numbers of GCs per galaxy and their formation times, but does not include metallicities. This limits the comparison with observations to only the GC ages, though the available measured metallicities can be used as indicators for the formation sites of the observed GCs. In contrast, for the modeled GCs this information is already known.

The GC model was applied to the merger tree of a DM-only simulation of side length 30 Mpc with a DM particle mass of $m_{\mathrm{DM}} = 7.90 \times 10^6\,\mathrm{M}_\odot$ that was run with the TreePM code Gadget-3 (Springel 2005). The empirical model emerge (Moster et al. 2018) provides the model with the baryonic matter content per galaxy. Because the model only tracks the number of GCs in each galaxy and at what times they were formed, the model parameters were fit to match observations of the numbers of GCs, since those are available for a sufficiently large sample: the GC numbers are taken from Burkert & Forbes (2020). The GC age distributions are consistent with those found by Usher et al. (2019) for the MW and three SLUGGS galaxies (SAGES Legacy Unifying Globulars and GalaxieS; Brodie et al. 2014), and the fractions of GCs formed through the wet merger pathway agree with the red GC fractions measured by Harris et al. (2015). For more information on the comparability to observations and how the model parameters affect the resulting GC properties, see Valenzuela et al. (2021).

17.1.2 Globular cluster observational data

A variety of observed GC age measurements from the literature are used in this work for selected galaxies in the Local Universe. These use different methods to obtain the GC ages and are presented in the following. For all of the measured samples, it is important to keep in mind that while the absolute ages have large uncertainties and are difficult to measure even in the MW itself (e.g., Ying et al. 2023, for M 92), within a given GC sample they are subjected to the same systematic uncertainties, resulting in much more precise relative ages. This is important for the study of GC age distributions, where the features in the distribution itself are given by the relative ages as opposed to the absolute ones.

Milky Way

The MW is the only galaxy besides its own satellites for which it is currently possible to obtain accurate CMDs of its GCs. This allows for a much more exact determination of their ages and has been done in multiple studies for different sized samples of GCs. In this work, we considered three of these as compiled by Kruijssen et al. (2019b), and additionally investigated the mean ages of those three studies in Section G.1.1:

- Forbes & Bridges (2010) with a sample of 92 GCs,
- Dotter et al. (2010, 2011) with a sample of 68 GCs,
- VandenBerg et al. (2013) with a sample of 54 GCs,
- Kruijssen et al. (2019b) with a sample of 96 GCs, which contains the mean GC ages from the previous three studies.

The sample from Forbes & Bridges (2010) is based on a number of previous age measurement studies (Salaris & Weiss 1998; Bellazzini et al. 2002; Catelan et al. 2002; De Angeli et al. 2005; Carraro et al. 2007; Dotter et al. 2008; Carraro 2009; Marín-Franch et al. 2009), of which 64 GCs were measured using the Advanced Camera for Surveys (ACS) from the Hubble Space Telescope (HST) through the ACS survey for Galactic GCs (Sarajedini et al. 2007; Marín-Franch et al. 2009) to obtain relative ages. They were normalized to absolute ages with the Dartmouth models of Dotter et al. (2007). While that sample is restricted to the inner 20 kpc of the MW, the age measurements of further GCs were supplemented from the other works. The sample from Dotter et al. (2010, 2011) is for the most part also based on the GCs measured through the ACS survey of Galactic GCs using the photometric catalog from Anderson et al. (2008), and the remaining GCs were observed with further HST/AST measurements. Lastly, the GC age measurements from VandenBerg et al. (2013) were computed from the same photometric catalog of the ACS survey of Galactic GCs as Marín-Franch et al. (2009) used, but employing the stellar evolutionary tracks from VandenBerg et al. (2012). It should be noted that while not all these objects are necessarily actual GCs, but in part also nuclear star clusters, metal complex clusters, or a combination thereof (e.g., McKenzie et al. 2022), we refer to all of them simply as GCs in this work.

In addition to the three CMD age samples of the MW GCs, we also included two GC age samples obtained through integrated measurements, as this is also what one is restricted to for other galaxies:

- Usher et al. (2019) with a sample of 61 GCs. Their measurements are obtained through combining photometry and spectroscopy, to which stellar population models are fitted using a Markov chain Monte Carlo (MCMC) method.
- Cabrera-Ziri & Conroy (2022) with a sample of 32 GCs, of which we removed the 3 spurious young GCs (see their section 6.1, where they detail how the spectral fit residuals indicate whether the best fit for a young GC is real or spurious, which is a result of the simple single population HB star model that they use). These have also been shown to be much older from CMD measurements. Compared to Usher et al. (2019), Cabrera-Ziri & Conroy (2022) used spectroscopy only, but additionally took the hot horizontal branch (HB) stars into account in their modeling of the integrated stellar population measurements.

For the MW, additional GC properties can be determined that are not possible to obtain for other galaxies at the moment. Six-dimensional phase space measurements have been made available for many MW GCs through Gaia (Gaia Collaboration 2018a; Vasiliev 2019), which Massari et al. (2019) used to assign the likely origin of the individual GCs. Their list of progenitors for the GCs consist of the MW itself (i.e., in situ formed GCs in the disk or bulge), the GSE galaxy, the Sagittarius dwarf, the Helmi Streams, the Sequoia galaxy, and unassociated high- and low-energy GCs. Forbes (2020) used the age-metallicity relation (AMR) to improve these progenitor assignments and propose that the unassociated low-energy GCs belong to a single progenitor dwarf satellite, which they dub Koala and is likely related to or overlaps with Kraken (Kruijssen et al. 2019b) and Heracles (Horta et al. 2021, 2023). Further work was done by Callingham et al. (2022), who used a chemo-dynamical model and hydrodynamical simulations of MW-like galaxies to associate the GCs with their progenitor hosts. Their assumed accretion events largely align with those used by Massari et al. (2019) and Forbes (2020). Chen & Gnedin (2024a) have recently applied clustering techniques to chemical, spatial, kinematic, and age properties of the GCs to associate the GCs with the MW, GSE, Sagittarius, and other ex-situ-formed GCs. It should be noted that due to the ongoing observations and work on this topic, this is a rapidly evolving field. The identifiers of the GCs were available to us for the CMD age samples and for the sample of Cabrera-Ziri & Conroy (2022), such that we could cross-match the ages for those four samples to the progenitor assignments. For this work, we use the assignments made by Forbes (2020), though using the assignments from Massari et al. (2019), Callingham et al. (2022), or Chen & Gnedin (2024a) do not change the statistical findings presented in this work when we did the analysis using those instead (also see Section G.1.2 for an analysis using the associations from Callingham et al. 2022 and Chen & Gnedin 2024a).

M 31

As the nearest more massive galaxy to the MW, the Andromeda galaxy (M 31) is an ideal galaxy for which GCs can be identified and analyzed, since observations have much better resolution and better signal-to-noise values than for more distant galaxies. For M 31, we used two different studies for the GC ages:

- Wang et al. (2021) with a sample of 343 clusters, of which we used the 293 old GCs ($t_{\rm age} > 1.5$ Gyr) in this work,
- Usher et al. (2024) with a sample of 290 clusters,
- Cabrera-Ziri et al. (in prep.) with a sample of 286 GCs, of which we used the 136 GCs whose ages are sufficiently constrained.

The sample from Wang et al. (2021) was observed with the Large Sky Area Multi-Object Fiber Spectroscopic Telescope (LAMOST; Cui et al. 2012; Luo et al. 2015). The GC ages were then determined based on the obtained integrated spectra and multi-band photometry from Beijing-Arizona-Taiwan-Connecticut (BATC; Ma et al. 2015) and Sloan Digital Sky Survey (SDSS; Peacock et al. 2010). For the old clusters, they fit the spectra using an empirical stellar spectra library and the measured colors using an MCMC method. Their ages are all younger than 10 Gyr, however, which is likely a consequence of their underlying models and almost certainly not actually the case for the majority of M 31's GCs (e.g., Beasley et al. 2005; Caldwell et al. 2011; Schiavon et al. 2013). Their ages should therefore be taken with caution. The GC age determinations from Usher et al. (2024) were also made from photometric and spectroscopic measurements, where the photometry was obtained with SDSS (mostly from Peacock et al. 2010) or from the Pan-Andromeda Archaeological Survey (PAndAS) Canada France Hawaii Telescope MegaCam for the halo GCs not covered by SDSS (Huxor et al. 2014). Usher et al. (2024) used the same method as Usher et al. (2019), for which they fit the stellar spectra using an MCMC method.

The integrated spectra measurements of Cabrera-Ziri et al. (in prep.) use the same method as applied for the MW GCs presented by Cabrera-Ziri & Conroy (2022). Their GC sample is selected from the inner halo of M 31, of which 150 have only a lower bound on their age, leaving 136 GCs with sufficiently constrained ages to study their distribution. The reason for the large number of lower age bounds is that their method is able to determine that the metal-poor GCs with a horizontal branch are very old, but not what exact age they have (>9 Gyr in all cases, and >12.5 Gyr is the median lower bound) due to degeneracies between the ages and horizontal branch properties. This also means that the resulting age distribution has a selection bias towards metal-rich GCs, which means that the metal-poor GCs typically accreted through smaller galaxies are removed. This should be kept in mind, though we believe that the consequences for this work are not severe since we focus on GCs formed during mergers, which produce younger GCs at generally higher metallicities. GCs formed through such mergers tend to be younger by on average 2–3 Gyr, having their formation peak at an age of roughly 10 Gyr (see fig. 2 of Valenzuela 2023).

NGC 3115 and NGC 1407

The age measurements for 116 GCs in NGC 3115 and 213 GCs in NGC 1407 were made by Usher et al. (2019) by combining photometry and spectroscopy to fit the stellar spectra using an MCMC method. The spectral data were obtained through the SLUGGS survey (Brodie et al. 2014) and the photometric data are from Arnold et al. (2011) using the Suprime-Cam of the Subaru telescope.

17.2 Age dating wet mergers with GCs in the Milky Way

Having the observational data, we investigated some reoccurring features in the GC age distributions with the aim of verifying if such features can be explained by the model. In the following, we present our initial findings from the observations and what predictions the model makes with respect to these.

17.2.1 GC age distribution observations in the Milky Way

As the galaxy for which the best data exists, we first considered the GC age distribution of the MW. In two of the available samples, the ages appear to have a bimodal or even multimodal distribution, which are shown in Figure 17.1. For both Forbes & Bridges (2010) and Usher et al. (2019), the main peak of the distribution is at 13 Gyr. There is also a slight second peak in the distribution of Forbes & Bridges (2010) at around 11 Gyr, while for Usher et al. (2019) there are two small peaks between 8 Gyr and 10 Gyr. Since the data from Forbes & Bridges (2010) are composed of multiple different studies, we show the age distribution only of the largest of the underlying GC age studies from Marín-Franch et al. (2009) in Section G.1.3 (it includes 64 of the 92 GCs), which also features the age bimodality. Thus, the bimodality seen for Forbes & Bridges (2010) is not the result of combining multiple studies with different systematic uncertainties. Studies of the age-metallicity relationship for MW GCs have shown that there are multiple branches of GCs corresponding to the in situ formed GCs and different progenitor galaxies that fell into the MW (e.g., Kruijssen et al. 2019b; Forbes 2020), which could be what is seen as a multimodal age distribution. The peaks in the age distributions align well with the estimated infall times of Sagittarius (8–9 Gyr ago) and Sequoia (~10 Gyr ago; Forbes 2020), and of the GSE merger event, the last major merger that the MW experienced (Helmi et al. 2018; Haywood et al. 2018): around 8 Gyr to 11 Gyr ago according to Belokurov et al. (2018) and around 10 Gyr ago according to Helmi et al. (2018). With an estimated merger mass ratio of 1:4 (Helmi et al. 2018; Gallart et al. 2019), GSE is expected to have been a gas-rich major merger that triggered a starburst in the disk of the MW (e.g., Helmi 2020; Ciucă et al. 2023). There is also evidence for this from stellar population measurements, where Gallart et al. (2019) found a clear peak of high star formation at around 9.5 Gyr ago.

Of course, the findings from the observed age distributions are accompanied by some caveats: First of all, GC age measurements are subject to large uncertainties, especially for the older ages (see the solid lines in Figure 17.1, which are the distributions smoothed by Gaussian

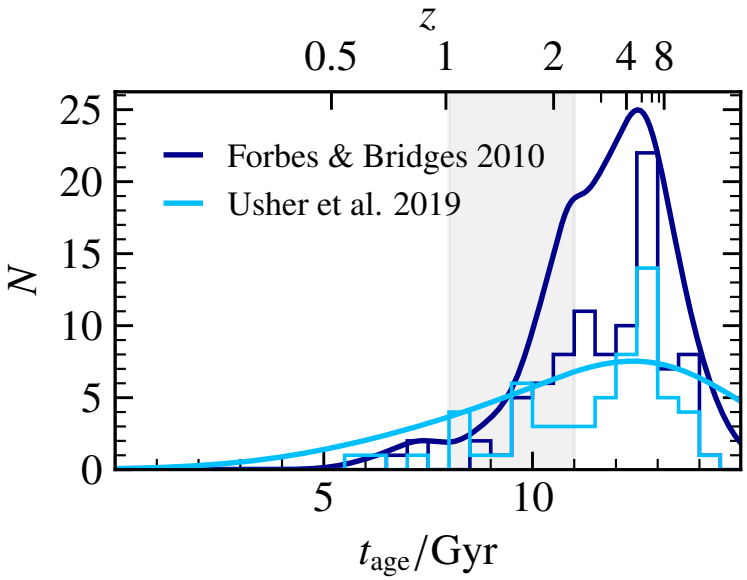


Figure 17.1: Globular cluster age distributions in the MW from Forbes & Bridges (2010) and Usher et al. (2019), with sample sizes of 92 and 61 GCs, respectively. The boxy lines are the actual histograms, while the smooth curves show the distributions smoothed by the measurement uncertainties. These are computed through a summation over normal distributions with the respective ages as the means and their uncertainties as the standard deviations. The shaded region between 8 Gyr and 11 Gyr indicates the estimated time of the GSE merger (Belokurov et al. 2018; Helmi et al. 2018).

kernels given by the measurement uncertainties). Still, a large part of these uncertainties are systematic effects, such that the relative ages can still be trusted more than individual absolute ages. Second, the sample sizes are not large enough to make any kind of statistically significant statements, in particular for the few GCs that make up the minor peaks in the age distributions. Third, bringing together the estimated time of the GSE merger event and the time of the GC age distribution peaks is far from having established a causal relation between the two. However, since the features are present in the data and the time also aligns with that of the GSE merger event, GC formation models can be employed to investigate if there is a theoretical basis for a causal connection.

17.2.2 Model predictions

The model introduced by Valenzuela et al. (2021) consists of two GC formation pathways, of which one allows GCs to form through wet mergers containing a sufficient amount of cold gas. To study what the model predicts for galaxies such as the MW, we first extracted MW-like galaxies from the simulation to which the GC model was applied. For this, we selected MW-mass galaxies by their virial mass of $M_{\rm vir} = 1\text{–}2 \times 10^{12}\,M_{\rm vir}$, which applies to 21 simulated galaxies. Out of these, there are two with GC age distributions that best match the distribution measured by Usher et al. (2019) for the MW in terms of their cumulative distributions, which is shown in the top panel of Figure 17.2. The analogs were selected using the measurements by Usher et al. (2019) instead of one of the CMD measurements since the model was originally calibrated by Valenzuela et al. 2021 to be in agreement with the ages

measured by Usher et al. 2019 to have a comparison with multiple galaxies. A recalibration of the model to the CMD age distributions is unsuitable because it would surpass the scope of this work and would only provide one single galaxy with a sufficient number of CMD-measured GC ages. The conclusions drawn in the following are still applicable to the model in general, independent of the age calibration that was used. We show the GC age distributions and the accretion histories of the other 19 MW-mass galaxies in Section G.2.

Both of the simulated galaxies have roughly bimodal GC age distributions with a minor peak at around 9 Gyr to 10 Gyr (middle panel of Figure 17.2). Assuming a measurement uncertainty of 0.75 Gyr for each GC age continues to show a clear bimodality in one case (orange distribution), but only leaves a hint for the other case (red distribution). This shows that even if there is a bimodal age distribution, the large measurement uncertainties for GC ages can make it difficult to actually confirm it in practice.

The underlying reason for these peaks in the age distributions becomes apparent when studying the accretion histories of the two galaxies: both of them experience a major merger in the same time period as the GC formation bursts (bottom panel of Figure 17.2). The mergers occur at the same time as the GSE merger is estimated to have happened (8–11 Gyr ago). The two accretion histories differ strongly in their later evolution, however: while the galaxy with the more pronounced bimodal GC age distribution only experiences mini to minor mergers afterwards (orange line in the bottom panel of Figure 17.2), the other galaxy has a second major merger at a later time of around 2–4 Gyr ago (red line). The lack of GCs having formed around that time is a clear indication that the merger was rather gas-poor (i.e., dry). The formation history of the first galaxy is therefore more similar to that inferred for the MW ("MW-analog"), while the other galaxy has had a much more violent recent history ("non-MW-analog"). The fact that the non-MW-analog GC age distribution seen in the middle panel of Figure 17.2 is more similar to the observed one by Usher et al. (2019) only indicates that the major merger around 10 Gyr ago is more similar to the GSE merger in terms of their GCs formed. However, the second major merger around 2–4 Gyr ago is in no way comparable to the MW, making it the non-MW-analog. As shown for the other 19 MW-mass galaxies in Section G.2, the peaks in their GC age distributions also correspond to gas-rich merger events, while those mergers that do not leave a strong imprint in the GC age distribution are the dry mergers that the galaxy experienced.

In conclusion, the model makes the following predictions: wet mergers with a large amount of cold gas are capable of producing a bimodal or even multimodal GC age distribution for a galaxy, providing an indication for a type of event that is generally difficult to trace through other means. However, dry mergers with little to no cold gas do not result in noticeable signatures in the GC age distributions. This is the case for the majority of late-time mergers, but at higher redshifts gas-rich mergers are increasingly more common and beyond $z \approx 2$ the most common kind of merger event (e.g., Bournaud et al. 2011). Thus, GC ages provide a means to probe the very early turbulent formation times of galaxies by tracing their massive wet merger events.

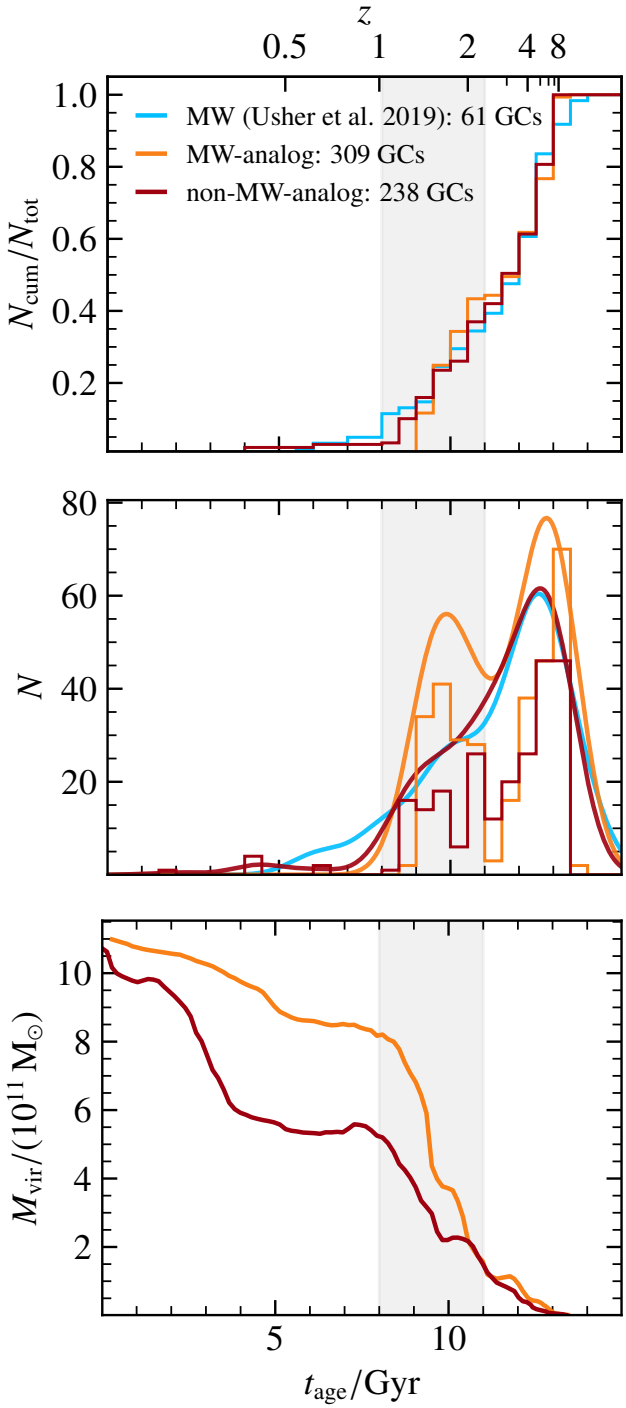


Figure 17.2: GC ages and virial mass evolutions of two selected modeled MW-mass galaxies compared to the observed GC ages in the MW. *Top*: Cumulative GC age distributions of the MW from Usher et al. (2019) (blue) and of two modeled GC populations in simulated MW-mass galaxies from Valenzuela et al. (2021) (red and orange). *Middle*: Age distributions of the same three GC populations as in the top panel. The smooth distributions are smoothed using an assumed uncertainty of 0.75 Gyr for the GC ages. These are computed through a summation over normal distributions with the respective ages as the means and their uncertainties as the standard deviations. For the sample from Usher et al. (2019), the distribution was scaled by a factor of four to be comparable to the modeled populations. *Bottom*: Dark matter virial mass evolution of the two modeled galaxies, showing their accretion histories. The shaded region between 8 Gyr and 11 Gyr indicates the estimated time of the GSE merger (Belokurov et al. 2018; Helmi et al. 2018).

17.3 Discussion: GCs in the Milky Way

Having the model prediction that wet mergers leave an imprint on the GC age distribution of a galaxy, we tested it through the available GC measurements in the MW. For this we could make use of additional properties currently unavailable for GCs around other galaxies, such as kinematic phase-space information and more accurate age measurements.

17.3.1 Milky Way diagnostics

To address some of the caveats brought up in Section 17.2.1, we used further data available on the MW GCs to study to what extent the model prediction can be applied to the MW and its GC population. Using the GC progenitor assignments by Forbes (2020), the age distributions for four of the samples (Forbes & Bridges 2010; Dotter et al. 2010, 2011; VandenBerg et al. 2013; Cabrera-Ziri & Conroy 2022) can be split up by those assignments. Figure 17.3 shows the age distributions for the GCs formed in situ in the MW and those associated with GSE and the other GC host progenitors, for each of the four samples. This figure uses the age uncertainties to smooth the distributions. For the total GC age distributions see Figure G.1, which shows that for the smoothed distributions, only the total age distribution from Forbes & Bridges (2010) shows a hint at a bimodality. This bimodality is smoothed out when taking the mean GC ages from Kruijssen et al. (2019b), which may lead to GC age biases (discussed in Section G.1.1). See Section G.1.4 for the unsmoothed age distributions plotted as histograms for the most relevant GC host progenitor groups that correspond to Figure 17.3.

The two smaller samples from VandenBerg et al. (2013) and Cabrera-Ziri & Conroy (2022) do not reveal further information besides an indication for the low-energy GCs to have formed at slightly later times for the measurements by VandenBerg et al. (2013). In contrast, both of the other samples show that there is a physical reason for the bimodal GC age distribution shown in Figure 17.1: in the largest sample by Forbes & Bridges (2010), it is clearly seen that the younger peak seen in Figure 17.1 at 11 Gyr is dominated by GSE-associated GCs, with contributions from the Helmi Streams and the high-energy GCs. This is less pronounced in the sample by Dotter et al. (2010, 2011), where the high-energy GCs contribute most of the young GCs, albeit there is also a significant contribution from GSE. The fact that these GCs have a different origin than the other MW GCs is known through the age-metallicity relation (e.g., Leaman et al. 2013; Kruijssen et al. 2019b; Forbes 2020), in which the GCs associated with GSE and the other progenitor galaxies follow their own tracks. While the Sagittarius dwarf is expected to have fallen into the MW around 8–9 Gyr ago on a most likely rather circular orbit, its extended time range of GC formation could be a result of tidally induced star cluster formation during its orbit around the MW while there was still enough cold gas available (e.g., Williams et al. 2022, for a study on young clusters with ages of around 2 Gyr in the Small Magellanic Cloud, which are suggested to have formed through tidal interactions with the Large Magellanic Cloud).

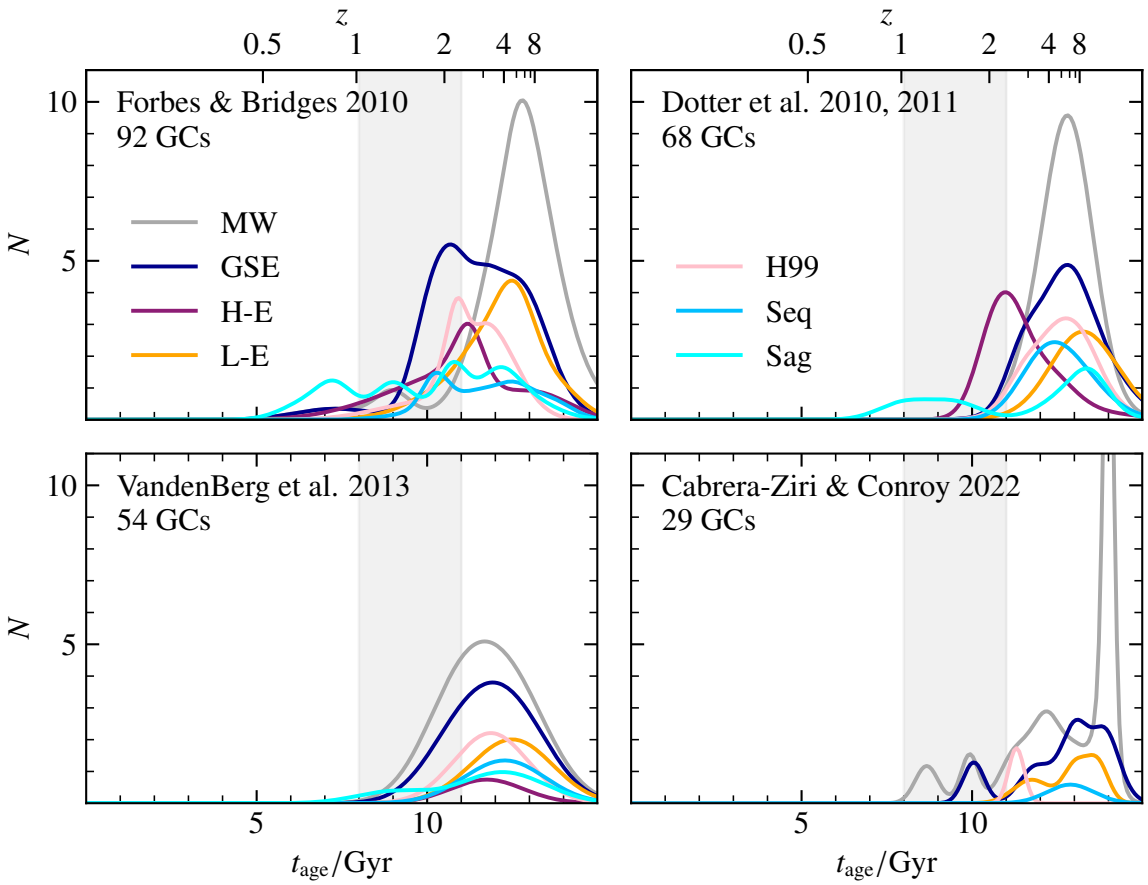


Figure 17.3: Globular cluster age distributions in the MW from Forbes & Bridges (2010), Dotter et al. (2010, 2011), VandenBerg et al. (2013), and Cabrera-Ziri & Conroy (2022), split up according to their likely progenitors from Forbes (2020). The shown classifications are the MW, GSE, unassociated high-energy GCs (H-E), unassociated low-energy GCs (L-E, which was given the name Koala by Forbes 2020), the Helmi Streams (H99), Sequoia (Seq), and Sagittarius (Sag). The total number of GCs in the respective sample is indicated in the top left. The distributions are computed from the GC ages and their uncertainties through a summation over normal distributions with the respective ages as the means and their uncertainties as the standard deviations. The shaded region between 8 Gyr and 11 Gyr indicates the estimated time of the GSE merger (Belokurov et al. 2018; Helmi et al. 2018). See Figure G.6 for the corresponding histograms of the most relevant GC progenitor groups without taking the uncertainties into account.

It is curious, however, that there appears to be a hint at a non-unimodal age distribution within the GSE GCs, which can be seen more clearly for Forbes & Bridges (2010) than for Dotter et al. (2010, 2011) in Figure 17.3. The bimodality is also present when only using the GC ages from the subsample of Marín-Franch et al. (2009) (Section G.1.3) as well as when using the mean GC ages from Kruijssen et al. (2019b). The bimodality is even slightly more prominent when using those ages, despite the overall distribution being more smoothed out (Section G.1.1). Additionally, it is also present when using the GC progenitor associations from any of Massari et al. (2019), Callingham et al. (2022), or Chen & Gnedin (2024a), and it is actually much more clearly visible for their classifications (Section G.1.2). The GCs associated with GSE are therefore shown to have an age bimodality across multiple different studies of their ages and association models with the GSE. The reason the bimodality is not seen in the samples from Dotter et al. (2010, 2011) and VandenBerg et al. (2013) is that they

each only contain 13 GCs associated with GSE, compared to 21 GCs from Forbes & Bridges (2010). Considering the raw age data without uncertainties, both distributions are actually bimodal (Figure G.6), with the caveat of there being a very small amount of GCs involved.

Still, if the signal is real, it can be brought together with the model prediction in a straightforward manner. As the model forms GCs in small halos at early times (first pathway as described in Section 17.1.1), a GSE satellite galaxy hosts its own GCs as it falls into the MW. We refer to these GCs as the accreted GCs in the following. Assuming there is enough cold gas available, the major merger event then triggers GC formation through the gas collision and tidal forces between the two galaxies (merger-induced GCs in the following, second pathway as described in Section 17.1.1; Ashman & Zepf 1992; Williams et al. 2022). This scenario leads to multiple properties arising for the GCs: (1) The age distribution of the combined early-formed accreted and merger-induced GCs is bimodal. (2) Assuming that GSE brings in its own cold gas, many of the merger-induced GCs are also formed from that gas, or a mixture of that and the MW's gas and therefore have similar metallicities and phase-space properties as those of the accreted GCs. This would then also lead to such GCs being associated with GSE through an analysis of phase-space and the age-metallicity relation. (3) Assuming the merger leads to violent gas interactions, it is possible that some recently formed merger-induced GCs are ejected from the overall orbit of GSE, leading to unassociated high-energy GCs. In that case, the high-energy GCs could also be associated with GSE and thus the bimodality in the GSE GC age distribution would be even more enhanced. It is also possible for GCs to distribute themselves further apart in phase space through other dynamical processes as shown by Pagnini et al. (2023), potentially ending up in the high-energy regime. This may occur in a similar fashion to the Splash (e.g., Bonaca et al. 2017; Belokurov et al. 2020), a group of more metal-rich stars in the MW halo that appear to have been formed in situ and dynamically ejected around the time of the GSE merger (e.g., Belokurov et al. 2020; Ciucă et al. 2023). Of course, this would not result in a change in age and metallicity of the formed GCs, though Ciucă et al. (2023) argue that the GSE merger could have first driven down the metallicity, which was then again enriched by the induced starburst.

While it is not possible to prove this theory with the current state of GC age precision and the difficulties of kinematic associations, the GC formation model indicates that the GCs associated with GSE are not only those that were brought in by the accreted galaxy (e.g., Côté et al. 1998), but also those that were formed through the wet merger (e.g., Ashman & Zepf 1992). Additionally, it is possible that some of the unassociated high-energy GCs were also formed in the process of the GSE merger, though it should be noted that many of those GCs have lower measured metallicities than those associated with GSE (Forbes 2020). In turn, this could be a result of the metallicity lowering through the merger (Ciucă et al. 2023). However, analyzing and modeling the details of GC metallicities in such a gas-rich major merger scenario are beyond the scope of this work and will be addressed in a future study.

Table 17.1: Predicted number of GCs, $N_{\mathrm{GC,formed}}$, formed through the GSE merger with the MW for different assumed MW total cold gas masses, $M_{\mathrm{gas,MW}}$. The GSE galaxy is assumed to have had a cold gas mass of $6.62 \times 10^9\,\mathrm{M}_\odot$ (Vincenzo et al. 2019).

$M_{\mathrm{gas,MW}}/\mathrm{M}_\odot$	$N_{\mathrm{GC,formed}}$
1.0×10^{10}	6
2.5×10^{10}	11
5.0×10^{10}	17
7.5×10^{10}	22

17.3.2 Model diagnostics

From Equation 17.3 it is possible to obtain the number of GCs expected from the model to form through a merger event based on the cold gas mass, M_{gas}. Vincenzo et al. (2019) estimated GSE to have brought in a cold gas mass of $6.62 \times 10^9\,\mathrm{M}_\odot$. For the MW, we estimated a range of possible cold gas masses by determining the cold gas masses of galaxies at $z = 2$ in a hydrodynamical cosmological simulation since the simulation that our GC model was applied to only contains DM particles. For this, we used Magneticum Pathfinder[2] Box4 (uhr) (with a side length of 68 Mpc and a gas particle mass of $m_{\mathrm{gas}} = 1.0 \times 10^7\,\mathrm{M}_\odot$) because it has the necessary resolution to resolve MW-like galaxies and their formation well, and at the same time it is large enough to contain a large sample of MW-like galaxies, from which we can draw conclusions about the expected gas mass at $z = 2$. The galaxies contained within it have been shown to agree well with observations across a broad range of properties (see Teklu et al. 2015 for details on the implementations and Valenzuela & Remus 2024 for an overview of comparisons to observations). For the galaxies at $z = 2$ with virial masses $5 \times 10^{11}\,\mathrm{M}_\odot \leq M_{\mathrm{vir}} \leq 8 \times 10^{11}\,\mathrm{M}_\odot$, the typical cold gas mass (which we define as star-forming gas particles with temperatures below 10^5 K) is $M_{\mathrm{gas}} = (2.1 \pm 0.6) \times 10^{10}\,\mathrm{M}_\odot$. We computed the expected numbers of formed GCs for a range of different MW cold gas masses between $1.0 \times 10^{10}\,\mathrm{M}_\odot$ and $7.5 \times 10^{10}\,\mathrm{M}_\odot$, leading to 6 to 22 GCs being formed (Table 17.1).

As seen in the GC age distribution from Forbes & Bridges (2010), there are 12 out of 21 GCs with available ages associated with GSE and 7 out of 9 unassociated high-energy GCs in the time range of GSE and the secondary peak of the overall MW GC age distribution. While the latter GCs are surely not all related to the GSE merger, the GC sample also does not include all GCs found in the MW (around 50–60%). Overall, the number of GCs expected from the model to be formed through such a merger aligns well with the observed number of GCs found to be associated with GSE or to be unassociated with high energies, while also taking into account the statistical incompleteness of the GC sample. This supports the prediction that multimodal GC age distributions can be used to trace wet mergers.

[2] www.magneticum.org

17.4 Discussion: Extension to nearby galaxies

While the GC age measurements are by far the most accurate for the MW due to resolved measurements of the clusters, the general properties from integrated GC age measurements can still give indications about the wet merger history of the host galaxy, through the relative ages between the GCs. One of the galaxies studied by Usher et al. (2019) is NGC 3115, a fast-rotating S0 field galaxy with stellar mass $M_* = 9 \times 10^{10}\,\mathrm{M}_\odot$ and virial mass $M_{\mathrm{vir}} = 1.2 \times 10^{12}\,\mathrm{M}_\odot$ (Forbes et al. 2016, assuming an NFW profile such that the virial mass is a factor 10 larger than the DM mass within $8\,R_e$, where R_e is the effective radius, the radius within which half the light of the galaxy is emitted). It has 550 ± 80 GCs (Harris et al. 2013) and features multimodal age distributions (based on 116 measured GC ages from Usher et al. 2019; top panel of Figure 17.4). The multimodal behavior of the ages is even retained when smoothing the histogram with a Gaussian kernel of 1.5 Gyr (smooth line), which is a value we selected to illustrate the effect of smoothing that can be caused by measurement uncertainties. There is in fact a galaxy in the simulation that has a very similar GC age distribution as NGC 3115, which can here be seen in the middle panel of Figure 17.4 (the similarity of the distributions is seen especially well in the cumulative distributions shown in fig. 17 of Valenzuela et al. 2021). The simulated galaxy has a virial mass of $M_{\mathrm{vir}} = 1.8 \times 10^{12}\,\mathrm{M}_\odot$, similar to that of NGC 3115, and a total of 525 GCs, consistent with NGC 3115, which places it 0.2 dex above the mean linear scaling relation from Burkert & Forbes (2020), but still within the observed scatter. Interestingly, both the observed and simulated ages feature three minor peaks in the distribution without smoothing over it, although this could very well be a coincidence given the large uncertainties for the observational measurements. For the simulation this means that there were overall three especially gas-rich mergers leading to an increased amount of GC formation. This occurred during a time of steady assembly between 6 Gyr and 12 Gyr ago (bottom panel of Figure 17.4).

This agrees well with the inferred formation history of NGC 3115 obtained through kinematics from IFU data and tracer populations, the metallicity profiles, its mass distribution, and the study of its morphological components: it is believed to have experienced an early gas-rich accreting phase followed by a lack of significant mergers thereafter (Arnold et al. 2011; Guérou et al. 2016; Zanatta et al. 2018; Poci et al. 2019; Dolfi et al. 2020; Buzzo et al. 2021). In particular, this supports the prediction of GC ages being able to trace wet mergers, also for galaxies outside the Local Group.

Such behavior is not the norm, however. This could already be seen from the median age distributions presented by Valenzuela et al. (2021) for all the virial mass bins, which show that generally GC populations are dominated by old GCs like those of the MW. For most galaxies, GC formation bursts are too close in time to the oldest GC populations to be able to distinguish them without having further properties available like in the MW, or the bursts are not significant enough due to a lack of cold gas as gas-rich merger events become less and less frequent with time.

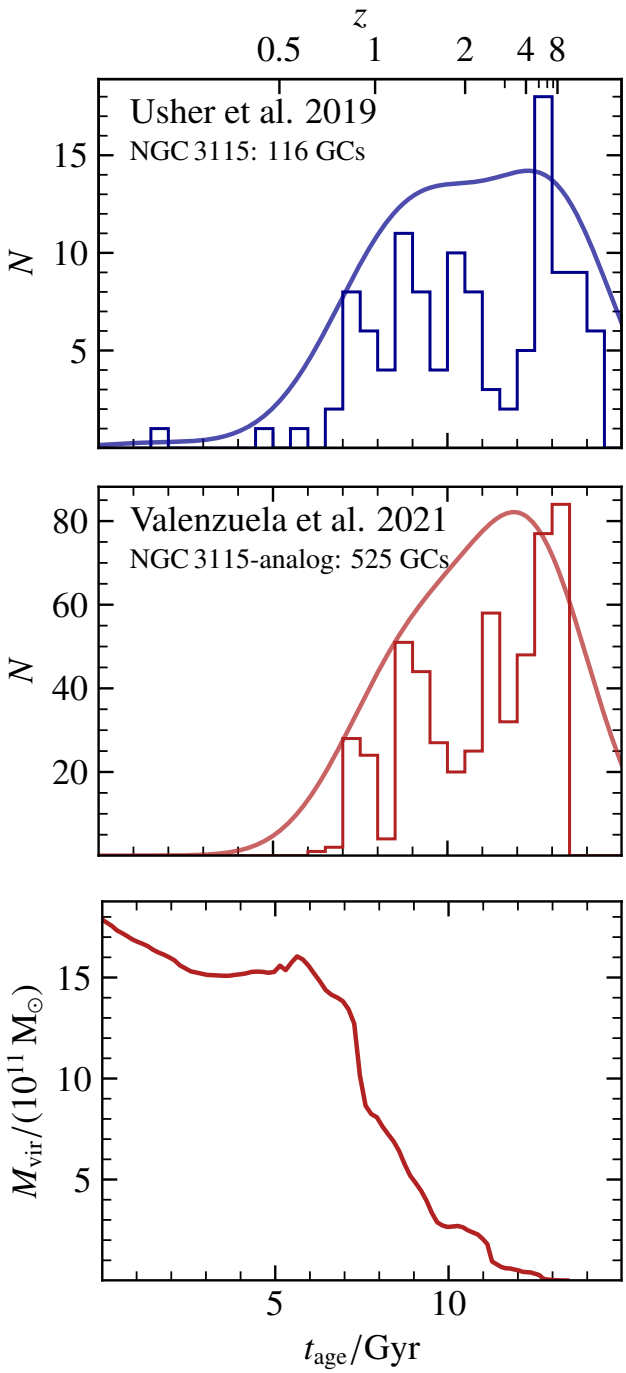


Figure 17.4: GC ages and virial mass evolution of the modeled NGC 3115-analog galaxy compared to the observed GC ages in NGC 3115. *Top and middle*: Age distributions of the GC population in NGC 3115 from Usher et al. (2019), with a sample of 116 GCs, and of the modeled GC population in an NGC 3115-analog galaxy from Valenzuela et al. (2021) with 525 GCs. The smooth distributions are smoothed using an assumed uncertainty of 1.5 Gyr for the GC ages. These are computed through a summation over normal distributions with the respective ages as the means and their uncertainties as the standard deviations. *Bottom*: Dark matter virial mass evolution of the simulated NGC 3115-analog galaxy, showing its accretion history.

One such case is M 31, for which the GC age measurements of Wang et al. (2021), Usher et al. (2024), and Cabrera-Ziri et al. (in prep.) show no clear bimodal distribution (Figure 17.5). There is a hint at some additional modes between 6 Gyr and 10 Gyr ago in the data from Usher et al. (2024) and Cabrera-Ziri et al. (in prep.) (middle and lower panel). The numbers of GCs

in these modes are small for the latter study (6 around 6–8 Gyr ago and 8 around 8–10 Gyr ago) and the uncertainties of the GC age measurements are large compared to the individual age peaks (smooth curves in the middle and lower panel), so we cannot exclude that they originate from statistical uncertainties. If they do not, this would indicate only small gas-rich mergers given the small numbers of GCs produced. As discussed in Section 17.1.2, the absolute ages of the measured distributions should not be compared with those of Wang et al. (2021) due to differences in the measurement techniques, which led to the much younger determined ages for Wang et al. (2021). In terms of their relative ages, however, all of the samples show that significant features in the GC age distributions are not found for all galaxies and strong features are only visible for mergers that have a sufficient amount of gas. Additionally, which features are identifiable in GC age distributions will always depend on how large the measurement errors are, which smooth out the data, which first removes the signatures from smaller mergers or those with smaller gas fractions. Thus, the method is the most reliable in detecting wet mergers with large mass fractions. Finally, note that the sample from Cabrera-Ziri et al. (in prep.) is biased towards metal-rich GCs (Section 17.1.2). However, gas-rich major mergers are expected to involve the more metal-rich GCs as opposed to metal-poor ones, such that we believe the implications of our analysis to be unaffected.

Observationally, it has been proposed that M 31 experienced a major merger at around 2 Gyr ago, possibly with the progenitor of M 32 (D'Souza & Bell 2018a,b; Hammer et al. 2018). A large peak in star formation between 2 Gyr and 4 Gyr ago in the disk and outskirts of M 31 (Bernard et al. 2012, 2015; Williams et al. 2017) is likely related to this event. Using planetary nebulae, Bhattacharya et al. (2023) find further evidence for a wet major merger of M 31 2.5 Gyr to 4 Gyr ago. In fact, the full sample by Wang et al. (2021) also includes young stellar clusters with ages below 1.5 Gyr, which could potentially also have been formed as a result of the gas brought in by the merger and would not be referred to as GCs yet. Similarly, the distribution by Usher et al. (2024) shows GCs with these kind of young ages as well as GCs with ages around 3–4 Gyr, and Cabrera-Ziri et al. (in prep.) also find one GC with an age of 2.5 Gyr, which could coincide with that merger.

It has also been determined that the star formation rate was very low before the recent peak, with most stars having formed prior to 8 Gyr ago (Williams et al. 2017). Due to the smooth and very massive stellar halo observed for M 31, it is estimated that the merger history was dominated by many smaller accretion events (e.g., Ibata et al. 2014; Mackey et al. 2019). This scenario is supported by the model prediction presented in this work, in which no single sufficiently massive merger exists that would lead to a significant GC formation burst.

Finally, the massive elliptical galaxy NGC 1407 also lacks a significant second peak in its GC age distribution, though there is a tail with a slight peak towards younger ages around 6–9 Gyr ago and potentially another around 10 Gyr ago (Figure 17.6). Due to the integrated age measurements, this could be the result of underestimated ages for those GCs as the peak again consists of only very few GCs. Overall, it appears that from the GC ages NGC 1407 has not experienced any massive wet mergers since the early buildup phase of the galaxy, and at most a later merger with a low cold gas fraction. In the latter case, it should be expected that

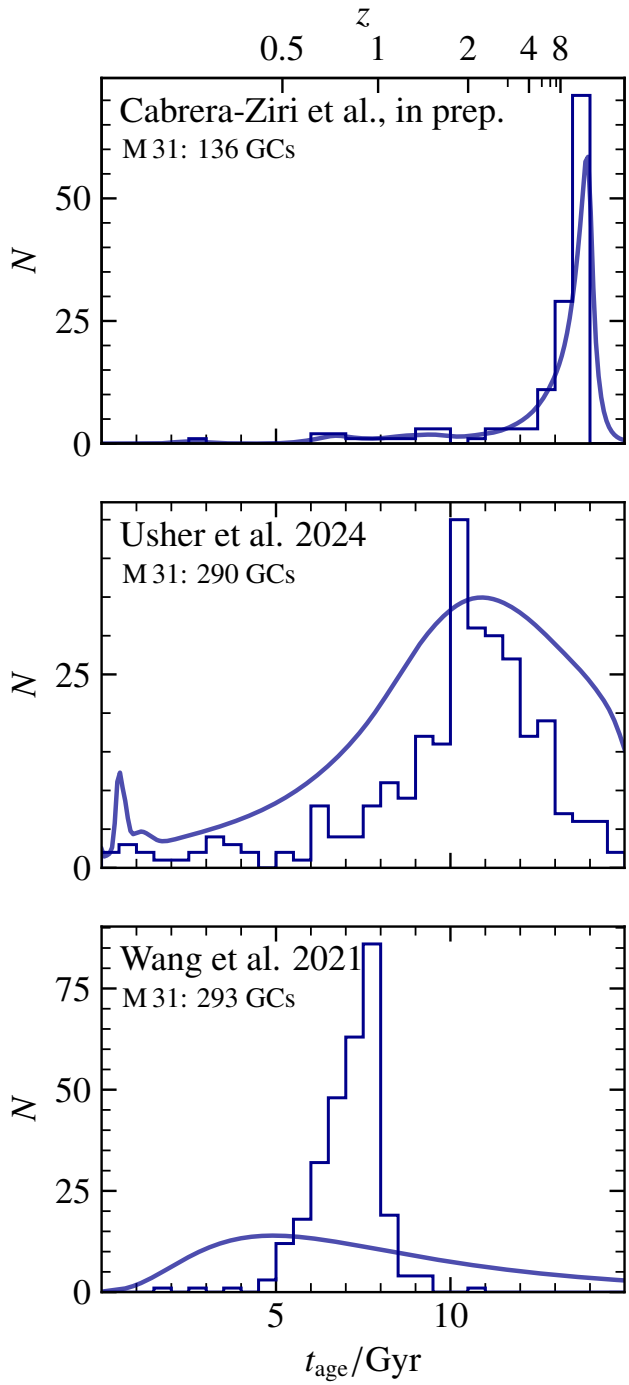


Figure 17.5: Globular cluster age distribution in M 31 from Cabrera-Ziri et al. (in prep.), Usher et al. (2024), and Wang et al. (2021), with sample sizes of 136 GCs, 290 GCs, and 293 GCs, respectively. The ages in the sample of Wang et al. (2021) correspond to their determined old clusters ($t_{age} > 1.5$ Gyr). For further comparisons with previous GC age determinations in M 31, see fig. 8 of Wang et al. (2021). The smooth lines show the distributions smoothed by the measurement uncertainties. These are computed through a summation over normal distributions with the respective ages as the means and their uncertainties as the standard deviations for Usher et al. (2024) and over log-normal distributions for the other two data sets. Note that for the logarithmic uncertainties, the visualization in linear space is skewed with respect to the peak.

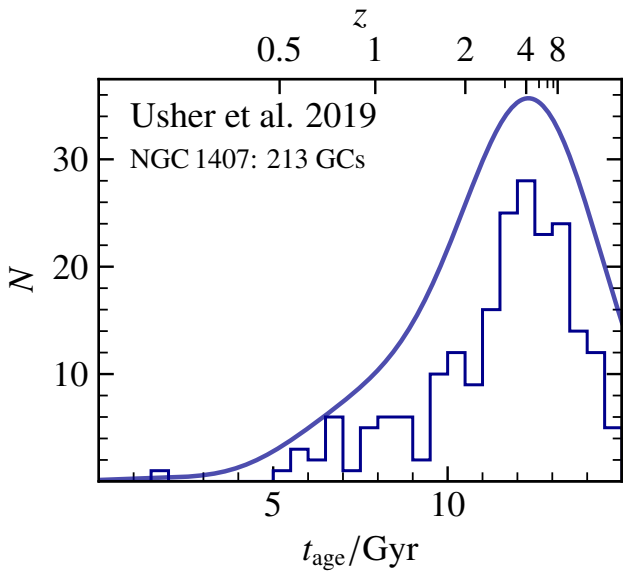


Figure 17.6: Globular cluster age distribution in NGC 1407 from Usher et al. (2019) with a sample size of 213 GCs. The smooth line shows the distribution smoothed using an assumed uncertainty of 1.5 Gyr for the GC ages. These are computed through a summation over normal distributions with the respective ages as the means and their uncertainties as the standard deviations.

there would also be a sign of late star formation activity in the stellar populations themselves. In fact, Spolaor et al. (2008) found from their stellar population measurements of NGC 1407 that the stars are uniformly old, having formed around 12 Gyr ago.

A kinematically decoupled core (KDC) hints at a major merger of NGC 1407 with gas fractions between 15% and 40% (Hoffman et al. 2010; Schulze et al. 2017). While Forbes & Remus (2018) find that a simulated galaxy from Magneticum with a similar size and mass as NGC 1407 had a late major merger around 8 Gyr ago, it was not selected based on further properties such as stellar ages or metallicity gradients. However, Ferré-Mateu et al. (2019) find in their observations of NGC 1407 that the KDC is slightly younger than the rest of the galaxy (we estimate a difference of around 1 Gyr based on their fig. 5), suggesting that a wet major merger could have occurred slightly later than the early buildup of the galaxy. This scenario is compatible with the GC age distribution found by Usher et al. (2019): the lack of late gas-rich mergers is consistent with no large amount of late GC formation, and the slight peak in the GC ages could be related to the wet major merger that formed the KDC. Such a merger is expected to have had a relatively high gas fraction (Hoffman et al. 2010), potentially forming many GCs as a result. However, due to the violent nature of such a merger, many of those systems would likely be disrupted in the same process, leading to a smaller peak in the age distribution. Since the GC sample analyzed by Usher et al. (2019) is biased towards central GCs due to the SLUGGS survey having been focused on the inner regions, it is expected that it would be more likely to pick up signatures from major mergers.

17.5 Conclusion

In this work, we have used the GC formation model from Valenzuela et al. (2021) with dual formation pathways to predict that massive wet mergers with enough cold gas can leave an imprint on the age distribution of the GC population in the host galaxy. This imprint results in a bimodal or even multimodal distribution, indicating when the wet mergers occurred. This prediction is in part also a consequence of the idea that red GCs tend to form through mergers that also induce star formation, thus resulting in properties that overall trace the underlying stellar component, such as spatial, kinematic, or chemical properties (e.g., Brodie & Strader 2006; Pota et al. 2013; Dolfi et al. 2021). In contrast, mergers with little to no gas are not traced by the GC ages since the lack of gas means that no significant number of GCs could be formed in the process.

The prediction is discussed for the MW in detail. We find that a hint at bimodality visible in the pure GC age distributions compiled by Forbes & Bridges (2010) can be further disentangled by combining the data with phase-space information on the GCs to map which galaxy progenitors the GCs are likely associated with (e.g., Massari et al. 2019; Forbes 2020; Callingham et al. 2022; Chen & Gnedin 2024a). We find the later peak in the GC age distribution to correspond to the GCs associated with GSE, the last major merger of the MW (Belokurov et al. 2018; Helmi et al. 2018), and in part also to the unassociated high-energy GCs and the GCs of the Helmi Streams. In fact, the age distribution of the GSE GCs appears to also have a bimodality. Since GSE is expected to have been a massive and gas-rich merger, we suggest that GSE not only brought in its own older GCs, but also formed a second group of GCs through the merger with the MW. The second group of GCs would be located near the first in phase space and lie on the same age-metallicity relation, as is also found for them in the observations. We further suggest that some of the unassociated high-energy GCs may also originate from the GSE merger, since it is possible that the violent merger dynamics would eject some GCs, or that GCs migrate away in phase space over time (Bonaca et al. 2017; Belokurov et al. 2020; Pagnini et al. 2023).

Two simulated MW-mass galaxies with similar GC age distributions as the MW are found to both have had a wet major merger around the same time as GSE (around 8 Gyr to 10 Gyr ago). One of the two then evolved only through smooth accretion and mini and minor mergers, as is believed to have been the case for the MW. In contrast, the other simulated galaxy encountered a dry merger at later times that is not traced by the GC ages, (for those kind of mergers, other kind of indicators have to be used).

We also tested the model with three other observed galaxies, NGC 3115, M 31, and NGC 1407, for which GC ages have been obtained. For NGC 3115, the observed GC age distribution is clearly multimodal with a considerable population of younger GCs that are 7–11 Gyr old. We were able to find a simulated galaxy of comparable virial mass and a similar GC age distribution. It underwent an early phase of multiple wet mini and minor mergers that led to the formation of the younger GC population, after which it experienced no further significant mergers. This agrees well with the expected formation history of NGC 3115

inferred from other tracers (Arnold et al. 2011; Guérou et al. 2016; Poci et al. 2019; Buzzo et al. 2021) and supports the prediction that additional modes in the GC age distribution trace wet mergers.

The GC age distribution of M 31 features no bimodality, indicating that it experienced no significant late wet mergers. However, it shows two or even three small peaks in the GC age distributions at 2–3 Gyr and at 7 and 9 Gyr, indicating either small merger events with large gas fractions or large merger events with low gas fractions, with the former being more likely than the latter. Since these peaks are small and the uncertainties are large, this is not conclusive, however. Similarly, NGC 1407 features no clear bimodality, but a possible second late peak in the GC age distribution may be related to an early wet major merger that led to the kinematically distinct core found in the overall very old galaxy. These are examples for the most common case for galaxies: the simulation predicts that strong peaks in the GC age distribution with GCs younger than around 12 Gyr clearly indicate a massive wet merger event and that small wet mergers can still leave minor peaks in the GC age distribution. Dry mergers, however, leave no imprints in the GC age distributions.

To conclude, the age distribution of GCs can be used as a tracer for wet mergers of galaxies, which are generally more difficult to infer from observations: while the old age peak of the GC age distribution does not help in constraining the merger history as here the old populations from the main progenitor of a galaxy mix with the old GCs brought in through other merging galaxies of all kind, the young GCs with ages less than around 11 Gyr are formed in the otherwise untraceable wet merger events. However, due to the current large observational uncertainties in determining GC ages from integrated measurements, further development of the age determination techniques will be essential to better understand individual galaxies' formation histories. Finally, increasing the number of galaxies with accurate GC age measurements will also help improve our understanding of GC formation and set more constraints on current GC formation models. We thus propose that this is a good method to infer the wet merger times of extragalactic galaxies from observations. With the advent of observatories such as Euclid, the Nancy Grace Roman Space Telescope, and the Vera C. Rubin Observatory, applying photometric methods to obtain GC ages from such observations has the great potential of providing deeper insight into the early gas-rich formation history of galaxies.

18

High-Redshift Stellar Clusters in GC Models

This chapter was published as Valenzuela et al. (2025a), MNRAS 537, 306[1]:
Globular cluster ages and their relation to high-redshift stellar cluster formation times from different globular cluster models

A matter of current research is how early the first star clusters were able to form. Observations with JWST are now revealing compact young star clusters in high-redshift galaxies at redshifts up to $z = 10$ in strongly lensed galaxies (e.g., Vanzella et al. 2022b, 2023; Adamo et al. 2024; Mowla et al. 2024). These measurements indicate that bursty star formation already occurs very early on in the Universe. However, the open question remains how these star clusters evolve with time and whether they could be the progenitors of the GCs we observe today at $z = 0$. Studies of intermediate- to high-redshift systems like the Sparkler galaxy suggest that GCs formed very early can at least survive to redshifts of $z = 1.4$ (e.g., Mowla et al. 2022; Forbes & Romanowsky 2023).

A natural approach to addressing the connection between the observed high-redshift star clusters and today's GCs is through models such as those summarized in Section 15.4. These models are not only diverse with respect to the implementation of GC formation and evolution, but also with respect to the galaxy formation model: some use the intrinsic properties of the hydrodynamic simulation (e.g., Pfeffer et al. 2018; Reina-Campos et al. 2022; Doppel

[1]Minor adjustments have been made, and the introduction has been adapted for this thesis.

et al. 2023), whereas most of the models use an underlying empirical or semi-analytic model for galaxy formation (e.g., Beasley et al. 2002a; Choksi et al. 2018; El-Badry et al. 2019; Valenzuela et al. 2021; Chen & Gnedin 2022). Even though such models are created to match some collection of properties at $z = 0$, they are highly diverse in their overall approach and implementation. Despite this diversity, there is a general lack of direct comparison between models in the literature. As none of the models is currently tuned to match high-redshift observations, they each make predictions with respect to the formation times and formation environments of GCs. In this work, we present the first side-by-side comparison of numerous different GC models, for which we study their predictions for GC ages and the formation redshifts of surviving GCs.

As the ages of GCs in the Milky Way (MW) can be measured through the distribution of their individual stars in the colour-magnitude diagram (CMD; see Section 15.2.3), they have significantly smaller uncertainties than measurements of GC ages in other galaxies. Additionally, most models have focused on MW-like galaxies or at least included such simulated host galaxies in their analyses. For these reasons, we perform the GC model comparison for MW-like galaxies and compare the results to the measurements in our own MW. We aim to present the range of direct predictions regarding the ages of GCs, thereby laying the groundwork for improving on these models in the future.

The paper is structured as follows: in Section 18.1, we introduce the observational data for our MW as well as the GC models that we use in our comparison. Next, we investigate in Section 18.2 whether the models are capable of reproducing the observational data for the GC age distribution in the MW, followed in Section 18.3 by the predicted GC age distributions for MW-mass galaxies for the models that have been applied to a larger number of such galaxies. In Section 18.4, we present the predicted formation redshift distributions of surviving GCs and compare these to recent high-redshift observations of young star clusters. Finally, we summarise and conclude in Section 18.5.

18.1 Data

For this work, we collected GC age data from multiple observational and theoretical studies. The observations are of the GCs in the MW and we selected GC formation models that have been run on MW-like galaxies. In the following, we introduce the data sets and detail which criteria were used to define *MW-like* galaxies for the theoretical studies. If applicable, we also state which selection criteria we apply to the GCs, such as mass or metallicity cuts. Note that the definition of a galaxy being "MW-like" or a MW analogue depends on the scientific question and has no single answer (see also Pillepich et al. 2024). As a result, the different theoretical studies have also applied several different approaches to selecting MW analogues, some more and some less restricting. In this work, we decided to use the term *MW-like* for any galaxy that was selected by more criteria than just halo or stellar mass, such as it being disc-dominated or having an early formation history, for example. In contrast, *MW-mass* refers to any galaxy having been purely selected based on mass criteria. For all the plots in this and

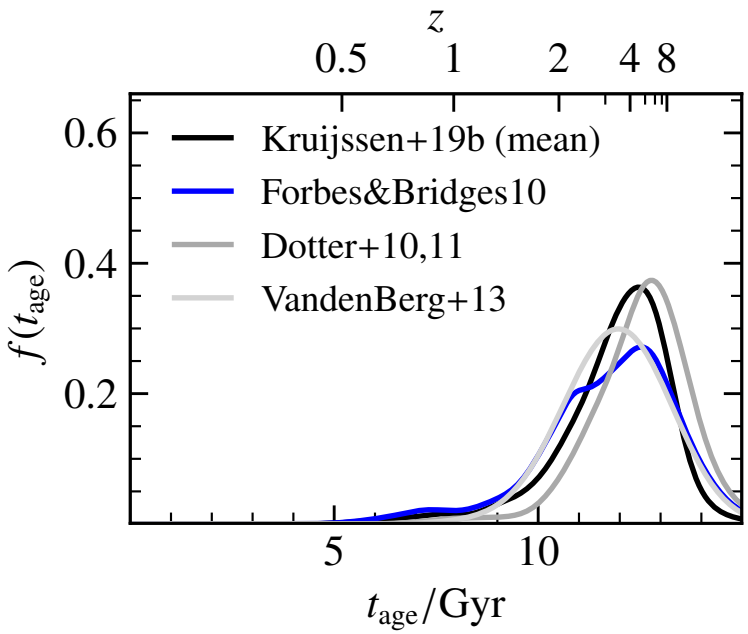


Figure 18.1: Age distributions of observed GCs in the MW. The ages are taken from Forbes & Bridges (2010), Dotter et al. (2010, 2011), VandenBerg et al. (2013), and Kruijssen et al. (2019b). The ages from the latter work are the mean ages from the other three studies, which we show as the black distribution. The smooth curves are determined from the sum of normal distributions at the individual age measurements with standard deviations equal to the individual age uncertainties.

the subsequent sections we show the ages and equivalent redshift scales at the bottom and top of the panels according to the cosmological parameters $h = 0.6781$ and $\Omega_M = 0.308$.

18.1.1 Observations

We include three compilations of MW GCs that use resolved CMD data to determine the GC ages, all of which have sample sizes of more than 50 GCs. We took the ages and their uncertainties from Kruijssen et al. (2019b) for the following samples, as well as their determined mean GC ages based on the three studies:

- Forbes & Bridges (2010): 92 GCs compiled from multiple previous studies that measured their ages (Salaris & Weiss 1998; Bellazzini et al. 2002; Catelan et al. 2002; De Angeli et al. 2005; Carraro et al. 2007; Dotter et al. 2008; Carraro 2009; Marín-Franch et al. 2009),
- Dotter et al. (2010, 2011): 68 GCs, whose ages were all obtained through the same method,
- VandenBerg et al. (2013): 54 GCs, whose absolute ages were measured consistently for the sample of Marín-Franch et al. (2009),
- Kruijssen et al. (2019b): 96 GCs with the mean ages determined from the three other studies.

The GC age distributions of the four studies are shown in Figure 18.1. The age distribution from Kruijssen et al. (2019b) is the one that we will also use to compare to the modelled GC ages as it takes the mean of the other studies, thereby giving us the current best absolute

estimate of an individual GC's age. This is the best approach for the purposes of this study, where absolute ages are our main concern. In contrast, in many cases the relative GC ages are of greater importance, such that combining different studies should then be avoided.

18.1.2 Stellar particle tracer model

The model for GC formation by Renaud et al. (2017) uses the stellar particles within a simulated galaxy as tracers for GC candidates. Only stellar particles that were formed at lookback times of more than 10 Gyr are considered for this and are classified as accreted and in-situ formed based on their formation sites. There is no maximum age that the GC candidates could have due to the first GC formation times still being unknown. This model was run on a cosmological hydrodynamic zoom-in simulation of a MW-like galaxy, which has a virial mass of $M_{200} = 1.3 \times 10^{12}\,\mathrm{M}_\odot$ at $z = 0$ in the parent simulation (where M_{200} is the mass within the radius enclosing a volume containing a density 200 times higher than the mean density of the Universe) and a stellar mass of $M_* = 4.1 \times 10^{10}\,\mathrm{M}_\odot$ at $z = 0.5$, the last point in time of the zoom-in simulation. The last major merger of the galaxy occurred at $z \approx 2$ with a mass ratio of 1:10, similar to the predicted last major merger of the MW, the GSE (e.g., Belokurov et al. 2018; Helmi et al. 2018).

The modelled GC candidates statistically represent the properties of the accreted and in-situ formed clusters. At the same time, as they were directly obtained from the stellar particles, their ages also trace the overall star formation history of a simulated MW-like galaxy before 10 Gyr ago. The ages we used in this work are those found in the bottom panel of fig. 8 of Renaud et al. (2017). Since the formation efficiency is likely different between accreted and in-situ formed GCs, we kept the two subpopulations of GCs separate in the analysis for this work. The total population of GC candidates is then a superposition of these two. Their used cosmological parameters are $h = 0.702$ and $\Omega_M = 0.272$. We show the relevant ranges of galaxy and GC population properties in Table 18.1 for this and the other models presented in the following.

18.1.3 E-MOSAICS model

The E-MOSAICS model (MOdelling Star cluster population Assembly In Cosmological Simulation within EAGLE; Pfeffer et al. 2018) couples MOSAICS (Kruijssen et al. 2011, 2012) onto the EAGLE galaxy formation model (Crain et al. 2015; Schaye et al. 2015) as a subgrid cluster model. When gas particles form stellar particles in the simulation, a certain fraction of the formed stellar particle mass is considered to be contained in stellar clusters in a subgrid fashion depending on the local gas density, velocity dispersion, and temperature. This designated cluster mass is distributed over a cluster population according to an initial cluster mass function (ICMF) set as an exponentially cut-off power law (Schechter 1976). Mass loss and disruption of GCs are accounted for according to the tidal forces measured throughout time. For the study of GCs, they only take the clusters with masses above $M_{\mathrm{GC}} > 10^5\,\mathrm{M}_\odot$ and low metallicities of $-2.5 < [\mathrm{Fe/H}] < -0.5$ into account to get around the issue of

Table 18.1: Galaxy properties of the GC model studies and from the our MW: the number of MW-mass galaxies analysed ($N_{\rm gal}$), their virial and stellar mass ranges ($M_{\rm vir}$ and M_*), the number of GCs contained in the individual galaxies ($N_{\rm GC}$), the mean and standard deviation of $N_{\rm GC}$, and the mean and standard deviation of the ages of all the GCs. The virial mass definitions are M_{200} for Renaud et al. (2017), Kruijssen et al. (2019a), Reina-Campos et al. (2022), and Valenzuela et al. (2024b); total mass of the system according to the applied subhalo finder for Chen & Gnedin (2024b); and halo mass for De Lucia et al. (2024). The GC-limited sample of De Lucia et al. (2024) is further selected according to $N_{\rm GC}$. Note that the differences in GC number and average GC age are the result of the different galaxy samples. For the values measured from observations, the virial mass estimate is from Bobylev & Baykova (2023), which has also been proposed to be larger by other more recent works (e.g., Kravtsov & Winney 2024), the stellar mass from Licquia & Newman (2015), $N_{\rm GC}$ from Garro et al. (2024), and we computed $\langle t_{\rm age}\rangle$ using the mean GC ages from Kruijssen et al. (2019b).

Model	Study	$N_{\rm gal}$	$M_{\rm vir}/(10^{12}\,{\rm M}_\odot)$	$M_*/(10^{10}\,{\rm M}_\odot)$	$N_{\rm GC}$	$\langle N_{\rm GC}\rangle$	$\langle t_{\rm age}\rangle$/Gyr
Stellar particle tracer	Renaud+17	1	1.3	4.1 (at $z = 0.5$)	–	–	11.4 ± 0.7
E-MOSAICS	Kruijssen+19	6	0.7–2.2	0.8–4	60–330	130 ± 100	10.3 ± 2.1
EMP-Pathfinder	ReinaCampos+22	21	0.6–2.3	0.4–6.5	140–1250	400 ± 240	8.1 ± 3.5
Rapid mass growth	Chen&Gnedin24	3	1.1–1.4	4–8	160–180	170 ± 10	11.2 ± 1.4
Two-phase	DeLucia+24	12 884	0.8–3	2–8	0–11 100	290 ± 590	9.5 ± 1.7
Two-phase (GC-limited)	DeLucia+24	1140	0.8–3	2–8	170–250	205 ± 25	10.8 ± 1.1
Dual formation pathway	Valenzuela+24	21	1–2	1.6–4.4	220–700	400 ± 120	11.1 ± 2.3
MW Observations		–	1.1 ± 0.4	6.1 ± 1.1	$\gtrsim$200	–	11.9 ± 1.3

"under-destruction" of GCs due to the multiphase ISM not being modelled. This would mostly affect younger, metal-rich GCs that spend more time orbiting the gas discs of their host galaxies.

Pfeffer et al. (2018) and Kruijssen et al. (2019a) ran the E-MOSAICS model for the volume-limited sample of 25 zoom-in cosmological simulations of present-day MW-mass galaxies contained in the 25 Mpc volume from the EAGLE project. The galaxies have virial masses of $M_{200} = 7 \times 10^{11}\,{\rm M}_\odot$–$3 \times 10^{12}\,{\rm M}_\odot$ and stellar masses of $M_* = 8 \times 10^9\,{\rm M}_\odot$–$4 \times 10^{10}\,{\rm M}_\odot$ at $z = 0$. For this work, we extracted the ages of the GC systems within the six galaxies found in fig. 3 of Kruijssen et al. (2019a). Those galaxies cover the full range of virial and stellar masses of the parent sample of 25 galaxies and were specifically chosen by Kruijssen et al. (2019a) to show the variation of GC system properties found within the whole sample of simulations. Their used cosmological parameters are $h = 0.6777$ and $\Omega_M = 0.307$.

18.1.4 EMP-Pathfinder model

The EMP-Pathfinder model (Reina-Campos et al. 2022) addresses the issue of clusters disrupting too slowly in E-MOSAICS by including the physics of the multiphase nature of the ISM in the simulations. The shock-driven disruption of clusters by the cold gas in the ISM is necessary to reproduce the mass distribution of old GCs in the MW. The model follows that of E-MOSAICS with some changes concerning GCs, including the ICMF model, the disruption treatment, and GC size prescriptions. Mass loss and disruption of GCs are accounted for through tidal forces. Dynamical friction is applied to the clusters in post-processing.

EMP-Pathfinder was run for 21 of the MW-mass galaxies used in the E-MOSAICS project with the same zoom-in initial conditions. All six galaxies for which we have the E-MOSAICS GC data are among these galaxies. The virial masses range from $M_{200} = 6 \times 10^{11}\,{\rm M}_\odot$–$2.3 \times 10^{12}\,{\rm M}_\odot$ and stellar masses from $M_* = 4 \times 10^9\,{\rm M}_\odot$–$6.5 \times 10^{10}\,{\rm M}_\odot$. While Reina-Campos

et al. (2022) focus their analysis on the clusters older than 10 Gyr for a large part of their work, this approach is not appropriate for our aim of studying the intrinsic predictions of GC models with respect to the GC ages. For this reason, we first set a GC mass cut of $M_{\rm GC} \geq 10^4\,{\rm M}_\odot$ to be comparable to the mass range of GCs observed in the MW (Baumgardt & Hilker 2018), and then applied the same metallicity cut as Kruijssen et al. (2019a) for E-MOSAICS of $-2.5 < [{\rm Fe/H}] < -0.5$. Additionally, we also consider the GC age distributions without the metallicity cut, though it should be noted that the large amount of young clusters is artificial and reflects their numerical choices for the star formation prescription. Their used cosmological parameters are $h = 0.6777$ and $\Omega_M = 0.307$, the same as used in E-MOSAICS.

18.1.5 Rapid mass growth model

The GC formation model employed by Chen & Gnedin (2024b) is based on that introduced by Choksi et al. (2018): when the relative virial mass accretion rate of a galaxy surpasses a certain threshold value (a free parameter of their model, found to be $\dot{M}_{\rm halo}/M_{\rm halo} > 0.5\,{\rm Gyr}^{-1}$), GC formation is triggered. To obtain the available cold gas mass, analytic stellar mass-halo mass and gas mass-stellar mass relations are applied to the virial masses of the galaxies as well as prescriptions for the evolution of their scatter. The available cold gas mass is then converted to the total formed GC mass by an efficiency factor. The number of GCs is obtained by sampling from a Schechter (1976) ICMF. Young stellar particles or DM particles in local density peaks are then tagged with the formed GCs to trace their evolution thereafter. Mass loss and disruption of GCs are accounted for according to the tidal forces measured throughout time.

Chen & Gnedin (2024b) presented three MW-like galaxies with this GC model. Those galaxies were selected by their total mass, circular velocity, and accretion history, where the last major merger must have occurred between 10–12 Gyr ago to resemble a GSE merger and secular evolution thereafter. Two of the MW-like galaxies are from TNG50, and one is from a DM-only zoom-in simulation of a galaxy group resembling the Local Group (introduced by Brown & Gnedin 2022; Chen & Gnedin 2023). The galaxies cover mass ranges of $M_{\rm vir} = 1.1 \times 10^{12}\,{\rm M}_\odot$–$1.4 \times 10^{12}\,{\rm M}_\odot$ and $M_* = 4 \times 10^{10}\,{\rm M}_\odot$–$8 \times 10^{10}\,{\rm M}_\odot$ at $z = 0$. For the GCs, we only take into account those with masses of $M_{\rm GC} \geq 10^4\,{\rm M}_\odot$ for comparability with the observed MW GCs, just as we also did for the EMP-Pathfinder GCs. The cosmological parameters are $h = 0.6774$ and $\Omega_M = 0.3089$ for TNG50 and $h = 0.68$ and $\Omega_M = 0.31$ for the Local Group simulation.

18.1.6 Two-phase model

De Lucia et al. (2024) use a semi-analytic two-phase model for GC formation and evolution based on the model of Kruijssen (2015), where stellar clusters are formed from cold gas in the galaxy disc depending on the cold gas surface density and the angular momentum. The galaxy properties are obtained from the semi-analytic model GAEA (GAlaxy Evolution and Assembly; Hirschmann et al. 2016; Xie et al. 2017), which is run on DM-only simulations

and populates the DM haloes with baryonic properties based on the merger histories. The stellar clusters are evolved through time taking into account mass loss and disruption until a galaxy merger is able to eject the clusters into the halo. Note that as a semi-analytic model, the actual GC spatial properties are not traced. Only the clusters that the model ejects into the halo as a consequence of a merger are considered to be GCs.

The model was run alongside GAEA for the Millenium Simulation (Springel et al. 2005), a DM-only cosmological simulation with a box length of 685 Mpc. They define their MW-like galaxy selection as being disc-dominated (bulge-to-total mass ratio $B/T < 0.2$) and that are central galaxies with virial masses of $M_{\rm vir} = 8 \times 10^{11}\,{\rm M}_\odot$–$3 \times 10^{12}\,{\rm M}_\odot$ at $z = 0$. To make the galaxy selection more comparable with those of the other studies selected in this work, we further add a stellar mass criterion of $M_* = 2 \times 10^{10}\,{\rm M}_\odot$–$8 \times 10^{10}\,{\rm M}_\odot$, leading to a total of 12 884 galaxies. For the GCs, we only take into account those with masses above $M_{\rm GC} \geq 10^4\,{\rm M}_\odot$, just as for some of the previously presented models. No metallicity cut is applied. As the number of GCs in those galaxies varies greatly (see Table 18.1), we also consider a second more limited sample of galaxies, taking only those into account with 170–250 GCs (this is the case for 1140 galaxies, whereas 8146 galaxies have fewer GCs and 3598 have more). This number range is based on the estimated number of GCs found in the MW of 170 with measured kinematics (Vasiliev & Baumgardt 2021) and more than 200 including newly identified GCs in the bulge region (Garro et al. 2024). Their used cosmological parameters are $h = 0.73$ and $\Omega_M = 0.25$.

18.1.7 Dual formation pathway model

The model by Valenzuela et al. (2021) employs two GC formation pathways, where GCs are either formed in low-mass galaxies when the virial mass surpasses a certain threshold value of around $6 \times 10^8\,{\rm M}_\odot$ or when a galaxy experiences a large accretion rate. The second formation pathway follows the rapid growth model introduced by Choksi et al. (2018) and on which the model by Chen & Gnedin (2024b) is based, see Section 18.1.5. The galaxy properties are obtained from the empirical galaxy formation model `EMERGE` (Moster et al. 2018). No GC mass loss or disruption is accounted for, therefore the model traces only the formation of surviving GCs. Since we only analyse the ages of GCs having survived until $z = 0$, this is not an issue for this work.

The model was run alongside `EMERGE` for a DM-only cosmological simulation of side length 30 Mpc. The MW-mass galaxies were selected as the 21 central galaxies with virial masses of $M_{\rm vir} = 1 \times 10^{12}\,{\rm M}_\odot$–$2 \times 10^{12}\,{\rm M}_\odot$, of which two were identified as having a similar GC age distribution to the MW, with one having an accretion history that resembles an early GSE-like merger followed by no significant accretions (Valenzuela 2023; Valenzuela et al. 2024b). The MW-mass galaxies have stellar masses ranging $M_* = 1.6 \times 10^{10}\,{\rm M}_\odot$–$4.4 \times 10^{10}\,{\rm M}_\odot$. Their used cosmological parameters are $h = 0.6781$ and $\Omega_M = 0.308$.

18.1.8 Other models

There are some GC models that do not create GCs according to a physical formation prescription, but place them into galaxies according to unrelated criteria that assume an already existing GC population in a particular circumstance. Even though these models are tuned to GC properties at $z = 0$, they therefore do not predict GC formation times, but rather inform about other GC properties. We mention two such models in the following, as well as one that was only very recently introduced.

The model by Boylan-Kolchin (2017) tests what the average host mass of GCs at $z = 6$ needs to be to reproduce the numbers of GCs in galaxies at $z = 0$, assuming that the surviving GCs already exist at $z = 6$. For this reason, their model simply places all GCs in the galaxies at $z = 6$, and can thus not be used to predict GC ages.

The GC model by Doppel et al. (2023) follows that of Ramos-Almendares et al. (2020) and places GCs in satellite galaxies at the time of accretion onto a more massive host galaxy by tagging DM particles, thus following the general spatial and orbital properties of the infalling satellite galaxy. This means that the model does not use any prescription to physically form GCs and thereby the GC "seeding times" only trace the GC infall time onto the host galaxy rather than the actual GC formation. The model therefore does not predict any GC ages. They apply the model to the 39 most massive groups and clusters in the cosmological simulation TNG50. Two of those systems are also among the objects classified as MW analogues by Pillepich et al. (2024). Those are galaxies with stellar discs, stellar masses of around $M_* = 3 \times 10^{10}\,\mathrm{M}_\odot$–$1.5 \times 10^{11}\,\mathrm{M}_\odot$, and have no other massive galaxies above $10^{10.5}\,\mathrm{M}_\odot$ within a 500 kpc environment. For completeness, we show the GC seeding times as tracers of their infall times onto the main galaxy in Section H.1.

Finally, a very recent addition to GC models is presented by Chen et al. (2025), where GCs are formed in subclouds that appear from fragmentation of turbulent gas when dark matter haloes accrete matter rapidly at high redshifts. Two populations of GCs are formed through two channels, the first by compression by gravity or supernova feedback, the second by cooling in metal-poor subclouds, which results in an older metal-poor and a younger metal-rich GC population. In this work, we discuss the results from the studied models with those presented by Chen et al. (2025) when possible.

18.2 GC age distributions for MW-like galaxies

In the following we compare the GC age predictions of the different models with each other and with observations. For the models which have been applied to a large sample of galaxies, we here focus on those galaxies with the most similar GC age distributions as the observed GCs in the MW.

18.2.1 Modelled GC age distributions

For each of the GC models introduced in the previous section, we show the modelled GC age distributions for some of the MW-like galaxies the models were applied to in Figure 18.2, always including the mean observed MW GC ages from Kruijssen et al. (2019b) for reference and better comparability (black line in each panel). To visualise the differences of the typically old GC ages the best, the age axis is restricted to values between $t_{\rm age}$ = 5 Gyr–15 Gyr. As not all the studies only have GC ages in that range, we additionally show the full age distributions in Section H.2.

In the top left panel, the in-situ (red) and accreted (blue) GC age distributions of Renaud et al. (2017) are shown, as well as the total GC age distribution (dotted), assuming equal numbers of in-situ and accreted GCs. In the top right panel, the GC age distributions are shown of all six E-MOSAICS galaxies from fig. 3 of Kruijssen et al. (2019a). In the middle left panel, the four galaxies with the on average oldest GCs are shown from EMP-Pathfinder (Reina-Campos et al. 2022) with solid lines, where the metallicity cut as described in Section 18.1.4 is applied. The age distributions of all star clusters without an additional metallicity cut are shown with dotted lines. This leads to the inclusion of a large population of metal-rich clusters that are young. In the middle right panel, the three MW-like galaxies from Chen & Gnedin (2024b) are shown. The distribution in the lightest colour is from the Local Universe simulation, the two darker ones from TNG50. In the bottom left panel, four galaxies from the GC-limited sample by De Lucia et al. (2024) are shown, meaning they have 170–250 GCs. The four galaxies were selected from the galaxies with the oldest GC populations. Finally, in the bottom right panel, four galaxies from Valenzuela et al. (2024b) are shown, two of which were selected by the authors as having similar GC age distributions as the MW (the two lighter colours), and two additional ones with old GC populations (the two darker colours).

Here we focus first on these galaxies selected to be similar to the MW in terms of their GC age distributions, but some of the models have GC ages available for more MW-mass galaxies that may have significantly different assembly histories and morphologies than our MW. We present and discuss their varieties of GC age distributions as predictions for other MW-mass galaxies in Section 18.3 for the models where this is possible. Before discussing these differences in more detail, we would like to reiterate what the aim is of this side-by-side comparison, and what it is not. All of the studies define a sample of MW-mass or MW-like simulated galaxies, for which they compare the respective GC populations to that of our MW. For this reason, the benchmark for these systems is the MW itself and our aim in this work is to lay out the predicted GC ages side by side of the current GC models for the MW-like galaxies. However, as each of the studies applied their GC model to one or multiple simulated galaxies or generated merger trees, and only the galaxies from E-MOSAICS and EMP-Pathfinder (Kruijssen et al. 2019a; Reina-Campos et al. 2022) overlap, the shown age distributions are results of potentially entirely different assembly histories and are subject to a whole range of baryonic physics and galaxy formation models. Furthermore, each study selects MW-mass/MW-like or MW analogue galaxies according to their own criteria, and

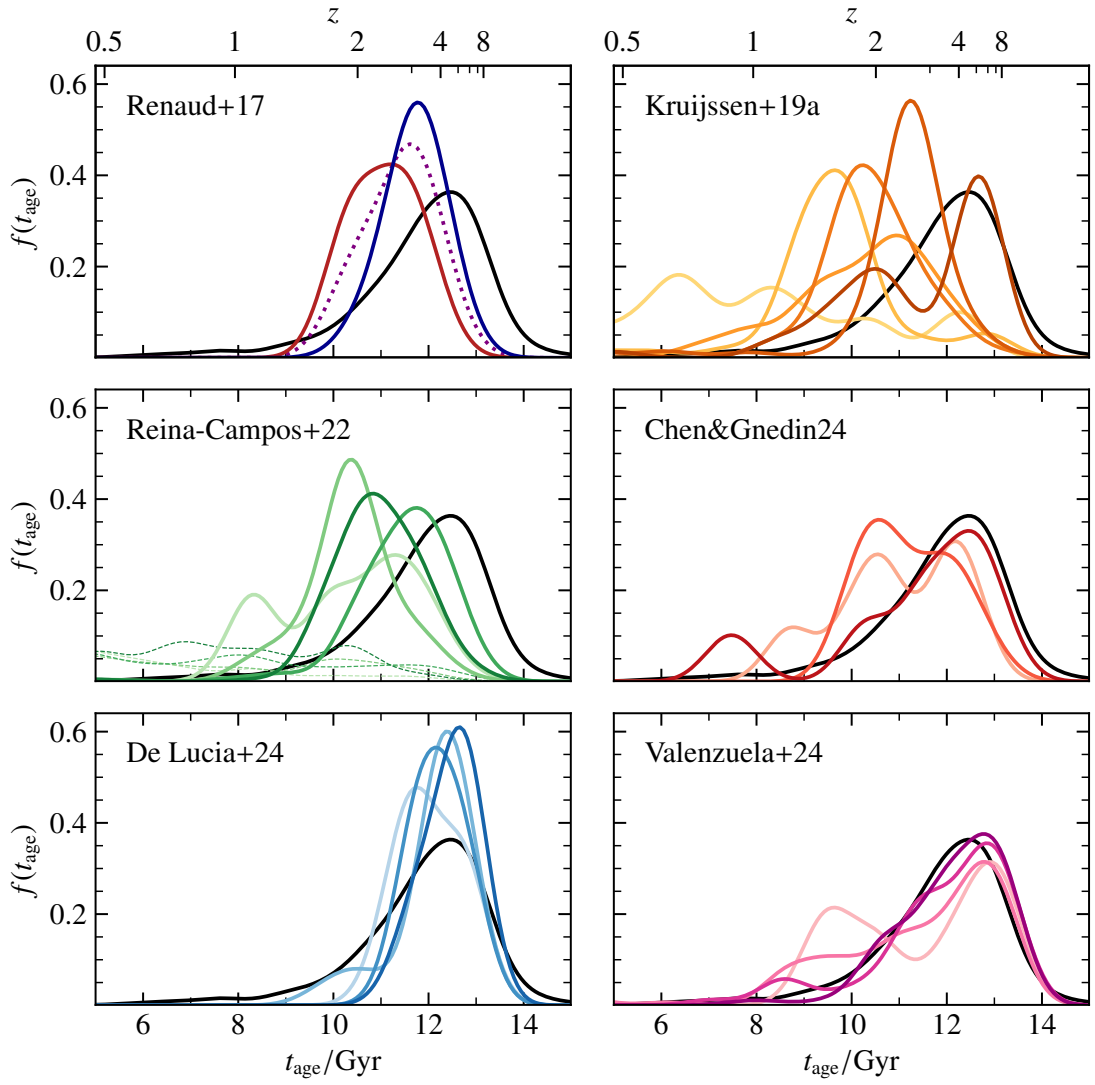


Figure 18.2: Age distributions of modelled GCs in MW analogues compared to the observed GC ages in the MW. The full age distributions reaching to $t_{\rm age} = 0$ Gyr are shown in Figure H.2. The observed GC ages are the mean values taken from Kruijssen et al. (2019b) and are shown in each panel as the black line. The modelled GC ages are from Renaud et al. (2017), Kruijssen et al. (2019a), Reina-Campos et al. (2022), Chen & Gnedin (2024b), De Lucia et al. (2024), and Valenzuela et al. (2024b). The dotted blackberry line for Renaud et al. (2017) is the combined age distribution of the in-situ (red) and accreted (blue) GC age distributions, assuming an equal number of underlying GCs for each group. For the other models the colours are selected to be darker for galaxies with older mean GC ages. The dashed lines for Reina-Campos et al. (2022) correspond to the same galaxies as the solid distributions of equal colour, with the difference that no metallicity cut was applied to the GCs, which results in a large population of young star clusters. This is best seen in Figure H.2. The age distributions are determined from the sum of normal distributions at the individual age measurements with standard deviations equal to the individual age uncertainties. For the modelled GCs, we assume a uniform age uncertainty of 0.5 Gyr.

different definitions concerning the resulting GC populations are used, such as the mass or metallicity cuts, which can in particular affect their age distribution. As a consequence, we do not claim to be able to fully interpret the differences found between the models as such differences will arise from a combination of factors that all play a role.

All the considered GC models are capable of producing GCs for certain MW-like galaxies that have overall old GCs ($t_{\rm age} \gtrsim 8\,$Gyr), just as is the case for the MW. To zeroth order, this means that these GC models are consistent with each other and with observations. Of course, having six models each with their own approach to GC formation, differences concerning their predicted GC formation times are not surprising as the details surrounding GC formation are still poorly understood. These differences can also be directly seen in Figure 18.2. Additionally, the observed GC ages have large systematic uncertainties on the order of 1 Gyr–2 Gyr, such that the observed age distribution has to be taken with caution. However, there is in general consensus about the MW GCs being particularly old, most likely as a result of the early formation history (e.g., Helmi et al. 2018).

18.2.2 Differences between the models

While the model by Renaud et al. (2017) simply assumes any stellar particle older than 10 Gyr to be a potential host of a GC, this means that their age distributions in fact traces the early star formation history of the MW-like galaxy until $t_{\rm age} = 10\,$Gyr. Clearly, the accreted (blue) stars are on average slightly older than the in-situ formed stars (red), by ∼1 Gyr. Still, the observed MW GCs are measured to be even older than the accreted stars, again by around 1 Gyr for the peak formation times. This shows that even the peak early star formation before $t_{\rm age} = 10\,$Gyr in their simulated MW-like galaxy occurs later than the peak GC formation in our MW. Other studies have also determined the GCs being older than the field stars (e.g., Harris & Harris 2002; Peng et al. 2008; Reina-Campos et al. 2019). Assuming this prediction from their simulation is correct and considering the findings that the cosmic star formation peaked around $z \sim 2$ (Madau & Dickinson 2014; Driver et al. 2018), this means that the formation of surviving GCs does not follow the early star formation history ($z > 2$) of a galaxy, but occurs earlier. The large systematic uncertainties of the observed ages could again bring the simulated and observed distributions into agreement, however.

For the E-MOSAICS and EMP-Pathfinder models, the GC ages tend to be younger than found in the MW, with the exception of the oldest E-MOSAICS GC system, which also appears to experience a second GC formation burst at around $t_{\rm age} \sim 10\,$Gyr. While this at first may look similar to the result of an early merger like the GSE, those younger GCs were actually formed in another galaxy that merged much later in time (Kruijssen et al. 2019a). The older measured MW GCs could be an indication that none of the 25 selected E-MOSAICS galaxies has an accretion history that is as early as that of the MW. However, for both E-MOSAICS and EMP-Pathfinder it is necessary to apply additional cuts to the metallicity to exclude especially metal-poor and metal-rich GCs, where the latter GCs are also mostly young. This cut is applied to differentiate the GCs from young/open clusters in those models. The effect of not applying such a cut can be seen for the EMP-Pathfinder GCs from the dashed lines. Being the only two subgrid models implemented within hydrodynamical cosmological simulations, this implies that there are still open questions concerning the exact GC formation conditions and their disruption. In particular for GC disruption, major advances were already made between

E-MOSAICS and EMP-Pathfinder by including the cold ISM, but this appears to not have strongly affected the first formation times of GCs.

Despite being the study with the by far largest sample of galaxies, even when only considering the galaxies with 170–250 GCs, the oldest GC age distributions from De Lucia et al. (2024) barely reach the high observed GC ages in the MW. This is also mentioned by the authors, who state that the GC systems are systematically younger than the observed MW GCs by ∼1 Gyr, though again the systematic uncertainties of the observations could be a part of the reason. Interestingly, the spread of GC ages is much smaller than for most of the other models except for Renaud et al. (2017). This is likely the result of individual merger events producing many GCs at once by ejecting clusters from the disc into the halo, or because of a coarse time binning, which would lead to the appearance of many GCs forming at once. In Section 18.3 we present further GC age distributions of different mean ages from De Lucia et al. (2024) and discuss why it is more likely that individual merger events are the cause for most of their GC formation.

Chen & Gnedin (2024b) selected three MW-like galaxies from two simulation suites using multiple criteria based on the properties and formation history of the MW to identify best-matching MW analogues. One of their galaxies has an especially old GC population with an age distribution similar to that of the MW (dark red), while both of the other galaxies have a more significant GC formation peak at $t_{\rm age}$ = 9 Gyr–11 Gyr, which roughly corresponds to the time range in which at least one major merger was enforced to exist to mimic the infall of GSE. Such a massive merger at early times will have been gas-rich and thus is expected to form a large population of GCs in the rapid mass growth model of Chen & Gnedin (2024b), as predicted by Valenzuela et al. (2024b) using the same model assumptions.

Similarly, the selected galaxies from Valenzuela et al. (2024b) show old GC ages consistent with the measured ones from the MW. These also feature secondary formation peaks between $t_{\rm age} \sim 8$ Gyr and 11 Gyr, indicating major merger events around that time. As their model includes a second formation pathway beyond the one employed by Chen & Gnedin (2024b), which populates dwarf galaxies in low-mass haloes with GCs at early times, it is not surprising that the GCs are slightly older than those of Chen & Gnedin (2024b) and that the secondary peaks at GSE infall times are less pronounced compared to the oldest GC population.

18.2.3 Empirical and subgrid GC models

Interestingly, the empirical models (i.e., models where the GC formation prescription is based on empirical or semi-analytic prescriptions, regardless of whether particle tagging is applied) tend to form the oldest GC populations. While Kruijssen et al. (2019a) find one galaxy in E-MOSAICS with an especially early burst of GC formation, that galaxy only has around 60 GCs in total with masses above $M_{\rm GC} \geq 10^5$ M$_\odot$ and also has a later GC formation peak with a longer tail towards younger ages ending at $t_{\rm age} \sim 8$ Gyr. While this does not affect the relative distribution of ages, it still means that none of the E-MOSAICS galaxies actually forms a large absolute number of GCs earlier than $t_{\rm age} \sim 12$ Gyr, which is also the case for EMP-Pathfinder.

The reason for the empirical models overall forming the earlier GCs is likely related to them being independent of the implemented baryonic physics in hydrodynamical cosmological simulations as they assume observationally-based scaling relations for the baryonic galaxy properties, such as star formation rate, cold gas mass, and stellar mass. As cosmological simulations have had issues with reproducing observed early star bursts, relying on these prescriptions for GC formation may be leading to GCs forming at the wrong times, even if the local physical formation conditions were perfectly understood.

On the other hand, the empirical models of Chen & Gnedin (2024b) and Valenzuela et al. (2024b) do not follow the self-consistent formation of galaxies within their DM haloes, but assume average scaling relations to apply. As a result, the GC populations of individual galaxies have to be considered as realisations based on correct galaxy merger histories, but with average baryonic properties. However, these scaling relations and the approach of forming GCs in gas-rich systems with rapid mass growth lead to very old GCs, as is expected from observations. Nevertheless, the disadvantage of using average scaling relations is that galaxies will overall have little gas at later times, therefore making late GC formation much rarer in galaxies, regardless of the individual assembly histories. This means that galaxies falling outside the norm with large gas amounts will not be directly covered by these models, in particular in the model by Valenzuela et al. (2021, 2024b), who directly employ the scaling relation for the gas depletion time without taking into account its scatter, whereas the stellar mass-halo mass relation is intrinsically dealt with in the underlying empirical galaxy formation model `EMERGE`. Chen & Gnedin (2024b) include prescriptions for the scatter of the scaling relations, among them that of Behroozi et al. (2013) for the stellar mass-halo mass relation. In particular for the stellar mass-halo mass relation, a large scatter may be necessary to obtain the amount of bright galaxies observed with JWST at high redshifts (e.g., Mason et al. 2023; Mirocha & Furlanetto 2023; Shen et al. 2023). Increasing this scatter would lead to a larger population of more massive galaxies, which in turn could give birth to more massive stellar clusters at formation time and modify the resulting age distribution of surviving GCs. This issue is in part circumvented in the model by Valenzuela et al. (2024b) through the free parameter of the formation pathway in low-mass galaxies.

The model by De Lucia et al. (2024) takes the middle ground between the subgrid and empirical models: implemented within a semi-analytic galaxy formation model, baryonic properties are inferred for the DM haloes through the semi-analytic model based on the merger histories. The model thus does not spatially resolve the internal gas behaviour, just like the empirical models. At the same time, it applies a similar GC formation prescription as employed in E-MOSAICS, being based on the approach of Kruijssen (2015).

As small time differences in the early Universe correspond to much larger differences in redshift than at later times, the variations of predicted GC formation ages in fact imply significantly different epochs of GC formation in cosmological terms. With the ongoing observations of heavily star-forming galaxies at high redshifts with JWST (e.g., Claeyssens et al. 2023; Adamo et al. 2024; Mowla et al. 2024), narrowing down our understanding of GC formation will be vital to compare the predictions of improved models with the observed

systems as well as to find to what extent massive star clusters at high redshifts are the progenitors of today's GCs. This will be further discussed in Section 18.4.

18.3 GC age distributions for other MW-mass galaxies

While some of the considered studies only have GC data available for a small number of MW-like galaxies that we could fully show in Figure 18.2, we have data available for a larger sample of MW-mass galaxies from EMP-Pathfinder (Reina-Campos et al. 2022), De Lucia et al. (2024), and Valenzuela et al. (2024b). These studies can therefore be used as a broader prediction to other MW-mass galaxies. In the case of De Lucia et al. (2024), this applies to MW-mass disc galaxies, whereas the galaxies from EMP-Pathfinder and Valenzuela et al. (2024b) are MW-mass galaxies of all types.

In Figure 18.3 we show the whole range of predicted GC age distributions for MW-mass galaxies from EMP-Pathfinder, De Lucia et al. (2024), and Valenzuela et al. (2024b). For De Lucia et al. (2024), we show the distributions considering all their selected galaxies (second row), and the distributions only considering the selected galaxies with 170–250 GCs contained in them (third row; see Table 18.1 for the properties of the galaxies and GC systems). Sorting the galaxies by their mean GC ages, we plotted the median and the 1σ and 2σ younger and older GC populations from each study, with darker colours indicating the older systems.

The first striking difference is the range that the age distributions of the three models cover. The youngest GC populations in EMP-Pathfinder include a significant fraction of GCs having ages smaller than $t_{\rm age} \sim 5\,$Gyr and even 3 Gyr, and the median to oldest GC populations have peak formation times of $t_{\rm age} \sim 10\,$Gyr to 12 Gyr. This indicates that most of their MW-mass galaxies have relatively old GC populations, but the younger half of the GC populations extends far into the late times of the Universe. Similarly, the six galaxies from E-MOSAICS seen in Figure 18.2 span a variety of different ages, with most of the GC populations having relatively old ages ($t_{\rm age} \gtrsim 10\,$Gyr). However, due to the GC data only being available for six galaxies, we cannot draw further conclusions from the spread of age distributions.

The model from De Lucia et al. (2024) has peak formation times between $t_{\rm age} \sim 7\,$Gyr and 13 Gyr. The five selected GC age distributions shown for the GC-limited galaxy sample (third row) have formation peaks relatively evenly distributed with time, indicating that the resulting mean GC ages of the galaxies are roughly normally distributed, with a slightly longer tail towards younger ages. It can also be seen that the spread of GC formation is larger the later the GCs are formed, also resulting in a lower relative age peak (as each age distribution is normalised). This would mean that GCs are formed over shorter periods of time in the early Universe. Besides two of the galaxies with constrained GC number having minor secondary GC formation peaks (the two with the younger GC populations), all of the shown galaxies have age distributions dominated by a single GC formation peak. For the full galaxy sample, the GC ages span the same range as for the GC-limited sample. In both galaxy samples the peaked GC ages imply that the formation of surviving GCs is actually tied to single events that create GCs in a very short period of time, as was already suggested in Section 18.2. This

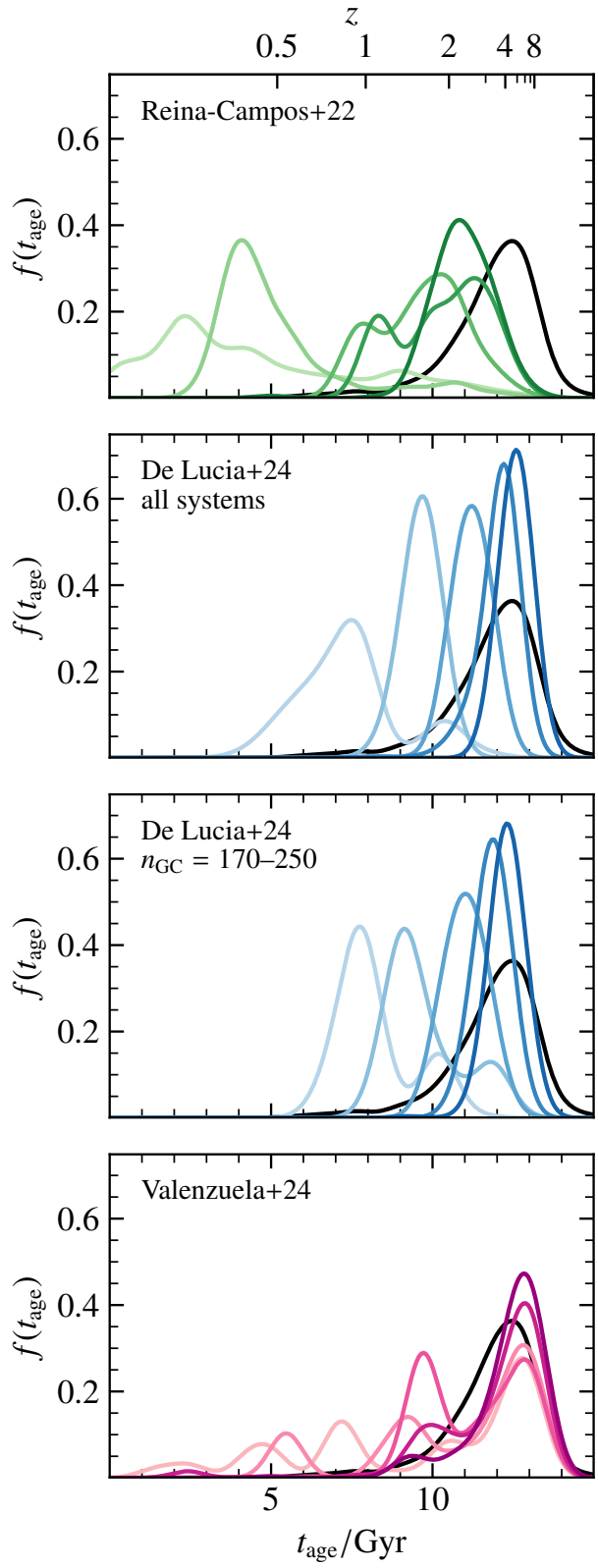


Figure 18.3: Age distributions of modelled GCs in MW-mass galaxies compared to the observed GC ages in the MW. The observed GC ages are the mean values taken from Kruijssen et al. (2019b) and are shown in each panel as the black line. The modelled GC ages are from Reina-Campos et al. (2022), De Lucia et al. (2024) when considering all MW-like galaxies (second row) and when considering only galaxies with 170–250 GCs (third row), and Valenzuela et al. (2024b). For each study, five example galaxies are shown: computing the mean GC age for each galaxy, here the median galaxy and the 1σ and 2σ outlier galaxies hosting younger or older GCs are shown. The colours are chosen to be darker for older GC populations.

is likely the result of merger events leading to the ejection of clusters from the disc into the halo, where they are considered as GCs in the model. Clusters are subject to mass loss and disruption in the disc before they are ejected, such that mergers will mostly only eject clusters having formed shortly before the event while older clusters would have already been disrupted for the most part.

In contrast to the first two studies, the model from Valenzuela et al. (2024b) always produces a dominant old population of GCs with ages of $t_{\rm age} > 11$ Gyr. The reason for this old population in their model is the formation pathway of forming GCs in small haloes as soon as they surpass a certain threshold virial mass. As this mass is rather low and in the regime of dwarf galaxies, this leads to significant GC formation at these early times. As these small haloes are the building blocks of the assembling more massive galaxies, they provide the proto-MW-mass galaxies with old GCs. Most of the younger GCs are then formed through the second formation pathway of rapid accretion onto the central galaxy, leading to the younger bumps of the GC age distribution seen for the five galaxies in the bottom panel of Figure 18.3.

As can seen by the vastly different possible GC age distributions predicted by the various models, there is still a large disagreement concerning how young the GC population of an individual MW-mass galaxy can actually be. While the studies by Kruijssen et al. (2019a), Reina-Campos et al. (2022), and De Lucia et al. (2024) predict the existence of some MW-mass galaxies having no or only very few old GCs and to varying degrees how young an entire GC population can be, the model from Valenzuela et al. (2024b) always contains a significant fraction of old GCs. On the even more extreme side, Boylan-Kolchin (2017) assumed that all GCs had been formed by $z = 6$ for their model. Traditionally, it has been assumed that the bulk of GCs are old with ages of $t_{\rm age} \gtrsim 10$ Gyr (Côté et al. 1998; Strader et al. 2005) based on the findings in our own MW and on more GC age estimates in nearby galaxies (e.g., Usher et al. 2019, 2024; Cabrera-Ziri et al. in prep.). Some galaxies also have been found to feature young massive clusters (YMCs), which have properties that are consistent with those expected for GCs right after formation time (e.g., Beasley et al. 2002a). Of the galaxies that have been studied for these purposes, NGC 3377 stands out as a peculiar galaxy having a large young population of GCs (Usher et al. 2019). However, even this early-type galaxy is measured to have many old GCs. The question thus stands whether MW-mass galaxies with purely younger GCs or YMCs exist, such as has been observed for certain lower-mass galaxies like the SMC (e.g., Parisi et al. 2014). More estimates of GC ages in other MW-mass galaxies will be needed to discern between the models. For this, even rough estimates of the ages will be sufficient, which may even be possible through photometric age determinations. This will especially be relevant for the recently launched and upcoming large area low surface brightness surveys like Euclid, Rubin, and Roman.

As an important point to keep in mind, we want to highlight that the definitions of GCs vary across models. Some differences are directly given by the mass-cuts intrinsically used by the models or applied by us to the GC data, such as the lower-mass cut: the GCs we show for E-MOSAICS have $M_{\rm GC} \geq 10^5\,{\rm M}_\odot$, for EMP-Pathfinder and Chen & Gnedin (2024b) $M_{\rm GC} \geq 10^4\,{\rm M}_\odot$, and the GCs from the model of Valenzuela et al. (2024b) have initial masses

of $M_{\rm GC,init} \geq 10^5\,{\rm M}_\odot$. Metallicity cuts to the E-MOSAICS and EMP-Pathfinder remove metal-rich GCs with mostly young ages that are assumed to be artificial due to under-disruption and an overproduction of clusters at $z < 1$, respectively. Finally, there is only a fuzzy line between what would be identified as a GC, a YMC, or an open cluster from observations as well as from models. It is therefore also difficult to tell in what way the GC output of a model would have to be compared with YMCs or even open clusters in addition to GCs.

Clearly, the currently available GC models have very different predictions concerning the variety of GC age distributions in MW-mass galaxies. These deviations are significant enough that the differences in galaxy masses, morphologies, or in the definitions of GCs will not be sufficient to bring all the predictions in agreement. To summarise the range that the models cover: some of them predict that every single MW-mass galaxy should have a dominant old GC population with $t_{\rm age} > 10\,{\rm Gyr}$ (e.g., Valenzuela et al. 2024b), whereas others predict that roughly a third of MW-mass disc galaxies have most of their GCs being younger than 5 Gyr (e.g., Reina-Campos et al. 2022). Having investigated the overall ages of the GCs in the models, we turn to the high-redshift formation times of surviving GCs from the same set of models in the next section.

18.4 Predictions for high-redshift clusters

For the recent and ongoing observations of clustered star formation in high-redshift galaxies with HST (e.g., Messa et al. 2024) and JWST (e.g., Claeyssens et al. 2023; Vanzella et al. 2023; Adamo et al. 2024; Mowla et al. 2024), we test in the following what predictions can be made from the GC models with respect to such star clusters in high-redshift potential progenitors of MW-mass galaxies. In Figure 18.4, we show the GC formation time distributions of the same set of galaxies from each of the six GC models as shown in Figure 18.2, just with the redshift plotted uniformly along the x-axis instead of age. For this, we converted the ages to the corresponding formation redshifts according to the original cosmologies applied by the respective authors (see Section 18.1). For the GCs by De Lucia et al. (2024), the ages were only available with equal-width age bins, such that the distribution becomes more discrete in redshift-space at high redshifts. For this reason, the lines are dashed and we included the age bin edges in grey for reference.

The redshifts of some of the high-redshift star clusters found with JWST are marked by short vertical black lines, which include the Sunrise arc ($z = 6.0$; Vanzella et al. 2023), the Cosmic Grapes ($z = 6.072$; Fujimoto et al. 2025), MACS J0416 ($z = 6.143$; Messa et al. 2025), the Firefly Sparkle ($z = 8.304$; Mowla et al. 2024), and the Cosmic Gems arc ($z = 10.2$; Adamo et al. 2024; Bradley et al. 2025). Their host galaxies are expected to grow to be MW-mass galaxies. For an overview of the current high-redshift observations of star clusters, see Pfeffer et al. (2025).

Taking the formation time distribution from Renaud et al. (2017) as tracer for the overall star formation history of a MW-like galaxy, it can be seen that the surviving GCs produced by the other models generally start forming at earlier times than the rest of the stars. All models

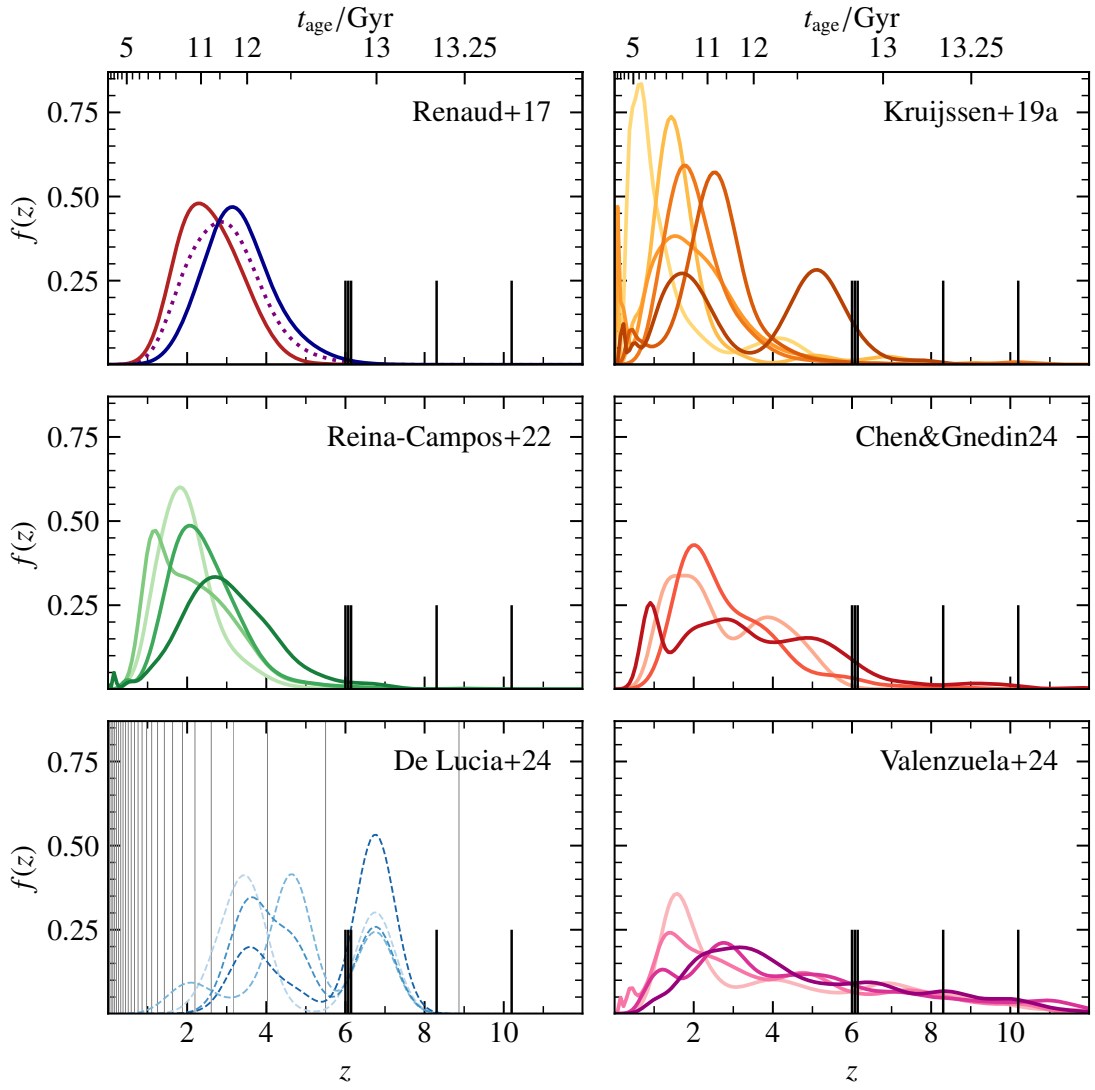


Figure 18.4: Formation redshift distributions of surviving modelled GCs in MW analogues. The formation redshifts are from Renaud et al. (2017), Kruijssen et al. (2019a), Reina-Campos et al. (2022), Chen & Gnedin (2024b), De Lucia et al. (2024), and Valenzuela et al. (2024b). The short vertical black lines denote the redshifts of star clusters from the strongly lensed systems observed by Vanzella et al. (2023), Fujimoto et al. (2025), Messa et al. (2025), Mowla et al. (2024), and Adamo et al. (2024), in increasing redshift order. The dotted blackberry curve for Renaud et al. (2017) is the combined age distribution of the in-situ (red) and accreted (blue) GC age distributions, assuming an equal number of underlying GCs for each group. As the GC ages for the galaxies from De Lucia et al. (2024) are only available in equally-spaced age bins that are relatively wide at high redshifts, the curves are plotted with dashes and the bin edges are indicated as vertical grey lines, with the last bin edge reaching a redshift of $z \approx 8.9$. For all the models, the formation redshift distributions are determined from the sum of normal distributions at the individual formation redshift with standard deviations equal to the individual redshift itself until $z = 0.5$, and beyond that equal to 0.5. This prevents the smoothed curves from surpassing $z = 0$ by too much in the plots.

have similar predictions with respect to the peak formation redshifts for the surviving GC populations: these lie around z = 1–3 and vary from galaxy to galaxy. This corresponds to the observed formation time of young massive clusters at z = 2.4 in the Sunburst galaxy (Vanzella et al. 2022a) and it is slightly after current observations at z = 4-5 of young massive clusters (e.g., Vanzella et al. 2022b; Messa et al. 2024). Only the oldest galaxies from the sample of De Lucia et al. (2024) all have no young GC population and have peak formation redshifts somewhere between z = 3 and z = 8. Most of the GC systems in their model do not have surviving GCs being formed before z = 6, however. Also Chen et al. (2025) show a peak age at z = 5 (see their fig. 9). Additionally, one of the E-MOSAICS galaxies has two similarly dominant formation peaks at $z \approx 2$ and at $z \approx 5$. While the peak formation time is therefore quite consistent among the models, the spread to higher redshifts varies significantly: the overall star formation as traced by the model of Renaud et al. (2017) begins at z = 5 and z = 6 for the in-situ and accreted components, respectively. This is also the case for EMP-Pathfinder, with one of the systems even reaching surviving GC formation times as early as z = 7. E-MOSAICS shows a similar behaviour for most of their galaxies, though one in particular has an especially early surviving GC formation burst starting at z = 7–8. For the high-redshift clusters formed in E-MOSAICS, Pfeffer et al. (2025) also compares the brightest cluster properties with recent JWST and HST observations.

The model by Chen & Gnedin (2024b) produces more surviving GCs at these larger redshifts, but only start their formation slightly earlier, at z = 6–10 for the very first GCs of some of their galaxies. The formation tail towards high redshifts is even longer for Valenzuela et al. (2024b), where for the shown MW-like galaxies the surviving GC formation rate per redshift slowly increases almost linearly, starting at around z = 12. For these models that use empirical scaling relations, increasing the scatter of the halo mass-stellar mass relation could lead to more massive galaxies and star clusters in lower-mass halos, resulting in earlier formed surviving GCs. This approach may be necessary to find better agreement with JWST observations of bright galaxies at high redshifts of $z \gtrsim 9$ (e.g., Mason et al. 2023; Shen et al. 2023). The initial formation time of surviving GCs in the model by Chen et al. (2025) is even slightly earlier at z = 14 (see their fig. 9). Finally, the only information at higher redshifts we can extract from the binned data of De Lucia et al. (2024) is that there is a non-significant number of surviving GCs formed in the range of z = 5.5–9, with none being formed before z = 9. However, as these are among the oldest GC systems of almost 700 galaxies, this prediction is not valid for the majority of their MW-mass galaxies. Linking this to the high-redshift observations marked with the vertical black lines, clearly the model that predicts that the star clusters at $z > 8$ could very well survive until today is the one by Valenzuela et al. (2024b). With a much lower probability of this happening, its is principally also possible according to E-MOSAICS and the model by Chen & Gnedin (2024b).

The models with younger surviving GC populations at z = 0 are therefore either inconsistent with these observational findings, or they predict that almost none of the high-redshift star clusters would turn into a GC at present day, as this would require more of the oldest GCs having formation times at higher redshifts. The models with the older GC populations (Chen

& Gnedin 2024b; Valenzuela et al. 2024b; and for certain galaxies Kruijssen et al. 2019a; De Lucia et al. 2024), in contrast, find a larger number of GCs formed at high redshifts ($z \gtrsim 6$), thereby suggesting that a larger fraction of the high-redshift star clusters could in fact be the progenitors of today's GCs around MW-mass galaxies.

High-resolution simulations of the early Universe have been able to trace the formation of potential proto-GCs at high redshifts. For instance, Phipps et al. (2020) list the properties of several stellar clusters having been formed in the cosmological simulation FiBY (First Billion Years) before $z = 6$, though the identified clusters all have masses below 3×10^5 $M_\odot$, which is at and below the lower end of the inferred cluster masses from observations at those redshifts (e.g., Messa et al. 2024; Mowla et al. 2024). It is therefore even less likely than for the observed clusters that the lower-mass systems identified in the simulation would survive to become GCs at $z = 0$. Mayer et al. (2025) find stellar clusters forming at $z > 7$ through disc fragmentation and discover a very similar mass surface density distribution of their objects compared to those observed at similar redshifts (e.g., Mowla et al. 2024; Adamo et al. 2024). The stellar clusters formed through high-resolution proto-galaxy mergers in the FIRE simulation (Kim et al. 2018) and in dwarf galaxy mergers (Lahén et al. 2019) are found to have masses up to 10^6 $M_\odot$ (Lahén et al. 2019), consistent with some of the observed high-redshift clusters.

One central question is how many of high-redshift galaxies actually contain massive star clusters, as current observations are still rather limited in number. Combining such a value with the GC models run for a diverse set of galaxies will be able to predict the surviving star cluster fraction as a function of redshift. Observations of systems at intermediate redshifts already indicate that their GCs must have formed at very early times of $z = 7$–11, as found by Mowla et al. (2022) for the Sparkler at $z \approx 1.4$, though also with significant systematic age uncertainties, which strongly affect the corresponding formation redshifts. This indicates that some of the early formed massive bound star clusters survive until at least intermediate redshifts.

More observations at high redshifts and further discriminating between the current GC models will bring further insight into the connection of GCs and star clusters and clumps at high and low redshifts, including what fraction of the observed high-redshift clumps would be expected to survive to present day, and if this depends on the mass or type of the galaxies in question.

18.5 Conclusion

In this work, we present the first side-by-side comparison of multiple current GC formation models, for which we collected GC age data from the GC models applied to MW-mass and MW-like galaxies to compare their age distributions with each other and with observations of the GCs in the MW as well as observations of star clusters at high redshifts. We give a detailed overview of the models and their methods for forming and evolving GCs side-by-side alongside their individual definitions for galaxies being MW-like and for the GCs themselves. Among the models are subgrid models applied to zoom-in hydrodynamical cosmological

simulations (Kruijssen et al. 2019a; Reina-Campos et al. 2022), empirical models applied to merger trees of cosmological simulations (Chen & Gnedin 2024b; Valenzuela et al. 2024b), and GC models implemented within semi-analytic models of galaxy formation (De Lucia et al. 2024), as well as a simple tagging prescription of old stellar particles in a hydrodynamical simulation (Renaud et al. 2017). The objective of this direct comparison of the model results is to present in a clear way the range of predictions that current GC models make, which lays the foundation for future development and improvement of such models.

For a selection of MW-like galaxies, we find that all of the considered models are in general capable of forming GCs at ages older than 10 Gyr as is observed for the MW. While the model by Renaud et al. (2017) can be used as a tracer of the regular star formation history at early times, the current best estimates for the MW GC ages indicate that GCs are formed earlier than the overall stellar population. While it should be noted that the MW GC absolute ages have large uncertainties, the E-MOSAICS (Kruijssen et al. 2019a) and EMP-Pathfinder (Reina-Campos et al. 2022) galaxies show slightly younger age distributions offset by 1–3 Gyr depending on the simulated galaxy. Only one old E-MOSAICS galaxy is directly consistent with the best age estimates for the MW GCs. For a carefully selected sample of MW-like galaxies according to their merger histories, Chen & Gnedin (2024b) find very similar age distributions. Valenzuela et al. (2024b) find the overall oldest GC age distributions, which are also similar to those observed. Finally, the oldest systems of the large sample by De Lucia et al. (2024) have peak surviving GC formation times consistent with the MW.

An important point to keep in mind for this is always that the different MW-like galaxies can have very different accretion histories, thus preventing an apples-to-apples comparison of the ages. For this reason, we also compared the variety of age distributions expected for MW-mass galaxies based on the larger galaxy samples from Reina-Campos et al. (2022), De Lucia et al. (2024), and Valenzuela et al. (2024b). While the model by Valenzuela et al. (2024b) predicts that every galaxy has a significant old GC population, the GC systems from De Lucia et al. (2024) show a roughly normal distribution of peak GC formation times, with half of their galaxies having most GCs being younger than 10–11 Gyr. The model by Reina-Campos et al. (2022) even predicts that roughly a third of MW-mass disc galaxies have most GCs being younger than 5 Gyr and lack an old GC population. Discerning between these models will therefore be possible by estimating rough ages of GCs in nearby galaxies. This means that it is critical that further observations of GCs around other galaxies in the MW mass range be performed and ages be estimated for them, such as what has been done for M 31 (e.g., Usher et al. 2024). Recent and upcoming large area low surface brightness surveys like Euclid, Rubin, and Roman will provide the means necessary to perform such rough measurements to increase the statistics of GC ages.

Finally, we compared the formation redshifts of surviving GCs from the models to the observed formation times of star clusters in high-redshift galaxies from HST and JWST. The models consistently predict a peak formation redshift of $z = 1$–3, depending on the individual galaxy. However, the tail towards higher redshifts varies significantly. Some models begin producing the first surviving GCs at $z = 5$–7 (Renaud et al. 2017; Kruijssen et al. 2019a;

Reina-Campos et al. 2022), while others produce surviving GCs even earlier at $z = 6$–10 (Chen & Gnedin 2024b) and $z = 12$ (Valenzuela et al. 2024b). Compared to recent observations of star clusters in strongly-lensed galaxies at $z = 6$–10 (e.g., Vanzella et al. 2023; Mowla et al. 2024; Adamo et al. 2024), the models with older GC populations predict that at least some of these systems could survive until present day, whereas other models are either inconsistent with these observations or predict that such systems are always disrupted over cosmic time. Increasing the sample of high-redshift star clusters in observations will be of great value for combining these with GC models to obtain predictions for the chances of survival and thus statistically quantifying how many of such star clusters are in fact proto-GCs.

In the future, this type of model comparison will be extended to further GC properties to test to what extent and for which use cases each of the models can be appropriately applied. To overcome the limitations of comparing GCs obtained within galaxies with different properties and accretion histories, this should ideally be carried out by running each of the models for the same galaxy initial conditions.

19

Globular Clusters as Dynamical Tracers

This chapter summarizes the results published by Veršič et al. (2024a, incl. Valenzuela), A&A 687, A80, for which I provided simulation data and contributed to the interpretations: *Shapes of dark matter haloes with discrete globular cluster dynamics: The example of NGC 5128 (Centaurus A)*

As bright sources that can be detected far out in the outskirts of galaxies, globular clusters (GCs) can provide the spatial and kinematic information necessary to constrain the underlying gravitational potential and its properties, thereby giving insights into the dark matter (DM) halo. Drawing on my expertise in galaxy outskirts and GCs from simulations and models, I contributed to a study targeting the nearby massive early-type galaxy Centaurus A (NGC 5128), which has a large number of GCs with line-of-sight velocity measurements. Centaurus A is furthermore a particularly interesting target due to strong evidence of recent accretion or even a major merger based on shells, streams, and young halo stars (e.g., Malin et al. 1983; Rejkuba et al. 2011; Crnojević et al. 2016; Wang et al. 2020).

Dynamical modeling techniques have enabled the study of the central stellar component of galaxies and their shapes in recent years (e.g., Jin et al. 2020; Santucci et al. 2022; Thater et al. 2025), though a similar approach for the outer halo is much more difficult because of the low surface brightness. These outer regions are dominated by DM (e.g., Deason et al. 2012; Cappellari et al. 2013) and can reach mass fractions of up to 90% for massive galaxies

(e.g., Harris et al. 2020). Predictions from DM-only cosmological simulations suggest that DM halos are nearly spherical in shape (e.g., Allgood et al. 2006; Valenzuela et al. 2024a) with tendencies toward being prolate or triaxial (e.g., Bailin & Steinmetz 2005; Hayashi et al. 2007). To probe the DM halo in observations, luminous tracer populations in the outskirts can be used to trace the underlying DM-dominated potential.

For Centaurus A, an elliptical or lenticular galaxy (Harris 2010) with stellar mass $M_* = 1.6 \times 10^{11}\,\mathrm{M}_\odot$ (Hui et al. 1995) and expected to host roughly 2000 GCs (Harris et al. 2006), the outskirts have long been studied through its population of planetary nebulae (PNe; Hui et al. 1993, 1995; Peng et al. 2004b; Walsh et al. 2015) and GCs (e.g., Peng et al. 2004a,c; Woodley et al. 2010a; Hughes et al. 2021). Based on those results, several studies have determined the spherical mass distribution of the halo using the kinematic tracers (e.g., Peng et al. 2004b; Woodley et al. 2007; Hughes et al. 2021; Dumont et al. 2024). Furthermore, in particular the PN kinematics have been used to predict a strong triaxiality of the stellar halo and the underlying potential (e.g., Hui et al. 1995; Peng et al. 2004b; Pulsoni et al. 2018). In this work, we use dynamical modeling to test how well the assumption of a spherical gravitational potential of its halo holds when considering GCs as dynamical tracers. In Section 19.1, we present the dynamical modeling technique and its results for the halo of Centaurus A. We then discuss the meaning of the results in light of cosmological simulations in Section 19.2 and finally conclude in Section 19.3.

19.1 Dynamically modeling the halo of Centaurus A

As tracers for the halo of Centaurus A, we use the photometric catalog of around 3200 GC candidates from Taylor et al. (2017) using the Dark Energy Camera (Taylor et al. 2016) for a region spanning radii out to over 150 kpc, which are shown as gray points in the left panel of Figure 19.1 (assuming a distance of 3.8 Mpc, 1 arcmin corresponds to 1.1 kpc, Harris 2010). Furthermore, we use the line-of-sight velocity measurements of the inner GCs from Hughes et al. (2021), where a sample of 482 GCs has both photometric and kinematic data available (blue points). Their spatial distribution already indicates an elongated structure reaching into the quadrants II and IV.

The dynamical modeling used in this work is the Jeans Anisotropic multi-Gaussian expansion (JAM; Cappellari 2008) method, which assumes relaxed and phase-mixed tracers of the underlying potential. However, Centaurus A has been suggested to have had a major merger around 6 Gyr ago with the final merger of the galaxies 2 Gyr ago (Wang et al. 2020), and the GC population has been found to also feature an intermediate-age and young subpopulation (e.g., Woodley et al. 2010b), indicating that not the entire GC population is relaxed. For this reason, we identified a relaxed subpopulation of GCs by analyzing different luminosity bins and the spatial distributions of the respective GCs in the inner and outer quadrants seen in the left panel of Figure 19.1, where the most promising subpopulation of GCs is that with intermediate luminosities (see Veršič et al. 2024a for details on the determination of this subpopulation). These GCs were then used to construct a relaxed tracer density profile.

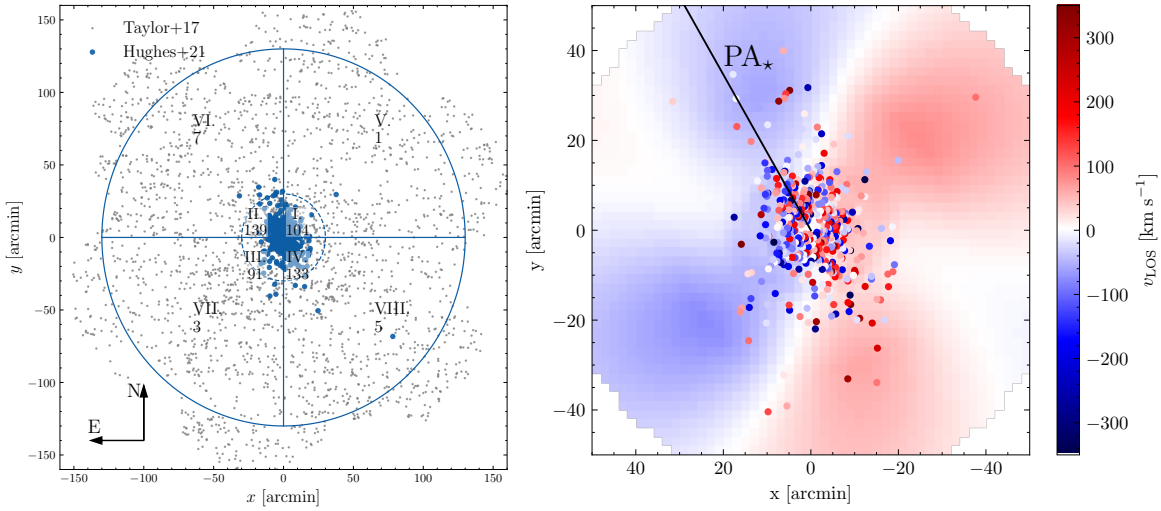


Figure 19.1: *Left*: Spatial distribution of GC candidates from Taylor et al. (2017, gray points) and GCs with kinematic measurements from Hughes et al. (2021, blue points) centered around Centaurus A. The dashed and solid blue circles indicate radii of 30 and 130 arcmin, respectively. The eight quadrants (inner and outer) are separated by the horizontal and vertical blue lines. The number of GCs with kinematic measurements in each quadrant are stated below the Roman quadrant number. *Right*: Underlying stellar velocity field for the inner halo region of Centaurus A (note the axis scale) obtained from PNe by Pulsoni et al. (2018), with overplotted line-of-sight velocities for the individual GCs from Hughes et al. (2021). The solid black line indicates the position angle (PA) of the stellar component from Dufour et al. (1979). The physical scale is 1.1 kpc per 1 arcmin. *These are figures 1 and 4 from Veršič et al. (2024a).*

We furthermore verified that the line-of-sight GC dynamics agree sufficiently well with the point-symmetric velocity map determined from PNe by Pulsoni et al. (2018), which can be seen in the right panel of Figure 19.1. Here, the underlying velocity map is that of the PNe, with the colored points indicating the line-of-sight velocities of the GCs from Hughes et al. (2021). For the stellar surface density of the halo, we combined data from the inner regions by Dufour et al. (1979) with red giant branch (RGB) star data for the outer regions by Rejkuba et al. (2022).

The dynamical model was then set up to include seven free parameters. The DM halo is described by an NFW profile (Navarro et al. 1996, 1997) with virial mass M_{200} and concentration c_{200}, and its shape is parametrized by the intrinsic flattening $q_{\rm DM}$, where the symmetry axis is fixed to that of the stellar component. The remaining four free parameters are the mass-to-light ratio M_*/L_B to scale the stellar surface density, the inclination i, and the orbital properties of the tracer population, the anisotropy β_z (radial vs. vertical motion) and rotation parameter κ (ordered vs. disordered motion). We then determined the best-fit parameters through axisymmetric JAM modeling and finding the posterior distributions based on the likelihood function determined from the line-of-sight velocities and the predicted velocity dispersion (for details refer to Veršič et al. 2024a). After several fitting iterations, the concentration was tied to the virial mass according to the mass-concentration relation (Correa et al. 2015), and the inclination was fixed to 90° because it was not possible to further constrain it throughout the first iterations.

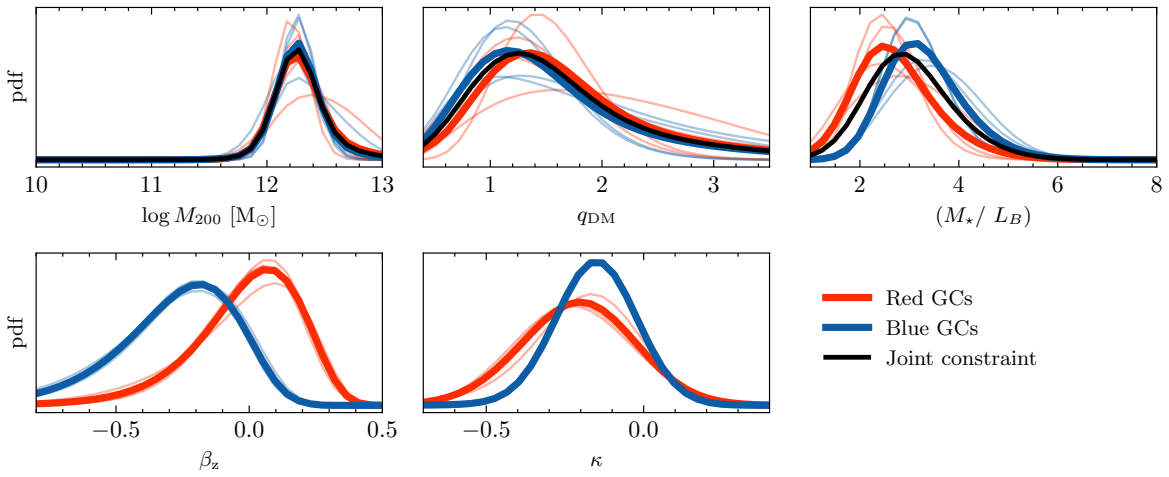


Figure 19.2: Posterior distributions of five free parameters for the JAM modeling, the DM halo mass M_{200}, its intrinsic flattening $q_{\rm DM}$, the stellar mass-to-light ratio M_*/L_B, the orbital tracer anisotropy β_z, and the orbital tracer rotation parameter κ, from the top left to the bottom right. The distributions for the red and blue GC subpopulations are indicated in red and blue, respectively, and the black lines indicate the joint posterior for the DM and stellar properties parameters (those in the first row). The thin lines indicate the posterior distributions for different parameter pairs, whereas the thick lines are the joint probabilities from all pairs. *This is figure 10 from Veršič et al. (2024a).*

Since the GCs around Centaurus A show a bimodal color distribution and the red and blue GCs exhibit distinct kinematics (e.g., Peng et al. 2004a), we model the two tracer subpopulations separately. The resulting posterior distributions of the five remaining free parameters are shown in Figure 19.2 for the red and blue GCs (thick red and blue lines, respectively), as well as the posterior distributions from the joint subpopulations for the DM and stellar parameters (black lines). The differing orbital parameters β_z and κ for the red and blue GCs show that they indeed have different kinematics in the halo, supporting the idea of them having experienced different formation pathways (e.g., Forbes et al. 2018a). Both subpopulations show slight rotation, with red GCs having larger rotation (κ) and exhibiting isotropic behavior. Blue GCs, on the other hand, have negative cylindrical anisotropy β_z. Both the red and blue GC dynamics lead to similar DM and stellar parameters, where we find a virial mass of $\log M_{200}/\mathrm{M}_\odot \approx 12.3$, an intrinsic DM halo flattening of $q_{\rm DM} = 1.45^{+0.78}_{-0.53}$, and a mass-to-light ratio of $M_*/L_B \approx 3.0\,\mathrm{M}_\odot\,\mathrm{L}_\odot{}^{-1}$. The value of $q_{\rm DM}$ greater than one means that the DM halo is prolate in shape. While the lower error bound means that it is still consistent with a spherical matter distribution, the posterior distribution clearly favors a prolate halo shape.

19.2 Comparison with simulations

Since the symmetry axis of the DM halo was fixed to that of the oblate stellar component, it is elongated along the stellar minor axis. This means that the major axis of the DM halo is misaligned with respect to that of the stellar component, which for instance is disfavored for the Milky Way (e.g., Law et al. 2009; Debattista et al. 2013; Han et al. 2023) and Milky Way-like disk galaxies in simulations (e.g., Prada et al. 2019). To assess the meaning of the configuration

found for Centaurus A, we measured the shapes of the galaxies and their DM halos in the Magneticum Box4 (uhr; Teklu et al. 2015; Dolag et al. 2025) and TNG100 Marinacci et al. 2018; Naiman et al. 2018; Nelson et al. 2018; Pillepich et al. 2018; Springel et al. 2018 simulations following a procedure similar to those described by Valenzuela et al. (2024a) and Pulsoni et al. (2021), which corresponds to method S1 from Zemp et al. (2011). For this, we selected simulated analog galaxies in the mass ranges of $M_{\rm vir} = 3 \times 10^{12}$–$3 \times 10^{13}\,{\rm M}_{\odot}$ and $M_{*} = 1$–$5 \times 10^{11}\,{\rm M}_{\odot}$ and that have oblate stellar distributions and prolate DM halos. We determined the shapes according to the triaxiality $T = (1 - q^2)/(1 - p^2)$ with axis ratios $q = b/a$ and $p = c/a$ for the three ellipsoidal axes $a \geq b \geq c$, where we define $T < 1/3$ as oblate and $T > 2/3$ as prolate.

We then determined the angles between the stellar minor axis and the DM halo major axis, where the preferred configuration of Centaurus A has a small such angle. In the two simulations, 12 galaxies in Magneticum Box4 and 17 galaxies in TNG100 have oblate stellar components and prolate DM halos. In each of the simulations, only one galaxy has a configuration similar to that expected for Centaurus A with a small angle ($\lesssim 20°$) between the stellar minor axis and the DM halo major axis. Both of the galaxies show clear signs of ongoing or recent interaction, indicating that this type of configuration is rare and most likely associated with significant mergers.

19.3 Conclusion

Using a photometric and kinematic sample of GCs in the outskirts of the massive early-type galaxy Centaurus A, we dynamically model the DM halo. The red and blue GCs exhibit distinct dynamical properties, pointing toward different formation pathways for the two subpopulations (e.g., Forbes et al. 2018a). The resulting DM halo and stellar properties are consistent between the best fits for the red and blue GCs. In particular, we constrain the intrinsic flattening of the halo, finding evidence that it is not spherical, but prolate and elongated along the minor axis of the oblate stellar component. By employing analog galaxies from the Magneticum Box4 (uhr) and TNG100 simulations based on virial mass, stellar mass, and the intrinsic galaxy and halo shapes, we investigate under what circumstances this galaxy-halo configuration occurs. Both simulations indicate that this orientation of a prolate DM halo along the minor axis of an oblate stellar component is very rare, where the sole galaxy in each of the two simulations with such a configuration shows clear signs of ongoing or recent interaction. The DM halo inferred from the GC system of Centaurus A therefore supports previous findings that the galaxy has undergone a significant merger in the past few Gyr that led to this particular elongation of the DM halo. We conclude that GCs are useful dynamical tracers and are capable of constraining halo properties that give insights into the past formation histories of their host galaxies.

20

Summary & Conclusion

Understanding the observed diversity of galaxies and deciphering their formation histories remains a central goal of galaxy physics. In this thesis, I explored this problem through three stellar tracers: the stellar component, planetary nebulae (PNe), and globular clusters (GCs). Using cosmological simulations, primarily the Magneticum Pathfinder simulation (Dolag, Remus, Valenzuela et al. 2025), and tracer population models, I investigated how these tracers encode information about galaxy assembly to make predictions for and compare to observations. In the following, I summarize the main results for each stellar tracer and conclude with an outlook on their complementary roles in future studies of galaxy formation in the era of large-scale surveys.

20.1 Results from the stellar component

For the stellar component, this thesis focuses on tidal features as tracers of galaxy assembly histories. A central result is that tidal shells preferentially occur around slowly rotating galaxies in simulations and observations, with streams showing the same but slightly weaker trend (Valenzuela & Remus 2024). For the shells, this indicates that outer tidal structures and inner galaxy kinematics are linked through radial merger events that lead to the formation of shells and simultaneously reduce the rotational support of the central galaxy. Some observational evidence indicates that this relation only holds for shell galaxies with younger stellar populations, implying that the connection between slow rotation and tidal features weakens as the latter dissipate over time (Rutherford et al. 2024, incl. Valenzuela). Prolate rotators are particularly likely to host tidal features, consistent with merger-driven formation scenarios. Galaxies with kinematically distinct cores (KDCs) show a preference for hosting

streams, suggesting assembly histories dominated by mini and minor mergers that preserve the inner galaxy rotation while reducing the outer rotational support. In contrast, I find no significant correlation between the inner galaxy kinematics and the presence of satellite planes, indicating that satellite configurations are more closely related to the larger-scale environment than to the galaxy itself.

Beyond these correlations, tidal features provide direct insight into the properties of their progenitor galaxies. I show that shells generally originate from more massive progenitors than streams, which is also reflected in their higher metallicities, and that both types tend to have lower velocity dispersions than the surrounding stellar halo (Stoiber, Valenzuela et al. 2025). Furthermore, I demonstrate that projected metallicity measurements in the feature region significantly underestimate the actual progenitor mass when directly applying the mass-metallicity relation because of contamination from halo stars. As a result, the biases predicted by simulations have to be taken into account when inferring progenitor galaxy properties such as mass, metallicity, or age. Tracing the evolution of streams and shells further reveals how their morphology and stellar populations change over time because of outside-in stripping (Stoiber, Valenzuela et al. 2026), and that some young stream-like features can arise in situ rather than through accretion.

By extending the analysis to galaxies that themselves are satellites of more massive galaxies, I further show that the occurrence of tidal features depends strongly on the environment and the satellite's location therein (Khalid et al. 2025, incl. Valenzuela). The results show a clear suppression of tidal features in the central regions of galaxy clusters, whereas they exhibit enhanced frequencies in the vicinity of field galaxies and at the center of galaxy groups.

To conclude, tidal features emerge as powerful tools for tracing a galaxy's formation history. In particular, the combination of tidal features with the inner galaxy kinematics offers a new avenue to disentangle specific formation pathways for galaxies, which will be of great interest with upcoming deep imaging surveys through Euclid, Rubin, and Roman.

20.2 Results from planetary nebulae

For PNe, this thesis focuses on establishing their theoretical connection to the underlying stellar populations and assessing their use as tracers of galaxy formation histories. A major outcome of this work is that the long-standing puzzle of bright PNe observed in old galaxies can largely be resolved through self-consistent modeling of PNe within their parent stellar populations and in galaxies with realistic star formation histories. Through the development of PICS (PNe In Cosmological Simulations; Valenzuela et al. 2025c), I show that the universal bright-end cutoff of the PN luminosity function (PNLF) can be reproduced across a wide range of stellar ages and metallicities. Metallicity emerges as a key ingredient in producing bright PNe at old ages, while circumnebular extinction is essential for regulating the bright end in younger populations (Valenzuela et al. 2025b).

By systematically varying the underlying model parameters and assumptions, I demonstrate that the details of the PNLF are sensitive to the initial-to-final mass relation (IFMR) of stars,

nebular physics, and circumnebular extinction. With PICS I am able to separate out the individual effects of these components, finding that in particular changes to the IFMR can lead to significantly brighter or dimmer PNLFs. Applying PICS to a simulated Milky Way-like galaxy successfully reproduces the shape and normalization of the observed local PNLF, supporting the reliability of the modeled PN populations (Valenzuela et al. 2025d).

Extending the application of PICS to the whole galaxy population obtained from different cosmological simulations, I find that the PNLF bright-end cutoff remains remarkably stable across galaxy masses and morphologies (Valenzuela et al. in prep. a). This is the first time that theoretical work fully models the PN populations for galaxies with cosmologically self-consistent star formation histories. It is finally capable of reproducing the universal bright-end cutoff of the PNLF, a long-standing problem in PN research. The universality even holds across different galaxy classifications including by morphology, star formation, inner kinematics, and stellar metallicity. However, there is still significant scatter toward dimmer bright-end cutoffs for some lower-mass galaxies, which I relate to their stellar age. In general, I find that the dominant driver for differences of the typical PNLF between the different classes is in fact the stellar age, where old galaxies have systematically fainter PNLFs with steeper slopes below the cutoff. Nevertheless, the PNLF cutoff is overall very similar between the other classes, and stronger differences can be seen in the shape of the faint PNLF, suggesting these can be leveraged to place constraints on the underlying stellar populations.

I further show that PNe are not only stellar population tracers, but also powerful tracers of diffuse structures. Applying PICS to a tidal stream around a simulated galaxy, I demonstrate that observations of the brightest PNe are sufficient to disentangle the stream kinematics from the underlying stellar halo (Valenzuela et al. 2026). This enables constraints on the host galaxy's gravitational potential and halo mass, establishing PNe as effective dynamical tracers that complement deep photometry of low-surface-brightness structures.

Comparisons with observed PN populations generally support the results from the PICS framework, where I find a consistent relation between intermediate-age stellar populations and the number of bright PNe for both the simulations and observations (Soemitro, Valenzuela et al. 2025). However, persistent discrepancies for old and metal-poor stellar populations indicate that the brightest PNe in these environments are not yet fully understood and may point either to limitations in current modeling or to a significant fraction of undetected intermediate-age stellar populations in the observations (Hartke, Ennis, Valenzuela et al. in prep.).

To conclude, this thesis has set a new milestone for theoretical PN modeling, which for the first time delivers a self-consistent theoretical explanation for much of the universality of the PNLF bright-end cutoff. First successful applications show that the details of the PNLF can provide insights into the underlying star formation history of a galaxy and that PNe are powerful tracers of low-surface-brightness dynamics. Simultaneously, the tensions still found between theory and observations highlight the key open questions that remain on PN populations.

20.3 Results from globular clusters

For the GCs, this thesis focuses on their use as tracers of assembly and merger histories as well as of halo dynamics. I show that GC populations encode information not only about halo mass, but also about accretion history. Building on an empirical GC model with two distinct formation pathways (Valenzuela et al. 2021, developed prior to this thesis), I find that deviations from the mean GC number-halo mass relation directly trace the amount of smooth accretion experienced by a galaxy, establishing GC populations as probes of halo growth and assembly history (Valenzuela 2023).

Leveraging the GC ages, I further demonstrate that their age distributions preserve signatures of past gas-rich merger events (Valenzuela et al. 2024b). For the observed Milky Way GCs, this allows me to connect a bimodality in the GC age distribution to Gaia-Sausage/Enceladus (GSE; the last major merger of the Milky Way ~8 Gyr ago), confirming the model prediction that significant gas-rich accretion events leave identifiable imprints in the GC ages. This is further supported by the successful application to several other nearby galaxies. More generally, I find that GC age distributions are effective tracers of early gas-rich mergers, while later gas-poor accretion events leave much weaker signatures.

To place these findings in a broader theoretical context, I conduct the first direct comparison of six state-of-the-art GC models with respect to their predicted age distributions for Milky Way-like galaxies (Valenzuela et al. 2025a). While all of the models are capable of successfully forming old GCs ($\gtrsim$10 Gyr), they differ substantially in their predictions for younger GC populations for a more general sample of Milky Way-mass galaxies, revealing systematic differences in their underlying formation assumptions. Forthcoming large photometric surveys like Euclid, Rubin, and Roman will help further distinguish between competing GC formation scenarios through coarse GC age estimates as the predictions differ so significantly.

I also investigate the possible connection between present-day GCs and the young stellar clusters now being observed at high redshift. While all GC models predict a consistent peak of GC formation at intermediate redshifts of z = 1–3, they differ strongly in the formation times of the first surviving clusters. This shows how the models offer different expectations for whether the high-redshift clusters can survive to become present-day GCs. More observations and age measurements will be needed to further establish the connection between high-redshift and present-day clusters, where additional work on the ages of high-redshift clusters has already appeared in the meantime (e.g., Claeyssens et al. 2026; Whitaker et al. 2026).

To conclude, GCs are effective tracers for galaxy formation across a wide range of timescales, as they originate from the earliest assembly phases of galaxies and act as powerful indicators for past gas-rich merger events. This thesis also lays the groundwork for more detailed model comparisons needed to improve on current approaches in the next generation of GC models.

20.4 A symphony on the past

Our understanding of galaxy formation has made large advances in recent years through new observational facilities as well as improved computational techniques. With multiple large-area surveys now coming online and upcoming extremely large telescopes, significantly more data will become available for present-day galaxies, which require robust theoretical frameworks for physical interpretation. As deciphering the entire past of an individual galaxy remains an exceptionally challenging task, it is of great importance to combine the different tracers available to us to gain comprehensive insights into its formation history. To this end, the three stellar tracers discussed in this thesis present different perspectives on the past, which I have addressed through a combination of simulations and models. While the faint stellar outskirts can be probed through deep photometry and trace the recent accretion and interactions well, adding PN measurements can deliver the corresponding kinematics and place constraints on the underlying stellar populations. Meanwhile, the red and blue GC populations may serve as distinct tracers for in-situ and accreted components as well as contribute to the overall spatial and dynamical properties of the halo. Lastly, the GCs and their stellar populations open up the window to the early formation times of their host galaxies and the otherwise elusive gas-rich merger events in the past. Taken together, the three stellar tracers provide complementary insights into galaxy formation histories, each probing different aspects of their past. In this sense, they form parts of a larger whole: a symphony on the past, reflecting the complexity of galaxy formation across cosmic time.



A

Rescaling the Cumulative Distribution

This is the appendix of the publication by Valenzuela & Remus (2024), A&A 686, A182, presented in Chapter 4.

The cumulative histogram of the simulated galaxies can be adapted to be directly comparable with that of the observations in the following way: Qualitatively, the λ_{R_e}-values are divided into bins. Each bin contains a different total number of observed and simulated galaxies, as well as different numbers of observed and simulated galaxies with a given tidal feature. To make the latter numbers directly comparable to each other, the number of either the observed or the simulated galaxies with the given feature has to be multiplied with the ratio of the total numbers of galaxies in that λ_{R_e} bin. In this work, we chose this to be the numbers of simulated galaxies with the given feature that are rescaled by the aforementioned ratio. The cumulative distribution is then obtained through summing over the individual bins up to a given value of λ_{R_e}.

Quantitatively, taking into account that there are different underlying distributions of values of λ_{R_e} in the observations and the simulation and that the samples have different sizes, this means that for any interval $\Delta\lambda_{R_e}$, there is a different number of observed galaxies $N_{\mathrm{obs}}(\Delta\lambda_{R_e})$ and of simulated galaxies $N_{\mathrm{sim}}(\Delta\lambda_{R_e})$. From these, the ratio of observed to simulated galaxies can be determined through $q(\Delta\lambda_{R_e}) = N_{\mathrm{obs}}(\Delta\lambda_{R_e})/N_{\mathrm{sim}}(\Delta\lambda_{R_e})$. We used this fraction $q(\Delta\lambda_{R_e})$ to then make the number of simulated galaxies with a given feature that lie within such an interval directly comparable with the number of observed galaxies with that feature $N_{\mathrm{obs,feat}}(\Delta\lambda_{R_e})$. For the λ_{R_e} values of the simulated galaxies that have a given feature, $\lambda^1_{R_e} \leq \cdots \leq \lambda^{N_{\mathrm{sim,feat}}}_{R_e}$, where $N_{\mathrm{sim,feat}}$ is the number of simulated

galaxies with the feature, it is sufficient for cumulative histograms to choose the intervals $\Delta\lambda^1_{R_e} = [0; \lambda^1_{R_e}], \Delta\lambda^2_{R_e} = (\lambda^1_{R_e}, \lambda^2_{R_e}]$, etc. This results in a set of $N_{\mathrm{sim,feat}}$ intervals, for which the weightings of the λ_{R_e} values of the simulated galaxies with the respective feature are given by the factors $q(\Delta\lambda_{R_e})$. The sum over all these weightings then defines the rescaled number of simulated galaxies with the given feature, and the cumulative histogram can be determined through

$$\frac{N_{\mathrm{cum}}(\leq\lambda^i_{R_e})}{N_{\mathrm{tot}}} = \frac{\sum_{j=1}^{i} q(\Delta\lambda^j_{R_e})}{\sum_{j=1}^{N_{\mathrm{sim,feat}}} q(\Delta\lambda^j_{R_e})}. \tag{A.1}$$



B

Tidal Feature Compilation

This is part of the appendix of the submitted publication by Stoiber, Valenzuela et al. (2025), presented in Chapter 5.

B.1 Overview of the extracted tidal shells and streams

For each of the tidal shells and streams found in the last snapshot of Magneticum Box4 (uhr), we identified their progenitor galaxies at the preceding snapshots (see Section 5.3). Here we show all the isolated shell and stream systems that we obtained by tracing forward the stars belonging to the progenitor galaxies. The isolated shell systems are shown in Figure B.1 and the streams in Figure B.2. The surface density maps were created in the same way as the right panels of Figure 5.4, where the maps are centered on the host galaxy, but the host itself is not shown. Note that some of the galaxies have streams from different progenitors and therefore show up in several panels (e.g., UID 0 and UID 1414).

B.2 Potential trigger for an in-situ stream-like feature

As discussed in Section 5.4, the stream-like feature shown in Figure 5.10 is formed in-situ within a gas ring around the host galaxy. A potential trigger for its formation is a brief encounter with a passing galaxy that has its pericenter on the side of the gas ring at $z = 0.14$ that begins forming stars shortly after. We show the flyby in Figure B.3 within the larger environment of the host galaxy from the face-on (top row; same orientation as Figure 5.10,

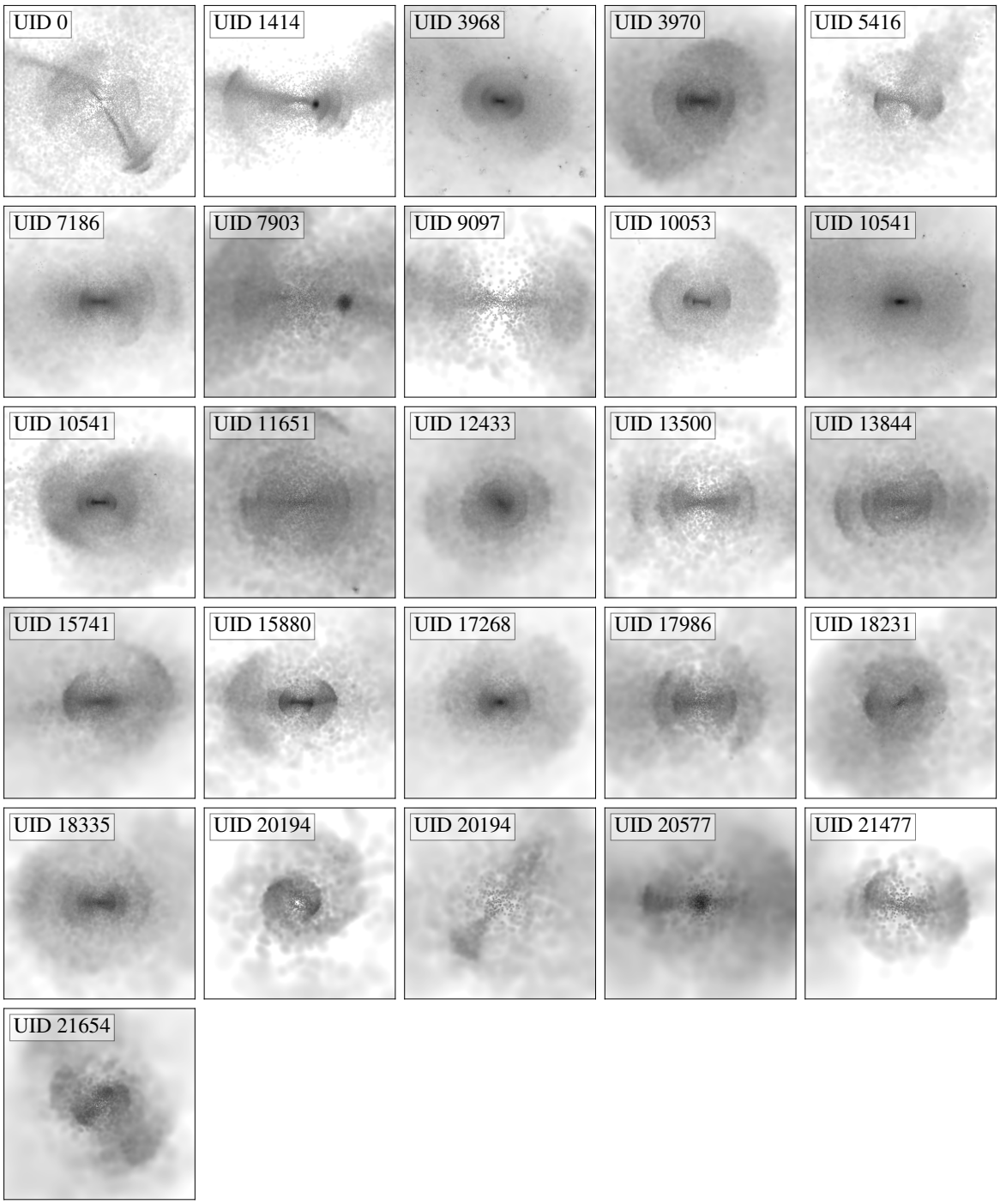


Figure B.1: Stellar surface density maps of the isolated shell systems in Magneticum Box4 (uhr), obtained by tracing the stars forward in time from the galaxy that was identified to be the progenitor of the shells. The projections and orientations of the maps are the same as in Figure 5.1. *This is figure B.1 from Stoiber et al. (2025).*

see the white square here) and edge-on (bottom row) views. Overplotted on the stellar surface density maps is the traced orbit of the flyby galaxy (dashed cyan line) and its velocity vectors along the orbit (blue arrows), where the first pericenter passage to the host galaxy occurs shortly before the second panel at $z = 0.14$. Less than 0.5 Gyr later, at $z = 0.10$, a significant amount of young stars have been formed within the gas ring in the direction of the incoming galaxy flyby. We thus propose that this encounter caused the in-situ star formation within the gas ring.

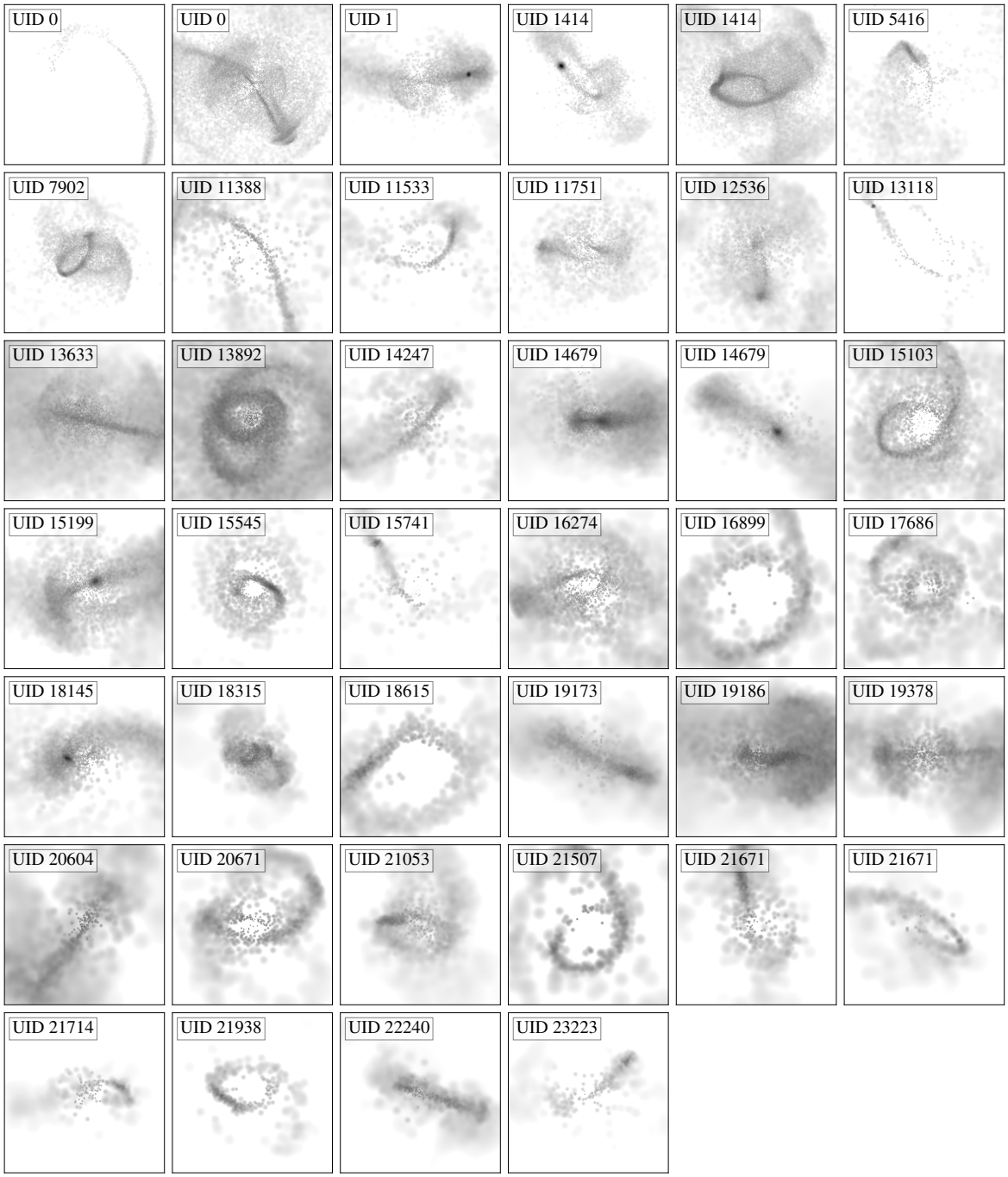


Figure B.2: Stellar surface density maps of the isolated streams in Magneticum Box4 (uhr), obtained by tracing the stars forward in time from the galaxy that was identified to be the progenitor of the streams. The projections and orientations of the maps are the same as in Figure 5.1. *This is figure B.2 from Stoiber et al. (2025).*

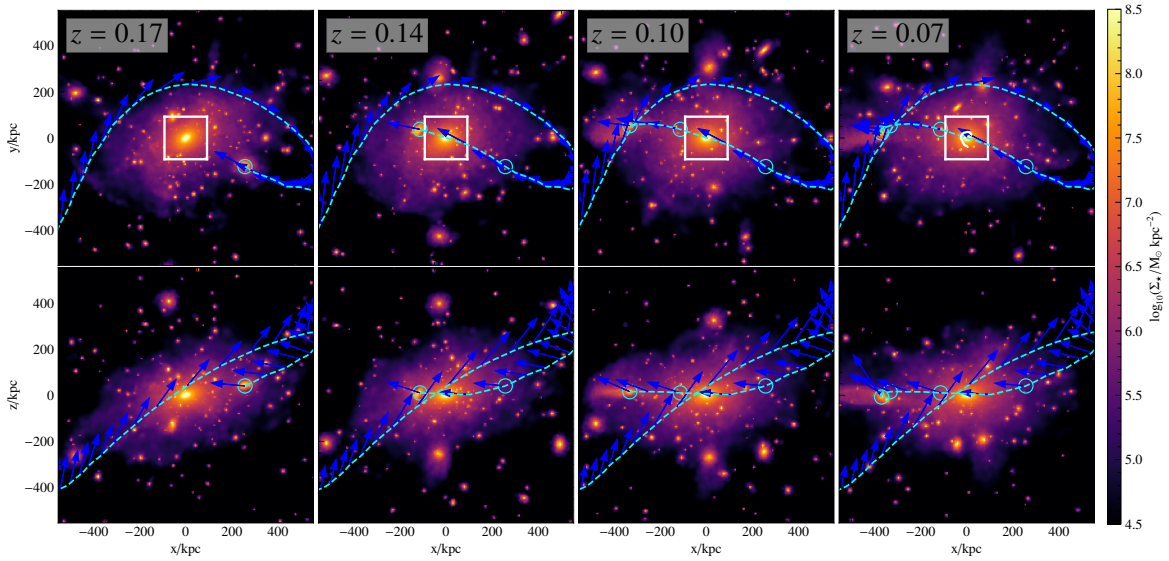


Figure B.3: Orbit of a galaxy passing by the host galaxy that forms a young stream-like feature in its gas ring across the same four snapshots as seen in Figure 5.10. The panels show the stellar surface density maps of the larger environment for the face-on (top) and edge-on projections of the host galaxy. The face-on projection is the same as found in Figure 5.10, where the white squares indicate the depicted regions in that figure. The flyby galaxy's orbit (cyan line) is traced until the respective snapshot, with the velocity vectors indicated along it (blue arrows). The positions at the four snapshots shown here are marked by the cyan circles.

C

Tidal features in projected phase space

This appendix presents the projected tidal feature fractions found in the publication by Khalid et al. (2025, incl. Valenzuela), MNRAS 543, 3391, presented in Chapter 6.

In Section 6.2, we show the tidal feature occurrences and fractions in 3D phase space around field galaxies, galaxy groups, and galaxy clusters. However, direct measurements in observations only deliver the projected distances and line-of-sight velocities of satellite galaxies for 2D phase space. While the actual intrinsic physical properties are obtained from 3D measurements as provided by the simulations, an important aspect is also the prediction for observations as a means to interpret incoming observational data. Furthermore, the comparison between intrinsic and projected information also reveals the extent to which trends are weakened and information is lost.

Figure C.1 shows the occurrence of tidal features in projected phase space for the same field galaxy, galaxy group, and galaxy cluster regimes as shown in Figure 6.2 for 3D phase space. The same overall trends are recovered as in the intrinsic 3D phase space, where fewer ancient infaller satellites show tidal features in the more massive environments. However, the intrinsically very high fractions are reduced for field galaxies and galaxy groups (from 73% to 60% and from 43% to 35%, respectively), and the intrinsically very low fraction is increased for clusters (from 8% to 13%) due to the projection leading to the intrinsic regions mixing somewhat. The intermediate and recent infaller regions as well as the outer satellites show small differences, indicating that the intrinsic predictions for these regions can also be applied to observations.

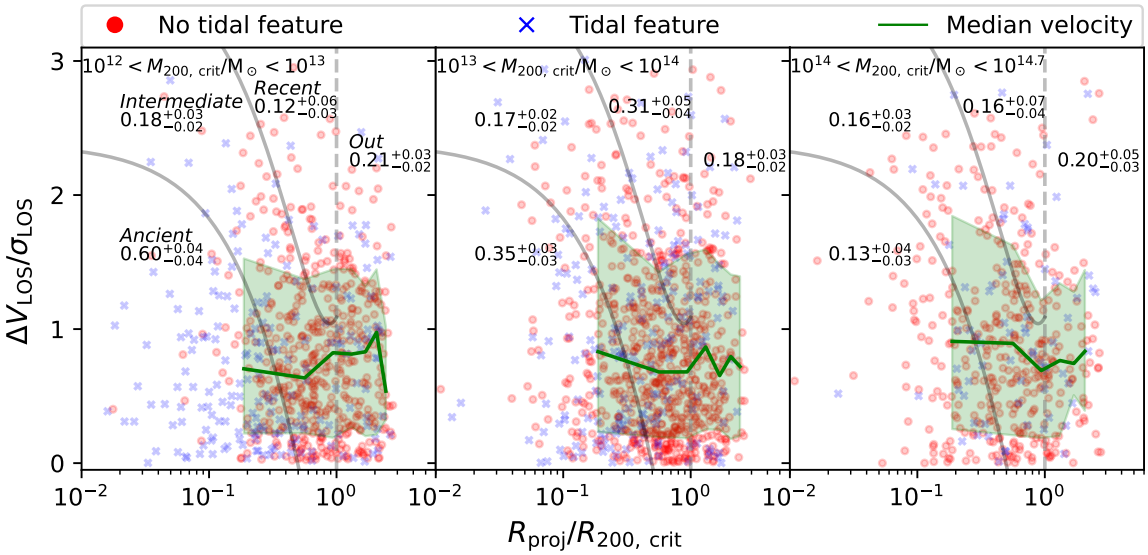
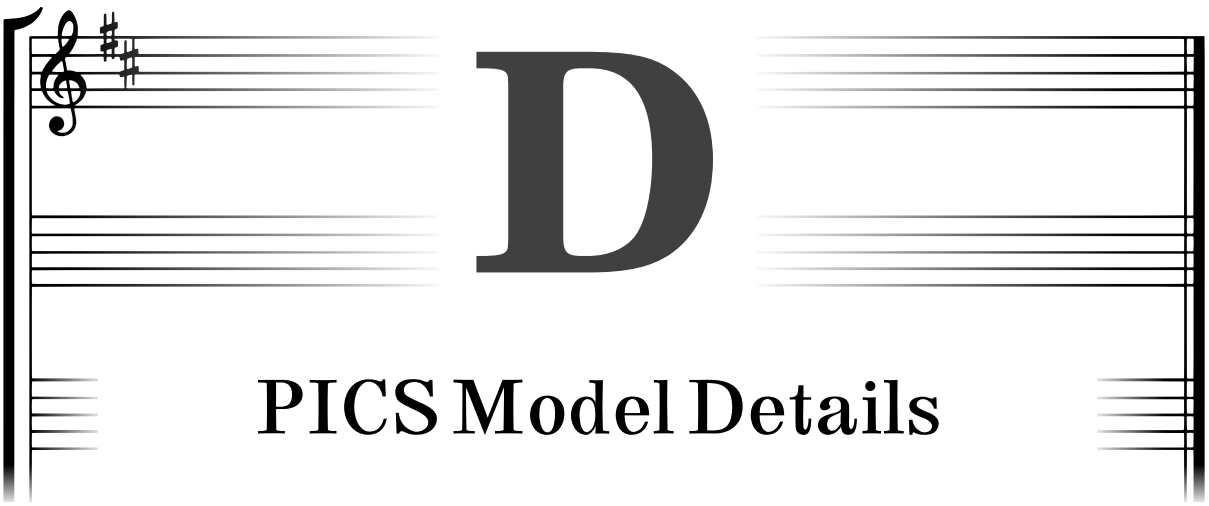


Figure C.1: Projected phase-space diagram of satellite galaxies in host halos of three different mass bins, for field galaxies (log M_{200} = 12–13, left), galaxy groups (log M_{200} = 13–14, center), and galaxy clusters (log M_{200} = 14–14.7, right), similar to Figure 6.2. The phase space is made up of the 2D projected radial distance to the host center R, normalized to $R_{200,\mathrm{crit}}$, and the line-of-sight velocity relative to the host ΔV_{LOS}, normalized to the halo line-of-sight velocity dispersion σ_{LOS}. The markers indicate the combined sample of satellite galaxies from Magneticum Box4, EAGLE, and TNG100, differentiating between galaxies with (blue crosses) and without (red circles) tidal features. The solid green line indicates the median velocity as a function of radius and the shaded region its 1σ scatter. The solid gray lines mark the borders of the ancient, intermediate, and recent infaller regions (as specified in the left panel, based on the definitions of Pasquali et al. 2019), and the vertical dashed gray line marks the halo border of $R_{200,\mathrm{crit}}$, separating the outer fourth region (Out). The fractions of galaxies having tidal features and their corresponding upper and lower errors are indicated in each region. *This is figure 4 from Khalid et al. (2025).*



D

PICS Model Details

This is the appendix of the publication by Valenzuela et al. (2025c), A&A 686, A182, presented in Chapter 8.

D.1 Post-AGB track interpolation

Here we present how the post-AGB tracks provided by Miller Bertolami (2016) are interpolated (see Section 8.1.4 for the corresponding section in the main text). For the post-AGB tracks, we take the output tables from Miller Bertolami (2016), which each consist of 101 points of equivalent position along the tracks in the Hertzsprung-Russel diagram, with precomputed luminosity, effective temperature, and post-AGB time since a temperature of $\log T_{\rm eff}/{\rm K} = 3.85$ was reached. The tables are available for between 12 and 20 final masses for each of the four metallicities $Z = 0.0001$ (12 between $M_{\rm final} = 0.525$ and $0.800\,{\rm M}_\odot$), $Z = 0.001$, $Z = 0.01$, and $Z = 0.02$ (each of them have 20 tables for final masses between $M_{\rm final} = 0.525$ and $1.000\,{\rm M}_\odot$). As we follow the approach of Valenzuela et al. (2019) in this work to define the post-AGB age as the time since a temperature of $T_{\rm eff} = 25\,000\,{\rm K}$ was reached, the precomputed post-AGB ages are shifted accordingly in the individual tables. To interpolate the tracks for arbitrary metallicities, final masses, and post-AGB ages, we perform linear interpolations on the logarithmic metallicity and the final mass to find the eight relevant equivalent points on the tracks corresponding to the two adjacent metallicities, final masses, and post-AGB ages. The luminosity and effective temperatures are then determined from these eight points by trilinear interpolation, the result of which can be seen in Figure 8.3.

D.2 Nebular model recipes

The nebular model by Valenzuela et al. (2019) as described in Section 8.1.5 employs empirical relations for the intensity ratio between $I(5007)$ and $I(\mathrm{H}\beta)$ and for the absorption factor that accounts for the possibility of optically thin nebulae and their dissipation over time. In this appendix we describe these recipes in more detail to present the final model from Valenzuela et al. (2019), which was built on previous versions by Méndez et al. (1993) and Méndez & Soffner (1997).

D.2.1 Intensity ratio recipe

After having obtained $I(\mathrm{H}\beta)$ assuming a blackbody spectrum based on the luminosity and effective temperature of the central star, the relative intensity of $I(5007)$ is determined empirically. For this we consider three different cases based on T_{eff}:

- $T_{\mathrm{eff}} \leq 30\,152\,\mathrm{K}$: $I(5007)$ is set to zero.
- $30\,152\,\mathrm{K} < T_{\mathrm{eff}} \leq 60\,000\,\mathrm{K}$: The intensity is set to $100\,I(5007)/I(\mathrm{H}\beta) = 0.0396\,T_{\mathrm{eff}}/\mathrm{K} - 1194$ based on the linear relation derived by Méndez et al. (1993) in their eq. 5.
- $T_{\mathrm{eff}} > 60\,000\,\mathrm{K}$: First, a random value I_{rel} is drawn from a normal distribution with a mean of 9.50 and a standard deviation of 3.75, truncated to 0 if a negative value is drawn. As Valenzuela et al. (2019) describe, the steep drop-off at the high end of the distribution has to be taken into account to avoid overly high values of $I(5007)$: First, for $I_{\mathrm{rel}} > 12$ the value is decreased by $((I_{\mathrm{rel}} - 12)/8)^{1.5}$. If it is then still larger than 15, it is further decreased by $(I_{\mathrm{rel}} - 15)/5$. Finally, if the value is still larger than 18, I_{rel} is simply set to a uniformly random value between 18 and 19 and then truncated to a maximum value of 18.5. In a last step, for low central star masses of $M_{\mathrm{final}} \leq 0.55\,\mathrm{M}_\odot$ that are hot and luminous with $\log(L/\mathrm{L}_\odot) > 3$ and $T_{\mathrm{eff}} > 75\,000\,\mathrm{K}$, the value of I_{rel} is multiplied with 0.4 as described by Valenzuela et al. (2019). This value of I_{rel} is finally used to obtain $I(5007)$ by $I(5007) = I_{\mathrm{rel}} I(\mathrm{H}\beta)$.

D.2.2 Absorption factor recipe

The absorption factor μ used by Valenzuela et al. (2019) is determined through a linear combination based on central star mass, effective temperature, and post-AGB age relative to reaching the highest combination of effective temperature and luminosity at the knee of the post-AGB tracks. The post-AGB time to the knee is approximated through the analytical relation $t_{\mathrm{knee}} = 0.0239 M_{\mathrm{final}}^{-21.82}$. The absorption factor is a value between 0 and 1 that is multiplied with the originally obtained value for $I(5007)$ to account for a lack of optical thickness and nebular dissipation. First, a generator value μ_{gen} is randomly drawn between 0 and 1 from a uniform distribution. For the cooling tracks with post-AGB ages larger than 1.1 times the time to reach the knee, the absorption factor is determined as $\mu = (0.1 + 0.9\mu_{\mathrm{gen}}^{0.9}) \times (1 - t_{\mathrm{post-AGB}}/30\,000\,\mathrm{yr})$ to account for the nebulae becoming transparent over time. For the heating tracks until the knee,

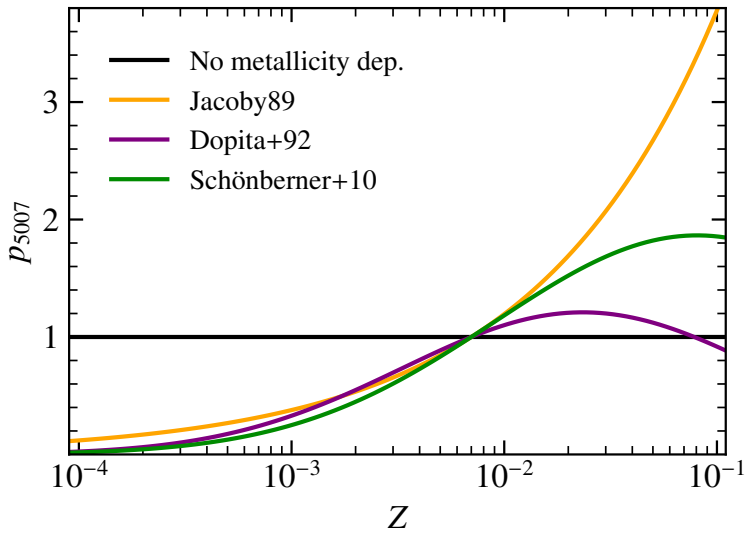


Figure D.1: Nebular metallicity correction factor p_{5007} as a function of metallicity for the relations given by Jacoby (1989), Dopita et al. (1992), and Schönberner et al. (2010), as well as for having no metallicity dependence. The relations are set up to reach a value of $p_{5007} = 1$ at the base metallicity $Z_{\mathrm{base}} = 0.007$.

three temperature ranges are considered, where linear interpolation is applied for temperatures between the respective limits:

- $\log T_{\mathrm{eff}}/\mathrm{K} < 4.51$: For the beginning of the heating track, μ is set to $\min(0.4 + \mu_{\mathrm{gen}}, 1)$ to account for generally more opaque PNe.
- $4.68 < \log T_{\mathrm{eff}}/\mathrm{K} < 4.85$: For low-mass central stars below $0.535\,\mathrm{M}_\odot$, $\mu = 0.03 + 0.17\mu_{\mathrm{gen}}$ is used to obtain overall low values of μ because of their slow post-AGB evolution, such that the nebulae already dissipate during this time. In contrast, for higher-mass central stars above $0.557\,\mathrm{M}_\odot$, $\mu = 0.2 + 0.8(1 - \mu_{\mathrm{gen}}^2)$ is applied, which allows for high values of μ. Linear interpolation is applied for the mass range in between these mass limits.
- $\log T_{\mathrm{eff}}/\mathrm{K} > 4.95$: For low-mass central stars below $0.535\,\mathrm{M}_\odot$, $\mu = 0.03 + 0.17\mu_{\mathrm{gen}}$ is again used to account for their slow evolution along the post-AGB tracks. For higher-mass central stars above $0.557\,\mathrm{M}_\odot$, $\mu = 0.1 + 0.9\mu_{\mathrm{gen}}$ is applied, which now leads to lower values of μ with a higher probability compared to at lower effective temperatures due to the time that has passed. Linear interpolation is again applied for the mass range in between these mass limits.

For the time between 1 and 1.1 times the time to reach the knee of the post-AGB track, and for the effective temperatures between the ranges listed above, linear interpolation is applied between the respective obtained values for μ. As a final step, μ is truncated to the range between 10^{-8} and 1.

D.3 Nebular metallicity

In Figure D.1 we show the nebular metallicity correction factor p_{5007}, which is multiplied by the obtained [O III] fluxes from the model by Valenzuela et al. (2019), as a function of metallicity. The relations are taken from Jacoby (1989), Dopita et al. (1992), and Schönberner et al. (2010) and are described in detail in Section 8.1.5. If no metallicity dependence is taken into account, the flux remains the same with a factor of 1 (black line). As we selected the base metallicity $Z_{\rm base} = 0.007$ based on which the corrections are computed, all lines run through p_{5007} at that metallicity. Because the values of p_{5007} do not lead to as heavily boosted or dimmed [O III] fluxes, we selected the relation by Dopita et al. (1992) for the fiducial PICS model.

D.4 Circumnebular extinction

The relations for circumnebular extinction by Jacoby & Ciardullo (2025) are only derived from the brightest PNe of M 31 and the LMC, and they are only dependent on the final stellar mass. In Section 8.1.6, we describe our choice of using PNe of metallicity $Z = 0.01$ to obtain the post-AGB ages at which the maximal brightness can be reached. Here we present the detailed derivation of this relation. We first modeled the intrinsic [O III] flux evolution throughout the PN lifetime of 30 000 yr for final masses $M_{\rm final} = 0.53$–$1.00\,{\rm M}_\odot$ at $Z = 0.01$, taking at each timestep the maximal brightness based on 10 000 realizations of the nebular model. For each final mass, we then determined the post-AGB age $t_{\rm post-AGB}$ at which the highest flux is reached. We selected 50 equally spaced values in the final mass range, for which the brightest post-AGB ages are shown in Figure D.2, using the stellar evolution relations by Miller Bertolami (2016) and the nebular model by Valenzuela et al. (2019).

As the relation for the logarithmic brightest post-AGB ages appears to be well-described by a broken-line fit, we fit two linear relations to the final masses smaller and larger than $0.60\,{\rm M}_\odot$ (red and orange lines, respectively). Since in our recipe we need to invert this relation to obtain the corresponding final mass for a given post-AGB age, we perform the fits as a function of post-AGB age. The analytical form is given in Equation 8.11. This approach ensures that a PN at its maximum brightness experiences the extinction from the derived relation from Jacoby & Ciardullo (2025), while simultaneously accounting for dust dissipating over time.

D.5 Luminosity-specific bright PN numbers

In Section 8.3.4 we presented the luminosity-specific PN numbers (α) and the visibility lifetimes ($\tau_{\rm PN}$) for all PNe with magnitudes brighter than $M(5007) = +3.5$, as obtained for the individual SSPs. This limiting magnitude is based on the assumption that PNe span roughly 8 magnitudes of brightness (e.g., Buzzoni et al. 2006). However, in practice it is impossible to measure the entire population of PNe in a galaxy, where for most galaxies outside the Local

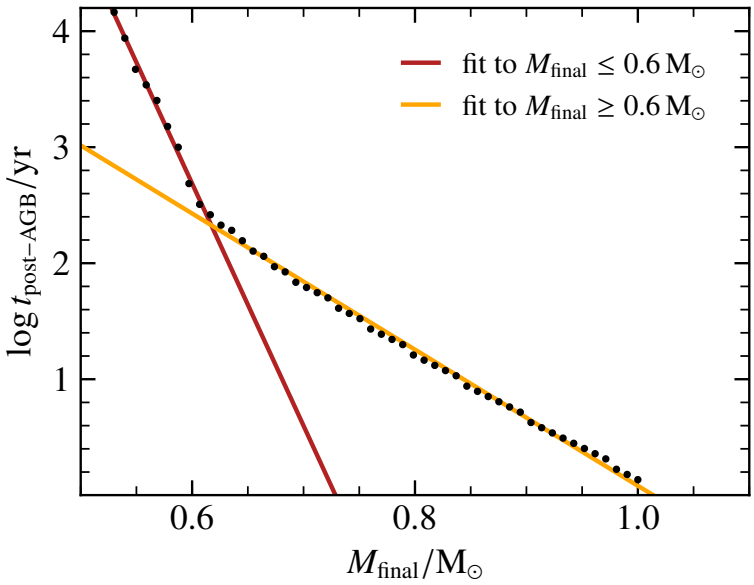


Figure D.2: Post-AGB age $t_{\rm post-AGB}$ at which PNe at metallicity $Z = 0.01$ reach the brightest possible [O III] flux as a function of final mass $M_{\rm final}$. The black data points mark the determined values from the model for 50 equally spaced final masses between 0.53 and 1.00 $\rm M_\odot$, and the red and orange lines are the linear fits to the values below and above $M_{\rm final} = 0.60\,{\rm M}_\odot$, respectively.

Table D.1: Luminosity-specific PN numbers $\alpha_{2.5}$ of the SSP PNLFs.

$t_{\rm age}$	Z					
(Gyr)	0.0001	0.001	0.01	0.02	0.04	0.08
0.25	–	–	–	9.000	–	–
0.5	–	0.006	0.049	0.040	0.090	0.415
1.0	–	0.103	0.443	0.364	0.255	0.483
2.0	–	0.173	0.807	0.682	0.631	0.389
4.0	–	0.340	1.116	0.814	1.086	0.869
6.0	–	0.584	1.531	1.173	1.074	1.164
8.0	–	0.001	1.082	0.849	1.280	1.438
10.0	–	–	0.052	0.214	0.850	0.655
12.0	–	–	–	0.087	0.138	0.681
13.0	–	–	–	–	0.094	0.579
$\alpha_{2.5}$ in units of $10^{-7}\,{\rm L}_\odot{}^{-1}$						

Notes. The luminosity-specific PN numbers $\alpha_{2.5}$ are given in units of $10^{-7}\,{\rm L}_\odot{}^{-1}$, and are given for the brightest PNe with $M(5007) \leq -2.0$ for each SSP PNLF. Each row corresponds to the given age $t_{\rm age}$ and each column to the given metallicity Z.

Table D.2: PN visibility lifetimes $\tau_{\mathrm{PN},2.5}$.

t_{age}	Z					
(Gyr)	0.0001	0.001	0.01	0.02	0.04	0.08
0.25	–	–	–	0.00	–	–
0.5	–	0.05	0.38	0.28	0.71	4.17
1.0	–	0.66	3.10	2.28	1.83	4.11
2.0	–	0.81	3.70	3.43	3.35	2.60
4.0	–	1.97	5.43	4.35	4.45	4.28
6.0	–	3.26	7.85	5.84	5.49	5.14
8.0	–	0.01	5.11	4.12	5.95	5.49
10.0	–	–	0.24	1.00	3.93	3.29
12.0	–	–	–	0.39	0.62	3.27
13.0	–	–	–	–	0.41	2.73
$\tau_{\mathrm{PN},2.5}$ in units of 10^3 yr						

Notes. The PN visibility lifetimes $\tau_{\mathrm{PN},2.5}$ are given in units of 10^3 yr and are determined from the PNe with $M(5007) \leq -2.0$ resulting from the SSPs. Each row corresponds to the given age t_{age} and each column to the given metallicity Z.

Group one is limited to the brightest couple of magnitudes. For this reason, $\alpha_{2.5}$ has become a relevant measure for the luminosity-specific PN number for those PNe with magnitudes within the brightest two and a half magnitudes of the PNLF (e.g., Jacoby et al. 1990a; Buzzoni et al. 2006; Longobardi et al. 2013; Hartke et al. 2017). For the values of each of the SSP PNLFs, we assume a fixed PNLF bright-end cutoff of $M(5007) = -4.5$ and count all PNe brighter with $M(5007) \leq -2.0$. In Table D.1 we show the values of $\alpha_{2.5}$ for the SSP PNLFs, analogously to Table 8.2 with the bolometric luminosities obtained through the GALAXEV CB07 SSP models of Bruzual & Charlot (2003) using a Chabrier (2003) IMF. Compared to α, these values are necessarily lower as the magnitude range is smaller. The values are generally compatible with results from observational work, where typically observed values are on the order of $\alpha_{2.5} \sim 10^{-8}\,\mathrm{L}_{\odot}{}^{-1}$ (e.g., Longobardi et al. 2013), which corresponds to values for ages of $t_{\mathrm{age}} \sim 10$–$12\,\mathrm{Gyr}$, depending on metallicity (see Table D.1). The corresponding PN visibility lifetimes $\tau_{\mathrm{PN},2.5}$ are shown in Table D.2, which indicate the time a PN spends being brighter than $M(5007) = -2.0$. These are also smaller than the values of τ_{PN} (Table 8.3) by necessity.

D.6 Extended PNLFs

In Figure D.3 we show the same set of SSP PNLFs as in Figure 8.10 for a grid of different ages and metallicities, just increasing the plotted magnitude range to fainter PNe at $M(5007) = +2$. Here it is much more obvious that most of the individual PNLFs drop towards fainter PNe and many in the young to intermediate age range ($t_{\mathrm{age}} \lesssim 6\,\mathrm{Gyr}$) then again have a rising number of PNe towards the faintest magnitudes. This "camel" shape has previously been found in both observations and simulations of PNe, in particular in younger systems (e.g., Jacoby & De Marco 2002; Reid & Parker 2010; Valenzuela et al. 2019), where the dip in the SMC occurs

at a slightly dimmer magnitude of $M(5007) \approx -0.5$ (Jacoby & De Marco 2002). This is consistent with the grid of PNLFs shown here, where the SSP models in Figure D.3 show that this shape can also arise within a pure SSP and it is not dependent on the correct superposition of different SSP PNLFs. In contrast, it is possible to wash out the camel shape by combining multiple SSP PNLFs as their peaks are located at different magnitudes and their shapes also differ in declining and increasing slope. The extreme rise in PN number at dim magnitudes for the youngest stellar populations of $t_{\rm age} \lesssim 0.5\,$Gyr arises from the circumnebular extinction decreasing with post-AGB age. This means that the extinction affects the intrinsically brightest PNe in the early post-AGB phase the strongest. In contrast, the older, but much dimmer PNe are hardly affected by the extinction. The PNLF is thereby effectively squashed towards dim magnitudes.

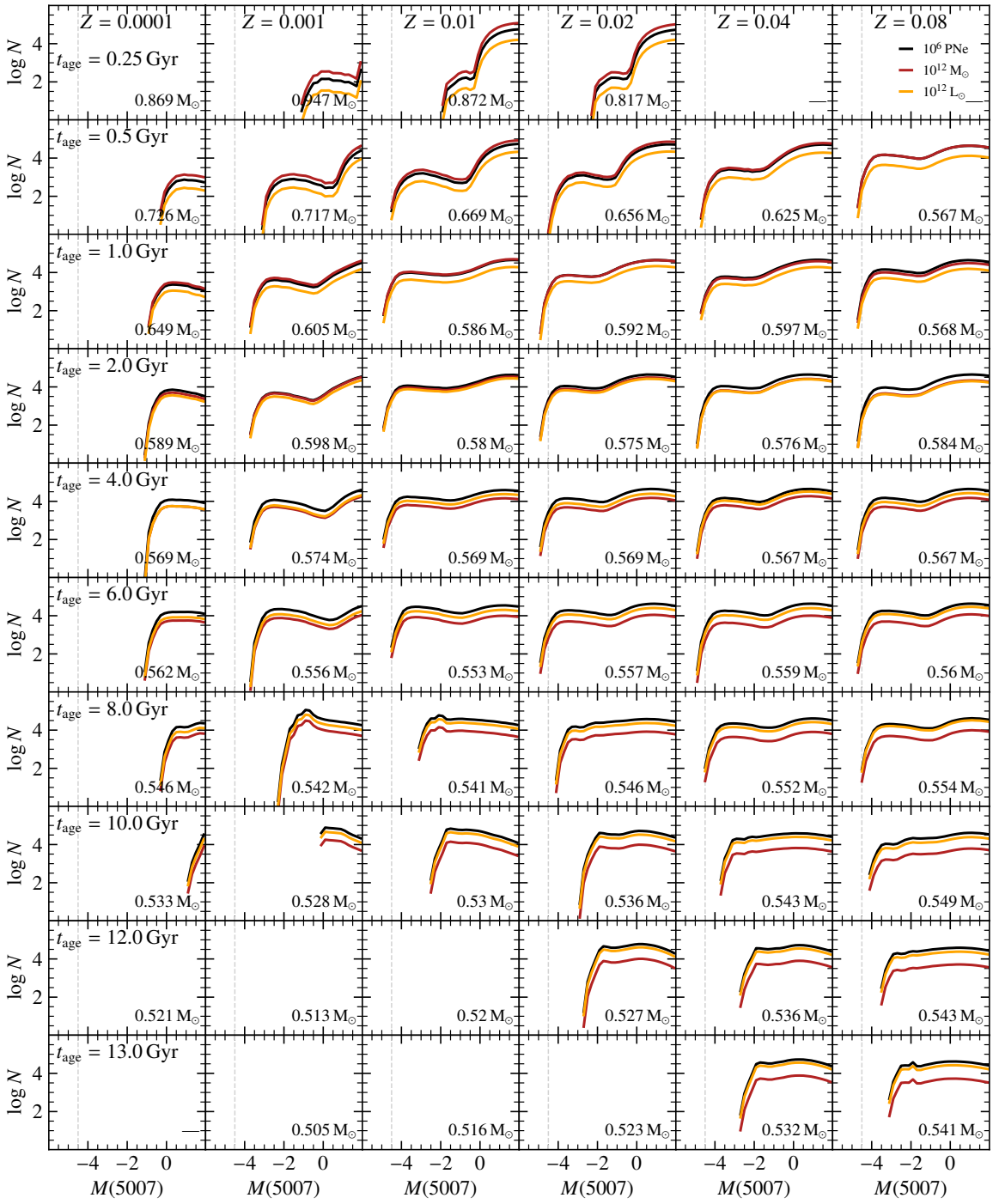


Figure D.3: Single stellar population PNLFs depending on the age and metallicity for the fiducial model with the nebular metallicity correction by Dopita et al. (1992) and circumnebular extinction by Jacoby & Ciardullo (2025), normalized to different quantities. This grid of PNLFs shows the same plots as seen in Figure 8.10, except that the λ5007 magnitude range is extended to dimmer PNe by four magnitudes. The black lines are the PNLFs obtained from 1×10^6 stars of the respective final mass with equally spaced post-AGB ages between 0 and 30 000 yr. The red PNLFs are normalized to a total mass of $10^{12}\,M_\odot$ assuming a Chabrier IMF (Chabrier 2003). The orange PNLFs are normalized to a total bolometric luminosity of $10^{12}\,L_\odot$ based on the GALAXEV CB07 SSP models by Bruzual & Charlot (2003) using a Chabrier IMF.



E

PNe at the Bright End of the PNLF

This is the appendix of the work to be submitted by Valenzuela et al. (in prep.), presented in Chapter 11.

E.1 Maximal metal-poor PN [O III] magnitude evolution

In Figure 11.2 we only show the PN brightness evolution for solar and super-solar metallicities. These are the metallicities most relevant to the bright-end of the PNLF for old and typically more metal-rich elliptical galaxies (see Figure 11.1). To capture the full metallicity dependence of the post-AGB evolution of the brightest PNe of a given stellar population, we show the $M^*(5007)$ evolution for lower metallicities of $Z = 0.001$, 0.005, and 0.01 in Figure E.1. The trends seen for the higher metallicities are continued into the metal-poor regime: the brightness of the youngest PNe (dark lines) becomes even dimmer due to their quicker heating and the strong circumnebular extinction right after the AGB phase. The oldest PNe (yellow and orange lines) heat much more slowly and reach their peak [O III] brightness towards the end of their PN lifetime of 30 000 yr. Additionally, the maximum PN brightness is dimmer for the metal-poor PNe. For the lowest metallicity of $Z = 0.001$, PNe of all ages are not able to reach the observed bright-end cutoff.

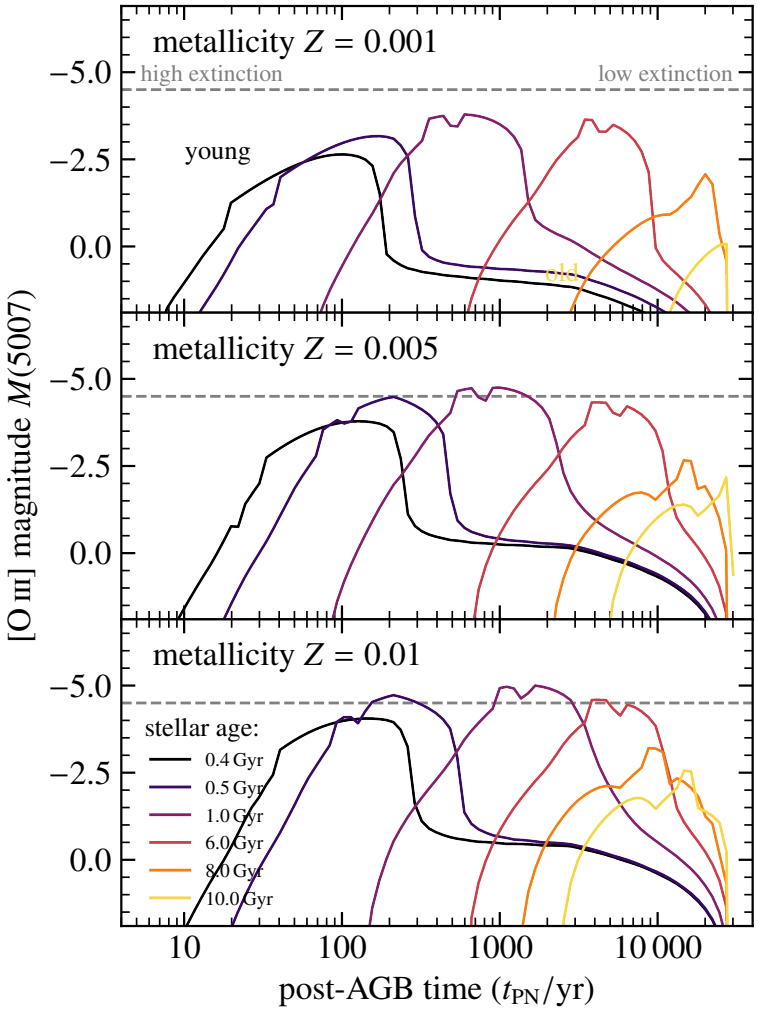


Figure E.1: Temporal evolution of the magnitude $M(5007)$ for optically thick PNe of different stellar ages (indicated by the colors) at sub-solar metallicities (Z = 0.001, 0.005, 0.01 from top to bottom, corresponding to $\log Z/Z_\odot = -1.2$, -0.5, and -0.2) over the PN lifetime of 30 000 yr from PICS (Valenzuela et al. 2025c). The circumnebular dust extinction decreases over the PN lifetime, which significantly dims the peak brightness of the youngest PNe. Metal-poor PNe have less oxygen available in their nebulae and are therefore more limited in their [O III] emission. The observed bright-end cutoff value of $M^*(5007) = -4.5$ is marked by the horizontal dashed lines.

E.2 PNLF bright end in Box4 at $z = 0$

Since Magneticum Box4 (uhr) was only run to $z = 0.06$, which corresponds to a lookback time of 0.88 Gyr, the stars are in fact younger than they would be at $z = 0$. While there would certainly be more stars that formed during this time span, we reran PICS for all Box4 galaxies assuming stellar ages increased by 0.88 Gyr to approximate the present-day PN populations. Their resulting PNLF bright-end cutoff magnitudes as a function of stellar mass are shown in Figure E.2 for elliptical and disk galaxies for direct comparison with Figure 11.4. The dip toward dimmer bright-end cutoffs around $10^{10}\,M_\odot$ becomes even deeper by around 0.2 mag as a result of the older stellar populations, where the maximum [O III] brightness becomes noticeably dimmer (Figure 11.2). While young PNe are missing entirely, many old elliptical galaxies will likely not have formed further stars during the last billion years, thereby leaving

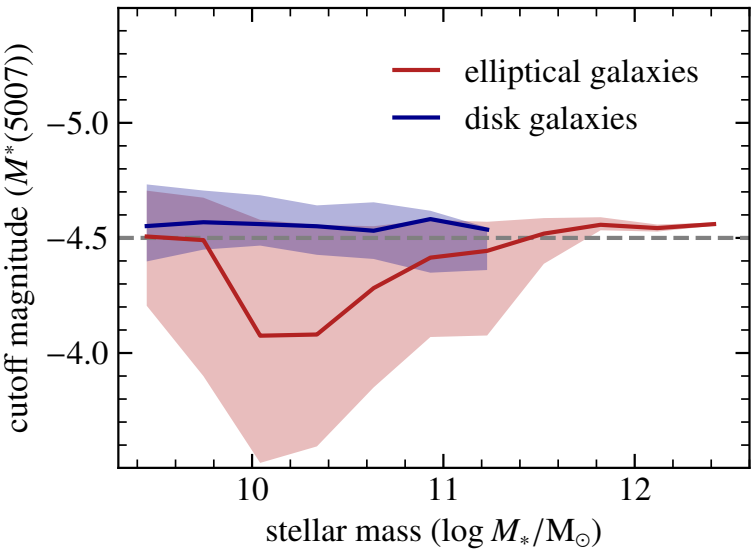


Figure E.2: Bright-end cutoff magnitude $M^*(5007)$ for stellar populations extrapolated to $z = 0$ by increasing the stellar ages by 0.88 Gyr, as a function of stellar mass for the simulated galaxies of the Magneticum Pathfinder Box4 (uhr) simulation, split by morphological type into disk (blue) and elliptical (red) galaxies. The solid lines show the respective median $M^*(5007)$ value, with the shaded regions indicating the 1σ scatter. The observed bright-end cutoff value of $M^*(5007) = -4.5$ is marked by the horizontal dashed line. The older stellar ages increase the magnitude dip at $10^{10}\,\mathrm{M}_\odot$ compared to Figure 11.4.

their PN populations and bright-end cutoff magnitudes unchanged. The importance of the stellar ages produced by the simulation is therefore high and affects the extent to which the bright-end cutoff is truly universal, which also motivates the inclusion of IllustrisTNG, a second simulation with different galaxy physics.

E.3 Stellar populations and bright-end cutoff in TNG50

As a second simulation, we also used the hydrodynamical cosmological simulation TNG50 at the highest available resolution (TNG50-1) (Nelson et al. 2019). It was run with the moving-mesh code Arepo (Springel 2010) and has a box side length of 52 Mpc, and a stellar particle mass of $8.5 \times 10^4\,\mathrm{M}_\odot$. The galaxies were identified with SubFind, just as for Magneticum. We selected all central and satellite galaxies from the last simulation snapshot at $z = 0$ with stellar masses of $M_* \geq 2 \times 10^9\,\mathrm{M}_\odot$, just as for Magneticum Box4. We computed all properties using the same methodology as for the other simulation. This results in a galaxy sample of 405 elliptical, 465 lenticular, and 1334 disk galaxies.

The stellar populations in TNG50 differ from those of Magneticum Box4: Figure E.3 shows significantly younger stellar populations across all masses compared to Box4 (seen in Figure 11.3), especially below $M_* = 10^{10}\,\mathrm{M}_\odot$. Additionally, the metallicities are higher in TNG50 for all stellar masses. This is due to the differences in the employed galaxy formation models including the stellar and active galactic nuclei (AGN) feedback prescriptions. The elliptical galaxies feature higher metallicities at the low-mass end compared to the more massive galaxies (dashed red line), which is the result of satellite galaxies having been enriched

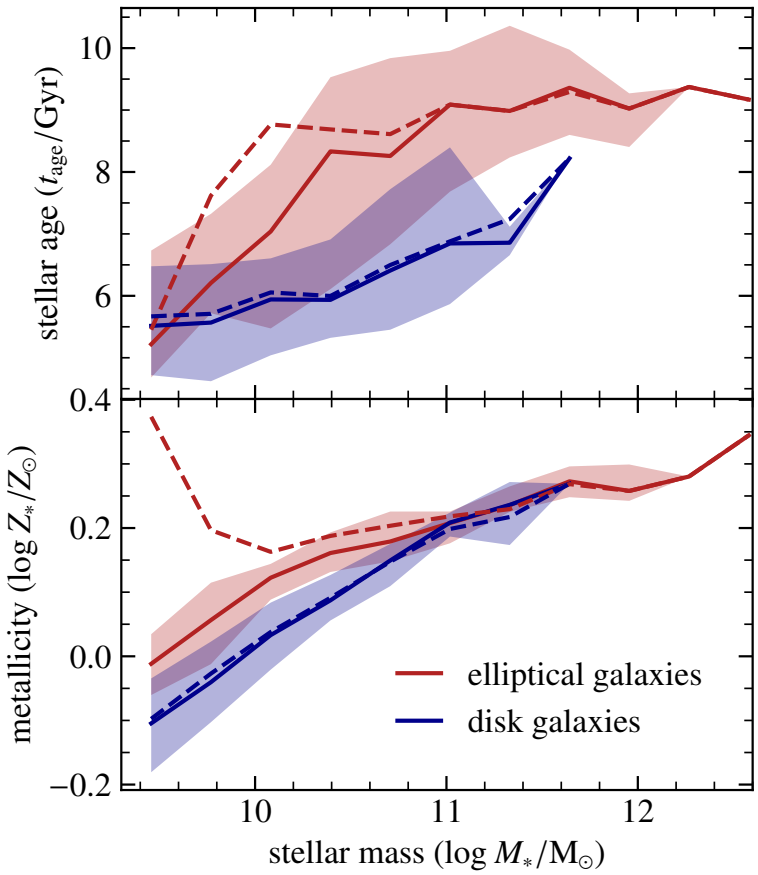


Figure E.3: Mass-weighted mean stellar age t_{age} (top) and metallicity Z_* (bottom) as functions of stellar mass for the simulated galaxies of the TNG50 simulation, split by morphological type into disk (blue) and elliptical (red) galaxies. The solid lines show the respective median age or metallicity value for the central galaxies only, with the shaded regions indicating the 1σ scatter. The dashed lines show the median values for the total galaxy sample including satellites, which have been significantly enriched with metals by their host galaxies, particularly seen by the metallicity rise at the low-mass end.

by their host galaxies. The large fraction of satellite galaxies at those lower masses dominates the scaling relation, such that we here also plot the relations for the central galaxy sample (solid lines), which recovers the expected mass-metallicity relation.

We show the TNG50 equivalent to Figure 11.4 of Magneticum Box4 with the PNLF bright-end cutoff $M^*(5007)$ as a function of stellar mass in Figure E.4. The universality of the PNLF cutoff across morphology and mass is even clearer here than in Box4, varying only by at most 0.1 mag, with disk galaxies having slightly brighter cutoffs than elliptical galaxies. The cutoff value at lower masses is brighter for TNG50 compared to Box4, which is a consequence of the TNG50 galaxies being systematically younger and more metal-rich than those in Box4 (Figure E.3). Still, while the stellar populations within TNG50 vary significantly between the two morphologies and across stellar masses, only the scatter of $M^*(5007)$ differs: it increases toward the low-mass end, and it is larger for elliptical compared to disk galaxies. The current theoretical state is therefore that the universal bright-end cutoff of the PNLF is robust against stellar population variations as long as the overall stellar age is not too old. Future improvements to the model such as through blue stragglers or variations of the IFMR

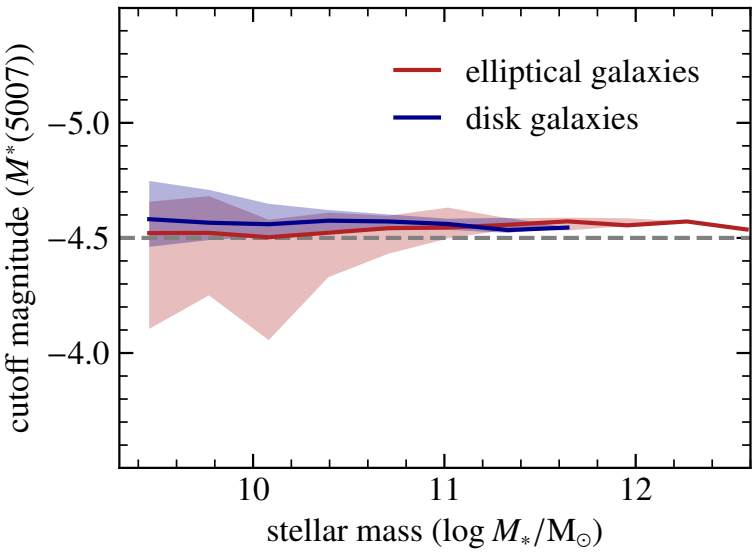


Figure E.4: Bright-end cutoff magnitude $M^*(5007)$ as a function of stellar mass for the simulated galaxies of TNG50, split by morphological type into disk (blue) and elliptical (red) galaxies. The solid lines show the respective median $M^*(5007)$ value, with the shaded regions indicating the 1σ scatter. The observed bright-end cutoff value of $M^*(5007) = -4.5$ is marked by the horizontal dashed line. Galaxies of both morphologies feature PNLF cutoffs around the observed value over a large range of stellar masses.

(e.g., Jacoby & Ciardullo 2025) could improve this for obtaining bright PNe even in old stellar populations.

F

PNLFs of Simulated Galaxy Classes

This is the appendix of the work to be submitted by Valenzuela et al. (in prep.), presented in Chapter 12.

F.1 Maximum likelihood estimation of the PNLF

The maximum likelihood estimation method includes summing over the individual probabilities $p(M)$ of a PN existing at its magnitude M given a specific PNLF function (see Section 12.1.2). These probabilities are determined through the integral over the PNLF multiplied with a Gaussian at the PN magnitude with a standard deviation of the magnitude uncertainty (Scheuermann et al. 2022), for which we use a fixed value of 0.01 mag:

$$p(M) = \int N(M')\phi(M', M, \sigma)\,\mathrm{d}M', \tag{F.1}$$

where $N(M')$ is the PNLF (Equation 7.2) and $\phi(M', M, \sigma)$ is the Gaussian function with mean M and standard deviation σ, evaluated at M':

$$\phi(M', M, \sigma) = \frac{1}{\sqrt{2\pi}\sigma} \exp\Big(-\frac{(M'-M)^2}{2\sigma^2}\Big). \tag{F.2}$$

The indefinite integral is solved with the error function:

$$\int N\phi\,\mathrm{d}M' = \frac{c_1}{2}\Big(e^{AM+A^2\sigma^2/2+3M^*}\,\mathrm{erf}\left(B(A\sigma^2+M-M')\right) \tag{F.3}$$

$$- e^{c_2 M + c_2^2 \sigma^2/2} \operatorname{erf}\left(B(c_2\sigma^2 + M - M')\right)\Big), \tag{F.4}$$

with $A = c_2 - 3$ and $B = 1/(\sqrt{2}\sigma)$. The definite integral from $M' = -\infty$ to $+\infty$ eliminates the error function terms because of the limits at $\pm\infty$ equaling ± 1. The resulting probability then becomes

$$p(M) = c_1\Big(e^{c_2 M + c_2^2 \sigma^2/2} - e^{AM + A^2\sigma^2/2 + 3M^*}\Big). \tag{F.5}$$

In practice, the analytical computation led to a speed-up of over two orders of magnitude compared to the numerical integration.

F.2 Corrected ages in Magneticum Box4 (uhr) for $z = 0$

Since Magneticum Box4 (uhr) was only run to $z = 0.066$, the stellar ages should be systematically older as that corresponds to a lookback time of $t_{\rm lb} \approx 880\,$Myr. In Section 12.2, we do not correct for this age difference since that would mean that the galaxy properties would not be self-consistent with the PN populations anymore, and stars that would theoretically form in that time span would not be accounted for. Figure F.1 shows the same grid of median PNLFs for the different classes for Box4 as Figure 12.1, but with all stellar ages increased by 880 Myr to account for the missing time span until $z = 0$. The main difference to the unmodified-age results is that the PNLFs shift slightly toward fainter magnitudes, which is especially noticeable for the elliptical, quiescent, slow rotator, old, and metal-rich galaxies. These correspond to the galaxies that are most likely to have old stellar populations, where the increased age leads to fainter PNLFs for the PICS model (see Valenzuela et al. 2025c).

F.3 Central galaxies in Magneticum Box4 (uhr)

In Section 12.2, we only show the PNLFs and $M^*(5007)$ values for the total population of galaxies. Figure F.2 shows the same grid of median PNLFs for the different classes for Box4 as Figure 12.5, but only for the central galaxies (i.e., without the satellite galaxies) Compared to the total galaxy sample, a clear difference is that the dip of $M^*(5007)$ toward fainter magnitudes at around $\log M_*/\mathrm{M}_\odot \sim 10.4$ seen for the elliptical galaxies is more shallow. This is a result of lower-mass old galaxies having overall brighter cutoff magnitudes, but also of the relatively smaller number of old central galaxies compared to the total sample (see Table 12.1. The other cutoff magnitudes remain very similar to the results for the total Box4 galaxy sample seen in Figure 12.5.

F.4 PNLF bright-end cutoff magnitudes in TNG50

Figure F.3 shows the bright-end cutoff magnitude of the PNLF $M^*(5007)$ as a function of stellar mass for the different classes and classification schemes for TNG50 in the same way as for Magneticum Box4 in Figure 12.5. Besides a slightly increased brightness of the

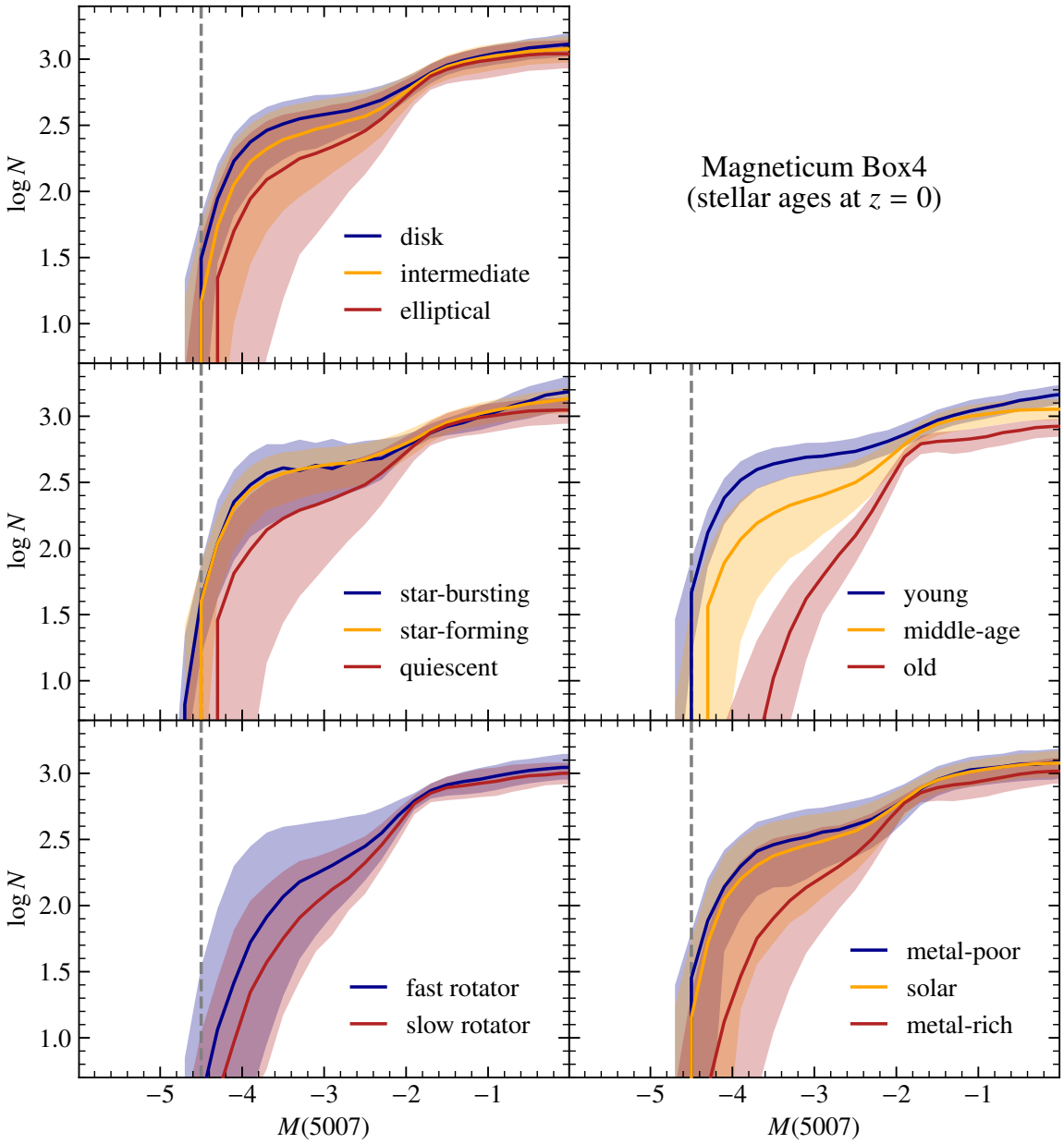


Figure F.1: Median PNLFs of galaxy classes from the different classification schemes for Magneticum Box4 (uhr) as in Figure 12.1, but with the PNe modeled with stellar ages increased by 880 Myr to modify the ages to the ones they would have at $z = 0$.

cutoffs compared to Box4 (at $M^*(5007) \approx -4.55$ mag), the central finding is that $M^*(5007)$ is significantly more constant across all classes except for the old galaxies, and it also has a much smaller scatter. Only the old galaxies show the same correlation of $M^*(5007)$ with stellar mass as Box4 featured, and for the same reasons: mass-metallicity relation, increased intermediate-age stellar mass fraction, and higher probability of populating the bright end of the PNLF with more stars.

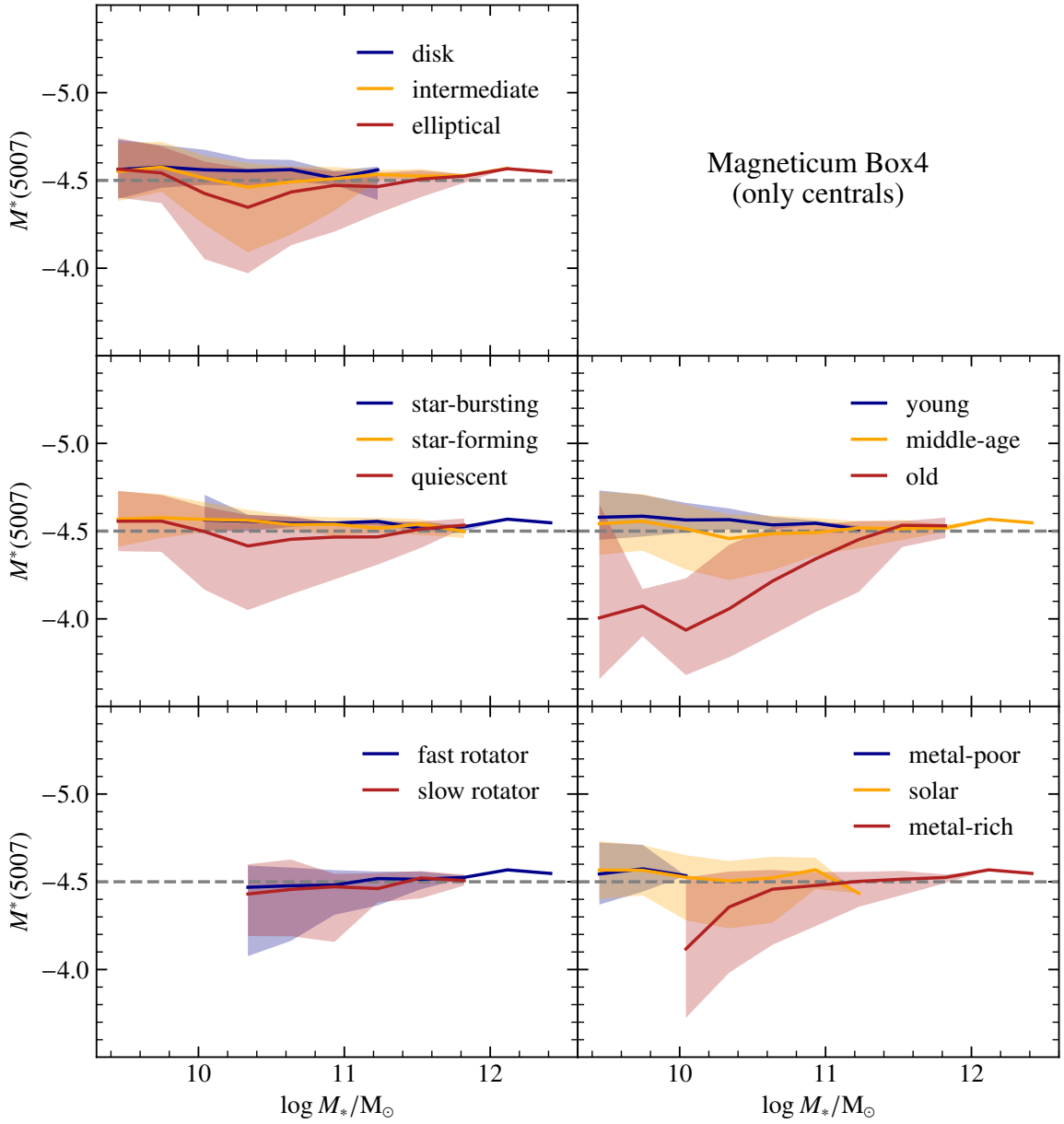


Figure F.2: Median PNLF bright-end cutoff magnitudes $M^*(5007)$ as a function of stellar mass M_* from the different classification schemes in Magneticum Box4 (uhr) as in Figure 12.5, but only for the central galaxies.

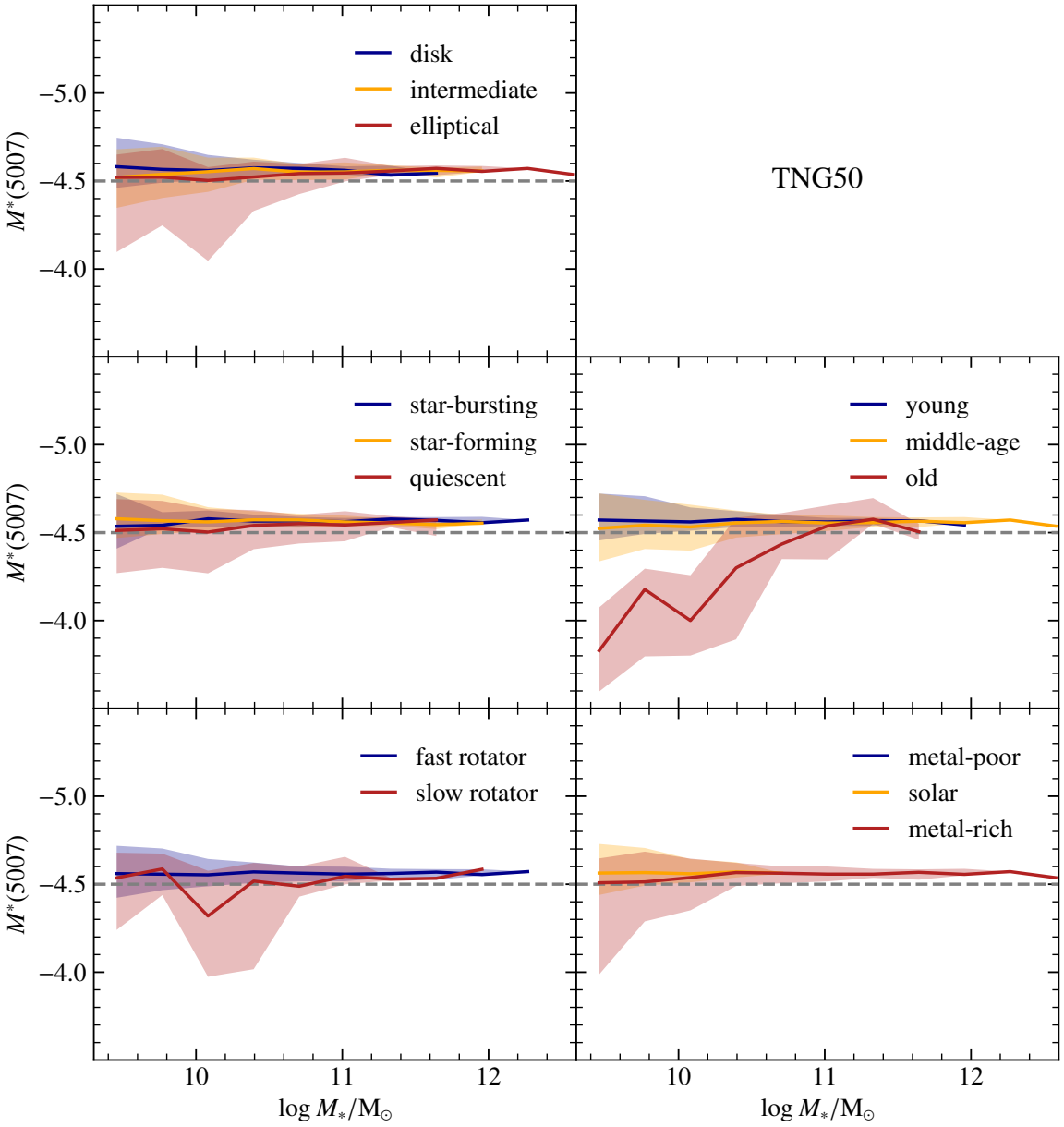


Figure F.3: Median PNLF bright-end cutoff magnitudes $M^*(5007)$ as a function of stellar mass M_* from the different classification schemes as in Figure 12.5, but for the galaxies in TNG50.

G

The Milky Way GC Age Distribution

This is the appendix of the publication by Valenzuela et al. (2024b), A&A 687, A104, presented in Chapter 17.

G.1 Milky Way globular cluster age distributions

G.1.1 Age distributions of all globular clusters

The age distributions of the full GC samples of Forbes & Bridges (2010), Dotter et al. (2010, 2011), VandenBerg et al. (2013), Kruijssen et al. (2019b), Usher et al. (2019), and Cabrera-Ziri & Conroy (2022) are shown in Figure G.1. The values from Kruijssen et al. (2019b) are obtained through the mean ages from the first three samples, all of which used CMD measurements, which leads to the total distribution being further smoothed out. Since not all of the CMD samples contain all 96 GCs from that study, the mean ages of the individual GCs will be biased towards younger or older ages depending on which samples they are contained in due to differences in the systematic uncertainties between the samples.

Nevertheless, the bimodality in the GSE GC age distribution is still clearly visible (Figure G.2), if not even clearer than in the top left panel of Figure 17.3 for the ages from Forbes & Bridges (2010). This strongly indicates that the found bimodality is an actual feature and not a statistical artifact.

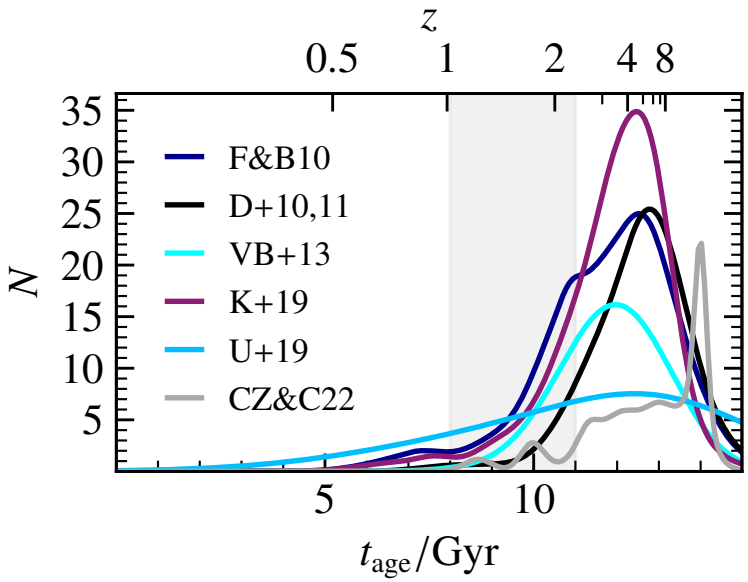


Figure G.1: Globular cluster age distributions in the MW from Forbes & Bridges (2010), Dotter et al. (2010, 2011), VandenBerg et al. (2013), Kruijssen et al. (2019b), Usher et al. (2019), and Cabrera-Ziri & Conroy (2022), smoothed by the measurement uncertainties. The curves are computed through a summation over normal distributions with the respective ages as the means and their uncertainties as the standard deviations. The shaded region between 8 Gyr and 11 Gyr indicates the estimated time of the GSE merger (Belokurov et al. 2018; Helmi et al. 2018).

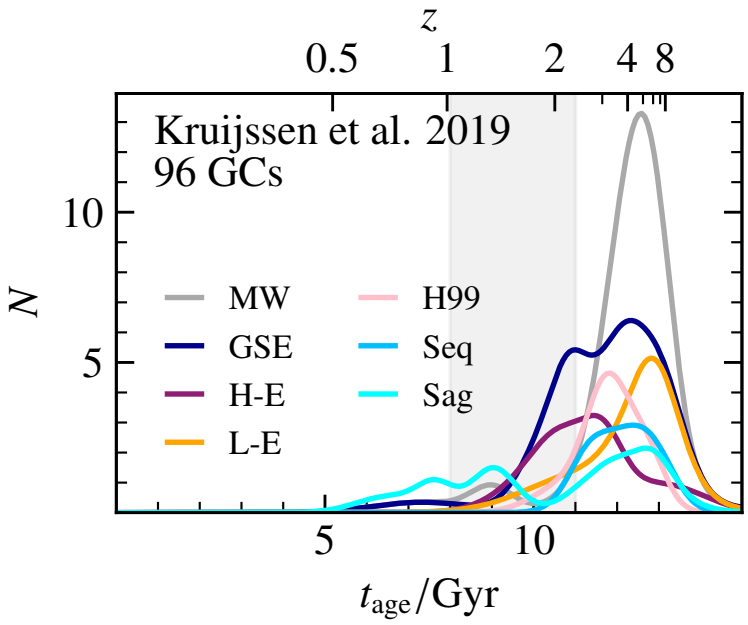


Figure G.2: Globular cluster age distributions in the MW from Kruijssen et al. (2019b), split up according to their likely progenitors from Forbes (2020). The shown classifications are the MW, GSE, unassociated high-energy GCs (H-E), unassociated low-energy GCs (L-E, which was given the name Koala by Forbes 2020), the Helmi Streams (H99), Sequoia (Seq), and Sagittarius (Sag). The curves are smoothed by the measurement uncertainties, which are computed through a summation over normal distributions with the respective ages as the means and their uncertainties as the standard deviations. The shaded region between 8 Gyr and 11 Gyr indicates the estimated time of the GSE merger (Belokurov et al. 2018; Helmi et al. 2018).

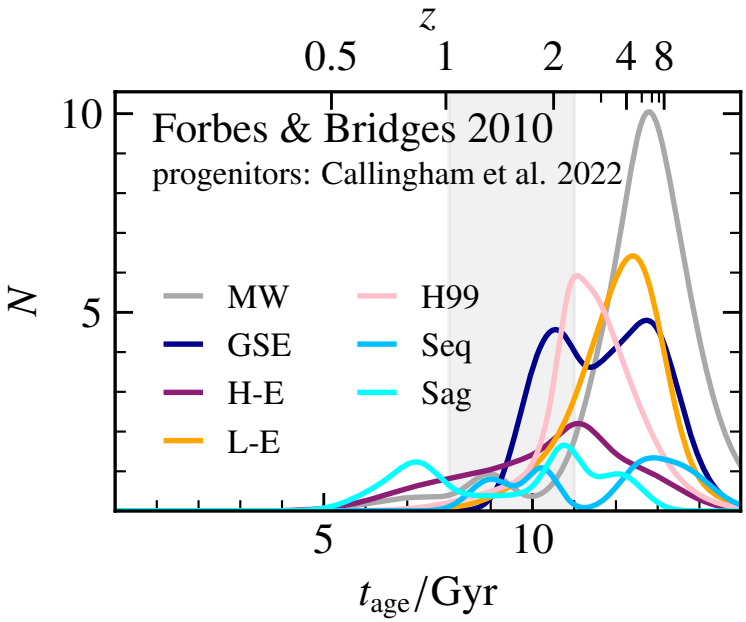


Figure G.3: Globular cluster age distributions in the MW from Forbes & Bridges (2010), split up according to their likely progenitors from Callingham et al. (2022). The shown classifications are the MW, GSE, unassociated high-energy GCs (H-E), unassociated low-energy GCs (L-E, which was given the name Koala by Forbes 2020), the Helmi Streams (H99), Sequoia (Seq), and Sagittarius (Sag). The shaded region between 8 Gyr and 11 Gyr indicates the estimated time of the GSE merger (Belokurov et al. 2018; Helmi et al. 2018).

G.1.2 Alternative progenitor associations

While we used the GC progenitor associations from Forbes (2020) in this work, it makes no qualitative difference to use the associations determined by other studies. For instance, the data from Callingham et al. (2022) show a somewhat different distribution of GCs among GSE, the Helmi Streams, and the low-energy GCs, but the GC age distributions of GSE still features a bimodal distribution (Figure G.3). This bimodality is visible in a much more distinct way when compared with the top left panel of Figure 17.3, which shows the distributions for the GC associations determined by Forbes (2020). Similarly, when using the associations from Chen & Gnedin (2024a), Figure G.4 shows that the age distributions change for GSE and Sagittarius (the only two ex-situ groups they specifically identify), but again the bimodality of the GSE-associated GCs persists. This time, the younger peak at 11 Gyr is significantly stronger than the ones seen from the associations of Forbes (2020) and Callingham et al. (2022), which would mean that potentially more GCs were formed through the GSE merger.

G.1.3 Age distributions of a single study

The GC sample of Forbes & Bridges (2010) is composed of multiple different studies (see Section 17.1.2), of which the largest subsample is of Marín-Franch et al. (2009), which includes 64 of the 92 GCs. As combining several GC studies could cause problems due to different systematic biases, we show the single GC study by Marín-Franch et al. (2009) in

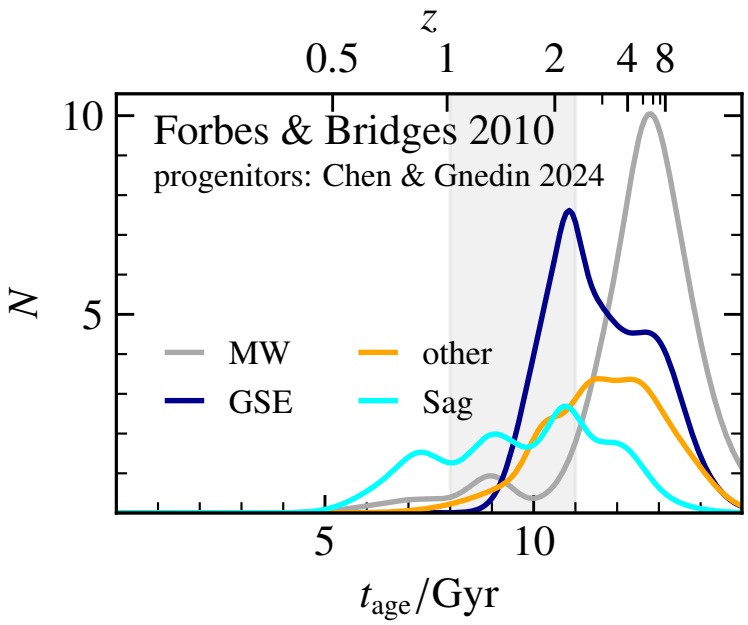


Figure G.4: Globular cluster age distributions in the MW from Forbes & Bridges (2010), split up according to their likely progenitors from Chen & Gnedin (2024a). The shown classifications are the MW, GSE, Sagittarius (Sag), and other ex-situ formed GCs (other). The shaded region between 8 Gyr and 11 Gyr indicates the estimated time of the GSE merger (Belokurov et al. 2018; Helmi et al. 2018).

Figure G.5. Both the bimodality of the overall GC age distribution as well as in the GSE GC age distribution are clearly visible. This demonstrates that these bimodalities do not result from combining several GC studies, but in fact come from a single study.

G.1.4 Age histograms

The unsmoothed age distribution of the MW are shown in Figure G.6 for the four GC samples by Forbes & Bridges (2010), Dotter et al. (2010, 2011), VandenBerg et al. (2013), and Cabrera-Ziri & Conroy (2022), using the progenitor associations given by Forbes (2020). It becomes apparent that GSE, the unassociated high-energy GCs, and the GCs from the Helmi Streams are important contributors to the second peak in the total GC age distribution. The smoothed distributions according to the measured age uncertainties are found in Figure 17.3.

G.2 Other Milky Way-mass modeled globular cluster age distributions

As we found 21 MW-mass galaxies in the simulation with virial masses of M_{vir} = 1–$2 \times 10^{12}\,M_{vir}$, but only discussed the two of them with GC age distributions most similar to those observed in the MW (see Section 17.2.2), we here present the other 19 simulated galaxies. Figure G.7 shows their GC age distributions (top of each of the four double panels) and their respective virial mass evolutions in the same color (bottom of the double panels). From the top left to the bottom right, the galaxies are sorted by their formation time, that

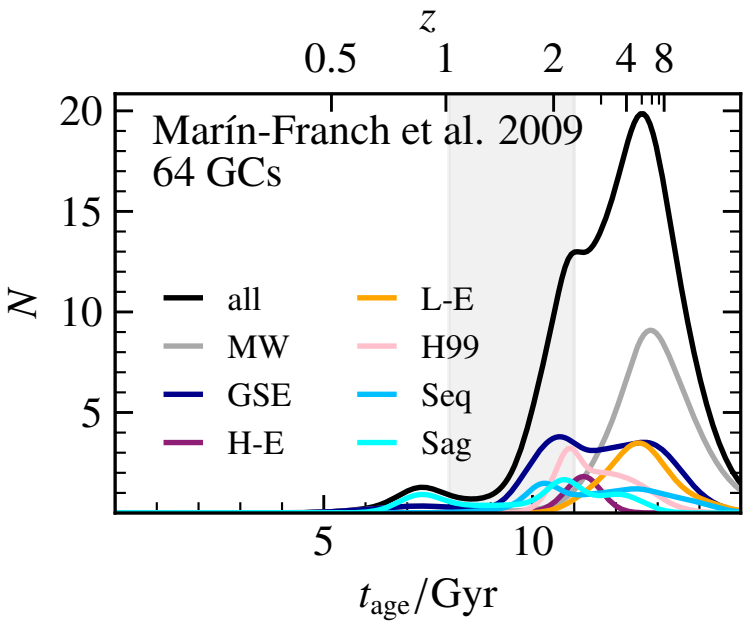


Figure G.5: Globular cluster age distributions in the MW from Marín-Franch et al. (2009), split up according to their likely progenitors from Forbes (2020). The shown classifications are the MW, GSE, unassociated high-energy GCs (H-E), unassociated low-energy GCs (L-E, which was given the name Koala by Forbes 2020), the Helmi Streams (H99), Sequoia (Seq), and Sagittarius (Sag). The curves are smoothed by the measurement uncertainties, which are computed through a summation over normal distributions with the respective ages as the means and their uncertainties as the standard deviations. The shaded region between 8 Gyr and 11 Gyr indicates the estimated time of the GSE merger (Belokurov et al. 2018; Helmi et al. 2018).

is at what time the galaxy reached half of the virial mass that it has at $z = 0$, where the galaxies formed the earliest are shown at the top left. It can immediately be seen that the galaxies formed the earliest also have the oldest GC populations, whereas the later-formed galaxies have increasingly young GC subpopulations. The time of the youngest GC formation peak is furthermore strongly correlated with the formation time as seen in Figure G.8. From the MW-analog, we also obtain a prediction for the formation of the MW itself of around 9–10 Gyr, which corresponds to $z = 1.3$–1.7. Overall, the ages of the youngest GCs also directly mark the time of the last major wet accretion event, as expected from the GC model.

Overall, the oldest GC population is almost always the dominant one (with the exception of the double-peaked age distributions in the upper left panel shown in pink and in the upper right panel shown in blue). In these two cases, there are nearly as many of the oldest GCs as the second youngest peak in the age distribution contains.

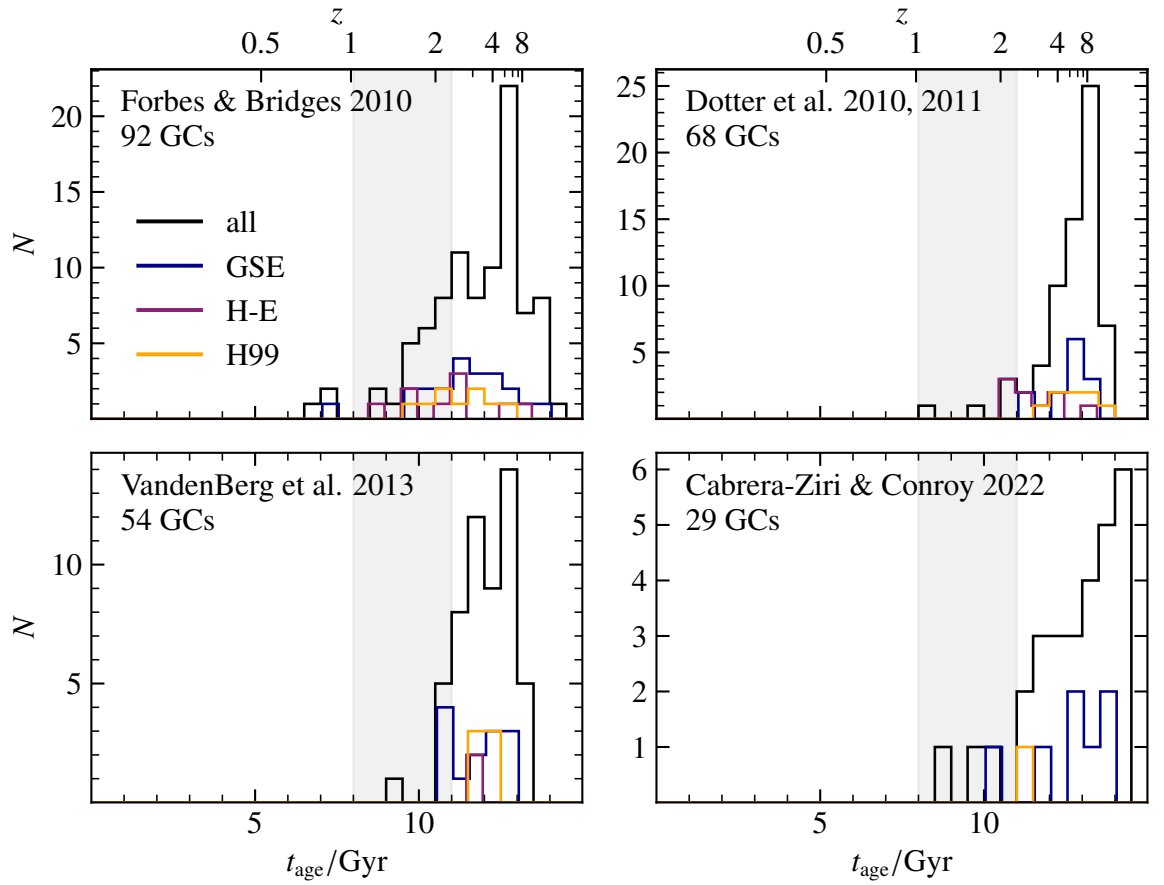


Figure G.6: Globular cluster age distributions in the MW from Forbes & Bridges (2010), Dotter et al. (2010, 2011), VandenBerg et al. (2013), and Cabrera-Ziri & Conroy (2022), split up according to their likely progenitors from Forbes (2020). The shown classifications are the total population (all), GSE, the unassociated high-energy GCs (H-E), and the Helmi Streams (H99). The total number of GCs in the respective sample is indicated in the top left. The shaded region between 8 Gyr and 11 Gyr indicates the estimated time of the GSE merger (Belokurov et al. 2018; Helmi et al. 2018). See Figure 17.3 for the corresponding age distributions smoothing the data points through their uncertainties.

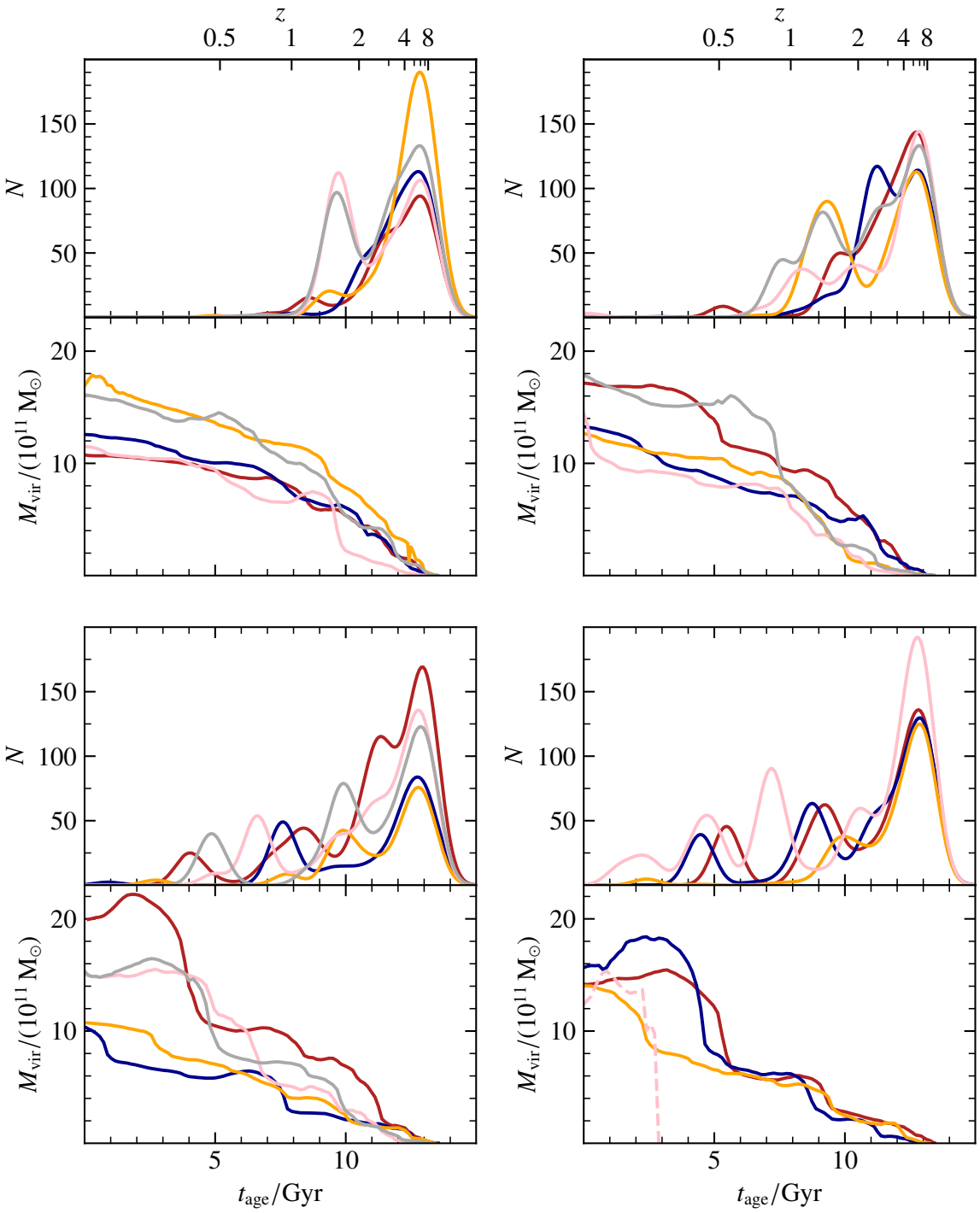


Figure G.7: Age distributions of the globular clusters in 19 simulated MW-mass galaxies and their virial mass evolutions plotted below the respective age distributions in the same colors for each galaxy. The distributions are smoothed using an assumed uncertainty of 0.5 Gyr for the GC ages. The galaxies shown in the top left panels are the galaxies that reached half of their $z = 0$ virial mass at the earliest time, followed by the galaxies in the top right panel. The galaxies in the bottom right panel are those that reach half of the current virial mass the latest. The galaxy with the dashed virial mass evolution line has an issue with the merger tree, but the GC population is correct.

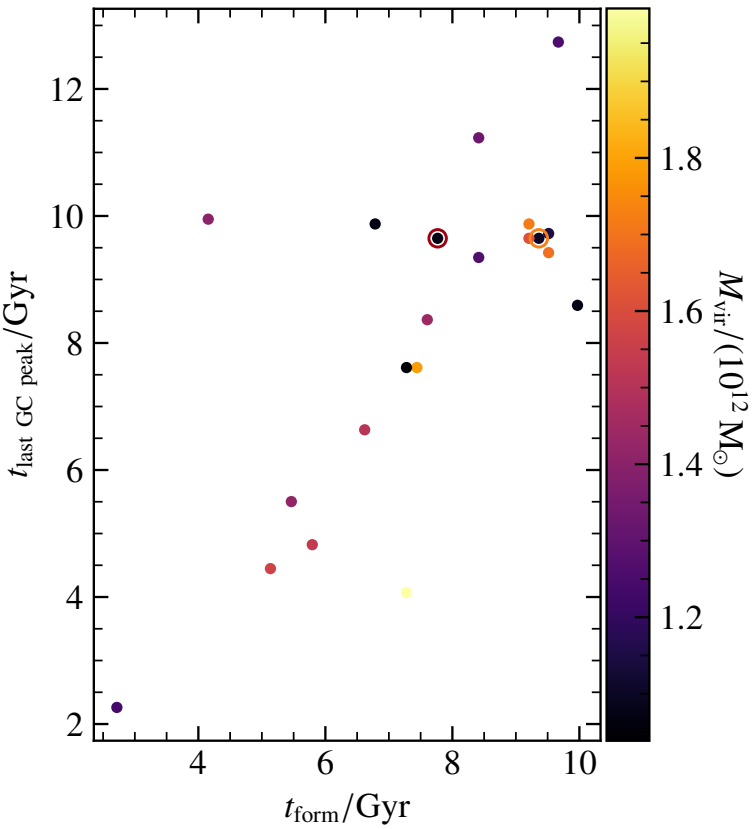


Figure G.8: Correlation between the age of the youngest GC peak in their age distribution ($t_{\text{last GC peak}}$) and the formation time of the MW-mass simulated galaxies (t_{form}), colored by the virial mass at $z = 0$. The youngest peak is required to have an absolute value above 10. The formation time of a galaxy is taken as the lookback time at which the galaxy has reached half of its virial mass at $z = 0$. The MW-analog and non-MW-analog from Figure 17.2 are additionally circled in orange and red, respectively.



H GC Model Age Comparisons

This is the appendix of the publication by Valenzuela et al. (2025a), MNRAS 537, 306, presented in Chapter 18.

H.1 Globular cluster formation time distributions of other models

As the GC seeding times from the model by Doppel et al. (2023) are not physical formation times due to the GCs being seeded at the time of infall of satellite galaxies (see Section 18.1.8), we did not include these times in the main analysis of this work. For completion, we show the distribution of GC seeding times for the two TNG50 MW analogue galaxies for which the GC model was run in Figure H.1. This is effectively the model's prediction for the time of GC accretion. The seeding times are overall much later than the observed and modelled GC ages as seen in Figure 18.2. While some GCs appear to be accreted earlier than 10 Gyr ago, the majority of GCs have been accreted within the last ∼3 Gyr. This indicates that these MW analogues have had a different accretion history than our MW, as the majority of observed MW GCs have either been formed in-situ in the early formation of the Galaxy or were accreted with GSE around 8 Gyr–11 Gyr ago.

The question still arises in what way this model also includes in-situ formed GCs, as these would be expected either to be formed in-situ in the main progenitor branch of the merger tree and thus not ever be accreted, or to be formed in another galaxy and "accreted" at very

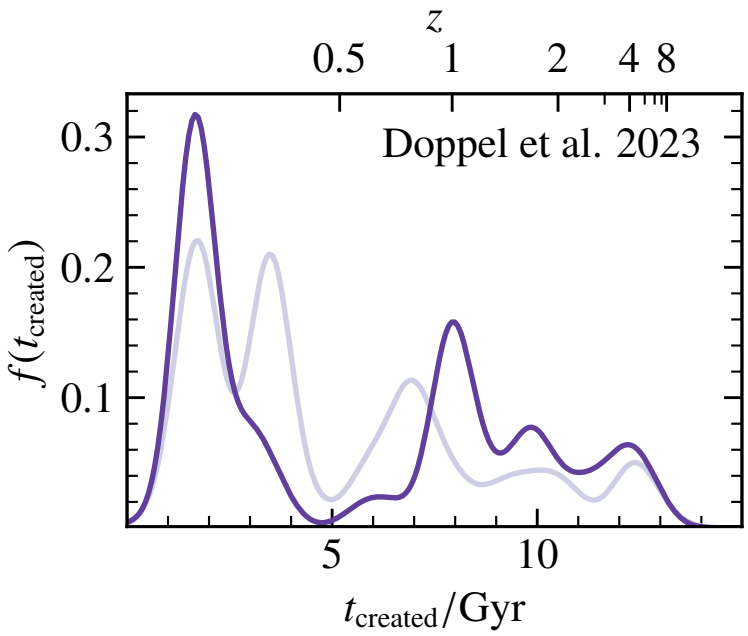


Figure H.1: Seeding time ($t_{\rm created}$) distributions of the modelled GCs in two simulated MW analogue galaxies in TNG50 from Doppel et al. (2023).

early times, thereby effectively belonging to the in-situ GC population. The overall lack of early accreted GCs indicates that either these galaxies have had much later accretion histories compared to the MW, leading to a very small early in-situ GC component, or that in-situ GCs are for the most part missing in the model.

H.2 Ages including young GCs

As some of the models like E-MOSAICS (Kruijssen et al. 2019a) and EMP-Pathfinder (Reina-Campos et al. 2022) include significant amounts of GCs younger than 5 Gyr, we show the full GC age distributions from Figure 18.2 with ages reaching until the present day in Figure H.2. The selected host galaxies are the same as those in Figure 18.2.

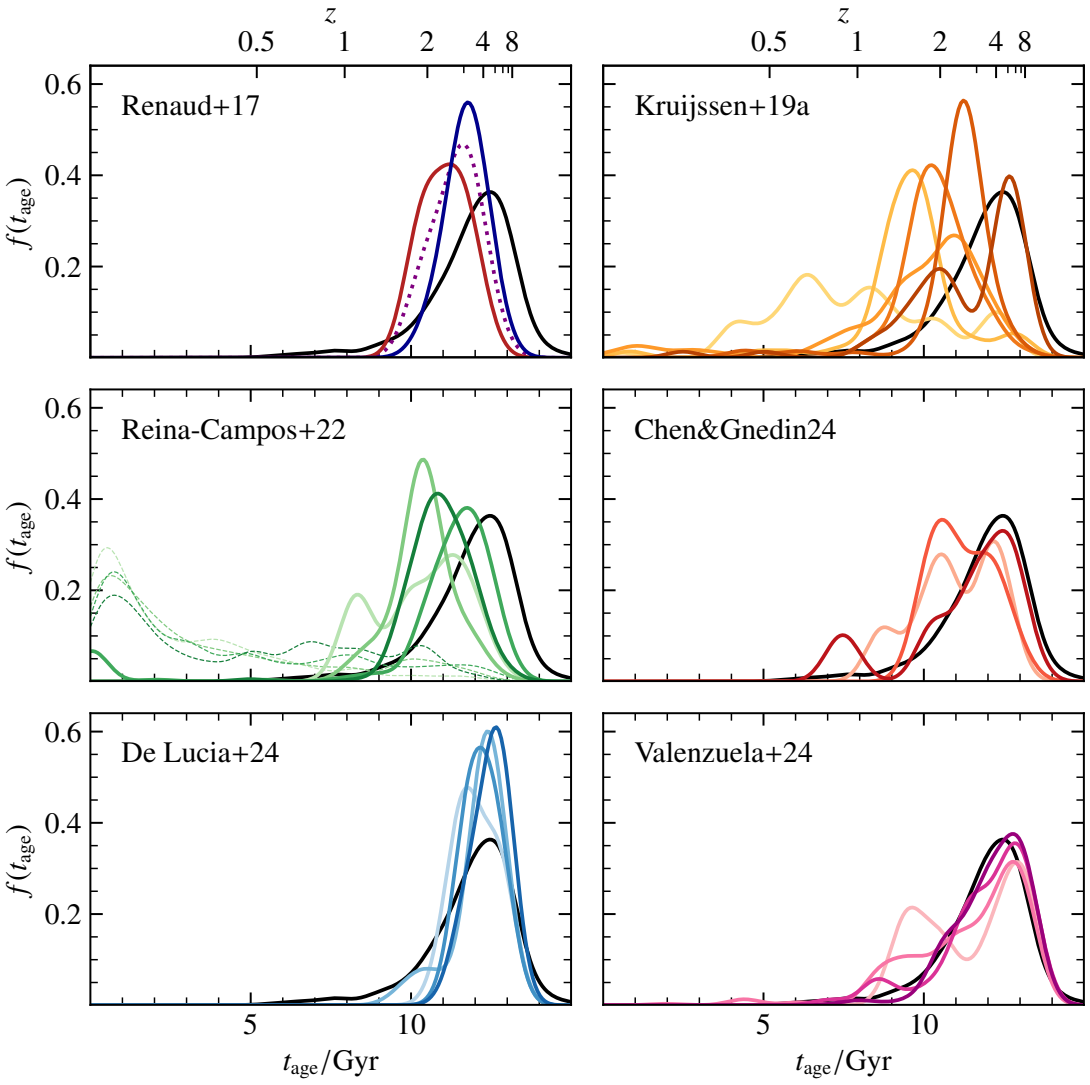
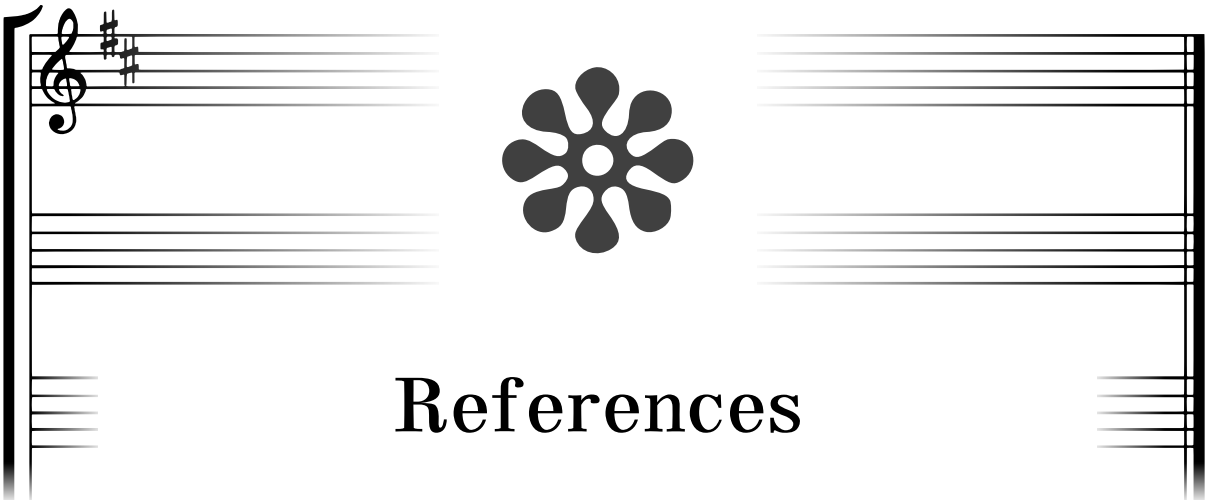


Figure H.2: Age distributions of modelled GCs in MW analogues compared to the observed GC ages in the MW. This plot shows the same GC age distributions as in Figure 18.2, but with ages extending to values of $t_{age} = 0$ Gyr. The dashed lines for EMP-Pathfinder correspond to the same galaxies as the solid distributions of equal colour, with the difference that no metallicity cut was applied to the GCs, which results in a large population of young stellar clusters.



References

Adamo A., Bradley L. D., Vanzella E., Claeyssens A., Welch B., Diego J. M., Mahler G., Oguri M., Sharon K., Abdurro'uf, et al.: *Bound Star Clusters Observed in a Lensed Galaxy 460 Myr after the Big Bang.* Nature **632**, 513 (2024)

Adams S. M., Zaritsky D., Sand D. J., Graham M. L., Bildfell C., Hoekstra H., & Pritchet C.: *The Environmental Dependence of the Incidence of Galactic Tidal Features.* AJ **144**, 128 (2012)

Aihara H., AlSayyad Y., Ando M., Armstrong R., Bosch J., Egami E., Furusawa H., Furusawa J., Goulding A., Harikane Y., et al.: *Second Data Release of the Hyper Suprime-Cam Subaru Strategic Program.* Publications of the Astronomical Society of Japan **71**, 114 (2019)

Alabi A. B., Forbes D. A., Romanowsky A. J., Brodie J. P., Strader J., Janz J., Usher C., Spitler L. R., Bellstedt S., & Ferré-Mateu A.: *The SLUGGS Survey: Dark Matter Fractions at Large Radii and Assembly Epochs of Early-Type Galaxies from Globular Cluster Kinematics.* MNRAS **468**, 3949 (2017)

Alcorn L. Y., Tran K.-V., Glazebrook K., Straatman C. M., Cowley M., Forrest B., Kacprzak G. G., Kewley L. J., Labbé I., Nanayakkara T., et al.: *ZFIRE: 3D Modeling of Rotation, Dispersion, and Angular Momentum of Star-forming Galaxies at $z \sim 2$.* ApJ **858**, 47 (2018)

Allgood B., Flores R. A., Primack J. R., Kravtsov A. V., Wechsler R. H., Faltenbacher A., & Bullock J. S.: *The Shape of Dark Matter Haloes: Dependence on Mass, Redshift, Radius and Formation.* MNRAS **367**, 1781 (2006)

Althaus L. G., Panei J. A., Romero A. D., Rohrmann R. D., Córsico A. H., García-Berro E., & Miller Bertolami M. M.: *Evolution and Colors of Helium-Core White Dwarf Stars with High-Metallicity Progenitors.* A&A **502**, 207 (2009)

Amorisco N. C.: *On Feathers, Bifurcations and Shells: The Dynamics of Tidal Streams across the Mass Scale.* MNRAS **450**, 575 (2015)

Amorisco N. C.: *Contributions to the accreted stellar halo: an atlas of stellar deposition.* MNRAS **464**, 2882 (2017)

Amorisco N. C.: *Globular Cluster Populations and the Kinematical Fingerprints of Minor Mergers.* MNRAS **482**, 2978 (2019)

Anand G. S., Tully R. B., Cohen Y., Makarov D. I., Makarova L. N., Jensen J. B., Blakeslee J. P., Cantiello M., Kourkchi E., & Raimondo G.: *The TRGB-SBF Project. I. A Tip of the Red Giant Branch Distance to the Fornax Cluster with JWST.* ApJ **973**, 83 (2024)

Anderson J., Sarajedini A., Bedin L. R., King I. R., Piotto G., Reid I. N., Siegel M., Majewski S. R., Paust N. E. Q., Aparicio A., et al.: *The ACS Survey of Globular Clusters. V. Generating a Comprehensive Star Catalog for Each Cluster.* AJ **135**, 2055 (2008)

Aniyan S., Freeman K. C., Arnaboldi M., Gerhard O. E., Coccato L., Fabricius M., Kuijken K., Merrifield M., & Ponomareva A. A.: *Resolving the Disc-Halo Degeneracy - I: A Look at NGC 628.* MNRAS **476**, 1909 (2018)

Aniyan S., Ponomareva A. A., Freeman K. C., Arnaboldi M., Gerhard O. E., Coccato L., Kuijken K., & Merrifield M.: *Resolving the Disc-Halo Degeneracy - II: NGC 6946.* MNRAS **500**, 3579 (2021)

Arnaboldi M., Freeman K. C., Hui X., Capaccioli M., & Ford H.: *The Kinematics of the Planetary Nebulae in the Outer Regions of NGC 1399.* The Messenger **76**, 40 (1994)

Arnaboldi M., Freeman K. C., Méndez R. H., Capaccioli M., Ciardullo R., Ford H., Gerhard O., Hui X., Jacoby G. H., Kudritzki R. P., & Quinn P. J.: *The Kinematics of the Planetary Nebulae in the Outer Regions of NGC 4406.* ApJ **472**, 145 (1996)

Arnaboldi M., Freeman K. C., Gerhard O., Matthias M., Kudritzki R. P., Méndez R. H., Capaccioli M., & Ford H.: *The Stellar Dynamics and Mass of NGC 1316 Using the Radial Velocities of Planetary Nebulae.* ApJ **507**, 759 (1998)

Arnaboldi M., Aguerri J. A. L., Napolitano N. R., Gerhard O., Freeman K. C., Feldmeier J., Capaccioli M., Kudritzki R. P., & Méndez R. H.: *Intracluster Planetary Nebulae in Virgo: Photometric Selection, Spectroscopic Validation, and Cluster Depth.* AJ **123**, 760 (2002)

Arnaboldi M., Gerhard O., Aguerri J. A. L., Freeman K. C., Napolitano N. R., Okamura S., & Yasuda N.: *The Line-of-Sight Velocity Distributions of Intracluster Planetary Nebulae in the Virgo Cluster Core.* ApJ **614**, L33 (2004)

Arnold J. A., Romanowsky A. J., Brodie J. P., Chomiuk L., Spitler L. R., Strader J., Benson A. J., & Forbes D. A.: *The Fossil Record of Two-Phase Galaxy Assembly: Kinematics and Metallicities in the Nearest S0 Galaxy.* ApJ **736**, L26 (2011)

Asada Y., Sawicki M., Abraham R., Bradač M., Brammer G., Desprez G., Estrada-Carpenter V., Iyer K., Martis N., Matharu J., et al.: *Bursty Star Formation and Galaxy-Galaxy Interactions in Low-Mass Galaxies 1 Gyr after the Big Bang.* MNRAS **527**, 11372 (2024)

Ashman K. M. & Zepf S. E.: *The Formation of Globular Clusters in Merging and Interacting Galaxies.* ApJ **384**, 50 (1992)

Asplund M., Grevesse N., Sauval A. J., & Scott P.: *The Chemical Composition of the Sun.* ARA&A **47**, 481 (2009)

Asplund M., Amarsi A. M., & Grevesse N.: *The Chemical Make-up of the Sun: A 2020 Vision.* A&A **653**, A141 (2021)

Athanassoula E.: *On the Nature of Bulges in General and of Box/Peanut Bulges in Particular: Input from N-body Simulations.* MNRAS **358**, 1477 (2005)

Atkinson A. M., Abraham R. G., & Ferguson A. M. N.: *Faint Tidal Features in Galaxies within the Canada-France-Hawaii Telescope Legacy Survey Wide Fields.* ApJ **765**, 28 (2013)

Bacon R., Accardo M., Adjali L., Anwand H., Bauer S., Biswas I., Blaizot J., Boudon D., Brau-Nogue S., Brinchmann J., et al.: *The MUSE Second-Generation VLT Instrument.* In: *Ground-Based and Airborne Instrumentation for Astronomy III.* Society of Photo-Optical Instrumentation Engineers (SPIE) Conference Series **7735**, 773508 (2010)

Baes M., Verstappen J., De Looze I., Fritz J., Saftly W., Vidal Pérez E., Stalevski M., & Valcke S.: *Efficient Three-dimensional NLTE Dust Radiative Transfer with SKIRT.* ApJS **196**, 22 (2011)

Bailin J. & Steinmetz M.: *Internal and External Alignment of the Shapes and Angular Momenta of ΛCDM Halos.* ApJ **627**, 647 (2005)

Balick B., Kwitter K. B., Corradi R. L. M., & Henry R. B. C.: *Metal-Rich Planetary Nebulae in the Outer Reaches of M31.* ApJ **774**, 3 (2013)

Barnes K. L., van Zee L., Dale D. A., Staudaher S., Bullock J. S., Calzetti D., Chandar R., & Dalcanton J. J.: *New Insights on the Formation and Assembly of M83 from Deep Near-infrared Imaging.* ApJ **789**, 126 (2014)

Bastian N. & Lardo C.: *Multiple Stellar Populations in Globular Clusters.* ARA&A **56**, 83 (2018)

Baumgardt H. & Hilker M.: *A Catalogue of Masses, Structural Parameters, and Velocity Dispersion Profiles of 112 Milky Way Globular Clusters.* MNRAS **478**, 1520 (2018)

Baumgardt H., Hilker M., Sollima A., & Bellini A.: *Mean Proper Motions, Space Orbits, and Velocity Dispersion Profiles of Galactic Globular Clusters Derived from Gaia DR2 Data.* MNRAS **482**, 5138 (2019)

Beasley M. A., Baugh C. M., Forbes D. A., Sharples R. M., & Frenk C. S.: *On the Formation of Globular Cluster Systems in a Hierarchical Universe.* MNRAS **333**, 383 (2002a)

Beasley M. A., Hoyle F., & Sharples R. M.: *Testing Stellar Population Models with Star Clusters in the Large Magellanic Cloud.* MNRAS **336**, 168 (2002b)

Beasley M. A., Brodie J. P., Strader J., Forbes D. A., Proctor R. N., Barmby P., & Huchra J. P.: *The Chemical Properties of Milky Way and M31 Globular Clusters. II. Stellar Population Model Predictions.* AJ **129**, 1412 (2005)

Bedin L. R., Piotto G., Anderson J., Cassisi S., King I. R., Momany Y., & Carraro G.: *ω Centauri: The Population Puzzle Goes Deeper.* ApJ **605**, L125 (2004)

Behroozi P. S., Wechsler R. H., & Conroy C.: *The Average Star Formation Histories of Galaxies in Dark Matter Halos from $z = 0$-8.* ApJ **770**, 57 (2013)

Bekki K., Beasley M. A., Brodie J. P., & Forbes D. A.: *Kinematics of Globular Cluster Systems and the Formation of Early-Type Galaxies.* MNRAS **363**, 1211 (2005)

Bekki K.: *Primordial Pollution of Globular Clusters within Their Host Dwarfs Embedded in Dark Matter Haloes at High Redshifts.* MNRAS **367**, L24 (2006)

Bell E. F., Wolf C., Meisenheimer K., Rix H.-W., Borch A., Dye S., Kleinheinrich M., Wisotzki L., & McIntosh D. H.: *Nearly 5000 Distant Early-Type Galaxies in COMBO-17: A Red Sequence and Its Evolution since Z~1.* ApJ **608**, 752 (2004)

Bell E. F., Zucker D. B., Belokurov V., Sharma S., Johnston K. V., Bullock J. S., Hogg D. W., Jahnke K., de Jong J. T. A., Beers T. C., et al.: *The Accretion Origin of the Milky Way's Stellar Halo.* ApJ **680**, 295 (2008)

Bellazzini M., Ferraro F. R., & Pancino E.: *A Step toward the Calibration of the Red Giant Branch Tip as a Standard Candle.* ApJ **556**, 635 (2001)

Bellazzini M., Ferraro F. R., & Ibata R.: *The Stellar Population of NGC 5634: A Globular Cluster in the Sagittarius dSph Stream?* AJ **124**, 915 (2002)

Belokurov V., Zucker D. B., Evans N. W., Gilmore G., Vidrih S., Bramich D. M., Newberg H. J., Wyse R. F. G., Irwin M. J., Fellhauer M., et al.: *The Field of Streams: Sagittarius and Its Siblings.* ApJ **642**, L137 (2006)

Belokurov V., Evans N. W., Irwin M. J., Lynden-Bell D., Yanny B., Vidrih S., Gilmore G., Seabroke G., Zucker D. B., Wilkinson M. I., et al.: *An Orphan in the "Field of Streams"*. ApJ **658**, 337 (2007)

Belokurov V., Erkal D., Evans N. W., Koposov S. E., & Deason A. J.: *Co-Formation of the Disc and the Stellar Halo.* MNRAS **478**, 611 (2018)

Belokurov V., Sanders J. L., Fattahi A., Smith M. C., Deason A. J., Evans N. W., & Grand R. J. J.: *The Biggest Splash.* MNRAS **494**, 3880 (2020)

Belokurov V. & Kravtsov A.: *In-Situ versus Accreted Milky Way Globular Clusters: A New Classification Method and Implications for Cluster Formation.* MNRAS **528**, 3198 (2024)

Bernard E. J., Ferguson A. M. N., Barker M. K., Hidalgo S. L., Ibata R. A., Irwin M. J., Lewis G. F., McConnachie A. W., Monelli M., & Chapman S. C.: *The Star Formation History and Dust Content in the Far Outer Disc of M31.* MNRAS **420**, 2625 (2012)

Bernard E. J., Ferguson A. M. N., Richardson J. C., Irwin M. J., Barker M. K., Hidalgo S. L., Aparicio A., Chapman S. C., Ibata R. A., Lewis G. F., et al.: *The Nature and Origin of Substructure in the Outskirts of M31 - II. Detailed Star Formation Histories.* MNRAS **446**, 2789 (2015)

Bhagavan S., de Koning B., Maddhashiya S., & Rackauckas C.: *DataInterpolations.jl: Fast Interpolations of 1D data.* Journal of Open Source Software **9**, 6917 (2024)

Bhattacharya S., Arnaboldi M., Hartke J., Gerhard O., Comte V., McConnachie A., & Caldwell N.: *The Survey of Planetary Nebulae in Andromeda (M 31). I. Imaging the Disc and Halo with MegaCam at the CFHT.* A&A **624**, A132 (2019)

Bhattacharya S., Arnaboldi M., Gerhard O., McConnachie A., Caldwell N., Hartke J., & Freeman K. C.: *The Survey of Planetary Nebulae in Andromeda (M 31). III. Constraints from Deep Planetary Nebula Luminosity Functions on the Origin of the Inner Halo Substructures in M 31.* A&A **647**, A130 (2021)

Bhattacharya S., Arnaboldi M., Hammer F., Yang Y., Gerhard O., Caldwell N., & Freeman K. C.: *The Survey of Planetary Nebulae in Andromeda (M 31) VI. Kinematics of M 31 Inner-Halo Substructures and Comparison with Major-Merger Simulation Predictions.* MNRAS (2023)

Biffi V., Dolag K., & Böhringer H.: *Investigating the Velocity Structure and X-ray Observable Properties of Simulated Galaxy Clusters with PHOX.* MNRAS **428**, 1395 (2013)

Binney J.: *Rotation and Anisotropy of Galaxies Revisited.* MNRAS **363**, 937 (2005)

Binney J.: *Dynamics for Galactic Archaeology.* New A Rev. **57**, 29 (2013)

Bittner A., Falcón-Barroso J., Nedelchev B., Dorta A., Gadotti D. A., Sarzi M., Molaeinezhad A., Iodice E., Rosado-Belza D., de Lorenzo-Cáceres A., et al.: *The GIST Pipeline: A Multi-Purpose Tool for the Analysis and Visualisation of (Integral-Field) Spectroscopic Data.* A&A **628**, A117 (2019)

Blakeslee J. P., Tonry J. L., & Metzger M. R.: *Globular Clusters in 19 Northern Abell Clusters.* AJ **114**, 482 (1997)

Blakeslee J. P., Jordán A., Mei S., Côté P., Ferrarese L., Infante L., Peng E. W., Tonry J. L., & West M. J.: *The ACS Fornax Cluster Survey. V. Measurement and Recalibration of Surface Brightness Fluctuations and a Precise Value of the Fornax-Virgo Relative Distance.* ApJ **694**, 556 (2009)

Blöcker T.: *Stellar Evolution of Low- and Intermediate-Mass Stars. II. Post-AGB Evolution.* A&A **299**, 755 (1995)

Bluck A. F. L., Maiolino R., Piotrowska J. M., Trussler J., Ellison S. L., Sánchez S. F., Thorp M. D., Teimoorinia H., Moreno J., & Conselice C. J.: *How Do Central and Satellite Galaxies Quench? - Insights from Spatially Resolved Spectroscopy in the MaNGA Survey.* MNRAS **499**, 230 (2020)

Blumenthal G. R., Faber S. M., Primack J. R., & Rees M. J.: *Formation of Galaxies and Large-Scale Structure with Cold Dark Matter.* Nature **311**, 517 (1984)

Blumenthal K. A., Moreno J., Barnes J. E., Hernquist L., Torrey P., Claytor Z., Rodriguez-Gomez V., Marinacci F., & Vogelsberger M.: *Galaxy Interactions in IllustrisTNG-100, I: The Power and Limitations of Visual Identification.* MNRAS **492**, 2075 (2020)

Bobylev V. V. & Baykova A. T.: *Modern Estimates of the Mass of the Milky Way.* Astronomy Reports **67**, 812 (2023)

Boecker A., Alfaro-Cuello M., Neumayer N., Martín-Navarro I., & Leaman R.: *Recovering Age-Metallicity Distributions from Integrated Spectra: Validation with MUSE Data of a Nearby Nuclear Star Cluster.* ApJ **896**, 13 (2020)

Boecker A., Neumayer N., Pillepich A., Frankel N., Ramesh R., Leaman R., & Hernquist L.: *The Origin of Stars in the Inner 500 Parsecs in TNG50 Galaxies.* MNRAS **519**, 5202 (2023)

Bois M., Bournaud F., Emsellem E., Alatalo K., Blitz L., Bureau M., Cappellari M., Davies R. L., Davis T. A., de Zeeuw P. T., et al.: *Formation of Slowly Rotating Early-Type Galaxies via Major Mergers: A Resolution Study.* MNRAS **406**, 2405 (2010)

Bois M., Emsellem E., Bournaud F., Alatalo K., Blitz L., Bureau M., Cappellari M., Davies R. L., Davis T. A., de Zeeuw P. T., et al.: *The ATLAS3D Project - VI. Simulations of Binary Galaxy Mergers and the Link with Fast Rotators, Slow Rotators and Kinematically Distinct Cores.* MNRAS **416**, 1654 (2011)

Boley A. C., Lake G., Read J., & Teyssier R.: *Globular Cluster Formation Within a Cosmological Context.* ApJ **706**, L192 (2009)

Bonaca A., Conroy C., Wetzel A., Hopkins P. F., & Kereš D.: *Gaia Reveals a Metal-Rich, in Situ Component of the Local Stellar Halo.* ApJ **845**, 101 (2017)

Borsato N. W., Martell S. L., & Simpson J. D.: *Identifying Stellar Streams in Gaia DR2 with Data Mining Techniques.* MNRAS **492**, 1370 (2020)

Bournaud F., Chapon D., Teyssier R., Powell L. C., Elmegreen B. G., Elmegreen D. M., Duc P.-A., Contini T., Epinat B., & Shapiro K. L.: *Hydrodynamics of High-Redshift Galaxy Collisions: From Gas-Rich Disks to Dispersion-Dominated Mergers and Compact Spheroids.* ApJ **730**, 4 (2011)

Boylan-Kolchin M.: *The Globular Cluster-Dark Matter Halo Connection.* MNRAS **472**, 3120 (2017)

Bradley L. D., Adamo A., Vanzella E., Sharon K., Brammer G., Coe D., Diego J. M., Kokorev V., Mahler G., Oguri M., et al.: *Unveiling the Cosmic Gems Arc at $z \sim 10$ with JWST NIRCam.* ApJ **991**, 32 (2025)

Brammer G. B., Whitaker K. E., van Dokkum P. G., Marchesini D., Franx M., Kriek M., Labbé I., Lee K.-S., Muzzin A., Quadri R. F., et al.: *The Number Density and Mass Density of Star-forming and Quiescent Galaxies at 0.4 <= z <= 2.2.* ApJ **739**, 24 (2011)

Bressan A., Marigo P., Girardi Léo., Salasnich B., Dal Cero C., Rubele S., & Nanni A.: *PARSEC: Stellar Tracks and Isochrones with the PAdova and TRieste Stellar Evolution Code.* MNRAS **427**, 127 (2012)

Bridges T., Gebhardt K., Sharples R., Faifer F. R., Forte J. C., Beasley M. A., Zepf S. E., Forbes D. A., Hanes D. A., & Pierce M.: *The Globular Cluster Kinematics and Galaxy Dark Matter Content of NGC 4649 (M60).* MNRAS **373**, 157 (2006)

Brodie J. P. & Strader J.: *Extragalactic Globular Clusters and Galaxy Formation.* ARA&A **44**, 193 (2006)

Brodie J. P., Romanowsky A. J., Strader J., & Forbes D. A.: *The Relationships among Compact Stellar Systems: A Fresh View of Ultracompact Dwarfs.* AJ **142**, 199 (2011)

Brodie J. P., Romanowsky A. J., Strader J., Forbes D. A., Foster C., Jennings Z. G., Pastorello N., Pota V., Usher C., Blom C., et al.: *The SAGES Legacy Unifying Globulars and GalaxieS Survey (SLUGGS): Sample Definition, Methods, and Initial Results.* ApJ **796**, 52 (2014)

Bromm V. & Clarke C. J.: *The Formation of the First Globular Clusters in Dwarf Galaxies before the Epoch of Reionization.* ApJ **566**, L1 (2002)

Brown G. & Gnedin O. Y.: *Testing Feedback from Star Clusters in Simulations of the Milky Way Formation.* MNRAS **514**, 280 (2022)

Brown T. M., Smith E., Ferguson H. C., Rich R. M., Guhathakurta P., Renzini A., Sweigart A. V., & Kimble R. A.: *The Detailed Star Formation History in the Spheroid, Outer Disk, and Tidal Stream of the Andromeda Galaxy.* ApJ **652**, 323 (2006)

Bruzual G. & Charlot S.: *Stellar Population Synthesis at the Resolution of 2003.* Monthly Notices of the Royal Astronomical Society **344**, 1000 (2003)

Bryant J. J., Owers M. S., Robotham A. S. G., Croom S. M., Driver S. P., Drinkwater M. J., Lorente N. P. F., Cortese L., Scott N., Colless M., et al.: *The SAMI Galaxy Survey: Instrument Specification and Target Selection.* MNRAS **447**, 2857 (2015)

Bullock J. S. & Johnston K. V.: *Tracing Galaxy Formation with Stellar Halos. I. Methods.* ApJ **635**, 931 (2005)

Bundy K., Bershady M. A., Law D. R., Yan R., Drory N., MacDonald N., Wake D. A., Cherinka B., Sánchez-Gallego J. R., Weijmans A.-M., et al.: *Overview of the SDSS-IV MaNGA Survey: Mapping Nearby Galaxies at Apache Point Observatory.* ApJ **798**, 7 (2015)

Burkert A. & Naab T.: *Major Mergers and the Origin of Elliptical Galaxies.* In: *Galaxies and Chaos.* **626**, 327, Springer (2003)

Burkert A. & Forbes D. A.: *High-Precision Dark Halo Virial Masses from Globular Cluster Numbers: Implications for Globular Cluster Formation and Galaxy Assembly.* AJ **159**, 56 (2020)

Buzzo M. L., Cortesi A., Hernandez-Jimenez J. A., Coccato L., Werle A., Beraldo e Silva L., Grossi M., Vika M., Barbosa C. E., Lucatelli G., et al.: *Recovering the Origins of the Lenticular Galaxy NGC 3115 Using Multiband Imaging.* MNRAS **504**, 2146 (2021)

Buzzoni A., Arnaboldi M., & Corradi R. L. M.: *Planetary Nebulae as Tracers of Galaxy Stellar Populations.* MNRAS **368**, 877 (2006)

Bílek M., Ebrová I., Jungwiert B., Jílková L., & Bartošková K.: *Shell Galaxies as Laboratories for Testing MOND.* Canadian Journal of Physics **93**, 203 (2015)

Bílek M., Cuillandre J.-C., Gwyn S., Ebrová I., Bartošková K., Jungwiert B., & Jílková L.: *Deep Imaging of the Shell Elliptical Galaxy NGC 3923 with MegaCam.* A&A **588**, A77 (2016)

Bílek M., Thies I., Kroupa P., & Famaey B.: *MOND Simulation Suggests an Origin for Some Peculiarities in the Local Group.* A&A **614**, A59 (2018)

Bílek M., Duc P.-A., Cuillandre J.-C., Gwyn S., Cappellari M., Bekaert D. V., Bonfini P., Bitsakis T., Paudel S., Krajnović D., et al.: *Census and Classification of Low-Surface-Brightness Structures in Nearby Early-Type Galaxies from the MATLAS Survey.* MNRAS **498**, 2138 (2020)

Bílek M., Fensch J., Ebrová I., Nagesh S. T., Famaey B., Duc P.-A., & Kroupa P.: *Origin of the Spectacular Tidal Shells of Galaxy NGC 474.* A&A **660**, A28 (2022)

Bílek M., Duc P. A., & Sola E.: *Origin of the Differences in Rotational Support among Early-Type Galaxies: The Case of Galaxies Outside Clusters.* A&A **672**, A27 (2023)

Cabrera-Ziri I. & Conroy C.: *Deriving Ages and Horizontal Branch Properties of Integrated Stellar Populations.* MNRAS **511**, 341 (2022)

Caffau E., Ludwig H. G., Steffen M., Freytag B., & Bonifacio P.: *Solar Chemical Abundances Determined with a CO5BOLD 3D Model Atmosphere.* Sol. Phys. **268**, 255 (2011)

Caldwell N., Schiavon R., Morrison H., Rose J. A., & Harding P.: *Star Clusters in M31. II. Old Cluster Metallicities and Ages from Hectospec Data.* AJ **141**, 61 (2011)

Callingham T. M., Cautun M., Deason A. J., Frenk C. S., Grand R. J. J., & Marinacci F.: *The Chemo-Dynamical Groups of Galactic Globular Clusters.* MNRAS **513**, 4107 (2022)

Camps P. & Baes M.: *SKIRT 9: Redesigning an Advanced Dust Radiative Transfer Code to Allow Kinematics, Line Transfer and Polarization by Aligned Dust Grains.* Astronomy and Computing **31**, 100381 (2020)

Capaccioli M., Held E. V., Lorenz H., & Vietri M.: *Photographic and CCD Surface Photometry of the Standard Elliptical Galaxy NGC 3379.* AJ **99**, 1813 (1990)

Cappellari M. & Copin Y.: *Adaptive Spatial Binning of Integral-Field Spectroscopic Data Using Voronoi Tessellations.* MNRAS **342**, 345 (2003)

Cappellari M. & Emsellem E.: *Parametric Recovery of Line-of-Sight Velocity Distributions from Absorption-Line Spectra of Galaxies via Penalized Likelihood.* Publications of the Astronomical Society of the Pacific **116**, 138 (2004)

Cappellari M., Emsellem E., Bacon R., Bureau M., Davies R. L., de Zeeuw P. T., Falcón-Barroso J., Krajnović D., Kuntschner H., McDermid R. M., et al.: *The SAURON Project - X. The Orbital Anisotropy of Elliptical and Lenticular Galaxies: Revisiting the* $(V/\sigma, \epsilon)$ *Diagram with Integral-Field Stellar Kinematics.* MNRAS **379**, 418 (2007)

Cappellari M.: *Measuring the Inclination and Mass-to-Light Ratio of Axisymmetric Galaxies via Anisotropic Jeans Models of Stellar Kinematics.* MNRAS **390**, 71 (2008)

Cappellari M., Emsellem E., Krajnović D., McDermid R. M., Scott N., Verdoes Kleijn G. A., Young L. M., Alatalo K., Bacon R., Blitz L., et al.: *The ATLAS3D Project - I. A Volume-Limited Sample of 260 Nearby Early-Type Galaxies: Science Goals and Selection Criteria.* MNRAS **413**, 813 (2011)

Cappellari M., Scott N., Alatalo K., Blitz L., Bois M., Bournaud F., Bureau M., Crocker A. F., Davies R. L., Davis T. A., et al.: *The ATLAS3D Project - XV. Benchmark for Early-Type Galaxies Scaling Relations from 260 Dynamical Models: Mass-to-Light Ratio, Dark Matter, Fundamental Plane and Mass Plane.* MNRAS **432**, 1709 (2013)

Cappellari M.: *Full Spectrum Fitting with Photometry in PPXF: Stellar Population versus Dynamical Masses, Non-Parametric Star Formation History and Metallicity for 3200 LEGA-C Galaxies at Redshift $z \approx 0.8$.* MNRAS **526**, 3273 (2023)

Cardelli J. A., Clayton G. C., & Mathis J. S.: *The Relationship between Infrared, Optical, and Ultraviolet Extinction.* ApJ **345**, 245 (1989)

Carlberg R. G. & Keating L. C.: *Simulating Globular Clusters in Dark Matter Subhalos.* ApJ **924**, 77 (2022)

Carleton T., Guo Y., Munshi F., Tremmel M., & Wright A.: *An Excess of Globular Clusters in Ultra-Diffuse Galaxies Formed through Tidal Heating.* MNRAS **502**, 398 (2021)

Carnall A. C., Walker S., McLure R. J., Dunlop J. S., McLeod D. J., Cullen F., Wild V., Amorin R., Bolzonella M., Castellano M., et al.: *Timing the Earliest Quenching Events with a Robust Sample of Massive Quiescent Galaxies at $2 < z < 5$.* MNRAS **496**, 695 (2020)

Carnall A. C., McLeod D. J., McLure R. J., Dunlop J. S., Begley R., Cullen F., Donnan C. T., Hamadouche M. L., Jewell S. M., Jones E. W., et al.: *A Surprising Abundance of Massive Quiescent Galaxies at $3 < z < 5$ in the First Data from JWST CEERS.* MNRAS **520**, 3974 (2023)

Carnall A. C., Cullen F., McLure R. J., McLeod D. J., Begley R., Donnan C. T., Dunlop J. S., Shapley A. E., Rowlands K., Almaini O., et al.: *The JWST EXCELS Survey: Too Much, Too Young, Too Fast? Ultra-massive Quiescent Galaxies at $3 < z < 5$.* MNRAS **534**, 325 (2024)

Carniani S., Hainline K., D'Eugenio F., Eisenstein D. J., Jakobsen P., Witstok J., Johnson B. D., Chevallard J., Maiolino R., Helton J. M., et al.: *Spectroscopic Confirmation of Two Luminous Galaxies at a Redshift of 14.* Nature **633**, 318 (2024)

Carraro G., Zinn R., & Moni Bidin C.: *Whiting 1: The Youngest Globular Cluster Associated with the Sagittarius Dwarf Spheroidal Galaxy.* A&A **466**, 181 (2007)

Carraro G.: *The Globular Cluster AM 4: Yet Another Young Globular Associated with the Sgr Dwarf Spheroidal Galaxy?* AJ **137**, 3809 (2009)

Casagrande L., Flynn C., Portinari L., Girardi L., & Jimenez R.: *The Helium Abundance and ΔY/ΔZ in Lower Main-Sequence Stars.* MNRAS **382**, 1516 (2007)

Catelan M., Borissova J., Ferraro F. R., Corwin T. M., Smith H. A., & Kurtev R.: *M75, A Globular Cluster with a Trimodal Horizontal Branch. I. Color-Magnitude Diagram.* AJ **124**, 364 (2002)

Catinella B., Saintonge A., Janowiecki S., Cortese L., Davé R., Lemonias J. J., Cooper A. P., Schiminovich D., Hummels C. B., Fabello S., et al.: *xGASS: total cold gas scaling relations and molecular-to-atomic gas ratios of galaxies in the local Universe.* MNRAS **476**, 875 (2018)

Chabrier G.: *Galactic Stellar and Substellar Initial Mass Function.* PASP **115**, 763 (2003)

Chandra V., Naidu R. P., Conroy C., Bonaca A., Zaritsky D., Cargile P. A., Caldwell N., Johnson B. D., Han J. J., & Ting Y.-S.: *Discovery of the Magellanic Stellar Stream Out to 100 Kpc.* ApJ **956**, 110 (2023)

Chang Y.-Y., van der Wel A., da Cunha E., & Rix H.-W.: *Stellar Masses and Star Formation Rates for 1M Galaxies from SDSS+WISE.* ApJS **219**, 8 (2015)

Chase O., Ciardullo R., Roth M. M., & Jacoby G. H.: *The Effect of Superpositions on the Planetary Nebula Luminosity Function.* ApJ **950**, 59 (2023)

Chen Y. & Gnedin O. Y.: *Modeling the Kinematics of Globular Cluster Systems.* MNRAS **514**, 4736 (2022)

Chen Y. & Gnedin O. Y.: *Formation of Globular Clusters in Dwarf Galaxies of the Local Group.* MNRAS **522**, 5638 (2023)

Chen Y. & Gnedin O. Y.: *Galaxy Assembly Revealed by Globular Clusters.* The Open Journal of Astrophysics **7**, 23 (2024a)

Chen Y. & Gnedin O. Y.: *Catalogue of Model Star Clusters in the Milky Way and M31 Galaxies.* MNRAS **527**, 3692 (2024b)

Chen Y., Mo H., & Wang H.: *A Two-Phase Model of Galaxy Formation: III. The Formation of Globular Clusters.* MNRAS **540**, 1235 (2025)

Chies-Santos A. L., Larsen S. S., Kuntschner H., Anders P., Wehner E. M., Strader J., Brodie J. P., & Santos J. F. C.: *An Optical/NIR Survey of Globular Clusters in Early-Type Galaxies. II. Ages of Globular Cluster Systems and the Relation to Galaxy Morphology.* A&A **525**, A20 (2011)

Choi H. & Yi S. K.: *On the Evolution of Galaxy Spin in a Cosmological Hydrodynamic Simulation of Galaxy Clusters.* ApJ **837**, 68 (2017)

Choksi N., Gnedin O. Y., & Li H.: *Formation of Globular Cluster Systems: From Dwarf Galaxies to Giants.* MNRAS **480**, 2343 (2018)

Chomiuk L., Strader J., & Brodie J. P.: *The Peculiar Globular Cluster System of the S0 Galaxy NGC 7457.* AJ **136**, 234 (2008)

Ciardullo R., Jacoby G. H., Ford H. C., & Neill J. D.: *Planetary Nebulae as Standard Candles. II. The Calibration in M31 and Its Companions.* ApJ **339**, 53 (1989)

Ciardullo R., Jacoby G. H., & Harris W. E.: *Planetary Nebulae as Standard Candles. VII. A Test versus Hubble Type in the NGC 1023 Group.* ApJ **383**, 487 (1991)

Ciardullo R. & Jacoby G. H.: *Planetary Nebulae as Standard Candles. VIII. Evidence for a Change in the Luminosity Function Cutoff at Low Metallicity.* ApJ **388**, 268 (1992)

Ciardullo R. & Jacoby G. H.: *The Circumstellar Extinction of Planetary Nebulae.* ApJ **515**, 191 (1999)

Ciardullo R., Feldmeier J. J., Jacoby G. H., Kuzio de Naray R., Laychak M. B., & Durrell P. R.: *Planetary Nebulae as Standard Candles. XII. Connecting the Population I and Population II Distance Scales.* ApJ **577**, 31 (2002)

Ciardullo R., Durrell P. R., Laychak M. B., Herrmann K. A., Moody K., Jacoby G. H., & Feldmeier J. J.: *The Planetary Nebula System of M33.* ApJ **614**, 167 (2004)

Ciardullo R., Sigurdsson S., Feldmeier J. J., & Jacoby G. H.: *Close Binaries as the Progenitors of the Brightest Planetary Nebulae.* ApJ **629**, 499 (2005)

Ciardullo R.: *The Planetary Nebula Luminosity Function: Pieces of the Puzzle.* PASA **27**, 149 (2010)

Ciardullo R.: *The Planetary Nebula Luminosity Function at the Dawn of Gaia.* Ap&SS **341**, 151 (2012)

Ciardullo R.: *The Planetary Nebula Luminosity Function in the Era of Precision Cosmology.* Frontiers in Astronomy and Space Sciences **9**, 896326 (2022)

Ciucă I., Kawata D., Ting Y.-S., Grand R. J. J., Miglio A., Hayden M., Baba J., Fragkoudi F., Monty S., Buder S., & Freeman K.: *Chasing the Impact of the Gaia-Sausage-Enceladus Merger on the Formation of the Milky Way Thick Disc.* MNRAS (2023)

Claeyssens A., Adamo A., Richard J., Mahler G., Messa M., & Dessauges-Zavadsky M.: *Star Formation at the Smallest Scales: A JWST Study of the Clump Populations in SMACS0723.* MNRAS **520**, 2180 (2023)

Claeyssens A., Adamo A., Kokorev V., Furtak L., Richard J., Beauchesne B., Dessauges-Zavadsky M., Atek H., Chisholm J., Endsley R., et al.: *A First GLIMPSE into Star Clusters Populations across Cosmic Time.* arXiv e-prints, arXiv:2601.16281 (2026)

Clontz C., Seth A. C., Wang Z., Souza S. O., Häberle M., Nitschai M. S., Neumayer N., Latour M., Milone A. P., Feldmeier-Krause A., et al.: *oMEGACat. V. Helium Enrichment in ω Centauri as a Function of Metallicity.* ApJ **984**, 162 (2025)

Coccato L., Gerhard O., Arnaboldi M., Das P., Douglas N. G., Kuijken K., Merrifield M. R., Napolitano N. R., Noordermeer E., Romanowsky A. J., et al.: *Kinematic Properties of Early-Type Galaxy Haloes Using Planetary Nebulae.* MNRAS **394**, 1249 (2009)

Coccato L., Arnaboldi M., & Gerhard O.: *Signatures of Accretion Events in the Haloes of Early-Type Galaxies from Comparing PNe and GCs Kinematics.* MNRAS **436**, 1322 (2013)

Cohen J. G., Blakeslee J. P., & Ryzhov A.: *The Ages and Abundances of a Large Sample of M87 Globular Clusters.* ApJ **496**, 808 (1998)

Congiu E., Scheuermann F., Kreckel K., Leroy A., Emsellem E., Belfiore F., Hartke J., Anand G., Egorov O. V., Groves B., et al.: *The MUSE View of the Sculptor Galaxy: Survey Overview and the Luminosity Function of Planetary Nebulae.* A&A **700**, A125 (2025)

Conselice C. J., Wilkinson A., Duncan K., & Mortlock A.: *The Evolution of Galaxy Number Density at $z < 8$ and Its Implications.* ApJ **830**, 83 (2016)

Cooper A. P., D'Souza R., Kauffmann G., Wang J., Boylan-Kolchin M., Guo Q., Frenk C. S., & White S. D. M.: *Galactic Accretion and the Outer Structure of Galaxies in the CDM Model.* MNRAS **434**, 3348 (2013)

Correa C. A., Wyithe J. S. B., Schaye J., & Duffy A. R.: *The Accretion History of Dark Matter Haloes - III. A Physical Model for the Concentration-Mass Relation.* MNRAS **452**, 1217 (2015)

Cortese L., Fogarty L. M. R., Bekki K., van de Sande J., Couch W., Catinella B., Colless M., Obreschkow D., Taranu D., Tescari E., et al.: *The SAMI Galaxy Survey: The Link between Angular Momentum and Optical Morphology.* MNRAS **463**, 170 (2016)

Cortesi A., Merrifield M. R., Arnaboldi M., Gerhard O., Martinez-Valpuesta I., Saha K., Coccato L., Bamford S., Napolitano N. R., Das P., et al.: *Unravelling the Origins of S0 Galaxies Using Maximum Likelihood Analysis of Planetary Nebulae Kinematics.* MNRAS **414**, 642 (2011)

Cortesi A., Arnaboldi M., Coccato L., Merrifield M. R., Gerhard O., Bamford S., Romanowsky A. J., Napolitano N. R., Douglas N. G., Kuijken K., et al.: *The Planetary Nebula Spectrograph Survey of S0 Galaxy Kinematics. Data and Overview.* A&A **549**, A115 (2013a)

Cortesi A., Merrifield M. R., Coccato L., Arnaboldi M., Gerhard O., Bamford S., Napolitano N. R., Romanowsky A. J., Douglas N. G., Kuijken K., et al.: *Planetary Nebula Spectrograph Survey of S0 Galaxy Kinematics - II. Clues to the Origins of S0 Galaxies.* MNRAS **432**, 1010 (2013b)

Côté P., Marzke R. O., & West M. J.: *The Formation of Giant Elliptical Galaxies and Their Globular Cluster Systems.* ApJ **501**, 554 (1998)

Crain R. A., Schaye J., Bower R. G., Furlong M., Schaller M., Theuns T., Dalla Vecchia C., Frenk C. S., McCarthy I. G., Helly J. C., et al.: *The EAGLE Simulations of Galaxy Formation: Calibration of Subgrid Physics and Model Variations.* MNRAS **450**, 1937 (2015)

Crnojević D., Sand D. J., Spekkens K., Caldwell N., Guhathakurta P., McLeod B., Seth A., Simon J. D., Strader J., & Toloba E.: *The Extended Halo of Centaurus A: Uncovering Satellites, Streams, and Substructures.* ApJ **823**, 19 (2016)

Croom S. M., Lawrence J. S., Bland-Hawthorn J., Bryant J. J., Fogarty L., Richards S., Goodwin M., Farrell T., Miziarski S., Heald R., et al.: *The Sydney-AAO Multi-object Integral Field Spectrograph.* MNRAS **421**, 872 (2012)

Croom S. M., Owers M. S., Scott N., Poetrodjojo H., Groves B., van de Sande J., Barone T. M., Cortese L., D'Eugenio F., Bland-Hawthorn J., et al.: *The SAMI Galaxy Survey: The Third and Final Data Release.* MNRAS **505**, 991 (2021)

Crosby E., Jerjen H., Müller O., Pawlowski M. S., Mateo M., & Lelli F.: *New Dwarf Galaxy Candidates in the Sphere of Influence of the Sombrero Galaxy.* MNRAS **527**, 9118 (2024)

Crosby E., Pawlowski M. S., Müller O., & Jerjen H.: *Detectability of Satellite Planes in Mock Observations of Isolated L* Galaxies.* MNRAS **547**, stag372 (2026)

Csukai A., Zijlstra A. A., McDonald I., & De Marco O.: *Central-star extinctions towards planetary nebulae.* MNRAS **543**, 3035 (2025)

Cui X.-Q., Zhao Y.-H., Chu Y.-Q., Li G.-P., Li Q., Zhang L.-P., Su H.-J., Yao Z.-Q., Wang Y.-N., Xing X.-Z., et al.: *The Large Sky Area Multi-Object Fiber Spectroscopic Telescope (LAMOST).* A&A **12**, 1197 (2012)

Cullen F., McLure R. J., Dunlop J. S., Khochfar S., Davé R., Amorín R., Bolzonella M., Carnall A. C., Castellano M., Cimatti A., et al.: *The VANDELS Survey: The Stellar Metallicities of Star-Forming Galaxies at 2.5 < z < 5.0.* MNRAS **487**, 2038 (2019)

Cummings J. D., Kalirai J. S., Tremblay P. E., Ramirez-Ruiz E., & Choi J.: *The White Dwarf Initial-Final Mass Relation for Progenitor Stars from 0.85 to 7.5 $M_{\odot}$.* ApJ **866**, 21 (2018)

Cunningham T., Tremblay P.-E., & W. O'Brien M.: *Initial-Final Mass Relation from White Dwarfs within 40 Pc.* MNRAS **527**, 3602 (2024)

Daddi E., Renzini A., Pirzkal N., Cimatti A., Malhotra S., Stiavelli M., Xu C., Pasquali A., Rhoads J. E., Brusa M., et al.: *Passively Evolving Early-Type Galaxies at 1.4 <~ z <~ 2.5 in the Hubble Ultra Deep Field.* ApJ **626**, 680 (2005)

Dage K. C., Usher C., Sobeck J., Chies Santos A. L., Szabó R., Reina-Campos M., Girardi L., Ripepi V., Di Criscienzo M., Sarajedini A., et al.: *Extragalactic Star Cluster Science with the Nancy Grace Roman Space Telescope's High Latitude Wide Area Survey and the Vera C. Rubin Observatory.* arXiv e-prints, arXiv2306.12620 (2023)

Davis B. D., Ciardullo R., Jacoby G. H., Feldmeier John. J., & Indahl B. L.: *The True Luminosities of Planetary Nebulae in M31's Bulge: Massive Central Stars from an Old Stellar Population.* ApJ **863**, 189 (2018)

Davis M., Efstathiou G., Frenk C. S., & White S. D. M.: *The Evolution of Large-Scale Structure in a Universe Dominated by Cold Dark Matter.* ApJ **292**, 371 (1985)

Davison T. A., Norris M. A., Pfeffer J. L., Davies J. J., & Crain R. A.: *An EAGLE's View of Ex Situ Galaxy Growth.* MNRAS **497**, 81 (2020)

De Angeli F., Piotto G., Cassisi S., Busso G., Recio-Blanco A., Salaris M., Aparicio A., & Rosenberg A.: *Galactic Globular Cluster Relative Ages.* AJ **130**, 116 (2005)

de Boer T. J. L., Belokurov V., & Koposov S.: *The Star Formation History of the Sagittarius Stream.* MNRAS **451**, 3489 (2015)

de Brito Silva D., Coelho P., Cortesi A., Bruzual G., Magris C. G., Chies-Santos A. L., Hernandez-Jimenez J. A., Ederoclite A., San Roman I., Varela J., et al.: *J-PLUS: Detecting and Studying Extragalactic Globular Clusters. The Case of NGC 1023.* A&A **664**, A129 (2022)

de Freitas Pacheco J. A. & Barbuy B.: *Horizontal Branch Morphology and Hβ Indices of Globular Clusters.* A&A **302**, 718 (1995)

de Graaff A., Setton D. J., Brammer G., Cutler S., Suess K. A., Labbé I., Leja J., Weibel A., Maseda M. V., Whitaker K. E., et al.: *Efficient Formation of a Massive Quiescent Galaxy at Redshift 4.9.* Nature **9**, 280 (2025)

De Lucia G., Kruijssen J. M. D., Trujillo-Gomez S., Hirschmann M., & Xie L.: *On the Origin of Globular Clusters in a Hierarchical Universe.* MNRAS **530**, 2760 (2024)

De Marco O., Aleman I., & Akras S.: *Planetary Nebulae.* arXiv e-prints, arXiv:2501.07869 (2025)

Deason A. J., Belokurov V., Evans N. W., & McCarthy I. G.: *Elliptical Galaxy Masses Out to Five Effective Radii: The Realm of Dark Matter.* ApJ **748**, 2 (2012)

Deason A. J. & Belokurov V.: *Galactic Archaeology with Gaia.* New A Rev. **99**, 101706 (2024)

Debattista V. P., Roškar R., Valluri M., Quinn T., Moore B., & Wadsley J.: *What's up in the Milky Way? The Orientation of the Disc Relative to the Triaxial Halo.* MNRAS **434**, 2971 (2013)

Dekel A., Birnboim Y., Engel G., Freundlich J., Goerdt T., Mumcuoglu M., Neistein E., Pichon C., Teyssier R., & Zinger E.: *Cold Streams in Early Massive Hot Haloes as the Main Mode of Galaxy Formation.* Nature **457**, 451 (2009)

Derkenne C., McDermid R. M., D'Eugenio F., Foster C., Khalid A., Harborne K. E., van de Sande J., Croom S. M., Lagos C. D. P., Bellstedt S., et al.: *The MAGPI Survey: Massive Slow Rotator Population in Place by z ~ 0.3.* MNRAS **531**, 4602 (2024)

D'Eugenio F., Colless M., Scott N., van der Wel A., Davies R. L., van de Sande J., Sweet S. M., Oh S., Groves B., Sharp R., et al.: *The SAMI Galaxy Survey: Stellar Population and Structural Trends across the Fundamental Plane.* MNRAS **504**, 5098 (2021)

Di Matteo P., Jog C. J., Lehnert M. D., Combes F., & Semelin B.: *Generation of Rotationally Dominated Galaxies by Mergers of Pressure-Supported Progenitors.* A&A **501**, L9 (2009)

Díaz-García S. & Knapen J. H.: *Gas fractions and depletion times in galaxies with different degrees of interaction.* A&A **635**, A197 (2020)

Dodd E., Callingham T. M., Helmi A., Matsuno T., Ruiz-Lara T., Balbinot E., & Lövdal S.: *Gaia DR3 View of Dynamical Substructure in the Stellar Halo near the Sun.* A&A **670**, L2 (2023)

Doherty M., Arnaboldi M., Das P., Gerhard O., Aguerri J. A. L., Ciardullo R., Feldmeier J. J., Freeman K. C., Jacoby G. H., & Murante G.: *The Edge of the M 87 Halo and the Kinematics of the Diffuse Light in the Virgo Cluster Core.* A&A **502**, 771 (2009)

Dolag K., Jubelgas M., Springel V., Borgani S., & Rasia E.: *Thermal Conduction in Simulated Galaxy Clusters.* ApJ **606**, L97 (2004)

Dolag K., Vazza F., Brunetti G., & Tormen G.: *Turbulent Gas Motions in Galaxy Cluster Simulations: The Role of Smoothed Particle Hydrodynamics Viscosity.* MNRAS **364**, 753 (2005)

Dolag K., Reinecke M., Gheller C., & Imboden S.: *Splotch: Visualizing Cosmological Simulations.* New Journal of Physics **10**, 125006 (2008)

Dolag K., Borgani S., Murante G., & Springel V.: *Substructures in Hydrodynamical Cluster Simulations.* MNRAS **399**, 497 (2009)

Dolag K., Remus R.-S., Valenzuela L. M., Kimmig L. C., Seidel B., Fortune S., Stoiber J., Ivleva A., Hoffmann T., Biffi V., et al.: *Encyclopedia Magneticum: Scaling Relations from Cosmic Dawn to Present Day.* arXiv e-prints, arXiv:2504.01061 (2025)

Dolfi A., Forbes D. A., Couch W. J., Ferré-Mateu A., Bellstedt S., Bekki K., Diaz J., Romanowsky A. J., & Brodie J. P.: *The Assembly History of the Nearest S0 Galaxy NGC 3115 from Its Kinematics out to Six Half-Light Radii.* MNRAS **495**, 1321 (2020)

Dolfi A., Forbes D. A., Couch W. J., Bekki K., Ferré-Mateu A., Romanowsky A. J., & Brodie J. P.: *The SLUGGS Survey: Combining Stars, Globular Clusters, and Planetary Nebulae to Understand the Assembly History of Early-Type Galaxies from Their Large Radii Kinematics.* MNRAS **504**, 4923 (2021)

Dolfi A., Pfeffer J., Forbes D. A., Couch W. J., Bekki K., Brodie J. P., Romanowsky A. J., & Kruijssen J. M. D.: *The Present-Day Globular Cluster Kinematics of Lenticular Galaxies from the E-MOSAICS Simulations and Their Relation to the Galaxy Assembly Histories.* MNRAS **511**, 3179 (2022)

Donlon T., II, Newberg H. J., Sanderson R., & Widrow L. M.: *The Milky Way's Shell Structure Reveals the Time of a Radial Collision.* ApJ **902**, 119 (2020)

Donlon T., II, Newberg H. J., Kim B., & Lépine S.: *The Local Stellar Halo Is Not Dominated by a Single Radial Merger Event.* ApJ **932**, L16 (2022)

Donlon T. & Newberg H. J.: *A Swing of the Pendulum: The Chemodynamics of the Local Stellar Halo Indicate Contributions from Several Radial Merger Events.* ApJ **944**, 169 (2023)

Donnert J., Dolag K., Brunetti G., & Cassano R.: *Rise and Fall of Radio Haloes in Simulated Merging Galaxy Clusters.* MNRAS **429**, 3564 (2013)

D'Onofrio M., Marziani P., & Chiosi C.: *Past, Present and Future of the Scaling Relations of Galaxies and Active Galactic Nuclei.* Frontiers in Astronomy and Space Sciences **8**, 157 (2021)

Dopita M. A. & Meatheringham S. J.: *Photoionization Modeling of Magellanic Cloud Planetary Nebulae. I.* ApJ **367**, 115 (1991a)

Dopita M. A. & Meatheringham S. J.: *Photoionization Modeling of Magellanic Cloud Planetary Nebulae. II.* ApJ **377**, 480 (1991b)

Dopita M. A., Jacoby G. H., & Vassiliadis E.: *A Theoretical Calibration of the Planetary Nebular Cosmic Distance Scale.* ApJ **389**, 27 (1992)

Doppel J. E., Sales L. V., Nelson D., Pillepich A., Abadi M. G., Peng E. W., Marinacci F., Naiman J., Torrey P., Vogelsberger M., et al.: *Modelling Globular Clusters in the TNG50 Simulation: Predictions from Dwarfs to Giant Galaxies.* MNRAS **518**, 2453 (2023)

Doroshkevich A. G.: *Spatial Structure of Perturbations and Origin of Galactic Rotation in Fluctuation Theory.* Astrophysics **6**, 320 (1970)

Dotter A., Chaboyer B., Jevremović D., Baron E., Ferguson J. W., Sarajedini A., & Anderson J.: *The ACS Survey of Galactic Globular Clusters. II. Stellar Evolution Tracks, Isochrones, Luminosity Functions, and Synthetic Horizontal-Branch Models.* AJ **134**, 376 (2007)

Dotter A., Sarajedini A., & Yang S.-C.: *Globular Clusters in the Outer Galactic Halo: AM-1 and Palomar 14.* AJ **136**, 1407 (2008)

Dotter A., Sarajedini A., Anderson J., Aparicio A., Bedin L. R., Chaboyer B., Majewski S., Marín-Franch A., Milone A., Paust N., et al.: *The ACS Survey of Galactic Globular Clusters. IX. Horizontal Branch Morphology and the Second Parameter Phenomenon.* ApJ **708**, 698 (2010)

Dotter A., Sarajedini A., & Anderson J.: *Globular Clusters in the Outer Galactic Halo: New Hubble Space Telescope/Advanced Camera for Surveys Imaging of Six Globular Clusters and the Galactic Globular Cluster Age-Metallicity Relation.* ApJ **738**, 74 (2011)

Douglas N. G., Arnaboldi M., Freeman K. C., Kuijken K., Merrifield M. R., Romanowsky A. J., Taylor K., Capaccioli M., Axelrod T., Gilmozzi R., et al.: *The Planetary Nebula Spectrograph: The Green Light for Galaxy Kinematics.* PASP **114**, 1234 (2002)

Douglas N. G., Napolitano N. R., Romanowsky A. J., Coccato L., Kuijken K., Merrifield M. R., Arnaboldi M., Gerhard O., Freeman K. C., Merrett H. R., et al.: *The PN.S Elliptical Galaxy Survey: Data Reduction, Planetary Nebula Catalog, and Basic Dynamics for NGC 3379.* ApJ **664**, 257 (2007)

Dowell J. L., Rhode K. L., Bridges T. J., Zepf S. E., Gebhardt K., Freeman K. C., & de Boer E. W.: *Beyond the Brim of the Hat: Kinematics of Globular Clusters out to Large Radii in the Sombrero Galaxy.* AJ **147**, 150 (2014)

Dressler A., Rieke M., Eisenstein D., Stark D. P., Burns C., Bhatawdekar R., Bonaventura N., Boyett K., Bunker A. J., Carniani S., et al.: *Building the First Galaxies—Chapter 2. Starbursts Dominate the Star Formation Histories of $6 < z < 12$ Galaxies.* ApJ **964**, 150 (2024)

Driver S. P., Andrews S. K., da Cunha E., Davies L. J., Lagos C., Robotham A. S. G., Vinsen K., Wright A. H., Alpaslan M., Bland-Hawthorn J., et al.: *GAMA/G10-COSMOS/3D-HST: The $0 < z < 5$ Cosmic Star Formation History, Stellar-Mass, and Dust-Mass Densities.* MNRAS **475**, 2891 (2018)

D'Souza R. & Bell E. F.: *The Andromeda Galaxy's Most Important Merger about 2 Billion Years Ago as M32's Likely Progenitor.* Nature **2**, 737 (2018a)

D'Souza R. & Bell E. F.: *The Masses and Metallicities of Stellar Haloes Reflect Galactic Merger Histories.* MNRAS **474**, 5300 (2018b)

Dubois Y., Pichon C., Welker C., Le Borgne D., Devriendt J., Laigle C., Codis S., Pogosyan D., Arnouts S., Benabed K., et al.: *Dancing in the Dark: Galactic Properties Trace Spin Swings along the Cosmic Web.* MNRAS **444**, 1453 (2014)

Duc P.-A., Cuillandre J.-C., Karabal E., Cappellari M., Alatalo K., Blitz L., Bournaud F., Bureau M., Crocker A. F., Davies R. L., et al.: *The ATLAS3D Project - XXIX. The New Look of Early-Type Galaxies and Surrounding Fields Disclosed by Extremely Deep Optical Images.* MNRAS **446**, 120 (2015)

Dufour R. J., van den Bergh S., Harvel C. A., Martins D. H., Schiffer F. H., III, Talbot R. J., Jr., Talent D. L., & Wells D. C.: *Picture Processing Analysis of the Optical Structure of NGC 5128 (Centaurus A).* AJ **84**, 284 (1979)

Dumont A., Seth A. C., Strader J., Sand D. J., Voggel K., Hughes A. K., Crnojević D., Forbes D. A., Mateo M., & Pearson S.: *Investigating the Dark Matter Halo of NGC 5128 Using a Discrete Dynamical Model.* A&A **685**, A132 (2024)

Ebrová I., Jungwiert B., Canalizo G., Bennert N., & Jílková L.: *Shell Galaxies: Dynamical Friction, Gradual Satellite Decay and Merger Dating*. In: *Galaxy Wars: Stellar Populations and Star Formation in Interacting Galaxies.* Astronomical Society of the Pacific Conference Series **423** (2010)

Ebrová I. & Łokas E. L.: *Galaxies with Prolate Rotation in Illustris.* ApJ **850**, 144 (2017)

Ebrová I., Bílek M., Vudragović A., Yıldız M. K., & Duc P.-A.: *Ubiquitous Signs of Interactions in Early-Type Galaxies with Prolate Rotation.* A&A **650**, A50 (2021)

El-Badry K., Rix H.-W., & Weisz D. R.: *An Empirical Measurement of the Initial-Final Mass Relation with Gaia White Dwarfs.* ApJ **860**, L17 (2018)

El-Badry K., Quataert E., Weisz D. R., Choksi N., & Boylan-Kolchin M.: *The Formation and Hierarchical Assembly of Globular Cluster Populations.* MNRAS **482**, 4528 (2019)

Elmegreen B. G. & Efremov Y. N.: *A Universal Formation Mechanism for Open and Globular Clusters in Turbulent Gas.* ApJ **480**, 235 (1997)

Emami R., Hernquist L., Alcock C., Genel S., Bose S., Weinberger R., Vogelsberger M., Shen X., Speagle J. S., Marinacci F., et al.: *Inferring the Morphology of Stellar Distribution in TNG50: Twisted and Twisted-Stretched Shapes.* ApJ **918**, 7 (2021)

Emsellem E., Cappellari M., Krajnović D., van de Ven G., Bacon R., Bureau M., Davies R. L., de Zeeuw P. T., Falcón-Barroso J., Kuntschner H., et al.: *The SAURON Project - IX. A Kinematic Classification for Early-Type Galaxies.* MNRAS **379**, 401 (2007)

Emsellem E., Cappellari M., Krajnović D., Alatalo K., Blitz L., Bois M., Bournaud F., Bureau M., Davies R. L., Davis T. A., et al.: *The ATLAS3D Project - III. A Census of the Stellar Angular Momentum within the Effective Radius of Early-Type Galaxies: Unveiling the Distribution of Fast and Slow Rotators.* MNRAS **414**, 888 (2011)

Ennis A. I., Hartke J., Bian F., Pulsoni C., Spiniello C., Arnaboldi M., & de Propris R.: *Planetary Nebulae as Tracers of Stellar Population Properties: A Pilot Study with MUSE.* MNRAS **545**, staf2036 (2026)

Erb D. K., Shapley A. E., Pettini M., Steidel C. C., Reddy N. A., & Adelberger K. L.: *The Mass-Metallicity Relation at Z>~2.* ApJ **644**, 813 (2006)

Espejo Salcedo J. M., Glazebrook K., Fisher D. B., Sweet S. M., Obreschkow D., & Schreiber N. M. F.: *A Shallow Slope for the Stellar Mass-Angular Momentum Relation of Star-Forming Galaxies at 1.5 < z < 2.5.* MNRAS **536**, 1188 (2025)

Euclid Collaboration: *Euclid Preparation. XVI. Exploring the Ultra-Low Surface Brightness Universe with Euclid/VIS.* A&A **657**, A92 (2022)

Fabjan D., Borgani S., Tornatore L., Saro A., Murante G., & Dolag K.: *Simulating the Effect of Active Galactic Nuclei Feedback on the Metal Enrichment of Galaxy Clusters.* MNRAS **401**, 1670 (2010)

Fahrion K., Lyubenova M., Hilker M., van de Ven G., Falcón-Barroso J., Leaman R., Martín-Navarro I., Bittner A., Coccato L., Corsini E. M., et al.: *The Fornax 3D Project: Globular Clusters Tracing Kinematics and Metallicities.* A&A **637**, A26 (2020)

Fahrion K., Beasley M. A., Gvozdenko A., van de Ven G., Rhode K. L., Chies-Santos A. L., Ferre-Mateu A., Rejkuba M., Müller O., & Emsellem E.: *Distance Measurements from the Internal Dynamics of Globular Clusters: Application to the Sombrero Galaxy (M 104).* The Open Journal of Astrophysics **9**, 55146 (2026)

Faifer F. R., Forte J. C., Norris M. A., Bridges T., Forbes D. A., Zepf S. E., Beasley M., Gebhardt K., Hanes D. A., & Sharples R. M.: *Gemini/GMOS Imaging of Globular Cluster Systems in Five Early-Type Galaxies*.* MNRAS **416**, 155 (2011)

Fall S. M. & Efstathiou G.: *Formation and Rotation of Disc Galaxies with Haloes.* MNRAS **193**, 189 (1980)

Fall S. M.: *Galaxy Formation - Some Comparisons between Theory and Observation.* In: *Internal Kinematics and Dynamics of Galaxies.* **100**, 391 (1983)

Fall S. M. & Rees M. J.: *A Theory for the Origin of Globular Clusters.* ApJ **298**, 18 (1985)

Fall S. M. & Romanowsky A. J.: *Angular Momentum and Galaxy Formation Revisited: Effects of Variable Mass-to-light Ratios.* ApJ **769**, L26 (2013)

Fang G., Kong X., Chen Y., & Lin X.: *Passive and Star-forming Galaxies at 1.4 <= z <= 2.5 in the AEGIS Field.* ApJ **751**, 109 (2012)

Feldmeier J. J., Ciardullo R., & Jacoby G. H.: *Planetary Nebulae as Standard Candles. XI. Application to Spiral Galaxies.* ApJ **479**, 231 (1997)

Fensch J., Duc P.-A., Lim S., Emsellem É., Bílek M., Durrell P., Liu C., Peng É., & Smith R.: *Shedding Light on the Formation Mechanism of Shell Galaxy NGC 474 with MUSE.* A&A **644**, A164 (2020)

Ferguson A. M. N. & Mackey A. D.: *Substructure and Tidal Streams in the Andromeda Galaxy and Its Satellites.* In: *Tidal Streams in the Local Group and Beyond.* Astrophysics and Space Science Library **420**, 191 (2016)

Fernando N., Arias V., Guglielmo M., Lewis G. F., Ibata R. A., & Power C.: *On the Stability of Satellite Planes - I. Effects of Mass, Velocity, Halo Shape and Alignment.* MNRAS **465**, 641 (2017)

Ferré-Mateu A., Forbes D. A., McDermid R. M., Romanowsky A. J., & Brodie J. P.: *Spatially Resolved Stellar Populations and Kinematics with KCWI: Probing the Assembly History of the Massive Early-Type Galaxy NGC 1407.* ApJ **878**, 129 (2019)

Forbes D. A., Brodie J. P., & Grillmair C. J.: *On the Origin of Globular Clusters in Elliptical and cD Galaxies.* AJ **113**, 1652 (1997)

Forbes D. A. & Bridges T.: *Accreted versus in Situ Milky Way Globular Clusters.* MNRAS **404**, 1203 (2010)

Forbes D. A., Spitler L. R., Strader J., Romanowsky A. J., Brodie J. P., & Foster C.: *Evidence for Two Phases of Galaxy Formation from Radial Trends in the Globular Cluster System of NGC 1407.* MNRAS **413**, 2943 (2011)

Forbes D. A., Ponman T., & O'Sullivan E.: *The Baryonic Haloes of Elliptical Galaxies: Radial Distribution of Globular Clusters and Diffuse Hot Gas.* MNRAS **425**, 66 (2012)

Forbes D. A., Alabi A., Romanowsky A. J., Brodie J. P., Strader J., Usher C., & Pota V.: *The SLUGGS Survey: Globular Clusters and the Dark Matter Content of Early-Type Galaxies.* MNRAS **458**, L44 (2016)

Forbes D. A., Sinpetru L., Savorgnan G., Romanowsky A. J., Usher C., & Brodie J.: *The SLUGGS Survey: Stellar Masses and Effective Radii of Early-Type Galaxies from Spitzer Space Telescope 3.6 μm Imaging.* MNRAS **464**, 4611 (2017)

Forbes D. A., Bastian N., Gieles M., Crain R. A., Kruijssen J. M. D., Larsen S. S., Ploeckinger S., Agertz O., Trenti M., Ferguson A. M. N., et al.: *Globular Cluster Formation and Evolution in the Context of Cosmological Galaxy Assembly: Open Questions.* Proceedings of the Royal Society of London Series A **474**, 20170616 (2018a)

Forbes D. A., Read J. I., Gieles M., & Collins M. L. M.: *Extending the Globular Cluster System-Halo Mass Relation to the Lowest Galaxy Masses.* MNRAS **481**, 5592 (2018b)

Forbes D. A. & Remus R.-S.: *Metallicity Gradients in the Globular Cluster Systems of Early-Type Galaxies: In Situ and Accreted Components?* MNRAS **479**, 4760 (2018)

Forbes D. A.: *Reverse Engineering the Milky Way.* MNRAS **493**, 847 (2020)

Forbes D. A. & Romanowsky A. J.: *Reconstructing the Genesis of a Globular Cluster System at a Look-Back Time of 9.1 Gyr with the JWST.* MNRAS **520**, L58 (2023)

Forbes D. A. & Gannon J. S.: *Do Ultra-Diffuse Galaxies Follow the Globular Cluster-halo Mass Relation?* MNRAS **543**, L1 (2025)

Ford H. C. & Jacoby G. H.: *Planetary Nebulae in Local Group Galaxies. V. The Andromeda Galaxy.* ApJ **219**, 437 (1978)

Forrest B., Marsan Z. C., Annunziatella M., Wilson G., Muzzin A., Marchesini D., Cooper M. C., Chan J. C. C., McConachie I., Gomez P., et al.: *The Massive Ancient Galaxies at z > 3 NEar-infrared (MAGAZ3NE) Survey: Confirmation of Extremely Rapid Star Formation and Quenching Timescales for Massive Galaxies in the Early Universe.* ApJ **903**, 47 (2020)

Förster P. U., Remus R.-S., Dolag K., Kimmig L. C., Teklu A., & Valenzuela L. M.: *Planes of Satellite Galaxies in the Magneticum Pathfinder Simulations.* arXiv e-prints, arXiv:2208.05496 (2022)

Forte J. C., Faifer F., & Geisler D.: *Globular Clusters as Tracers of Stellar Bimodality in Elliptical Galaxies: The Case of NGC 1399.* MNRAS **357**, 56 (2005)

Fortuné S., Remus R.-S., Kimmig L. C., Burkert A., & Dolag K.: *Die Hard: The on-off Cycle of Galaxies on the Star Formation Main Sequence.* A&A **704**, A185 (2025)

Foster C., Spitler L. R., Romanowsky A. J., Forbes D. A., Pota V., Bekki K., Strader J., Proctor R. N., Arnold J. A., & Brodie J. P.: *Global Properties of 'ordinary' Early-Type Galaxies: Photometry and Spectroscopy of Stars and Globular Clusters in NGC 4494.* MNRAS **415**, 3393 (2011)

Foster C., Pastorello N., Roediger J., Brodie J. P., Forbes D. A., Kartha S. S., Pota V., Romanowsky A. J., Spitler L. R., Strader J., et al.: *The SLUGGS Survey: Stellar Kinematics, Kinemetry and Trends at Large Radii in 25 Early-Type Galaxies.* MNRAS **457**, 147 (2016)

Freeman K. C.: *On the Disks of Spiral and S0 Galaxies.* ApJ **160**, 811 (1970)

Freeman K. & Bland-Hawthorn J.: *The New Galaxy: Signatures of Its Formation.* ARA&A **40**, 487 (2002)

Frew D. J.: *Planetary Nebulae in the Solar Neighbourhood: Statistics, Distance Scale and Luminosity Function.* Macquarie University, Department of Physics and Astronomy (2008)

Fritz T. K., Di Cintio A., Battaglia G., Brook C., & Taibi S.: *The Mass of Our Galaxy from Satellite Proper Motions in the Gaia Era.* MNRAS **494**, 5178 (2020)

Fujimoto S., Ouchi M., Kohno K., Valentino F., Giménez-Arteaga C., Brammer G. B., Furtak L. J., Kohandel M., Oguri M., Pallottini A., et al.: *Primordial Rotating Disk Composed of at Least 15 Dense Star-Forming Clumps at Cosmic Dawn.* Nature **9**, 1553 (2025)

Gadotti D. A.: *Robust Galaxy Image Decompositions with Differential Evolution Optimization and the Problem of Classical Bulges in and beyond the Nearby Universe.* MNRAS **545**, staf2072 (2026)

Gaia Collaboration: *Gaia Data Release 1. Summary of the Astrometric, Photometric, and Survey Properties.* A&A **595**, A2 (2016)

Gaia Collaboration: *Gaia Data Release 2. Kinematics of Globular Clusters and Dwarf Galaxies around the Milky Way.* A&A **616**, A12 (2018a)

Gaia Collaboration: *Gaia Data Release 2. Summary of the Contents and Survey Properties.* A&A **616**, A1 (2018b)

Gaia Collaboration: *Gaia Data Release 3. Summary of the Content and Survey Properties.* A&A **674**, A1 (2023)

Galán-de Anta P. M., Sarzi M., Spriggs T. W., Nedelchev B., Pinna F., Martín-Navarro I., Coccato L., Corsini E. M., de Zeeuw P. T., Falcón-Barroso J., et al.: *The Fornax 3D Project: PNe Populations and Stellar Metallicity in Edge-on Galaxies.* A&A **652**, A109 (2021)

Galera-Rosillo R., Mampaso A., Corradi R. L. M., García-Rojas J., Balick B., Jones D., Kwitter K. B., Magrini L., & Villaver E.: *On the Most Luminous Planetary Nebulae of M 31.* A&A **657**, A71 (2022)

Gallart C., Bernard E. J., Brook C. B., Ruiz-Lara T., Cassisi S., Hill V., & Monelli M.: *Uncovering the Birth of the Milky Way through Accurate Stellar Ages with Gaia.* Nature **3**, 932 (2019)

Gallazzi A., Charlot S., Brinchmann J., White S. D. M., & Tremonti C. A.: *The Ages and Metallicities of Galaxies in the Local Universe.* MNRAS **362**, 41 (2005)

Gallazzi A., Bell E. F., Zibetti S., Brinchmann J., & Kelson D. D.: *Charting the Evolution of the Ages and Metallicities of Massive Galaxies since $z = 0.7$.* ApJ **788**, 72 (2014)

Garro E. R., Minniti D., & Fernández-Trincado J. G.: *Over 200 Globular Clusters in the Milky Way and Still None with Super-Solar Metallicity.* A&A **687**, A214 (2024)

Genzel R., Tacconi L. J., Gracia-Carpio J., Sternberg A., Cooper M. C., Shapiro K., Bolatto A., Bouché N., Bournaud F., Burkert A., et al.: *A Study of the Gas-Star Formation Relation over Cosmic Time.* MNRAS **407**, 2091 (2010)

Georgiev I. Y., Goudfrooij P., & Puzia T. H.: *New Insights into the Star Formation Histories of Candidate Intermediate-Age Early-Type Galaxies from K'-Band Imaging of Globular Clusters.* MNRAS **420**, 1317 (2012)

Gerhard O. E.: *N-Body Simulations of Disc-Halo Galaxies - Isolated Systems, Tidal Interactions and Merging.* MNRAS **197**, 179 (1981)

Gerhard O., Arnaboldi M., Freeman K. C., Kashikawa N., Okamura S., & Yasuda N.: *Detection of Intracluster Planetary Nebulae in the Coma Cluster.* ApJ **621**, L93 (2005)

Gesicki K., Zijlstra A. A., & Miller Bertolami M. M.: *The Mysterious Age Invariance of the Planetary Nebula Luminosity Function Bright Cut-Off.* Nature **2**, 580 (2018)

Gillman S., Tiley A. L., Swinbank A. M., Harrison C. M., Smail I., Dudzevičiūtė U., Sharples R. M., Cortese L., Obreschkow D., Bower R. G., et al.: *From Peculiar Morphologies to Hubble-type Spirals: The Relation between Galaxy Dynamics and Morphology in Star-Forming Galaxies at $z \sim 1.5$.* MNRAS **492**, 1492 (2020)

Gnedin O. Y.: *Tidal Effects in Clusters of Galaxies.* ApJ **582**, 141 (2003)

Gonçalves G., Coelho P., Schiavon R., & Usher C.: *How Well Can We Determine Ages and Chemical Abundances from Spectral Fitting of Integrated Light Spectra?* MNRAS **499**, 2327 (2020)

Gordon A. J., Ferguson A. M. N., & Mann R. G.: *Uncovering Tidal Treasures: Automated Classification of Faint Tidal Features in DECaLS Data.* MNRAS **534**, 1459 (2024)

Goudfrooij P., Alonso M. V., Maraston C., & Minniti D.: *The Star Cluster System of the 3-Gyr-Old Merger Remnant NGC 1316: Clues from Optical and near-Infrared Photometry.* MNRAS **328**, 237 (2001a)

Goudfrooij P., Mack J., Kissler-Patig M., Meylan G., & Minniti D.: *Kinematics, Ages and Metallicities of Star Clusters in NGC 1316: A 3-Gyr-Old Merger Remnant.* MNRAS **322**, 643 (2001b)

Gratton R., Bragaglia A., Carretta E., D'Orazi V., Lucatello S., & Sollima A.: *What Is a Globular Cluster? An Observational Perspective.* A&A Rev. **27**, 8 (2019)

Gray E. I., Read J. I., Taylor E., Orkney M. D. A., Rey M. P., Yates R. M., Kim S. Y., Noël N. E. D., Agertz O., Andersson E. P., & Pontzen A.: *EDGE: A New Model for Nuclear Star Cluster Formation in Dwarf Galaxies.* MNRAS **539**, 1167 (2025)

Gu M., Conroy C., & Behroozi P.: *Hierarchical Galaxy Growth and Scatter in the Stellar Mass-Halo Mass Relation.* ApJ **833**, 2 (2016)

Guérou A., Emsellem E., Krajnović D., McDermid R. M., Contini T., & Weilbacher P. M.: *Exploring the Mass Assembly of the Early-Type Disc Galaxy NGC 3115 with MUSE.* A&A **591**, A143 (2016)

Gunn J. E. & Gott J. R., III: *On the Infall of Matter Into Clusters of Galaxies and Some Effects on Their Evolution.* ApJ **176**, 1 (1972)

Guszejnov D., Markey C., Offner S. S. R., Grudić M. Y., Faucher-Giguère C.-A., Rosen A. L., & Hopkins P. F.: *Cluster Assembly and the Origin of Mass Segregation in the STARFORGE Simulations.* MNRAS **515**, 167 (2022)

Habas R., Marleau F. R., Duc P.-A., Durrell P. R., Paudel S., Poulain M., Sánchez-Janssen R., Sreejith S., Ramasawmy J., Stemock B., et al.: *Newly Discovered Dwarf Galaxies in the MATLAS Low-Density Fields.* MNRAS **491**, 1901 (2020)

Hammer F., Yang Y. B., Wang J. L., Ibata R., Flores H., & Puech M.: *A 2-3 Billion Year Old Major Merger Paradigm for the Andromeda Galaxy and Its Outskirts.* MNRAS **475**, 2754 (2018)

Han J. J., Conroy C., & Hernquist L.: *A Tilted Dark Halo Origin of the Galactic Disk Warp and Flare.* Nature **7**, 1481 (2023)

Harris G. L. H.: *NGC 5128: The Giant Beneath.* PASA **27**, 475 (2010)

Harris J. & Zaritsky D.: *The Star Formation History of the Large Magellanic Cloud.* AJ **138**, 1243 (2009)

Harris W. E. & Pudritz R. E.: *Supergiant Molecular Clouds and the Formation of Globular Cluster Systems.* ApJ **429**, 177 (1994)

Harris W. E. & Harris G. L. H.: *The Halo Stars in NGC 5128. III. An Inner Halo Field and the Metallicity Distribution.* AJ **123**, 3108 (2002)

Harris W. E., Harris G. L. H., Barmby P., McLaughlin D. E., & Forbes D. A.: *Structural Parameters for Globular Clusters in NGC 5128. II. Hubble Space Telescope ACS Imaging and New Clusters.* AJ **132**, 2187 (2006)

Harris W. E., Harris G. L. H., Layden A. C., & Wehner E. M. H.: *The Leo Elliptical NGC 3379: A Metal-Poor Halo Emerges.* ApJ **666**, 903 (2007)

Harris W. E., Harris G. L. H., & Alessi M.: *A Catalog of Globular Cluster Systems: What Determines the Size of a Galaxy's Globular Cluster Population?* ApJ **772**, 82 (2013)

Harris W. E., Harris G. L., & Hudson M. J.: *Dark Matter Halos in Galaxies and Globular Cluster Populations. II. Metallicity and Morphology.* ApJ **806**, 36 (2015)

Harris W. E., Blakeslee J. P., Whitmore B. C., Gnedin O. Y., Geisler D., & Rothberg B.: *Globular Cluster Systems in Brightest Cluster Galaxies. II. NGC 6166.* ApJ **817**, 58 (2016)

Harris W. E., Blakeslee J. P., & Harris G. L. H.: *Galactic Dark Matter Halos and Globular Cluster Populations. III. Extension to Extreme Environments.* ApJ **836**, 67 (2017a)

Harris W. E., Ciccone S. M., Eadie G. M., Gnedin O. Y., Geisler D., Rothberg B., & Bailin J.: *Globular Cluster Systems in Brightest Cluster Galaxies. III: Beyond Bimodality.* ApJ **835**, 101 (2017b)

Harris W. E., Remus R.-S., Harris G. L. H., & Babyk I. V.: *Measuring Dark Matter in Galaxies: The Mass Fraction within Five Effective Radii.* ApJ **905**, 28 (2020)

Harris W. E., Reina-Campos M., Keatley K. E., Bradač M., Martis N. S., Muzzin A., Noirot G., Sarrouh G. T. E., Sawicki M., Willott C. J., & Berek S. C.: *JWST Photometry of Globular Cluster Populations in MACS0417.5-1154.* ApJ **993**, 210 (2025)

Harrison C. M., Johnson H. L., Swinbank A. M., Stott J. P., Bower R. G., Smail I., Tiley A. L., Bunker A. J., Cirasuolo M., Sobral D., et al.: *The KMOS Redshift One Spectroscopic Survey (KROSS): Rotational Velocities and Angular Momentum of $z \approx 0.9$ Galaxies.* MNRAS **467**, 1965 (2017)

Hartke J., Arnaboldi M., Longobardi A., Gerhard O., Freeman K. C., Okamura S., & Nakata F.: *The Halo of M 49 and Its Environment as Traced by Planetary Nebulae Populations.* A&A **603**, A104 (2017)

Hartke J., Arnaboldi M., Gerhard O., Coccato L., Pulsoni C., Freeman K. C., Merrifield M., Cortesi A., & Kuijken K.: *The Halo of M 105 and Its Group Environment as Traced by Planetary Nebula Populations. I. Wide-field Photometric Survey of Planetary Nebulae in the Leo I Group.* A&A **642**, A46 (2020)

Hartke J., Arnaboldi M., Gerhard O., Coccato L., Merrifield M., Kuijken K., Pulsoni C., Agnello A., Bhattacharya S., Spiniello C., et al.: *The Halo of M 105 and Its Group Environment as Traced by Planetary Nebula Populations. II. Using Kinematics of Single Stars to Unveil the Presence of Intragroup Light around the Leo I Galaxies NGC 3384 and M 105.* A&A **663**, A12 (2022)

Hartke J.: *Planetary Nebulae as Tracers of Accreted Stellar Populations in Massive Galaxies in Groups and Clusters.* Frontiers in Astronomy and Space Sciences **12**, 1673373 (2025)

Hartke J., Arnaboldi M., Pulsoni C., Bhattacharya S., Bureau M., Congiu E., Flint G., Gerhard O., Roth M., Soemitro A., et al.: *Extragalactic Planetary Nebulae – Tracers of Kinematics and Stellar Populations out to 100 Mpc.* arXiv e-prints, arXiv:2601.11324 (2026)

Hayashi E., Navarro J. F., & Springel V.: *The Shape of the Gravitational Potential in Cold Dark Matter Haloes.* MNRAS **377**, 50 (2007)

Haywood M., Di Matteo P., Lehnert M. D., Snaith O., Khoperskov S., & Gómez A.: *In Disguise or Out of Reach: First Clues about In Situ and Accreted Stars in the Stellar Halo of the Milky Way from Gaia DR2.* ApJ **863**, 113 (2018)

Heesters N., Habas R., Marleau F. R., Müller O., Duc P.-A., Poulain M., Durrell P., Sánchez-Janssen R., & Paudel S.: *Flattened Structures of Dwarf Satellites around Massive Host Galaxies in the MATLAS Low-to-Moderate Density Fields.* A&A **654**, A161 (2021)

Hegde S., Bryan G. L., & Genel S.: *Reorientation Rates of Structural and Kinematic Axes in Simulated Massive Galaxies and the Origins of Prolate Rotation.* ApJ **937**, 38 (2022)

Heggie D. C.: *Binary Evolution in Stellar Dynamics.* MNRAS **173**, 729 (1975)

Helmi A., White S. D. M., de Zeeuw P. T., & Zhao H.: *Debris Streams in the Solar Neighbourhood as Relicts from the Formation of the Milky Way.* Nature **402**, 53 (1999)

Helmi A., Babusiaux C., Koppelman H. H., Massari D., Veljanoski J., & Brown A. G. A.: *The Merger That Led to the Formation of the Milky Way's Inner Stellar Halo and Thick Disk.* Nature **563**, 85 (2018)

Helmi A.: *Streams, Substructures, and the Early History of the Milky Way.* ARA&A **58**, 205 (2020)

Hendel D. & Johnston K. V.: *Tidal Debris Morphology and the Orbits of Satellite Galaxies.* MNRAS **454**, 2472 (2015)

Henize K. G. & Westerlund B. E.: *Dimensions of Diffuse and Planetary Nebulae in the Small Magellanic Cloud.* ApJ **137**, 747 (1963)

Hernández-Martínez L. & Peña M.: *Emission line objects in NGC 6822. New planetary nebula candidates.* A&A **495**, 447 (2009)

Hernquist L. & Quinn P. J.: *Formation of Shell Galaxies. I. Spherical Potentials.* ApJ **331**, 682 (1988)

Hillenbrand L. A. & Hartmann L. W.: *A Preliminary Study of the Orion Nebula Cluster Structure and Dynamics.* ApJ **492**, 540 (1998)

Hills J. G.: *Encounters between Binary and Single Stars and Their Effect on the Dynamical Evolution of Stellar Systems.* AJ **80**, 809 (1975)

Hilz M., Naab T., Ostriker J. P., Thomas J., Burkert A., & Jesseit R.: *Relaxation and Stripping - The Evolution of Sizes, Dispersions and Dark Matter Fractions in Major and Minor Mergers of Elliptical Galaxies.* MNRAS **425**, 3119 (2012)

Hilz M., Naab T., & Ostriker J. P.: *How Do Minor Mergers Promote Inside-out Growth of Ellipticals, Transforming the Size, Density Profile and Dark Matter Fraction?* MNRAS **429**, 2924 (2013)

Hirschmann M., Dolag K., Saro A., Bachmann L., Borgani S., & Burkert A.: *Cosmological Simulations of Black Hole Growth: AGN Luminosities and Downsizing.* MNRAS **442**, 2304 (2014)

Hirschmann M., De Lucia G., & Fontanot F.: *Galaxy Assembly, Stellar Feedback and Metal Enrichment: The View from the GAEA Model.* MNRAS **461**, 1760 (2016)

Hoffman L., Cox T. J., Dutta S., & Hernquist L.: *Orbital Structure of Merger Remnants. I. Effect of Gas Fraction in Pure Disk Mergers.* ApJ **723**, 818 (2010)

Hohl F.: *Numerical Experiments with a Disk of Stars.* ApJ **168**, 343 (1971)

Hollands M. A., Littlefair S. P., & Parsons S. G.: *Measuring the Initial-Final Mass Relation Using Wide Double White Dwarf Binaries from Gaia DR3.* MNRAS **527**, 9061 (2024)

Horta D., Schiavon R. P., Mackereth J. T., Beers T. C., Fernández-Trincado J. G., Frinchaboy P. M., García-Hernández D. A., Geisler D., Hasselquist S., Jönsson H., et al.: *The Chemical Compositions of Accreted and in Situ Galactic Globular Clusters According to SDSS/APOGEE.* MNRAS **493**, 3363 (2020)

Horta D., Schiavon R. P., Mackereth J. T., Pfeffer J., Mason A. C., Kisku S., Fragkoudi F., Allende Prieto C., Cunha K., Hasselquist S., et al.: *Evidence from APOGEE for the Presence of a Major Building Block of the Halo Buried in the Inner Galaxy.* MNRAS **500**, 1385 (2021)

Horta D., Schiavon R. P., Mackereth J. T., Weinberg D. H., Hasselquist S., Feuillet D., O'Connell R. W., Anguiano B., Allende-Prieto C., Beaton R. L., et al.: *The Chemical Characterization of Halo Substructure in the Milky Way Based on APOGEE.* MNRAS **520**, 5671 (2023)

Hubble E. P.: *Extragalactic Nebulae.* ApJ **64**, 321 (1926)

Hubble E. P.: *Realm of the Nebulae.* Yale University Press (1936)

Hughes A. K., Sand D. J., Seth A., Strader J., Voggel K., Dumont A., Crnojević D., Caldwell N., Forbes D. A., Simon J. D., et al.: *NGC 5128 Globular Cluster Candidates Out to 150 Kpc: A Comprehensive Catalog from Gaia and Ground-based Data.* ApJ **914**, 16 (2021)

Hui X., Ford H. C., Ciardullo R., & Jacoby G. H.: *The Planetary Nebula System and Dynamics of NGC 5128. I. Planetary Nebulae as Standard Candles.* ApJ **414**, 463 (1993)

Hui X., Ford H. C., Freeman K. C., & Dopita M. A.: *The Planetary Nebula System and Dynamics of NGC 5128. III. Kinematics and Halo Mass Distributions.* ApJ **449**, 592 (1995)

Huxor A. P., Mackey A. D., Ferguson A. M. N., Irwin M. J., Martin N. F., Tanvir N. R., Veljanoski J., McConnachie A., Fishlock C. K., Ibata R., & Lewis G. F.: *The Outer Halo Globular Cluster System of M31 - I. The Final PAndAS Catalogue.* MNRAS **442**, 2165 (2014)

Ibata R. A., Gilmore G., & Irwin M. J.: *A Dwarf Satellite Galaxy in Sagittarius.* Nature **370**, 194 (1994)

Ibata R. A., Lewis G. F., Conn A. R., Irwin M. J., McConnachie A. W., Chapman S. C., Collins M. L., Fardal M., Ferguson A. M. N., Ibata N. G., et al.: *A Vast, Thin Plane of Corotating Dwarf Galaxies Orbiting the Andromeda Galaxy.* Nature **493**, 62 (2013)

Ibata R. A., Lewis G. F., McConnachie A. W., Martin N. F., Irwin M. J., Ferguson A. M. N., Babul A., Bernard E. J., Chapman S. C., Collins M., et al.: *The Large-Scale Structure of the Halo of the Andromeda Galaxy. I. Global Stellar Density, Morphology and Metallicity Properties.* ApJ **780**, 128 (2014)

Iben I.: *Planetary Nebulae and Their Central Stars — Origin and Evolution.* Phys. Rep. **250**, 1 (1995)

Iben I., Jr. & Renzini A.: *Asymptotic Giant Branch Evolution and Beyond.* ARA&A **21**, 271 (1983)

Iodice E., Sarzi M., Bittner A., Coccato L., Costantin L., Corsini E. M., van de Ven G., de Zeeuw P. T., Falcón-Barroso J., Gadotti D. A., et al.: *The Fornax3D Project: Tracing the Assembly History of the Cluster from the Kinematic and Line-Strength Maps.* A&A **627**, A136 (2019a)

Iodice E., Spavone M., Capaccioli M., Peletier R. F., van de Ven G., Napolitano N. R., Hilker M., Mieske S., Smith R., Pasquali A., et al.: *The Fornax Deep Survey with the VST. V. Exploring the Faintest Regions of the Bright Early-Type Galaxies inside the Virial Radius.* A&A **623**, A1 (2019b)

Ito K., Valentino F., Brammer G., Faisst A. L., Gillman S., Gómez-Guijarro C., Gould K. M. L., Heintz K. E., Ilbert O., Jespersen C. K., et al.: *Size-Stellar Mass Relation and Morphology of Quiescent Galaxies at $z \geq 3$ in Public JWST Fields.* ApJ **964**, 192 (2024)

Ito K., Tanaka T. S., Shimasaku K., Ando M., Onoue M., Tanaka M., Matsui S., Kakimoto T., & Valentino F.: *Black Hole Mass of a Quiescent Galaxy Hosting a Type 1 AGN at $z = 2.09$: Implications for Black Hole-Galaxy Coevolution and AGN Quenching at High Redshift.* MNRAS **538**, 1501 (2025)

Ivezić Ž., Kahn S. M., Tyson J. A., Abel B., Acosta E., Allsman R., Alonso D., AlSayyad Y., Anderson S. F., Andrew J., et al.: *LSST: From Science Drivers to Reference Design and Anticipated Data Products.* ApJ **873**, 111 (2019)

Izotov Y. I. & Thuan T. X.: *Systematic Effects and a New Determination of the Primordial Abundance of 4He and dY/dZ from Observations of Blue Compact Galaxies.* ApJ **602**, 200 (2004)

Jacoby G. H.: *The Luminosity Function for Planetary Nebulae and the Number of Planetary Nebulae in Local Group Galaxies.* ApJS **42**, 1 (1980)

Jacoby G. H.: *Planetary Nebulae as Standard Candles. I. Evolutionary Models.* ApJ **339**, 39 (1989)

Jacoby G. H., Ciardullo R., Ford H. C., & Booth J.: *Planetary Nebulae as Standard Candles. III. The Distance to M81.* ApJ **344**, 704 (1989)

Jacoby G. H., Ciardullo R., & Ford H. C.: *Planetary Nebulae as Standard Candles. V. The Distance to the Virgo Cluster.* ApJ **356**, 332 (1990a)

Jacoby G. H., Walker A. R., & Ciardullo R.: *Planetary Nebulae as Standard Candles. VI. A Test in the Magellanic Clouds.* ApJ **365**, 471 (1990b)

Jacoby G. H. & De Marco O.: *A Survey for Very Faint Planetary Nebulae in the SMC. I. Identification, Confirmation, and Preliminary Analysis.* AJ **123**, 269 (2002)

Jacoby G. H., Hillwig T. C., Jones D., Martin K., De Marco O., Kronberger M., Hurowitz J. L., Crocker A. F., & Dey J.: *Binary Central Stars of Planetary Nebulae Identified with Kepler/K2.* MNRAS **506**, 5223 (2021)

Jacoby G. H., Ciardullo R., Roth M. M., Arnaboldi M., & Weilbacher P. M.: *Toward Precision Cosmology with Improved Planetary Nebula Luminosity Function Distances Using VLT-MUSE. II. A Test Sample from Archival Data.* ApJS **271**, 40 (2024)

Jacoby G. H. & Ciardullo R.: *The Critical Role of Dust on the [O III] Planetary Nebula Luminosity Function's Bright-end Cutoff.* ApJ **983**, 129 (2025)

Jeong H., Yi S. K., Bureau M., Davies R. L., Bacon R., Cappellari M., de Zeeuw P. T., Emsellem E., Falcón-Barroso J., Krajnović D., et al.: *The SAURON Project - XXI. The Spatially Resolved UV-line Strength Relations of Early-Type Galaxies.* MNRAS **423**, 1921 (2012)

Jesseit R., Cappellari M., Naab T., Emsellem E., & Burkert A.: *Specific Angular Momentum of Disc Merger Remnants and the {\ensuremath{\lambda}}$_{R}$-Parameter.* MNRAS **397**, 1202 (2009)

Jester S., Schneider D. P., Richards G. T., Green R. F., Schmidt M., Hall P. B., Strauss M. A., Vanden Berk D. E., Stoughton C., Gunn J. E., et al.: *The Sloan Digital Sky Survey View of the Palomar-Green Bright Quasar Survey.* AJ **130**, 873 (2005)

Jian H.-Y., Lin L., & Chiueh T.: *Environmental Dependence of the Galaxy Merger Rate in a ΛCDM Universe.* ApJ **754**, 26 (2012)

Jimenez R., Flynn C., MacDonald J., & Gibson B. K.: *The Cosmic Production of Helium.* Science **299**, 1552 (2003)

Jin Y., Zhu L., Long R. J., Mao S., Wang L., & van de Ven G.: *SDSS-IV MaNGA: Internal Mass Distributions and Orbital Structures of Early-Type Galaxies and Their Dependence on Environment.* MNRAS **491**, 1690 (2020)

Johnston K. V., Zhao H., Spergel D. N., & Hernquist L.: *Tidal Streams as Probes of the Galactic Potential.* ApJ **512**, L109 (1999)

Johnston K. V., Bullock J. S., Sharma S., Font A., Robertson B. E., & Leitner S. N.: *Tracing Galaxy Formation with Stellar Halos. II. Relating Substructure in Phase and Abundance Space to Accretion Histories.* ApJ **689**, 936 (2008)

Jones D. & Boffin H. M. J.: *Binary Stars as the Key to Understanding Planetary Nebulae.* Nature **1**, 0117 (2017)

Kado-Fong E., Greene J. E., Hendel D., Price-Whelan A. M., Greco J. P., Goulding A. D., Huang S., Johnston K. V., Komiyama Y., Lee C.-H., et al.: *Tidal Features at $0.05 < z < 0.45$ in the Hyper Suprime-Cam Subaru Strategic Program: Properties and Formation Channels.* ApJ **866**, 103 (2018)

Kakimoto T., Tanaka M., Onodera M., Shimakawa R., Wu P.-F., Gould K. M. L., Ito K., Jin S., Kubo M., Suzuki T. L., et al.: *A Massive Quiescent Galaxy in a Group Environment at $z = 4.53$.* ApJ **963**, 49 (2024)

Kang J. & Lee M. G.: *Globular Cluster Systems of Massive Compact Elliptical Galaxies in the Local Universe: Evidence for Relic Red Nuggets?* ApJ **914**, 20 (2021)

Karachentsev I. D. & Kroupa P.: *A Co-Rotating Gas and Satellite Structure around the Interacting Galaxy Pair NGC 4490/85.* MNRAS **528**, 2805 (2024)

Karademir G. S., Remus R.-S., Burkert A., Dolag K., Hoffmann T. L., Moster B. P., Steinwandel U. P., & Zhang J.: *The Outer Stellar Halos of Galaxies: How Radial Merger Mass Deposition, Shells, and Streams Depend on Infall-Orbit Configurations.* MNRAS **487**, 318 (2019)

Kashino D., Lilly S. J., Renzini A., Daddi E., Zamorani G., Silverman J. D., Ilbert O., Peng Y.-j., Mainieri V., Bardelli S., et al.: *The Stellar Mass versus Stellar Metallicity Relation of Star-forming Galaxies at $1.6 \leq z \leq 3.0$ and Implications for the Evolution of the α-Enhancement.* ApJ **925**, 82 (2022)

Kauffmann G., White S. D. M., Heckman T. M., Ménard B., Brinchmann J., Charlot S., Tremonti C., & Brinkmann J.: *The Environmental Dependence of the Relations between Stellar Mass, Structure, Star Formation and Nuclear Activity in Galaxies.* MNRAS **353**, 713 (2004)

Kawinwanichakij L., Glazebrook K., Nanayakkara T., Kacprzak G. G., Chittenden H. G., Jacobs C., Chandro-Gómez Á., Lagos C., Marchesini D., Martìnez-Marìn M., et al.: *Connecting Environment, Star Formation History, and Morphology of Massive Quiescent Galaxies at $3 < z < 4$ with JWST.* ApJ **997**, 29 (2026)

Kelson D. D.: *Decoding the Star-Forming Main Sequence or: How I Learned to Stop Worrying and Love the Central Limit Theorem.* arXiv e-prints, arXiv:1406..5191 (2014)

Keszthelyi Z., Puls J., Chiaki G., Nagakura H., ud-Doula A., Takiwaki T., & Tominaga N.: *The Effects of Surface Fossil Magnetic Fields on Massive Star Evolution: V. Models at Low Metallicity.* MNRAS **533**, 3457 (2024)

Khalid A., Brough S., Martin G., Kimmig L. C., Lagos C. D. P., Remus R. S., & Martinez-Lombilla C.: *Characterizing Tidal Features around Galaxies in Cosmological Simulations.* MNRAS **530**, 4422 (2024)

Khalid A., Brough S., Martin G., Kimmig L. C., Remus R.-S., Lagos C. d. P., Valenzuela L. M., & Wright R. J.: *Tidal Features around Simulated Groups and Cluster Galaxies: Enhancement and Suppression of Merger Events through Environment in LSST-like Mock Observations.* MNRAS **543**, 3391 (2025)

Khalid A., Brough S., Martin G., Kimmig L. C., Remus R.-S., Lagos C. d. P., Canepa L., & Desmons A.: *Investigating the Imprints of Tidal Features on Simulated Galaxy Outskirts in LSST-like Mock Observations.* MNRAS **545**, staf1989 (2026)

Kim D., Sheen Y.-K., Jaffé Y. L., Kelkar K., Ranjan A., Piraino-Cerda F., Crossett J. P., Costa Lourenço A. C., Martin G., Nantais J. B., et al.: *Distribution of Merging and Post-merger Galaxies in Nearby Galaxy Clusters.* ApJ **966**, 124 (2024)

Kim J.-h., Ma X., Grudić M. Y., Hopkins P. F., Hayward C. C., Wetzel A., Faucher-Giguère C.-A., Kereš D., Garrison-Kimmel S., & Murray N.: *Formation of Globular Cluster Candidates in Merging Proto-Galaxies at High Redshift: A View from the FIRE Cosmological Simulations.* MNRAS **474**, 4232 (2018)

Kimmig L. C., Remus R.-S., Seidel B., Valenzuela L. M., Dolag K., & Burkert A.: *Blowing Out the Candle: How to Quench Galaxies at High Redshift—An Ensemble of Rapid Starbursts, AGN Feedback, and Environment.* ApJ **979**, 15 (2025)

Kippenhahn R., Weigert A., & Weiss A.: *Stellar Structure and Evolution.* Springer Berlin (2013)

Kirby E. N., Cohen J. G., Guhathakurta P., Cheng L., Bullock J. S., & Gallazzi A.: *The Universal Stellar Mass-Stellar Metallicity Relation for Dwarf Galaxies.* ApJ **779**, 102 (2013)

Klessen R. S. & Glover S. C. O.: *The First Stars: Formation, Properties, and Impact.* ARA&A **61**, 65 (2023)

Kluge M., Neureiter B., Riffeser A., Bender R., Goessl C., Hopp U., Schmidt M., Ries C., & Brosch N.: *Structure of Brightest Cluster Galaxies and Intracluster Light.* ApJS **247**, 43 (2020)

Kluge M., Remus R.-S., Babyk I. V., Forbes D. A., & Dolfi A.: *A Trail of the Invisible: Blue Globular Clusters Trace the Radial Density Distribution of the Dark Matter - Case Study of NGC 4278.* MNRAS **521**, 4852 (2023)

Klypin A., Kravtsov A. V., Valenzuela O., & Prada F.: *Where Are the Missing Galactic Satellites?* ApJ **522**, 82 (1999)

Knowles A. T., Sansom A. E., Allende Prieto C., & Vazdekis A.: *sMILES: A Library of Semi-Empirical MILES Stellar Spectra with Variable [α/Fe] Abundances.* MNRAS **504**, 2286 (2021)

Knowles A. T., Sansom A. E., Vazdekis A., & Allende Prieto C.: *sMILES SSPs: A Library of Semi-Empirical MILES Stellar Population Models with Variable [α/Fe] Abundances.* MNRAS **523**, 3450 (2023)

Kobayashi C. & Arimoto N.: *Gradients of Absorption-Line Strengths in Elliptical Galaxies.* ApJ **527**, 573 (1999)

Kobayashi C., Karakas A. I., & Lugaro M.: *The Origin of Elements from Carbon to Uranium.* ApJ **900**, 179 (2020)

Komatsu E., Smith K. M., Dunkley J., Bennett C. L., Gold B., Hinshaw G., Jarosik N., Larson D., Nolta M. R., Page L., et al.: *Seven-Year Wilkinson Microwave Anisotropy Probe (WMAP) Observations: Cosmological Interpretation.* ApJS **192**, 18 (2011)

Koposov S. E., Rix H.-W., & Hogg D. W.: *Constraining the Milky Way Potential with a Six-Dimensional Phase-Space Map of the GD-1 Stellar Stream.* ApJ **712**, 260 (2010)

Koposov S. E., Erkal D., Li T. S., Da Costa G. S., Cullinane L. R., Ji A. P., Kuehn K., Lewis G. F., Pace A. B., Shipp N., et al.: *S* ^{5}*: Probing the Milky Way and Magellanic Clouds Potentials with the 6D Map of the Orphan-Chenab Stream.* MNRAS **521**, 4936 (2023)

Kormendy J. & Kennicutt R. C., Jr.: *Secular Evolution and the Formation of Pseudobulges in Disk Galaxies.* ARA&A **42**, 603 (2004)

Krajnović D., Emsellem E., Cappellari M., Alatalo K., Blitz L., Bois M., Bournaud F., Bureau M., Davies R. L., Davis T. A., et al.: *The ATLAS3D Project - II. Morphologies, Kinemetric Features and Alignment between Photometric and Kinematic Axes of Early-Type Galaxies.* MNRAS **414**, 2923 (2011)

Kravtsov A. V. & Gnedin O. Y.: *Formation of Globular Clusters in Hierarchical Cosmology.* ApJ **623**, 650 (2005)

Kravtsov A. & Winney S.: *Effect of the Large Magellanic Cloud on the Kinematics of Milky Way Satellites and Virial Mass Estimate.* The Open Journal of Astrophysics **7**, 50 (2024)

Kreckel K., Groves B., Bigiel F., Blanc G. A., Kruijssen J. M. D., Hughes A., Schruba A., & Schinnerer E.: *A Revised Planetary Nebula Luminosity Function Distance to NGC 628 Using MUSE.* ApJ **834**, 174 (2017)

Kroupa P.: *On the Variation of the Initial Mass Function.* MNRAS **322**, 231 (2001)

Kroupa P., Theis C., & Boily C. M.: *The Great Disk of Milky-Way Satellites and Cosmological Sub-Structures.* A&A **431**, 517 (2005)

Kruijssen J. M. D., Pelupessy F. I., Lamers H. J. G. L. M., Portegies Zwart S. F., & Icke V.: *Modelling the Formation and Evolution of Star Cluster Populations in Galaxy Simulations.* MNRAS **414**, 1339 (2011)

Kruijssen J. M. D., Pelupessy F. I., Lamers H. J. G. L. M., Portegies Zwart S. F., Bastian N., & Icke V.: *Formation versus Destruction: The Evolution of the Star Cluster Population in Galaxy Mergers.* MNRAS **421**, 1927 (2012)

Kruijssen J. M. D.: *Globular Clusters as the Relics of Regular Star Formation in 'normal' High-Redshift Galaxies.* MNRAS **454**, 1658 (2015)

Kruijssen J. M. D., Pfeffer J. L., Crain R. A., & Bastian N.: *The E-MOSAICS Project: Tracing Galaxy Formation and Assembly with the Age-Metallicity Distribution of Globular Clusters.* MNRAS **486**, 3134 (2019a)

Kruijssen J. M. D., Pfeffer J. L., Reina-Campos M., Crain R. A., & Bastian N.: *The Formation and Assembly History of the Milky Way Revealed by Its Globular Cluster Population.* MNRAS **486**, 3180 (2019b)

Kruijssen J. M. D.: *The formation of globular clusters.* In: *Encyclopedia of Astrophysics (First Edition).* **4**, 500 (2026)

Kudritzki R.-P., Teklu A. F., Schulze F., Remus R.-S., Dolag K., Burkert A., & Zahid H. J.: *Galaxy Look-back Evolution Models: A Comparison with Magneticum Cosmological Simulations and Observations.* ApJ **910**, 87 (2021)

Kudritzki R.-P., Urbaneja M. A., Bresolin F., Macri L. M., Yuan W., Li S., Anand G. S., & Riess A. G.: *The Hubble Constant Anchor Galaxy NGC 4258: Metallicity and Distance from Blue Supergiants.* ApJ **977**, 217 (2024)

Kumar P., Pawlowski M. S., Kanehisa K. J., Li P., Júlio M. P., & Taibi S.: *The Effect of Measurement Uncertainties on the Inferred Stability of Planes of Satellite Galaxies.* A&A **699**, A363 (2025)

Lagos C. d. P., Stevens A. R. H., Bower R. G., Davis T. A., Contreras S., Padilla N. D., Obreschkow D., Croton D., Trayford J. W., Welker C., & Theuns T.: *Quantifying the Impact of Mergers on the Angular Momentum of Simulated Galaxies.* MNRAS **473**, 4956 (2018)

Lagos C. d. P., Emsellem E., van de Sande J., Harborne K. E., Cortese L., Davison T., Foster C., & Wright R. J.: *The Diverse Nature and Formation Paths of Slow Rotator Galaxies in the EAGLE Simulations.* MNRAS **509**, 4372 (2022)

Lahén N., Naab T., Johansson P. H., Elmegreen B., Hu C.-Y., & Walch S.: *The Formation of Low-metallicity Globular Clusters in Dwarf Galaxy Mergers.* ApJ **879**, L18 (2019)

Laine S., Grillmair C. J., Capak P., Arendt R. G., Romanowsky A. J., Martínez-Delgado D., Ashby M. L. N., Davies J. E., Majewski S. R., Brodie J. P., et al.: *Metallicity and Age of the Stellar Stream around the Disk Galaxy NGC 5907.* AJ **152**, 72 (2016)

Lake W., Naoz S., Chiou Y. S., Burkhart B., Marinacci F., Vogelsberger M., & Kremer K.: *The Supersonic Project: SIGOs, A Proposed Progenitor to Globular Clusters, and Their Connections to Gravitational-Wave Anisotropies.* ApJ **922**, 86 (2021)

Lançon A., Larsen S., Voggel K., Cuillandre J. C., Duc P. A., Chantereau W., Jain R., Sánchez-Janssen R., Cantiello M., Rejkuba M., et al.: *Extragalactic Globular Clusters with Euclid and Other Wide Surveys.* In: *SF2A-2021: Proceedings of the Annual Meeting of the French Society of Astronomy and Astrophysics.* 447 (2021)

Lange R., Driver S. P., Robotham A. S. G., Kelvin L. S., Graham A. W., Alpaslan M., Andrews S. K., Baldry I. K., Bamford S., Bland-Hawthorn J., et al.: *Galaxy And Mass Assembly (GAMA): mass-size relations of $z < 0.1$ galaxies subdivided by Sérsic index, colour and morphology.* MNRAS **447**, 2603 (2015)

Law D. R., Majewski S. R., & Johnston K. V.: *Evidence for a Triaxial Milky Way Dark Matter Halo from the Sagittarius Stellar Tidal Stream.* ApJ **703**, L67 (2009)

Law D. R. & Majewski S. R.: *The Sagittarius Dwarf Galaxy: A Model for Evolution in a Triaxial Milky Way Halo.* ApJ **714**, 229 (2010)

Leaman R., VandenBerg D. A., & Mendel J. T.: *The Bifurcated Age-Metallicity Relation of Milky Way Globular Clusters and Its Implications for the Accretion History of the Galaxy.* MNRAS **436**, 122 (2013)

Lee B., Giavalisco M., Whitaker K., Williams C. C., Ferguson H. C., Acquaviva V., Koekemoer A. M., Straughn A. N., Guo Y., Kartaltepe J. S., et al.: *The Intrinsic Characteristics of Galaxies on the SFR-M $*$ Plane at $1.2 < z < 4$: I. The Correlation between Stellar Age, Central Density, and Position Relative to the Main Sequence.* ApJ **853**, 131 (2018)

Lee J.-W., Kang Y.-W., Lee J., & Lee Y.-W.: *Enrichment by Supernovae in Globular Clusters with Multiple Populations.* Nature **462**, 480 (2009)

Lee M. G., Freedman W. L., & Madore B. F.: *The Tip of the Red Giant Branch as a Distance Indicator for Resolved Galaxies.* ApJ **417**, 553 (1993)

Lee M. G., Park H. S., Hwang H. S., Arimoto N., Tamura N., & Onodera M.: *The Globular Cluster System of the Virgo Giant Elliptical Galaxy NGC 4636. II. Kinematics of the Globular Cluster System.* ApJ **709**, 1083 (2010)

Lee M. G. & Jang I. S.: *Dual Stellar Halos in the Standard Elliptical Galaxy M105 and Formation of Massive Early-type Galaxies.* ApJ **822**, 70 (2016)

Lee Y.-W., Joo J.-M., Sohn Y.-J., Rey S.-C., Lee H.-C., & Walker A. R.: *Multiple Stellar Populations in the Globular Cluster ω Centauri as Tracers of a Merger Event.* Nature **402**, 55 (1999)

Lequeux J., Peimbert M., Rayo J. F., Serrano A., & Torres-Peimbert S.: *Chemical Composition and Evolution of Irregular and Blue Compact Galaxies.* A&A **80**, 155 (1979)

Leslie S. K., Schinnerer E., Liu D., Magnelli B., Algera H., Karim A., Davidzon I., Gozaliasl G., Jiménez-Andrade E. F., Lang P., et al.: *The VLA-COSMOS 3 GHz Large Project: Evolution of Specific Star Formation Rates out to $z \sim 5$.* ApJ **899**, 58 (2020)

Li B., Peng E. W., Zhang H.-x., Blakeslee J. P., Côté P., Ferrarese L., Jordán A., Liu C., Mei S., Puzia T. H., et al.: *A Gemini/GMOS Study of Intermediate Luminosity Early-type Virgo Cluster Galaxies. I. Globular Cluster and Stellar Kinematics.* ApJ **806**, 133 (2015)

Li H. & Gnedin O. Y.: *Modeling the Formation of Globular Cluster Systems in the Virgo Cluster.* ApJ **796**, 10 (2014)

Li H., Mao S., Cappellari M., Ge J., Long R. J., Li R., Mo H. J., Li C., Zheng Z., Bundy K., et al.: *SDSS-IV MaNGA: Global Stellar Population and Gradients for about 2000 Early-Type and Spiral Galaxies on the Mass-Size Plane.* MNRAS **476**, 1765 (2018)

Li S., Riess A. G., Busch M. P., Casertano S., Macri L. M., & Yuan W.: *A Sub-2% Distance to M31 from Photometrically Homogeneous Near-infrared Cepheid Period-Luminosity Relations Measured with the Hubble Space Telescope.* ApJ **920**, 84 (2021)

Li Z.-Z., Jing Y. P., Qian Y.-Z., Yuan Z., & Zhao D.-H.: *Determination of Dark Matter Halo Mass from Dynamics of Satellite Galaxies.* ApJ **850**, 116 (2017)

Liao L.-W. & Cooper A. P.: *Colour Gradients of Low-Redshift Galaxies in the DESI Legacy Imaging Survey.* MNRAS **518**, 3999 (2023)

Licquia T. C. & Newman J. A.: *Improved Estimates of the Milky Way's Stellar Mass and Star Formation Rate from Hierarchical Bayesian Meta-Analysis.* ApJ **806**, 96 (2015)

Lin L., Ellison S. L., Pan H.-A., Thorp M. D., Su Y.-C., Sánchez S. F., Belfiore F., Bothwell M. S., Bundy K., Chen Y.-M., et al.: *ALMaQUEST. IV. The ALMA-MaNGA QUEnching and STar Formation (ALMaQUEST) Survey.* ApJ **903**, 145 (2020)

Longobardi A., Arnaboldi M., Gerhard O., Coccato L., Okamura S., & Freeman K. C.: *The Planetary Nebula Population in the Halo of M 87.* A&A **558**, A42 (2013)

Longobardi A., Arnaboldi M., Gerhard O., & Hanuschik R.: *The Outer Regions of the Giant Virgo Galaxy M 87 Kinematic Separation of Stellar Halo and Intracluster Light.* A&A **579**, A135 (2015)

Longobardi A., Arnaboldi M., Gerhard O., Pulsoni C., & Söldner-Rembold I.: *Kinematics of the outer halo of M 87 as mapped by planetary nebulae.* A&A **620**, A111 (2018)

Luo A. L., Zhao Y.-H., Zhao G., Deng L.-C., Liu X.-W., Jing Y.-P., Wang G., Zhang H.-T., Shi J.-R., Cui X.-Q., et al.: *The First Data Release (DR1) of the LAMOST Regular Survey.* A&A **15**, 1095 (2015)

Lynden-Bell D.: *Dwarf Galaxies and Globular Clusters in High Velocity Hydrogen Streams.* MNRAS **174**, 695 (1976)

Ma J., Wang S., Wu Z., Zhang T., Zou H., dan Nie J., Zhou Z., Zhou X., Wu J., Du C., & Yuan Q.: *Spectral Energy Distributions and Masses of 304 M31 Old Star Clusters.* AJ **149**, 56 (2015)

Mackereth J. T., Schiavon R. P., Pfeffer J., Hayes C. R., Bovy J., Anguiano B., Allende Prieto C., Hasselquist S., Holtzman J., Johnson J. A., et al.: *The Origin of Accreted Stellar Halo Populations in the Milky Way Using APOGEE, Gaia, and the EAGLE Simulations.* MNRAS **482**, 3426 (2019)

Mackey A. D. & van den Bergh S.: *The Properties of Galactic Globular Cluster Subsystems.* MNRAS **360**, 631 (2005)

Mackey A. D., Ferguson A. M. N., Huxor A. P., Veljanoski J., Lewis G. F., McConnachie A. W., Martin N. F., Ibata R. A., Irwin M. J., Côté P., et al.: *The Outer Halo Globular Cluster System of M31 - III. Relationship to the Stellar Halo.* MNRAS **484**, 1756 (2019)

Madau P. & Dickinson M.: *Cosmic Star-Formation History.* ARA&A **52**, 415 (2014)

Madau P., Lupi A., Diemand J., Burkert A., & Lin D. N. C.: *Globular Cluster Formation from Colliding Substructure.* ApJ **890**, 18 (2020)

Maiolino R., Nagao T., Grazian A., Cocchia F., Marconi A., Mannucci F., Cimatti A., Pipino A., Ballero S., Calura F., et al.: *AMAZE. I. The Evolution of the Mass-Metallicity Relation at z > 3.* A&A **488**, 463 (2008)

Malhan K., Ibata R. A., Sharma S., Famaey B., Bellazzini M., Carlberg R. G., D'Souza R., Yuan Z., Martin N. F., & Thomas G. F.: *The Global Dynamical Atlas of the Milky Way Mergers: Constraints from Gaia EDR3-Based Orbits of Globular Clusters, Stellar Streams, and Satellite Galaxies.* ApJ **926**, 107 (2022)

Malin D. F. & Carter D.: *A Catalog of Elliptical Galaxies with Shells.* ApJ **274**, 534 (1983)

Malin D. F., Quinn P. J., & Graham J. A.: *Shell Structure in NGC 5128.* ApJ **272**, L5 (1983)

Mancera Piña P. E., Posti L., Fraternali F., Adams E. A. K., & Oosterloo T.: *The Baryonic Specific Angular Momentum of Disc Galaxies.* A&A **647**, A76 (2021)

Mancillas B., Duc P.-A., Combes F., Bournaud F., Emsellem E., Martig M., & Michel-Dansac L.: *Probing the Merger History of Red Early-Type Galaxies with Their Faint Stellar Substructures.* A&A **632**, A122 (2019)

Marigo P., Girardi L., Weiss A., Groenewegen M. A. T., & Chiosi C.: *Evolution of Planetary Nebulae. II. Population Effects on the Bright Cut-off of the PNLF.* A&A **423**, 995 (2004)

Marigo P., Cummings J. D., Curtis J. L., Kalirai J., Chen Y., Tremblay P.-E., Ramirez-Ruiz E., Bergeron P., Bladh S., Bressan A., et al.: *Carbon Star Formation as Seen through the Non-Monotonic Initial-Final Mass Relation.* Nature **4**, 1102 (2020)

Marín-Franch A., Aparicio A., Piotto G., Rosenberg A., Chaboyer B., Sarajedini A., Siegel M., Anderson J., Bedin L. R., Dotter A., et al.: *The ACS Survey of Galactic Globular Clusters. VII. Relative Ages.* ApJ **694**, 1498 (2009)

Marinacci F., Vogelsberger M., Pakmor R., Torrey P., Springel V., Hernquist L., Nelson D., Weinberger R., Pillepich A., Naiman J., & Genel S.: *First Results from the IllustrisTNG Simulations: Radio Haloes and Magnetic Fields.* MNRAS **480**, 5113 (2018)

Martin G., Bazkiaei A. E., Spavone M., Iodice E., Mihos J. C., Montes M., Benavides J. A., Brough S., Carlin J. L., Collins C. A., et al.: *Preparing for Low Surface Brightness Science with the Vera C. Rubin Observatory: Characterization of Tidal Features from Mock Images.* MNRAS **513**, 1459 (2022)

Martínez-Delgado D., Peñarrubia J., Gabany R. J., Trujillo I., Majewski S. R., & Pohlen M.: *The Ghost of a Dwarf Galaxy: Fossils of the Hierarchical Formation of the Nearby Spiral Galaxy NGC 5907.* ApJ **689**, 184 (2008)

Martínez-Delgado D., Cooper A. P., Román J., Pillepich A., Erkal D., Pearson S., Moustakas J., Laporte C. F. P., Laine S., Akhlaghi M., et al.: *Hidden Depths in the Local Universe: The Stellar Stream Legacy Survey.* A&A **671**, A141 (2023a)

Martínez-Delgado D., Roca-Fàbrega S., Miró-Carretero J., Gómez-Flechoso M. A., Romàn J., Donatiello G., Schmidt J., Lang D., Akhlaghi M., & Hanson M.: *A Giant Umbrella-like Stellar Stream around the Tidal Ring Galaxy NGC 922.* A&A **669**, A103 (2023b)

Martínez-Delgado D., Stein M., Sakowska J. D., Maurice Weigelt M., Román J., Donatiello G., Roca-Fàbrega S., Schirmer M., Grebel E. K., Saifollahi T., et al.: *Stellar Tidal Streams around Nearby Spiral Galaxies with Deep Imaging from Amateur Telescopes.* A&A **701**, A182 (2025)

Martocchia S., Cabrera-Ziri I., Lardo C., Dalessandro E., Bastian N., Kozhurina-Platais V., Usher C., Niederhofer F., Cordero M., Geisler D., et al.: *Age as a Major Factor in the Onset of Multiple Populations in Stellar Clusters.* MNRAS **473**, 2688 (2018)

Mason C. A., Trenti M., & Treu T.: *The Brightest Galaxies at Cosmic Dawn.* MNRAS **521**, 497 (2023)

Massari D., Koppelman H. H., & Helmi A.: *Origin of the System of Globular Clusters in the Milky Way.* A&A **630**, L4 (2019)

Massari D., Aguado-Agelet F., Monelli M., Cassisi S., Pancino E., Saracino S., Gallart C., Ruiz-Lara T., Fernández-Alvar E., Surot F., et al.: *Cluster Ages to Reconstruct the Milky Way Assembly (CARMA). I. The Final Word on the Origin of NGC 6388 and NGC 6441.* A&A **680**, A20 (2023)

Mateu C.: *Galstreams: A Library of Milky Way Stellar Stream Footprints and Tracks.* MNRAS **520**, 5225 (2023)

Matthee J.: *JWST Provides a New View of Cosmic Dawn: Latest Developments in Studies of Early Galaxies.* Contemporary Physics **66**, 116 (2025)

Mayer L., van Donkelaar F., Messa M., Capelo P. R., & Adamo A.: *In Situ Formation of Star Clusters at z > 7 via Galactic Disk Fragmentation: Shedding Light on Ultracompact Clusters and Overmassive Black Holes Seen by JWST.* ApJ **981**, L28 (2025)

McDermid R. M., Alatalo K., Blitz L., Bournaud F., Bureau M., Cappellari M., Crocker A. F., Davies R. L., Davis T. A., de Zeeuw P. T., et al.: *The ATLAS3D Project - XXX. Star Formation Histories and Stellar Population Scaling Relations of Early-Type Galaxies.* MNRAS **448**, 3484 (2015)

McDonald S. L. E., Davies B., & Beasor E. R.: *Red Supergiants in M31: The Humphreys-Davidson Limit at High Metallicity.* MNRAS **510**, 3132 (2022)

McKenzie M. & Bekki K.: *Simulations of Globular Clusters within Their Parent Galaxies: Multiple Stellar Populations and Internal Kinematics.* MNRAS **500**, 4578 (2021)

McKenzie M., Yong D., Marino A. F., Monty S., Wang E., Karakas A. I., Milone A. P., Legnardi M. V., Roederer I. U., Martell S., & Horta D.: *The Complex Stellar System M 22: Confirming Abundance Variations with High Precision Differential Measurements.* MNRAS **516**, 3515 (2022)

McLaughlin D. E. & Fall S. M.: *Shaping the Globular Cluster Mass Function by Stellar-Dynamical Evaporation.* ApJ **679**, 1272 (2008)

McMillan R., Ciardullo R., & Jacoby G. H.: *Planetary Nebulae as Standard Candles. IX. The Distance to the Fornax Cluster.* ApJ **416**, 62 (1993)

Meatheringham S. J., Dopita M. A., Ford H. C., & Webster B. L.: *The Kinematics of the Planetary Nebulae in the Large Magellanic Cloud.* ApJ **327**, 651 (1988)

Méndez R. H., Kudritzki R. P., & Herrero A.: *On Central Star Luminosities and Optical Thicknesses in Planetary Nebulae.* A&A **260**, 329 (1992)

Méndez R. H., Kudritzki R. P., Ciardullo R., & Jacoby G. H.: *The Bright End of the Planetary Nebula Luminosity Function.* A&A **275**, 534 (1993)

Méndez R. H. & Soffner T.: *Improved Simulations of the Planetary Nebula Luminosity Function.* A&A **321**, 898 (1997)

Méndez R. H., Riffeser A., Kudritzki R.-P., Matthias M., Freeman K. C., Arnaboldi M., Capaccioli M., & Gerhard O. E.: *Detection, Photometry, and Slitless Radial Velocities of 535 Planetary Nebulae in the Flattened Elliptical Galaxy NGC 4697.* ApJ **563**, 135 (2001)

Méndez R. H., Thomas D., Saglia R. P., Maraston C., Kudritzki R. P., & Bender R.: *Oxygen and Neon Abundances of Planetary Nebulae in the Elliptical Galaxy NGC 4697.* ApJ **627**, 767 (2005)

Méndez R. H., Teodorescu A. M., Schönberner D., Jacob R., & Steffen M.: *Toward Better Simulations of Planetary Nebulae Luminosity Functions.* ApJ **681**, 325 (2008)

Méndez R. H., Teodorescu A. M., Kudritzki R.-P., & Burkert A.: *Kinematics of Planetary Nebulae in the Outskirts of the Elliptical Galaxy NGC 4697.* ApJ **691**, 228 (2009)

Méndez R. H.: *The Planetary Nebulae Luminosity Function (PNLF): Current Perspectives.* In: *Planetary Nebulae: Multi-Wavelength Probes of Stellar and Galactic Evolution.* IAU Symposium **323**, 298 (2017)

Messa M., Dessauges-Zavadsky M., Adamo A., Richard J., & Claeyssens A.: *Properties of the Brightest Young Stellar Clumps in Extremely Lensed Galaxies at Redshifts 4 to 5.* MNRAS **529**, 2162 (2024)

Messa M., Vanzella E., Loiacono F., Bergamini P., Castellano M., Sun B., Willott C., Windhorst R. A., Yan H., Angora G., et al.: *Anatomy of a $z = 6$ Lyman-α Emitter down to Parsec Scales: Extreme UV Slopes, Metal-Poor Regions, and Possibly Leaking Star Clusters.* A&A **694**, A59 (2025)

Mestel L.: *On the Galactic Law of Rotation.* MNRAS **126**, 553 (1963)

Mihos J. C.: *Interactions and Mergers of Cluster Galaxies.* In: *Clusters of Galaxies: Probes of Cosmological Structure and Galaxy Evolution.* Carnegie Observatories Astrophysics Series **3**, 277 (2004)

Mihos J. C., Harding P., Feldmeier J., & Morrison H.: *Diffuse Light in the Virgo Cluster.* ApJ **631**, L41 (2005)

Miller Bertolami M. M.: *New Models for the Evolution of Post-Asymptotic Giant Branch Stars and Central Stars of Planetary Nebulae.* A&A **588**, A25 (2016)

Mirocha J. & Furlanetto S. R.: *Balancing the Efficiency and Stochasticity of Star Formation with Dust Extinction in $z \gtrsim 10$ Galaxies Observed by JWST.* MNRAS **519**, 843 (2023)

Miskolczi A., Bomans D. J., & Dettmar R.-J.: *Tidal Streams around Galaxies in the SDSS DR7 Archive. I. First Results.* A&A **536**, A66 (2011)

Miyazaki S., Komiyama Y., Sekiguchi M., Okamura S., Doi M., Furusawa H., Hamabe M., Imi K., Kimura M., Nakata F., et al.: *Subaru Prime Focus Camera – Suprime-Cam.* Publications of the Astronomical Society of Japan **54**, 833 (2002)

Mo H., van den Bosch F. C., & White S.: *Galaxy Formation and Evolution.* Cambridge University Press (2010)

Moore B., Ghigna S., Governato F., Lake G., Quinn T., Stadel J., & Tozzi P.: *Dark Matter Substructure within Galactic Halos.* ApJ **524**, L19 (1999)

Mora M. D., Larsen S. S., & Kissler-Patig M.: *Spectroscopy of Globular Clusters in the Low-Luminosity Spiral Galaxy NGC 45.* A&A **489**, 1065 (2008)

Morales G., Martínez-Delgado D., Grebel E. K., Cooper A. P., Javanmardi B., & Miskolczi A.: *Systematic Search for Tidal Features around Nearby Galaxies. I. Enhanced SDSS Imaging of the Local Volume.* A&A **614**, A143 (2018)

Morisset C., Corradi R. L. M., García-Rojas J., Mampaso A., Jones D., Kwitter K. B., Magrini L., & Villaver E.: *The Computation of Interstellar Extinction in Photoionized Nebulae.* A&A **674**, L6 (2023)

Moster B. P., Naab T., & White S. D. M.: *EMERGE - an Empirical Model for the Formation of Galaxies since $z \sim 10$.* MNRAS **477**, 1822 (2018)

Mowla L., Iyer K. G., Desprez G., Estrada-Carpenter V., Martis N. S., Noirot G., Sarrouh G. T., Strait V., Asada Y., Abraham R. G., et al.: *The Sparkler: Evolved High-Redshift Globular Cluster Candidates Captured by JWST.* ApJ **937**, L35 (2022)

Mowla L., Iyer K., Asada Y., Desprez G., Tan V. Y. Y., Martis N., Sarrouh G., Strait V., Abraham R., Bradač M., et al.: *Formation of a Low-Mass Galaxy from Star Clusters in a 600-Million-Year-Old Universe.* Nature **636**, 332 (2024)

Mozumdar P., Cappellari M., Fassnacht C. D., & Treu T.: *MAGNUS I: A MUSE-DEEP Sample of Early-Type Galaxies at Intermediate Redshift.* arXiv e-prints, arXiv:2510.23863 (2025a)

Mozumdar P., Cappellari M., Fassnacht C. D., & Treu T.: *MAGNUS II: Rotational Support of Massive Early-Type Galaxies Decreased over the Past 7 Billion Years.* arXiv e-prints, arXiv:2510.23888 (2025b)

Müller O., Pawlowski M. S., Jerjen H., & Lelli F.: *A Whirling Plane of Satellite Galaxies around Centaurus A Challenges Cold Dark Matter Cosmology.* Science **359**, 534 (2018)

Myeong G. C., Evans N. W., Belokurov V., Sanders J. L., & Koposov S. E.: *The Sausage Globular Clusters.* ApJ **863**, L28 (2018)

Myeong G. C., Vasiliev E., Iorio G., Evans N. W., & Belokurov V.: *Evidence for Two Early Accretion Events That Built the Milky Way Stellar Halo.* MNRAS **488**, 1235 (2019)

Naab T., Johansson P. H., & Ostriker J. P.: *Minor Mergers and the Size Evolution of Elliptical Galaxies.* ApJ **699**, L178 (2009)

Naab T., Oser L., Emsellem E., Cappellari M., Krajnović D., McDermid R. M., Alatalo K., Bayet E., Blitz L., Bois M., et al.: *The ATLAS3D Project - XXV. Two-Dimensional Kinematic Analysis of Simulated Galaxies and the Cosmological Origin of Fast and Slow Rotators.* MNRAS **444**, 3357 (2014)

Naiman J. P., Pillepich A., Springel V., Ramirez-Ruiz E., Torrey P., Vogelsberger M., Pakmor R., Nelson D., Marinacci F., Hernquist L., et al.: *First Results from the IllustrisTNG Simulations: A Tale of Two Elements - Chemical Evolution of Magnesium and Europium.* MNRAS **477**, 1206 (2018)

Nanayakkara T., Glazebrook K., Jacobs C., Kawinwanichakij L., Schreiber C., Brammer G., Esdaile J., Kacprzak G. G., Labbe I., Lagos C., et al.: *A Population of Faint, Old, and Massive Quiescent Galaxies at 3.* Scientific Reports **14**, 3724 (2024)

Nanni A., Bressan A., Marigo P., & Girardi L.: *Evolution of Thermally Pulsing Asymptotic Giant Branch Stars - III. Dust Production at Supersolar Metallicities.* MNRAS **438**, 2328 (2014)

Naoz S. & Narayan R.: *Globular Clusters and Dark Satellite Galaxies through the Stream Velocity.* ApJ **791**, L8 (2014)

Navarro J. F., Frenk C. S., & White S. D. M.: *The Structure of Cold Dark Matter Halos.* ApJ **462**, 563 (1996)

Navarro J. F., Frenk C. S., & White S. D. M.: *A Universal Density Profile from Hierarchical Clustering.* ApJ **490**, 493 (1997)

Nelson D., Pillepich A., Springel V., Weinberger R., Hernquist L., Pakmor R., Genel S., Torrey P., Vogelsberger M., Kauffmann G., et al.: *First Results from the IllustrisTNG Simulations: The Galaxy Colour Bimodality.* MNRAS **475**, 624 (2018)

Nelson D., Pillepich A., Springel V., Pakmor R., Weinberger R., Genel S., Torrey P., Vogelsberger M., Marinacci F., & Hernquist L.: *First Results from the TNG50 Simulation: Galactic Outflows Driven by Supernovae and Black Hole Feedback.* MNRAS **490**, 3234 (2019)

Neumann J., Thomas D., Maraston C., Hill L., Nanni L., Wenman O., Lian J., Comparat J., Gonzalez-Perez V., Westfall K. B., et al.: *The MaNGA FIREFLY Value Added Catalogue: Resolved Stellar Populations of 10 010 Nearby Galaxies.* MNRAS **513**, 5988 (2022)

Newman A. B., Belli S., Ellis R. S., & Patel S. G.: *Resolving Quiescent Galaxies at $z \gtrsim 2$. II. Direct Measures of Rotational Support.* ApJ **862**, 126 (2018)

Nipoti C.: *Evolution of massive quiescent galaxies via envelope accretion.* A&A **697**, A74 (2025)

Norris M. A., Gebhardt K., Sharples R. M., Faifer F. R., Bridges T., Forbes D. A., Forte J. C., Zepf S. E., Beasley M. A., Hanes D. A., et al.: *The Globular Cluster Kinematics and Galaxy Dark Matter Content of NGC 3923.* MNRAS **421**, 1485 (2012)

Obreschkow D. & Glazebrook K.: *Fundamental Mass-Spin-Morphology Relation Of Spiral Galaxies.* ApJ **784**, 26 (2014)

Obreschkow D., Glazebrook K., Bassett R., Fisher D. B., Abraham R. G., Wisnioski E., Green A. W., McGregor P. J., Damjanov I., Popping A., & Jørgensen I.: *Low Angular Momentum in Clumpy, Turbulent Disk Galaxies.* ApJ **815**, 97 (2015)

Odenkirchen M., Grebel E. K., Dehnen W., Rix H.-W., Yanny B., Newberg H. J., Rockosi C. M., Martínez-Delgado D., Brinkmann J., & Pier J. R.: *The Extended Tails of Palomar 5: A 10° Arc of Globular Cluster Tidal Debris.* AJ **126**, 2385 (2003)

Oh K. S., Lin D. N. C., & Aarseth S. J.: *On the Tidal Disruption of Dwarf Spheroidal Galaxies around the Galaxy.* ApJ **442**, 142 (1995)

Oh S., Yi S. K., Cortese L., van de Sande J., Mahajan S., Jeong H., Sheen Y.-K., Allen J. T., Bekki K., Bland-Hawthorn J., et al.: *The SAMI Galaxy Survey: Galaxy Interactions and Kinematic Anomalies in Abell 119.* ApJ **832**, 69 (2016)

Oh S., Kim K., Lee J. H., Sheen Y.-K., Kim M., Ree C. H., Ho L. C., Kyeong J., Sung E.-C., Park B.-G., & Yi S. K.: *KYDISC: Galaxy Morphology, Quenching, and Mergers in the Cluster Environment.* ApJS **237**, 14 (2018)

Omori K. C., Bottrell C., Walmsley M., Yesuf H. M., Goulding A. D., Ding X., Popping G., Silverman J. D., Takeuchi T. T., & Toba Y.: *Galaxy Mergers in Subaru HSC-SSP: A Deep Representation Learning Approach for Identification, and the Role of Environment on Merger Incidence.* A&A **679**, A142 (2023)

Oser L., Ostriker J. P., Naab T., Johansson P. H., & Burkert A.: *The Two Phases of Galaxy Formation.* ApJ **725**, 2312 (2010)

Osterbrock D. E. & Ferland G. J.: *Astrophysics of Gaseous Nebulae and Active Galactic Nuclei.* University Science Books (2006)

Padmanabhan T.: *Structure Formation in the Universe.* Cambridge University Press (1993)

Padovani P. & Matteucci F.: *Stellar Mass Loss in Elliptical Galaxies and the Fueling of Active Galactic Nuclei.* ApJ **416**, 26 (1993)

Pagnini G., Di Matteo P., Khoperskov S., Mastrobuono-Battisti A., Haywood M., Renaud F., & Combes F.: *The Distribution of Globular Clusters in Kinematic Spaces Does Not Trace the Accretion History of the Host Galaxy.* A&A **673**, A86 (2023)

Pal F. A., Martell S. L., & Iles E. J.: *The Fate of Globular Cluster Substructure: A Kinematic Response to Galaxy Assembly.* MNRAS **548**, stag622 (2026)

Panithanpaisal N., Sanderson R. E., Wetzel A., Cunningham E. C., Bailin J., & Faucher-Giguère C.-A.: *The Galaxy Progenitors of Stellar Streams around Milky Way-mass Galaxies in the FIRE Cosmological Simulations.* ApJ **920**, 10 (2021)

Parikh T., Thomas D., Maraston C., Westfall K. B., Andrews B. H., Boardman N. F., Drory N., & Oyarzun G.: *SDSS-IV MaNGA: Radial Gradients in Stellar Population Properties of Early-Type and Late-Type Galaxies.* MNRAS **502**, 5508 (2021)

Parisi M. C., Geisler D., Carraro G., Clariá J. J., Costa E., Grocholski A. J., Sarajedini A., Leiton R., & Piatti A. E.: *Age Determination of 15 Old to Intermediate-Age Small Magellanic Cloud Star Clusters.* AJ **147**, 71 (2014)

Pasquali A., Smith R., Gallazzi A., De Lucia G., Zibetti S., Hirschmann M., & Yi S. K.: *Physical Properties of SDSS Satellite Galaxies in Projected Phase Space.* MNRAS **484**, 1702 (2019)

Pawlowski M. S., Kroupa P., & de Boer K. S.: *Making Counter-Orbiting Tidal Debris. The Origin of the Milky Way Disc of Satellites?* A&A **532**, A118 (2011)

Pawlowski M. S., Famaey B., Jerjen H., Merritt D., Kroupa P., Dabringhausen J., Lüghausen F., Forbes D. A., Hensler G., Hammer F., et al.: *Co-Orbiting Satellite Galaxy Structures Are Still in Conflict with the Distribution of Primordial Dwarf Galaxies.* MNRAS **442**, 2362 (2014)

Pawlowski M. S.: *It's Time for Some Plane Speaking.* Nature **5**, 1185 (2021)

Peacock M. B., Maccarone T. J., Knigge C., Kundu A., Waters C. Z., Zepf S. E., & Zurek D. R.: *The M31 Globular Cluster System: Ugriz and K-Band Photometry and Structural Parameters.* MNRAS **402**, 803 (2010)

Pearson S., Price-Whelan A. M., Hogg D. W., Seth A. C., Sand D. J., Hunt J. A. S., & Crnojević D.: *Mapping Dark Matter with Extragalactic Stellar Streams: The Case of Centaurus A.* ApJ **941**, 19 (2022)

Pearson W. J., Wang L., Hurley P. D., Małek K., Buat V., Burgarella D., Farrah D., Oliver S. J., Smith D. J. B., & van der Tak F. F. S.: *Main Sequence of Star Forming Galaxies beyond the Herschel Confusion Limit.* A&A **615**, A146 (2018)

Peebles P. J. E. & Dicke R. H.: *Origin of the Globular Star Clusters.* ApJ **154**, 891 (1968)

Peebles P. J. E.: *Origin of the Angular Momentum of Galaxies.* ApJ **155**, 393 (1969)

Peña M., Reyes-Pérez J., Hernández-Martínez L., & Pérez-Guillén M.: *A Catalog of Planetary Nebula Candidates in the Sculptor Spiral Galaxy NGC 300.* A&A **547**, A78 (2012)

Peng E. W., Ford H. C., & Freeman K. C.: *The Globular Cluster System of NGC 5128. II. Ages, Metallicities, Kinematics, and Formation.* ApJ **602**, 705 (2004a)

Peng E. W., Ford H. C., & Freeman K. C.: *The Planetary Nebula System and Dynamics in the Outer Halo of NGC 5128.* ApJ **602**, 685 (2004b)

Peng E. W., Ford H. C., & Freeman K. C.: *The Globular Cluster System of NGC 5128. I. Survey and Catalogs.* ApJS **150**, 367 (2004c)

Peng E. W., Jordán A., Côté P., Takamiya M., West M. J., Blakeslee J. P., Chen C.-W., Ferrarese L., Mei S., Tonry J. L., & West A. A.: *The ACS Virgo Cluster Survey. XV. The Formation Efficiencies of Globular Clusters in Early-Type Galaxies: The Effects of Mass and Environment.* ApJ **681**, 197 (2008)

Penzias A. A. & Wilson R. W.: *A Measurement of Excess Antenna Temperature at 4080 Mc/s.* ApJ **142**, 419 (1965)

Pérez-Martínez J. M., Ziegler B., Dannerbauer H., Böhm A., Verdugo M., Díaz A. I., & Hoyos C.: *Evolution of Galaxy Scaling Relations in Clusters at 0.5 < z < 1.5.* A&A **646**, A53 (2021)

Perina S., Galleti S., Fusi Pecci F., Bellazzini M., Federici L., & Buzzoni A.: *HST/ACS Color-Magnitude Diagrams of Candidate Intermediate-Age M 31 Globular Clusters. The Role of Blue Horizontal Branches.* A&A **531**, A155 (2011)

Pfeffer J., Kruijssen J. M. D., Crain R. A., & Bastian N.: *The E-MOSAICS Project: Simulating the Formation and Co-Evolution of Galaxies and Their Star Cluster Populations.* MNRAS **475**, 4309 (2018)

Pfeffer J., Forbes D. A., Romanowsky A. J., Bastian N., Crain R. A., Kruijssen J. M. D., Bekki K., Brodie J. P., Chevance M., Couch W. J., & Gannon J. S.: *Comparing E-MOSAICS Predictions of High-Redshift Proto-Globular Clusters with JWST Observations in Lensed Galaxies.* MNRAS **536**, 1878 (2025)

Pham K., Kravtsov A., & Manwadkar V.: *Spatial and Orbital Planes of the Milky Way Satellites: Unusual but Consistent with ΛCDM.* MNRAS **520**, 3937 (2023)

Phipps F., Khochfar S., Varri A. L., & Dalla Vecchia C.: *The First Billion Years Project: Finding Infant Globular Clusters at $z = 6$.* A&A **641**, A132 (2020)

Piatti A. E.: *Formation Imprints in the Kinematics of the Milky Way Globular Cluster System.* ApJ **882**, 98 (2019)

Pietrinferni A., Cassisi S., Salaris M., & Hidalgo S.: *The BaSTI Stellar Evolution Database: Models for Extremely Metal-Poor and Super-Metal-Rich Stellar Populations.* A&A **558**, A46 (2013)

Pillepich A., Nelson D., Hernquist L., Springel V., Pakmor R., Torrey P., Weinberger R., Genel S., Naiman J. P., Marinacci F., & Vogelsberger M.: *First Results from the IllustrisTNG Simulations: The Stellar Mass Content of Groups and Clusters of Galaxies.* MNRAS **475**, 648 (2018)

Pillepich A., Nelson D., Springel V., Pakmor R., Torrey P., Weinberger R., Vogelsberger M., Marinacci F., Genel S., van der Wel A., & Hernquist L.: *First Results from the TNG50 Simulation: The Evolution of Stellar and Gaseous Discs across Cosmic Time.* MNRAS **490**, 3196 (2019)

Pillepich A., Sotillo-Ramos D., Ramesh R., Nelson D., Engler C., Rodriguez-Gomez V., Fournier M., Donnari M., Springel V., & Hernquist L.: *Milky Way and Andromeda Analogues from the TNG50 Simulation.* MNRAS **535**, 1721 (2024)

Piotrowska J. M., Bluck A. F. L., Maiolino R., & Peng Y.: *On the Quenching of Star Formation in Observed and Simulated Central Galaxies: Evidence for the Role of Integrated AGN Feedback.* MNRAS **512**, 1052 (2022)

Pippert J.-N., Kluge M., & Bender R.: *Modeling Tidal Streams and Tidal Tails around Galaxies Using Deep Wendelstein Imaging Data.* ApJ **980**, 244 (2025)

Planck Collaboration: *Planck 2015 Results. XIII. Cosmological Parameters.* A&A **594**, A13 (2016)

Planck Collaboration: *Planck 2018 Results. VI. Cosmological Parameters.* A&A **641**, A6 (2020)

Poci A., McDermid R. M., Zhu L., & van de Ven G.: *Combining Stellar Populations with Orbit-Superposition Dynamical Modelling: The Formation History of the Lenticular Galaxy NGC 3115.* MNRAS **487**, 3776 (2019)

Pop A.-R., Pillepich A., Amorisco N. C., & Hernquist L.: *Galaxies with Shells in the Illustris Simulation: Metallicity Signatures.* Galaxies **5**, 34 (2017)

Pop A.-R., Pillepich A., Amorisco N. C., & Hernquist L.: *Formation and Incidence of Shell Galaxies in the Illustris Simulation.* MNRAS **480**, 1715 (2018)

Popesso P., Concas A., Cresci G., Belli S., Rodighiero G., Inami H., Dickinson M., Ilbert O., Pannella M., & Elbaz D.: *The Main Sequence of Star-Forming Galaxies across Cosmic Times.* MNRAS **519**, 1526 (2023)

Posti L., Fraternali F., Di Teodoro E. M., & Pezzulli G.: *The Angular Momentum-Mass Relation: A Fundamental Law from Dwarf Irregulars to Massive Spirals.* A&A **612**, L6 (2018)

Pota V., Forbes D. A., Romanowsky A. J., Brodie J. P., Spitler L. R., Strader J., Foster C., Arnold J. A., Benson A., Blom C., et al.: *The SLUGGS Survey: Kinematics for over 2500 Globular Clusters in 12 Early-Type Galaxies.* MNRAS **428**, 389 (2013)

Pota V., Brodie J. P., Bridges T., Strader J., Romanowsky A. J., Villaume A., Jennings Z., Faifer F. R., Pastorello N., Forbes D. A., et al.: *A SLUGGS and Gemini/GMOS Combined Study of the Elliptical Galaxy M60: Wide-Field Photometry and Kinematics of the Globular Cluster System.* MNRAS **450**, 1962 (2015)

Pottasch S. R.: *Planetary Nebulae. A Study of Late Stages of Stellar Evolution.* D. Reidel Publishing Company (1984)

Power C., Navarro J. F., Jenkins A., Frenk C. S., White S. D. M., Springel V., Stadel J., & Quinn T.: *The Inner Structure of ΛCDM Haloes - I. A Numerical Convergence Study.* MNRAS **338**, 14 (2003)

Prada J., Forero-Romero J. E., Grand R. J. J., Pakmor R., & Springel V.: *Dark Matter Halo Shapes in the Auriga Simulations.* MNRAS **490**, 4877 (2019)

Press W. H. & Schechter P.: *Formation of Galaxies and Clusters of Galaxies by Self-Similar Gravitational Condensation.* ApJ **187**, 425 (1974)

Prieur J.-L.: *The Shell System around NGC 3923 and Its Implications for the Potential of the Galaxy.* ApJ **326**, 596 (1988)

Prudil Z., Koch-Hansen A. J., Lemasle B., Grebel E. K., Marchetti T., Hansen C. J., Crestani J., Braga V. F., Bono G., Chaboyer B., et al.: *Milky Way Archaeology Using RR Lyrae and Type II Cepheids. II. High-Velocity RR Lyrae Stars and Milky Way Mass.* A&A **664**, A148 (2022)

Pulsoni C., Gerhard O., Arnaboldi M., Coccato L., Longobardi A., Napolitano N. R., Moylan E., Narayan C., Gupta V., Burkert A., et al.: *The Extended Planetary Nebula Spectrograph (ePN.S) Early-Type Galaxy Survey: The Kinematic Diversity of Stellar Halos and the Relation between Halo Transition Scale and Stellar Mass.* A&A **618**, A94 (2018)

Pulsoni C., Gerhard O., Arnaboldi M., Pillepich A., Nelson D., Hernquist L., & Springel V.: *The Stellar Halos of ETGs in the IllustrisTNG Simulations: The Photometric and Kinematic Diversity of Galaxies at Large Radii.* A&A **641**, A60 (2020)

Pulsoni C., Gerhard O., Arnaboldi M., Pillepich A., Rodriguez-Gomez V., Nelson D., Hernquist L., & Springel V.: *The Stellar Halos of ETGs in the IllustrisTNG Simulations. II. Accretion, Merger History, and Dark Halo Connection.* A&A **647**, A95 (2021)

Puzia T. H., Kissler-Patig M., Thomas D., Maraston C., Saglia R. P., Bender R., Goudfrooij P., & Hempel M.: *VLT Spectroscopy of Globular Cluster Systems. II. Spectroscopic Ages, Metallicities, and [α/Fe] Ratios of Globular Clusters in Early-Type Galaxies.* A&A **439**, 997 (2005)

Quinn P. J.: *On the Formation and Dynamics of Shells around Elliptical Galaxies.* ApJ **279**, 596 (1984)

Ramos-Almendares F., Sales L. V., Abadi M. G., Doppel J. E., Muriel H., & Peng E. W.: *Simulating the Spatial Distribution and Kinematics of Globular Clusters within Galaxy Clusters in Illustris.* MNRAS **493**, 5357 (2020)

Reid W. A. & Parker Q. A.: *A New Population of Planetary Nebulae Discovered in the Large Magellanic Cloud - III. The Luminosity Function.* MNRAS **405**, 1349 (2010)

Reina-Campos M., Kruijssen J. M. D., Pfeffer J. L., Bastian N., & Crain R. A.: *Formation Histories of Stars, Clusters, and Globular Clusters in the E-MOSAICS Simulations.* MNRAS **486**, 5838 (2019)

Reina-Campos M., Keller B. W., Kruijssen J. M. D., Gensior J., Trujillo-Gomez S., Jeffreson S. M. R., Pfeffer J. L., & Sills A.: *Introducing EMP-Pathfinder: Modelling the Simultaneous Formation and Evolution of Stellar Clusters in Their Host Galaxies.* MNRAS **517**, 3144 (2022)

Reina-Campos M., Trujillo-Gomez S., Pfeffer J. L., Sills A., Deason A. J., Crain R. A., & Kruijssen J. M. D.: *Constraining the Shape of Dark Matter Haloes with Globular Clusters and Diffuse Stellar Light in the E-MOSAICS Simulations.* MNRAS **521**, 6368 (2023)

Reina-Campos M., Gnedin O. Y., Sills A., & Li H.: *The Star Clusters as Links between Galaxy Evolution and Star Formation Project. I. Numerical Method.* ApJ **978**, 15 (2025)

Rejkuba M., Harris W. E., Greggio L., & Harris G. L. H.: *How Old Are the Stars in the Halo of NGC 5128 (Centaurus A)?* A&A **526**, A123 (2011)

Rejkuba M., Harris W. E., Greggio L., Crnojević D., & Harris G. L. H.: *The Outermost Stellar Halo of NGC 5128 (Centaurus A): Radial Structure.* A&A **657**, A41 (2022)

Rekola R., Richer M. G., McCall M. L., Valtonen M. J., Kotilainen J. K., & Flynn C.: *Distance to NGC 253 Based on the Planetary Nebula Luminosity Function.* MNRAS **361**, 330 (2005)

Remus R.-S., Dolag K., Naab T., Burkert A., Hirschmann M., Hoffmann T. L., & Johansson P. H.: *The Co-Evolution of Total Density Profiles and Central Dark Matter Fractions in Simulated Early-Type Galaxies.* MNRAS **464**, 3742 (2017)

Remus R.-S. & Forbes D. A.: *Accreted or Not Accreted? The Fraction of Accreted Mass in Galaxies from the Magneticum Simulations and Observations.* ApJ **935**, 37 (2022)

Remus R.-S. & Kimmig L. C.: *Relight the Candle: What Happens to High-redshift Massive Quenched Galaxies.* ApJ **982**, 30 (2025)

Renaud F., Agertz O., & Gieles M.: *The Origin of the Milky Way Globular Clusters.* MNRAS **465**, 3622 (2017)

Renzini A.: *Energetics of Stellar Populations.* Annales de Physique **6**, 87 (1981)

Renzini A. & Buzzoni A.: *Global Properties of Stellar Populations and the Spectral Evolution of Galaxies.* In: *Proceedings of the Fourth Workshop.* Astrophysics and Space Science Library **122**, 195 (1986)

Renzini A.: *Stellar Population Diagnostics of Elliptical Galaxy Formation.* ARA&A **44**, 141 (2006)

Renzini A.: *Origin of Multiple Stellar Populations in Globular Clusters and Their Helium Enrichment.* MNRAS **391**, 354 (2008)

Renzini A.: *Finding Forming Globular Clusters at High Redshifts.* MNRAS **469**, L63 (2017)

Rhee J., Smith R., Choi H., Yi S. K., Jaffé Y., Candlish G., & Sánchez-Jánssen R.: *Phase-Space Analysis in the Group and Cluster Environment: Time Since Infall and Tidal Mass Loss.* ApJ **843**, 128 (2017)

Richer M. G.: *Bright Planetary Nebulae as Probes of Chemical Evolution.* ApJ **415**, 240 (1993)

Riley A. H. & Strigari L. E.: *The Milky Way's Stellar Streams and Globular Clusters Do Not Align in a Vast Polar Structure.* MNRAS **494**, 983 (2020)

Rizzi L., Tully R. B., Makarov D., Makarova L., Dolphin A. E., Sakai S., & Shaya E. J.: *Tip of the Red Giant Branch Distances. II. Zero-Point Calibration.* ApJ **661**, 815 (2007)

Rodriguez-Gomez V., Pillepich A., Sales L. V., Genel S., Vogelsberger M., Zhu Q., Wellons S., Nelson D., Torrey P., Springel V., et al.: *The Stellar Mass Assembly of Galaxies in the Illustris Simulation: Growth by Mergers and the Spatial Distribution of Accreted Stars.* MNRAS **458**, 2371 (2016)

Rodriguez-Gomez V., Snyder G. F., Lotz J. M., Nelson D., Pillepich A., Springel V., Genel S., Weinberger R., Tacchella S., Pakmor R., et al.: *The Optical Morphologies of Galaxies in the IllustrisTNG Simulation: A Comparison to Pan-STARRS Observations.* MNRAS **483**, 4140 (2019)

Rodríguez-González A., Hernández-Martínez L., Esquivel A., Raga A. C., Stasińska G., Peña M., & Mayya Y. D.: *A Two-Mode Planetary Nebula Luminosity Function.* A&A **575**, A1 (2015)

Romanowsky A. J. & Fall S. M.: *Angular Momentum and Galaxy Formation Revisited.* ApJS **203**, 17 (2012)

Romero A. D., Campos F., & Kepler S. O.: *The Age-Metallicity Dependence for White Dwarf Stars.* MNRAS **450**, 3708 (2015)

Roth M. M., Jacoby G. H., Ciardullo R., Davis B. D., Chase O., & Weilbacher P. M.: *Toward Precision Cosmology with Improved PNLF Distances Using VLT-MUSE I. Methodology and Tests.* ApJ **916**, 21 (2021)

Ruiz-Lara T., Helmi A., Gallart C., Surot F., & Cassisi S.: *Unveiling the Past Evolution of the Progenitor of the Helmi Streams.* A&A **668**, L10 (2022)

Rutherford T. H., van de Sande J., Croom S. M., Valenzuela L. M., Remus R.-S., D'Eugenio F., Vaughan S. P., Zovaro H. R. M., Casura S., Barsanti S., et al.: *The SAMI Galaxy Survey: Using Tidal Streams and Shells to Trace the Dynamical Evolution of Massive Galaxies.* MNRAS **529**, 810 (2024)

Salaris M., Degl'Innocenti S., & Weiss A.: *The Age of the Oldest Globular Clusters.* ApJ **479**, 665 (1997)

Salaris M. & Weiss A.: *Metal-Rich Globular Clusters in the Galactic Disk: New Age Determinations and the Relation to Halo Clusters.* A&A **335**, 943 (1998)

Sales L. V., Wetzel A., & Fattahi A.: *Baryonic Solutions and Challenges for Cosmological Models of Dwarf Galaxies.* Nature **6**, 897 (2022)

Sambhus N., Gerhard O., & Méndez R. H.: *Kinematic Evidence for Different Planetary Nebula Populations in the Elliptical Galaxy NGC 4697.* AJ **131**, 837 (2006)

Sandage A.: *The Hubble Atlas of Galaxies.* Carnegie Institution of Washington (1961)

Santini P., Fontana A., Castellano M., Di Criscienzo M., Merlin E., Amorin R., Cullen F., Daddi E., Dickinson M., Dunlop J. S., et al.: *The Star Formation Main Sequence in the Hubble Space Telescope Frontier Fields.* ApJ **847**, 76 (2017)

Santucci G., Brough S., van de Sande J., McDermid R. M., van de Ven G., Zhu L., D'Eugenio F., Bland-Hawthorn J., Barsanti S., Bryant J. J., et al.: *The SAMI Galaxy Survey: The Internal Orbital Structure and Mass Distribution of Passive Galaxies from Triaxial Orbit-superposition Schwarzschild Models.* ApJ **930**, 153 (2022)

Saracco P., Marchesini D., La Barbera F., Gargiulo A., Annunziatella M., Forrest B., Lange Vagle D. J., Marsan Z. C., Muzzin A., Stefanon M., & Wilson G.: *The Rapid Buildup of Massive Early-type Galaxies: Supersolar Metallicity, High Velocity Dispersion, and Young Age for an Early-type Galaxy at $z = 3.35$.* ApJ **905**, 40 (2020)

Saracco P., La Barbera F., De Propris R., Bevacqua D., Marchesini D., De Lucia G., Fontanot F., Hirschmann M., Nonino M., Pasquali A., et al.: *The Star Formation History and the Nature of the Mass-Metallicity Relation of Passive Galaxies at $1.0 < z < 1.4$ from VANDELS.* MNRAS **520**, 3027 (2023)

Sarajedini A., Bedin L. R., Chaboyer B., Dotter A., Siegel M., Anderson J., Aparicio A., King I., Majewski S., Marín-Franch A., et al.: *The ACS Survey of Galactic Globular Clusters. I. Overview and Clusters without Previous Hubble Space Telescope Photometry.* AJ **133**, 1658 (2007)

Sarzi M., Mamon G. A., Cappellari M., Emsellem E., Bacon R., Davies R. L., & de Zeeuw P. T.: *The Planetary Nebulae Population in the Central Regions of M32: The SAURON View.* MNRAS **415**, 2832 (2011)

Savino A., Weisz D. R., Skillman E. D., Dolphin A., Kallivayalil N., Wetzel A., Anderson J., Besla G., Boylan-Kolchin M., Bullock J. S., et al.: *The Hubble Space Telescope Survey of M31 Satellite Galaxies. I. RR Lyrae-based Distances and Refined 3D Geometric Structure.* ApJ **938**, 101 (2022)

Sawala T., Cautun M., Frenk C., Helly J., Jasche J., Jenkins A., Johansson P. H., Lavaux G., McAlpine S., & Schaller M.: *The Milky Way's Plane of Satellites Is Consistent with ΛCDM.* Nature **7**, 481 (2023)

Schauer A. T. P., Bromm V., Boylan-Kolchin M., Glover S. C. O., & Klessen R. S.: *Globular Clusters and Streaming Velocities: Testing the New Formation Channel in High-Resolution Cosmological Simulations.* ApJ **922**, 193 (2021)

Schaye J., Crain R. A., Bower R. G., Furlong M., Schaller M., Theuns T., Dalla Vecchia C., Frenk C. S., McCarthy I. G., Helly J. C., et al.: *The EAGLE Project: Simulating the Evolution and Assembly of Galaxies and Their Environments.* MNRAS **446**, 521 (2015)

Schaye J., Chaikin E., Schaller M., Ploeckinger S., Huško F., McGibbon R. J., Trayford J. W., Benítez-Llambay A., Correa C., Frenk C. S., et al.: *The COLIBRE Project: Cosmological Hydrodynamical Simulations of Galaxy Formation and Evolution.* MNRAS **548**, stag375 (2026)

Schechter P.: *An Analytic Expression for the Luminosity Function for Galaxies.* ApJ **203**, 297 (1976)

Scheuermann F., Kreckel K., Anand G. S., Blanc G. A., Congiu E., Santoro F., Van Dyk S. D., Barnes A. T., Bigiel F., Glover S. C. O., et al.: *Planetary Nebula Luminosity Function Distances for 19 Galaxies Observed by PHANGS-MUSE.* MNRAS **511**, 6087 (2022)

Schiavon R. P., Caldwell N., Conroy C., Graves G. J., Strader J., MacArthur L. A., Courteau S., & Harding P.: *Star Clusters in M31. V. Evidence for Self-Enrichment in Old M31 Clusters from Integrated Spectroscopy.* ApJ **776**, L7 (2013)

Schlafly E. F. & Finkbeiner D. P.: *Measuring Reddening with Sloan Digital Sky Survey Stellar Spectra and Recalibrating SFD.* ApJ **737**, 103 (2011)

Schönberner D.: *Late Stages of Stellar Evolution. II. Mass Loss and the Transition of Asymptotic Giant Branch Stars into Hot Remnants.* ApJ **272**, 708 (1983)

Schönberner D., Jacob R., Steffen M., & Sandin C.: *The Evolution of Planetary Nebulae. IV. On the Physics of the Luminosity Function.* A&A **473**, 467 (2007)

Schönberner D., Jacob R., Sandin C., & Steffen M.: *The Evolution of Planetary Nebulae. VII. Modelling Planetary Nebulae of Distant Stellar Systems.* A&A **523**, A86 (2010)

Schuberth Y., Richtler T., Hilker M., Dirsch B., Bassino L. P., Romanowsky A. J., & Infante L.: *The Globular Cluster System of NGC 1399. V. Dynamics of the Cluster System out to 80 Kpc.* A&A **513**, A52 (2010)

Schulze F., Remus R.-S., & Dolag K.: *On the Kinematics, Stability and Lifetime of Kinematically Distinct Cores: A Case Study.* Galaxies **5**, 41 (2017)

Schulze F., Remus R.-S., Dolag K., Burkert A., Emsellem E., & van de Ven G.: *Kinematics of Simulated Galaxies - I. Connecting Dynamical and Morphological Properties of Early-Type Galaxies at Different Redshifts.* MNRAS **480**, 4636 (2018)

Schulze F., Remus R.-S., Dolag K., Bellstedt S., Burkert A., & Forbes D. A.: *Kinematics of Simulated Galaxies II: Probing the Stellar Kinematics of Galaxies out to Large Radii.* MNRAS **493**, 3778 (2020)

Scoville N., Aussel H., Brusa M., Capak P., Carollo C. M., Elvis M., Giavalisco M., Guzzo L., Hasinger G., Impey C., et al.: *The Cosmic Evolution Survey (COSMOS): Overview.* ApJS **172**, 1 (2007)

Seo C., Yoon S.-J., Paudel S., An S.-H., & Moon J.-S.: *A New Rarity Assessment of the "Disk of Satellites": The Milky Way System Is the Exception Rather Than the Rule in the ΛCDM Cosmology.* ApJ **976**, 253 (2024)

Sesto L. A., Faifer F. R., Smith Castelli A. V., Forte J. C., & Escudero C. G.: *Young Globular Clusters in NGC 1316.* MNRAS **479**, 478 (2018)

Sextl E., Kudritzki R.-P., Zahid H. J., & Ho I.-T.: *Mass-Metallicity Relationship of SDSS Star-forming Galaxies: Population Synthesis Analysis and Effects of Star Burst Length, Extinction Law, Initial Mass Function, and Star Formation Rate.* ApJ **949**, 60 (2023)

Shao S., Cautun M., & Frenk C. S.: *Evolution of Galactic Planes of Satellites in the EAGLE Simulation.* MNRAS **488**, 1166 (2019)

Shapiro K. L., Genzel R., & Förster Schreiber N. M.: *Star-Forming Galaxies at z ~ 2 and the Formation of the Metal-Rich Globular Cluster Population.* MNRAS **403**, L36 (2010)

Sharina M. E., Afanasiev V. L., & Puzia T. H.: *Ages, Metallicities and [α/Fe] Ratios of Globular Clusters in NGC 147, 185 and 205.* MNRAS **372**, 1259 (2006)

Sheen Y.-K., Yi S. K., Ree C. H., & Lee J.: *Post-Merger Signatures of Red-sequence Galaxies in Rich Abell Clusters at z <~ 0.1.* ApJS **202**, 8 (2012)

Shen X., Vogelsberger M., Boylan-Kolchin M., Tacchella S., & Kannan R.: *The Impact of UV Variability on the Abundance of Bright Galaxies at z ≥ 9.* MNRAS **525**, 3254 (2023)

Shi R., Wang W., Li Z., Zhu L., Smith A., Cole S., Gao H., Chen X., Li Q., & Han J.: *Inferring the Mass Content of Galaxy Clusters with Satellite Kinematics and Jeans Anisotropic Modeling.* ApJ **973**, 82 (2024)

Shipp N., Drlica-Wagner A., Balbinot E., Ferguson P., Erkal D., Li T. S., Bechtol K., Belokurov V., Buncher B., Carollo D., et al.: *Stellar Streams Discovered in the Dark Energy Survey.* ApJ **862**, 114 (2018)

Smith R., Duc P. A., Bournaud F., & Yi S. K.: *A Formation Scenario for the Disk of Satellites: Accretion of Satellites during Mergers.* ApJ **818**, 11 (2016)

Smoot G. F., Bennett C. L., Kogut A., Wright E. L., Aymon J., Boggess N. W., Cheng E. S., de Amici G., Gulkis S., Hauser M. G., et al.: *Structure in the COBE Differential Microwave Radiometer First-Year Maps.* ApJ **396**, L1 (1992)

Soemitro A. A., Roth M. M., Weilbacher P. M., Ciardullo R., Jacoby G. H., Monreal-Ibero A., Castro N., & Micheva G.: *MUSE Crowded Field 3D Spectroscopy in NGC 300. IV. Planetary Nebula Luminosity Function.* A&A **671**, A142 (2023)

Soemitro A. A., Valenzuela L. M., Roth M. M., Ciardullo R., Jacoby G. H., Arnaboldi M., Couto G. S., & Jakob Walcher C.: *Towards Precision Cosmology with Improved PNLF Distances Using VLT-MUSE: III. Impact of Stellar Populations in Early-Type Galaxies.* A&A **704**, A303 (2025)

Soker N.: *Accreting White Dwarfs among the Planetary Nebulae Most Luminous in [O III] λ5007 Emission.* ApJ **640**, 966 (2006)

Sola E., Duc P.-A., Richards F., Paiement A., Urbano M., Klehammer J., Bílek M., Cuillandre J.-C., Gwyn S., & McConnachie A.: *Characterization of Low Surface Brightness Structures in Annotated Deep Images.* A&A **662**, A124 (2022)

Sola E., Chemaly D., Belokurov V., Müller O., Ardern-Arentsen A., Davies E. Y., Laguna-Miralles J., Myeong G., Panagiotakis K., Zhang H., et al.: *STRRINGS: STReams in Residual Images of Nearby GalaxieS.* MNRAS **544**, 735 (2025a)

Sola E., Duc P.-A., Urbano M., Richards F., Paiement A., Bílek M., Yıldız M. K., Boselli A., Côté P., Cuillandre J.-C., et al.: *Low Surface Brightness Structures from Annotated Deep CFHT Images: Effects of the Host Galaxy's Properties and Environment.* MNRAS **541**, 3015 (2025b)

Souropanis D., Chiotellis A., Boumis P., Jones D., & Akras S.: *Planetary Nebulae Hosting Accreting White Dwarfs: A Possible Solution for the Mysterious Cut-off of Planetary Nebula Luminosity Function?* MNRAS **521**, 1808 (2023)

Spiniello C., Napolitano N. R., Arnaboldi M., Tortora C., Coccato L., Capaccioli M., Gerhard O., Iodice E., Spavone M., Cantiello M., et al.: *The Fornax Cluster VLT Spectroscopic Survey II - Planetary Nebulae Kinematics within 200 Kpc of the Cluster Core.* MNRAS **477**, 1880 (2018)

Spitler L. R. & Forbes D. A.: *A New Method for Estimating Dark Matter Halo Masses Using Globular Cluster Systems.* MNRAS **392**, L1 (2009)

Spitzer L., Jr.: *Equipartition and the Formation of Compact Nuclei in Spherical Stellar Systems.* ApJ **158**, L139 (1969)

Spolaor M., Forbes D. A., Proctor R. N., Hau G. K. T., & Brough S.: *The Early-Type Galaxies NGC 1407 and NGC 1400 - II. Star Formation and Chemical Evolutionary History.* MNRAS **385**, 675 (2008)

Spriggs T. W., Sarzi M., Napiwotzki R., Galán-de Anta P. M., Viaene S., Nedelchev B., Coccato L., Corsini E. M., de Zeeuw P. T., Falcón-Barroso J., et al.: *Fornax 3D Project: Automated Detection of Planetary Nebulae in the Centres of Early-Type Galaxies and First Results.* A&A **637**, A62 (2020)

Spriggs T. W., Sarzi M., Galán-de Anta P. M., Napiwotzki R., Viaene S., Nedelchev B., Coccato L., Corsini E. M., Fahrion K., Falcón-Barroso J., et al.: *The Fornax3D Project: Planetary Nebulae Catalogue and Independent Distance Measurements to Fornax Cluster Galaxies.* A&A **653**, A167 (2021)

Springel V., White S. D. M., Tormen G., & Kauffmann G.: *Populating a Cluster of Galaxies - I. Results at $z = 0$.* MNRAS **328**, 726 (2001)

Springel V.: *The Cosmological Simulation Code GADGET-2.* MNRAS **364**, 1105 (2005)

Springel V., White S. D. M., Jenkins A., Frenk C. S., Yoshida N., Gao L., Navarro J., Thacker R., Croton D., Helly J., et al.: *Simulations of the Formation, Evolution and Clustering of Galaxies and Quasars.* Nature **435**, 629 (2005)

Springel V.: *E Pur Si Muove: Galilean-invariant Cosmological Hydrodynamical Simulations on a Moving Mesh.* MNRAS **401**, 791 (2010)

Springel V., Pakmor R., Pillepich A., Weinberger R., Nelson D., Hernquist L., Vogelsberger M., Genel S., Torrey P., Marinacci F., & Naiman J.: *First Results from the IllustrisTNG Simulations: Matter and Galaxy Clustering.* MNRAS **475**, 676 (2018)

Starkman N., Bovy J., Webb J. J., Calvetti D., & Somersalo E.: *On the Fast Track: Rapid Construction of Stellar Stream Paths.* MNRAS **522**, 5022 (2023)

Steinborn L. K., Dolag K., Hirschmann M., Prieto M. A., & Remus R.-S.: *A Refined Sub-Grid Model for Black Hole Accretion and AGN Feedback in Large Cosmological Simulations.* MNRAS **448**, 1504 (2015)

Stoiber J., Valenzuela L. M., Remus R.-S., Kimmig L. C., Pippert J.-N., Sola E., & Dolag K.: *Living the Stream: Properties and Progenitors of Tidal Shells and Streams around Galaxies from Magneticum.* arXiv e-prints, arXiv:2509.25307 (2025)

Stoiber J., Valenzuela L. M., Remus R.-S., & Dolag K.: *Stream on: Evolution of stellar shells and streams – A case study.* arXiv e-prints, arXiv2604.14280 (2026)

Strader J., Brodie J. P., Cenarro A. J., Beasley M. A., & Forbes D. A.: *Extragalactic Globular Clusters: Old Spectroscopic Ages and New Views on Their Formation.* AJ **130**, 1315 (2005)

Strader J., Romanowsky A. J., Brodie J. P., Spitler L. R., Beasley M. A., Arnold J. A., Tamura N., Sharples R. M., & Arimoto N.: *Wide-Field Precision Kinematics of the M87 Globular Cluster System.* ApJS **197**, 33 (2011)

Strateva I., Ivezić Ž., Knapp G. R., Narayanan V. K., Strauss M. A., Gunn J. E., Lupton R. H., Schlegel D., Bahcall N. A., Brinkmann J., et al.: *Color Separation of Galaxy Types in the Sloan Digital Sky Survey Imaging Data.* AJ **122**, 1861 (2001)

Sturm E., Davies R., Alves J., Clénet Y., Kotilainen J., Monna A., Nicklas H., Pott J.-U., Tolstoy E., Vulcani B., et al.: *The MICADO First Light Imager for the ELT: Overview and Current Status.* In: *Ground-Based and Airborne Instrumentation for Astronomy X.* **13096**, 1309611 (2024)

Sweet S. M., Fisher D., Glazebrook K., Obreschkow D., Lagos C., & Wang L.: *Revisiting the Stellar Mass-Angular Momentum-Morphology Relation: Extension to Higher Bulge Fraction and the Effect of Bulge Type.* ApJ **860**, 37 (2018)

Sweet S. M., Fisher D. B., Savorgnan G., Glazebrook K., Obreschkow D., Gillman S., Tiley A. L., Lagos C. D. P., Wang L., Swinbank A. M., et al.: *Angular Momentum of $z \sim 1.5$ Galaxies and Their Local Analogues with Adaptive Optics.* MNRAS **485**, 5700 (2019)

Swinbank A. M., Papadopoulos P. P., Cox P., Krips M., Ivison R. J., Smail I., Thomson A. P., Neri R., Richard J., & Ebeling H.: *The Interstellar Medium in Distant Star-forming Galaxies: Turbulent Pressure, Fragmentation, and Cloud Scaling Relations in a Dense Gas Disk at $z = 2.3$.* ApJ **742**, 11 (2011)

Swinbank A. M., Harrison C. M., Trayford J., Schaller M., Smail I., Schaye J., Theuns T., Smit R., Alexander D. M., Bacon R., et al.: *Angular Momentum Evolution of Galaxies over the Past 10 Gyr: A MUSE and KMOS Dynamical Survey of 400 Star-Forming Galaxies from $z = 0.3$ to 1.7.* MNRAS **467**, 3140 (2017)

Tacconi L. J., Genzel R., & Sternberg A.: *The Evolution of the Star-Forming Interstellar Medium Across Cosmic Time.* ARA&A **58**, 157 (2020)

Tal T., van Dokkum P. G., Nelan J., & Bezanson R.: *The Frequency of Tidal Features Associated with Nearby Luminous Elliptical Galaxies From a Statistically Complete Sample.* AJ **138**, 1417 (2009)

Taylor M. A., Muñoz R. P., Puzia T. H., Mieske S., Eigenthaler P., & Bovill M. S.: *The Survey of Centaurus A's Baryonic Structures (SCABS). I. Survey Description and Initial Source Catalogues.* arXiv e-prints, arXiv:1608.07285 (2016)

Taylor M. A., Puzia T. H., Muñoz R. P., Mieske S., Lançon A., Zhang H., Eigenthaler P., & Bovill M. S.: *The Survey of Centaurus A's Baryonic Structures (SCABS) - II. The Extended Globular Cluster System of NGC 5128 and Its Nearby Environment.* MNRAS **469**, 3444 (2017)

Teklu A. F., Remus R.-S., Dolag K., Beck A. M., Burkert A., Schmidt A. S., Schulze F., & Steinborn L. K.: *Connecting Angular Momentum and Galactic Dynamics: The Complex Interplay between Spin, Mass, and Morphology.* ApJ **812**, 29 (2015)

Teklu A. F., Remus R.-S., Dolag K., & Burkert A.: *The Morphology-Density Relation: Impact on the Satellite Fraction.* MNRAS **472**, 4769 (2017)

Teklu A., Kudritzki R.-P., Dolag K., Remus R.-S., & Kimmig L.: *On the Decline of Star Formation during the Evolution of Galaxies.* ApJ **954**, 182 (2023)

Teodorescu A. M., Méndez R. H., Bernardi F., Thomas J., Das P., & Gerhard O.: *Planetary Nebulae in the Elliptical Galaxy NGC 4649 (M 60): Kinematics and Distance Redetermination.* ApJ **736**, 65 (2011)

Thater S., Jethwa P., Lilley E. J., Zocchi A., Santucci G., & van de Ven G.: *Dynamical Modelling of ATLAS3D Galaxies.* In: IAU Symposium **379**, 314 (2025)

Tiley A. L., Gillman S., Cortese L., Swinbank A. M., Dudzevičiūtė U., Harrison C. M., Smail I., Obreschkow D., Croom S. M., Sharples R. M., & Puglisi A.: *The KMOS Galaxy Evolution Survey (KGES): The Angular Momentum of Star-Forming Galaxies over the Last ≈10 Gyr.* MNRAS **506**, 323 (2021)

Tonry J. L., Dressler A., Blakeslee J. P., Ajhar E. A., Fletcher A. B., Luppino G. A., Metzger M. R., & Moore C. B.: *The SBF Survey of Galaxy Distances. IV. SBF Magnitudes, Colors, and Distances.* ApJ **546**, 681 (2001)

Tonry J. & Schneider D. P.: *A New Technique for Measuring Extragalactic Distances.* AJ **96**, 807 (1988)

Toomre A. & Toomre J.: *Galactic Bridges and Tails.* ApJ **178**, 623 (1972)

Toomre A.: *Mergers and Some Consequences.* In: *Evolution of Galaxies and Stellar Populations.* 401 (1977)

Tornatore L., Borgani S., Matteucci F., Recchi S., & Tozzi P.: *Simulating the Metal Enrichment of the Intracluster Medium.* MNRAS **349**, L19 (2004)

Tornatore L., Borgani S., Dolag K., & Matteucci F.: *Chemical enrichment of galaxy clusters from hydrodynamical simulations.* MNRAS **382**, 1050 (2007)

Tortora C., Napolitano N. R., Cardone V. F., Capaccioli M., Jetzer Ph., & Molinaro R.: *Colour and Stellar Population Gradients in Galaxies: Correlation with Mass.* MNRAS **407**, 144 (2010)

Trager S. C., Faber S. M., Worthey G., & González J. J.: *The Stellar Population Histories of Local Early-Type Galaxies. I. Population Parameters.* AJ **119**, 1645 (2000)

Tremonti C. A., Heckman T. M., Kauffmann G., Brinchmann J., Charlot S., White S. D. M., Seibert M., Peng E. W., Schlegel D. J., Uomoto A., et al.: *The Origin of the Mass-Metallicity Relation: Insights from 53,000 Star-forming Galaxies in the Sloan Digital Sky Survey.* ApJ **613**, 898 (2004)

Trujillo-Gomez S., Kruijssen J. M. D., Reina-Campos M., Pfeffer J. L., Keller B. W., Crain R. A., Bastian N., & Hughes M. E.: *The Kinematics of Globular Cluster Populations in the E-MOSAICS Simulations and Their Implications for the Assembly History of the Milky Way.* MNRAS **503**, 31 (2021)

Trujillo I., D'Onofrio M., Zaritsky D., Madrigal-Aguado A., Chamba N., Golini G., Akhlaghi M., Sharbaf Z., Infante-Sainz R., Román J., et al.: *Introducing the LBT Imaging of Galactic Halos and Tidal Structures (LIGHTS) Survey. A Preview of the Low Surface Brightness Universe to Be Unveiled by LSST.* A&A **654**, A40 (2021)

Turnbull A. J., Bridges T. J., & Carter D.: *Imaging of the Shell Galaxies NGC 474 and 7600, and Implications for Their Formation.* Monthly Notices, Volume 307, Issue 4, pp. 967-976. **307**, 967 (1999)

Tutukov A. V., Vereshchagin S. V., & Sizova M. D.: *Destruction of Galaxies as a Cause of the Appearance of Stellar Streams.* Astronomy Reports **65**, 1085 (2021)

Urbano M., Duc P.-A., Saifollahi T., Sola E., Lançon A., Voggel K., Annibali F., Baes M., Bouy H., Cantiello M., et al.: *Euclid: Early Release Observations of Diffuse Stellar Structures and Globular Clusters as Probes of the Mass Assembly of Galaxies in the Dorado Group.* A&A **700**, A104 (2025)

Usher C., Forbes D. A., Brodie J. P., Foster C., Spitler L. R., Arnold J. A., Romanowsky A. J., Strader J., & Pota V.: *The SLUGGS Survey: Calcium Triplet-Based Spectroscopic Metallicities for over 900 Globular Clusters.* MNRAS **426**, 1475 (2012)

Usher C., Brodie J. P., Forbes D. A., Romanowsky A. J., Strader J., Pfeffer J., & Bastian N.: *The SLUGGS Survey: Measuring Globular Cluster Ages Using Both Photometry and Spectroscopy.* MNRAS **490**, 491 (2019)

Usher C., Dage K. C., Girardi L., Barmby P., Bonatto C. J., Chies-Santos A. L., Clarkson W. I., Gómez Camus M., Hartmann E. A., Ferguson A. M. N., et al.: *Rubin Observatory LSST Stars Milky Way and Local Volume Star Clusters Roadmap.* Publications of the Astronomical Society of the Pacific **135**, 074201 (2023)

Usher C., Caldwell N., & Cabrera-Ziri I.: *Measuring M31 Globular Cluster Ages and Metallicities Using Both Photometry and Spectroscopy.* MNRAS **528**, 6010 (2024)

Valentini M. & Dolag K.: *Hydrodynamic Methods and Sub-Resolution Models for Cosmological Simulations.* arXiv e-prints, arXiv:2502.06954 (2025)

Valenzuela L. M., Méndez R. H., & Miller Bertolami M. M.: *Revised Simulations of the Planetary Nebulae Luminosity Function.* ApJ **887**, 65 (2019)

Valenzuela L. M., Moster B. P., Remus R.-S., O'Leary J. A., & Burkert A.: *Globular Cluster Numbers in Dark Matter Haloes in a Dual Formation Scenario: An Empirical Model within EMERGE.* MNRAS **505**, 5815 (2021)

Valenzuela L. M.: *Lights in the Dark: Globular clusters as dark matter tracers.* In: *Memorie della Societa Astronomica Italiana.* **94**, 47 (2023)

Valenzuela L. M. & Remus R.-S.: *A Stream Come True: Connecting Tidal Tails, Shells, Streams, and Planes with Galaxy Kinematics and Formation History.* A&A **686**, A182 (2024)

Valenzuela L. M., Remus R.-S., Dolag K., & Seidel B. A.: *Galaxy Shapes in Magneticum: I. Connecting Stellar and Dark Matter Shapes to Dynamical and Morphological Galaxy Properties and the Large-Scale Structure.* A&A **690**, A206 (2024a)

Valenzuela L. M., Remus R.-S., McKenzie M., & Forbes D. A.: *Galaxy Archaeology for Wet Mergers: Globular Cluster Age Distributions in the Milky Way and Nearby Galaxies.* A&A **687**, A104 (2024b)

Valenzuela L. M., Forbes D. A., & Remus R.-S.: *Globular Cluster Ages and Their Relation to High-Redshift Stellar Cluster Formation Times from Different Globular Cluster Models.* MNRAS **537**, 306 (2025a)

Valenzuela L. M., Jacoby G. H., Remus R.-S., Miller Bertolami M. M., & Méndez R. H.: *The PICS Project: II. Circumnebular Extinction Variations and Their Effect on the Planetary Nebula Luminosity Function.* Frontiers in Astronomy and Space Sciences **12**, 1709047 (2025b)

Valenzuela L. M., Miller Bertolami M. M., Remus R.-S., & Méndez R. H.: *The PICS Project: I. The Impact of Metallicity and Helium Abundance on the Bright End of the Planetary Nebula Luminosity Function.* A&A **699**, A371 (2025c)

Valenzuela L. M., Remus R.-S., Miller Bertolami M. M., & Méndez R. H.: *PICS: Planetary Nebulae in Cosmological Simulations - Revelations of the Planetary Nebula Luminosity Function from Realistic Stellar Populations.* In: IAU Symposium **384**, 69 (2025d)

Valenzuela L. M., Stoiber J., & Remus R.-S.: *Deep Imaging Meets Motion: Complementing Stream Photometry Through Planetary Nebula Kinematics.* arXiv e-prints, arXiv2604.14272 (2026)

van de Sande J., Bland-Hawthorn J., Fogarty L. M. R., Cortese L., d'Eugenio F., Croom S. M., Scott N., Allen J. T., Brough S., Bryant J. J., et al.: *The SAMI Galaxy Survey: Revisiting Galaxy Classification through High-order Stellar Kinematics.* ApJ **835**, 104 (2017)

van de Sande J., Lagos C. D. P., Welker C., Bland-Hawthorn J., Schulze F., Remus R.-S., Bahé Y., Brough S., Bryant J. J., Cortese L., et al.: *The SAMI Galaxy Survey: Comparing 3D Spectroscopic Observations with Galaxies from Cosmological Hydrodynamical Simulations.* MNRAS **484**, 869 (2019)

van de Sande J., Vaughan S. P., Cortese L., Scott N., Bland-Hawthorn J., Croom S. M., Lagos C. D. P., Brough S., Bryant J. J., Devriendt J., et al.: *The SAMI Galaxy Survey: A Statistical Approach to an Optimal Classification of Stellar Kinematics in Galaxy Surveys.* MNRAS **505**, 3078 (2021)

van der Wel A., Franx M., van Dokkum P. G., Skelton R. E., Momcheva I. G., Whitaker K. E., Brammer G. B., Bell E. F., Rix H.-W., Wuyts S., et al.: *3D-HST+CANDELS: The Evolution of the Galaxy Size-Mass Distribution since $z = 3$.* ApJ **788**, 28 (2014)

van der Wel A., Martorano M., Häußler B., Nedkova K. V., Miller T. B., Brammer G. B., van de Ven G., Leja J., Bezanson R. S., Muzzin A., et al.: *Stellar Half-mass Radii of 0.5 z < 2.3 Galaxies: Comparison with JWST/NIRCam Half-light Radii.* ApJ **960**, 53 (2024)

van Donkelaar F., Mayer L., Capelo P. R., Tamfal T., Quinn T. R., & Madau P.: *Stellar Cluster Formation in a Milky Way-Sized Galaxy at z > 4 - I. The Proto-Globular Cluster Population and the Imposter amongst Us.* MNRAS **522**, 1726 (2023)

VandenBerg D. A., Bergbusch P. A., Dotter A., Ferguson J. W., Michaud G., Richer J., & Proffitt C. R.: *Models for Metal-poor Stars with Enhanced Abundances of C, N, O, Ne, Na, Mg, Si, S, Ca, and Ti, in Turn, at Constant Helium and Iron Abundances.* ApJ **755**, 15 (2012)

VandenBerg D. A., Brogaard K., Leaman R., & Casagrande L.: *The Ages of 55 Globular Clusters as Determined Using an Improved \Delta VĤB_TO Method along with Color-Magnitude Diagram Constraints, and Their Implications for Broader Issues.* ApJ **775**, 134 (2013)

Vanzella E., Castellano M., Bergamini P., Meneghetti M., Zanella A., Calura F., Caminha G. B., Rosati P., Cupani G., Meštrić U., et al.: *High Star Cluster Formation Efficiency in the Strongly Lensed Sunburst Lyman-Continuum Galaxy at z = 2.37.* A&A **659**, A2 (2022a)

Vanzella E., Castellano M., Bergamini P., Treu T., Mercurio A., Scarlata C., Rosati P., Grillo C., Acebron A., Caminha G. B., et al.: *Early Results from GLASS-JWST. VII. Evidence for Lensed, Gravitationally Bound Protoglobular Clusters at z = 4 in the Hubble Frontier Field A2744.* ApJ **940**, L53 (2022b)

Vanzella E., Claeyssens A., Welch B., Adamo A., Coe D., Diego J. M., Mahler G., Khullar G., Kokorev V., Oguri M., et al.: *JWST/NIRCam Probes Young Star Clusters in the Reionization Era Sunrise Arc.* ApJ **945**, 53 (2023)

Vasiliev E.: *Proper Motions and Dynamics of the Milky Way Globular Cluster System from Gaia DR2.* MNRAS **484**, 2832 (2019)

Vasiliev E. & Baumgardt H.: *Gaia EDR3 View on Galactic Globular Clusters.* MNRAS **505**, 5978 (2021)

Vasiliev E., Belokurov V., & Evans N. W.: *Radialization of Satellite Orbits in Galaxy Mergers.* ApJ **926**, 203 (2022)

Vasiliev E.: *Dear Magellanic Clouds, Welcome Back!* MNRAS **527**, 437 (2024)

Vassiliadis E. & Wood P. R.: *Post–Asymptotic Giant Branch Evolution of Low- to Intermediate-Mass Stars.* ApJS **92**, 125 (1994)

Vaughan S. P., Barone T. M., Croom S. M., Cortese L., D'Eugenio F., Brough S., Colless M., McDermid R. M., van de Sande J., Scott N., et al.: *The SAMI Galaxy Survey: Galaxy Size Can Explain the Offset between Star-Forming and Passive Galaxies in the Mass-Metallicity Relationship.* MNRAS **516**, 2971 (2022)

Vazdekis A., Peletier R. F., Beckman J. E., & Casuso E.: *A New Chemo-evolutionary Population Synthesis Model for Early-Type Galaxies. II. Observations and Results.* ApJS **111**, 203 (1997)

Veljanoski J., Ferguson A. M. N., Mackey A. D., Huxor A. P., Irwin M. J., Côté P., Tanvir N. R., Bernard E. J., Chapman S. C., Ibata R. A., et al.: *Kinematics of Outer Halo Globular Clusters in M31.* ApJ **768**, L33 (2013)

Veljanoski J., Mackey A. D., Ferguson A. M. N., Huxor A. P., Côté P., Irwin M. J., Tanvir N. R., Peñarrubia J., Bernard E. J., Fardal M., et al.: *The Outer Halo Globular Cluster System of M31 - II. Kinematics.* MNRAS **442**, 2929 (2014)

Veljanoski J. & Helmi A.: *The Kinematics of Globular Clusters Systems in the Outer Halos of the Aquarius Simulations.* A&A **592**, A55 (2016)

Ventura P., Dell'Agli F., Schneider R., Di Criscienzo M., Rossi C., La Franca F., Gallerani S., & Valiante R.: *Dust from Asymptotic Giant Branch Stars: Relevant Factors and Modelling Uncertainties.* MNRAS **439**, 977 (2014)

Vera-Casanova A., Gómez F. A., Monachesi A., Gargiulo I., Pallero D., Grand R. J. J., Marinacci F., Pakmor R., Simpson C. M., Frenk C. S., & Morales G.: *Linking the Brightest Stellar Streams with the Accretion History of Milky Way like Galaxies.* MNRAS **514**, 4898 (2022)

Veršič T., Rejkuba M., Arnaboldi M., Gerhard O., Pulsoni C., Valenzuela L. M., Hartke J., Watkins L. L., van de Ven G., & Thater S.: *Shapes of Dark Matter Haloes with Discrete Globular Cluster Dynamics: The Example of NGC 5128 (Centaurus A).* A&A **687**, A80 (2024a)

Veršič T., Thater S., van de Ven G., Watkins L. L., Jethwa P., Leaman R., & Zocchi A.: *Total mass slopes and enclosed mass constrained by globular cluster system dynamics.* A&A **681**, A46 (2024b)

Vincenzo F., Spitoni E., Calura F., Matteucci F., Silva Aguirre V., Miglio A., & Cescutti G.: *The Fall of a Giant. Chemical Evolution of Enceladus, Alias the Gaia Sausage.* MNRAS **487**, L47 (2019)

Vitvitska M., Klypin A. A., Kravtsov A. V., Wechsler R. H., Primack J. R., & Bullock J. S.: *The Origin of Angular Momentum in Dark Matter Halos.* ApJ **581**, 799 (2002)

Vogelsberger M., Genel S., Springel V., Torrey P., Sijacki D., Xu D., Snyder G., Nelson D., & Hernquist L.: *Introducing the Illustris Project: Simulating the Coevolution of Dark and Visible Matter in the Universe.* MNRAS **444**, 1518 (2014)

Vogelsberger M., Marinacci F., Torrey P., & Puchwein E.: *Cosmological Simulations of Galaxy Formation.* Nature **2**, 42 (2020)

von Steiger R. & Zurbuchen T. H.: *Solar Metallicity Derived from in Situ Solar Wind Composition.* ApJ **816**, 13 (2016)

Walder M., Erkal D., Collins M., & Martínez-Delgado D.: *Probing the Dark Matter Halos of External Galaxies with Stellar Streams.* ApJ **994**, 36 (2025)

Walsh J. R., Jacoby G. H., Peletier R. F., & Walton N. A.: *The Light Element Abundance Distribution in NGC 5128 from Planetary Nebulae.* A&A **544**, A70 (2012)

Walsh J. R., Rejkuba M., & Walton N. A.: *An Imaging and Spectroscopic Study of the Planetary Nebulae in NGC 5128 (Centaurus A). Planetary Nebulae Catalogues.* A&A **574**, A109 (2015)

Wang J., Kauffmann G., Overzier R., Catinella B., Schiminovich D., Heckman T. M., Moran S. M., Haynes M. P., Giovanelli R., & Kong X.: *The GALEX Arecibo SDSS Survey - III. Evidence for the inside-out Formation of Galactic Discs.* MNRAS **412**, 1081 (2011)

Wang J., Frenk C. S., & Cooper A. P.: *The Spatial Distribution of Galactic Satellites in the Λ Cold Dark Matter Cosmology.* MNRAS **429**, 1502 (2013)

Wang J., Hammer F., Rejkuba M., Crnojević D., & Yang Y.: *A Recent Major Merger Tale for the Closest Giant Elliptical Galaxy Centaurus A.* MNRAS **498**, 2766 (2020)

Wang S., Chen B., & Ma J.: *Estimating Ages and Metallicities of M31 Star Clusters from LAMOST DR6.* A&A **645**, A115 (2021)

Watkins A. E., Salo H., Laurikainen E., Díaz-García S., Comerón S., Janz J., Su A. H., Buta R., Athanassoula E., Bosma A., et al.: *Stellar Masses, Sizes, and Radial Profiles for 465 Nearby Early-Type Galaxies: An Extension to the Spitzer Survey of Stellar Structure in Galaxies (S4G).* A&A **660**, A69 (2022)

Webb J. J., Reina-Campos M., & Kruijssen J. M. D.: *A Systematic Analysis of Star Cluster Disruption by Tidal Shocks - I. Controlled N-body Simulations and a New Theoretical Model.* MNRAS **486**, 5879 (2019)

Wei L. H., Keto E., & Ho L. C.: *Two Populations of Molecular Clouds in the Antennae Galaxies.* ApJ **750**, 136 (2012)

Weibel A., de Graaff A., Setton D. J., Miller T. B., Oesch P. A., Brammer G., Lagos C. D. P., Whitaker K. E., Williams C. C., Baggen J. F. W., et al.: *RUBIES Reveals a Massive Quiescent Galaxy at $z = 7.3$.* ApJ **983**, 11 (2025)

Welker C., Dubois Y., Pichon C., Devriendt J., & Chisari N. E.: *Caught in the Rhythm. I. How Satellites Settle into a Plane around Their Central Galaxy.* A&A **613**, A4 (2018)

Wetzel A. R., Hopkins P. F., Kim J.-h., Faucher-Giguère C.-A., Kereš D., & Quataert E.: *Reconciling Dwarf Galaxies with ΛCDM Cosmology: Simulating a Realistic Population of Satellites around a Milky Way-mass Galaxy.* ApJ **827**, L23 (2016)

Whitaker K. E., Cutler S. E., Chandar R., Pan R., Setton D. J., Furtak L. J., Bezanson R., Labbe I., Leja J., Suess K. A., et al.: *Discovery of Ancient Globular Cluster Candidates in the Relic, a Quiescent Galaxy at z = 2.5.* ApJ **1001**, 107 (2026)

White S. D. M. & Rees M. J.: *Core Condensation in Heavy Halos: A Two-Stage Theory for Galaxy Formation and Clustering.* MNRAS **183**, 341 (1978)

White S. D. M. & Frenk C. S.: *Galaxy Formation through Hierarchical Clustering.* ApJ **379**, 52 (1991)

Wiersma R. P. C., Schaye J., & Smith B. D.: *The Effect of Photoionization on the Cooling Rates of Enriched, Astrophysical Plasmas.* MNRAS **393**, 99 (2009)

Williams B. F., Dolphin A. E., Dalcanton J. J., Weisz D. R., Bell E. F., Lewis A. R., Rosenfield P., Choi Y., Skillman E., & Monachesi A.: *PHAT. XIX. The Ancient Star Formation History of the M31 Disk.* ApJ **846**, 145 (2017)

Williams M. L., Bekki K., & McKenzie M.: *Star Cluster Formation from Giant Molecular Clouds in the Small Magellanic Cloud about 2 Gyr Ago: Their Origin, Structures, and Kinematics.* MNRAS **512**, 4086 (2022)

Woodley K. A., Harris W. E., Beasley M. A., Peng E. W., Bridges T. J., Forbes D. A., & Harris G. L. H.: *The Kinematics and Dynamics of the Globular Clusters and Planetary Nebulae of NGC 5128.* AJ **134**, 494 (2007)

Woodley K. A., Gómez M., Harris W. E., Geisler D., & Harris G. L. H.: *The Kinematics of the Globular Cluster System of NGC 5128 with a New Large Sample of Radial Velocity Measurements.* AJ **139**, 1871 (2010a)

Woodley K. A., Harris W. E., Puzia T. H., Gómez M., Harris G. L. H., & Geisler D.: *The Ages, Metallicities, and Alpha Element Enhancements of Globular Clusters in the Elliptical NGC 5128: A Homogeneous Spectroscopic Study with Gemini/Gemini Multi-Object Spectrograph.* ApJ **708**, 1335 (2010b)

Worthey G.: *Comprehensive Stellar Population Models and the Disentanglement of Age and Metallicity Effects.* ApJS **95**, 107 (1994)

Xie L., De Lucia G., Hirschmann M., Fontanot F., & Zoldan A.: *H2-Based Star Formation Laws in Hierarchical Models of Galaxy Formation.* MNRAS **469**, 968 (2017)

Xu Y., Kang X., & Libeskind N. I.: *A Rotating Satellite Plane around Milky Way-like Galaxy from the TNG50 Simulation.* ApJ **954**, 128 (2023)

Yao P. Z. & Quataert E.: *The Origin of the Consistent Planetary Nebula Luminosity Function Bright-End Cutoff.* ApJ **957**, 30 (2023)

Ying J. M., Chaboyer B., Boudreaux E. M., Slaughter C., Boylan-Kolchin M., & Weisz D.: *The Absolute Age of M92.* AJ **166**, 18 (2023)

Yoon Y., Kim J.-W., & Ko J.: *The Most Massive Early-type Galaxies Exhibit Tidal Features More Frequently in Lower-density Environments.* ApJ **974**, 299 (2024a)

Yoon Y., Ko J., Chung H., Byun W., & Chun K.: *Shell-Type Tidal Features Are More Frequently Detected in Slowly Rotating Early-type Galaxies than Stream- and Tail-type Features.* ApJ **965**, 158 (2024b)

York D. G., Adelman J., & SDSS Collaboration: *The Sloan Digital Sky Survey: Technical Summary.* AJ **120**, 1579 (2000)

Zahid H. J., Kewley L. J., & Bresolin F.: *The Mass-Metallicity and Luminosity-Metallicity Relations from DEEP2 at z ~ 0.8.* ApJ **730**, 137 (2011)

Zanatta E. J. B., Cortesi A., Chies-Santos A. L., Forbes D. A., Romanowsky A. J., Alabi A. B., Coccato L., Mendes de Oliveira C., Brodie J. P., & Merrifield M.: *Chromodynamical Analysis of Lenticular Galaxies Using Globular Clusters and Planetary Nebulae.* MNRAS **479**, 5124 (2018)

Zaritsky D., Gil de Paz A., & Bouquin A. Y. K.: *An Empirical Connection between the Ultraviolet Color of Early-type Galaxies and the Stellar Initial Mass Function.* ApJ **780**, L1 (2014)

Zel'dovich Ya. B.: *Gravitational Instability: An Approximate Theory for Large Density Perturbations.* A&A **5**, 84 (1970)

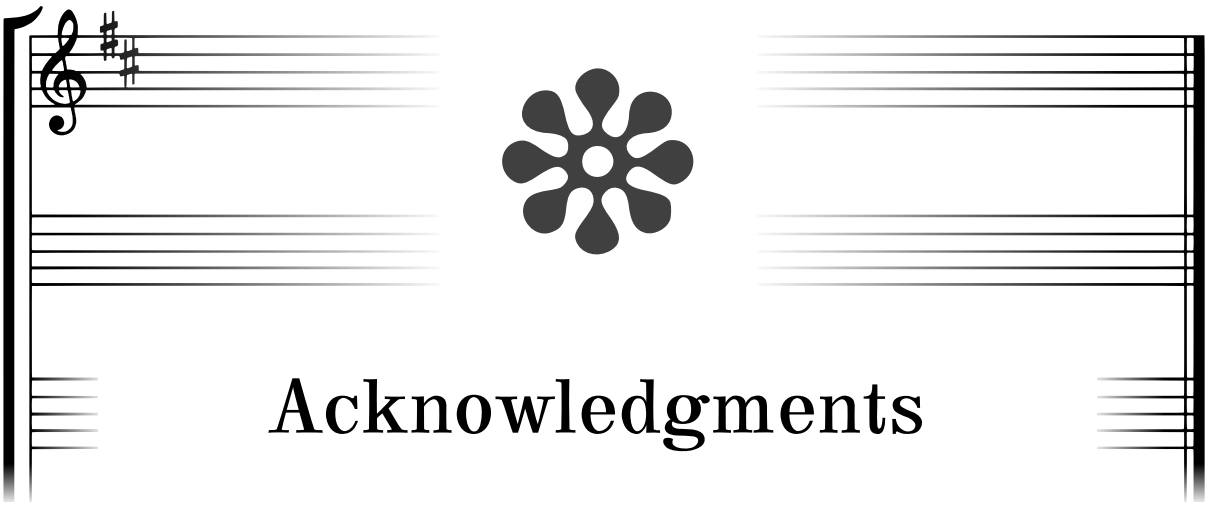
Zemp M., Gnedin O. Y., Gnedin N. Y., & Kravtsov A. V.: *On Determining the Shape of Matter Distributions.* ApJS **197**, 30 (2011)

Zhang H.-X., Peng E. W., Côté P., Liu C., Ferrarese L., Cuillandre J.-C., Caldwell N., Gwyn S. D. J., Jordán A., Lançon A., et al.: *The Next Generation Virgo Cluster Survey. VI. The Kinematics of Ultra-compact Dwarfs and Globular Clusters in M87.* ApJ **802**, 30 (2015)

Zhu L., Long R. J., Mao S., Peng E. W., Liu C., Caldwell N., Li B., Blakeslee J. P., Côté P., Cuillandre J.-C., et al.: *The Next Generation Virgo Cluster Survey. V. Modeling the Dynamics of M87 with the Made-to-Measure Method.* ApJ **792**, 59 (2014)

Zibetti S., Gallazzi A. R., Hirschmann M., Consolandi G., Falcón-Barroso J., van de Ven G., & Lyubenova M.: *Insights into Formation Scenarios of Massive Early-Type Galaxies from Spatially Resolved Stellar Population Analysis in CALIFA.* MNRAS **491**, 3562 (2020)

Zinn R.: *The Globular Cluster System of the Galaxy. IV. The Halo and Disk Subsystems.* ApJ **293**, 424 (1985)



Acknowledgments

This thesis marks the end of one of the most exciting and rewarding phases of my life. During these years, I have grown both scientifically and personally through many adventures, ranging from working on cutting-edge research and building international collaborations to traveling the world and developing skills that will remain valuable far beyond academia. Yet this journey was never one I took alone. These past years would not have been nearly as fulfilling without the people around me who brightened every step along the way. I would like to use these final pages to express my gratitude to them.

This thesis would not have been the same without my supervisor, Rhea-Silvia Remus. Your support from the very beginning, in designing a tailor-made project for my PhD thesis, set the direction for the years that followed. Throughout this journey, you have believed in me, invested time and energy to help me realize my full potential, and encouraged me to try things out and become independent as both a researcher and person. Your approach to science with joyful curiosity and deep physical understanding has been a true inspiration, showing me the kind of scientist I aspire to become. Thank you for everything.

I also want to thank Klaus Dolag for accompanying me throughout my PhD thesis. Your advice on so many topics, from scientific and technical matters to the finer details of dealing with journals and other aspects of scientific work, has been invaluable to me. Thank you for welcoming me into your group, investing in me, and supporting me in all my endeavors over the last few years.

I furthermore want to thank Andreas Burkert for many stimulating discussions, your never-ending enthusiasm for my projects and progress, and for providing an enriching environment

in the CAST[1] group. It was through you that I was able to start my journey in astrophysical research back during my undergraduate studies. Thank you for opening those doors for me.

My journey in physics started some years before that, however, and I want to say a special thank you to Lucas Kimmig. I met you on day one of our physics studies, and we have been able to learn and grow side by side ever since. It is one of the biggest pleasures to discuss science with you, and I have always been amazed at your incredible skill of connecting diverse topics intuitively and asking insightful questions on any matter you come across. Thank you for the journey together.

Everyday life at the institute would not have been the same without the DRAGONS[2] team. The team has grown over time, and I want to thank Rhea-Silvia Remus, Lucas Kimmig, Silvio Fortuné, Benjamin Seidel, Anna Ivleva, Johannes Stoiber, Anita Schiller, Alexandra Konrad, and Tadziu Hoffmann, for all the enriching moments of discussing science and working together as a group on joint projects. The group has taught me that scientific work flourishes in a collaborative environment. Thank you for the times filled with joy and laughter, and for looking out for one another.

Thank you also to Tadziu Hoffmann for the amazing technical support in all aspects of hardware and software. You always seem to find a solution to any problem, even in the most creative ways. Thank you for providing your help so generously and selflessly.

Having spent significant amounts of time abroad, I also want to particularly thank Duncan Forbes, Marcelo Miller Bertolami, and Jesse van de Sande for hosting me during my visits and for the support that has opened so many doors for me. I am also grateful to Ana Ennis, Jonah Gannon, Bill Harris, Antonela Monachesi, Danail Obreschkow, Florent Renaud, Martin Roth, Alison Sills, Azlizan Soemitro, Ulrich Steinwandel, and Glenn van de Ven for the kind hospitality and allowing me to engage with the local scientific communities through talks and discussions.

I want to thank Rhea-Silvia Remus, Lucas Kimmig, Johanna Hartke, and Benjamin Seidel for reading parts of this thesis and providing valuable feedback on the content. I also thank Tadziu Hoffmann for helping to polish the final graphics and prepare the document for printing. This thesis would furthermore not have been possible without the support of the German Academic Scholarship Foundation (Studienstiftung des deutschen Volkes) and the Marianne-Plehn-Program of the Elite Network of Bavaria, which together enabled me to pursue the project of my choosing.

And finally, I am incredibly grateful to my close friends and family, who have always supported and cared for me in all my endeavors. I know I can count on you in all circumstances, which is one of the greatest gifts one could wish for. Thank you.

[1] Computational ASTrophysics

[2] Dynamics, enviRonment, and Assembly of Galaxies in Observations and Numerical Simulations (astrophysicists like acronyms very much)